***Darijani M, 2018, Investigating modeling and inversion techniques for overburden stripping for uranium exploration in the Athabasca basin, Canada, MSc Thesis, Memorial U, NL, 322 p.***

NSERC-CMIC Mineral Exploration Footprints Project Contribution 144.

# Investigating Modelling and Inversion Techniques for Overburden Stripping for Uranium Exploration in the Athabasca Basin, Canada

by

© Mehrdad Darijani

A thesis submitted to the School of Graduate Studies in partial fulfilment of the requirements for the degree of Doctor of Philosophy

**Department of Earth Sciences**

**Memorial University of Newfoundland**

August, 2018

St. John's Newfoundland and Labrador

# Abstract

This thesis investigates ways to remove the overburden contribution to geophysical data (via modelling and inversion) so that deeper targets that are what's of interest can be detected and delineated. This is being done in the context of exploration for uranium in the Athabasca Basin, Canada. For this purpose, the variable thickness of overburden is tried to find using new, modern, state-of-the-art modelling and (constrained and joint) inversion of geophysical methods such as seismic refraction, gravity, magnetic and electromagnetic methods. This research project is a part of the CMIC Footprints project (www.cmic-footprints.ca), and is a very challenging exploration problem and very useful of successful for the most places in Canada, not just the Athabasca Basin and uranium exploration.

The Athabasca Basin is a Proterozoic sedimentary basin which is located in northwest Saskatchewan and northeast Alberta, Canada, which supplies around 20% of the world's uranium. The uranium deposits are surrounded by alteration zones at the unconformity between Proterozoic sedimentary rocks and the Archean and Aphebian metamorphic basement. The sedimentary rocks are covered by Quaternary glacial deposits. In the eastern Athabasca Basin, McArthur River mine has the world's largest high-grade uranium deposits in a depth of about 500 m where the faults intersect the unconformity.

Because of the small size of uranium deposits and their location at depth, geophysical methods look for structures which host the uranium deposits, for example, electromagnetic (EM) methods can locate graphitic faults which is the primary target. The gravity method

can potentially detect the alteration zones. In this exploration, seismic can image the boundary between layers such as unconformity and basement faults. And, magnetic data can delineate basement structures. The benefit of using multiple data-types can provide complementary information (e.g. the seismic and gravity). Also, all these methods can be used for the overburden stripping if there is a good physical property contrast between the overburden and the sandstone. In the Athabasca Basin, overburden can be conductive while density and seismic velocity of the overburden is less than sandstone. Some rocks in unconsolidated glacial deposits have magnetic susceptibilities (e.g. granite), whereas sandstone is non-magnetic.

Based on these features, the synthetic modelling and inversion of the geophysical data are performed for (mainly) the overburden stripping as well as reconstructing the geological structure in depths. Magnetic, gravity, first-arrival seismic traveltimes and time- and frequency-domain electromagnetic data are synthetized using forward modelling of 2D and 3D models. For inversion methods, independent, joint and constrained methods are applied for 1D, 2D and 3D cases. Acceptable results can be obtained from the independent inversion of seismic data and EM data, but good results can be achieved from magnetic and gravity data if constrained and joint (or both of them) inversions are used. Also, inversions give reasonable results if there are good physical properties contrast. Among all tested geophysical methods, the seismic refraction and frequency domain electromagnetic methods give better results for the overburden stripping while constrained joint inversion of gravity and magnetic data can image the near surface and deep structures well. In this research, real data are inverted and investigated for the most of the geophysical methods.

# Acknowledgements

My greatest appreciation goes to my supervisor, Dr. Colin G. Farquharson, for his patience, invaluable advices and continuous support and help throughout this project. And, special thanks go to Dr. Peter Lelièvre for providing the software as well as guidance. I would also like to thank the members of my supervisory committee Dr. Charles Hurich and Dr. Alison Leitch.

I am also grateful for the financial support provided by the Footprints Project and a MUN School of Graduate Studies Fellowship. The Footprints Project is by the Canadian Mining Innovation Council (CMIC www.cmic-footprints.ca), with funding from lots of industry sponsors and Natural Sciences and Engineering Research Council of Canada (NSERC). This is NSERC-CMIC-Footprints Publication #144. I would also like to thank Dr. Kevin Ansdell (uranium-subproject leader), Dr. Kurt Kyser (uranium-subproject co-leader), Ken Wasyliuk (uranium-subproject research associate) as well as Garnet Wood, Clare O'Dowd and Gerard Zaluski of Cameco Corporation and Robert Hearst (now at Quantec Geoscience) and David Quirt of Orano Canada Inc. (formerly AREVA Resources Canada) for their helpful review and comments on my quarterly reports of the CMIC-Footprints Project and this thesis.

Last but certainly not least, I address my deepest gratitude to my family to whom I owe a great deal; to my late father, Mohammad Darijani, who showed me that the key to life is knowledge; to my mother, Zahra Jazinizadeh, who has been a constant source of support and encouragement, and has made an untold number of sacrifices for the family; to my sister, Iren, and my brother, Meghdad, for their spiritual supports.

# Table of Contents

# List of Tables

# List of Figures

# List of Appendices

# Chapter 1

# Introduction

Most parts of Canada are covered by the overburden especially glacial deposits (Fulton, 1995). The erosion and deposition due to the glacial process have provided a variable thickness in the overburden. These variations can be problematic in a geophysical interpretation. For example, the research problem in this project is due to the thickness of glacial deposits, which varies greatly in the eastern Athabasca Basin (Schreiner, 1984a; Campbell, 2007). Because glacial deposits are generally less dense than bedrock, local thickening of these deposits causes an anomalously low gravity response (Wood and Thomas, 2002). Such a low response can mimic or mask the gravity low associated with the hydrothermal alteration at depth that is an intrinsic component of the footprint of uranium deposits. This research as a part of the larger Canadian Mining Innovation Council (CMIC; www.cmic-footprints.ca) Footprints project has been done in the context of uranium exploration in the Athabasca Basin, but it has implications for exploration for many different resource types.

Uranium is a radioactive element, which was discovered in 1789 by Martin Heinrich Klaproth and named after the planet Uranus. Uranium has an abundance of 0.91 ppm (parts per million) in the Earth's crust and 0.003 ppm in the ocean (Tuncer et al., 2006a). One of

the primary mineral ores of uranium, containing 50–80 percent of that element, is pitchblende. Uranium is mostly used as a fuel in nuclear reactors. It is mostly found in unconformity deposits as Uraninite (more than one third of the uranium resource) where grades can be 3-100 times higher than the other type of the deposits (Fayek and Kyser, 1997; Gandhi, 1989; Kyser et al., 2000; Jefferson et al., 2007). Uraninite (formerly pitchblende) has mostly a chemical composition of $UO_2$, but due to oxidation has typically variable proportions of $U_3O_8$ (www.wikipedia.com). Note that Uraninite is the term usually reserved for macrocrystalline (well crystallized) uranium oxide close to the ideal formula of $UO_2$. The (old) term pitchblende is usually used to refer to microcrystalline to crypto-crystalline or amorphous uranium oxide, often with botryoidal, massive, sooty, or earthy textures which is usually more oxidized (CMIC-Footprints project).

The Athabasca Basin of Canada hosts this type of uranium deposit (Jefferson et al., 2003; Ramaekers, 1990; Ramaekers and Catuneanu, 2004). In the Athabasca Basin, McArthur River is the world's largest high-grade uranium deposit (16.5% $U_3O_8$ after allowance for dilution). Also, McArthur River is the world's largest in terms of annual production (13% of world mine production in 2012; adapted from www.world-nuclear.org). This mine is owned by Cameco (70%) and Orano Canada Inc. (formerly AREVA Resources Canada; 30%), with Cameco being the mine operator. The price of uranium was around US$30 per pound in early 2017 (adapted from www.cameco.com).

Exploration for uranium in the Athabasca Basin began in the mid-1960's, with companies looking for sandstone-hosted and/or paleochannel-type uranium deposits (Gandhi, 1995). At the beginning, the focus was on the shallower parts of the basin, but recently, it has moved to deeper levels (Tuncer et al., 2006a; O'Dowd et al., 2006). These

deeper deposits, which are associated with the unconformity at the base of the Basin, have traditionally been explored using EM methods based on a graphitic conductor model (Irvine and Witherly, 2006; Tuncer et al., 2006a; Farquharson and Craven, 2009). Seismic methods have begun to be applied for detecting the location of the unconformity and post-Athabasca fault zones (Juhojuotti et al., 2012; Hajnal et al., 2007; White et al., 2007). Seismic data can provide a structural framework from the near surface to a few kilometres below the unconformity (Györfi et al., 2007), calibrated with the aid of borehole geophysics (Mwenifumbo et al., 2004). Airborne magnetic surveys can provide maps of basement geology based on the magnetic gradients between Archean gneiss and the Wollaston Supergroup (Pilkington, 1989; Card, 2006; Thomas and McHardy, 2007). Ground and airborne gravity can, it is hoped, detect alteration zones as negative gravity anomalies (desilicified zones) or positive anomalies (silicified zones) that surround the small uranium deposits (Wood and Thomas, 2002; Thomas and Wood, 2007; McGill et al., 1993; Matthews et al., 1997; Thomas et al., 2002).

The focus of this research is on a corridor between the McArthur River and Millennium areas in the Athabasca Basin, which has a total size of 50×20 km. NE-SW structures in this corridor are associated with the transition between the Wollaston and the Mudjatik domains in the underlying Archean and Paleoproterozoic basement rocks (Yeo and Delaney, 2007; Thomas, 1983; Annesley et al., 2005). The sediments of the Athabasca Basin rest unconformably on these basement rocks and under the glacial sediments (Bernier, 2004; Ramaekers et al., 2007; Hoeve and Quirt, 1984). Unconformity deposits in this corridor are generally found where a fault intersects the unconformity (Figure 1.1; Hoeve and Quirt, 1987; Ramaekers, 1990).

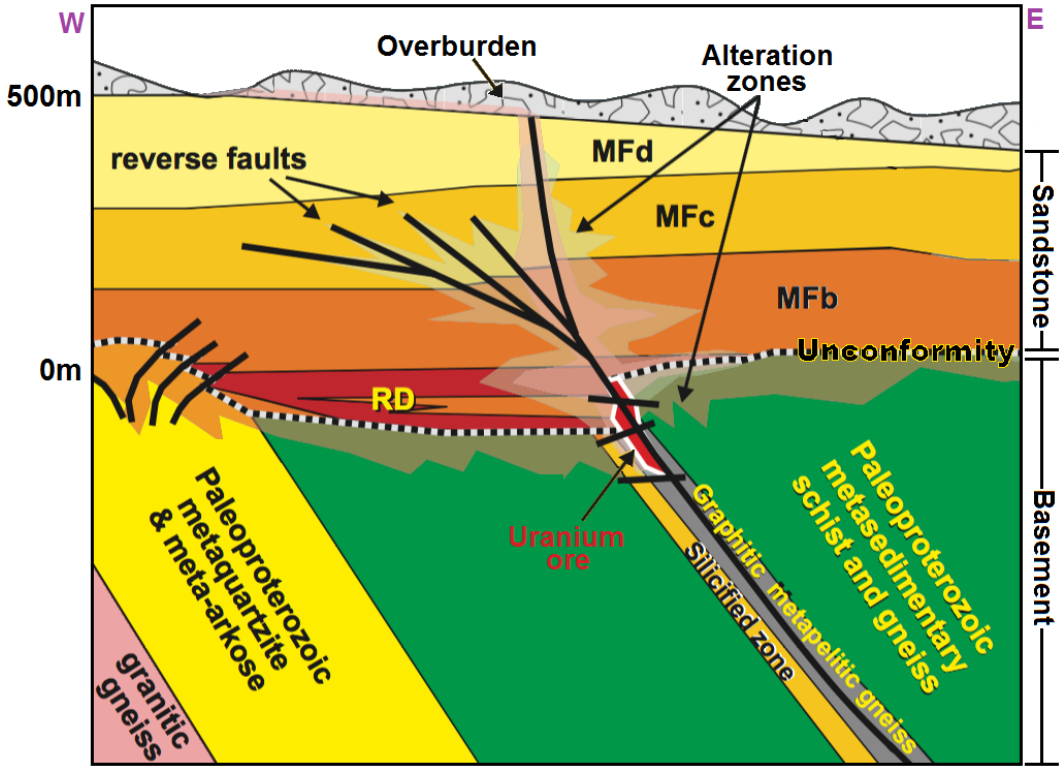


Figure 1.1: Generic model of an unconformity type uranium deposit (adapted from Jefferson et al., 2007). The Athabasca Basin consists of three major strata from top to bottom: overburden (glacial deposits), sandstone (Manitou Falls Formations MFd, MFc, MFb and RD), and metamorphic basement.

The goal is that the subtle geophysical responses of uranium deposit alteration systems at depth can be confused with or masked by the geophysical response of the overburden. By more accurately modeling the response of the overburden, it can be more effectively separated (or stripped) from the geophysical signatures of the deposit. Therefore, in this project we investigate and assess methods for "stripping" off the effect of the glacial cover from geophysical data, primarily from gravity and magnetic data, using modelling and the inversion methods. For the inversion, constrained and joint methods will be investigated over the McArthur-Millennium site. 2D and 3D inversions of synthetized data will be

performed on the geophysical data-set constrained by sediment cover thickness derived from geophysical inversions and physical properties of Quaternary sediments in order to reconstruct a model incorporating both sediment cover and mineralization from geophysical methods. And finally, best inversion methods obtained from synthetic modelling will be applied on the real data.

These will be applied on geophysical methods such as gravity, magnetic, electromagnetic and seismic refraction methods in different chapters of this thesis. First chapters will introduce the geology and physical properties of the rocks of the study area as well as geophysical methods and the theory of forward modelling and inversion methods. Synthetic forward modelling of gravity data (free-air and Bouguer anomalies) will be investigated in the following chapter. Also, the spectral analysis and filtering methods will be performed on the gravity data in a different chapter. For the seismic refraction method, a chapter will show the results related to the 2D modelling and inversion as well as the joint inversion with the gravity method. In the next chapter, in addition to the 3D forward modelling of gravity and magnetic data, the independent, joint and constrained inversions will be done to model the geological structures. In the last chapter, for electromagnetic methods, both frequency- and time-domain methods will be assessed using 3D forward modelling and 1D inversion codes.

# Chapter 2

# Geological Attributes and Physical Properties in the McArthur-Millennium Region

## 2.1 Introduction

The Athabasca Basin is a Proterozoic sedimentary basin which is located in northwest Saskatchewan and northeast Alberta (Figure 2.1; Jefferson et al., 2007). In the Athabasca Basin, the uranium deposits are located at the unconformity between Proterozoic sedimentary rocks and the Archean and Paleoproterozoic metamorphic basement where the Athabasca Group unconformably overlies the western Wollaston and Wollaston–Mudjatik transition basement domains. The sedimentary rocks are unmetamorphosed strata which are covered by Quaternary glacial deposits. Sedimentation began in the Athabasca Basin at about 1740-1730 Ma.

The basement is tectonically interleaved Paleoproterozoic metasedimentary and Archean to Proterozoic granitoid rocks which were last metamorphosed at 1800 Ma by the Trans Hudson Orogen (Jefferson et al., 2007; Alexandre et al., 2007).

Uranium deposits in the Athabasca Basin are related to hydrothermal ore-generating events at around 1600 and 1350 Ma which were overprinted by further alteration and uranium remobilization events at around 1176 Ma, 900 Ma and 300 Ma (Fayek et al., 2002a).

Geological structures have different physical properties. Their rock properties present a quantitative link between geology and geophysics. Physical properties depend on the mineralogy, composition of the rocks, porosity, fractures, material in pores and fractures, geometry of minerals and fractures, and etc (Nur et al., 1998; Schön, 1996). Geophysical data are responsive to variations in physical rock properties in the earth. Resistivity, density and seismic velocity depend on the porosity and the nature of the pore fluid (Mavko, 2009; Schön, 2011). Density and seismic velocity of strata in the Athabasca Basin mostly increase with increasing depth. Resistivity and magnetic susceptibility can be variable for any geological structure. Physical property measurements including resistivity, density, magnetic susceptibility, seismic velocity and porosity are made on both drill-hole and surface samples (Mwenifumbo et al., 2004).

In this chapter, topics such as the geology and the stratigraphy as well as the quaternary geology (e.g. nature of deposits and stratigraphy) of the McArthur-Millennium region will be discussed. In addition to the investigation of the relationship between uranium deposition and geological attributes, the main physical properties of region such as density, magnetic susceptibility, conductivity and seismic velocity will be assessed.

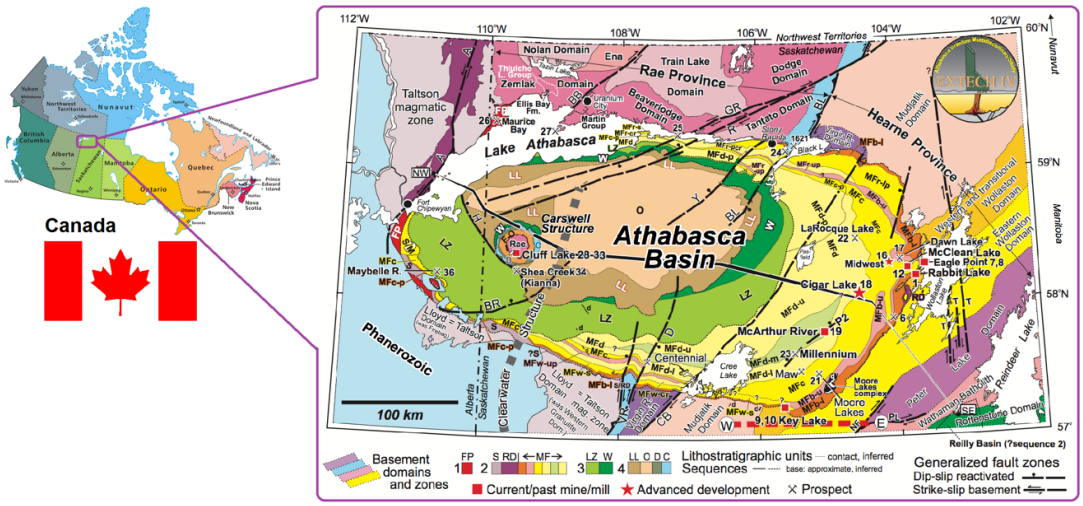


Figure 2.1: Geology of the Athabasca Basin and uranium deposits (adapted from Jefferson et al., 2007).

## 2.2 Geology and stratigraphy of the McArthur-Millennium corridor

In the McArthur-Millennium area, the near surface structure is overburden comprising glacial sediments with a variable thickness (from 0 to more than 100 m; Figures 2.2 and 2.3). The underlying layer (Figure 1.1) is sandstone of late Paleo- to Meso-Proterozoic age (Rainbird et al., 2007). In the McArthur area, from top to bottom, sandstone consists of the D, C and B units of Manitou Falls formation as well as the Read Formation (formerly MFa). Manitou Falls D consists of fine grained, well sorted sandstone. Manitou Falls C comprises quartzarenite with minor quartz pebbly beds, mudstone interbeds, clay intraclasts and conglomerate interbeds. Manitou Falls D contains the greater abundance of clay intraclasts compared to Manitou Falls C. The Manitou Falls B is distinguished by conglomeratic pebble beds (Ramaekers, 1981; McGill et al., 1993; Jefferson et al., 2007). Read Formation (RD) consists of discontinuous basal conglomerate, intercalated coarse sandstone,

conglomerate and red mudstone (McMullan et al., 1987; Mwenifumbo et al., 2004).

Two alteration patterns are observed in the Athabasca (Manitou Falls Formation) sandstones: 1) desilicification and illitization, and 2) silicification, kaolinization and dravitization. Desilicification and silicification mostly occured in the northeast portion and the south portion of the Athabasca Basin, respectively. Strong silicification is quite unique to the McArthur River deposit and it is very restricted to the deposit itself. Therefore, the silicification, while mostly in the Read formation, is very limited laterally – i.e. especially at the scale of the greater McArthur-Millennium study area (McGill et al., 1993; Matthews et al., 1997). During silicification, silica is deposited by hydrothermal fluids and fills pore spaces and replaces the other minerals. This increases the resistivity and density of the rocks. In contrast, the bleaching (desilicification) is caused by hydrothermal fluid flow that removes the coloured minerals from the sandstone, and decreases the density of the rocks. Altered clay minerals such as illite, dravite, kaolinite, chlorite and dickite can be seen in the sediments as well as upper part of the basement. They show a low electrical resistivity.

In the CMIC-Footprints project, the 3D shells of the distribution of altered clays minerals are modelled by researchers (called SWIR; see Section 3.4). Illite is the dominant alteration mineral in the area which can extend laterally to more than 10 kilometres and cover the uranium mineralization. Mineralization is mostly under the zones of silicification and dravitization. In the case of alteration associated with basement-hosted deposits, the uranium mineralization is surrounded by an outer illitic halo as well as an inner illitic-chloritic halo. Silicification is mostly located and laterally extended in the RD formation while disilicification surrounds the reverse faults in the sandstone like a thick cover (see

Figure 1.1; Fayek and Kyser, 1997; Alexandre et al., 2007).

Since faults and fracture zones permit the flow of fluids that contain uranium, uranium deposits are mostly formed where the unconformity intersects underlying fold and thrust belts (Jefferson et al., 2007). In these zones, graphite rich faults often underlie uranium deposits. The low electrical resistivity of graphite acts as a good target for electromagnetic exploration methods. Also, the hydrothermal circulation causes alteration of the host rocks including changing their densities which make them a possible target for the gravity exploration method.

At the McArthur River mine, the deposit formed where the reverse P2 fault intersects the basement with an offset up to 80 metres (see Figures 2.2 and 2.3). The age of the faulting is around 1.8 Ga, and the age of first uranium mineralization is around 1.6 Ga (Jefferson et al., 2007). The basement below the unconformity includes two different types of metasedimentary rocks: pelite (making up the hanging-wall rocks of the fault) and quartzite (the footwall rocks; McGill et al., 1993). Alternating units of quartzite and granitic rocks as well as metamorphosed graphitic pelitic rocks are the main structures in the basement. Most deposits are located near metapelitic rocks. Since the silicification within the sandstone at McArthur River is located above units of basement quartzite, quartzite units are also important for gravity exploration (Marlatt et al., 1992).

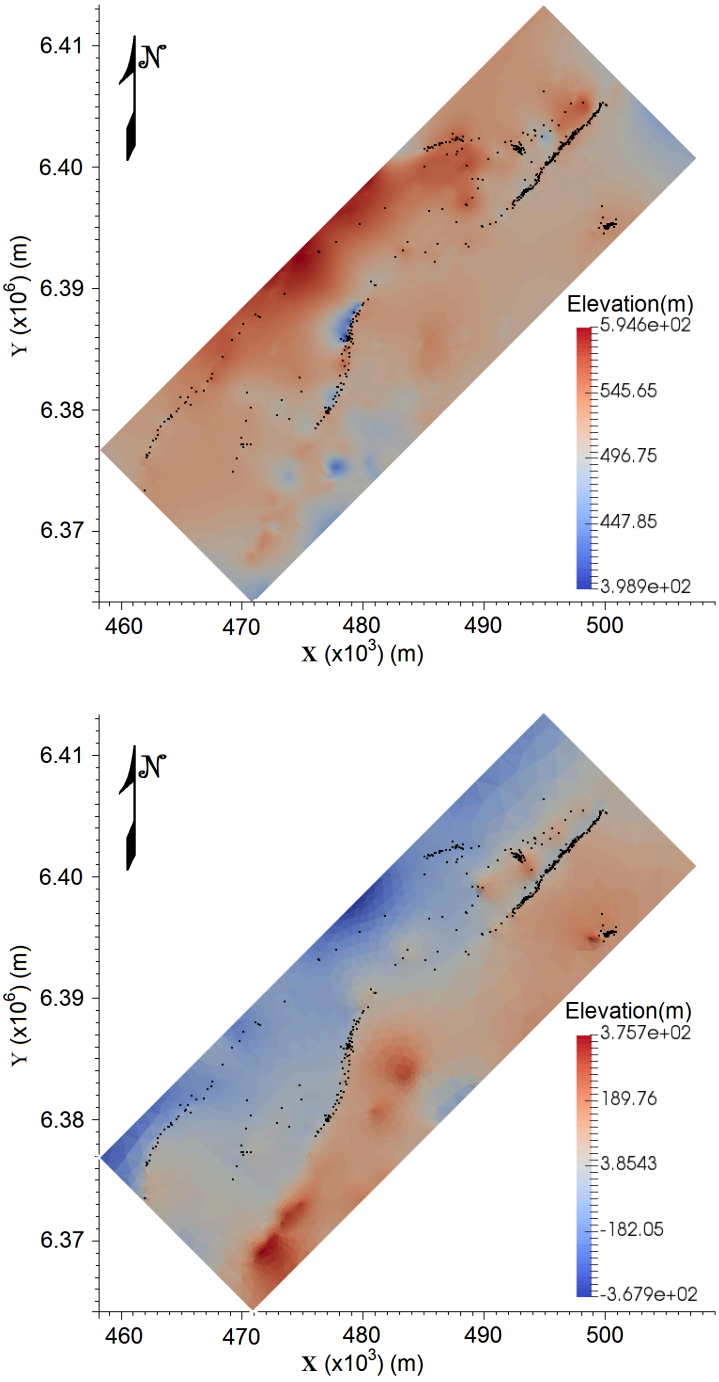


Figure 2.2: Topography of the base of overburden (top) and unconformity (bottom) in the McArthur-Millennium corridor (20×50km) made using drill-hole data (adapted from CMIC-Footprints project; made by Mohamed Gouiza and Mira Geoscience Ltd.). Some of the drill-holes in the area are shown by black dots.

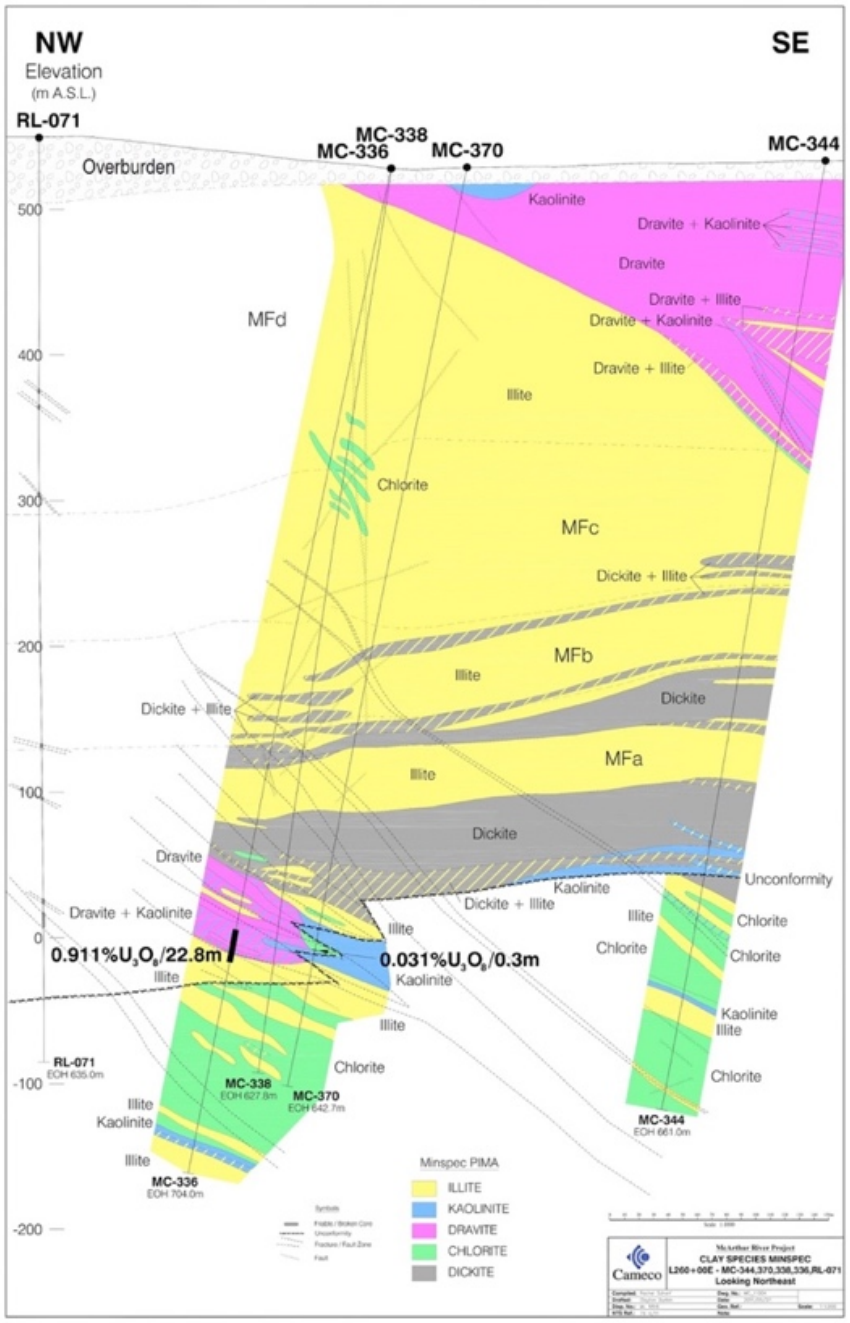


Figure 2.3: Geological cross-section made using drill-hole data in the McArthur area. It shows the structure of the altered clay in the sandstone and top of the basement (adapted from CMIC-Footprints project). Note that these are the clays identified using SWIR, however the rocks are all completely dominated by quartz in the sandstones.

## 2.3 Uranium deposition and geological attributes

Uranium deposits in the Athabasca Basin can be categorized into different types (Jefferson et al., 2007). One of the categorizations, which is based on the location of the uranium deposits, has two types (Figure 2.4). The first type is the fracture-controlled basement ore deposit which occurs below the unconformity in dipping shear zones. The second type is the clay-bounded ore deposit which occurs along and/or above the unconformity. Also, some deposits are considered as a combination of both types.

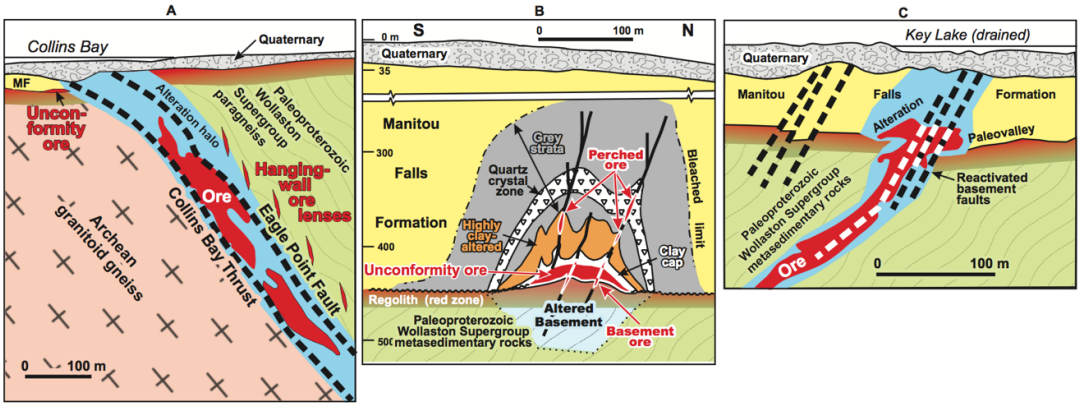


Figure 2.4: A) Basement hosted uranium deposit, B) typical unconformity ore and C) both basement hosted and unconformity type deposit (Tuncer et all., 2006a; Jefferson et al., 2007).

Unconformity-associated uranium deposits can also be categorized, based on the metals which are present with uranium, into monometallic and polymetallic deposits (Figure 2.5; Ruzicka, 1996). Monometallic deposits, which are fracture controlled basement hosted deposits, contain only traces of metals other than uranium and copper. Polymetallic deposits, which are mostly clay bounded, contain sulphide and arsenide minerals with significant amounts of Ni, Co, Cu, Pb, Zn and Mo (Jefferson et al., 2007). Unconformity

deposits can be either polymetallic or simple in mineralogy.

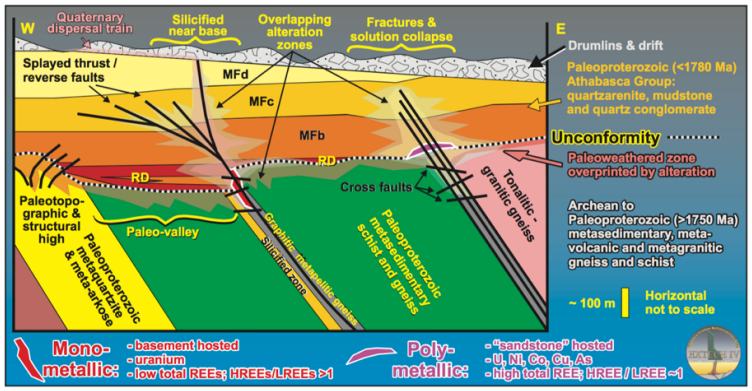


Figure 2.5: Monometallic and polymetallic type uranium deposits (Jefferson et al., 2007).

Another categorization comes from the fluid flow directions as well as the type of alteration. If the fluid flows from the basement to the sandstones, this will generate an egress type uranium deposit (Figure 2.6). In contrast, the ingress type deposit is one in which the fluid flows from sandstones to the basement. Weak alteration occurs in ingress type deposits. Because of the complexity of hydrothermal systems, some deposits such as McArthur River have both ingress and egress types (Jefferson et al., 2007).

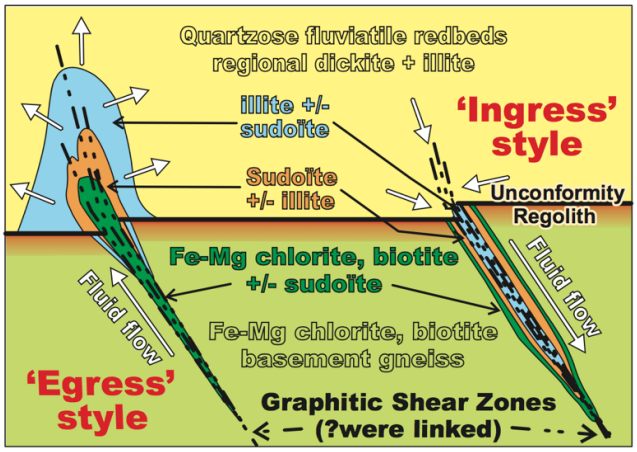


Figure 2.6: Ingress and egress type uranium deposits (Jefferson et al., 2007).

## 2.4 Quaternary geology

### 2.4.1 Glaciers

Glaciers are accumulations of large quantities of ice, air, water, and sediments (rock debris) moving downhill under the pull of gravity very slowly, from tens of metres to thousands of metres per year (from 0.01-0.1 m per day for large Continental glaciers to 0.1–2 m per day for Alpine glaciers). They cover one-tenth of the Earth's surface (Jain, 2014).

There are several types of glaciers that fall into two main categories. One category is "continental glaciers" which are thick masses of ice that cover vast areas in which the ice can be hundreds to thousands of metres thick. Continental glaciers, based on their size, are subdivided into two main types: ice caps (smaller than 50,000 $km^2$) and ice sheets (bigger than 50,000 $km^2$). The other category is "Alpine glacier" which is much smaller than continental glaciers, and originates in a mountain range. Alpine glaciers produce some of the most remarkable natural features such as U-shaped valleys, hanging valleys, arêtes, cirques, horns, tarns, and roches moutonnée. Rocks are incorporated into a glacier by "Abrasion" and "Plucking" (Figure 2.7). Abrasion produces silt-sized (0.002–0.0625 mm) sediments when debris-rich ice slides over the bedrock and abrades it. Plucking removes blocks of bedrock and incorporates them into the glacier when ice flows into or refreezes in fractures in the bedrock.

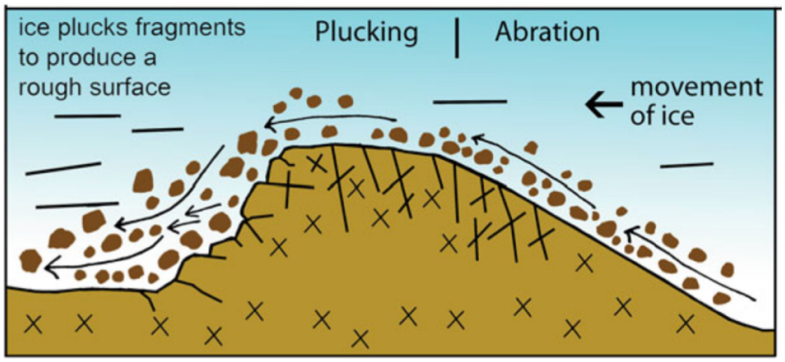


Figure 2.7: Abrasion, plucking and the movement of ice (Jain, 2014).

The term "glacial drift" applies to all sediments which have glacial origin. There are two types of glacial drift: till (glacial deposits) and stratified drift (glaciofluvial deposits). Till deposits include till, erratics, moraines and drumlins. Till is an unsorted and unstratified glacial drift, deposited directly from ice. The grain size in till ranges from clay to boulder. The finer sediments (rock flour) and the larger pieces of sediment (boulders) in till come from abrasion and plucking, respectively. Erratics are large boulders transported by glaciers and left behind when the ice melts. Moraines are concentrated deposits of till, and there are five different types of them: terminal moraine, ground moraines, recessional moraines, lateral moraines, and medial moraine. Drumlins are hills made of till and some partly of bedrock which are molded by the flow of the continental ice sheet. They are usually about 1–2 km long and about 15– 50 m high (Figure 2.8).

Stratified drift deposits are sorted and layered sediments deposited by glacial melt-water such as kettles, kames, eskers, outwash and loess (Figure 2.8). Depressions formed underneath the glacier and filled by water generate small lakes which are called kettles. Kames are low, cone shaped, steep-sided hills. They are stratified sediments by streams on top of the glacier which are deposited when the glacier melts. Eskers are long sinuous ridges

of sediment, with a height of a few to several tens of metres, deposited by streams that flow under a glacier. Outwash deposits are made by the meltwater flowing away from the ice. Loess is silt-rich rock flour which is picked up and distributed by wind across wide areas.

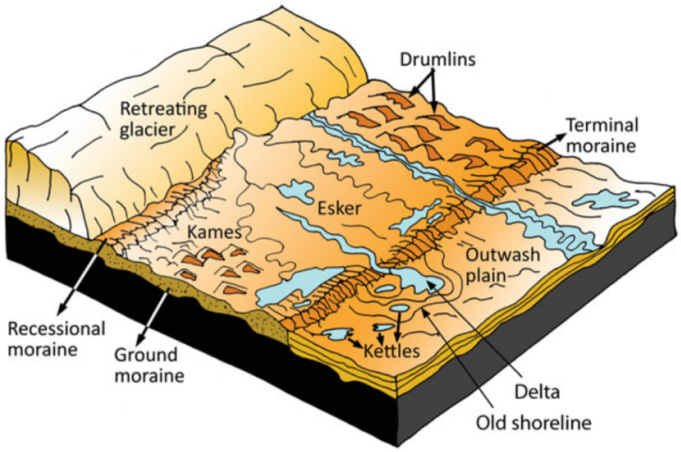


Figure 2.8: Various landforms produced by continental glaciers (Jain, 2014).

### 2.4.2 Quaternary geology of the eastern Athabasca Basin

The overburden of Athabasca Basin is a product of the advance and retreat of the last ice sheet belonging to Late Wisconsinan. Deglaciation of the eastern Athabasca Basin began in the southwest around 9000–8700 BP (Before Present), and it was completely ice-free by 8200 BP. The thickness of glacial deposits is variable and ranges from 0 up to 100 m. The area is mostly covered by drumlin, hummocky moraine, esker complexes, and ground moraine. The bedrock surface topography is undulating and variable due to glacial erosion (Campbell, 2007; Campbell and Flory, 1999). Ice-flow direction in the eastern basin has been determined southwestward (208°–245°) by glacially streamlined features such as drumlins and flutings.

### 2.4.2.1 Nature of deposits

Till deposits, which form ground and streamlined moraines, are dominant surface materials. Other surficial deposits include glaciofluvial and glaciolacustrine sediments, block fields, and eolian and organic deposits. Drumlins and streamlined features are the most prevalent landforms in the Athabasca Basin (Figure 2.9; Sproule, 1939). Figure 2.10 shows the topography map which is dominated by glacial features. Northern and western parts of the eastern Athabasca Basin are covered by outwash plains with sporadic drumlins and esker systems. These geological features are described as follows:

Organic deposits: Organic deposits with a thickness of less than 3m, consisting of bogs, are found as surface deposits in depressions close to lakes and rivers.

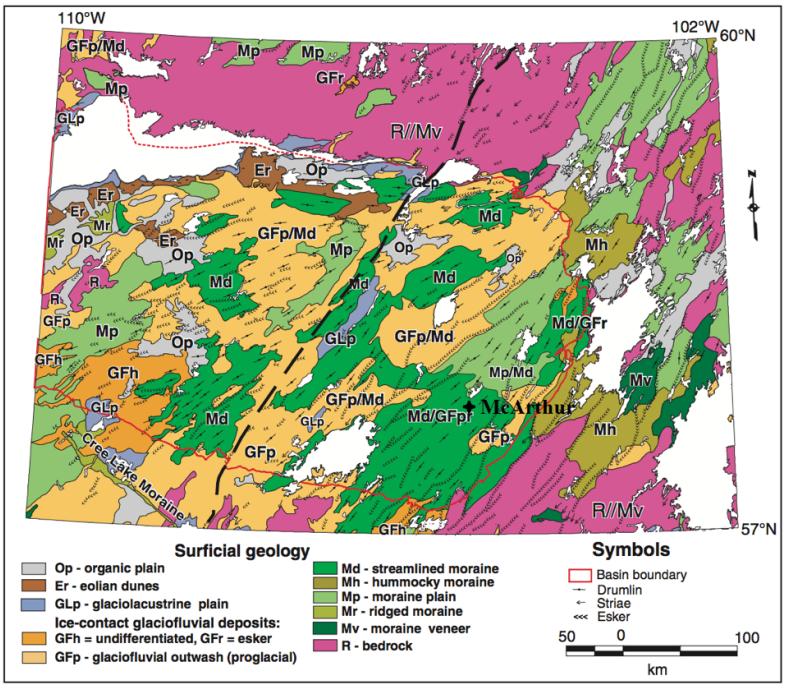


Figure 2.9: Regional surficial geology map of the Athabasca Basin and northern Saskatchewan (modified from 1:1000000 scale maps; Simpson, 1997; Schreiner, 1984a).

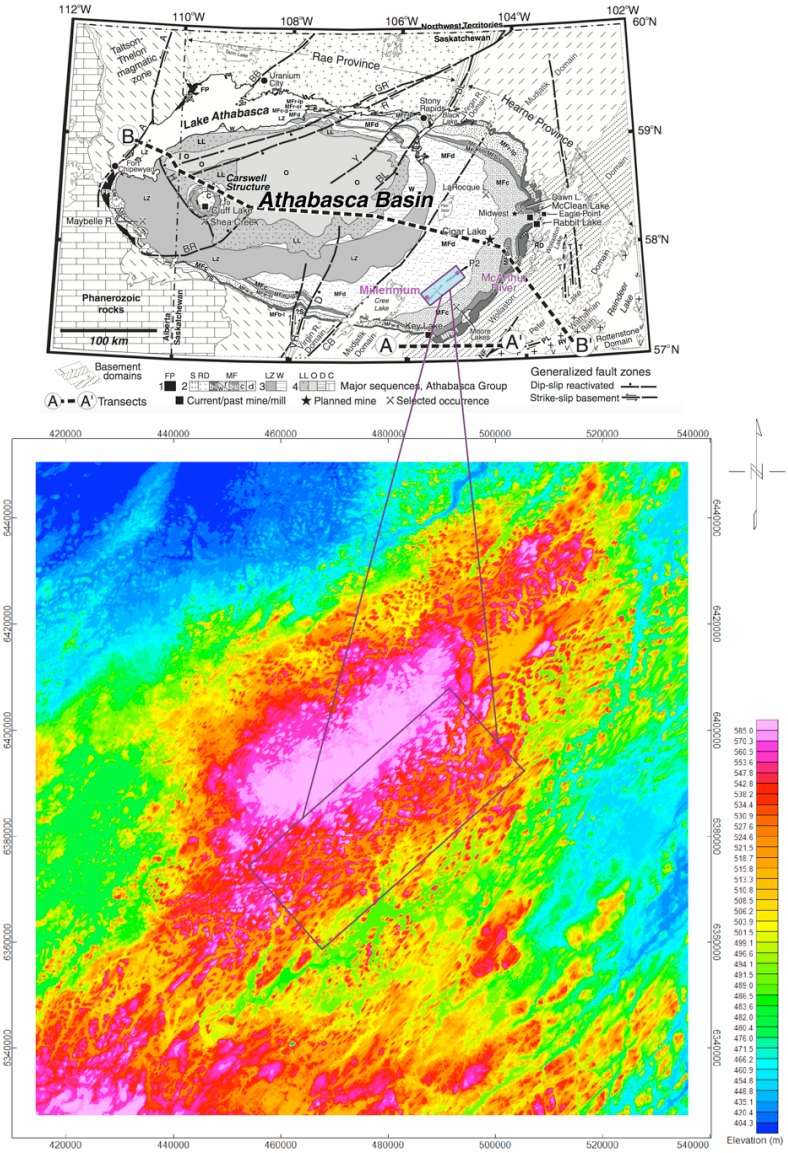


Figure 2.10: Topography of the eastern Athabasca Basin. Rectangular frame shows McArthur-Millennium corridor.

Till: Tills on the Athabasca Basin are mostly composed of sand, silt, clay and gravels. Tills are very sandy and range from very sandy to silty sand (sand ranges from 51% to 95%; Schreiner, 1984a; Campbell and Flory, 1999). Tills with intrabasinal and extrabasinal sources are typically white to pinkish grey and very sandy with less than 15% clasts, and

grey to brownish grey with a silty-sand matrix containing a higher clay component and 35–100% basement clasts, respectively. The extrabasinal materials were derived from the northeast margin of the basin in Nunavut, and have been moved several 100 km from sources (Campbell, 2007). They comprise pebble- to boulder-size igneous and metamorphic rock and pink feldspar. In general, the thin veneer of till over bedrock is composed mostly of locally derived sandstone (intrabasinal material). By increasing the thickness of till deposits the proportion of extrabasinal detritus increases.

Streamlined deposits: Drumlins in the basin are composed generally of till (Millard, 1988). The core of the large drumlins is predominantly richer in extrabasinal materials. They have been capped by a thin and surficial till unit with a higher sandstone component of intrabasinal materials (Aario and Peuraniemi, 1992). By moving from lee to stoss, the sandstone component in the surface till changes slightly towards the crystalline shield clasts. Some drumlins have a core composed of water-sorted sediments capped by a thin deposit of poorly sorted till (Shaw and Kvill, 1984).

Hummocky moraine: It is formed at the ice margin, and is composed of till that is mostly looser and sandier with a higher proportion of clasts ranging from pebble to boulder which is often sorted by meltwater.

Block fields: They consist of 0.5–2.0 m diameter angular sandstone boulders which are observed in the region.

Glaciofluvial deposits: Sand and gravel in the area are mostly related to esker complexes, ice-walled channels, recessional moraines, and stagnant-ice hummocky moraine. Esker

systems form a dendritic drainage pattern, ranging from tens of metres to several kilometres wide, adjacent to kames, kettles, and/or outwash plains. Ice-walled channels in the area have been eroded through the previously deposited drift, and can have up to 1 km wide (Schreiner, 1983, 1984a).

Glaciolacustrine deposits: Due to the sandy nature of glaciolacustrine sediments, this kind of deposit is mostly well sorted, comprising fine- to medium-grained sand and silty sand. They form sand plains, beaches, and spit deposits.

Eolian deposits: Eolian deposits in the eastern Athabasca Basin (less than 5%) have been mostly covered and stabilized by vegetation. Rare dunes and blowouts indicate some eolian activity still occurs. Loess has a thickness up to 20 cm which fills shallow depressions in till surfaces.

### 2.4.2.2 Quaternary stratigraphy

Based on information gathered from the eastern Athabasca Basin during the 1970s, Geddes (1982) identified three 'till' units. There are also three nonglacial deposits called 'stratified sediments' (Table 2.1). These units are described as follows:

Till 1: Till 1 is the oldest or lowermost till which has been largely eroded by subsequent glaciations. It was largely derived from crystalline shield rocks, and has a fine- to medium-grained, silty sand matrix with variable silt/clay content. Its thickness ranges from less than 1 m to 18 m, and is capped by silt and clay of the 'lower stratified sediments'. It has been deposited by a glacial event that predated the Late Wisconsinan ice advance.

Table 2.1: The regional Quaternary stratigraphic units along the eastern margin of the Athabasca Basin (modified after Geddes, 1982).

| Stratigraphic unit | Subunits, materials | Distribution | Associated ice-flow direction |
|---|---|---|---|
| RECENT DEPOSITS | Peat, lacustrine, eolian | Throughout | |
| UPPER STRATIFIED SEDIMENTS (UPPER DEGLACIAL SEDIMENTS, Geddes (1982)) | Sand, gravel; minor silt and clay | Sporadic, throughout Eskerine complexes, outwash plains | |
| TILL 3 (UPPER TILL, Averill (1977a, b); Geddes (1982)) | Ablation till (flow and meltout) | Related to re-advance dominantly west of unconformity Discontinuous Hummocky, drift, thin veneer, small drumlins | 190–200° |
| MIDDLE STRATIFIED SEDIMENTS (MIDDLE DEGLACIALS, Geddes (1982)) | Sand, gravel; minor silt and clay | Uncommon; mixed with till 3 | |
| TILL 2 (MIDDLE TILL, Averill (1977a, b); LOWER TILL, Geddes (1982)) | Ablation till | Throughout Most common unit Associated with drumlins, fluted and featureless till plains | Drumlins: 210–225° Striae: 205–225° |
| | Basal till (melt-out and lodgement facies) | | |
| LOWER STRATIFIED SEDIMENTS (LOWER GRAVELS, Geddes (1982)) | Clay and silt; sand and gravel | Rare No surface expression | |
| TILL 1 (LOWER TILL; Averill (1977a, b); OLD DRIFT, Geddes (1982)) | Till | Very rare, preserved in bedrock lows | Maybe related to 240° |
| BEDROCK | | | |

Lower stratified sediments: The ‘lower stratified sediments’, which overlie Till 1 or bed-rock, consist of two units: 1) glaciofluvial sand and thin clay layers, and 2) glaciolacustrine silt and clay. The thickest deposits are up to 27 m.

Till 2: Till 2 is the most extensive till deposit in the area, which forms drumlins and ground moraines. It is hard with a texturally mottled sandy and silty-sand matrix (Averill, 1976a). Till 2 contains crystalline shield detritus, and where it overlies the bedrock, it is mostly derived from sandstone. It was deposited by the main Late Wisconsinan ice advance.

Middle stratified sediments: ‘Middle stratified sediments’ is a discontinuous layer of sand and gravel or a thin (<1 m) deposit of silt (Geddes, 1982).

Till 3: Till 3 discontinuously overlies Till 2 with a variable thickness of 0 to 23 m. Hummocky moraine and the smaller-scale drumlins and fluted moraines are mostly composed of Till 3 (Campbell and Flory, 1999). It is loose, sandy, and often bouldery, and often has a higher component of locally derived material than Till 2.

Upper stratified sediments: The 'upper stratified sediments' unit is comprised of ice-contact and proglacial stratified sediments related to deglaciation.

Recent deposits: These include organic deposits, eolian deposits, and modern alluvial and lacustrine sediments.

Recent researches (adapted from Shawn Scott and Martin Ross reports in CMIC-Footprints quarterly Y2Q4 and Y3Q1 reports) on a cross section (exposure) of a drumlin at the McArthur area show that oxidized stratified coarse sands related to the pre-late Wisconsinan are located at the base of the section. The lower till has fewer clasts, higher silt and more distally (basement) derived material. The lower till preserved in the core of drumlins can contain magnetic rocks. Above the lower till, layers of stratified sandy diamict dominated most of the section are located. These layers are covered by a more proximal sandstone rich till. The surface of area is dominated by local till which is covered by dispersed altered boulders. Also, it has been found that all the tills are very sandy. The lower till has more shield clasts and finer material while the upper till has more sandstone clasts and coarser material.

## 2.5 Physical properties

Physical properties used in this thesis in the next chapters are based on papers and updated values from CMIC-Footprints project. In the following, these updated values of the physical properties are brought. They are based on the expanded and refined measurements with a better statics (i.e. means and standard deviations).

### 2.5.1 Seismic velocity

In the eastern Athabasca basin, seismic velocity values as well as acoustic properties (density, P-wave seismic velocity $V_p$ and acoustic impedance) increase with increasing depth. It means that the acoustic properties of basement blocks are usually higher than the overlying sandstone, and also the acoustic properties of sandstone are higher than the overlying overburden (glacial deposits). Variations in acoustic properties in the sandstone depend on the degree of silicification. Highly (altered) silicified zones have higher acoustic impedance. Seismic data cannot show the ore-body, mostly because of a lack of seismic reflectivity due to the small size of mineralization. But, the unconformity can be observed due to the change/increase in the velocity associated with this surface.

Shi et al. (2014) used a 2D model for the numerical wavefield simulation which is shown in Figure 2.11. In this model, the Athabasca Group sandstone consists of three subunits: a gradual velocity increasing layer (above 300 m), a thin layer within the sedimentary sequence (300-350m) and the high-velocity Read Formation (350-650m). The seismic velocities of sandstone vary form lower values which can be observed near the top of

sandstone to higher values which are near the basement rocks. The velocity contrast along the unconformity within the transition zone between the sandstone and basement rocks has a low contrast of ~500 m/s. Faults and alteration mineralization zones has different seismic velocities from the surrounding rocks. Overburden is not considered in this model.

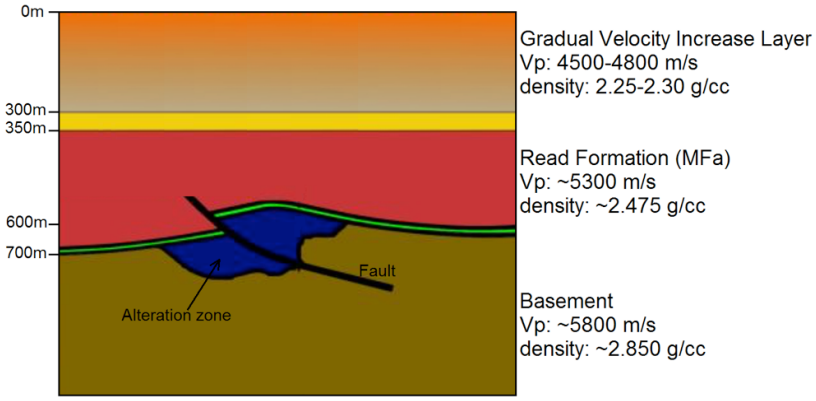


Figure 2.11: Seismic velocity model of the McArthur-Millennium area (Shi et al. 2014; CMIC-Footprints project).

Figure 2.12 shows a conceptual model for the overburden and the top of sandstone in the Athabasca Basin (from CMIC-Footprints project). It shows that the probability of a blind layer (see 5.2.3) being present in the overburden is high, which could be problematic for the seismic refraction method.

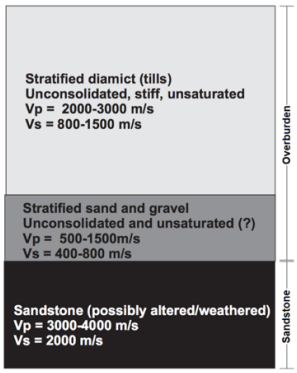


Figure 2.12: Seismic velocities for the overburden and sandstone of the McArthur-Millennium area (adapted from CMIC-Footprints project).

### 2.5.2 Density

Gravity anomalies result from the difference in density. The density of a rock is dependent on both its mineral composition and porosity. Figures 2.13 to 2.17 show approximate density ranges of some rocks in the Athabasca Basin based on the different sample populations (adapted from CMIC-Footprints project; Thomas and Wood, 2007).

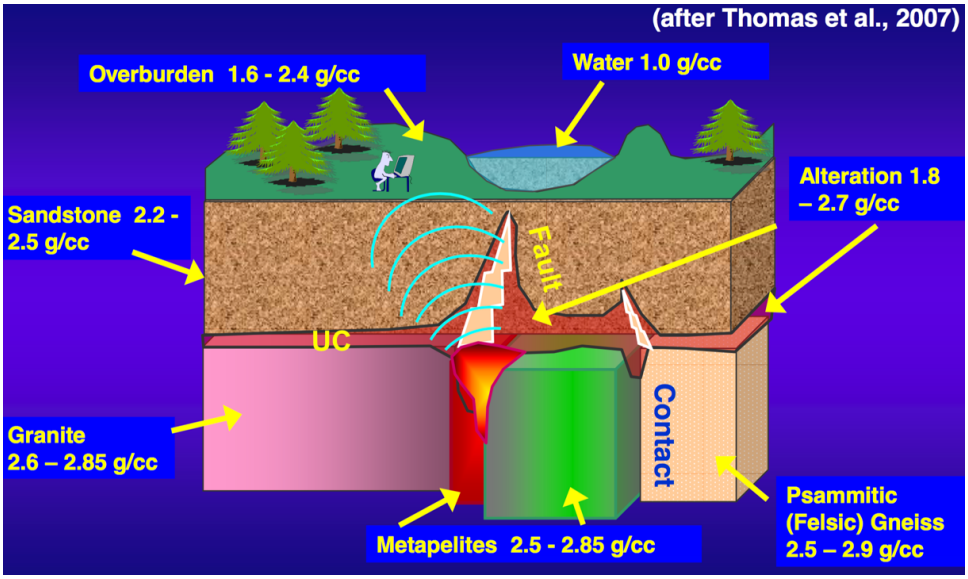


Figure 2.13: Density model for the Athabasca Basin (Thomas and Wood, 2007; adapted from CMIC-Footprints project).

Due to the small number of samples, they only show the measurement of pebbles/boulders in the till, and so not relevant for the till overall. They show that the mean density for the overburden (Quaternary deposits) is around 2.6 g/cc (gram per cube centimeter) which is much higher than what is expected (around 2 g/cc). But, recent researches in the CMIC-Footprints confirm that the average density of overburden in the McArthur-Millennium corridor is around 2 g/cc (adapted from from Shawn Scott and Martin Ross reports in CMIC-Footprints quarterly Y3Q3 report).

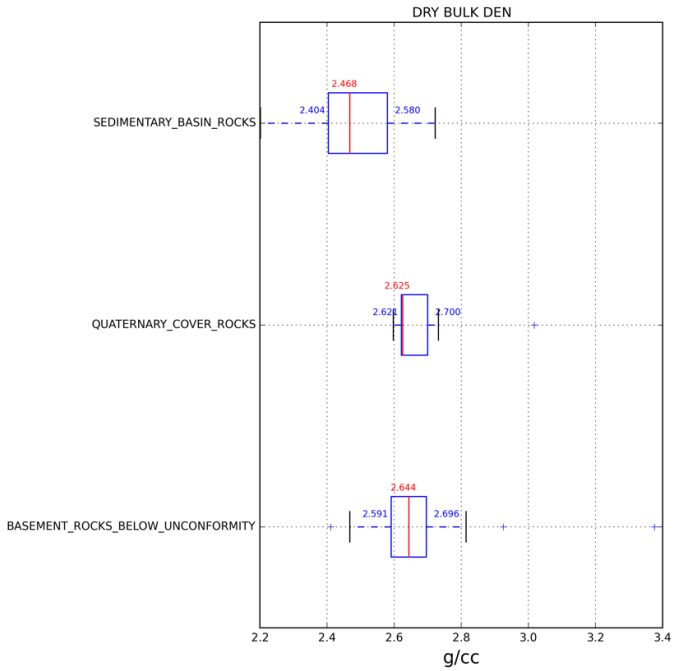


Figure 2.14: Density estimations for the lithology groups of the McArthur-Millennium area (adapted from CMIC-Footprints project).

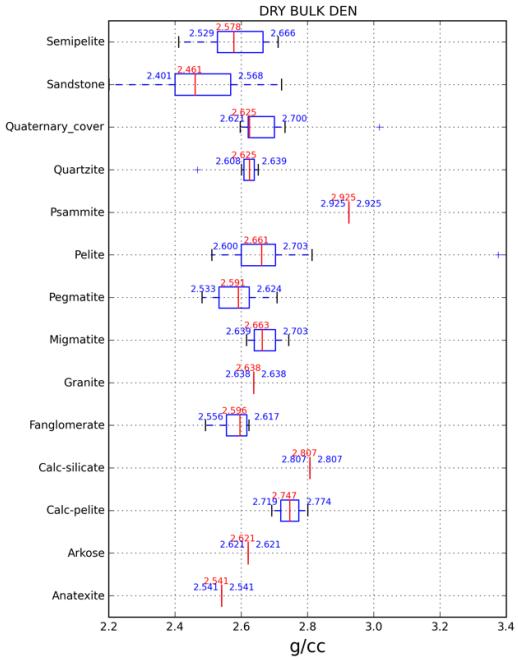


Figure 2.15: Density estimations for the lithology of the McArthur-Millennium area (adapted from CMIC-Footprints project).

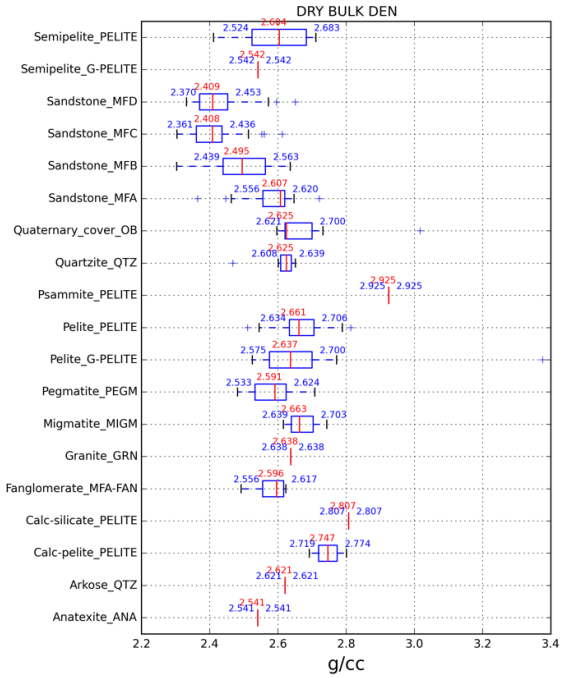


Figure 2.16: Density estimations for the rock-type of the McArthur-Millennium area (adapted from CMIC-Footprints project).

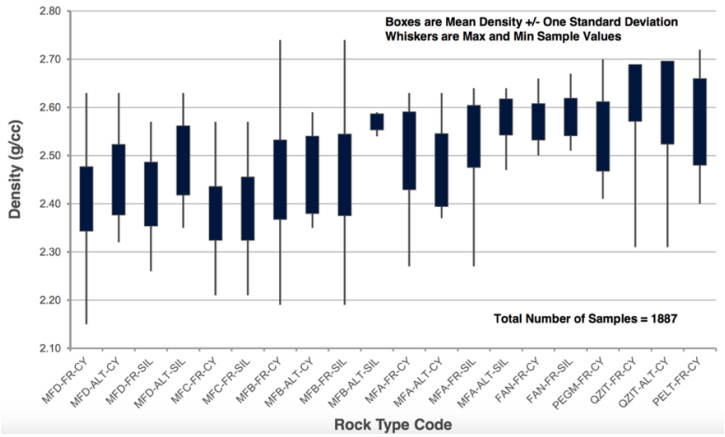


Figure 2.17: Density estimations from drill core from McArthur River/Read Lake (adapted from CMIC-Footprints project). ALT: altered; FR: not altered; CY: clay; SIL: silicification; MFA, MFB, MFC and MFD: sandstone strata, Manito-Falls A, B, C, and D; FAN, PEGM, QZIT and PELT: basement rocks.

Manito-Falls Formations have different ranges of densities especially due to the altered structures (e.g. silicifcation and disilicification; Figures 2.3 and 2.13). Regional sandstone

density is in the 2.4-2.5g/cc range (with an average of 2.43g/cc), silicified sandstone density is generally more than 2.6g/cc, while desilicified altered sandstone density is often around 2.2g/cc. The average densities for the clay-altered samples are lower than the average densities for the silicified samples for all of the lithologies, except for altered Fanglomerate and non-altered Quartzite (adapted from CMIC-Footprints project). MFA samples shows that there is a decrease in Illite, Chlorite and Dravite and an increase in Dickite in the silicified altered samples compared to the clay altered samples. Also, there is a decrease in Chlorite and increase in Dickite in the silicified altered MFB samples compared to the clay altered MFB samples. There is a decrease in Illite and increase in Chlorite and Dravite in the silicified altered MFC samples compared to the clay altered MFC samples. For MFD, there is a decrease in Chlorite and increase in Kaolinite and Dravite in the silicified altered samples compared to the clay altered samples (adapted from CMIC-Footprints project). Note that the total amount of any of the clay minerals in the sandstones is small (no more than a few %), and so there is only a small affect on the total density.

Basement rocks (Figures 1.1 and 2.13) can be categorized into three main groups of density: 1) 2.66–2.67g/cc including granitoid rocks, pegmatite, psammitic gneiss, and chloritic schist; 2) 2.69–2.71g/cc including graphitic pelitic schist, quartzo-feldspathic gneiss, albite gneiss, and pelitic and/or psammo-pelitic gneiss; and 3) 2.81–2.95g/cc including calc-silicate gneiss and metadiorite, metagabbro, and amphibolite (Thomas and Wood, 2007). The mean densities for the non-altered rocks (in both sandstone and basement rocks) are lower than the altered rocks for all of the lithologies, except for Quartzite and Pelite. However, the non-altered rocks vary in density more than the altered rocks (adapted

from CMIC-Footprints project).

### 2.5.3 Magnetic susceptibility

The magnetic susceptibilities, in SI units, of some rocks and minerals from drill core from the McArthur-Millennium area are given in Figures 2.18 to 2.20. There is not very much information and samples related to the magnetic susceptibility of the overburden. But, based on the available samples, the variable magnetic susceptibility of the overburden is due to the presence of granite clasts among some glacial deposits especially in the lower layers in drumlins. Different layers of glacial deposits can have different magnetic suscebtibility starting from 0SI to $1\times10^{-2}$SI with an average value of $5\times10^{-3}$SI (adapted from CMIC-Footprints project). Also, the sandstone layers (MF members) have very small values, lower than $10^{-5}$SI, which are considered as non-magnetic. Basement blocks have different magnetic susceptibility values. In the McArthur River area, the magnetic susceptibility of rocks in the footwall of P2 fault is less than hanging-wall (adapted from CMIC-Footprints project; Thomas and Wood, 2007).

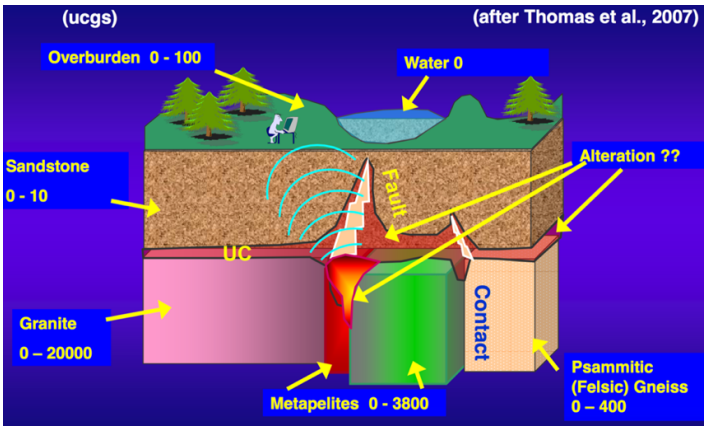


Figure 2.18: Magnetic model for the Athabasca Basin (Thomas and Wood, 2007; adapted from CMIC-Footprints project).

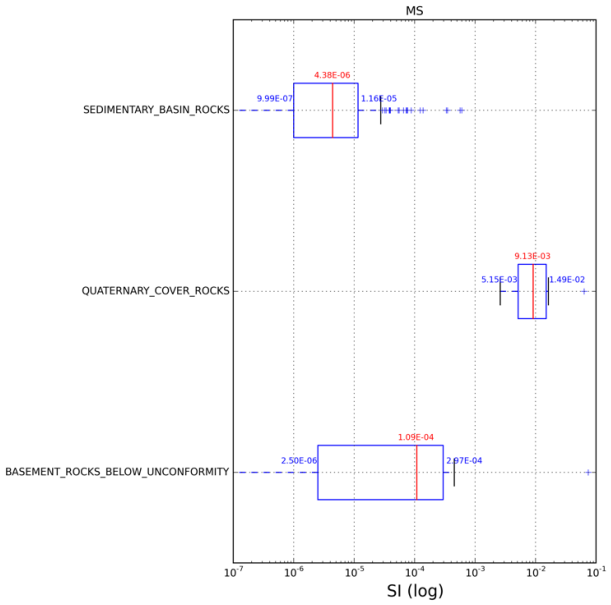


Figure 2.19: Magnetic susceptibility estimations for the lithology groups of the McArthur-Millennium area (adapted from CMIC-Footprints project).

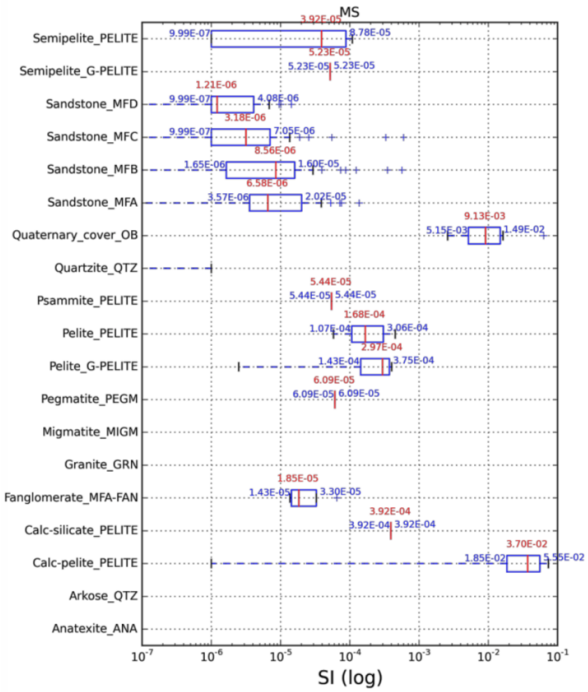


Figure 2.20: Magnetic susceptibility estimations for the rock-type of the McArthur-Millennium area (adapted from CMIC-Footprints project).

Magnetic susceptibilities of basement rocks have a wide range from metasedimentary pelitic, psammitic and calc-silicate gneisses (susceptibility $\mu = 0$ to 4 SI $\times 10^{-3}$) as units with lowest magnetic susceptibility to granitoid rocks (susceptibility $\mu = 0$ to 20 SI $\times 10^{-3}$) which have the highest magnetic susceptibility. The magnetic susceptibility of meta-quartzite rocks ranges from 0 to 0.2 SI $\times 10^{-3}$ (Wood and Thomas, 2002).

### 2.5.4 Resistivity

The resistivity (i.e. reciprocal of conductivity) of some rocks and minerals of the Athabasca Basin are shown in Figures 2.21 to 2.25 based on the different sample populations. Resistivity values related to the overburden is variable in the Athabasca Basin. However, there is not a good conductivity contrast between the overburden and the sandstone. The presence of water in the unconsolidated materials of overburden can decrease the resistivity. An average of 2000 Ohm-m can be considered for the sandstone resistivity (Figures 2.21 to 2.23). Altered clay in sandstone has a lower resistivity than the host. For the basement blocks (Figures 2.23 to 2.25), the resistivity is variable from 10 Ohm-m for graphitic rocks to 80000 Ohm-m for Archean granitoid gneiss (adapted from CMIC-Footprints project).

Silicification in the Read Formation and MFb increase the resistivity. The low resistivity observed in MFc can be due to less intense early hydrothermal silicification or the increase in porosity caused by hydrothermal quartz dissolution. The low resistivity of MFd can be due to the absence of the silisification. Resistivity contrast between silicified and nonsilicified sandstone is significant (McGill et al., 1993; Mwenifumbo et al., 2007).

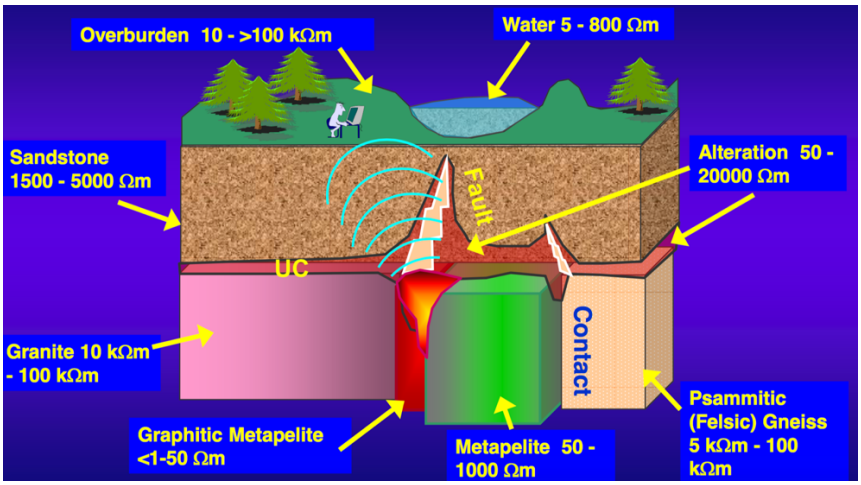


Figure 2.21: Resistivity model for the Athabasca Basin (adapted from CMIC-Footprints project).

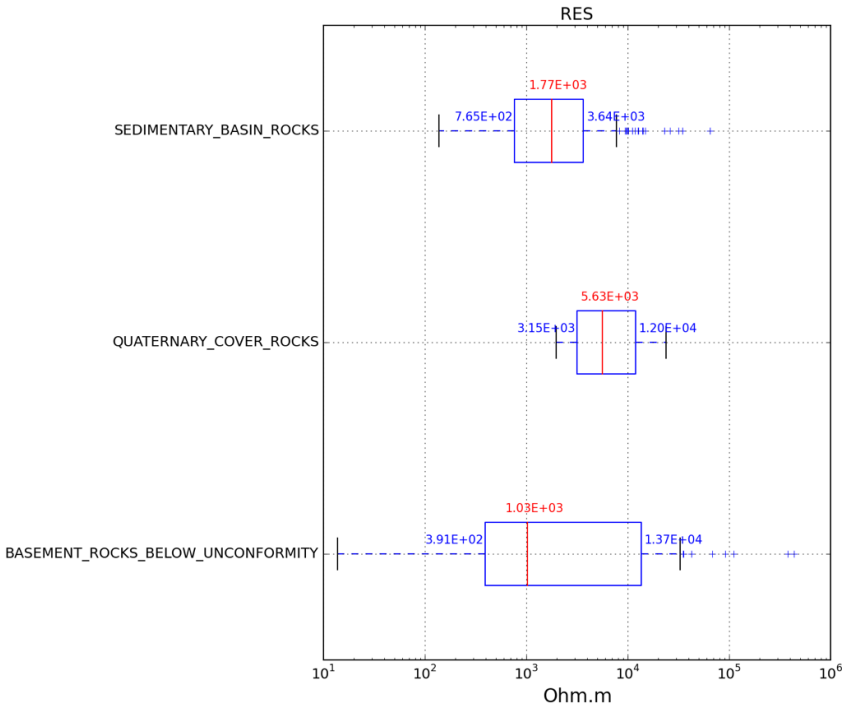


Figure 2.22: Resistivity estimations for the lithology groups of the McArthur-Millennium area (adapted from CMIC-Footprints project).

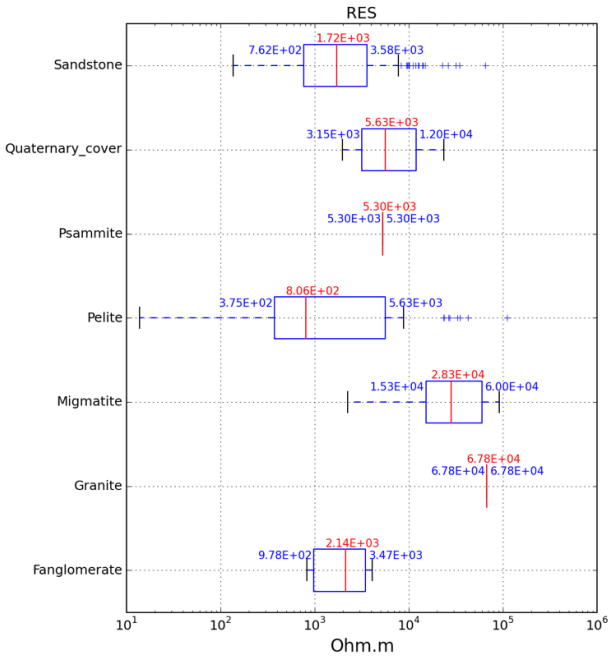


Figure 2.23: Resistivity estimations for the lithology of the McArthur-Millennium area (adapted from CMIC-Footprints project).

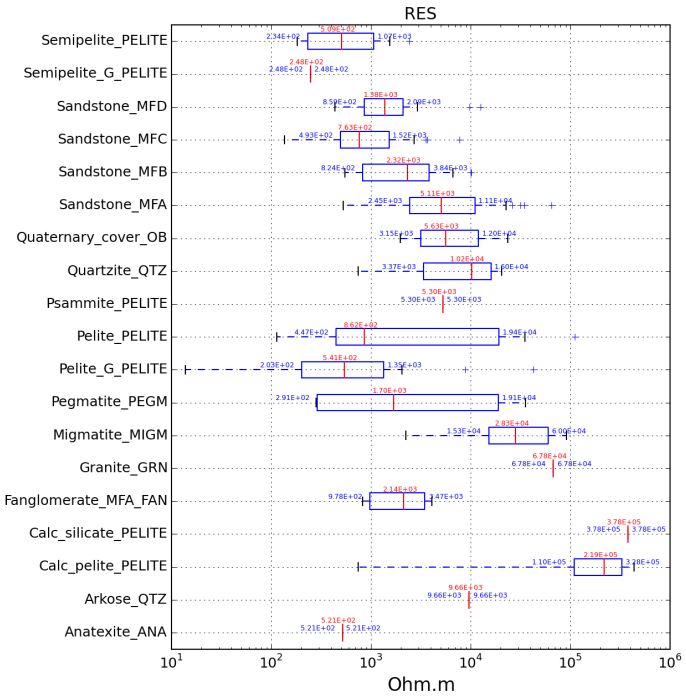


Figure 2.24: Resistivity estimations for the rock-type of the McArthur-Millennium area (adapted from CMIC-Footprints project).

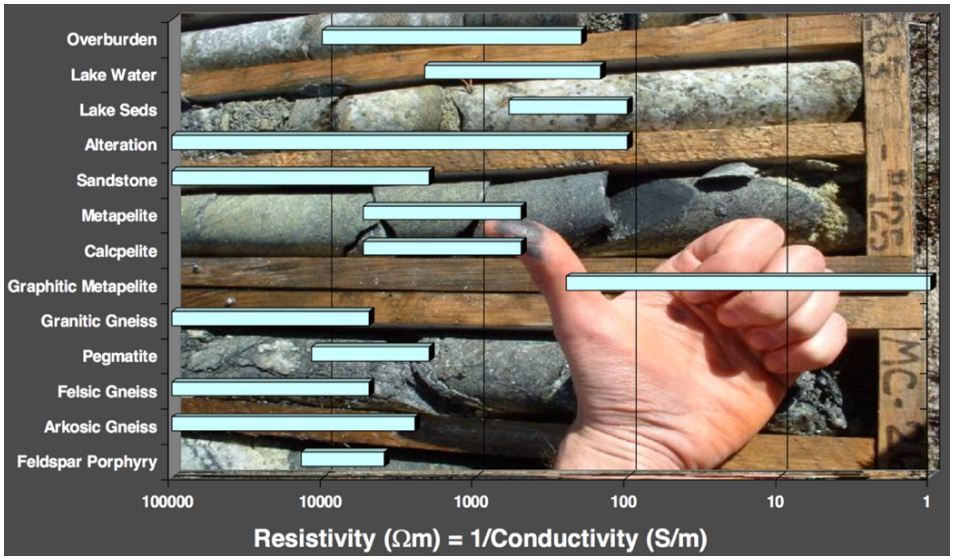


Figure 2.25: Resistivity estimations for the rocks of the Athabasca Basin (adapted from CMIC-Footprints project; U-site workshop 2014).

### 2.5.5 Geophysical logs

Borehole studies, including measurements of resistivity, density, P-wave velocity and porosity, are used in order to improve the lithological information as well as the physical properties of sandstone and basement rocks (Figure 2.26). They confirm the physical properties obtained from measurements on samples. Geophysical logs from MAC-218, shown in Figures 2.26, demonstrate a change in physical properties at a depth of 300m. Above 300m, the density, seismic velocity (p-wave), and resistivity are low (2.27 g/cc, 4800 m/s, and 2000ohm-m, respectively) and below 300 m they are high (2.48 g/cc, 5670 m/s, and 14000ohm-m, respectively). The increase in values is due to the decrease of porosity in the alteration (silicification) zone. The relatively high gamma-ray activity in MFb and MFa is mostly due to Th and the lesser amount of U (Mwenifumbo et al., 2007).

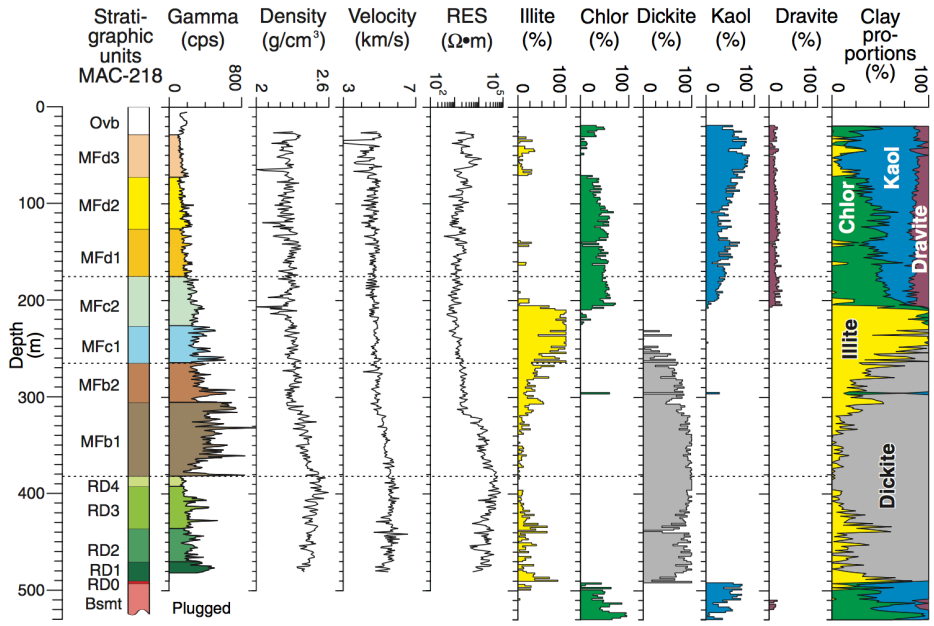


Figure 2.26: Borehole MAC-218 in eastern Athabasca near the McArthur River mine. Geophysical logs including gamma-ray, density, resistivity, seismic velocity and clay minerlogical results are shown while the P2 ore zone is located around 500 m (Chlor = chlorite; Kaol = kaolinite; RES = normal resistivity; stratigraphic codes in ascending order: RD = Read Formation; MFb, MFc, MFd = Bird, Collins, and Dunlop members of Manitou Falls Formation; Ovb = overburden; Mwenifumbo et al., 2007). Note that the clays % are proportion of the clays in the rock. They only make up a few % maximum of the sandstones.

## 2.6 Summary

In the eastern Athabasca Basin, most uranium deposits are located in the McArthur-Millennium region where graphitic faults intersect the unconformity between the sandstone and the basement at depth. Uranium deposits are mostly surrounded by alteration zones. Overburden (unconsolidated glacial deposits) which is located on the top of the sandstone concludes drumlin, hummocky moraine, esker complexes, and ground moraine.

Physical properties of the geological structures have a wide range of values which help to detect the approximate location of the uranium mineralization using geophysical methods. These physical properties (such as density, resistivity, magnetic susceptibility and seismic velocity) will be used later in the next chapters for synthetic modellings. Density and seismic velocity of the geological layers increase by increasing the depth. There is no specific pattern for the resistivity and magnetic susceptibility of the rocks as they are variable. But, graphitic faults are conductive, and alteration zones can have different density from the host rocks. Blocks in the basement have a better contrast for the resistivity and magnetic susceptibility than the density and seismic velocity. However, the contrast between overburden and sandstone for the resistivity and magnetic susceptibility can be less than the density and seismic velocity in some parts of the area.

# Chapter 3

# Geophysical Methods: Gravity, Magnetic, Seismic Refraction and Electromagnetic Methods

## 3.1 Introduction

Geophysical methods used in this research, such as magnetic, gravity, seismic refraction and electromagnetic methods, are explained in detail in this chapter. First, the gravity method will be discussed. The signature of the density anomaly on the gravity data will be investigated. Different reductions on the gravity data as well as the definition and the nature of free-air and Bouguer anomalies will be explained. For the magnetic method, in addition to the corrections and processing, the interpretation will be explained.

Then, for the seismic refraction method, seismic surveys and the behaviour of the acoustic wave at the interfaces as well as interpretation methods will be discussed. Also, common problems in this method will be mentioned. For the electromagnetic method, both frequency- and time-domain for the airborne cases will be considered. For frequency domain and time domain, DIGHEM and VTEM methods will be investigated, respectively. And, finally some examples of the previous geophysical studies will be shown.

## 3.2 Gravity method

The gravity method involves measuring the variation in the earth's gravitational field due to the changes in the density of the subsurface rocks. Thus, like the magnetic, magnetotelluric and SP methods, gravity is a natural source method. The gravity field due to the density variation of local mass is very small in comparison with the background field of the earth (often of the order of 1 part in $10^6$ to $10^7$; Telford et al, 1976). In exploration, the gravity method is surveyed by surface, air-borne, marine and borehole measurements.

After applying the correction methods necessary to take into account all but local effects, gravity data is ready for interpretation. Forward modelling is one of the main methods for interpretation in which the data will be mathematically synthetized based on some physical or mathematical model with a given set of model parameters. The calculated data can be compared with the real data. In order to fit these two data sets, the geometries and physical properties in the forward model can be changed. This process can be done repeatedly to reconstruct a model similar to the real geological structure.

### 3.2.1 Basic theory

The (attraction) force of gravity, proposed by Newton based on the masses ($m_1$ and $m_2$) of two particles and the distance ($r$) between their centres, is given by (Kearey et al., 2002; Telford et al, 1976):

$$F = \frac{Gm_1m_2}{r^2} \tag{3.1}$$

where $G$ is the Gravitational constant ($6.67 \times 10^{-11}$ $m^3$ $kg^{-1}$ $s^{-2}$).

Consider the gravitational attraction of the earth (a spherical, non-rotating and homogeneous Earth) with the mass $M$ and the radius $R$ on a small mass m with the small mass a located on the earth'e surface. Thus:

$$F = \frac{GM}{R^2} m = mg \tag{3.2}$$

where $g$ is the gravitational acceleration (or simply gravity) and is known by:

$$g = \frac{GM}{R^2} \tag{3.3}$$

On such an Earth, gravity would be constant. But, gravity on the Earth's surface varies because of the rotation, ellipsoidal shape, internal mass distribution and irregular surface relief (Kearey et al., 2002).

Equipotential surfaces (sea-level surface or geoid) can be defined on which the magnitude of $g$ is constant. The elevation of the points on the land are determined with respect to the equipotential surfaces. The mean value of gravity on the Earth's surface is about 9.8 $ms^{-2}$ (=980665mGal). The c.g.s. unit of gravity is the milligal (1 mgal = $10^{-3}$ gal = $10^{-3}$ cm $s^{-2}$), which is equivalent to 10 gu (gravity unit).

### 3.2.2 Gravity surveying

Since the contribution to the total gravity from density variations in the upper crust are very small, gravimeters need to be very sensitive. Previous generations of measuring instruments

were based on small pendulums or the oscillation of torsion fibres which took a lot of time for reading. New instruments, known as gravimeters, are based on the changes of the length of a spring which is connected to a mass. Variations in the weight of the mass are due to variations in gravity (Kearey et al., 2002; Telford et al, 1976). Gravimeters can measure one part in 100 million of the earth's gravity field (980 gals or 980,000 milligals) in units of milligals (mGal) or microgals. Some ground measuring systems have a reading resolution of 0.001mGal (www.scintrexltd.com). Today, airborne systems are frequently used in the exploration as they are a fast method for data acquisition and they can measure both gravity and gradiometry (see Appendix D) data. Airborne surveying is complex because of the large possible errors in applying corrections (Kearey et al., 2002). Modern airborne systems can provide a spatial resolution of around 150m with an accuracy of 0.1mGal (www.cgg.com). The station spacing in the gravity survey can vary from a few metres in the case of small mineral or geotechnical surveys to several kilometres in regional reconnaissance surveys.

Since the Earth is not a perfect homogeneous sphere, gravity is not constant. Gravity's magnitude depends on the following parameters: latitude, elevation, topography of the surrounding terrain, earth tides and density variations in the subsurface (Telford et al, 1976). Gravity exploration is based on the last of these parameters the value of which is less than latitude and elevation effects. Therefore, the effects of these parameters should be removed from observed data to achieve data belonging to the density variations in the subsurface.

### 3.2.3 Gravity corrections

Before interpretation, one needs to correct for all variations in the Earth's gravitational field which do not result from the subsurface anomalies. This process is called gravity reduction or reduction to the geoid, as sea-level is mostly considered as datum level (Kearey et al., 2002). The geoid surface, which is based on the mean sea-surface level, is irregular but smoother than the Earth's physical surface. Although the physical Earth has variation from +8,000 m to −418 m, the geoid's variation ranges from −106 to +85 m. For the corrections, the location of the gravimeter should be known precisely. Gravity corrections are as follows (Blakely, 1995):

**Drift correction:** The instrument's components can change slowly due to the fluctuations in temperature etc. This causes the measurement recorded by the gravimeter tend to change slowly as well. This problem can be solved by repeating the readings at a base station at recorded times during the day. Drift is assumed to be linear between repeated base readings. The drift correction, determined for each datum at the corresponding times, should be subtracted from the observed values (Blakely, 1995; Kearey et al., 2002; Figure 3.1). Modern gravimeters can measure and estimate their drift (although not during an actual survey).

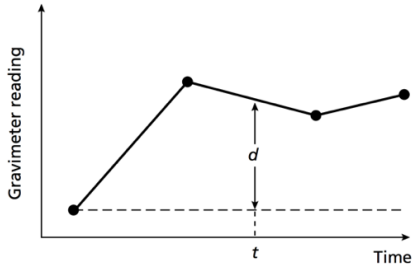


Figure 3.1: A gravimeter drift curve and a drift correction value (d) constructed from repeated readings at a fixed location (Kearey et al., 2002).

**Latitude corrections (gf):** Earth is approximately an oblate spheroid due to its constant rotation which creates centrifugal forces that make Earth wider at the equator than the poles, where the difference in equatorial and polar radii is about 21 km. Thus, points near the equator are farther from the centre of mass of the Earth than those near the poles. This causes gravity to increase from the equator to the poles. Also, the centripetal acceleration generated by this rotation causes gravity to decrease from pole to equator. The gravity value that would be observed if Earth was a perfect (no geologic or topographic complexities) rotating ellipsoid would be as follow (Blakely, 1995; Kearey et al., 2002):

$$gf = 978031.85\ (1.0 + 0.005278895\ sin^2(lat) + 0.000023462\ sin^4(lat)) \quad \text{mGal} \tag{3.4}$$

where *lat* is latitude [degree]. For a small scale area, after applying the correction for the most northerly point, which is based on and relative to the absolute gravity in the base station, we can use the following linearized correction for subsequent points (Blakely, 1995):

$$\Delta gl = 0.000812\ sin(2\ lat) \quad \text{mGal/m (N-S)} \tag{3.5}$$

The correction is added to *g* as we move toward the equator.

**Free-air correction (FAC):** The free-air correction accounts for gravity variations caused by elevation differences in the observation locations (Blakely, 1995; Kearey et al., 2002; Figure 3.2a),

$$FAC = 0.3086\ h \quad \text{mGal} \tag{3.6}$$

where $h$ is the elevation [metres] of each gravity station above the datum (typically sea level). The FAC is positive for an observation point above datum to correct for the decrease in gravity with elevation. In airborne surveys, $h$ is the elevation of the observation point (height of the aircraft) above the datum.

**Bouguer correction (BC):** The Bouguer correction attempts to remove the gravitational effect of the rock present between the observation point and datum by approximating the rock layer beneath the observation point by an infinite horizontal slab with a thickness equal to the elevation of the observation above datum (Blakely, 1995; Kearey et al., 2002; Figure 3.2b).

$$\text{BC} = 2\pi G\rho h \approx 0.04192\,\rho h \quad \text{mGal} \tag{3.7}$$

where $G$ is the Gravitational constant, $\rho$ is the average density of the underlying rocks in g/cc (the usual value is 2.67 g/cc) and $h$ is the elevation in metres. On land the Bouguer correction must be subtracted, and for sea surface observations must be added (to account for the lack of rock between sea surface and sea bed). For the sea water, the correction can be done by considering the replacement of the water layer (with a density of $\rho_w$=1.023g/cc) by a specified rock (with a usual density of $\rho_s$=2.67g/cc). Therefore, $h$ is the water depth and $\rho = \rho_s - \rho_w$. In airborne surveys, $h$ is the height (thickness) of the ground (directly beneath the observation) above the datum.

**Terrain correction (TC):** Bouguer correction which is based on a horizontal slab is only an approximation as the topography has an effect on the gravity data as well. Terrain

correction is based on the topographic effect in the vicinity of the gravity station. This correction is always positive regardless of whether the local topography consists of a mountain or a valley (Blakely, 1995; Kearey et al., 2002; Figure 3.2c). But, in airborne surveys terrain correction is positive for heights above the surface height directly beneath the airborne measurement and vice versa (Hinze et al., 2013). In this research, a complete Bouguer correction based on the forward modelling with an accurate representation of topography will be done (Chapter 5).

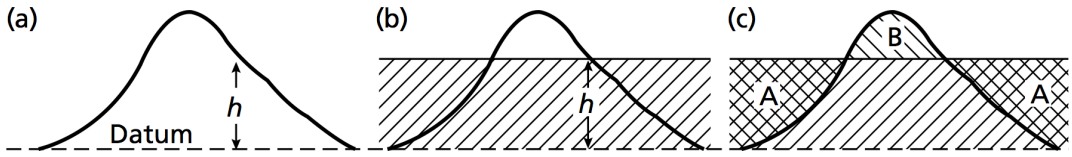


Figure 3.2: (a) The free-air correction (b) The Bouguer correction (c) The terrain correction (Kearey et al., 2002).

**Tidal correction:** Gravity in a fixed location changes with time because of the periodic variation in the gravitational effects of the Sun and Moon, and correction must be made for this variation which is predictable and quantifiable. The tidal effect never exceeds 0.3mGal (Blakely, 1995; Kearey et al., 2002).

**Eötvös correction (EC):** The Eötvös correction is applied to gravity data taken on a moving vehicle such as a ship or a plane. The motion of the vehicle generates a centrifugal acceleration associated with the movement of the vehicle over the Earth's surface and relative to the Earth's axis of rotation. Therefore, the readings are lower when the vehicle moves eastwards, and higher when it moves westward (Blakely, 1995; Kearey et al., 2002).

$$EC = 7.503\, V \sin(a) \cos(f) + 0.004154\, V^2 \quad \text{mGal} \tag{3.8}$$

where $V$ is the speed of the vehicle in knots, $a$ is the heading and $f$ is the latitude of the observation.

### 3.2.4 Gravity anomalies

**Free-air and Bouguer anomalies:** The free-air anomaly (FAA) and Bouguer anomaly (BA) are defined by (Kearey et al., 2002):

$$FAA=gobs-gf+FAC(\pm EC) \tag{3.9}$$

$$BA=gobs-gf+FAC\pm BC+TC(\pm EC) \tag{3.10}$$

The interpretation of gravity data on land is mostly based on the Bouguer anomaly. In marine surveys, Bouguer anomaly is not appropriate for deeper water surveys but can be calculated for inshore and shallow water areas. Thus, the free-air anomaly is frequently used for interpretation in such areas.

In general, the observed gravity is composed of various component as follow (Blakley, 1995):

observed gravity = [attraction of the reference ellipsoid]
+ [effect of elevation above sea level (free-air)]
+ [effect of "normal" mass above sea level (Bouguer and terrain)]
+ [time-dependent variations (tidal)]
+ [effect of moving platform (Eötvös)]
+ [effect of masses that support topographic loads (isostatic)]
+ [effect of crust and upper mantle density variations ("geology")].

Blakely (1995) illustrated the various contributions to observed gravity by Figures 3.3 to 3.7. Figure 3.3 shows the variations in density in a cross section as well as the gravity data along a west-east profile which is observed at the topographic surface. The crust and mantle have densities of 2.67 and 3.07g/cc, respectively. The mountain is isostatically compensated by a crustal root. The aim is to isolate the square-shaped anomaly with a high density of 2.97g/cc in the upper crust.

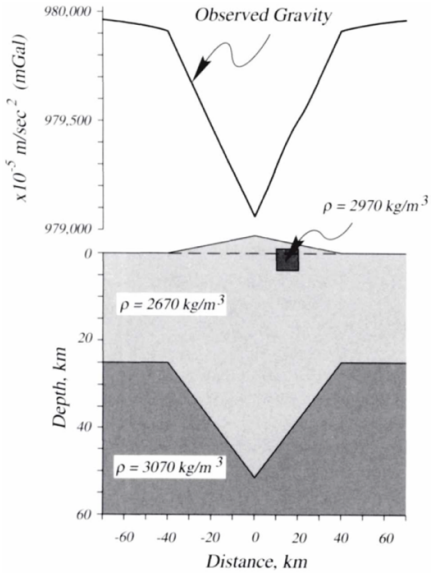


Figure 3.3: Crustal cross section and observed gravity (vertical exaggeration 2; Blakely, 1995).

Theoretical gravity, which is the normal gravitational attraction of a mathematical model representing a physically homogeneous-smoothed Earth (Earth ellipsoid), can be theoretically calculated and then subtracted from gravity data. The remainder represents departures of the earth's density from the homogeneous ellipsoid which includes the effects of altitude, tides, and various other factors. In this example, 0m elevation is considered as the datum (reference ellipsoid), and a density of 2.67g/cc is considered for the homogeneous-smoothed Earth (Figure 3.4; Blakley, 1995).

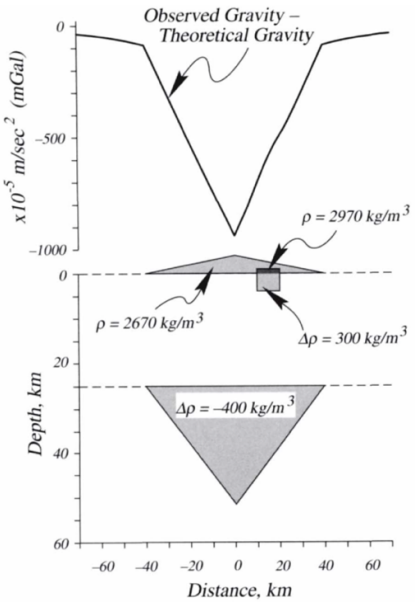


Figure 3.4: Crustal cross section and gravity data after subtraction the theoretical gravity (Blakely, 1995).

Tidal and Eötvös corrections need to be applied as well. The large negative anomaly in Figure 3.4 is due to the changes (increasing) in distance between the elevation of gravity meter and the center of the earth (reference ellipsoid) as the profile rises over the topographic edifice. This large negative anomaly can be eliminated by the free-air correction (Figure 3.5; Blakely, 1995). It can be seen that the free-air correction has not accounted for the additional mass represented by the topographic edifice as well as the crustal root (which produces a long-wavelength, relatively low-amplitude, negative component in the free-air anomaly). But, the free-air correction adjusts measured gravity to what would have been measured at a reference (ellipsoid) level. This reference level is commonly taken as the mean sea level. Note that the concept of the free-air correction as 'moving' the observation location to the reference level is correct only if there is no other effect such as the contribution due to a crustal density anomaly. For this case, it is important to not move the observation location but keep it where it is, so that the contribution from

the density anomaly can be correctly evaluated.

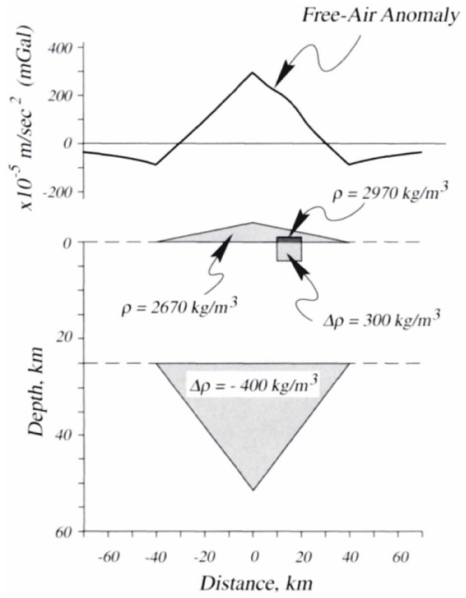


Figure 3.5: Crustal cross section and gravity data after the free-air correction (Blakely, 1995).

The gravity signature of the additional mass that exists between the level of observation and datum (here sea level) can be removed from the data using the Bouguer correction. Here, the additional mass has a density of 2.67g/cc (Figure 3.5). In addition to the Bouguer correction, the terrain correction is essential in order to remove the effect of the topography on the data. In Figure 3.6, the dashed line shows the data after Bouguer correction, and the solid line shows the data after both Bouguer and terrain corrections (Blakely, 1995).

Although the Bouguer correction has accounted for the direct effects of the topographic edifice, it has not accounted for the low-density root that isostatically supports the topography. The extra mass of large topographic features is generally compensated at depth by mass deficiencies (Figure 3.6), whereas large topographic depressions are matched at depth by mass excesses. This is called isostatic compensation. This can be removed from

gravity data using a digital terrain model, in which first we need to calculate the shape of the crust-mantle interface consistent with the Airy model for isostatic compensation, and second calculate at each observation point the gravitational effect of the volume (Blakely, 1995).

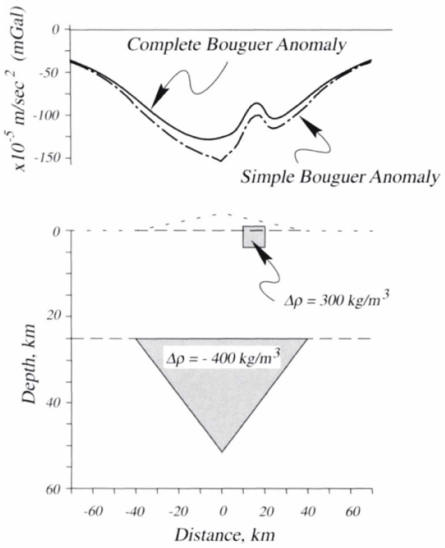


Figure 3.6: Crustal cross section and gravity data after the Bouguer correction (dashed line) and both Bouguer and terrain corrections (solid line; Blakely, 1995).

According to the Airy's hypothesis of isotacy, the mountain range can be thought of as a block of lithosphere (crust) floating in the asthenosphere (mantle). Mountains have roots, while ocean basins have anti-roots (Figure 3.7). The depth below sea level of the compensating root ($d_m$) can be calculated by (Blakely, 1995):

$$d_m = h\frac{\rho_t}{\rho_m - \rho_c} + d_s \tag{3.11}$$

where $\rho_c$ is crustal density, $\rho_m$ is mantle density, $\rho_t$ is the average density of rocks that make up the terrain, $d_s$ is the depth of compensation at shorelines, and $h$ is elevation of the

observation point above sea level. Isostatic residual anomaly can be obtained by subtraction the isostatic regional anomaly from the data (Figure 3.8). The isostatic regional is negative over continents and positive over oceans (Blakely, 1995).

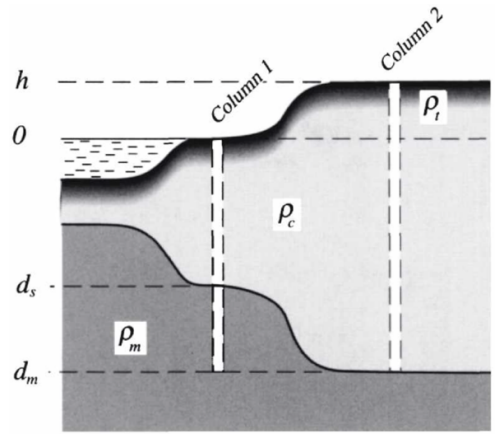


Figure 3.7: Airy model of isostatic compensation (Blakely, 1995).

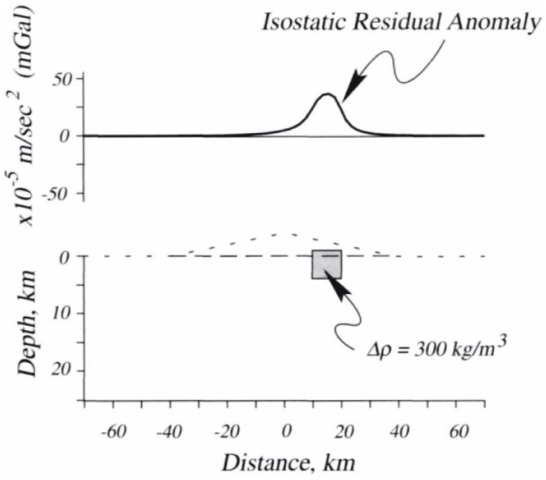


Figure 3.8: Isostatic residual gravity profile over crustal cross section (Blakely, 1995).

**Residual anomalies:** Bouguer anomaly fields (shorter wavelength) are often affected and covered by regional anomaly fields (longer wavelength; Figure 3.9). The removal of the regional field, to isolate the residual anomalies, is performed by analytical methods such as trend surface analysis and low-pass filtering. Upward continuation is employed in gravity

interpretation to determine the form of regional gravity variation over a survey area, since the regional field is assumed to originate from deep structures (Kearey et al., 2002).

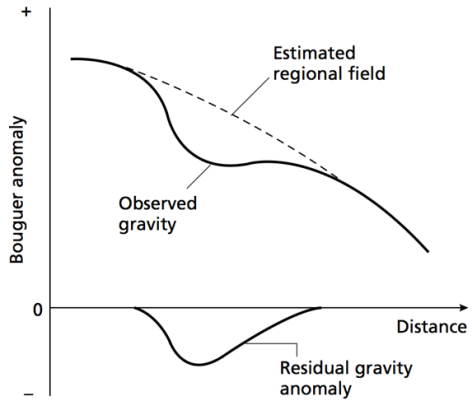


Figure 3.9: Regional and residual gravity anomalies from the observed Bouguer anomaly (Kearey et al., 2002).

## 3.3 Magnetic method

The magnetic method investigates subsurface features based on their magnetic properties. Although most rocks are non-magnetic, a few types contain sufficient magnetic minerals that they can contribute to the measureable magnetic field. When a magnetic rock is placed in the Earth's magnetic field, it generates an induced magnetic field with these variations being considered as a magnetic anomaly. The possibility of remanent magnetization can also contribute to a magnetic anomaly. Magnetic surveying is common, and an initial method in many exploration situations. In exploration applications, the magnetic method is surveyed by surface, air-borne, marine and borehole measurements.

### 3.3.1 Basic theory

As everybody knows, the same polarity or opposite polarity of the poles of two magnets causes the force of repulsion or attraction between two poles, respectively. This magnetic

force can also be seen in two adjacent current-carrying wires. The current in a (infinitely long straight) wire generates magnetic field ($B$) which can be calculated using Ampère's law as

$$B = \frac{\mu_0 I}{2\pi r} \tag{3.12}$$

where $\mu_0$ is constant corresponding to the magnetic permeability of vacuum (= $4\pi\times10^{-7}$ $Hm^{-1}$), $I$ is the current, and $r$ is the distance to the wire (Craik, 1995).

The SI unit of magnetic field strength (in the geomagnetic exploration field) is *nanotesla* (nT). 1nT is numerically equivalent to 1 *gamma* (*g*) in c.g.s. units. Also, 1nT is equivalent to $10^{-5}$ *gauss* (*G*). In a vacuum, the magnetic field strength $B$ and magnetizing field $H$ (with unit $A\ m^{-1}$) inside a material are related by $B= \mu_0 H$.

$$B = \mu_0 H + \mu_0 kH = (1 + k)\mu_0 H \tag{3.13}$$

where $k$ is the magnetic susceptibility of the material indicating the response of the materials to an applied field. Susceptibility is dimensionless in the SI and c.g.s. systems (SI susceptibility value = $4\pi\times$ c.g.s susceptibility value). The magnetic induction $B$ is the total field including the effect of magnetization. Susceptibility is useful for induced magnetization when magnetization is proportional to the applied field (Blakely, 1995). Earth's materials have a wide a range of magnetic susceptibility. Section 2.5.3 shows the range of susceptibilities for the Athabasca Basin.

### 3.3.2 Geomagnetic field

The geomagnetic field mostly originates from the Earth's core. The flow of liquid iron in the outer core, resulting from the Earth's spin, generates electric currents, which in turn produce magnetic fields. Charged metals passing through these fields go on to create electric currents of their own, and so the cycle continues. This self-sustaining loop is known as the geodynamo (Fowler, 2005).

Declination (*D*; the angle on the horizontal plane between magnetic north and true north), inclination (*I*; the angle at which the magnetic field lines intersect the Earth's surface) and the total field vector (*B*) are represented as geomagnetic elements (Figure 3.10). The magnetic intensity of the Earth's magnetic field varies over the surface of the Earth with latitude in strength from around 25,000 nT at the magnetic equator to 70,000 nT at the magnetic poles (Kearey et al., 2002). Also, due to the external origin, geomagnetic field varies on a daily basis to produce diurnal variations (less than 50nT).

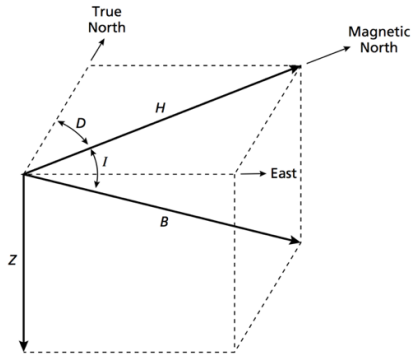


Figure 3.10: Geomagnetic elements (Kearey et al., 2002).

### 3.3.3 Magnetic corrections, processing and interpretation

The International Geomagnetic Reference Field (IGRF) is a standard mathematical

description of the Earth's main magnetic field and its secular variation. In magnetic processing, removing the effects of diurnal variation from the observed data is called "diurnal variation correction". Some days the amplitude of diurnal variations is not regular, up to 1000nT, which it is known as magnetic storms. Magnetic surveying should be discontinued during such days. Also, the IGRF value is removed from the magnetic data which is called "geomagnetic correction". After applying diurnal and geomagnetic corrections, the remaining magnetic field variations, called residual data or magnetic anomaly are caused by regional, remnant and anomaly variations. Regional variations can be removed from data, and remnant variation mostly has a small value and could be ignored as they are not typically as common as induced magnetization. Anomaly variations are referred to as magnetic anomalies (Telford et al., 1976; Kearey et al., 2002),

$$F = F_{IGRF} + F_{Anomaly} + F_{Remnant} + F_{Regional} \tag{3.14}$$

There are many methods for the processing of magnetic data such as "reduction to pole" (RTP; to transform dipolar magnetic anomalies to vertical dipolar anomalies which is symmetric and centred over their bodies), "upward and downward continuations" (to emphasize the effects of deep or shallow structures), "analytic signal" (another way to try to symmetrize the response directly over the source) and "Euler deconvolution" (to determine the depth to magnetic sources; Telford et al., 1976; Reid et al. 1990). Since these processing methods are not going to be used in this thesis, they are not described any further here.

The interpretation of magnetic data is similar to that of gravity data. But, there are a few

differences between them. Although, the gravity anomaly of a body is positive or negative (depending on more or less dense in comparison with its surroundings), the magnetic anomaly of a body contains mostly both positive and negative elements which arise from the dipolar nature of magnetism (Figure 3.11). Also, the different direction of magnetization in bodies with identical shape can causes different magnetic anomalies. Nowadays, inversion is considered as the main method for the interpretation of magnetic data.

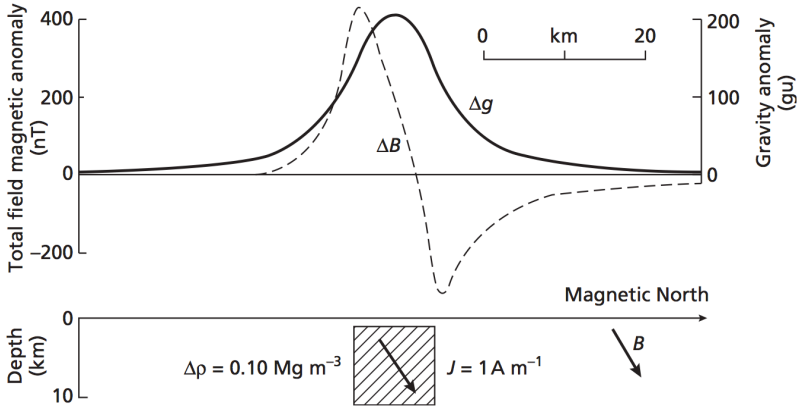


Figure 3.11: Gravity *(*Δ*g*) and magnetic *(*Δ*B*) anomalies over the same two-dimensional body (Kearey et al., 2002).

## 3.4 Seismic refraction method

Seismic methods are based on the laws of elastic wave propagation in the ground. This propagation of elastic waves is under the influence of mechanical properties (e.g. elasticity and hence seismic velocity as well as density) of the subsurface rocks. Using the travel times between the source and the receiver, we can determine the depth of different geological boundaries and the type of rocks. Seismic exploration is divided into refraction and reflection surveys. The seismic method is good for mapping the geological structures

using the difference in the seismic velocity of structures and materials (Telford et al. 1976; Sjörgen, 1984; Reynolds, 1997).

The seismic refraction method is based on the measurement of the travel time of refracted waves. One of the main applications of seismic refraction is for determining depth to bedrock. Seismic waves refract/bent by velocity gradient and velocity contrast across interfaces. Since velocity generally increases with depth, seismic energy is refracted back to the surface eventually. This can tell us about vertical and lateral variation in velocity, particularly sub-horizontal interfaces like the base of the overburden (Redpath, 1973; Okwueze; 1988; Lankston, 1990)

### 3.4.1 Seismic waves and ray paths

There are two groups of seismic waves, "body waves" (P and S) and "surface waves" (Love and Rayleigh). Due to the type of the source as well as the surface wave effect, body waves can have a higher frequency and velocity than surface waves. P (primary or compressional) wave, which is the fastest, moves particles in the direction of wave propagation. S (secondary or shear) waves move particles side-to-side perpendicular to the direction of wave propagation. S wave can only move through solid rock, not through any liquid medium. Love wave is the fastest surface wave moving the ground horizontally from side-to-side. A Rayleigh (or ground- roll) wave moves the ground up and down, and backwards-and-forwards in the same direction as the wave is moving similar to a wave rolls across a lake or an ocean. The P (or compressional) wave is mostly used for seismic exploration (Cerveny and Ravindra, 1971; Kearey et al., 2002)

In seismics, “wavefront” is defined as the location of all points at which the wave has reached at a particular time by contouring (joining together) all points corresponding to the same part of the wave. “Seismic rays” are everywhere perpendicular to wavefronts, and usually show direction in which energy is being transferred. Figure 3.12 shows Snell’s Law of Refraction,

$$\frac{sin\theta_1}{sin\theta_2} = \frac{v_1}{v_2} \tag{3.15}$$

where $v_1$ and $v_2$ are the seismic velocity of upper and lower layers, respectively. Also, if $v_2 > v_1$ then $\theta_2 > \theta_1$. Critical angle ($\theta_c$) is defined when the angle of refraction is 90°. In the refraction method, the critically refracted ray travels along the interface at the higher velocity $v_2$ (underlying layer) based on Huygen’s principle. Seismic energy returns to the surface by the “head wave” (Figure 3.13). Rays can bend if there is a gradual change in the velocity.

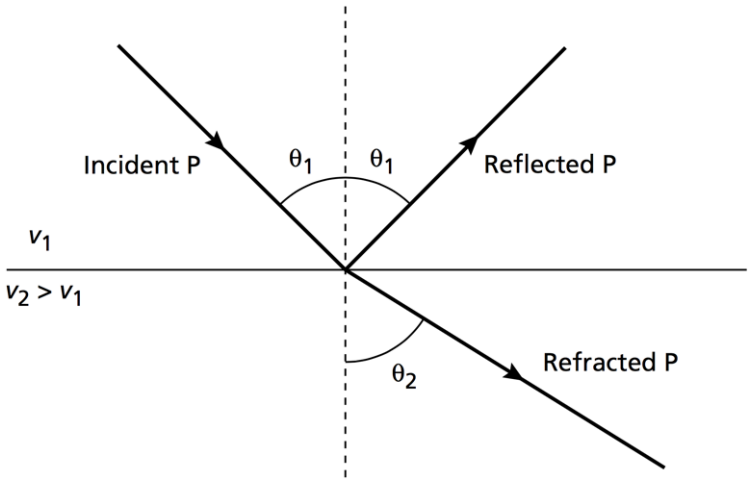


Figure 3.12: Reflected and refracted P-wave rays at an interface between two layers of differing seismic velocity (Kearey et al., 2002).

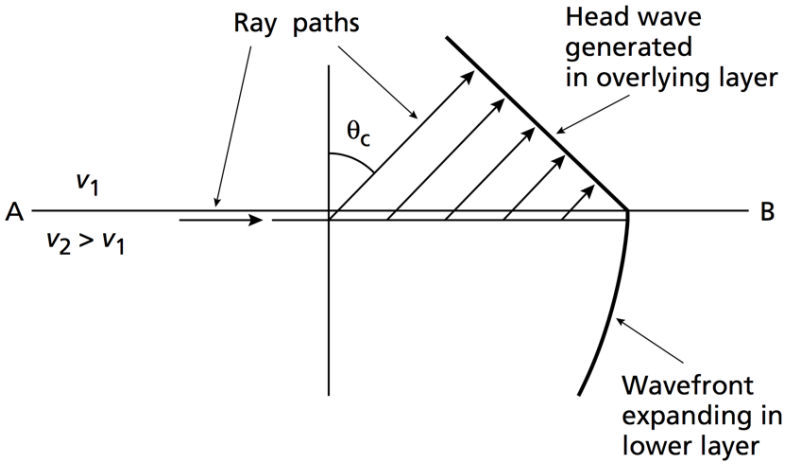

Figure 3.13: Generation of a head wave (Kearey et al., 2002).

### 3.4.2 Practicalities of seismic surveying

The ideal seismic source signal would produce a spike as it has high energy, and a nice and localized in time, which would make interpretation much easier (for picking arrival times). Seismic sources can be categorized into two main groups, explosive sources and non-explosive sources. Vibroseis, shotguns, rifles, weight drops and hammers are a few samples of non- explosive land sources. Air guns and water guns are used in marine surveys. Weight drops have a diversity from dropping a weight of several tonnes to a sledgehammer. They can be fast and efficient especially for refraction seismic surveying (Telford et al. 1976; Reynolds, 1997; Kearey et al., 2002).

Geophones and hydrophones are devices to detect seismic motions on land and for marine surveys, respectively. In a geophone, a cylindrical coil is suspended from a spring close to a permanent magnet. The geophone is fixed by a spike base into the ground. Movement of the coil, due to the ground motion, in the magnetic field generates a voltage across the terminals of the coil. Vertical movements of P-waves and horizontal movement

of S-waves can be detected when the coil within the geophone is mounted vertically and horizontally, respectively. Hydrophones detect the passage of a P-wave using pressure changes. Hydrophones are fixed to a cable called a streamer. Two sheets of piezoelectric material generate a voltage difference between the opposite faces when subjected to mechanical bending due to pressure changes (Sheriff and Geldart, 1995).

Seismic refraction is generally applicable only where the seismic velocities of layers increase with depth. It can be applied in a wide range from engineering site investigation surveys (Redpath, 1973; Lim and Jones; 1989) to the study of the structure of the crust or the lithosphere (Bamford et al., 1978; Stoffa and Buhl, 1979; Wright et al., 1990). Refraction profiles should be about five times bigger than the depth of investigation (Telford et al. 1976; Kearey et al., 2002).

Consider a simple geological section as shown in Figure 3.14c ($v_2 > v_1$). There are three types of ray paths. The direct ray which travels through the top layer ($v_1$) from the source to the receiver along a straight line. The reflected ray, travelling at the speed of the top layer ($v_1$), reflects back from the interface through the top layer to the detector. The refracted ray goes down to the interface at velocity $v_1$, moves along the interface at the higher velocity $v_2$, and back up through the upper layer at $v_1$.

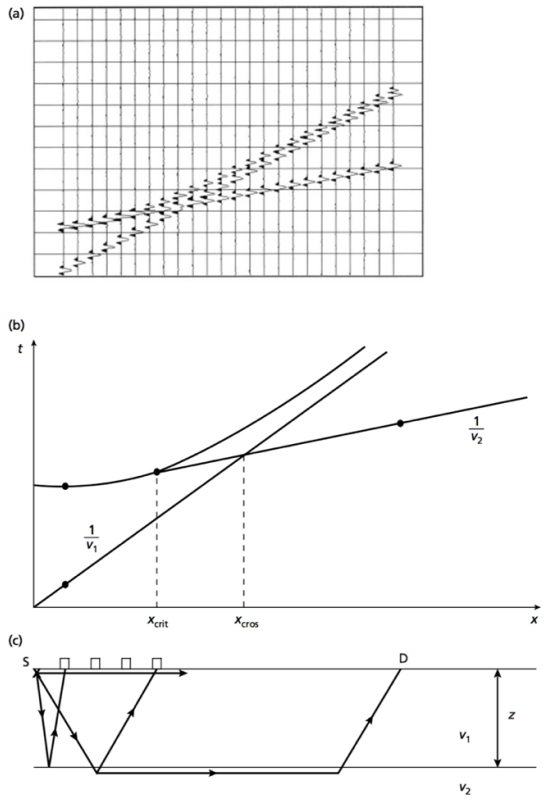


Figure 3.14: Top: Seismogram of traces along the Earth's surface as a function of time. Middle: Travel-time curves for direct, reflected and refracted rays. Bottom: Direct, reflected and refracted ray paths from a source to a receiver (Kearey et al., 2002).

According to Figure 3.14, before the crossover distance $x_{cros}$, the first arrival is a direct ray. Beyond this offset distance the first arrival is always a refracted ray. At the critical distance $x_{cros}$, the travel times of reflected rays and refracted rays coincide. The reflection from an interface at angles near the critical angle often leads to strong wide-angle reflections. These wide-angle reflections can be used for indicating the presence of a low-velocity layer which would not be revealed by refracted arrivals alone.

Figure 3.15 illustrates progressive positions of the wavefront for the first-arrival as well as the direct and refracted ray paths for a two-layer case with horizontal interface. The travel-time equation is given by:

$$t = \frac{x}{v_2} + \frac{2z(v_2^2 + v_1^2)^{1/2}}{v_1 v_2} = \frac{x}{v_2} + t_i \tag{3.16}$$

where $t_i$ is the intercept on the time axis of a travel-time plot and the straight line has a slope of $1/v_2$ (Figure 3.16). $v_1$ and $v_2$ can be obtained from the reciprocal of the gradient of travel-time plots, and the depth, $z$, can be determined from the intercept time $t_i$.

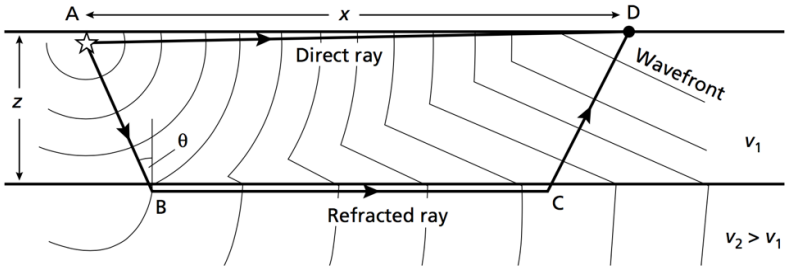


Figure 3.15: Positions of the wavefronts for direct and refracted waves (Kearey et al., 2002).

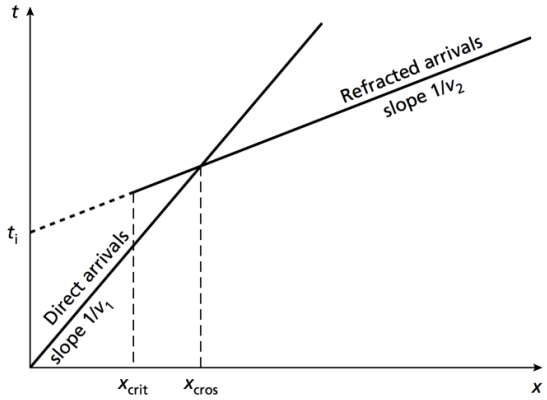


Figure 3.16: Travel-time curves for the direct and refracted waves from a two-layer model (Kearey et al., 2002).

### 3.4.3 Interpretation of seismic refraction data

In the refraction method, hidden layers produce head waves but no first arrivals may result

(Figure 3.17a). This may result from the thinness of the layer, or from the closeness of its velocity to the overlying layer. A blind layer results from a low-velocity layer (Figure 3.17b) (for example, a peat layer in muds and sands above bedrock) in which rays cannot be critically refracted. This leads to an overestimation of the depth to underlying interfaces (Domzalski, 1959; Kearey et al., 2002).

Figure 3.18 shows the traveltime–distance graphs for a few models. The data in Figure 3.18 illustrate two points: 1- "Parallelism" in which travel time graphs from the same interface, recorded in the same direction with different source locations, are parallel, meaning if the branches are not parallel, then the two arrivals at the relevant detectors did not come from the same layer; 2- "Reciprocal time ($T_{Recip}$)" in which the time to travel between two points is the same regardless of the direction of travel of the waves. Surface topography, subsurface irregularities, and anomalies within layers have effects on the traveltime-distance curve (Figure 3.19; Hauck and Kneisel, 2008).

There are several methods to determine subsurface structure from travel times such as (conventional) reciprocal method (CRM) (or plus–minus method) and generalized reciprocal method (GRM; Palmer, 1980; Derecke, 1981). Nowadays, inversion can be considered as one of the main approaches for interpretation (Zhang and Toksoz, 1998; Lelièvre et al., 2012).

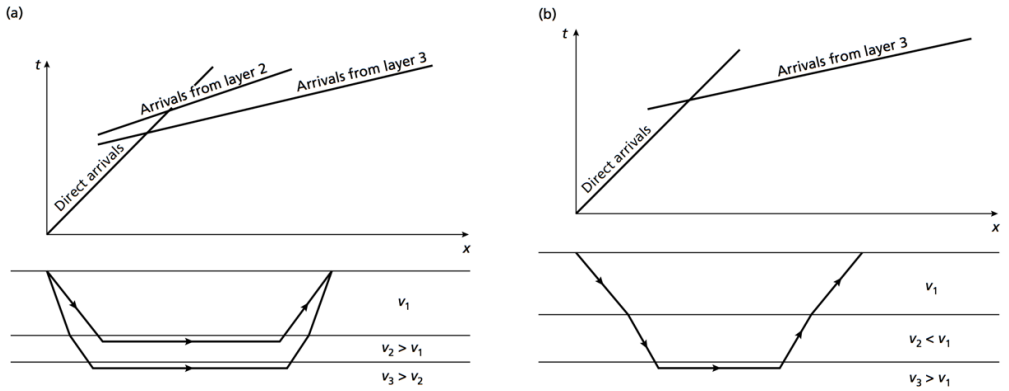


Figure 3.17: Left: hidden layer. Right: blind layer (Kearey et al., 2002).

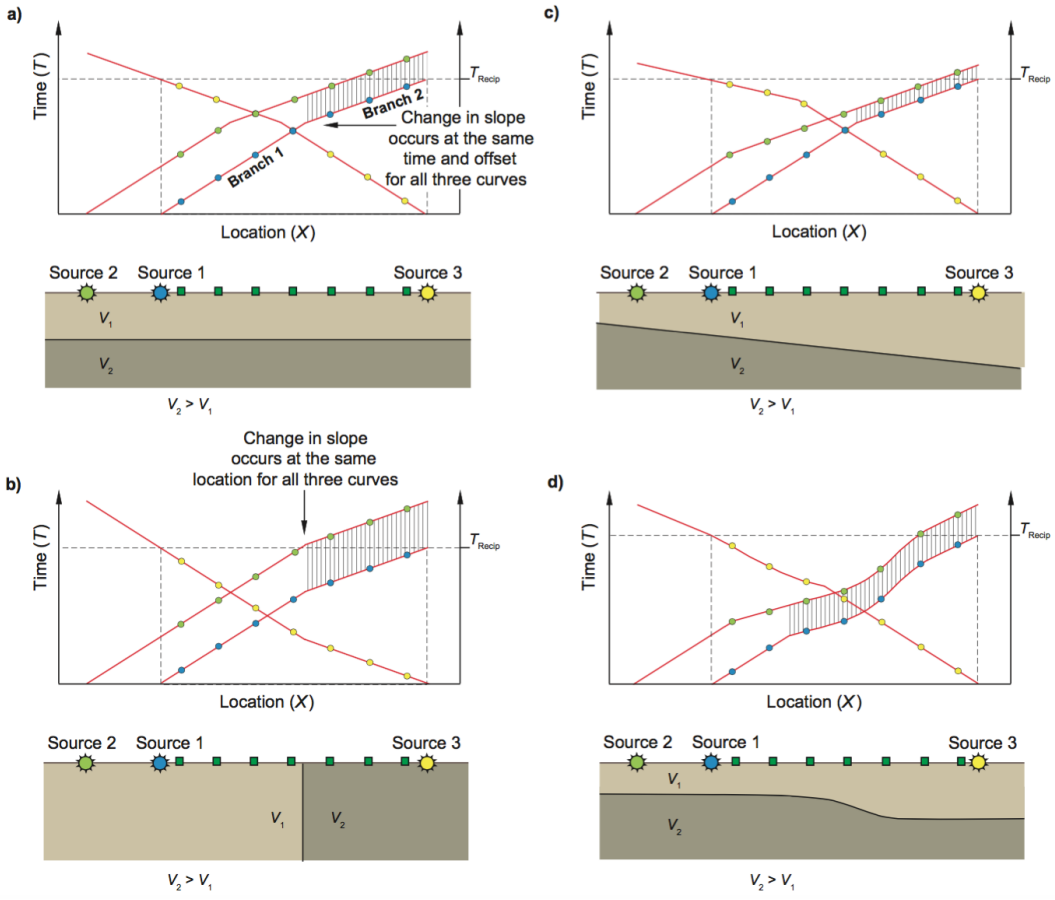


Figure 3.18: Time–distance (T–X) graphs produced by various subsurface velocity distributions. The vertical hatching indicates the locations where the T–X graphs for sources 1 and 2 are parallel. $T_{Recip}$: reciprocal time (modified after Reynolds, 1997).

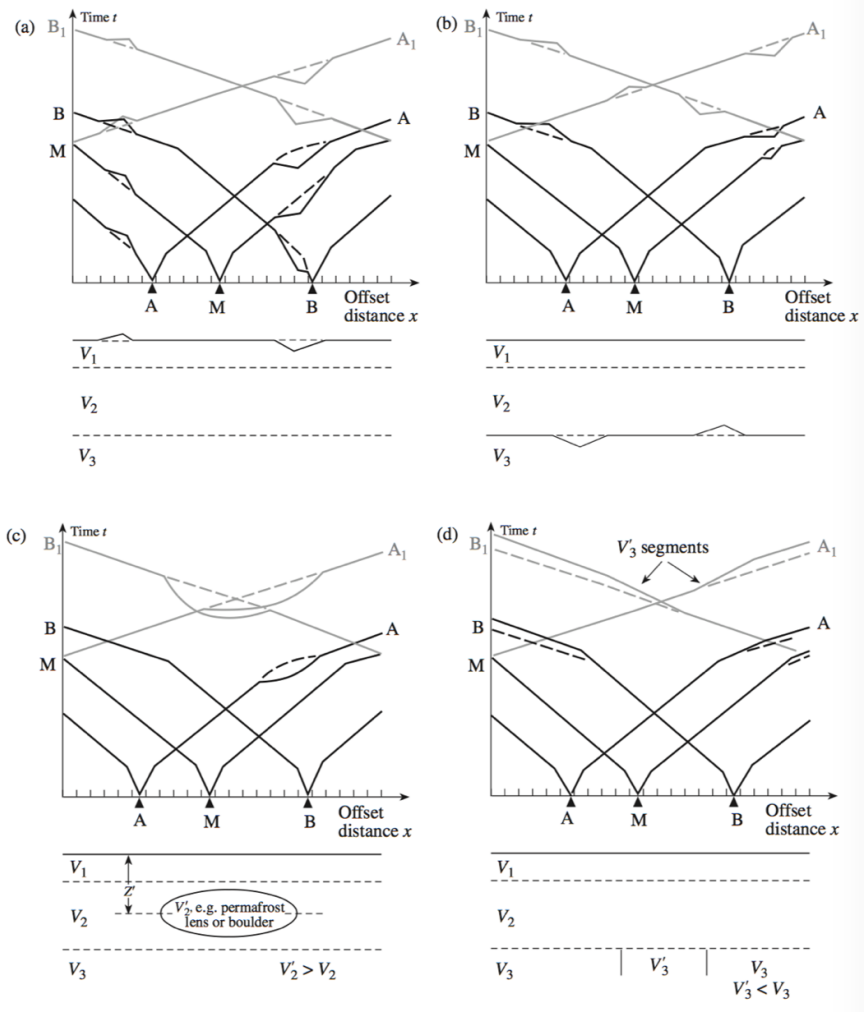


Figure 3.19: Examples of traveltime anomalies and their causes: the effect of the topography of Earth-air interface (a), the effect of the topography of refractor (b), the effect of a high-velocity mass within a layer (c) and the effect of the vertical low-velocity block in lower layers (d). Solid lines indicate traveltimes and dashed lines indicate regular traveltimes (Hauck and Kneisel, 2008).

## 3.5 Electromagnetic method

Electromagnetic (EM) geophysical methods can detect conductive structures in the ground. Some EM methods have a natural source such as the magnetotelluric method, while in the controlled source EM (CSEM) and ground penetrating radar (GPR) methods sources and

receivers are loops of wires. The CSEM method can be categorized into frequency-domain (FDEM) and time-domain (TDEM) electromagnetic methods.

### 3.5.1 Frequency-domain EM (FDEM)

In FDEM, a time-varying electric current flows through a transmitter coil (Figure 3.20). This current is varying sinusoidally with time at a particular frequency or set of frequencies (i.e., a very particular variation with time that's characteristic of the FDEM method). The current in the transmitter coil generates a magnetic field which penetrates the Earth. In the presence of a conductive body, time variations of the primary magnetic field induce an electromotive force (emf) within the conductor. The emf generates eddy currents in the conductive Earth, which then generate a secondary magnetic field. The resultant of the arriving primary and secondary fields in the receiver, according to phase and amplitude, is different from the primary field. The secondary magnetic field due to the eddy currents in the ground comprises components both in-phase and out-of-phase with the primary magnetic field because of the conductivity distribution in the subsurface.

In this research for FDEM, a helicopter-borne method (DIGHEM; Fraser, 1986; Cain, 2000) is applied for overburden stripping (Figure 3.21). There is no real DIGHEM data-set available in the uranium project, but the method will nevertheless be investigated as a possible means for overburden stripping (see Appendix E for the real DIGHEM data of Au project). DIGHEM typically uses five frequencies from 880Hz to 55840Hz with two coil configurations: coaxial (horizontal dipole; 5848Hz and 1082Hz) coil pairs and coplanar (vertical dipole; 880Hz, 7213Hz and 55840Hz) coil pairs (Figure 3.22). Coil separation

(between receiver and transmitter) is 8 m except for 55840Hz which is 6.3 m. Receiver and transmitter coils have a diameter of about half a metre. DIGHEM is suited to mapping the top 150m or so of the subsurface which makes it a good method for overburden stripping (Holladay and Lo, 1997; Hodges, 1999).

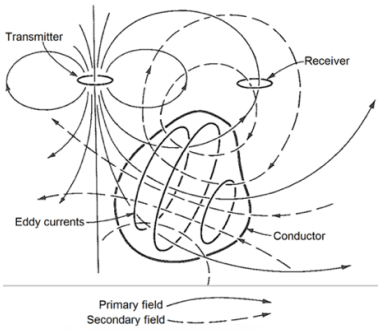


Figure 3.20: General principle of FDEM method (Grant and West, 1965).

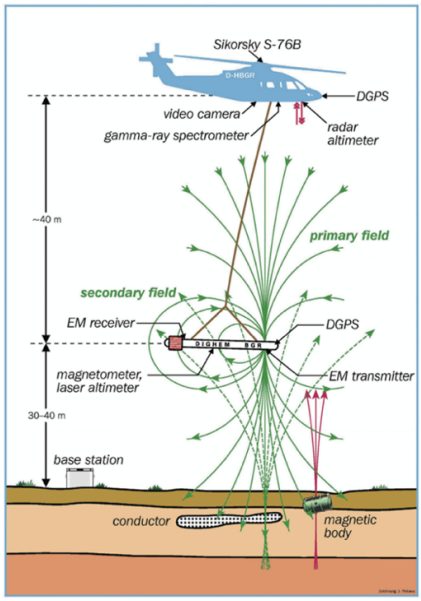


Figure 3.21: DIGHEM helicopter-borne geophysical system (adapted from BGR website).

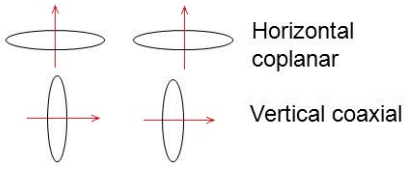


Figure 3.22: Loop configurations for DIGHEM.

### 3.5.2 Time-domain EM (TDEM)

If the transmitters be larger (i.e. bigger loop) and hence larger transmitter moment and deeper penetration into the subsurface, therefore a small secondary field can be measured. This can be done by the time-domain electromagnetic surveying (TDEM) method (sometimes called pulsed or transient-field EM; Figure 3.23) which measures the secondary field in the off time that allows for measuring much smaller secondary fields. The investigation depth for TDEM is more than for FDEM. In this method the primary field is not continuous but is a series of pulses which are separated by time intervals. During these intervals, when the primary field is absent, the secondary field is measured. Actually, eddy currents decay in the subsurface conductor during these intervals. Measurement of the rate of decay of the eddy currents can provide the information of the location and conductivity of anomalies. The observations can be values of voltage (i.e., dB/dt) or magnetic field (Nabighian and Macnae, 1991).

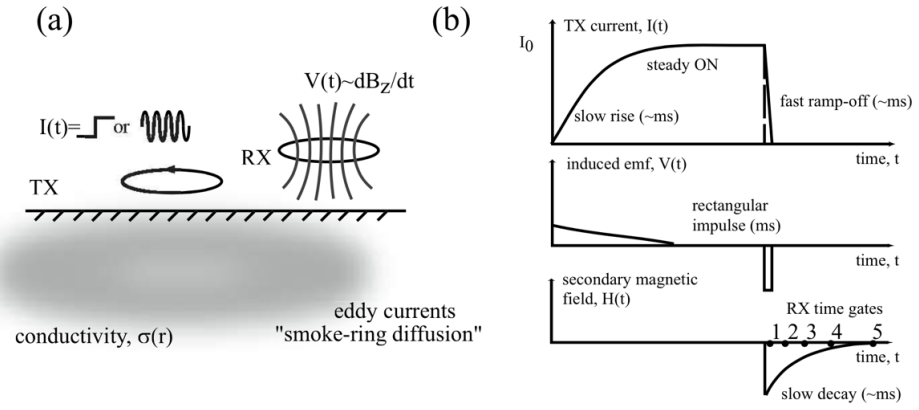


Figure 3.23: General principle of TDEM method (Everett and Meju, 2005).

In this research, for TDEM a helicopter-borne method (VTEM) is considered (Figure 3.24; Witherly et al., 2004; Witherly and Irvine, 2006). The standard VTEM system has a 13 m radius (vertical axis) with a 4 turn transmitter coil which can produce over 500,000 $Am^2$ of dipole-moment. The recent high power VTEM™35 system has a 17.5 m radius loop and 1,000,000 $Am^2$ dipole-moment that has increased the depth penetration (adapted from geotech.ca). The VTEM system measures a voltage that is proportional to the time derivative of the vertical magnetic field (dBz⁄dt) in 44 off-time channels.

Early time TDEM data can be suitable for shallow investigations in addition to deeper exploration (Legault et al., 2011). Early-time measurements in VTEM (early-channel closer to the transmitter current turn-off) from 20μs after the current turn-off (versus ~100μs for standard VTEM) led to improvements in the investigation of shallow structures. Thus, early-time VTEM can be a suitable method for overburden stripping if there is a good conductivity contrast.

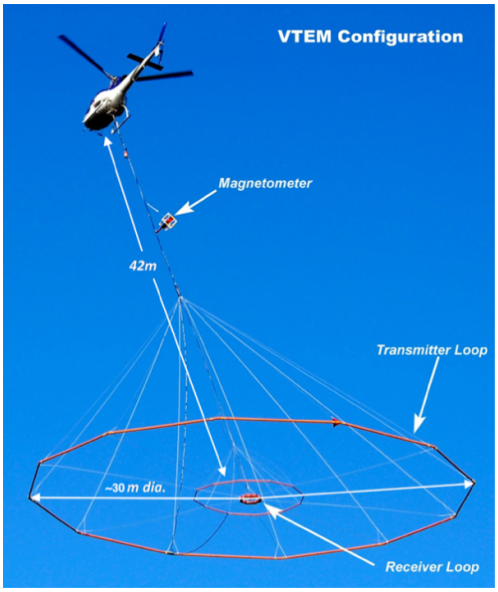

Figure 3.24: System for VTEM method (Geotech Ltd., 2013).

## 3.6 Previous geophysical studies for mineral exploration in the Athabasca Basin

Exploration for uranium using geophysical methods can be classified into direct and indirect methods. Direct methods can directly detect the zone of uranium mineralization, such as radiometry that is used for defining areas with radioactive minerals such as K, U and Th. The problem is that the direct methods are only effective for shallow deposits. Indirect methods look for structures which host the uranium deposits, for example, the gravity method can potentially detect the alteration zones. Electromagnetic (EM) methods can locate graphitic faults. Seismic can image the unconformity and the basement faults. Magnetic data can delineate basement structures.

Regional airborne geophysical methods (such as airborne radiometry, airborne EM, aeromagnetic and airborne gravity surveys) are initial and reconnaissance methods in order to define areas of potential uranium mineralization. Then, ground geophysical surveys, such as electrical and EM, gravity, magnetic, seismic and radiometry, are used in order to explore for the mineralization zones with greater accuracy.

### 3.6.1 Airborne radiometry

The radiometric, or gamma-ray spectrometry, method is a geophysical technique to estimate concentrations of the radioelements potassium, uranium and thorium by measuring the gamma-rays which the radioactive isotopes of these elements emit during radioactive decay.

Airborne radiometric data cover the entire Athabasca Basin. These data reveal the presence of radioactive minerals in the upper few metres of the subsurface (Milsom, 1989). Note that most near surface material has been transported by the glaciation (Campbell et al., 2002). The regional radiometry data are shown in Figure 3.25. It can be seen that these maps do not show a good correlation with the location of uranium deposits located at the eastern part. Thus, this method is mostly used as a reconnaissance exploration.

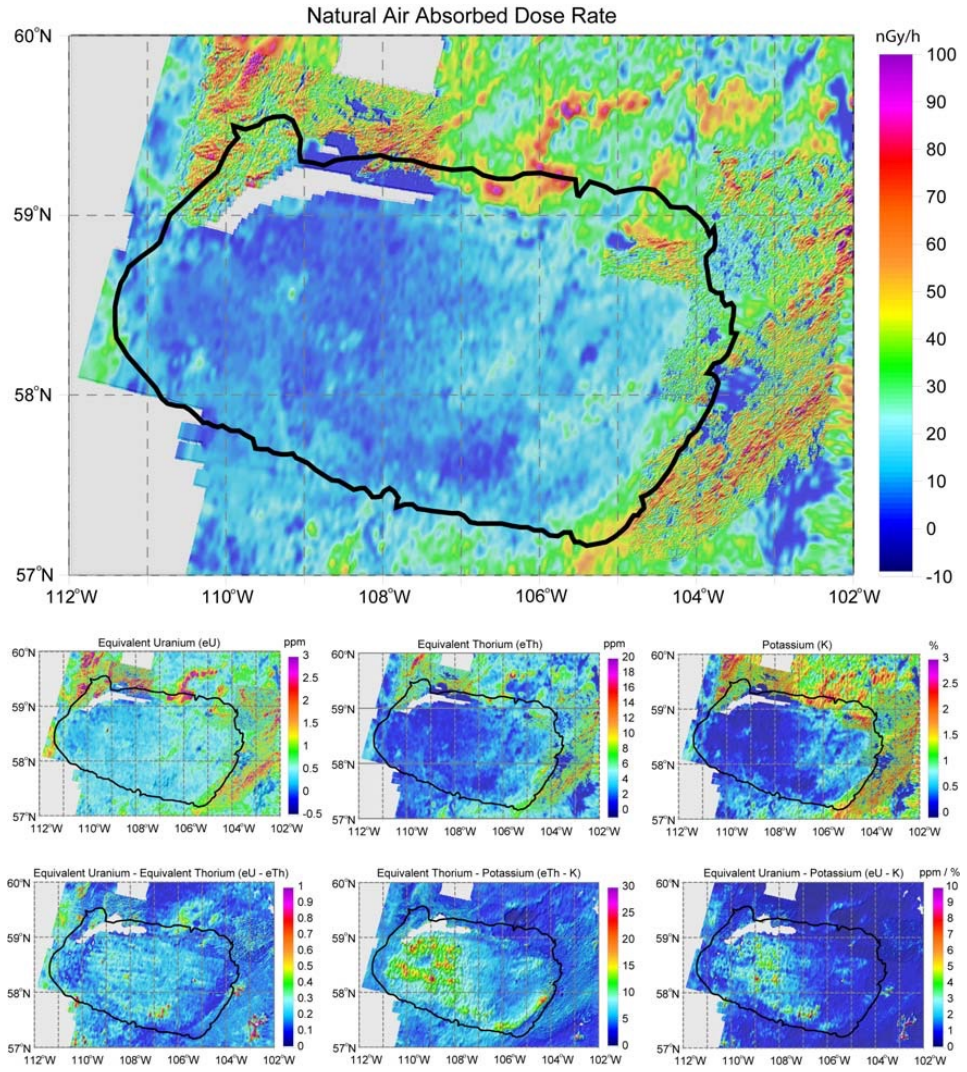


Figure 3.25: Regional radiometry data from the Athabasca Basin. Black line shows the limit of the Basin (Tuncer et al., 2006a).

### 3.6.2 Seismic imaging

As mentioned before (Section 2.5.1), seismic (reflection) data cannot distinguish between different members of the Manitou Falls formation nor the signature of the uranium ore-body itself, but the unconformity and fault zones are well imaged (Juhojuotti et al., 2012). In Figure 3.26, the reflections are vague in the vicinity of the ore-body and are interpreted as a hydrothermal alteration zone. Apparently, there are significant time delays in the unconformity reflections due to variable overburden. Accurate refraction static corrections are essential to correct for these effects. This refraction data can be used to determine the thickness of the overburden as well. Also, seismic data can map the depth of the basement and other regional features such as the Moho (White et al., 2007). Note that the seismic sections need constraints from drilling to relate them to the geological structures.

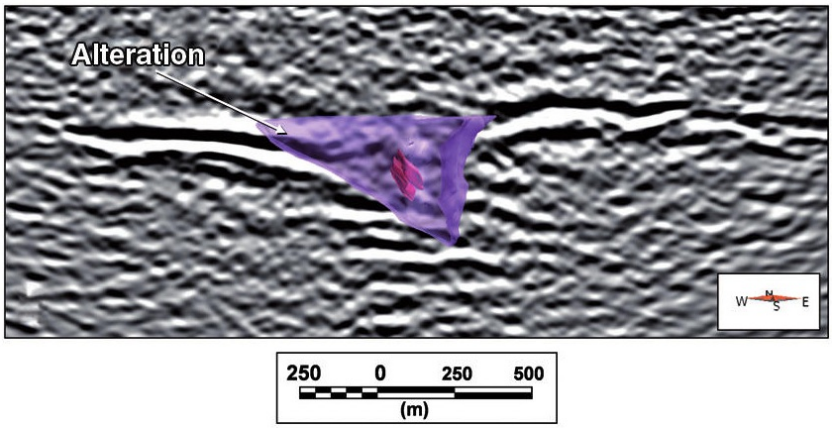


Figure 3.26: Vertical depth section of Millennium site showing the unconformity surface and the alteration zone in the vicinity of the orebody; seismic image in the background (Juhojuotti et al., 2012).

### 3.6.3 Magnetic studies

Regional aeromagnetic coverage delineates the basement structures such as fault systems and alteration features (Matthews et al., 1997). Most of the uranium deposits are located in the magnetic low trends (blue colors) in the eastern Athabasca Basin, which is coincident with the boundary of the Mudjatik and Wollaston domains (Figure 3.27).

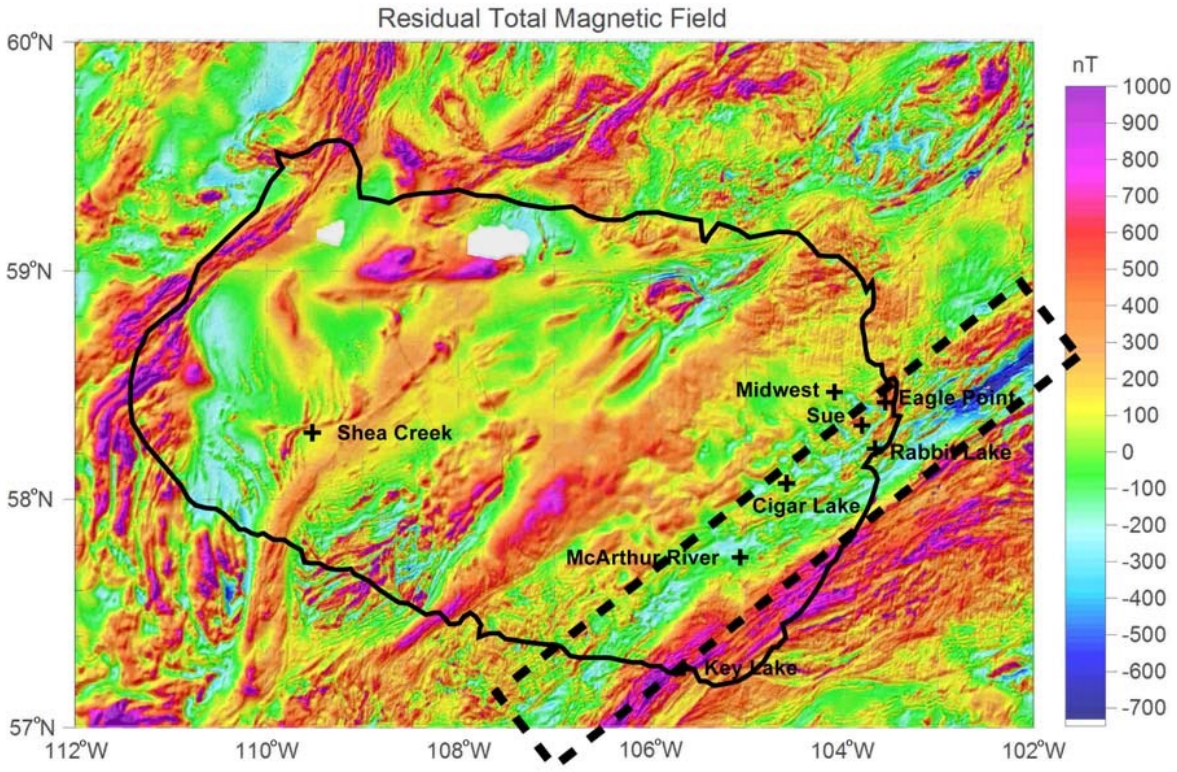


Figure 3.27: Total residual magnetic field in the Athabasca Basin. Dashed line shows one of the magnetic low trends interpreted as the Wollaston Domain–Mudjatik Domain transition zone (Matthews et al., 1997)

Thomas and McHardy (2007) mention that the magnetic lows near the McArthur River deposit are associated with pelitic - psammopelitic gneiss and lesser quartzite, intermediate levels with psammatic gneiss and highs with granitoid units. Although the magnetic low

can often determine structures related to the uranium deposits, it is not able to directly detect the uranium deposit or locate graphitic faults. Thomas and Wood (2007) modelled a 2D magnetic susceptibility structure along a profile (B-B') close to the McArthur area using magnetic data (Figures 3.28 and 3.29). For the forward modelling, they got help from seismic reflection images to shape the blocks in the basement. To fit the data, the appropriate magnetic susceptibilities are given to these blocks using drill-hole data. Overburden and sandstone are considered as non-magnetic in this modelling. Figure 3.29 shows that different blocks in the basement such as granitoid rocks, psammitic gneiss and pelitic gneiss have a wide range of magnetic susceptibility from $0.1\times10^{-3}$ SI (for pelitic gneiss) to $23\times10^{-3}$ SI (for high-susceptibility granitoid rocks)

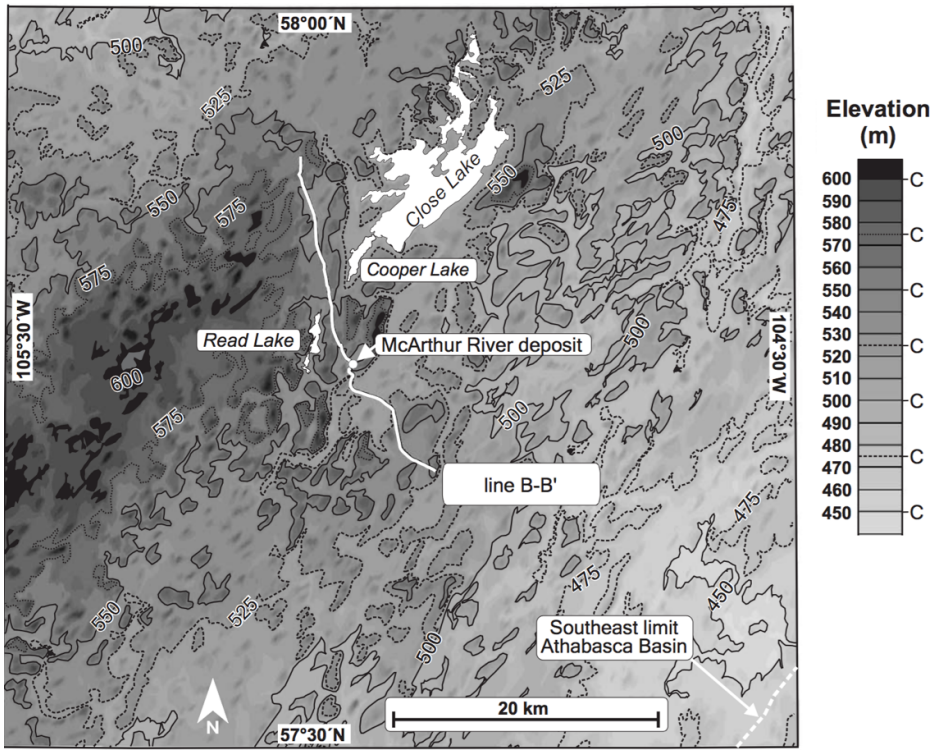


Figure 3.28: Topography map of region around the survey line B-B' (Thomas and Wood, 2007).

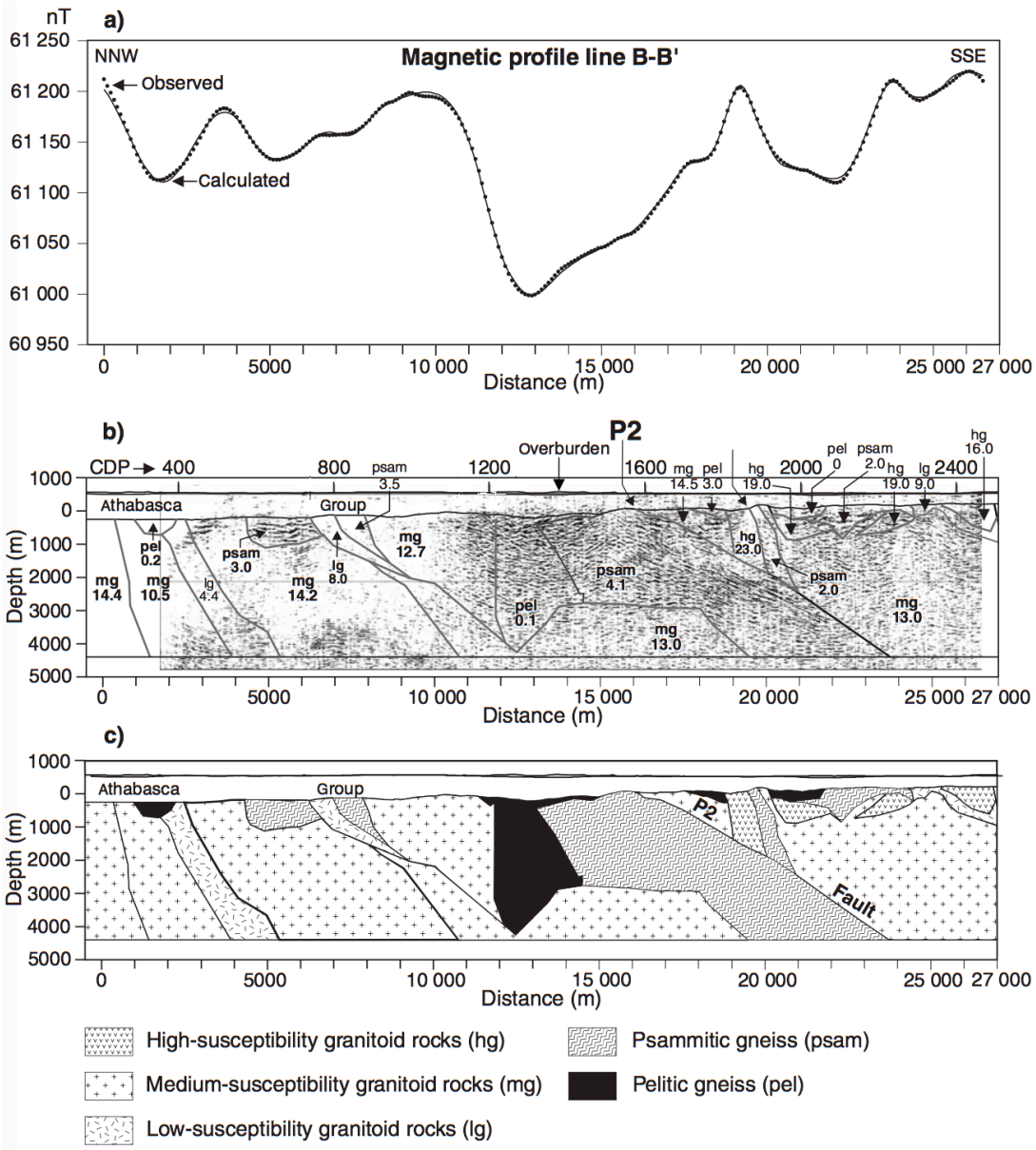


Figure 3.29: Geological section interpreted from a) magnetic profile along B-B'. b) Section illustrating boundaries of interpreted geological units and seismic reflection image. Magnetic susceptibilities ($\times 10^{-3}$ SI) of units are indicated; P2 is location of P2 fault. c) Patterned geological section. High-, medium-, and low-susceptibility granitoid rocks show arbitrary subdivision of interpreted granitoid units based on relative magnetic susceptibility (Thomas and Wood, 2007).

There has not been a detailed, comprehensive study of the overburden signature in the magnetic data in the Athabasca Basin, but similar research has been done for another area in Canada, namely, Quaternary glacial paleo-channels infilled by fluvial sediment in the Western Canadian Sedimentary Basin (WCSB). The resulting data indicates that the sediments have higher susceptibility values (0.2-0.8 $\times 10^{-3}$ SI) than the underlying bedrock (0.05-0.4 $\times 10^{-3}$ SI). The high susceptibility value of tills results from Canadian Shield-derived igneous and metamorphic rock materials. An aeromagnetic survey was done using the HELI-TRIAX system with a sensor height of 30m and a flight line spacing of 50 m. After data processing, it can be seen that several magnetic anomalies with a pattern of drainage are clearly imaged (Figure 3.30; Davies et al., 2004).

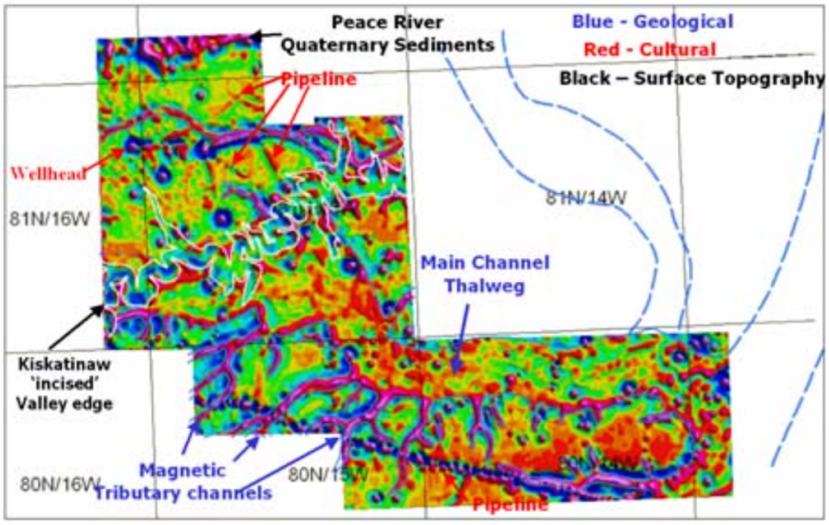


Figure 3.30: Residual HELI-TRIAX total magnetic intensity with interpretation (Davies et al., 2004).

### 3.6.4 Gravity exploration

Regional gravity data have been used to map the basement structures in the Athabasca

Basin with average data spacing ranging from 5 to 10 km (Figure 3.31). An average overburden density of 2.1 g/cc was used for the Bouguer correction (see Section 3.2.3; Matthews et al. 1997). The Bouguer anomaly is dominated by variations in the basement densities. The high values are associated with granulite facies metamorphic rocks and metamorphic terranes. The low values are often correlated with amphibolite facies terranes, in part retrograde granulites (Matthews et al., 1997).

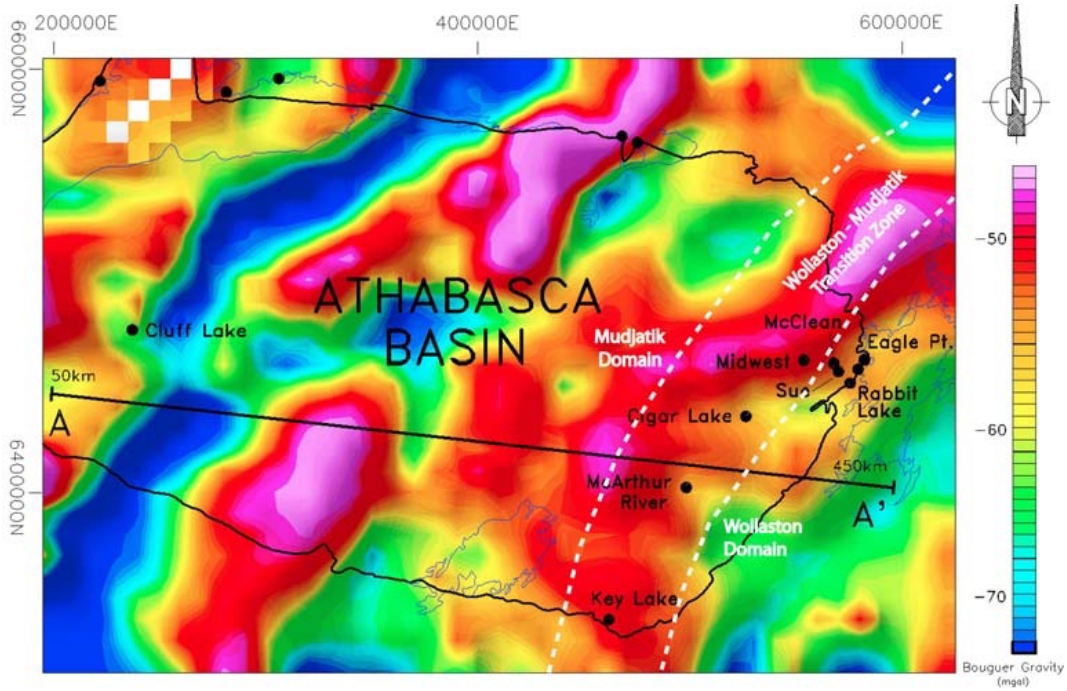


Figure 3.31: Corrected Bouguer gravity anomaly map for the Athabasca Basin. Black line shows the limit of Athabasca Basin (Matthews et al., 1997).

A high resolution ground gravity data-set was modelled along a profile (B-B') by Wood and Thomas (2002) using forward modelling (Figure 3.32). The Bouguer anomaly was computed with a density of 2 g/cc. The Bouguer anomaly data show a variation of less than 3 mGal along the profile. Short wavelengths less than 500m and intermediate wavelengths (500–1800 m) belong to the overburden and alteration zones, respectively. Zones of

alteration are anticipated to give gravity lows in the range 0.4 – 1 mGal. Desilicification decreases the density and gives a small negative Bouguer anomaly, whereas silicification increases the density and gives a small positive Bouguer anomaly (see Section 2.5.2). Sandstone, silicification and desilicification have a density of 2.42 g/cc, 2.47 g/cc and 2.39 g/cc, respectively. Long wavelength components (>2500 m) in the range 0.5 - 1 mGal are due to the deeper structures such as variations in the basement densities. The density of different blocks in the basement has a range from 2.65 g/cc (for quartzite) to 2.77 g/cc (for pelitic gneiss).

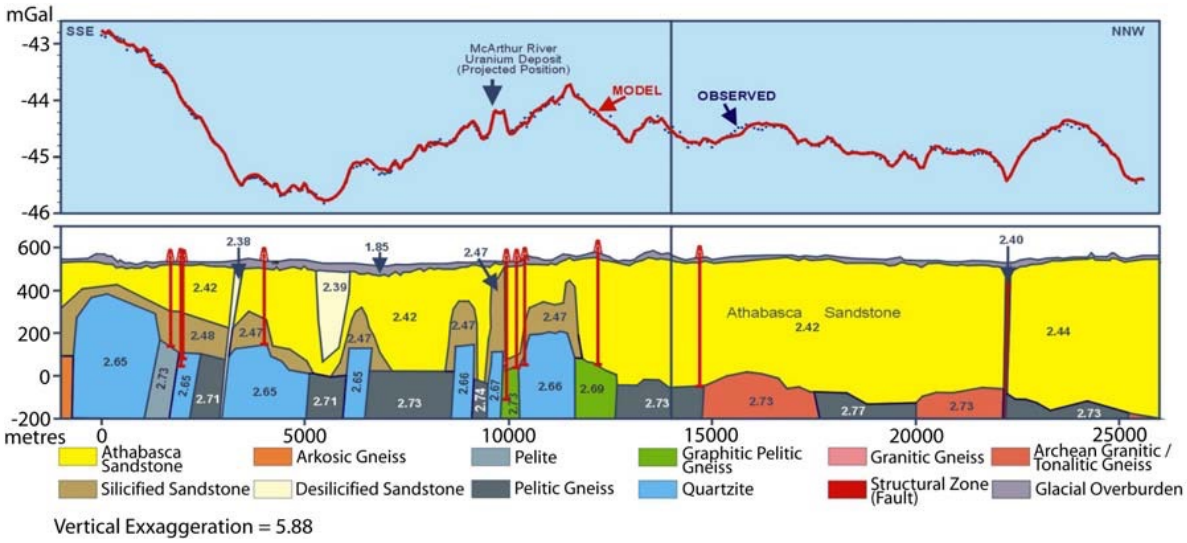


Figure 3.32: Observed and modelled gravity profiles along the high-resolution gravity profile (the same profile shown in Figure 3.28) at McArthur area (Wood and Thomas, 2002). Densities (g/cc) of modelled geological units are indicated.

A better modelling (Figure 3.33) is done on another high resolution ground gravity data-set by Thomas and Wood (2007) along the profile B-B' shown in Figure 3.28. Modelling was started by assigning densities to all blocks shown in Figure 3.29. Psammitic gneiss and granitoid pelitic gneiss units were assigned a density of 2.67 g/cc, 2.67 g/cc and 2.71 g/cc,

respectively. Also, densities of 2.46 g/cc, 2.48 g/cc, 2.52 g/cc, and 2.60 g/cc were assigned to the MFd, MFc, MFb, and RD members, respectively. In the next step, the inversion is applied to seek the best match between the observed and modelled profiles. As shown in Figure 3.33, the inverted densities for granitoid units varies within the range 2.634–2.682 g/cc, which is compatible with values for Archean and Proterozoic granitoid rocks. Also, inverted densities for psammitic gneiss and pelitic gneiss units range from 2.640 g/cc to 2.689 g/cc and from 2.674 g/cc to 2.875 g/cc, respectively. There is a good match between calculated densities and drill-hole data.

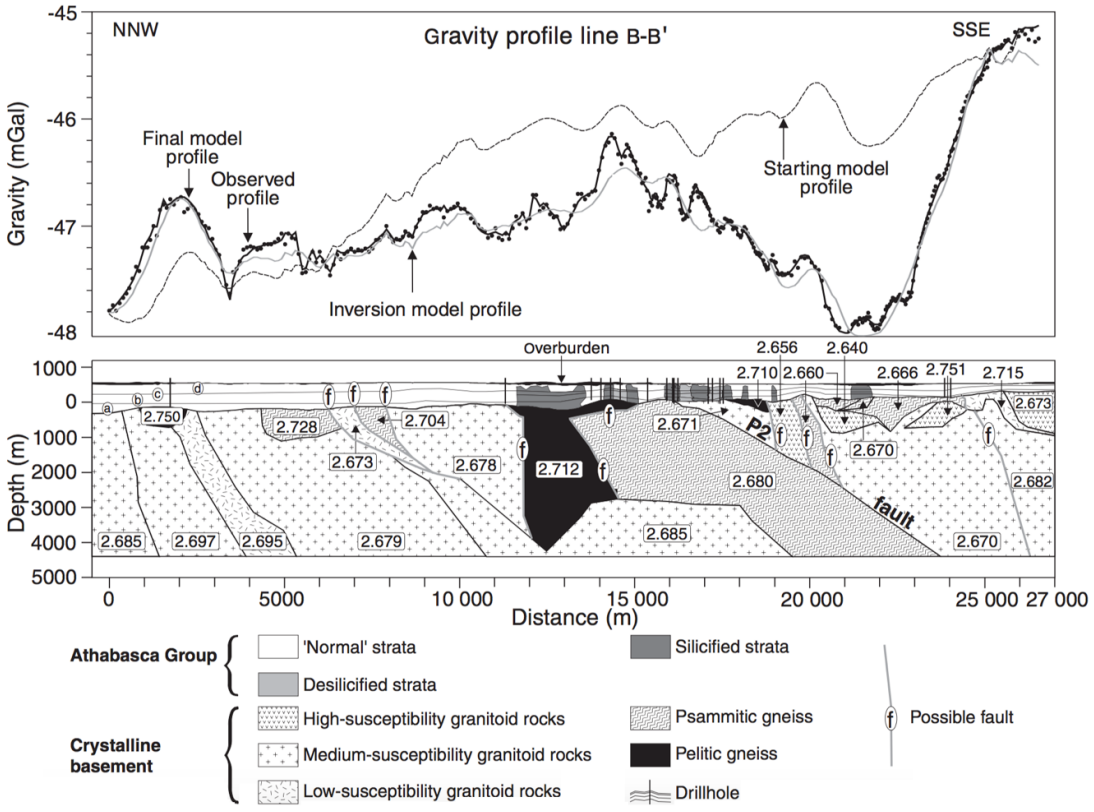


Figure 3.33: Gravity model along profile B-B' shown Figure 3.28 using inversion method by considering the basement subdivisions which are based on the magnetic model shown in Figure 3.29. Densities (g/cc) of units are indicated by numbers in boxes (Thomas and Wood, 2007).

### 3.6.5 Electromagnetic studies

As mentioned before, uranium deposits are often found in the vicinity of graphite in the Athabasca Basin (Jefferson et al., 2007). Graphite is considered as an electrical conductor which can easily be detected using EM methods. Figure 3.34 shows a smooth model 1D inversion of ground EM data (the in-loop data from Step Loop) in the Athabasca Basin (but not McArthur area; Powell et al., 2006). The unconformity is well resolved in a depth of 175 m. A large conductive body (< 200 Ohm-m) with hints of a steeply dipping fault represents the lower Wollaston Group which contain the graphitic conductors.

Figure 3.35 shows a vertical section of electrical resistivity in the Athabasca Basin (but not McArthur area) determined from airborne time domain MEGATEM data (Irvine and Witherly, 2006). The sandstone and the basement are associated with high values of electrical resistivity. Silicified zones and desilicified zones have relatively high resistivities (due to the silica content in pore spaces) and low resistivities (due to the clay content in the pore space), respectively. The overburden has mostly low resistivity in the Athabasca Basin, because of the deposit compositions and/or the presence of penetrated water and lake waters. In some regions in the Athabasca Basin, therefore, the overburden can be investigated using EM methods. In Figure 3.34, the overburden can be seen as a narrow conductive shallow layer along the vertical section represented by green color.

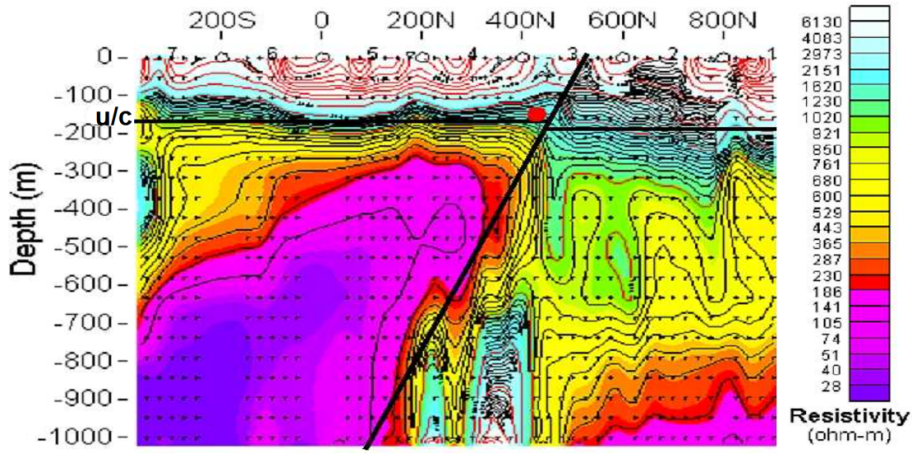


Figure 3.34: Resistivity model of the 1D inversion of ground (Step Loop) EM data in the Athabasca Basin. The location of mineralization is shown in a red circle (Powell et al., 2006).

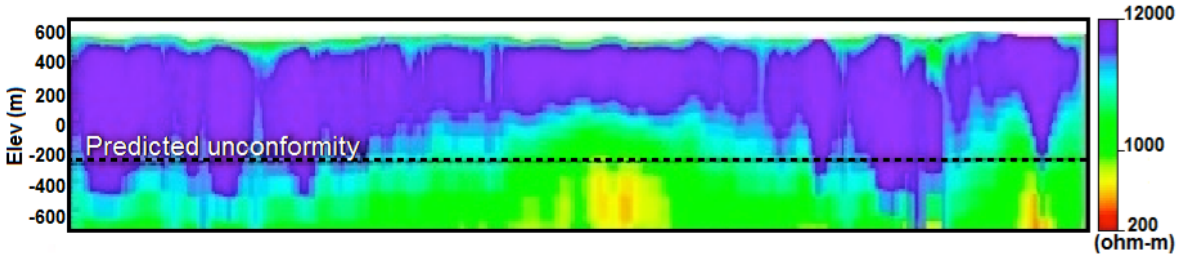


Figure 3.35: Resistivity depth section along a profile in the Athabasca Basin (Irvine and Witherly, 2006).

## 3.7 Conclusions

Geophysical methods can help to reveal the subsurface structures. A few of them such as gravity, magnetic, seismic refraction and electromagnetic methods are explained in this chapter. These methods are used in this research for the overburden stripping. Gravity method is the response of density of geological structures. But, before any interpretation the reduction should be done on the data. The corrected data can be end up in two types of data: free-air data or Bouguer data. Magnetic method is the response of magnetic

susceptibility of geological structures. Geomagnetic correction, which is subtracting the IGRF's value, as well as diurnal variation correction, which is subtracting the diurnal variations, should be applied on the magnetic data before the interpretation.

The seismic refraction method measures the travel time of refracted waves in order to determine the depth of different geological boundaries and the type of rocks. This method works when by increasing the depth, the seismic velocity of the geological structures is increasing. There are several methods for the interpretation of seismic data such as (conventional) reciprocal method (CRM; or plus–minus method), generalized reciprocal method (GRM) and inversion method. EM method includes the response of the conductive structures in the ground. In the controlled source EM (CSEM) method, magnetic fields (or electrical currents) flowing in the subsurface generates electromotive force (emf) in the conductive body. emf generates a secondary magnetic field which can be detected by receivers. The CSEM method is divided into two frequency domain (FDEM) and time domain (TDEM) methods.

# Chapter 4

# Forward Modelling and Inverse Theory

## 4.1 Introduction

The basic concept of the forward theory is a mathematical solution for obtaining the calculated data from the model parameters. Forward modelling is applied for different geophysical methods to synthetize the data. Also, in this research the inversion method will be applied on both synthetic and real data to reconstruct the geological structures from different observed data such as seismic refraction, gravity, magnetic and electromagnetic data. Therefore, the basic concept of the inverse theory will be introduced in this chapter as it is a mathematical process of estimating the values of model parameters from a set of observed data (see Appendix C for a simple example of linear gravity inversion). In this research, the latest-and-greatest modelling and inversion methods and codes are used (it is not just the same old methods and codes). Hence, conclusions from all the synthetic modelling studies could well be different (more successful) from what people might expect using old technology.

In this chapter, the theory of the forward modelling of gravity, magnetic, first-arrival seismic traveltime and electromagnetic methods will be explained. The methods used for

gravity and magnetics are based on analytical solutions while the methods for first-arrival seismic traveltime and electromagnetics are based on the numerical methods (finite difference and finite element). Subsequently, the minimum-structure approach for inverse, which is the approach used in this thesis, will be discussed.

## 4.2 Gravity and magnetic forward modelling

In this research, 2D and 3D gravity and magnetic data were synthesized using the forward modelling code of Lelièvre et al. (2011). The analytical solution is used for the forward modeling based on the unstructured tetrahedral meshes using a method presented by Okabe (1979). Okabe develops the analytical expressions for the derivatives of the gravitational potential in an arbitrary direction due to a polyhedral body composed of polygonal facets using the divergence theory. Gravity and magnetic anomalies are similar in the forward modelling expressions. Also, the magnetic potential due to a magnetized body can be directly derived from the first derivative of the gravitational potential in a given direction (Okabe, 1979). Here, I will simply and initially describe this method for a 2D case on a triangular mesh (see Appendix B for Fortran code). And then it will be briefly expanded for a 3D case.

Okabe (1979) applies the divergence theorem for 2-D polygonal and 3-D polyhedral bodies to gravity theory. He develops analytical expressions for gravity anomalies due to a homogeneous polyhedral body composed of polygonal facets. For a 2D case, in the 2D basic Cartesian system, $(p_0,q_0)$ and $(p,q)$ are considered as observation points and vertices points, respectively.

$z = p - p_0$ and $x = q - q_0$ (4.1)

In two dimensions, with due attention to Figure 4.1 for the i*th* edge in a coordinate rotation case we have

$$\begin{bmatrix} X \\ Z \end{bmatrix} = \begin{bmatrix} cos\psi & sin\psi \\ -sin\psi & cos\psi \end{bmatrix} \begin{bmatrix} x_0 \\ z_0 \end{bmatrix} \tag{4.2}$$

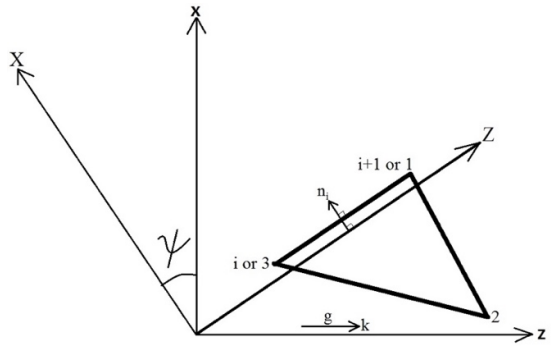


Figure 4.1: The edge rotation of the Cartesian system for calculating the *k*th component of the gravity due to a uniform triangular prism.

Finally, we have the forward modeling equation as

$$U_k = \rho\, G \sum_{i=1} \boldsymbol{k}^T \boldsymbol{n}_i \boldsymbol{I}_i \tag{4.3}$$

where

$$\boldsymbol{n}_i = \begin{bmatrix} -sin\psi \\ cos\psi \end{bmatrix} \tag{4.4}$$

is the direction vector specifying the outward normal on the i*th* edge. Note that $U_k$ in the gravity theory is the first derivative of potential in k-direction, and in the magnetic theory is the magnetic potential by assuming $\rho G$=1. In the gravity theory, $\boldsymbol{k}$ and $\boldsymbol{I}$ are the given direction of measurement. In the magnetic theory, $\boldsymbol{k}$ is the magnetic intensity vector for the

potential or given direction for the field, and $\boldsymbol{I}$ is the magnetic intensity vector for the field. Supposing that the vertices of the triangle are numbered clockwise, and the i*th* edge has two vertices *i* and *i*+1 (for the last edge, vertex *i*+1 corresponds to vertex 1), then we have

$$\boldsymbol{I}_i = [Z\ ln(Z^2 + X^2) + 2Xtan^{-1}\left(\frac{Z}{X}\right) - 2Z]_{Z_i}^{Z_{i+1}} \tag{4.5}$$

where the direction vector $\boldsymbol{k}^T$ (*T* means transverse) is

$$\boldsymbol{k}^T = (k_z, k_x) = [\cos(z,k), \cos(x,k)] = [1 \quad 0] \tag{4.6}$$

and

$$cos\psi = \frac{z_{i+1}-z_i}{\sqrt{(z_{i+1}+z_i)^2+(x_{i+1}+x_1)^2}} \tag{4.7}$$

and

$$sin\psi = \frac{x_{i+1}-x_i}{\sqrt{(z_{i+1}+z_i)^2+(x_{i+1}+x_1)^2}} \tag{4.8}$$

We should also consider the following conditions in solving the forward equation: 1) If in the first term of the $I_i$, $Z\ ln(Z^2 + X^2)$, $Z^2 + X^2$ converge to zero, thus the whole first term is equal to zero. 2) If $x = 0$, the second term of $I_i$, $2X\ tan^{-1}(Z/X)$ is equal to zero.

In three dimensions, with due attention to Figure 4.2, it is need to first rotate the x- and y-axes around the z-axis until the rotated x-direction is coincident with the projected direction of the outward normal onto the x-y plane. And then we rotate the z- and x- axes around the Y-axis until the rotated z-direction is coincident with the direction of the

outward normal. By these rotations we obtain the target system (X, Y, Z) which can be written as (Okabe, 1979):

$$\begin{bmatrix} X \\ Y \\ Z \end{bmatrix} = \begin{bmatrix} cos\phi & 0 & -sin\phi \\ 0 & 1 & 0 \\ sin\phi & 0 & cos\phi \end{bmatrix} \begin{bmatrix} cos\theta & sin\theta & 0 \\ -sin\theta & cos\theta & 0 \\ 0 & 0 & 1 \end{bmatrix} \begin{bmatrix} x \\ y \\ z \end{bmatrix} \tag{4.9}$$

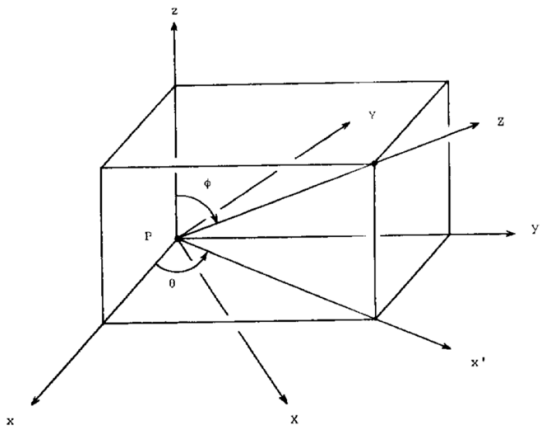


Figure 4.2: The surface rotation of the Cartesian system (Okabe, 1979).

where $0 \leq \theta < 2\pi$ and $0 \leq \phi \leq \pi$. Hence, the forward modelling equation can be written

$$U_k = \rho\, G \sum_i \sum_j \boldsymbol{k}^T \boldsymbol{n}_i \boldsymbol{J}_j(i) \tag{4.10}$$

where

$$\boldsymbol{n}_i = \begin{bmatrix} sin\phi\, cos\theta \\ sin\phi\, sin\theta \\ cos\phi \end{bmatrix} \tag{4.11}$$

is the direction vector specifying the outward normal on the i*th* facet. Supposing that the j*th* edge of the polygon has vertices *j* and *j*+1 (for the last edge, vertex *j*+1 corresponds to vertex 1), then we have (see, Okabe, 1979, for more information):

$$\boldsymbol{J}_j(i) = \left\{ (X\ sin\psi - Y\ cos\psi) \ln[X\ cos\psi + Y\ sin\psi + (X^2 + Y^2 + Z^2)^{\frac{1}{2}}] - \right.$$

$$\left. 2Z\ tan^{-1} \frac{(1+sin\psi)\left[Y+(X^2+Y^2+Z^2)^{\frac{1}{2}}\right]+X\ cos\psi}{Z\ cos\psi} \right\}_{(X_j,Y_j)}^{(X_{j+1},Y_{j+1})} \tag{4.12}$$

Note that these equations for a 3D case can give the solution for the magnetic potential by assuming $\rho G$=1 and regarding the direction vector $\boldsymbol{k}$ as the magnetic intensity vector. The gravity and magnetic theory can be treated in the same expressions. The contributions from all the cells in the model (each contribution computed using the appropriate formula above) are added up (superposition) to get the gravity or magnetic datum for the whole density or susceptibility model.

## 4.3 Modelling of first-arrival seismic traveltimes

The forward problem for the first-arrival seismic traveltimes is solved using the Fast Marching Method (FMM). FMM is a numerical method which is used for propagating first-arrival seismic wavefronts through a velocity distribution. In this method, first each cell in the mesh is assigned a constant slowness value. The solution starts by initializing the traveltimes at near-source nodes. This can be done by defining a radius for the source and calculating the traveltime at nodes within that radius (by assuming uniform slowness within this radius) by multiplication of the slowness by the distance from each node to the source (Lelièvre et al., 2011).

Figure 4.3 shows the FMM solution on a rectilinear grid after initialization stage. In this grid, nodes can be categorized into “upwind” or “downwind” nodes. Upwind nodes have firm traveltime values that can not be changed at later stages in the FMM solution. The downwind nodes can also be categorized into “close” nodes which are connected to upwind nodes at which the traveltimes are calculated based on the traveltimes at their neighbouring upwind nodes, and “far” nodes which are not immediately connected to upwind nodes. For a close node, there can be several calculations due to the adjacent nodes. Actually, the FMM calculates first arrivals so the actual traveltime taken by a node is the minimum of all those calculated traveltimes coming from the local adjacent nodes. Thus, the close node with the smallest traveltime is chosen as an upwind node. Afterwards, the far nodes which are now connected to the new upwind node will be considered as the close nodes. The solution goes forward until all nodes have been visited, and have been considered as the upwind nodes (Lelièvre et al., 2011).

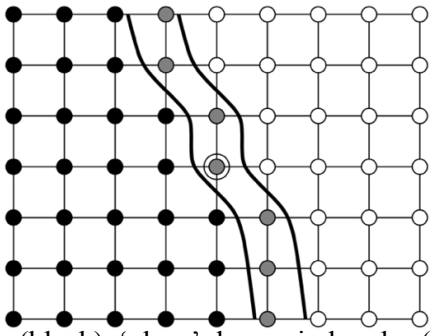

Figure 4.3: Upwind nodes (black), ‘close’ downwind nodes (grey) and ‘far’ downwind nodes (white) in a section of a rectilinear 2D grid through which an FMM solution is progressing. Thin connecting lines indicating the grid cells. Two parallel thick lines show the sides of a narrow band of ‘close’ nodes (Lelièvre et al., 2011).

The mathematical equations for the FMM method for a 2D mesh made up of triangular cells can be described using Figure 4.4. Suppose that the traveltimes at nodes $A$ and $B$ ($t_A$ and $t_B$) are calculated at previous stages in the FMM solution. Thus, the traveltime at node

$C$ ($t_C$) corresponding to a wave transmitted through the cell can be calculated using (Lelièvre et al., 2011)

$$t_C = t_A + u\xi_0 + wc^{-1}\rho_0 \tag{4.13}$$

with

$$w^2 = s^2c^2 - u^2 \tag{4.14}$$

where $u = t_B - t_A$, $c$ is the length of line $AB$, $s$ is the homogeneous slowness of the triangular cell, $\xi_0$ is the normalized projection of node $C$ onto line $AB$, and $\rho_0$ is the length of the normal from node $C$ to the point at $\xi_0$. However, traveltime $t_C$ could also be due to a head wave travelling along side $AC$ or $BC$. Therefore, in general we have

$$t_C = \min\left(t_A + u\xi_0 + wc^{-1}\rho_0 \ , \ t_A + sb \ , \ t_B + sa\right) \tag{4.15}$$

where $a$ is the length of line $BC$, and $b$ is the length of line $AC$.

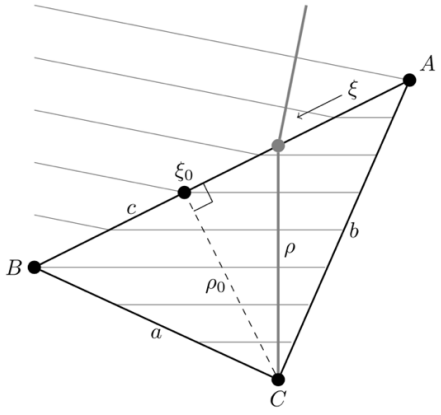


Figure 4.4: A geometrical scheme for the traveltime calculating procedure in triangular cell lies between three nodes A, B and C. A traversing ray hitting node C is drawn as a thick grey line perpendicular to the (linear) wavefronts which are drawn as thin grey lines (Lelièvre et al., 2011).

## 4.4 Electromagnetic modelling

Maxwell's equations are the fundamental equations of electromagnetic theory. For a conductive medium, they can be expressed as:

$$\nabla \times \boldsymbol{E} = -\frac{\partial \boldsymbol{B}}{\partial t} \qquad \text{Faraday's law} \qquad (4.16)$$

$$\nabla \times \boldsymbol{H} = \boldsymbol{J} - \frac{\partial \boldsymbol{D}}{\partial t} \qquad \text{Ampère's law} \qquad (4.17)$$

$$\nabla . \boldsymbol{B} = 0 \qquad \text{No-monopole law} \qquad (4.18)$$

$$\nabla . \boldsymbol{D} = q \qquad \text{Coulomb's law} \qquad (4.19)$$

where $\boldsymbol{E}$ [V/m] is the electric field intensity, $\boldsymbol{B}$ [Wb/m$^2$] is the magnetic induction, $\boldsymbol{H}$ [A/m] is the magnetic field intensity, $\boldsymbol{J}$ [A/m$^2$] is the current density, $\boldsymbol{D}$ [C/m$^2$] is the electric displacement, and $q$ [C/m$^3$] is the electric charge density. Faraday's law describes the generation of the electric field by a time-varying magnetic field. Ampere's law describes that the conduction and displacement currents are sources of the magnetic field. Coulomb's law states that $\boldsymbol{D}$ is produced by electric charge q, and can be monopolar in nature. No-monopole law states that $\boldsymbol{B}$ cannot be a monopole, and must be dipolar in nature (Fitterman and Lasbon, 2005).

For an isotropic medium, $\boldsymbol{E}$ and $\boldsymbol{H}$ are related to $\boldsymbol{D}$ and $\boldsymbol{B}$, and $\boldsymbol{J}$ and $\boldsymbol{E}$ are linked through the following equations

$$\boldsymbol{B} = \mu \boldsymbol{H}, \quad \boldsymbol{D} = \epsilon \boldsymbol{E} \quad \text{and} \quad \boldsymbol{J} = \sigma \boldsymbol{E} \qquad (4.20)$$

where $\mu$ [H/m] is the magnetic permeability, $\epsilon$ [F/m] is the electric permittivity, and $\sigma$ [S/m] is the electrical conductivity which is the main physical property in the EM method. In the earth, $\mu$, $\epsilon$ and $\sigma$ are variable, and describe the physical properties of the materials. Magnetic permeability and electric permittivity are

$$\mu = \mu_r \mu_0 \quad \text{and} \quad \epsilon = \epsilon_r \epsilon_0 \tag{4.21}$$

where $\mu_0 = 4\pi \times 10^{-7} \mathrm{H/m}$ is the magnetic permittivity of vacuum, and $\epsilon_0 = 8.85 \times 10^{-12} \mathrm{F/m}$ is the dielectric permittivity of vacuum. $\mu_r$ and $\epsilon_r$ are dimensionless multipliers. Relative permeability $\mu_r$ is the ratio of permeability of material to that of vacuum. Relative permittivity $\epsilon_r$ (also called dielectric constant) is the ratio of permittivity of material to that of vacuum.

The Fourier transform pair between time and frequency are as follows (Ward and Hohmann, 1988)

$$F(\omega) = \int_{-\infty}^{+\infty} f(t) e^{-i\omega t} dt \qquad \text{(time-domain to frequency-domain)} \tag{4.22}$$

$$f(t) = \frac{1}{2\pi} \int_{-\infty}^{+\infty} F(\omega) e^{i\omega t} d\omega \qquad \text{(frequency-domain to time-domain)} \tag{4.23}$$

where $i^2$=-1 and $\omega$ is the angular frequency. Faraday's and Ampère's laws can be transformed from the time-domain to the frequency-domain using the Fourier transform as

$$\boldsymbol{\nabla} \times \boldsymbol{E} = -i\omega \boldsymbol{B} \tag{4.24}$$

$$\boldsymbol{\nabla} \times \boldsymbol{H} = \boldsymbol{J} + i\omega \boldsymbol{D} \tag{4.25}$$

By taking the curl of the Faraday's and Ampere's laws we have "wave equations" which in the time-domain are given by

$$\boldsymbol{\nabla}\times\boldsymbol{\nabla}\times\boldsymbol{E} + \mu\boldsymbol{\nabla}\times\frac{\partial}{\partial t}\boldsymbol{H} = 0 \tag{4.26}$$

$$\boldsymbol{\nabla}\times\boldsymbol{\nabla}\times\boldsymbol{H} - \epsilon\boldsymbol{\nabla}\times\frac{\partial}{\partial t}\boldsymbol{E} = \sigma\nabla\times\boldsymbol{E} \tag{4.27}$$

Using the vector identity

$$\boldsymbol{\nabla}\times\boldsymbol{\nabla}\times\boldsymbol{T} = \boldsymbol{\nabla}(\boldsymbol{\nabla}.\boldsymbol{T}) - \boldsymbol{\nabla}^2\boldsymbol{T} \tag{4.28}$$

where $\boldsymbol{T}$ is a vector, and considering that in a homogeneous medium $\nabla.\mathrm{H} = 0$ and $\nabla.\mathrm{E} = 0$, the wave equations (in time-domain) will be as

$$\boldsymbol{\nabla}^2\boldsymbol{E} - \mu\epsilon\frac{\partial^2\boldsymbol{E}}{\partial^2 t} - \mu\sigma\frac{\partial\boldsymbol{E}}{\partial t} = 0 \tag{4.29}$$

$$\boldsymbol{\nabla}^2\boldsymbol{H} - \mu\epsilon\frac{\partial^2\boldsymbol{H}}{\partial^2 t} - \mu\sigma\frac{\partial\boldsymbol{H}}{\partial t} = 0 \tag{4.30}$$

These wave equations can be written in the frequency-domain as

$$\boldsymbol{\nabla}^2\boldsymbol{E} + (\mu\epsilon\omega^2 - i\mu\sigma\omega)\boldsymbol{E} = 0 \tag{4.31}$$

$$\boldsymbol{\nabla}^2\boldsymbol{H} + (\mu\epsilon\omega^2 - i\mu\sigma\omega)\boldsymbol{H} = 0 \tag{4.32}$$

These two equations are also known as Helmholtz equations for $\boldsymbol{E}$ and $\boldsymbol{H}$ fields. For common values of μ, ϵ and σ of earth materials, and for frequencies smaller than $10^5$ Hz (which is common in EM geophysical surveys except GPR), it can be seen that the

displacement current term ($\mu\epsilon\omega^2$) is much smaller than the conduction current term ($\mu\sigma\omega$). Therefore, displacement currents can be neglected. This assumption is called the "quasi-static approximation" in which the primary magnetic field in free space generated by a source loop of alternating current is in-phase with current; and the primary electric field is in quadrature with current, being generated by the time derivative of the magnetic field (West and Macnae, 1991). Therefore, wave equations can be transformed into

$$\boldsymbol{\nabla}^2\boldsymbol{E} - \mu\sigma\frac{\partial \boldsymbol{E}}{\partial t} = 0 \tag{4.33}$$

$$\boldsymbol{\nabla}^2\boldsymbol{H} - \mu\sigma\frac{\partial \boldsymbol{H}}{\partial t} = 0 \tag{4.34}$$

and

$$\boldsymbol{\nabla}^2\boldsymbol{E} - i\mu\sigma\omega\,\boldsymbol{E} = 0 \tag{4.35}$$

$$\boldsymbol{\nabla}^2\boldsymbol{H} - i\mu\sigma\omega\,\boldsymbol{H} = 0 \tag{4.36}$$

These equations are "diffusion equations" in homogeneous media. And,

$$k = \sqrt{-i\mu\sigma\omega} \tag{4.37}$$

where k [1/m] is "wavenumber". Actually, the propagation of the electromagnetic signals in the Earth is along with the diffusion. When the time-varying magnetic field penetrates into the ground, it induces an oscillating electric current. While this electric current flows, a part of energy is converted to heat which consequently it cannot be converted back into electric or magnetic fields. Thus, the amplitudes of the EM signals in a medium generally

decrease by a factor of 1/*e* over the distance δ which is known as the "skin depth" given by

$$\delta = \sqrt{\frac{2}{\omega\mu\sigma}} \approx \frac{500}{\sqrt{\sigma f}} \tag{4.38}$$

It can be seen that by increasing frequency and/or conductivity, the skin depth decreases. Therefore, a low conductivity or a low frequency is necessary for the deep imaging. Note that the skin depth is only truly applicable to plane waves. For a localized source, there is the additional geometric decay with distance from the source.

All the equations presented so far are based on the "direct EM-field formulation". In order to solve the electromagnetic problems more effectively, we can use the "potential method" in which a vector potential is used from which E and H can both be derived (Grant and West, 1965). The benefit is that the linear system of equations we end up having to solve is not as ill-conditioned. The problem can be formulated in terms of magnetic vector potential ($\boldsymbol{A}$) and electric scalar potential ($\phi$) rather than electric ($\boldsymbol{E}$) and magnetic ($\boldsymbol{H}$) fields. As a result of the no-monopole law and the Helmholtz equation, $\boldsymbol{B}$ can be considered as the curl of a vector potential $\boldsymbol{A}$. Thus, magnetic induction can be written as

$$\boldsymbol{B} = \nabla \times \boldsymbol{A} \tag{4.39}$$

Thus, by substituting this into Equation 4.16 in frequency-domain, we have

$$\nabla \times (\boldsymbol{E} + i\omega\boldsymbol{A}) = 0 \tag{4.40}$$

It can be seen that the curl of the vector ($\boldsymbol{E} + i\omega\boldsymbol{A}$) is equal to zero. If the curl of a vector is zero, the vector can be zero or equal to the gradient of a scalar function, as curl of a gradient of anything is zero. Since, the curl of a vector is equal to the negative gradient of a scalar potential ($-\boldsymbol{\nabla}\phi$), we have

$$\boldsymbol{E} = -i\omega\boldsymbol{A} - \boldsymbol{\nabla}\phi \tag{4.41}$$

The scalar and vector potentials are not unique, because any function whose curl is zero can be added to $\boldsymbol{A}$ without changing the value of $\boldsymbol{B}$. To keep the electric field unique, $\phi$ should be changed accordingly. These changes in the scalar and vector potentials are called "gauge transformations" (Griffiths, 1999). This freedom of choosing the values of the potentials can be exploited to adjust the divergence of $\boldsymbol{A}$ (i.e., gauge fixing). The simplest choice is a vanishing divergence:

$$\boldsymbol{\nabla}.\boldsymbol{A} = 0 \tag{4.42}$$

which is called the "Coulomb gauge" (Griffiths, 1999; Jahandari, 2015).

For controlled source EM (CSEM), the source can be incorporated using a current density. Thus, if we consider the current density of EM source ($\boldsymbol{J^s}$), Faraday's and Ampère's laws in the frequency domain can be rewritten as

$$\boldsymbol{\nabla}\times\boldsymbol{E} = -i\omega\boldsymbol{B} \tag{4.43}$$

$$\boldsymbol{\nabla}\times\boldsymbol{H} = \boldsymbol{J^s} + \sigma\boldsymbol{E} \tag{4.44}$$

Thus, the E-field Helmholtz equation will be as

$$\boldsymbol{\nabla}\times\boldsymbol{\nabla}\times\boldsymbol{E} + i\mu_0\sigma\omega\boldsymbol{E} = -i\mu_0\omega\boldsymbol{J^s} \tag{4.45}$$

Replacing $\boldsymbol{E}$ in Equation 4.41 into the E-field Helmholtz equation we have

$$\boldsymbol{\nabla}\times\boldsymbol{\nabla}\times\boldsymbol{A} + i\mu_0\sigma\omega\boldsymbol{A} + \mu_0\sigma\boldsymbol{\nabla}\phi = \mu_0\boldsymbol{J^s} \tag{4.46}$$

Using Ohm's law ($\boldsymbol{J} = \sigma\boldsymbol{E}$) and substituting Equation 4.41 into equation (conservation of charge)

$$\boldsymbol{\nabla}.\sigma\boldsymbol{E} = -\boldsymbol{\nabla}.\boldsymbol{J^s} \tag{4.47}$$

gives

$$i\omega\boldsymbol{\nabla}.\sigma\boldsymbol{A} + \boldsymbol{\nabla}.\sigma\boldsymbol{\nabla}\phi = \boldsymbol{\nabla}.\boldsymbol{J^s} \tag{4.48}$$

This equation and Equation 4.47 constitute a system of equations. In order to solve this system, homogeneous Dirichlet boundary conditions on $\boldsymbol{A}$ and $\phi$ by introducing Ω for the whole domain of the physical EM problem with Λ as its outer boundary. The boundary conditions are as follow

$$(\boldsymbol{n}\times\boldsymbol{A})_\Lambda = 0 \tag{4.49}$$

and

$$\phi_\Lambda = 0 \tag{4.50}$$

where $\boldsymbol{n}$ is the normal vector for the boundary surfaces of the domain. This means that if the EM sources are located inside the numerical domain (as in the CSEM methods) and

they are far enough away from the boundaries of the domain, then the EM fields vanish on the boundaries due to the attenuation. Thus, EM fields can be considered as zero values on the boundary surfaces of the numerical domain.

The geophysical EM problem needs boundary value problem at the interfaces of the media with different EM properties as well. It also needs conditions to be satisfied on the interfaces between media with different EM properties. These interface conditions for the EM potentials can be derived by integrating Maxwell's equations in terms of the scalar and vector potentials ($\phi$ and $\boldsymbol{A}$) over infinitesimal Gaussian pill-boxes (Griffiths, 1999; Jahandari, 2015):

$$\boldsymbol{A}_{t1} = \boldsymbol{A}_{t2} \tag{4.51}$$

This boundary condition shows that the tangential components of the vector potential ($\boldsymbol{A}_t$) are continuous across interfaces between two media 1 and 2, so is the normal component if one is using the Coulomb gauge (i.e., to satisfy $\boldsymbol{\nabla}.\boldsymbol{A} = 0$ right on the interface).

Finally, the system of equations can be solved and discretized using numerical methods such as finite-difference approaches (Weiss, 2010), finite-volume approaches (Madsen and Ziolkowski, 1990; Jahandari and Farquharson, 2014), and finite-element approaches (Jin, 2002; Börner, 2010). In this research, the code of Ansari and Farquharson (2014) is used which is based on the finite-element method in the frequency domain. The finite-element discretization in this research is based on the Galerkin method of weighted residuals in

which a residual function is formed which gives the error ($\boldsymbol{R}$) between the true solution and the approximate solution. The residual is weighted by the same basis functions ($\boldsymbol{N}$) that are used for approximating the unknowns (Jahandari et al., 2017). Then, the weighted residual over the whole domain is set to zero, which then enables the approximate solution to be found. The weighted vector and scalar residuals can be written as

$$\boldsymbol{R} = \boldsymbol{N}.(\boldsymbol{\nabla}\times\boldsymbol{\nabla}\times\widetilde{\boldsymbol{A}} + i\mu_0\sigma\omega\widetilde{\boldsymbol{A}} + \mu_0\sigma\boldsymbol{\nabla}\tilde{\phi} - \mu_0\boldsymbol{J^s}) \tag{4.52}$$

$$R = N(i\omega\boldsymbol{\nabla}.\sigma\widetilde{\boldsymbol{A}} + \boldsymbol{\nabla}.\sigma\boldsymbol{\nabla}\tilde{\phi} - \boldsymbol{\nabla}.\boldsymbol{J^s}) \tag{4.53}$$

where $\widetilde{\boldsymbol{A}}$ and $\tilde{\phi}$ are approximate vector and scalar potentials, respectively. Inside each tetrahedral element these approximated potentials can be defined as (Ansari and Farquharson, 2014)

$$\widetilde{\boldsymbol{A}} = \sum_{u=1}^{6} \boldsymbol{N}_u\tilde{A}_u \tag{4.54}$$

$$\tilde{\phi} = \sum_{u=1}^{4} N_u\tilde{\phi}_u \tag{4.55}$$

where $\boldsymbol{N}_u$ and $\tilde{A}_u$ are vector basis functions and approximate vector potentials corresponding to the edges, respectively, and $N_u$ and $\tilde{\phi}_u$ are scalar basis functions and scalar potentials corresponding to the nodes, respectively. Integrating the weighted residuals over the entire numerical domain Ω and equating to zero gives

$$\sum_{q=1}^{\bar{m}} \widetilde{A}_q \int_\Omega (\boldsymbol{\nabla}\times\boldsymbol{N}_m).\left(\boldsymbol{\nabla}\times\boldsymbol{N}_q\right)d\Omega + i\omega\mu_0 \sum_{q=1}^{\bar{m}} \widetilde{A}_q \int_\Omega \sigma\boldsymbol{N}_m.\boldsymbol{N}_q d\Omega +$$
$$\mu_0 \sum_{k=1}^{\bar{n}} \widetilde{\phi}_k \int_\Omega \sigma\boldsymbol{N}_m.\nabla N_k d\Omega = \mu_0 \int_\Omega \boldsymbol{N}_m.\boldsymbol{J}_P d\Omega \tag{4.56}$$

$$i\omega \sum_{q=1}^{\bar{m}} \widetilde{A}_q \int_\Omega \nabla N_n . \left(\sigma \boldsymbol{N}_q\right) d\Omega + \sum_{k=1}^{\bar{n}} \widetilde{\phi}_k \int_\Omega \nabla N_n . (\sigma \nabla N_k) d\Omega = - \int_\Omega N_n \nabla . \boldsymbol{J}_P d\Omega \quad (4.57)$$

where $\bar{m}$ and $\bar{n}$ are the numbers of edges and nodes in the mesh, respectively, $m = 1, \ldots, \bar{m}$ and $n = 1, \ldots, \bar{n}$. These two equations are solved for the coefficients $\tilde{A}_q$ of the approximate vector potential and the coefficients $\tilde{\phi}_k$ of the approximate scalar potential. When the system has been solved for the real and imaginary parts of the vector and scalar potentials, the electric field can be obtained using Equation 4.41. Also, the magnetic field can be calculated by taking the curl of the vector potential and using the edge-element basis functions as

$$\boldsymbol{H} = \frac{1}{\mu_0} \sum_{q=1}^{\bar{m}} \tilde{A}_q \boldsymbol{\nabla} \times \boldsymbol{N}_q \quad (4.58)$$

## 4.5 Inverse theory

The inversion approach used in this research is that of the code of Lelièvre et al. (2012). This uses the minimum-structure approach in which an objective function is minimized using a Gauss-Newton method. It should be noted that inversion problems are not typically well-posed problems. This means that they do not usually satisfy the three conditions 1-existence, 2-uniqueness and 3-stability of a solution. In these cases, regularization helps to solve the inversion problem. For a single dataset, the typical objective function can be written as

$$\boldsymbol{\Phi} = \phi_d + \beta \phi_m \quad (4.59)$$

where $\beta$ is the trade-off parameter which controls the relative contributions of the data misfit term ($\phi_d$) and the regularization (or model) term ($\phi_m$). The data misfit term controls the fit to the data, and the regularization term controls the amount and type of structure in the recovered model (Lelièvre and Oldenburg, 2009). The data misfit and regularization terms have the general forms

$$\phi_d = \phi_d(\boldsymbol{u}) \tag{4.60}$$

$$\phi_m = \sum_k \alpha_k \phi_k(\boldsymbol{v}_k) \tag{4.61}$$

where

$$\boldsymbol{u} = \mathbf{W}_d(\boldsymbol{d}^{obs} - \boldsymbol{d}^{prd}) \tag{4.62}$$

$$\boldsymbol{v}_k = \mathbf{W}_k\left(\boldsymbol{m} - \boldsymbol{m}_k^{ref}\right) \tag{4.63}$$

where $\boldsymbol{d}^{obs}$ is the vector of observed data, $\boldsymbol{d}^{prd}$ is the vector of data calculated for the vector, **m**, of model parameters, and the data-weighting matrix, $\mathbf{W}_d$, is a diagonal matrix whose elements are the reciprocals of the estimates of the standard deviations of the noise in the observations (Farquharson, 2008). Data misfit, $\phi_d$, can be written as

$$\phi_d = \sum_{i=1}^{N} \left(\frac{F[\boldsymbol{m}]_i - d_i}{\sigma_i}\right)^2 \tag{4.64}$$

where $N$ is the number of measured data, $d_i$, $F[\boldsymbol{m}]_i$ are calculated data, and $\sigma_i$ are the estimated uncertainties. In the code of Lelièvre et al. (2012), if the uncertainty value is unknown, it will be considered to be 5% of the datum. Also, $\phi_m$ can be written as

$$\phi_m = \alpha_s \phi_s(\boldsymbol{v}_s) + \alpha_m \phi_m(\boldsymbol{v}_m) = \alpha_s \phi_s(\boldsymbol{W}_s(\boldsymbol{m} - \boldsymbol{m}^{ref})) + \alpha_t \phi_t(\boldsymbol{W}_t \boldsymbol{m}) \quad (4.65)$$

where $\boldsymbol{W}_s$ contains cell volume information, $\boldsymbol{W}_t$ calculates model differences between adjacent grid cells (weighted by cell volumes), and $\alpha_s$ and $\alpha_t$ are constant values during the inversion which are used to adjust the relative amount of structure recovered in the physical property models. Thus, the objective function can be written as (Farquharson and Oldenburg, 1998)

$$\boldsymbol{\Phi} = \phi_d(\mathbf{W}_d(\boldsymbol{d}^{obs} - \boldsymbol{d}^{prd})) + \beta[\alpha_s \phi_s(\boldsymbol{W}_s(\boldsymbol{m} - \boldsymbol{m}^{ref})) + \alpha_t \phi_t(\boldsymbol{W}_t \boldsymbol{m})] \quad (4.66)$$

To solve the inverse problem, we minimize $\boldsymbol{\Phi}$ by differentiating with respect to the model parameters, $\boldsymbol{m}$, and equating the resulting derivatives to zero.

In a general form, $\phi_d$ and $\phi_m$ can be written as

$$\phi(\boldsymbol{x}) = \sum_j \gamma(x_j) \quad (4.67)$$

The measure proposed by Ekblom (1973, 1987), used in this research, is a modified version of the $l_p$ norm:

$$\gamma(x) = (x^2 + \varepsilon^2)^{p/2} \quad (4.68)$$

where $\varepsilon$ is a very small positive number, and $p$ is the order of norm (e.g. $p$=1 and $p$=2 for L1-norm and L2-norm, respectively). The final linear system of inversion equations obtained by minimizing the objective function $\boldsymbol{\Phi}$ is

$$[\beta \alpha_s \boldsymbol{W}_s^T \boldsymbol{R}_s \boldsymbol{W}_s + \beta \alpha_t \boldsymbol{W}_t^T \boldsymbol{R}_t \boldsymbol{W}_t + \boldsymbol{G}^T \boldsymbol{W}_d^T \boldsymbol{R}_d \boldsymbol{W}_d \boldsymbol{G}]\boldsymbol{m} = \boldsymbol{G}^T \boldsymbol{W}_d^T \boldsymbol{R}_d \boldsymbol{W}_d \boldsymbol{d}^{obs} +$$

$$\beta\alpha_s \boldsymbol{W}_s^T \boldsymbol{R}_s \boldsymbol{W}_s \boldsymbol{m}^{ref} \tag{4.69}$$

where $\boldsymbol{G}$ is a kernel or Jacobian matrix for the general non-linear case that contains all the physics of this problem, and *T* indicates the transpose of a matrix. Since $\boldsymbol{R}_s$, $\boldsymbol{R}_t$ and $\boldsymbol{R}_d$ are diagonal matrices depending on the model $\boldsymbol{m}$, this equation is non-linear. This problem can be solved with an iterative procedure:

$$\boldsymbol{m}^{k+1} = \boldsymbol{M}_k^{-1} \boldsymbol{y}^k \tag{4.70}$$

where

$$\boldsymbol{M}_k = \left[\beta\alpha_s \boldsymbol{W}_s^T \boldsymbol{R}_s^k \boldsymbol{W}_s + \beta\alpha_t \boldsymbol{W}_t^T \boldsymbol{R}_t^k \boldsymbol{W}_t + \boldsymbol{G}^T \boldsymbol{W}_d^T \boldsymbol{R}_d^k \boldsymbol{W}_d \boldsymbol{G}\right] \tag{4.71}$$

and

$$\boldsymbol{y}^k = \boldsymbol{G}^T \boldsymbol{W}_d^T \boldsymbol{R}_d^k \boldsymbol{W}_d \boldsymbol{d}^{obs} + \beta\alpha_s \boldsymbol{W}_s^T \boldsymbol{R}_s^k \boldsymbol{W}_s \boldsymbol{m}^{ref} \tag{4.72}$$

where *k* is the iteration number and $\boldsymbol{R}_d^k = \boldsymbol{R}_d(\boldsymbol{m}^k)$, etc. At the first iteration, for the starting model, $\boldsymbol{R}_s$=$\boldsymbol{R}_t$=$\boldsymbol{R}_d$=$\boldsymbol{I}$ where $\boldsymbol{I}$ is the identity matrix. These matrices will be computed at each iteration in order to solve the inversion equation to obtain a new model. The iterations are terminated when the model no longer changes by a significant amount.

The iteration procedure of the inversion code (Lelièvre et al., 2012) will terminate when "*omega (ω)*" reaches 1. This means that a good fit between the observed and calculated data is obtained (Carter-McAuslan et al., 2013). Therefore, the normalized data residuals should ideally reach zero (or close to zero and between -1 and 1).

$$\text{Normalized Data Residual} = \frac{d_i^{cal} - d_i^{obs}}{\sigma_i} \tag{4.73}$$

where $d_i^{cal}$ is the *i*th datum calculated by the model constructed by the inversion, $d_i^{obs}$ is the *i*th datum from the (observed) dataset that was provided for the inversion, and $\sigma_i$ is the uncertainty on the *i*th datum.

The fitting can be controlled by changing the value of "*chifact*". "*chifact*" and "$\omega$" are

$$chifact = \frac{target\ misfit\ (\phi_d^*)}{number\ of\ data\ (N)} \tag{4.74}$$

$$omega\ (\omega) = \frac{data\ misfit\ (\phi_d)}{target\ misfit\ (\phi_d^*)} \tag{4.75}$$

The use of *chifact* to yield the optimal model is based upon the assumption that noise and error on the data are random and have a Gaussian distribution. Thus, if uncertainties are well chosen, the appropriate target misfit will have a value of *N* (number of data). For noisy data, if we know the standard deviations of the noise in each measurement we should be able to get to a *chifact* of *N*. If we do not know the standard deviations of the noise, we can guess them. If our guessed standard deviations are too small, then we will probably need to aim for a target misfit that is larger than *N*, and if our guessed standard deviations are too big, we should really end up with a misfit lower than *N*. Therefore, the target misfit may have to be larger than *N*, thus *chifact* would be specified as more than 1. And, for clean data, *chifact* can be set less than 1.

Therefore, the code inverts by searching and finding a value for the trade-off parameter

$\beta$ that provides a misfit value close to the number of data (target misfit, and $\omega = 1$). A typical procedure is that the value of $\beta$ reduces slowly from one iteration to the next from an initially large value. By decreasing values of $\beta$, a model can be obtained that fits the data better but that contains more structure. However, a very low value of $\beta$ can fit noise in the data which leads to spurious structures in the model (Lelièvre et al., 2012). In the code of Lelièvre et al. (2012), $\beta$ can be controlled and reduced using

$$\beta^{(k+1)} = \frac{\beta^{(k)}}{\nu_\beta} = \frac{\beta^{(k)}}{1+\tau_\beta|\omega-1|} \tag{4.76}$$

where $\tau_\beta = 1$, and $\nu_\beta \in [1+\epsilon, 2]$ with $\epsilon$ some small value (i.e. here 0.05). The value of $\nu_\beta$ should lie on $[1+\epsilon, 2]$ so that the adjustment of $\beta$ is neither too large nor too small from one iteration to the next. During the inversion process, various parts of the objective function such as data misfit term ($\phi_d$), model term ($\phi_m$), objective function ($\mathbf{\Phi}$) and trade-off parameter ($\beta$) change at each iteration. Ideally, their values decrease during the inversion process except the value of model term which increases.

### 4.5.1 Joint inversion

Independent single-property inversion can often encounter difficulties when the geology is complicated. Inverting a data-set jointly with another complementary data-set can solve and improve the construction of a single earth model. This process is called joint inversion. With two data-sets in the joint inversion, the objective function can be written as (Lelièvre et al., 2012)

$$\boldsymbol{\Phi}(\boldsymbol{m}_1, \boldsymbol{m}_2) = \lambda_1 \phi_{d1}(\boldsymbol{m}_1) + \lambda_2 \phi_{d2}(\boldsymbol{m}_2) + \alpha_1 \phi_{m1}(\boldsymbol{m}_1) + \alpha_2 \phi_{m2}(\boldsymbol{m}_2) + \Phi_j(\boldsymbol{m}_1, \boldsymbol{m}_2)$$

$$= \lambda(\phi_{d1}(\boldsymbol{m}_1) + \gamma \phi_{d2}(\boldsymbol{m}_2)) + \alpha_1 \phi_{m1}(\boldsymbol{m}_1) + \alpha_2 \phi_{m2}(\boldsymbol{m}_2) + \Phi_j(\boldsymbol{m}_1, \boldsymbol{m}_2) \qquad (4.77)$$

where the two $\phi_d$ and two $\phi_m$ terms are the data misfit and regularization terms for each of the two data sets $\boldsymbol{d}_1$ and $\boldsymbol{d}_2$ and models $\boldsymbol{m}_1$ and $\boldsymbol{m}_2$, respectively. And, $\alpha_1$ and $\alpha_2$ are constant parameters for adjusting the relative amount of structure constructed in the models. By increasing one of them, the influence of the related data-set on the constructed models will be more than the other. Lelièvre et al. (2012) position the trade-off parameters $\lambda_1 (= \lambda)$ and $\lambda_2 (= \lambda\gamma)$ in front of the data misfit terms (instead of regularization terms). In order to avoid confusion, $\lambda$ is used instead of $\beta$ as the symbol for the tradeoff parameters when multiplying the data misfit terms. The coupling term, $\Phi_j$, measures the dis-similarity (as this quantity gets larger the more unlike the models are) between the two models:

$$\Phi_j = \sum_i \rho_i \Psi_i(\boldsymbol{m}_1, \boldsymbol{m}_2) \qquad (4.78)$$

where $\rho_i$ is the coupling factor, and $\Psi_i$ is a joint coupling measure.

The iteration procedure of the joint inversion code of Lelièvre et al. (2012) will terminate when "*omega (ω)*" reaches 1. This average "$\omega$" is

$$\omega = \frac{(\omega_1 + \omega_2)}{2} = \frac{(\frac{\phi_{d1}}{\phi^*_{d1}} + \frac{\phi_{d2}}{\phi^*_{d2}})}{2} \qquad (4.79)$$

The joint inversion algorithm searches for the appropriate values of parameters λ and γ to have both misfits equal their respective targets. The approach is to set γ to some value

(initially equal to 1) and then search for the value of λ that best yields the target misfits. Then γ can be adjusted as misfits move toward their targets. λ can be calculated using

$$\lambda^{(k+1)} = \lambda^{(k)}\ \nu_\lambda = \lambda^{(k)}\ (1 + \tau_\lambda|\tfrac{\omega_1+\omega_2}{2} - 1|) \tag{4.80}$$

where $\tau_\lambda = 1$, and $\nu_\lambda \in [1+\epsilon, 2]$. In this case, the value of $\nu_\lambda$ multiplies the value of λ such that it slowly increases. After adjusting λ, we can adjust γ using

$$\gamma^{(k+1)} = \gamma^{(k)}\ \nu_\gamma = \gamma^{(k)}\ (1 + \tau_\gamma(|\omega_1 - 1| + |\omega_2 - 1|)) \tag{4.81}$$

where $\tau_\gamma = 2$, and $\nu_\gamma \in [1+\epsilon, 2]$. The process of adjusting λ and γ values will go on at each iteration until the misfits reach to their targets, and "$\omega$" reaches 1.

Since there are several possible measures for the joint coupling measure ($\Psi_i$), there are different types of possible coupling. In this research, the fuzzy c-mean clustering method and the correlation method have been used. In the fuzzy c-mean method, a relationship between the physical properties can be specified that lies in discrete clusters (Paasche and Tronicke, 2007):

$$\Psi(\boldsymbol{r}, \boldsymbol{s}) = \sum_{i=1}^{C} \sum_{k=1}^{M} w_{ik}^{f} z_{ik}^{2} \tag{4.82}$$

where *C* is the number of clusters, *M* is the number of cells, and *f* is typically set to a value of 2. The terms $z_{ik}$ and $w_{ik}$ relate the model parameter set (physical property values) for the $k^{th}$ cell to the $i^{th}$ cluster (Lelièvre et al., 2012). Vectors **r** and **s** are two inversion models (e.g. density and slowness models) on a grid containing *M* cells. This method can be used

where there is not a strict linear relationship between the physical properties, and therefore a statistical relationship between the two physical properties can be used. Thus, the physical properties of geological structures should be used as initial/input information in the inversion code. Also, the similarity parameter ($\rho$) needs to be provided to the code. If $\rho$ is set too low, there won't be enough similarity imposed between the two models. By increasing the $\rho$ value and imposing a greater degree of similarity the model begins to improve (although this can make the inverse problem harder to solve).

In the correlation method for joint inversion a statistical relationship between the two physical properties is used. In this method a correlation measure from statistics is used, which measures the degree of the implicit linear relationship between two sets of values. It does not require any knowledge of the range of the physical properties. The correlation measure is

$$\Psi(\boldsymbol{r},\boldsymbol{s}) = \left(\frac{\sum_{i=1}^{M}(r_i-\mu_r)(s_i-\mu_s)}{M\sigma_r\sigma_s} \pm 1\right)^2 \tag{4.83}$$

where $M$ is the number of cells in the model, $r_i$ and $s_i$ are the two physical properties (e.g. density and slowness) of the ith cell, $\sigma_r$ and $\sigma_s$ are the standard deviations, and $\mu_r$ and $\mu_r$ are the means of the physical property distributions. The positive or negative linear correlation between the physical properties can be defined by choosing the negative or positive sign in the equation. Both fuzzy c-mean and correlation methods are considered as "compositional" approaches, because their coupling defines a relationship between the physical properties involved.

### 4.5.2 Depth/distance weighting

Note that magnetic and gravity data have no inherent depth resolution (Li and Oldenburg, 1998). Therefore, the susceptibilities or densities constructed using a typical minimum-structure inversion method would tend to be concentrated close to the observation points. To deal with this, the objective function (the model norm part) includes a term to overcome the natural decay of the field (which is $1/r^2$ for the gravity and $1/r^3$ for the magnetic method, where r is distance between causative feature and sensor). Lelièvre et al. (2012) considered a "depth weighting" for a cell as

$$(z - w_z)^{-w_p} \tag{4.84}$$

where $z$ is the depth of the cell centroid, $w_z$ is the average survey height in the input coordinate system, and $w_p$ is a constant. For surface data, the sensitivity (effect of a feature on a measurement) decays in the depth direction so a weighting which overcomes the decay in the vertical direction is appropriate, so long as the elevation of measurements is properly accounted for. Lelièvre et al. (2012) considered a "sensitivity weighting" for a cell as

$$\sum \left( \left| \frac{gj}{v} \right|^{w_n} \right)^{(w_b/w_n)} \tag{4.85}$$

where $gj$ is a column of the sensitivity matrix, $v$ is the cell volume, and $w_n$ and $w_b$ are constants. Sometimes a weighting function that varies in three dimensions is needed (e.g. for data sets that contain borehole measurements). Therefore, a generalized version of depth weighting called "distance weighting" is used which accounts for the distance between each

model cell and measurement. Lelièvre et al. (2012) considered the "distance weighting" for a cell as

$$\sum\left(|r + w_z|^{(-w_p \times w_n)}\right)^{(w_b/w_n)} \tag{4.86}$$

where $r$ is the distance between cell centroids and observation points. For the distance weighting, $w_z$ should be a small value, such as half the smallest cell dimension.

### 4.5.3 Constraints via reference model and bounds

In this thesis, triangular cells (for 2D) and tetrahedral cells (for 3D) are used for all inversion meshes (as well as modelling meshes). The advantage of these meshes, in comparison with rectangular and rectangular cube meshes, is the ability of modelling an accurate topography. Also, the constrained inversion method used in this thesis is based on the two methods: 1- constraining by being close to the reference model, 2- constraining via upper and lower bounds. In the first constraining method, there are two "reference" and "weight" models which use the same mesh as the model being constructed. Each number in the "reference" model represents a physical property value, and each number in the "weight" model is a weight given to the equivalent physical property value in the "reference" model. By increasing the weight of a cell, the initial physical property considered in the "reference" model for the cell will change less during the inversion process. In the second constraining method, the physical property of each cell can be controlled by upper and lower bounds. A wider range of the bounds gives more freedom to the inversion code to assign an appropriate value. When the physical property of a/some

cell/s is known (e.g. from borehole data), the range of the bounds can be as narrow as having both bounds share the same value.

### 4.5.4 Heating/cooling schedules

In the code of Lelièvre et al. (2012), inversions start from an initial model which can be a model with uniform values of physical properties. Since the minimum structure method (the method used in the inversion) is not dependent on the initial model, the assigned values can be zero except for the seismic method for which the values should be more than zero. For the joint inversion there are two initial models/values for one mesh. And, for each of the two data-types we need to consider specific values for the *chifact* and trade-off parameter ($\beta$). In the code of Lelièvre et al. (2012), the process of joint inversion (i.e., how the trade-off parameter(s) is varied during an inversion) can be run in different ways: heating joint inversion without pre-heating (JwP) and heating joint inversion after pre-heating (JaP). In the "JwP", the joint inversion directly starts by considering the coupling factor, thus the inversion will converge when both *omega* values of the two data-sets as well as the total *omega* value (related to the all data misfit terms in the objective function) reach to 1. The coupling factor can be heated in different stages in which each stage is a separate and complete process of joint inversion. The number of stages can be defined by the user. During these stages, the coupling factor starts from a smaller value than the assigned value, and in each stage the value of the coupling factor will increase until it reaches the assigned value in the final stage. The models and trade-off parameters obtained in each stage will be used as initial models and initial trade-off parameters in the next stage.

In the “JaP”, the objective function is first minimized without any joint coupling (which is called "stage 0"), followed by heating in the joint coupling measure over one/several stage/s.

In the codes EM1DFM (Farquharson and Oldenburg, 2000) and EM1DTM (Farquharson and Oldenburg, 2006), which are 1D modelling and inversion codes for electromagnetic frequency- and time-domain data, there are different methods to find the appropriate value for the trade-off parameter (Farquharson and Oldenburg, 2004). I have used the generalized cross-validation (GCV; Haber, 1997; Haber and Oldenburg, 2000; Farquharson and Oldenburg, 2004) method in which the trade-off parameter is automatically chosen using the GCV criterion. As a conceptual description, the GCV method is based on inverting all but the first observation using a trial value of $\beta$, and then computing the individual misfit between the first observation and the first forward-modelled datum for the model produced by the inversion (for linear problems). This can be repeated leaving out all the other observations in turn using the same value of $\beta$. The best value of $\beta$ can then be defined as the one which gives the smallest sum of all the individual misfits. The GCV function for the $n$th iteration is given by:

$$GCV(\beta) = \frac{\left\| \boldsymbol{W}_d\left(d^{obs} - d^{n-1}\right) - \boldsymbol{W}_d \boldsymbol{G}^{\boldsymbol{n-1}} \boldsymbol{M}^{-1}\left(\boldsymbol{G}^{n-1T} \boldsymbol{W}_d^T \boldsymbol{W}_d\left(d^{obs} - d^{n-1}\right) + \beta \sum_{i=1}^{2} \boldsymbol{W}_i^T \boldsymbol{W}_i\left(\boldsymbol{m}_i^{ref} - \boldsymbol{m}^{n-1}\right)\right)\right\|^2}{\left[trace\left(\boldsymbol{I} - \boldsymbol{W}_d \boldsymbol{G}^{n-1} \boldsymbol{M}^{-1} \boldsymbol{G}^{n-1T} \boldsymbol{G}_d^T\right)\right]^2} \tag{4.87}$$

where

$$\boldsymbol{M}(\beta) = \boldsymbol{G}^{n-1T} \boldsymbol{W}_d^T \boldsymbol{W}_d \boldsymbol{G}^{n-1} + \beta \sum_{i=1}^{2} \boldsymbol{W}_i^T \boldsymbol{W}_i \tag{4.88}$$

If $\beta^*$ is the value of the trade-off parameter that minimizes GCV function at the $n$th

iteration, the actual value of $\beta$ used to compute the new model is given by:

$$\beta^n = \max\left(\beta^*, bfac \times \beta^{n-1}\right) \tag{4.89}$$

where the user-supplied factor *bfac* is such that $0.01 < bfac < 0.5$. Also, the codes are considered to have converged when both of the following equations are satisfied (Gill et al., 1981).

$$\boldsymbol{\Phi^{n-1} - \Phi^n} < \vartheta(1 + \boldsymbol{\Phi}^n) \tag{4.90}$$

$$\| \boldsymbol{m}^{n-1} - \boldsymbol{m}^n \| < \sqrt{\vartheta}(1 + \| \boldsymbol{m}^n \|) \tag{4.91}$$

where $\vartheta$ is a user-specified parameter with a default value of 0.01.

### 4.5.5 Mesh generation

In this research, "Triangle" (Shewchuk, 1996) and "Tetgen" (Si, 2015) codes are used to generate 2D triangular and 3D tethrahedral meshes, respectively. Many codes are used in order to format conversion, data processing and model processing as well (see appendix A; Lelièvre and Farquharson, 2015). Models and results are mostly shown using Paraview software (www.paraview.org). Data are plotted using the Generic Mapping Tools (GMT; Wessel and Smith, 1991)

## 4.6 Summary

Forward modelling is a mathematical solution to calculated data from the model parameters while inversion is a mathematical process of estimating the model parameters from the

observed data. Therefore, the forward modelling can be a part of the inversion process. For the forward modelling, the gravity and magnetic methods can be solved easily using the analytical solution but the values for the seismic and electromagnetic methods should be estimated by the numerical methods such as finite difference and finite element methods.

There are many methods to solve for the inversion problem. In this research, we use the minimum structure approach in which an objective function is minimized using a Gauss-Newton method. Due to the complicated geology, joint and constrained inversions can also help to improve the results. Joint inversion can be define as inverting a data-set jointly with another complementary data-set. Also, the constrained inversion method can be based on the two methods: 1- constraining by being close to the reference model; 2- constraining via upper and lower bounds.

# Chapter 5

# Gravity Forward Modelling of the Athabasca Basin

## 5.1 Introduction

As mentioned before, using the forward modelling we will be able to synthetize the data in order to compare with real data to investigate the subsurface. The gravity data involves the variations in the density of geophysical structures. Therefore, forward modelling of gravity data can give us a better understanding of relationship between the gravity data and variations in density.

Therefore, synthesizing the gravity response of different components of the geology in the McArthur-Millennium corridor, and as a result assess the size and character of the various responses will be done in this chapter. This includes the "target" responses, i.e., alteration zones in the sandstones, as well as all the other non-target responses/signals including from the overburden/glacial sediments and basement.

In this chapter, two synthetic models will be built up component by component, with the gravity contribution being assessed component by component in order to investigate the free-air and Bouguer anomalies of the McArthur-Millennium region. Realistic models were build taking into account everything that is known (such as topography as well as location of structures from boreholes) and structures that are estimated or speculated (such as base of overburden and unconformity) as wells as allowing an assessment to be made of the various contributions to gravity data over the Athabasca Basin, the data-sets generated here will be used to test inversion procedures for overburden stripping in subsequent chapters.

## 5.2 3D gravity forward modelling of an anomaly

The size, depth and density of anomalies are the main effects in gravity data, whereas the shape has less effect. As a first example of 3D modelling, gravity data were synthesized using the forward modelling code of Lelièvre et al. (2011) for one irregular-shaped anomaly and one cylinder-shaped anomaly (Figure 5.1).

In Figure 5.2, it can be seen that the gravity response due to the cylinder with a diameter of 300 m (shown by grey color in Figures 5.1 and 5.2) is similar to that due to the irregular, more realistic, density anomaly (red color) at the same depth and of the same density (2.47 g/cc). There is no topography in this modelling as all stations along the profile have the same elevation.

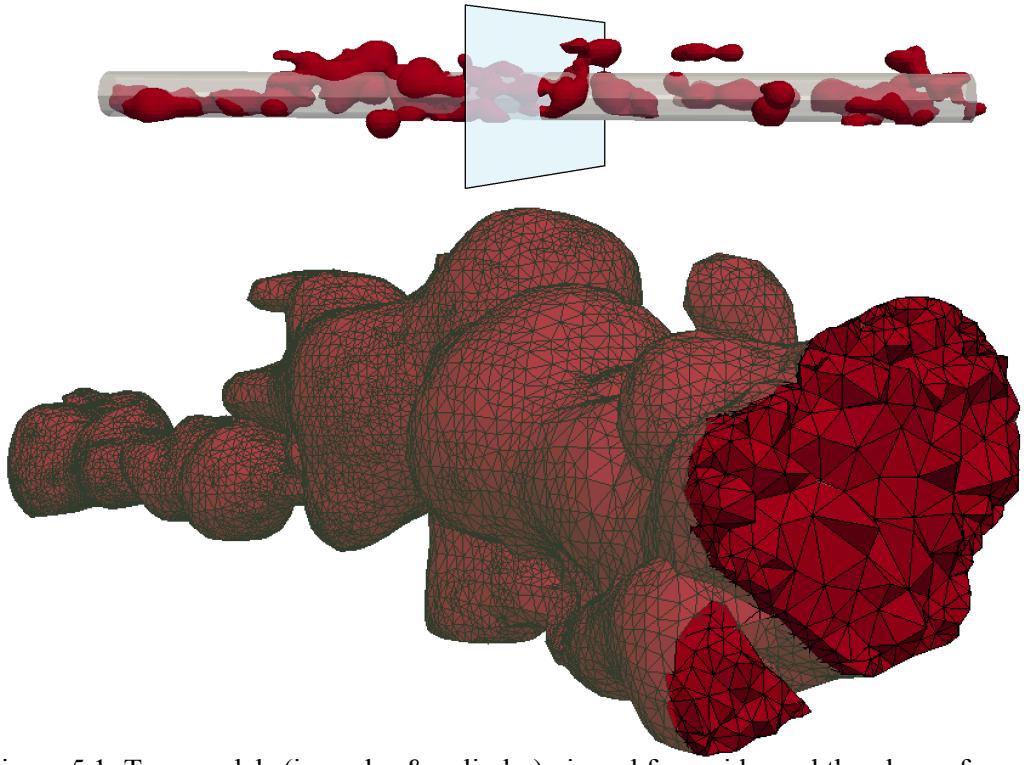

Figure 5.1: Top: models (irregular & cylinder) viewed from side, and the plane of cross-section. Bottom: cross-section of 3D tetrahedral mesh of irregular body.

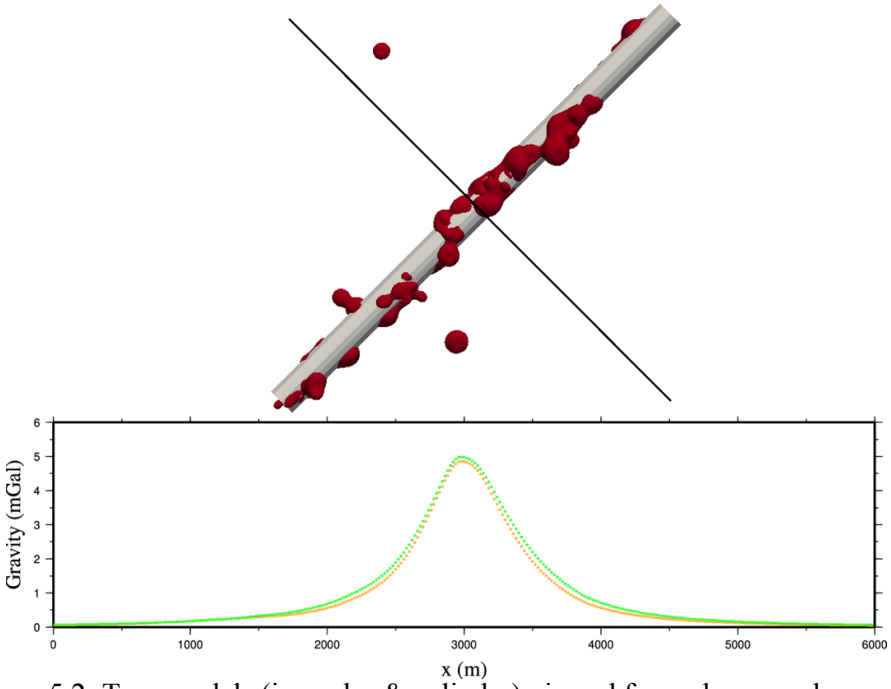


Figure 5.2: Top: models (irregular & cylinder) viewed from above, and a survey line (black line) of length 6 km. Bottom: gravity data over the cylinder (green) and irregular density anomaly (orange).

Here, in order to make the irregular anomaly I got help from isosurfaces of SWIR data (modified by GOCAD software; www.pdgm.com). SWIR 3D shells represent an isotropic estimate of the 3D distribution of alteration minerals (altered clays such as illite, drivite, kaolinite, dickite and chlorite). They are a function of drilling distribution so need to be used knowing where the drill-holes are. They are based on cut off %, which means all data inside the threshold will be equal or higher than the % value. For example, dravite_65 captures all data points having a % value of 65 or higher in Dravite content. SWIR data could be the best direct representation of the clay alteration halos. Note that the "alteration zone" is actually weak, with only a small amount of clay. Thus, more than 65% dravite in clays, might mean 0.65% dravite and 0.35% by volume of another clay in 99% quartz (see Section 2.2).

For the second modelling, gravity data were computed for a 3D model corresponding to an overburden and alteration scenario. The models incorporate real topography with a digital resolution of around 10 to 30 m in the McArthur-Millennium corridor made using about 1.5 million stations (Figure 5.3). The orientation of the corridor is in agreement with the main direction of mineralization (e.g. along the P2 fault in the McArthur area) as well as the direction of ice flow (and hence the main direction of the drumlins). The contributions to the gravity data from the components of the models (i.e. overburden and alteration zones) were assessed and compared (Figure 5.4).

The initial alteration model was the irregular anomaly (see Figures 5.1 and 5.2). A density of 2.47g/cc was assigned to the alteration zone (see Section 2.5; Wood and Thomas, 2002). Gravity data were computed at 20m intervals along a 6 km line across the

mineralization zone (see Figure 5.4). The alteration zone in the model comprised approximately 50,000 tetrahedral cells. Similarity between the overburden and alteration signatures can be seen in the gravity data. It can be seen that the strengths of the respective signatures are similar, as are the lateral extents of the peak in the alteration signature and the features in the overburden signature. Therefore, the alteration signature can be masked by the variations in the overburden.

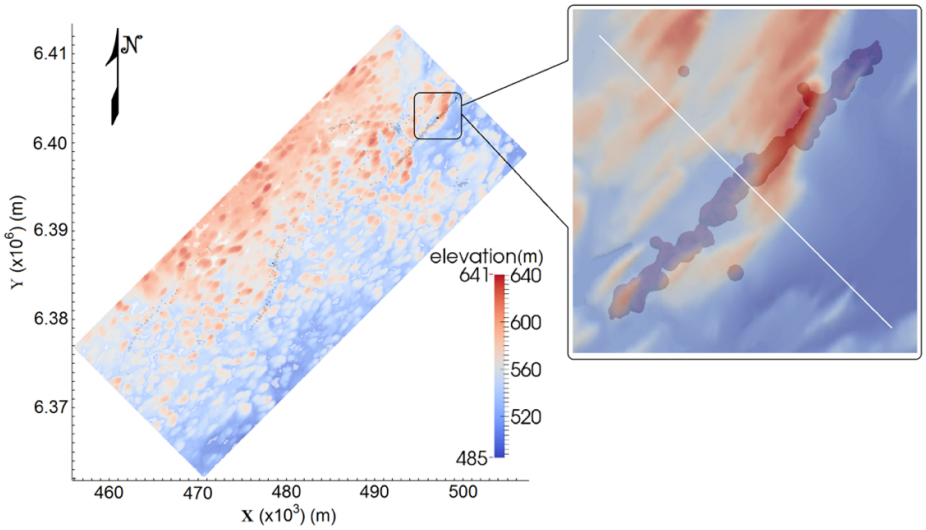


Figure 5.3: Topography of McArthur-Millennium corridor. Inset shows modelled area (5×5km - McArthur area) as well as location of survey line (white line) over alteration zone (red bodies) for the gravity forward modelling. The X and Y axes show real UTM Easting and Northing.

Note that (in the concept of uranium exploration in the Athabasca Basin) one is interest in the gravity signature from the alteration – a tell-tale indicator in uranium mineralization – but as Figure 5.4 shows, it is going to be challenging to discriminate from the signature from the overburden.

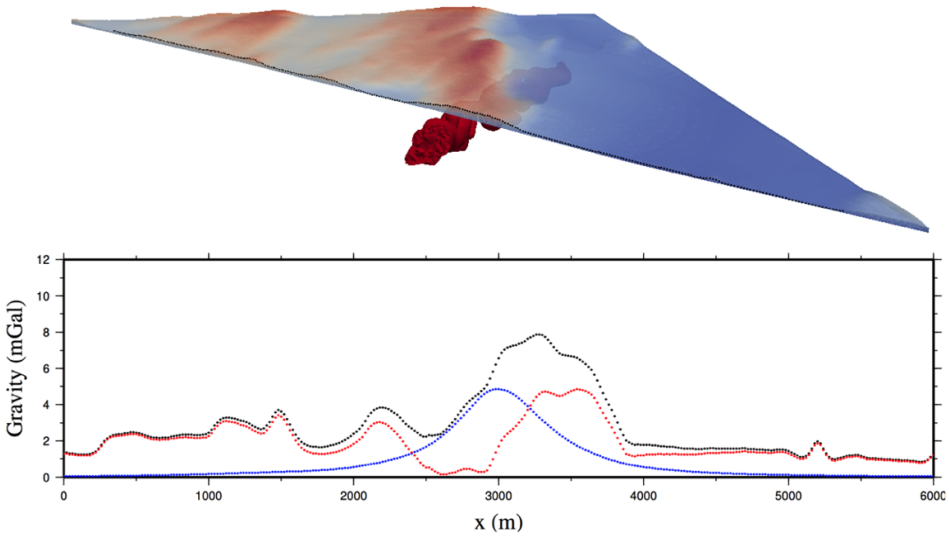


Figure 5.4: Top: cross-section along the profile through the model including alteration zones (red bodies), overburden and location of survey line (black dots). Bottom: gravity data along the survey line for overburden (red), alteration zone (blue), and both overburden and alteration zone (black).

## 5.3 Modelling of free-air and Bouguer anomalies (McArthur area #1)

For geological models, gravity data computed directly using the code of Lelièvre et al. (2011) are equivalent to the free-air anomaly data. In these modelling, a datum (mostly sea level) is considered as the "reference ellipsoid". The layers (or structures) above the reference ellipsoid have real densities while the layers (or structures) below the reference ellipsoid have relative density.

relative density = (real density of the structure) – (2.67 g/cc)

Bouguer anomaly is calculated after applying the Bouguer correction on the free-air anomaly (see Section 3.2.3). Two main scenarios (#1 and #2) are considered in this chapter in order to investigate the free-air and Bouguer anomalies in the McArthur area based on

Wood and Thomas (2002; see Figure 3.32) and Thomas and Wood (2007; see Figure 3.33), respectively. The structure of the basement is the main difference between these two models. These modellings were done before the basement model in the CMIC model was completed (see Section 9.4 and Figure 9.17). The McArthur area is chosen for modelling because of the previous studies of geology, geophysics and physical properties for this area, as it can be seen from the two papers mentioned above.

For the scenario #1, gravity data (free-air and Bouguer anomalies) were computed for 3D models for the McArthur area based on Wood and Thomas (2002; Figure 5.5). Models varied from simple to complicated in order to investigate the different contributions to gravity data. The complicated model (which is the last one; Model 8 in Table 5.1) tried to be similar to the model shown in Figure 5.5 in densities, the basement structure and the thickness of the model. But the interfaces (topography, top of sandstone and unconformity) are modified using the available borehole and elevation data from the CMIC-Footprints project. In this scenario (#1), densities of 1.85 g/cc, 2.42 g/cc, 2.47 g/cc are considered for the overburden, sandstone and alteration zone, respectively. For the blocks in the basement different densities ranging from 2.66 g/cc to 2.74 g/cc are used.

In the following, each model is similar to the previous model, but with a small difference. Table 5.1 briefly demonstrates some of the characteristics of the models. The images of the 3D models in this section show the central 5 by 5 km. The actual 3D models used for the computations had a size of 500 by 500 km in order to avoid any effect of the edges on the gravity data. Needing such a big model, for which the edges no longer affect the computed data, is especially true since we want to have the option of modelling for real

densities, not just anomalous densities for which large parts of the model could be zero.

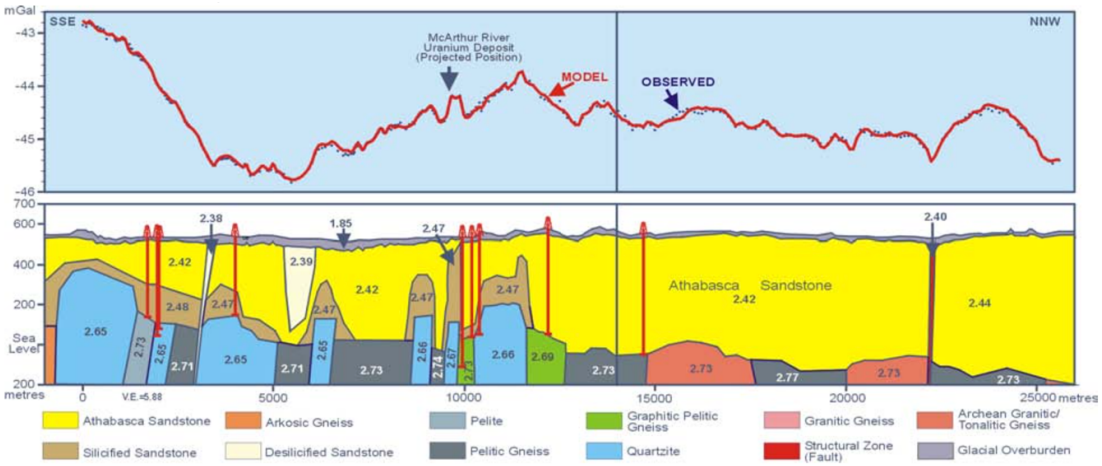


Figure 5.5: Density model made for gravity data along a profile crossing the McArthur area in the Athabasca Basin (Wood and Thomas, 2002).

Table 5.1: Characteristics of the models.

| | Number of layers | Topography | Interface(s) | Datum in BC | Reference ellipsoid | Thickness of model | Anomaly |
|---|---|---|---|---|---|---|---|
| **Model 1** | 2 | flat | flat | at 0m | at 0m | 950m | - |
| **Model 2** | 2 | real | flat | at 0m | at 0m | ~1000m | - |
| **Model 3** | 2 | real | flat | at 500m | at 500m | ~1000m | - |
| **Model 4** | 2 | real | flat | at 500m | at 500m | ~1000m | cylinder |
| **Model 5** | 2 | real | real | at 500m | at 500m | ~1000m | cylinder |
| **Model 6A** | 3 | real | flat | at 500m & 0m | at 0m | ~1000m | cylinder |
| **Model 6B** | 3 | real | flat | at 500m & 0m | at 500m | ~1000m | cylinder |
| **Model 6C** | 3 | real | flat | at 500m & 0m | at 500m | ~1000m | cylinder |
| **Model 7** | 3 | real | flat | at 500m | at 500m | ~5000m | cylinder |
| **Model 8A** | 3 | real | real | at 0m & upper real interface | upper real interface | ~5000m | irregular (small) |
| **Model 8B** | 3 | real | real | upper real interface | upper real interface | ~5000m | irregular( big) |

The effect of the edge can be seen in Table 5.2; in which three models are tested with sizes 20×20 km, 100×100 km and 500×500 km. All models are made of a simple block (layer) with a density of 2 g/cc. The observation point is located at the centre of the model on the surface (0m elevation). Gravity data are calculated for these three models, and then

the Bouguer correction is applied on the data. For the Bouguer correction a density of 2 g/cc is considered, thus it is expected that the Bouguer anomaly (= gravity data – Bouguer correction) be equal to zero (see Section 3.2.3). Table 5.2 show that by (lateral) increasing the size of the model, the Bouguer anomalies are getting close to zero. It also shows the effect of the thickness of layer (10 m and 100 m) on the gravity data and the Bouguer anomaly. It's not so much that the Bouguer anomaly calculated for the slab is zero (it's closer to zero for the smaller slabs). It's that the computed gravity value asymptotes to a constant value as the width of the slab gets larger. The thickness of the slab should just cause a constant shift from one thickness to another. According to these results, in this research a size of 500×500 km is considered for the all modelling. Note that in the gravity forward modelling (like magnetic method and unlike electromagnetic method; see Chapter 4) the quality of mesh (here tetrahedral cells), number and size of the cells have no effect on the results (data).

Table 5.2: Edge effect on synthetic gravity data.

| | *Thickness of 10m* | | | *Thickness of 100m* | | |
|---|---|---|---|---|---|---|
| | 20×20km | 100×100km | 500×500km | 20×20km | 100×100km | 500×500km |
| Gravity data (*mGal*) | 0.83828321 | 0.838585234 | 0.838645639 | 8.348855191 | 8.379056809 | 8.385097282 |
| Bouguer anomaly (mGal) | -0.00011679 | 0.000185234 | 0.000245639 | -0.035144809 | -0.004943191 | 0.001097282 |

**Model 1:** Gravity data (free-air and Bouguer) were first computed for a simple model (Figure 5.6) which has two horizontal layers and a total thickness of 950 m (elevation from -400 m to 550 m). The measurement locations are located on the ground surface (at the elevation of 550 m). The interface between the two layers is located at an elevation of 0 m. Gravity data were computed at 20 m intervals along a 6 km line across the model.

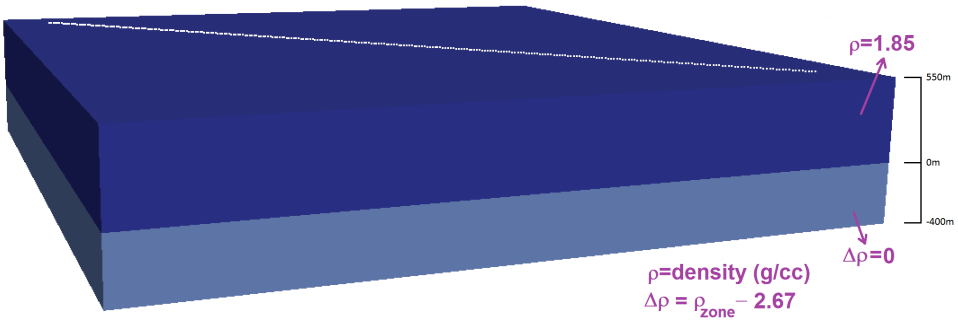


Figure 5.6: Model 1; 3D structure (5×5×1 km) for the simple model with two layers. White line on the surface is the survey line of a length of 6 km.

In this model, I consider the one elevation as the datum for the "reference ellipsoid". Therefore, since in Model 1 the sea level (0m) is considered as the reference ellipsoid, the upper layer has a real density of 1.85 g/cc whereas the lower layer has a relative density of 0 g/cc. This would correspond to the real density of the lower layer being 2.67 g/cc.

As mentioned before, the Bouguer correction (BC) removes the gravitational effect of the rock present between the observation point and the datum, and does so by approximating the rock layer beneath the observation point by an infinite horizontal slab with a thickness equal to the elevation of the observation above the datum (see Section 3.2.3). For the BC for Model 1, I consider the datum to be 0m elevation with ρ=1.85 g/cc. As expected, the free-air anomaly is a constant value for all stations (see Figure 5.7). Thus, after the BC the value of Bouguer anomaly is 0mGal for all the stations.

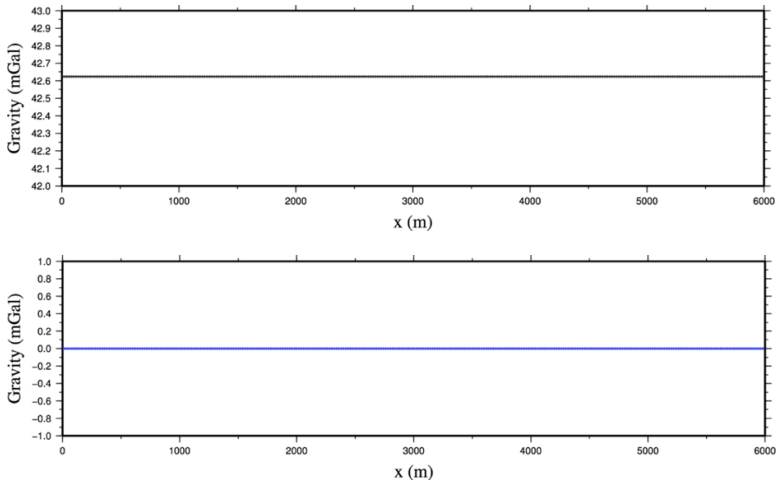


Figure 5.7: Top: free-air anomaly over Model1 (black dots). Bottom: Bouguer anomaly over Model 1 (blue dots). For the Bouguer correction, the datum is at 0m and ρ=1.85 g/cc.

**Model 2:** Model 2 (Figure 5.8) is similar to Model 1, but with real topography (from McArthur). The measurement locations are still on the ground surface (all stations in the modelling in this chapter are located on the ground surface). The profile is the same as used in Figure 5.3. Figure 5.9 shows the corresponding free-air and Bouguer anomalies. Both anomalies are correlated with the topography (free-air anomaly is very correlated). It can be seen that the Bouguer anomaly still has a non-zero value, whereas it should be 0 mGal (if all the mass above the reference level up to the topography were truly taken into account). This is due to the terrain effect. Including a real topography with digital resolution of around 20 m increases the size of the tetrahedral mesh to around 280,000 cells.

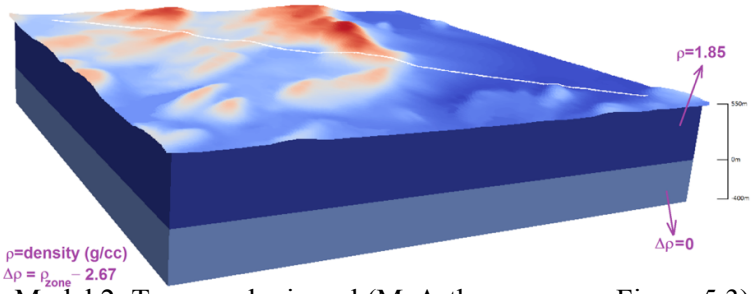


Figure 5.8: Model 2; Topography is real (McArthur area; see Figure 5.3). White line is the survey line on the topography.

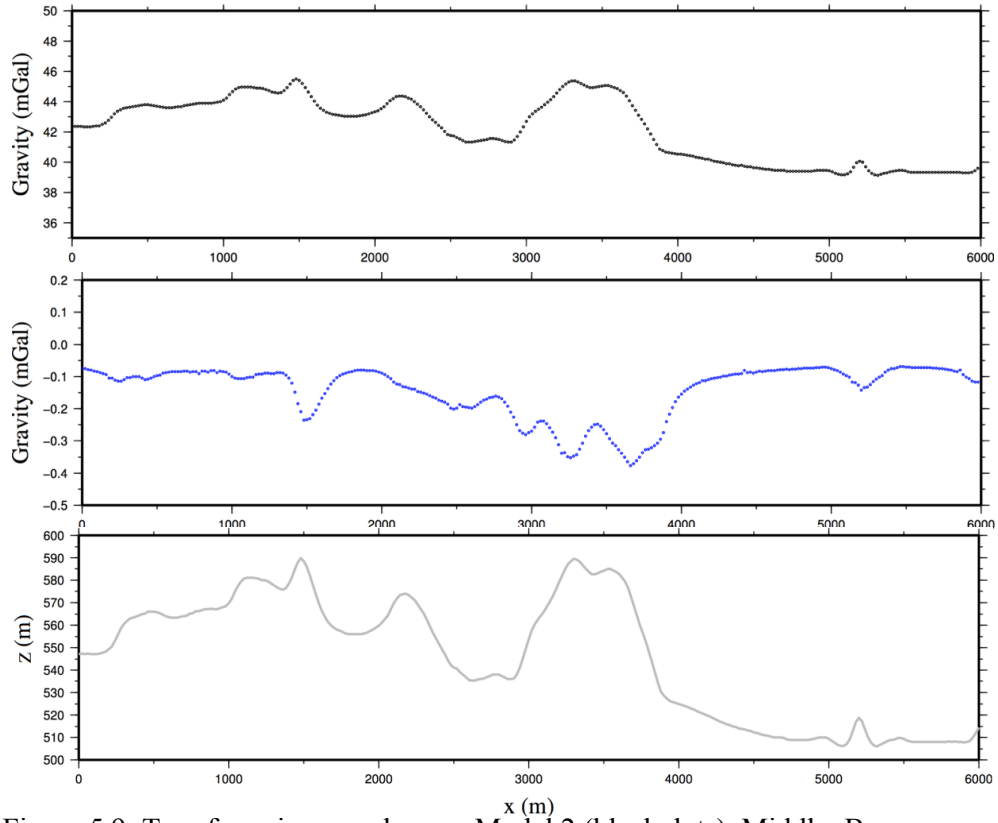


Figure 5.9: Top: free-air anomaly over Model 2 (black dots). Middle: Bouguer anomaly over Model 2 (blue dots). For the Bouguer correction, the datum is at 0m and ρ=1.85 g/cc. Bottom: topography along the survey line.

**Model 3:** Model 3 is similar to Model 2, but the thickness of the upper layer has been reduced. The interface between the two layers has been moved from 0m elevation to 500m as the base of the overburden in the McArthur area is located around 500m. Both the reference ellipsoid and the datum for the BC are now considered to be at 500m (Figure 5.10). It can be seen that the data after BC still have values similar to those for Model 2 (Figure 5.11). These values, ranging from 0.5 to 0.35mGal, are due to the terrain effect. This range is mentioned in Wood and Thomas (2002). The terrain correction (TC) takes into account the terrain and topographic effect in the vicinity of a gravity measurement. The residual data in the lower panel in Figure 5.11 are used as the TC for all subsequent

examples.

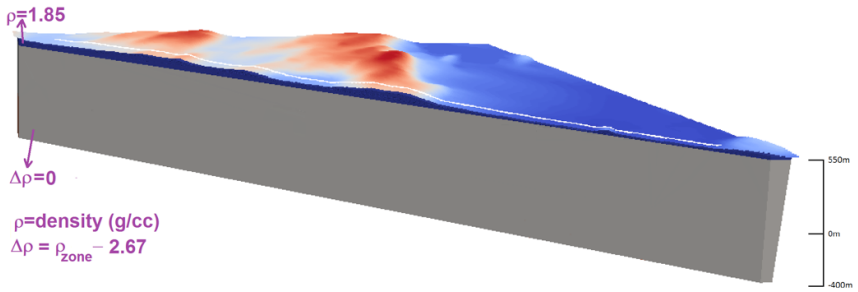


Figure 5.10: Model 3; A cross-section along the survey line. Interface between two layers is located at 500m elevation. White line is the survey line on the topography.

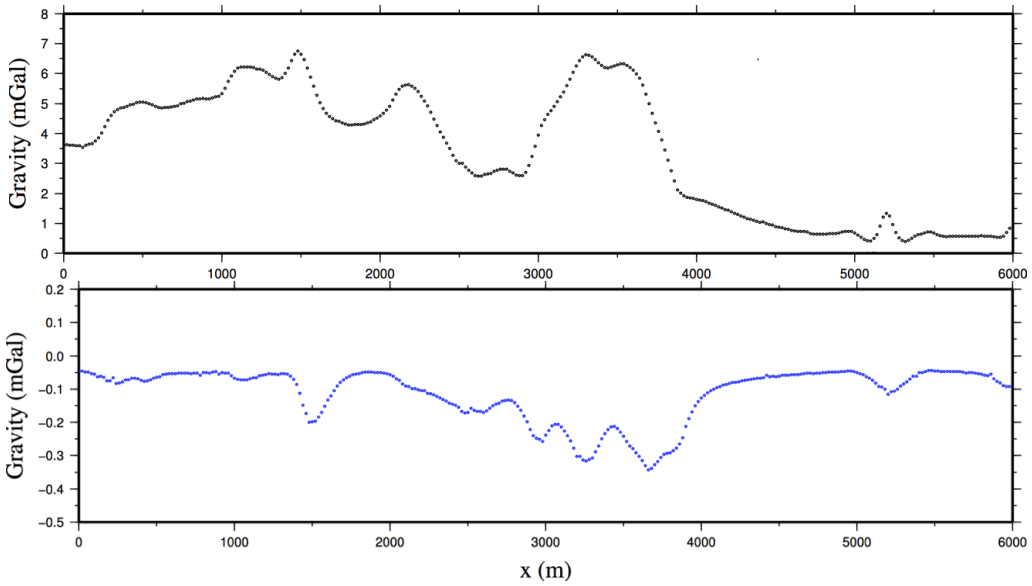


Figure 5.11: Top: free-air anomaly over Model 3 (black dots). Bottom: Bouguer anomaly over Model 3 (blue dots). For the Bouguer correction, the datum is at 500m and ρ=1.85 g/cc.

**Model 4:** Model 4 is similar to Model 3, but for this model I add a cylinder (perpendicular to the profile) with a diameter of 300m (from an elevation of 0m to 300m). It has a density of 2.47 g/cc, but since the reference ellipsoid is at 500m, it has a relative density of -0.2 g/cc (relative to 2.67g/cc; see Figures 5.12 and 5.13). It can be seen that, as expected, the Bouguer anomaly (after BC+TC) is similar to the gravity signature of cylinder anomaly.

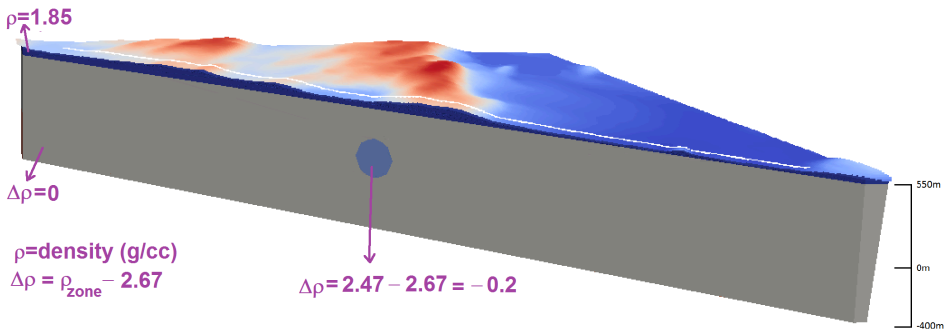


Figure 5.12: Model 4; cross-section of two layers plus a cylinder anomaly.

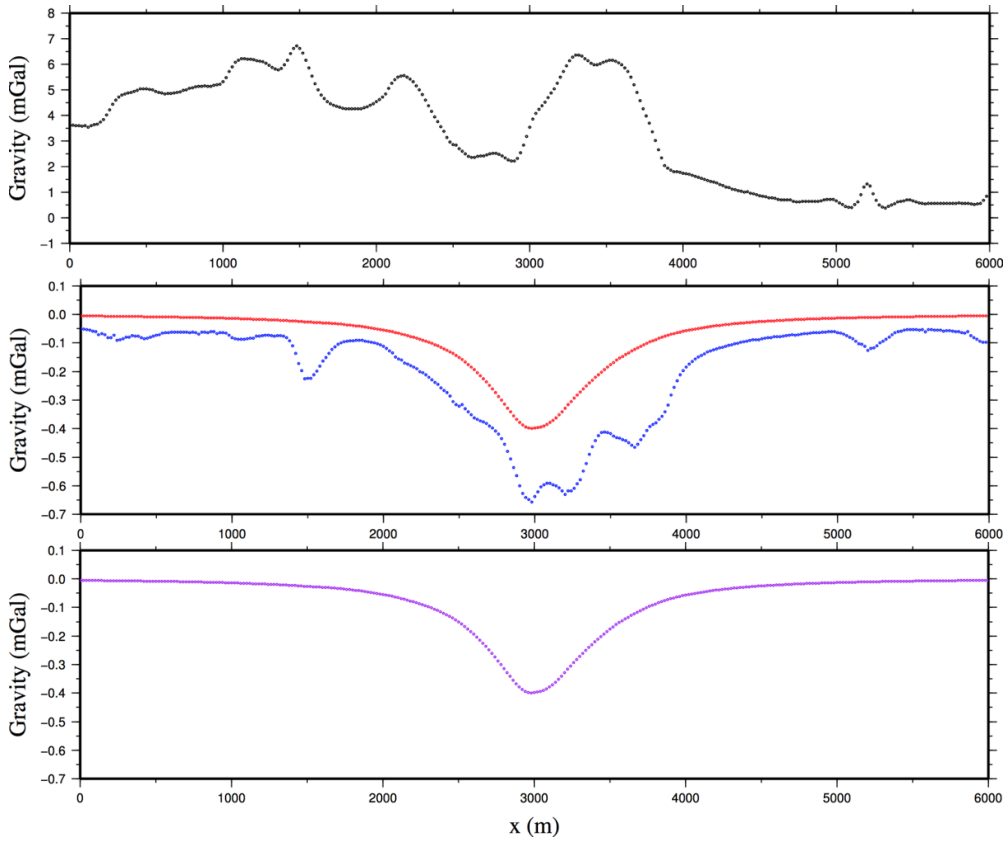


Figure 5.13: Top: free-air anomaly over Model 4 (black dots). Middle: Bouguer anomaly over Model 4 after BC (blue dots) and after BC+TC (red dots). For the Bouguer correction, the datum is at 500m and ρ=1.85 g/cc. Bottom: gravity signature of cylinder anomaly (Δρ=-0.2 g/cc).

**Model 5:** Model 5 (Figure 5.14) is similar to Model 4, but with a rugged interface between the two layers (based on McArthur drill-hole data; see Figure 2.2). For the BC, I still

consider a plane interface at an elevation of 500 m as the datum. As can be seen from Figure 5.15 the Bouguer anomaly along the profile has a shape that mimics the topography of the interface between the two layers under the survey line. There is no obvious indication of the cylinder in the Bouguer anomaly.

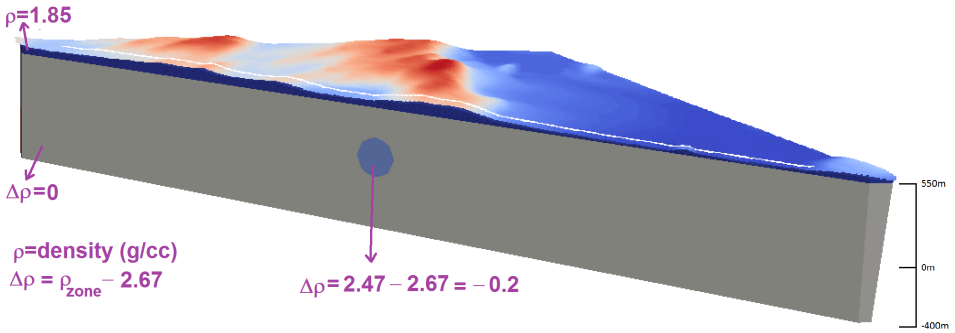


Figure 5.14: Model 5; cross-section of two layers with a rugged interface.

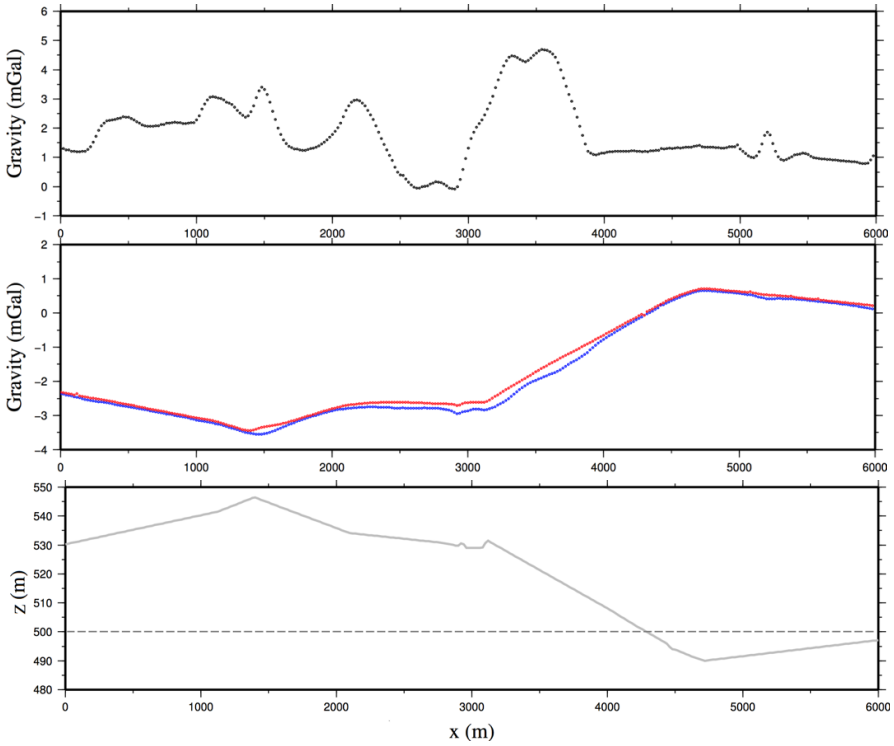


Figure 5.15: Top: free-air anomaly over Model 5 (black dots). Middle: Bouguer anomaly over Model 5 after BC (blue dots) and after BC+TC (red dots). For the Bouguer correction, the datum is at 500 m (dashed line in the bottom panel) and ρ=1.85 g/cc. Bottom: Topography of interface between the layers under the survey line.

**Model 6:** Model 6 is similar to Model 4 (i.e. flat base of the top layer), but with a third layer (lower layer from 0m to -400 m; i.e. basement of McArthur area). This also has different vertical blocks in three different variants of the model. The interface between the upper layer and the middle layer is again a plane at an elevation of 500 m. The interface between the middle layer and the lower layer is a plane et 0 m (sea level). The approximate locations of these layers as well as their densities are taken from Wood and Thomas (2002). For this model, three different scenarios (A, B and C) are considered.

**Model 6A:** In Model 6A (Figure 5.16), the sea level (0 m) is considered as the reference ellipsoid. Therefore, the densities below 0m (actually the densities of the units in the third layer) are relative density with respect to 2.67 g/cc. In this variant of Model 6, I assume that the third (lower) layer has a constant density of 2.67 g/cc, and hence a relative density of 0 g/cc. The cylinder now has a positive real density more than the real density of the middle layer (Figure 5.17). Therefore, the cylinder shows up as a positive contribution to the Bouguer anomaly.

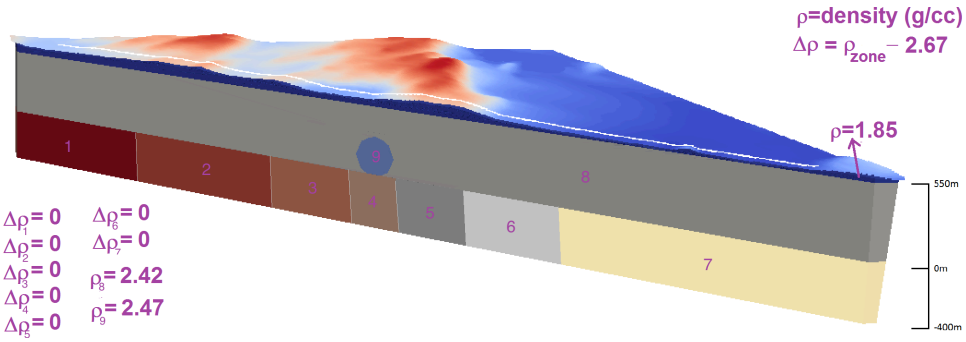


Figure 5.16: Model 6A; Reference ellipsoid and Bouguer correction datum are located at 0m and 500m elevations, respectively. The lowest layer has a relative density of 0g/cc.

Figure 5.17 indicates the importance of the TC. There is a significant difference between the Bouguer anomaly after BC and the Bouguer anomaly after BC+TC. In this figure for

the BC I consider the interface between the upper and the middle layer as datum (500 m), and after BC and TC I get a good result. However, the base level of the Bouguer anomaly is not around 0 mGal. Figure 5.18 represents the Bouguer anomaly after BC and TC when I consider sea level (0 m) as the datum in the BC for two densities ρ=1.85 g/cc and ρ=2.67 g/cc. It can be clearly seen that considering a density of 2.67 g/cc is not a good choice.

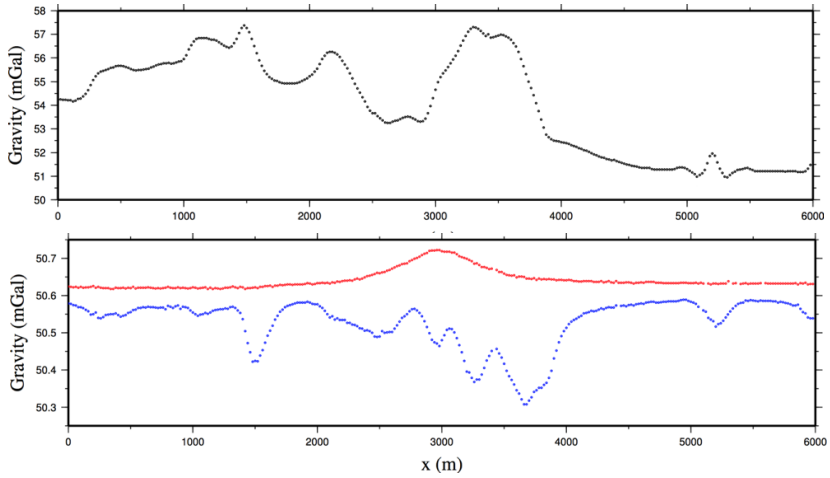


Figure 5.17: Top: free-air anomaly over Model 6A (black dots). Bottom: Bouguer anomaly over Model 6A after BC (blue dots) and after BC+TC (red dots). For the Bouguer correction, the datum is at 500 m and ρ=1.85 g/cc.

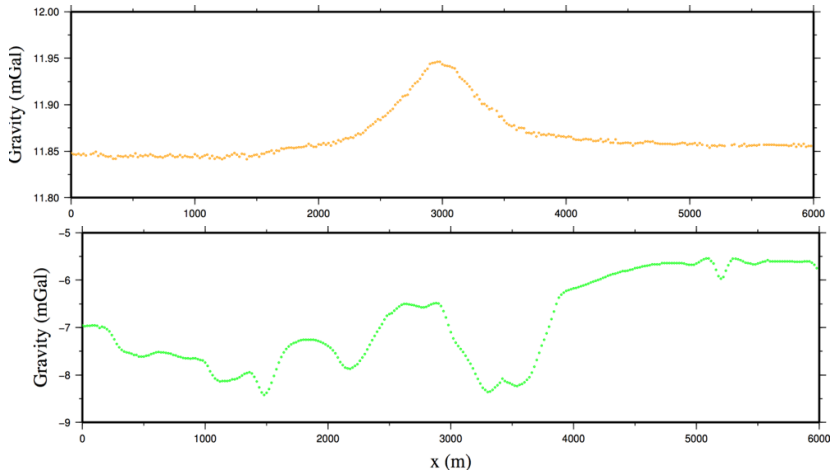


Figure 5.18: Bouguer anomaly over Model 6A after BC+TC, but for the Bouguer correction with the datum at 0 m and two densities: ρ=1.85 g/cc (top - orange dots) and ρ=2.67 g/cc (bottom – green dots).

**Model 6B:** The base level of the Bouguer anomaly of Model 6A is unexpectedly too far from a value close to 0 mGal (as can be seen it is around 50 mGal; Figure 5.17). This can be solved by considering the same datum for both the reference ellipsoid and Bouguer correction which is the same as correct estimations mentioned in Section 3.2.4. Thus, for Model 6B, I consider the interface between the upper and middle layer (which is at 500m) as the reference ellipsoid. Thus, the structures under 500m in the model have a relative density (actually the densities of the units in the second and third layers in addition to the cylinder anomaly; Figure 5.19). The Bouguer anomaly (after BC+TC) in Figure 5.20 show a good result when the datum is at 500 m and ρ=1.85 g/cc, as the signature of the cylinder anomaly can be clearly seen. Note that I considered a density for the Bouguer correction which is the same as the density of the materials of the upper layer (i.e. the density of overburden located above the reference ellipsoid). Also, I considered the same datum for the reference ellipsoid and Bouguer correction.

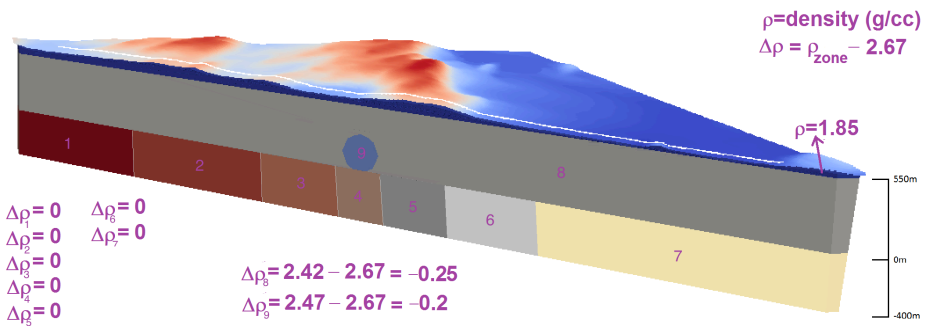


Figure 5.19: Model 6B; Reference ellipsoid is located at the base of the upper layer, and for the Bouguer correction two scenarios (0m and 500m) are considered for datum. The lowest layer has a relative density of 0g/cc.

Assume that for Model 6B the accurate value for the density in the BC is not known. Thus, I try two values (ρ=1.7 g/cc and ρ=2 g/cc) for density which are close to the accurate value (ρ=1.85 g/cc). The results are shown in Figure 5.21. It can be seen that those

approximate densities don't give good results. This shows the importance of getting the density that is used in the Bouguer correction as close as possible to the density of the material that the topography is going up and down through.

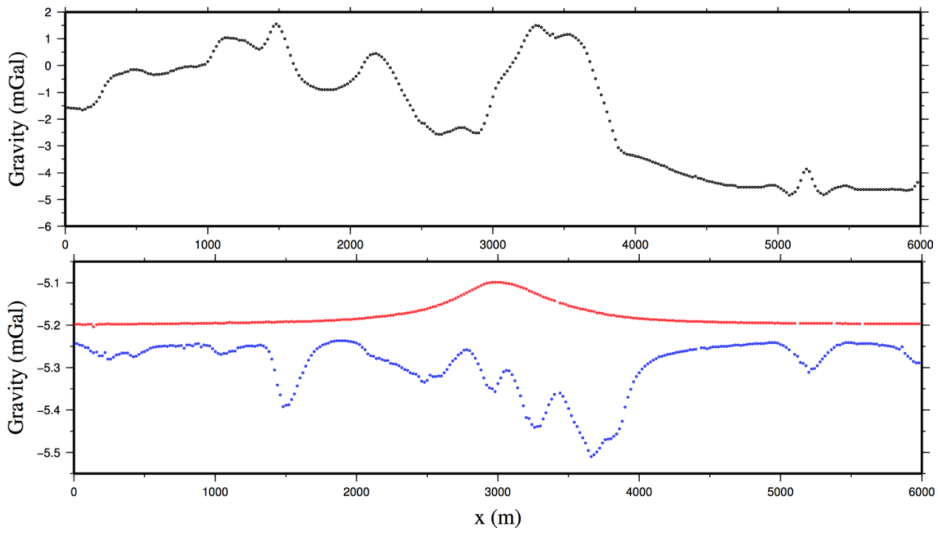


Figure 5.20: Top: free-air anomaly over Model 6B (black dots). Bottom: Bouguer anomaly over Model 6B after BC (blue dots) and after BC+TC (red dots). For the Bouguer correction, the datum is at 500m and ρ=1.85 g/cc.

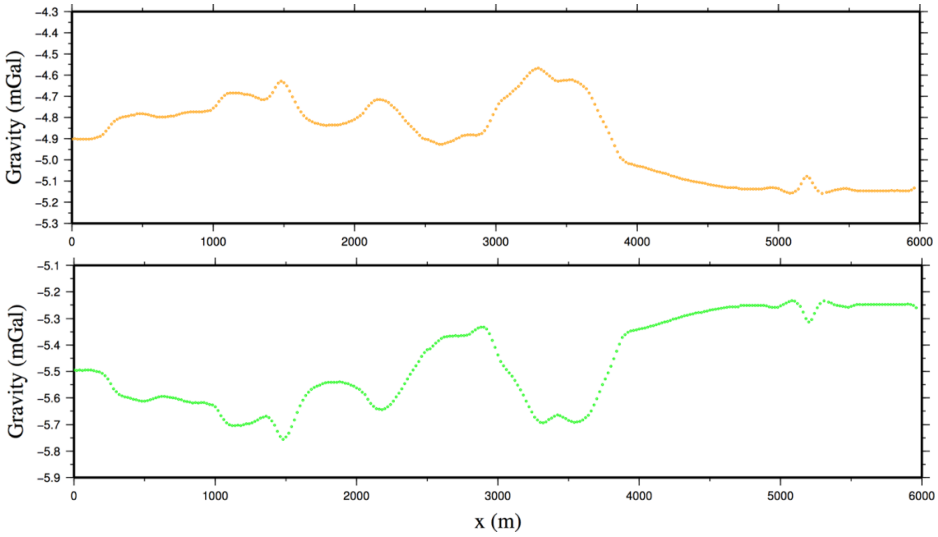


Figure 5.21: Bouguer anomaly over Model 6B after BC+TC for the Bouguer correction using the datum at 500m and with two densities: ρ=1.7 g/cc (top - orange dots) and ρ=2 g/cc (bottom – green dots).

Now, assume that for Model 6B the location of the base of the upper layer is unknown to be used in the BC. Therefore, I consider an arbitrary datum for the BC at 0 m elevation. The Bouguer anomaly (after BC+TC) in Figure 5.22 shows that for a datum at 0 m in the BC, ρ=1.85 g/cc gives a much better result than ρ=2.67 g/cc. For the BC when the datum is at 0m, I again try two values (ρ=1.7 g/cc and ρ=2 g/cc) for the density which are close to the true value (of the upper layer; ρ=1.85 g/cc). The results are shown in Figure 5.23. It can be seen that a good estimate of density of which part of the subsurface in the BC is necessary for obtaining a good result even when I did not consider a good approximate for the datum in the BC.

However, there is a static shift in the Bouguer anomalies in Figures 5.22 and 5.23 around -40 to -60 mGal which is due to the considering a datum for BC (0 m) lower than the reference ellipsoid. This happened because for BC I considered a density of 1.85 g/cc for all the structures above 0m elevation while from 0m to 500m the structures had small values of the relative density ($\Delta\rho_8$=-0.25 g/cc and $\Delta\rho_9$=-0.2 g/cc ; Figure 5.19) as they are located under the reference ellipsoid. Thus, when the BC is subtracted from the free-air data, actually a slab with a thickness of 500 m (from 0 m to 500 m) and a density of 1.85 g/cc is subtracted while it had a small value of the relative densities.

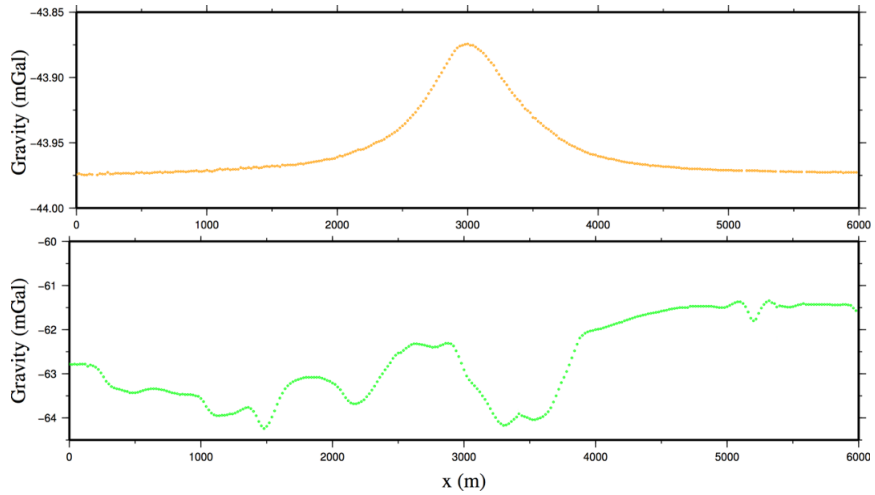


Figure 5.22: Bouguer anomaly over Model 6B after BC+TC for the Bouguer correction using the datum at 0 m and with two densities: ρ=1.85 g/cc (top - orange dots) and ρ=2.67 g/cc (bottom – green dots).

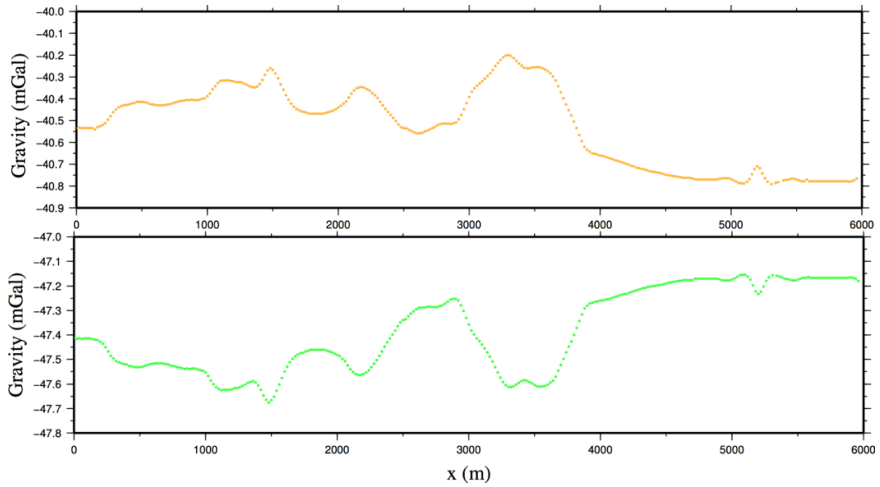


Figure 5.23: Bouguer anomaly over Model 6B after BC+TC for the Bouguer correction using the datum at 0 m and with two densities: ρ=1.7 g/cc (top - orange dots) and ρ=2 g/cc (bottom – green dots).

**Model 6C:** Model 6C is similar to Model 6B, but in this model I consider different densities for the vertical blocks in the lower layer (Figure 5.24). These blocks represent the different geological structures in the basement (see Figure 5.5). In Figure 5.25, for the BC a datum of 500 m and a density of 1.85 g/cc are considered. The graphs show that the different

densities in the lower layer have a big effect on the gravity data. The subsequent graphs in Figure 5.26 emphasize that for the BC with a datum at 0m, a density of 2.67 g/cc is not a good choice as there is no similarity between this graph (with a density of 2.67 g/cc) and the graph in Figure 5.25 (with a density of 1.85 g/cc). Also, this graph is following the same pattern of the variations of topography (but in opposite values which means by increasing topography the data is decreasing and vice versa; see Figure 5.9). Note that in Figure 5.26 the static shift is again present as expected.

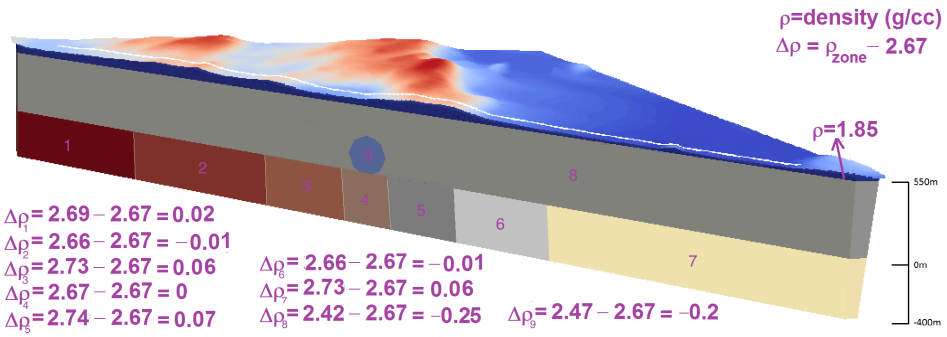


Figure 5.24: Model 6C; Reference ellipsoid is located at the base of the upper layer, and for the Bouguer correction two scenarios (0 m and 500 m) are considered for datum. The lowest layer has blocks with different relative densities.

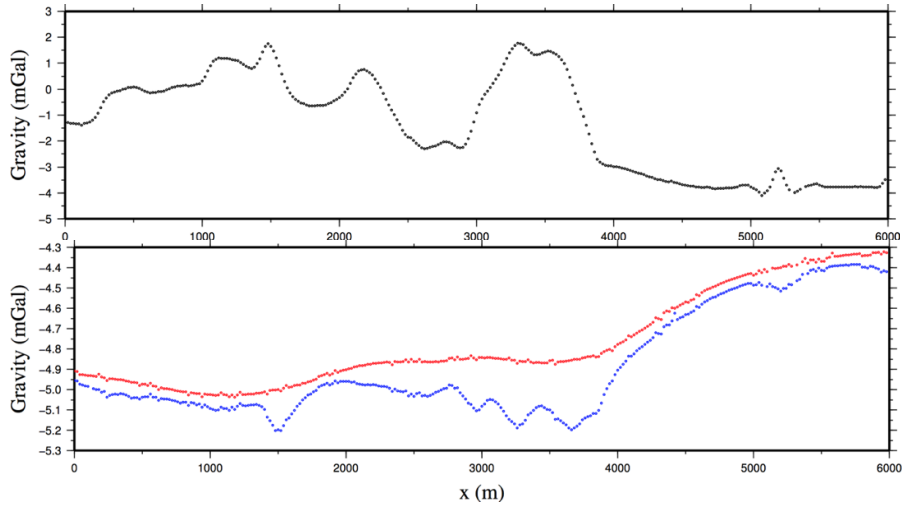


Figure 5.25: Top: free-air anomaly over Model 6C (black dots). Bottom: Bouguer anomaly over Model 6C after BC (blue dots) and after BC+TC (red dots). For the Bouguer correction, the datum is at 500m and ρ=1.85 g/cc.

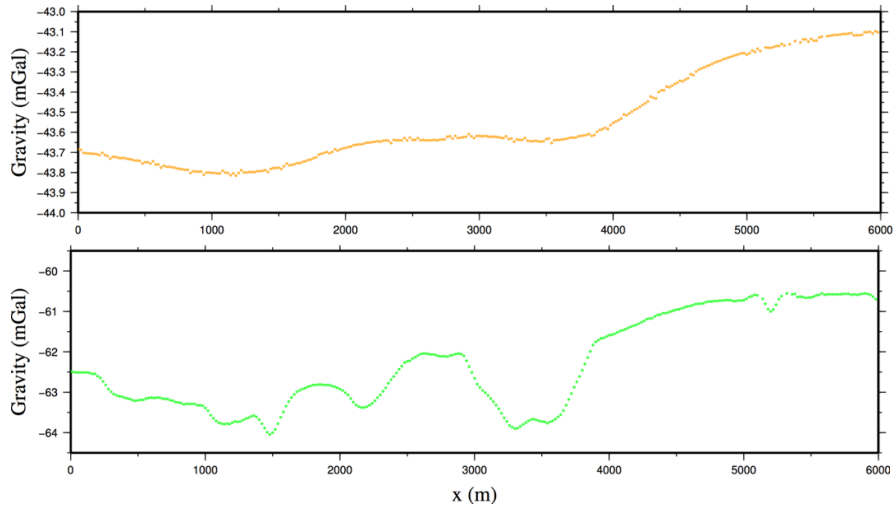


Figure 5.26: Bouguer anomaly over Model 6C after BC+TC for the Bouguer correction using the datum at 0m and with two densities: ρ=1.85 g/cc (top - orange dots) and ρ=2.67 g/cc (bottom – green dots).

**Model 7:** Model 7 is similar to Model 6C, but in this model based on Wood and Thomas (2002) the thickness of the lower layer was increased from 400m to 4500m (Figure 5.27). By this work, the effect of the thickness of the model on the computed data can be investigated (Figure 5.28). For the Bouguer correction, the datum is at 500m and $\rho$=1.85 g/cc. By comparing Figures 5.25 and 5.28, it can be seen that both free-air and Bouguer anomalies are shifted around 5 mGal for Model 7 which is due to the increasing of the thickness of the model. However, in both figures the signature of the cylinder anomaly cannot be seen because it is masked by the variations of the density of the basement blocks. Also, it can be seen that the Bouguer anomaly of Model 7 is a little bit smoother than Model 6C. This is because, by increasing the thickness of basement blocks to depth, longer wavelength components from the deeper parts of the blocks are now contributing to the response. Therefore, the summation of these longer wavelengths gives a smoother data in which the variation of amplitude is less sharp.

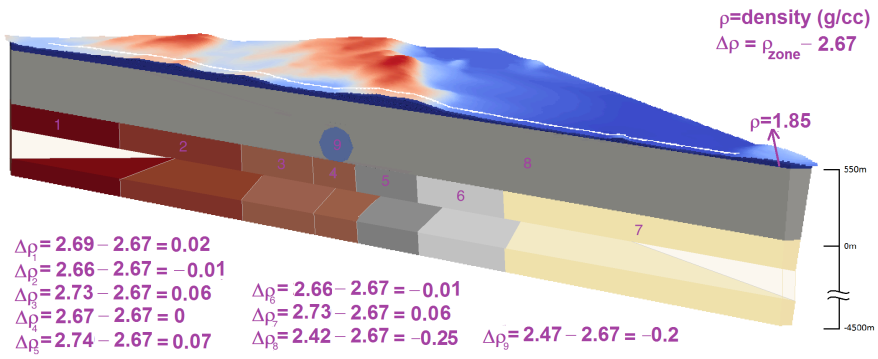


Figure 5.27: Model 7; For the Bouguer correction, the datum is at 500m and $\rho$=1.85 g/cc. The thickness of the lowest layer which has different blocks with different relative densities has increased.

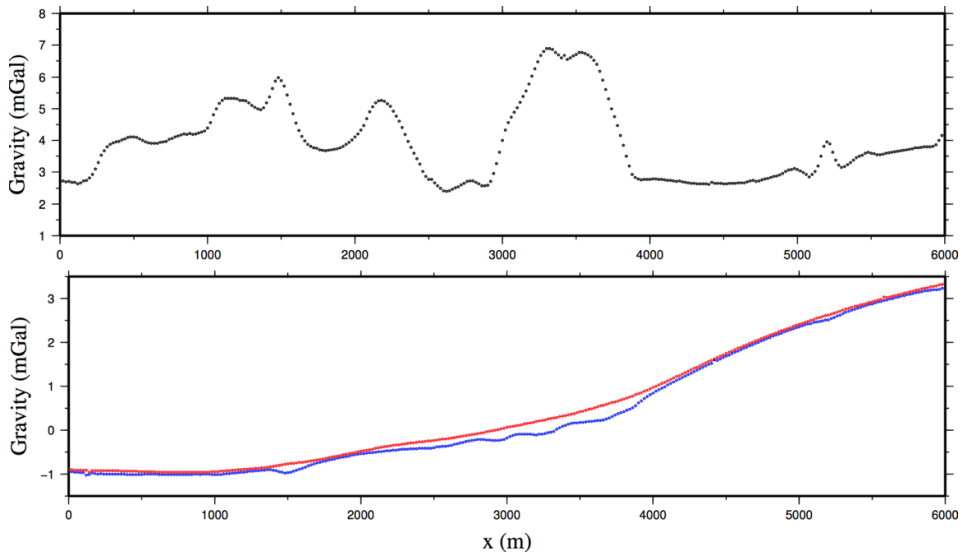


Figure 5.28: Top: free-air anomaly over Model 7 (black dots). Bottom: Bouguer anomaly over Model 7 after BC (blue dots) and after BC+TC (red dots). For the Bouguer correction, the datum is at 500m and ρ=1.85 g/cc.

**Model 8:** Model 8 is similar to Model 7, but it has realistic interfaces between the layers (Figure 5.29). Thus, both the base of overburden and top of basement (unconformity) are not planar in Model 8. These changes are made using the available drill-hole data (see Section 2.2 and Figure 2.2). Also, instead of the cylinder the irregular density anomaly is used (see Section 5.2).

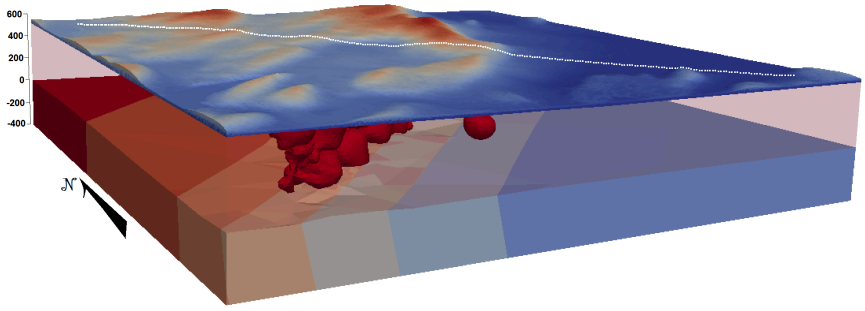


Figure 5.29: A 3D perspective view of Model 8 (to the depth -400m). This model has an irregular density anomaly as well as realistic interfaces between the layers.

**Model 8A:** For Model 8, I investigate two variations (8A and 8B) in which the anomaly within the second layer (#9 in Figures 5.30 and 5.34) is two times larger in Model 8B than in Model 8A.

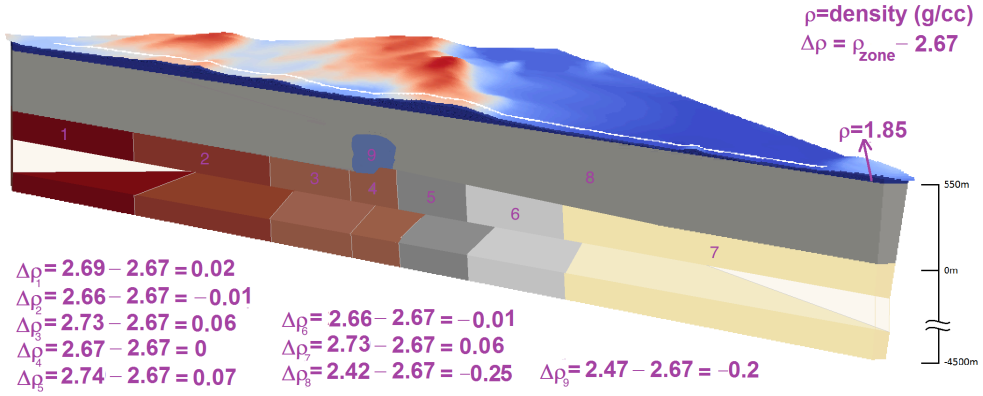


Figure 5.30: Model 8A; This model has a small irregular density anomaly as well as realistic interfaces between the layers.

It can be seen that the small variation in the data due to the anomaly within the second layer (which could be the alteration zone) is very small compared with the variation due to the heterogeneous lower layer (i.e., basement; Figure 5.31). Also, there are sharp variations due to the topography of the interface between upper and lower layers (Figure 5.32). In Figure 5.33 the individual contributions of the upper layer (i.e., overburden) and the lower layer (i.e., basement) are shown. Also shown are the data for the complete model after

removing the contribution of the upper layer which is similar to the Bouguer anomaly (BC+TC) as expected.

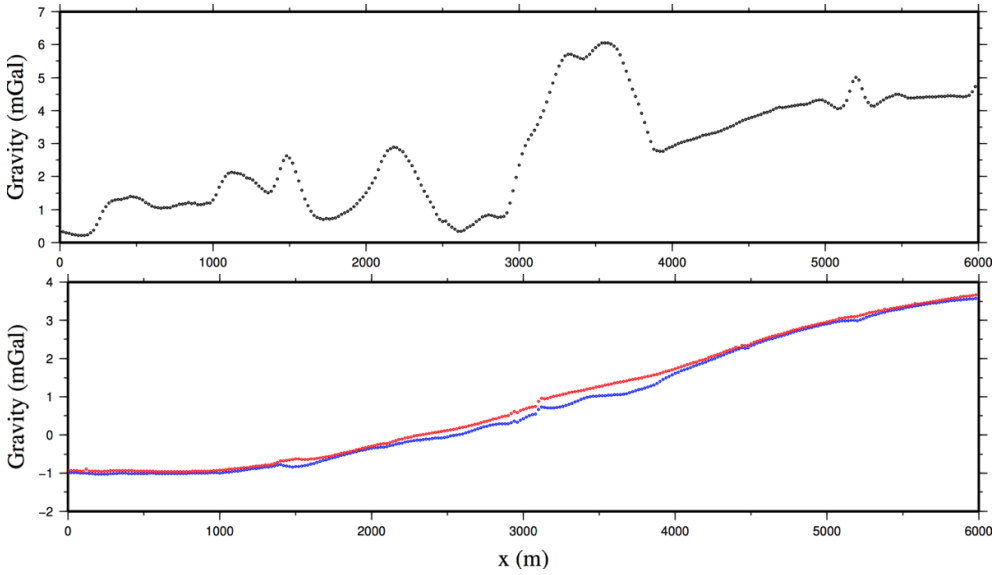


Figure 5.31: Top: free-air anomaly over Model 8A (black dots). Bottom: Bouguer anomaly over Model 8A after BC (blue dots) and after BC+TC (red dots). For the Bouguer correction, the datum is the interface between the upper and lower layers and ρ=1.85 g/cc.

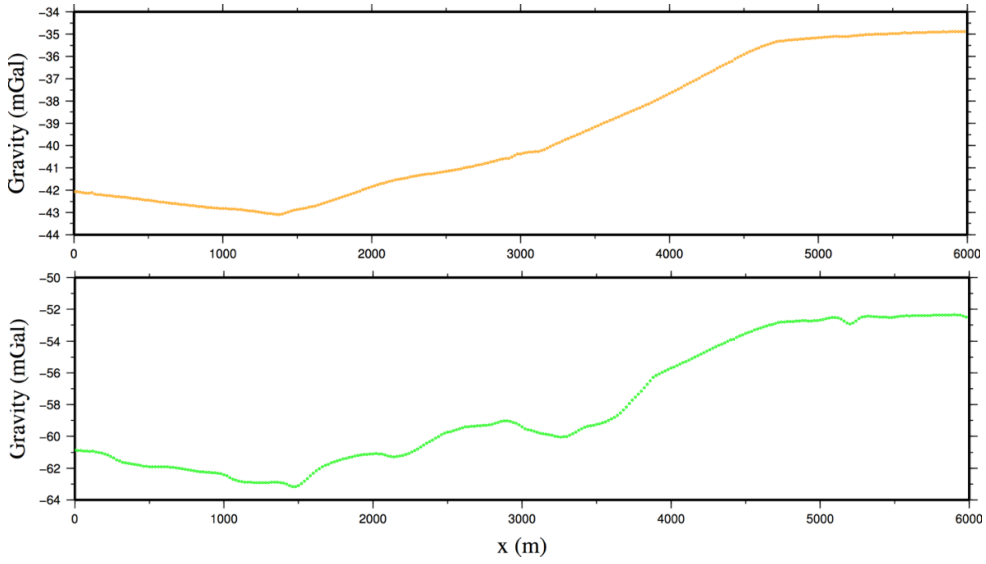


Figure 5.32: Bouguer anomaly over Model 8A after BC+TC for the Bouguer correction using the datum at 0m and with two densities: ρ=1.85 g/cc (top - orange dots) and ρ=2.67 g/cc (bottom – green dots).

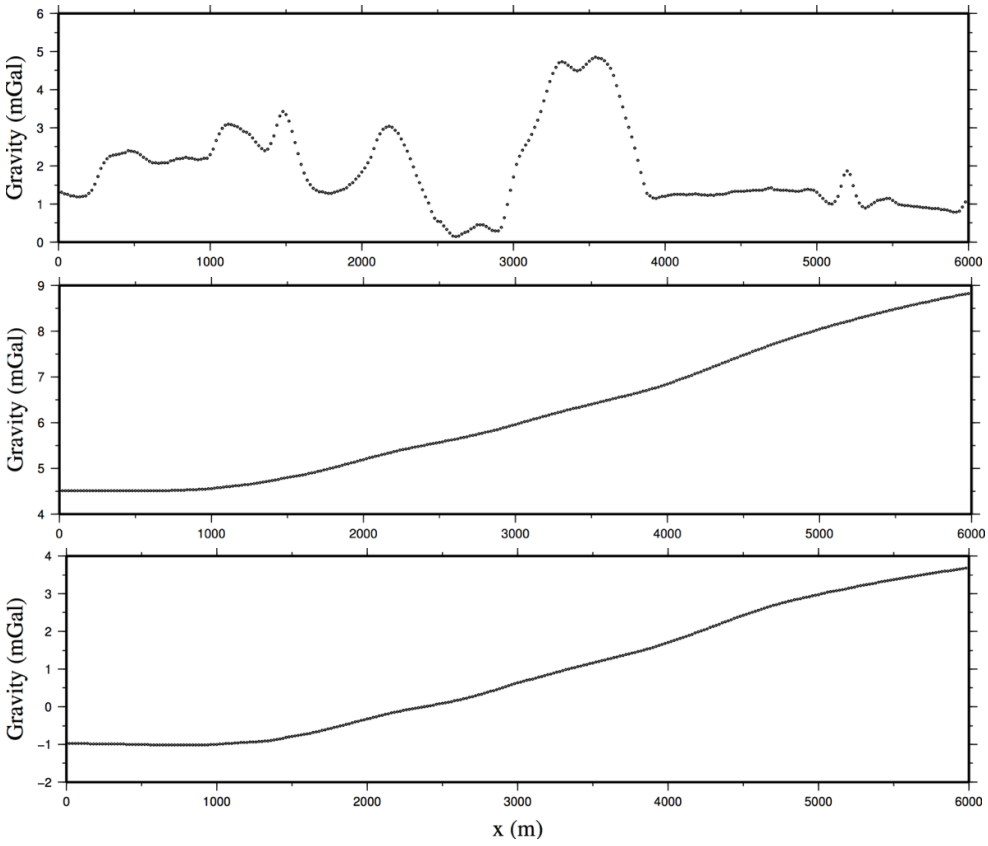


Figure 5.33: Top: Gravity data along the survey line on the topography for the upper layer (overburden). Middle: Gravity data along the survey line on the topography for the lower layer (basement). Bottom: Gravity data along the survey line on the topography for the entire model after removing the upper layer (overburden) contribution.

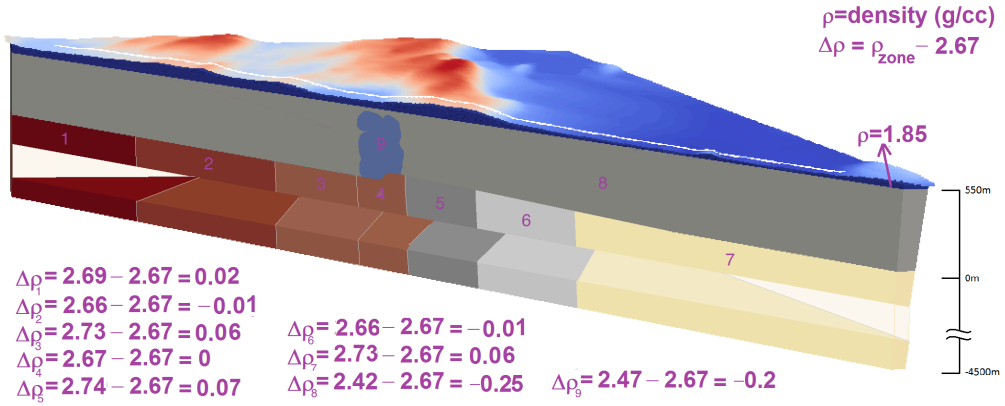


Figure 5.34: Model 8B; This model has a large irregular density anomaly as well as realistic interfaces between the layers.

**Model 8B:** In Model 8B the anomaly in the second layer (#9 in Figure 5.34) is larger in width and vertical extent (same density). Comparing the data due to the two Models, 8A and 8B, shows an increase of 0.1 mGal in the amplitude of gravity data for Model 8B (Figure 5.35).

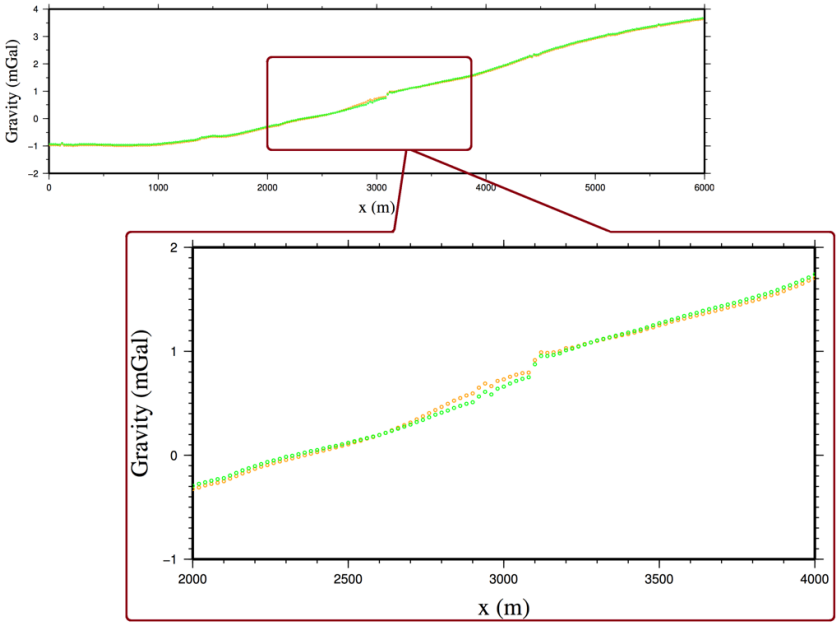


Figure 5.35: Comparing the Bouguer anomaly (BC+TC) for the two Models 8A (green) and 8B (orange). It can be seen that they are similar except in the middle of the profile where the 8B data are 0.1 mGal larger than the 8A data.

## 5.4 Modelling of free-air and Bouguer anomalies (McArthur area #2)

As mentioned before, the structure of the basement is the main difference between scenarios (#1) and (#2). For Model (#2), the density model was made based on Wood and Thomas (2007; Figures 5.36 and 5.37). In this model, the effect of the (different) basement on gravity data is investigated. Gravity data (free-air and Bouguer anomalies) were computed for representative 3D models of the McArthur area. The images of the 3D models in this section again show the central 5 by 5 km. The actual 3D models used for the

computations had a size of 500 by 500 km in order to avoid any effect of the edges on the gravity data. The total thickness of these models was 5000 m based on the results of the previous section. Gravity data were computed at 20 m intervals along a 6 km line across the model over the topography. The tetrahedral mesh has around 320,000 cells starting with an edge size of 20 m on the surface. Note that, as mentioned before, in the gravity forward modelling the quality of mesh, number and size of the cells have no effect on the results (data).

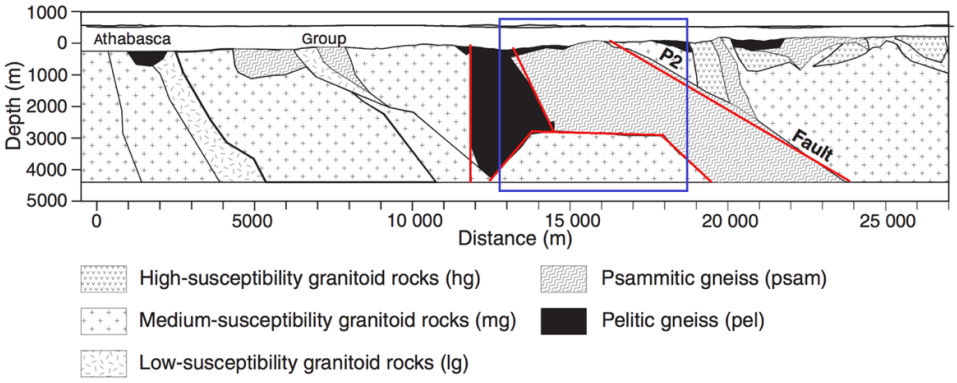


Figure 5.36: McArthur geological section from Thomas and Wood (2007). Blue square shows the part which forms the basis of the models considered here. Red lines show the modelled interfaces between the blocks. Small zones and variations are ignored in the modelling.

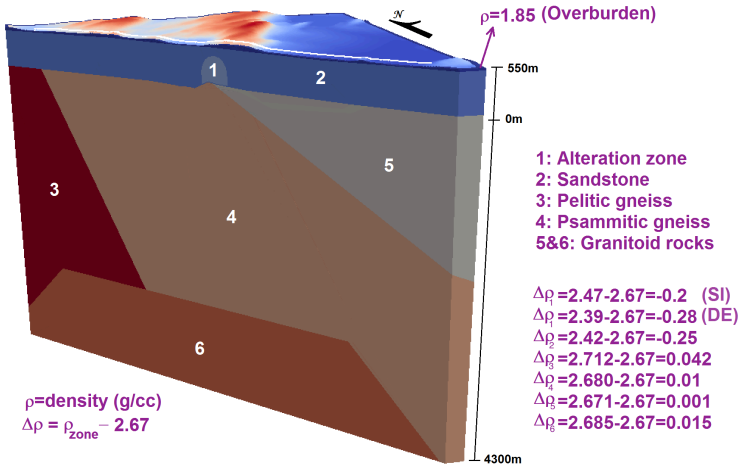


Figure 5.37: Density model including different geological structures based on Wood and Thomas (2007). Basement blocks are adapted from Figure 5.36.

Two different scenarios, named DE and SI, are considered. Also, instead of the irregular density (SWIR) used in previous Models (Model 8; Figure 5.29) a cylinder anomaly is used for this new model as the alteration zone. The density of the alteration zone in Model DE is less than the sandstone, and in Model SI is more than the sandstone. The base of the overburden is considered as datum for the reference ellipsoid and the Bouguer correction. The layers (or structures) above the reference ellipsoid have real densities while the layers (or structures) below the reference ellipsoid have relative density. The relative densities were with respect to 2.67g/cc. Therefore, overburden has a real density of 1.85 g/cc and the lower layers have a relative density. This model has realistic topography as well as realistic interfaces for the base of overburden and the top of basement (unconformity). The unconformity has a step of more than 50 m where it is intersected by the fault (the interface between block #4 and block #5 in Figure 5.37). A density of 1.85 g/cc in applied for the BC.

**Model DE:** Figures 5.38 and 5.39 show the gravity data for the DE scenario. In this model a density of 2.39 g/cc (a relative density of -0.28 g/cc) is considered for the alteration zone. It can be seen that the free-air anomaly is dominated by variations in topography. The Bouguer anomaly (Figure 5.38) shows a decrease in the middle of the profile that is due to the alteration zone. Other variations, specially a large step at 3000 m, in the Bouguer anomaly along the profile can be due to the variations in the interface between overburden and sandstone. Also, in Figure 5.39 gravity data after removing overburden contribution shows a decrease in the middle of the profile (between 2500 m and 4000 m) which is due to the alteration zone.

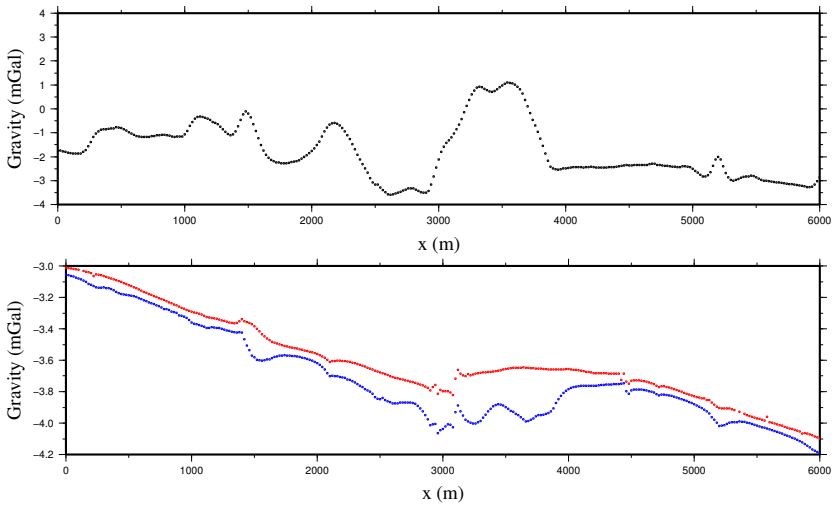


Figure 5.38: Top: free-air anomaly over Model DE (black dots). Bottom: Bouguer anomaly over Model DE after BC (blue dots) and after BC+TC (red dots). For the Bouguer correction, the datum is the interface between the upper and lower layers and ρ=1.85 g/cc.

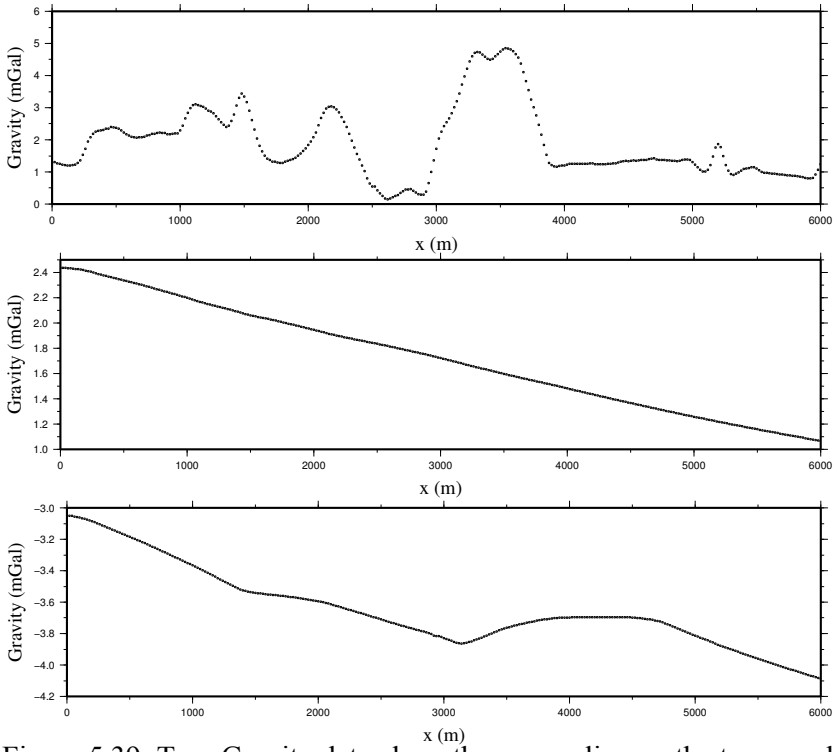


Figure 5.39: Top: Gravity data along the survey line on the topography for the overburden. Middle: Gravity data along the survey line on the topography for the basement. Bottom: Gravity data along the survey line on the topography for the entire model after removing overburden contribution.

**Model SI:** Figures 5.40 and 5.41 show the gravity data for the SI scenario. In this model, a density of 2.47g/cc (a relative density of -0.2) is considered for the alteration zone. Similar to the previous model, the free-air anomaly is strongly influenced by variations of topography. The Bouguer anomaly shows an increase in the middle of the profile that is due to the alteration zone. A large step at 3000 m in the Bouguer anomaly is due to the variations in the interface between overburden and sandstone. The Bouguer anomaly (Figure 5.40) shows an increase in the middle of the profile that is due to the alteration zone. Also, in Figure 5.41 gravity data after removing overburden contribution shows an increase in the middle of the profile (between 2500m and 4000m) which is due to the alteration zone as well.

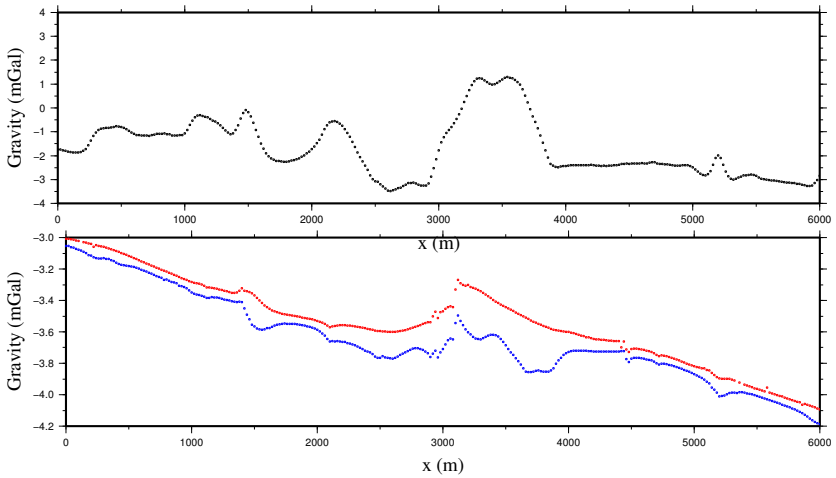


Figure 5.40: Top: free-air anomaly over Model SI (black dots). Bottom: Bouguer anomaly over Model SI after BC (blue dots) and after BC+TC (red dots). For the Bouguer correction, the datum is the interface between the upper and lower layers and ρ=1.85 g/cc.

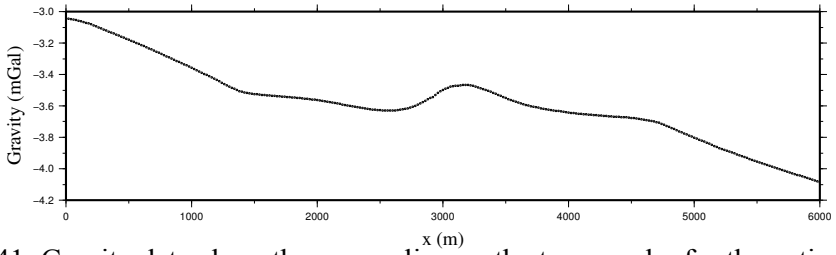


Figure 5.41: Gravity data along the survey line on the topography for the entire model after removing overburden contribution.

It can be seen that considering the interface between overburden and sandstone as the reference ellipsoid is a good choice (however it is not flat) as the signature of alteration zone can be clearly seen in the Bouguer anomaly and the free-air anomaly after removing the overburden contribution.

I also investigated a case in which the datum for the reference ellipsoid and the Bouguer correction is flat and is located at 450 m elevation for both Models DE and SI. Therefore, the overburden and the upper part of the sandstone has a real density of 1.85 g/cc and 2.42 g/cc, respectively; whereas the lower layers have a relative density.

**Model DE:** Figure 5.42 shows the gravity data for the DE scenario in which the datum for the reference ellipsoid and the Bouguer correction is located at 450 m elevation, and a density of 2.39 g/cc (a relative density of -0.28 g/cc) is considered for the alteration zone. It can be seen that the free-air anomaly is dominated by variations in topography. Variations in the Bouguer anomaly along the profile are due to the variations in the interface between the overburden and the sandstone. No variation can be seen in the Bouguer anomaly as well as the free-air anomaly associated with the alteration zone after removing the overburden contribution.

**Model SI:** Figures 5.43 shows the gravity data for the SI scenario in which the datum for the reference ellipsoid and Bouguer correction is located at 450 m elevation, and a density of 2.47 g/cc (a relative density of -0.2 g/cc) is considered for the alteration zone. The Bouguer anomaly shows an increase in the middle (between 2500 m and 3500 m) of the profile that is due to the alteration zone. But, no clear variation can be seen in the free-air

anomaly after removing the overburden contribution associated with the alteration zone.

For the McArthur area model (Figure 5.37), it is not possible to consider a flat datum for the reference ellipsoid higher than the base of the overburden (somewhere in the overburden). Because, in some places the elevation of the highest point of the base of overburden is more than the elevation of the lowest point of the topography in other places (see Figure 5.44). In the model in Figure 5.37, the topography varies from 506 m to 624 m, while the base of the overburden varies from 494 m to 550 m.

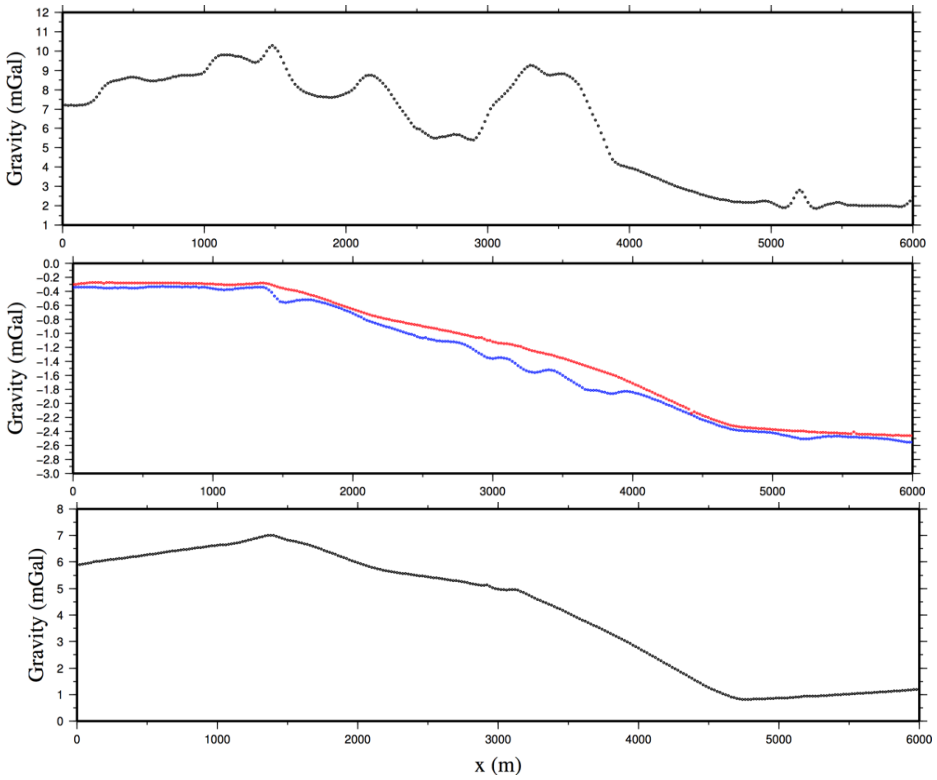


Figure 5.42: Top: free-air anomaly over Model DE (black dots). Middle: Bouguer anomaly over Model DE after BC (blue dots) and after BC+TC (red dots). For the Bouguer correction, the datum is at 450 m elevation and ρ=1.85 g/cc. Bottom: gravity data along the survey line on the topography for the entire model after removing overburden contribution.

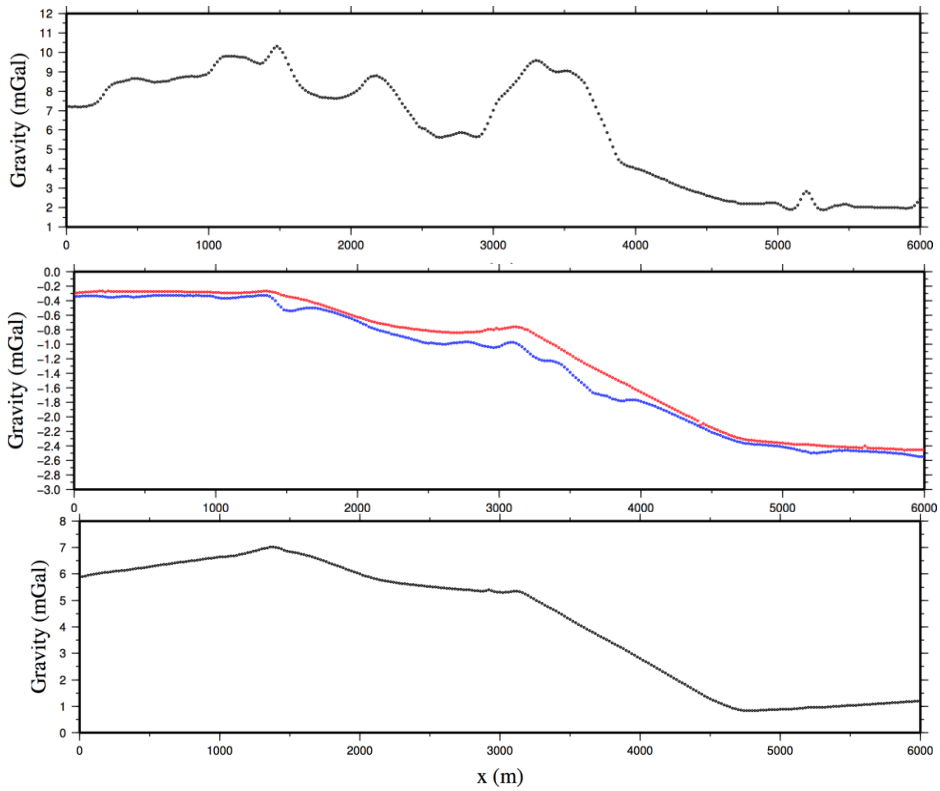


Figure 5.43: Top: free-air anomaly over Model SI (black dots). Middle: Bouguer anomaly over Model SI after BC (blue dots) and after BC+TC (red dots). For the Bouguer correction, the datum is at 450 m elevation and ρ=1.85 g/cc. Bottom: gravity data along the survey line on the topography for the entire model after removing overburden contribution.

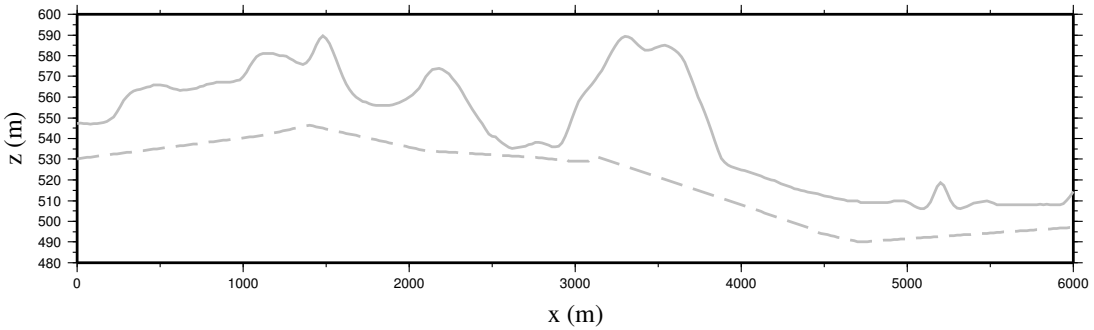


Figure 5.44: Topography along the survey line (solid line), and the interface between the overburden and sandstone under the survey line (dashed line).

Figures 5.43 and 5.44 show also that a variation less than 10m in the base of overburden can provide a similar response to the alteration signature. New researches (CMIC-Footprints project; see Section 2.5.2) show that the density of alteration zone can changes in a wider range from 2.2 g/cc (disilicification) to 2.6 g/cc (silicification). This means that a larger response (amplitude) related to the alteration zone might be seen in the Bouguer anomaly.

## 5.5 Conclusions

In this chapter, I was working to build realistic models taking into account everything I know and structures that are estimated or speculated to do forward modelling. Also, the concept of the free-air anomaly and the Bouguer anomaly were explained by synthetic models. Different models were made to investigate the contribution of different geological structures of the McArthur area in gravity data. It was shown that the free-air data is dominated by the variations of topography. Also, the basement has a significant effect on the Bouguer anomaly. And, the density contrast between sandstone and alteration is an important factor for detecting the alteration signature in the Bouguer anomaly. Therefore, it is not easy to provide a minimum contrast that is needed in order to resolve the alteration zone as the shape, depth and density of other structures have a very large effect on the results. If I be able to remove the overburden signature from the gravity data, there can be more factors (e.g. topography between the overburden and sandstone) which are able to mask the alteration signature.

It was shown that the location of the datum in the Bouguer correction has no significant

effect on the Bouguer anomaly. But, a good estimate of density of which part of the subsurface in the BC is necessary for obtaining a good result even when I did not consider a good approximate for the datum in the the Bouguer correction.

# Chapter 6

# Spectral Analysis and Filtering for Separation of Overburden and Deep Signals

## 6.1 Introduction

Different sources at different depths (and of different scales) can give signals of different wavelengths/wavenumbers. And hence this looks like a possible way to separate out overburden effect and deeper structures. For example, gravity and magnetic measurements are a combination of several sources at different depths which the separation of the contributions of each source is not always easily possible (Telford et al., 1976; Blakely, 1995). But, there is a relationship between the wavenumber/wavelength and the depth of the source, which this relationship can help for estimating the depth as well as the source separation (Blakely, 1995; Naidu and Mathew, 1998). Therefore, differences in wavenumber/wavelength content can be used for this purpose.

For this purpose, the data should transform from the space (or time) domain to the frequency domain using the mathematical method of Fourier transform (Papoulis, 1962; Bracewell, 1965). Spectral analysis and frequency filtering are used in this research.

Spectral analysis can separate (under certain assumption and simplification as I am about to show, essentially, in this chapter) and represent each source contribution as well as the the depth to the source in the frequency domain if all sources have the same size and geometry (Naidu, 1968; Spector and Grant, 1970; Rayner, 1971; Treitel et al., 1971). Frequency filtering means the separation of data into its individual components. Frequency filters (e.g. low-pass, high-pass and band-pass) are employed as each source has different frequency characteristics and can therefore be separated on this basis (Cowan and Cowan, 1993; Hsu et al., 1996; Naidu and Mathew, 1998; Smith et al., 1998). Low-pass filter passes signals with a frequency lower than a certain cut-off frequency, and attenuates signals with frequencies higher than the cut-off frequency. In the high-pass filter, high frequencies are passed, and low frequencies are attenuated. Also in the band-pass filter, only frequencies in a frequency band are passed.

In this chapter, spectral analysis as well as filtering are applied to both synthetic and real gravity data. I start with synthetic data. For the synthetic case, gravity data are synthesized for an area (9×9 km) over a 3D model along a number of profiles (adapted from real data) with station spacing and profile spacing of around 50 m and 300 m, respectively (Figure 6.1). The 3D model is similar to the model used in Figure 5.37. For the spectral analysis, 2D power spectrum and radially averaged power spectrum are investigated on the synthetic data. Also, frequency filtering (such as low-pass, high-pass, band-pass and derivatives) are applied on the synthetic data. After finding the appropriate spectral analysis and filtering methods, they will be applied to the real data.

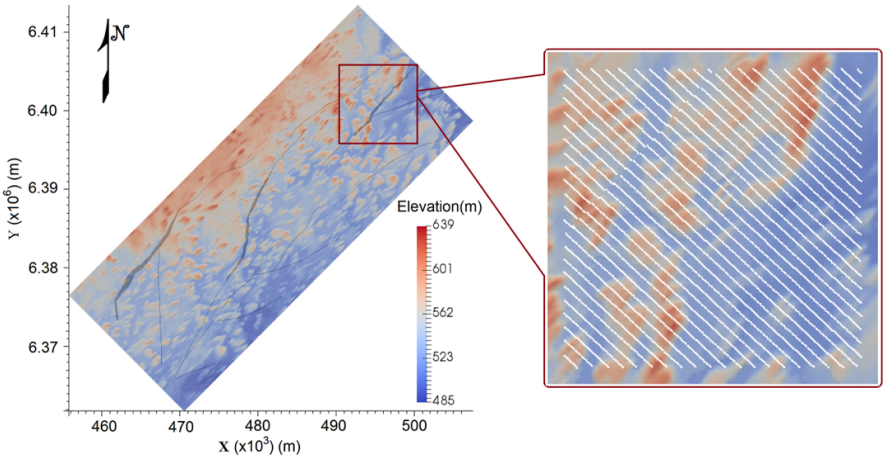


Figure 6.1: Topography of McArthur-Millennium corridor. Main faults are shown by grey irregular lines. Inset (9×9km) shows location of airborne survey lines (white lines; adapted from real data).

## 6.2 3D gravity modelling

The gravity model with the densities of the various geological units, made based on Wood and Thomas (2007; Figure 6.2), is shown in Figure 6.3. This model is an initial model with the rough estimate of density values and block locations. It is similar to Model (#2) in Section 5.4, but it has a density of 2 g/cc for the overburden.

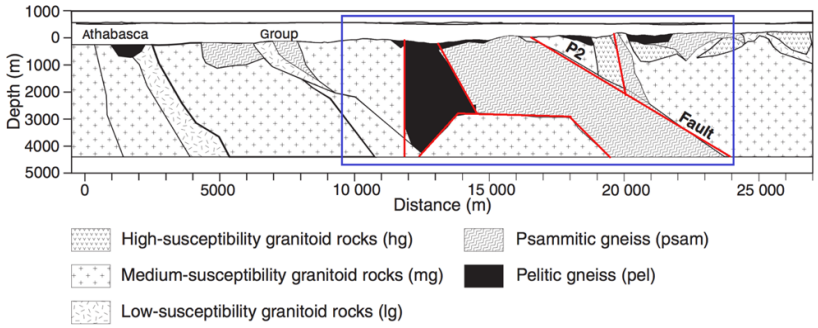


Figure 6.2: McArthur geological section from Thomas and Wood (2007). Blue rectangle shows the part which forms the basis of models in this chapter. Red lines show the modelled interfaces between the blocks. Small zones and variations are ignored in the modelling.

The images of the 3D models in this report show the central 9 by 9 km. The actual 3D models used for the computations had a size of 500 by 500 km in order to avoid any effect

of the edges on the gravity data. The total thickness of this model is around 4500 m. In this model, a cylinder anomaly is considered as an alteration zone. Gravity data (free-air data, overburden signature data, basement signature data and gravity data after removing overburden signature) were computed using the forward modelling code of Lelièvre et al. (2011). The base of the upper layer (overburden) is considered as the reference ellipsoid (see Section 5.4). The layers (or structures) above the reference ellipsoid have real densities while the layers (or structures) below the reference ellipsoid have relative density. The relative densities are with respect to 2.67 g/cc. Therefore, the overburden has a real density of 2 g/cc whereas the lower layers have a relative density. In this model, I use the real topography with a digital resolution of around 20 m. The tetrahedral mesh has around 530,000 cells. For this chapter, synthetic data are plotted, analysed and filtered by Oasis Montaj software (2006; www.geosoft.com).

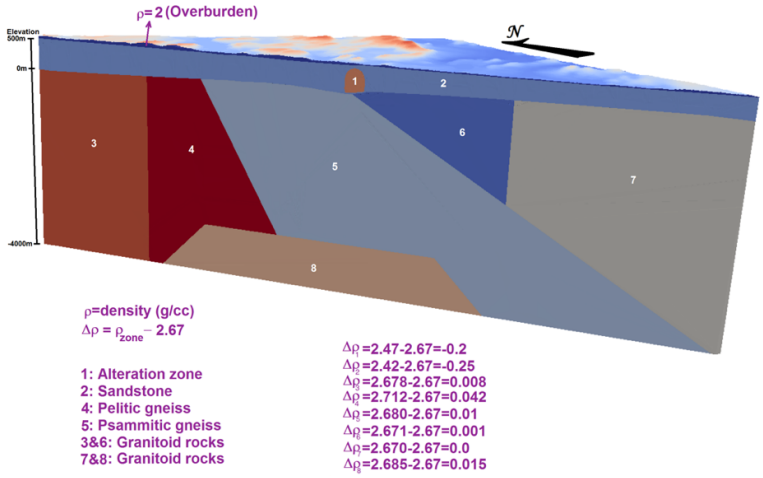


Figure 6.3: Density (free-air) model of McArthur area made using Figure 6.2.

By comparing free-air data with the overburden signature data, it can be seen that the free-air gravity data is strongly influenced by the variations of topography (Figures 6.4 and 6.5). In Figure 6.4, for the Bouguer correction (BC) a density of 2.0 g/cc is considered.

Since the base of the overburden is considered as the reference ellipsoid, it is considered as datum for the Bouguer correction as well.

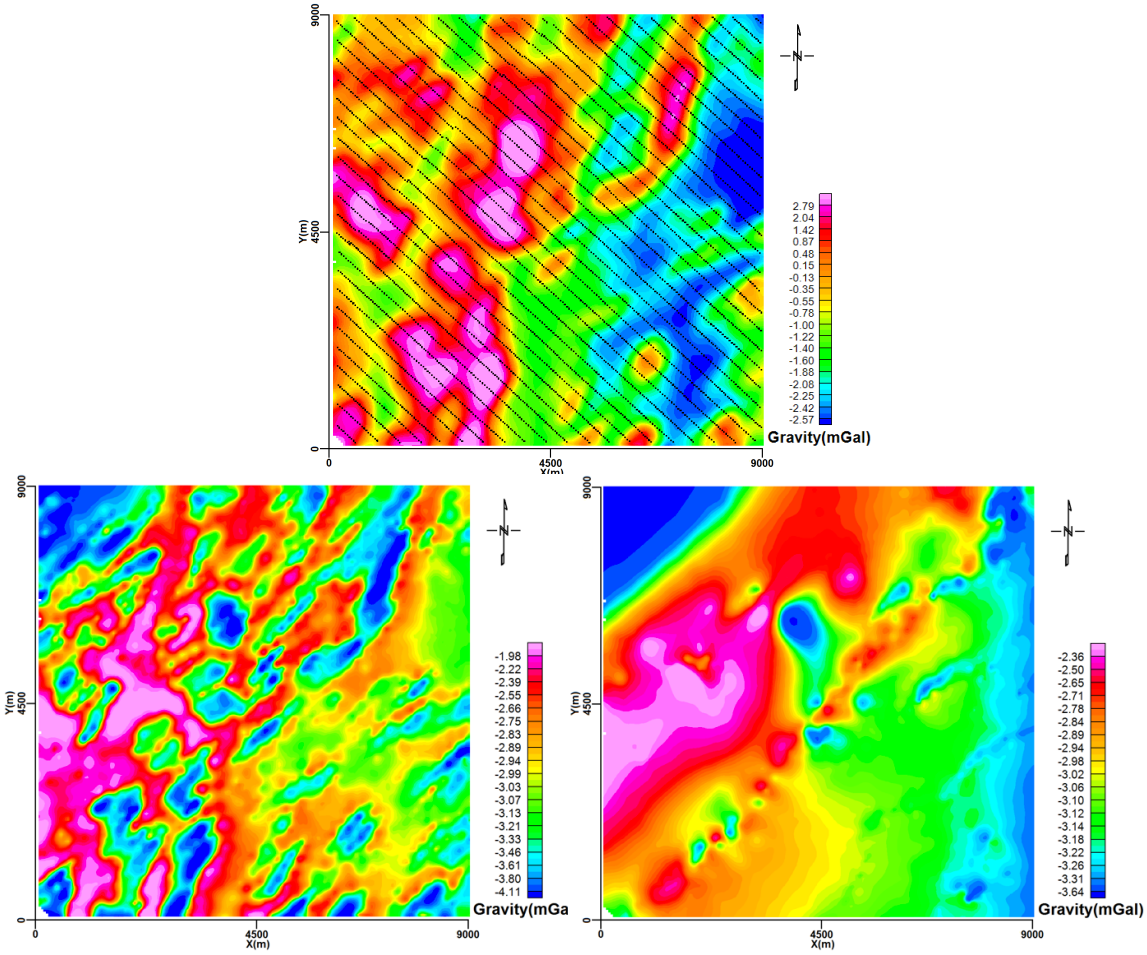


Figure 6.4: Top: grid of synthetic free-air data along the airborne survey lines (black dots). Station spacing: ~50 m. Profile spacing: ~300 m. Number of stations: 4597. Bottom: Bouguer anomaly after BC (left) and BC+TC (right; gridded by Oasis Montaj).

For the terrain correction (TC), the terrain effect is calculated by synthetizing the gravity data over a simple model with the same topography and the same stations used in Figure 6.3 with an uniform density of 2.0 g/cc. The bottom of the model is a flat surface at 450 m elevation. After applying the Bouguer correction (in which *h* is the thickness of the ground directly beneath the observation to 450 m, and the density equals to 2.0 g/cc; see Section

3.2.3) on the synthetized data, the Bouguer anomaly (which should be zero) has variable values which are due to the terrain effect. These values are applied for the terrain correction by subtracting them from the data (see Section 5.3, Models 2 and 3).

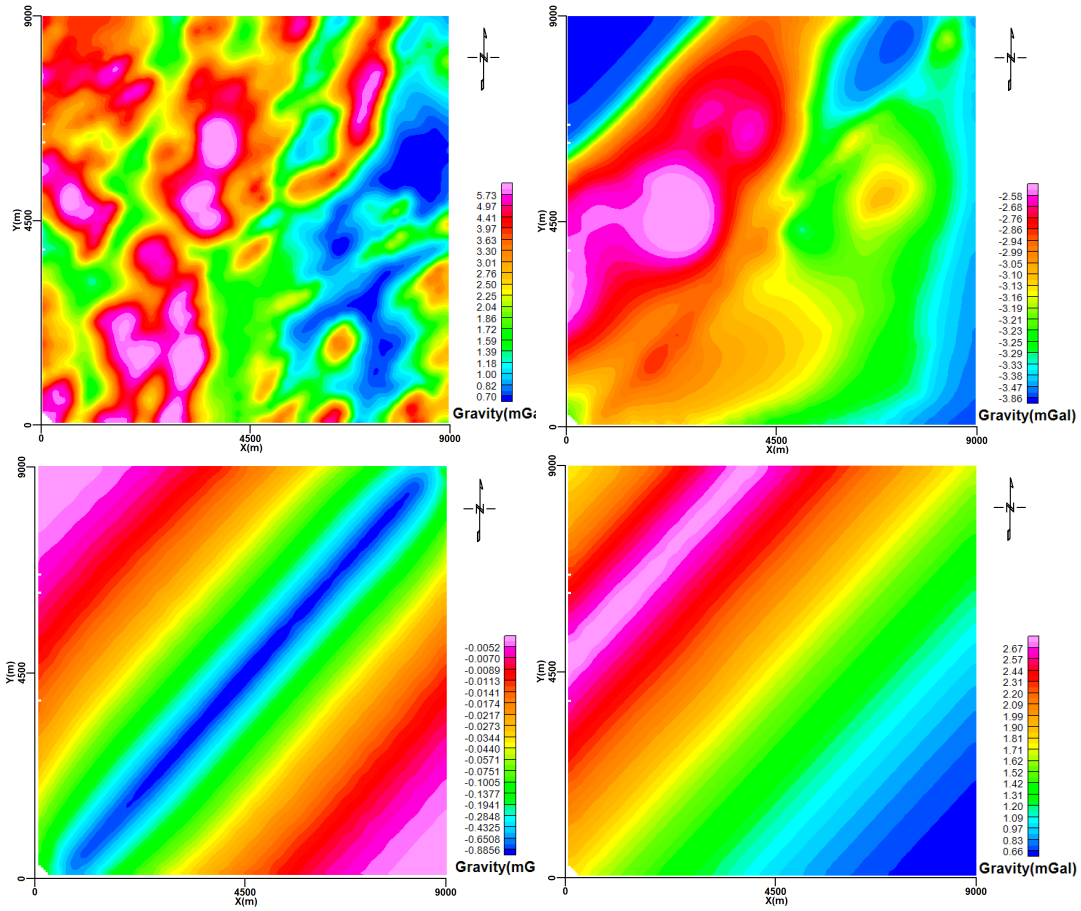


Figure 6.5: Grid of gravity free-air data after removing overburden signature (FwOB; top-right side), overburden signature gravity data (top-left side), alteration signature gravity data (bottom-left side) and basement signature gravity data (bottom-right side). The data shown here are on the same area shown in Figure 6.4 (gridded by Oasis Montaj).

Grid of "free-air data without overburden signature" (FwOB) shows some variations in the data (Figure 6.5). These variations are mainly due to the following factors: 1-variations in the topography of interface between overburden and sandstone; 2-alteration zone and 3-basement. FwOB data is similar to the Bouguer anomaly after BC and TC (Figure 6.4) as

expected. The data-sets (maps) are consistent with the profiles shown in Chapter 5 for these same contributions to the full gravity data-set. In Figure 6.5, the portion related to the alteration zone in the data can be seen as a strip with high value and a narrow extent in the across strike direction oriented from the bottom left to the top right. Other short lateral extent variations in the FwOB data are due to the variations in the topography of interface between overburden and sandstone. Large lateral extents are due to the variations in the basement. Figure 6.6 shows the topography of the interface between the overburden and the sandstone made using data from around 600 drill-holes mostly located along the faults in the area (see Section 2.2).

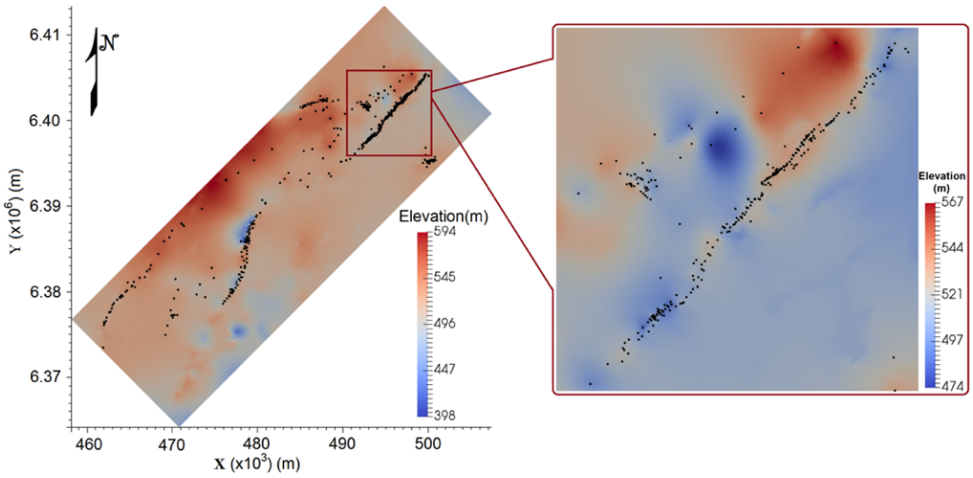


Figure 6.6: Topography of the interface between overburden and sandstone of McArthur-Millennium corridor (20×50km; made by Mohamed Gouiza and Mira Geoscience Ltd.). Inset shows the topography of the 10×10km study area. Some of the drill-holes in the area are shown by black dots.

## 6.3 Spectral analysis theory

Fourier spectral analyses are done for processing and interpretation of gravity data. Both 2D power spectra (2DPS) and radially averaged power spectra (RAPS) were calculated and

analysed for all data. Spectral analyses are done using Oasis Montaj software (2006) over different grid cell sizes. The idea is to investigate the various contributions of gravity data for the model in Figure 6.3 in the wavenumber domain based on their power spectra. The data can transform from the space domain to the wavenumber domain using the mathematical method of Fourier transform (Papoulis, 1962; Bracewell, 1965). 2D continuous Fourier transform equation for transforming from space domain to frequency/wavenumber domain is as follow:

$$F(u,v) = \int_{-\infty}^{\infty}\int_{-\infty}^{\infty} f(x,y)e^{-j2\pi(ux+vy)}dxdy$$

where $u$ and $v$ are wavenumbers (i.e., spatial frequencies). And, for transforming from frequency/wavenumber domain to space domain the 2D continuous Fourier transform equation is as follow:

$$f(x,y) = \int_{-\infty}^{\infty}\int_{-\infty}^{\infty} F(u,v)e^{-j2\pi(ux+vy)}dudv$$

"Aliasing" and "*sinc* function" are two undesired effects which can be seen in the wavenumber domain especially in the 2D power spectrum.

**Aliasing:** Aliasing can be an issue with sampling of potential field data such as gravity and magnetic in an airborne survey, or sparse locations on the ground because of access and expense of collecting ground data. In order to describe aliasing, the "sampling rate" and "Nyquist theorem" will be first defined. The sampling rate (*SR*) is the rate at which values are digitized from the true signal. It is measured in "sample per unit". The "unit" can be in space domain (metre). Higher sampling rates allow the signal to be more accurately

represented (Figure 6.7). In this study (Figure 6.4), the (minimum) station spacing is around 50 m. So a rough estimate for *SR* is 0.02 samples/metre (or 20 samples/km).

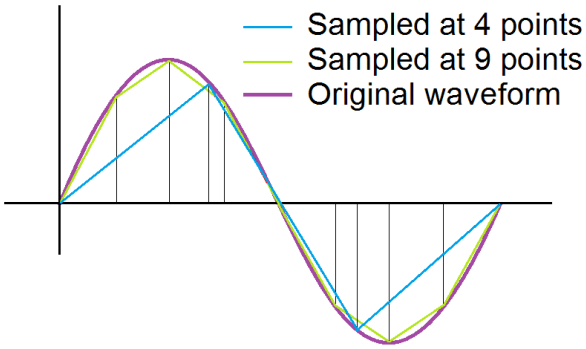


Figure 6.7: Examples for different sampling rates.

**Nyquist theorem:** One can digitally represent only frequencies (in time domain) or wavenumbers (in space domain) up to half the sampling rate. Frequencies (*f*), or wavenumbers (*k*), above the Nyquist frequency (or wavenumber) "fold over" to masquerade as lower frequencies (or wavenumbers). This foldover is called “aliasing” which gives the overlapped frequency spectrum. Aliased frequency (*f'*) in range [*SR/2*, *SR*] is equal to |*f* - *SR*|. In this study, the *SR* is 0.02 samples/metre (or 20 samples/km). So, Nyquist wavenumber is 0.01 samples/metre (or 10 samples/km; Figure 6.8). Both the grid cell size and measurement spacing have consequences on the Nyquist.

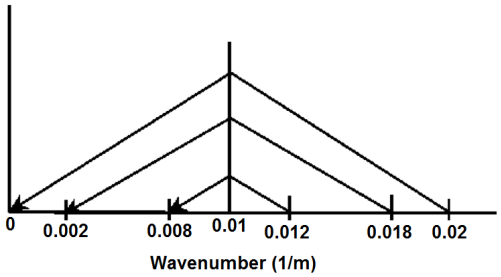


Figure 6.8: Examples for some aliased wavenumbers with an *SR* of 0.02 $m^{-1}$ and Nyquist wavenumber of 0.01 $m^{-1}$ (adapted from www.cse.ust.hk).

**Gridding:** For two-dimensional data, the data can be represented by determining its value at equally spaced grid of nodes (Figure 6.9). The process of gridding takes data and interpolates the readings to determine the values at the nodes of a grid. For gridding, the cell size should not be much less than half the nominal data point interval. This is because a very small cell size in not useful as it can consume more processing time than necessary. Also, it should not be too big as when working with gridded data, we cannot see detail smaller than the grid cell size (adapted from www.geosoft.com).

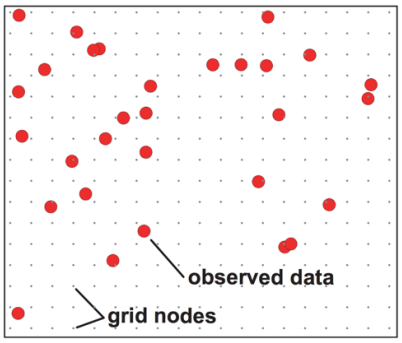


Figure 6.9: Observed data and grid nodes (adapted from www.geosoft.com).

***Sinc* function:** The *sinc* function is the Fourier transform of the rectangular (or boxcar) function. The rectangular function can contain the data (here gravity data in the space domain; left side of Figure 6.10). According to Figure 6.10 (right side) there will be the variations/oscillations out of the range from $-f_o$ to $+f_o$ in the *sinc* function ($f_o \approx 1/t$).

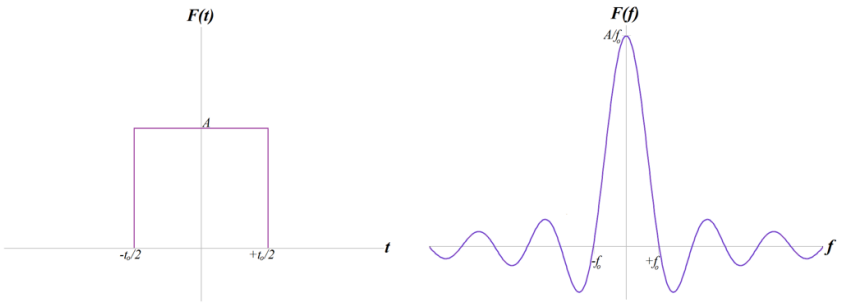


Figure 6.10: Fourier transform pair showing the rectangular pulse signal (left) and its Fourier transform, the *sinc* function (right; adapted from Sheriff and Geldart, 1995).

A 2D power spectrum represents the spectral content of data along with the azimuth of sources at all wavenumbers. It does not give quantitative information on the number of sources with a particular frequency (Spector and Grant, 1970; Clement, 1972). Figure 6.11 shows the basic principle of the 2D power spectrum between space domain and wavenumber domain. Patterns in the space domain show a rotation by 90˚ (i.e. a phase shift of $\pi/2$ radians) in the wavenumber domain. Spectrum (power) has a unit of $mGal^2$.

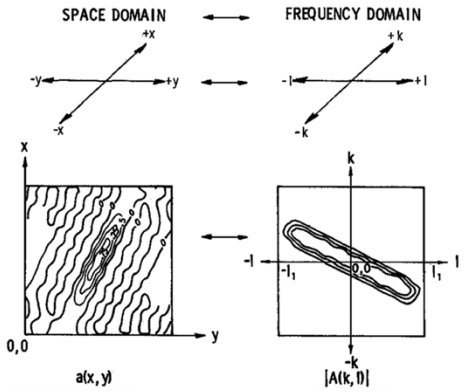


Figure 6.11: Top: coordinate axes in the space and frequency/wavenumber domains. Bottom: the two dimensional continuous function and its continuous spectrum (Clement, 1972). The symbols *k* and *l* refer to the frequency components in the *x* and *y* direction, respectively.

A 2D power spectrum can be converted to a one dimensional plot as a radially averaged power spectrum (RAPS) in order to ease the presentation. It means that each point in the RAPS is an average of all points lying on a circle with a fixed frequency (or wavenumber). RAPS can give more quantitative insight, and it gives averages over the spectral window (Bhattacharya, 1966; Spector and Grant, 1970; Maus and Dimri, 1996). RAPS decreases with increasing depth to source (*d*) by a factor *exp(-2dk)*, where *k* is the wavenumber. Therefore, if the shape of the power spectrum is dominated by the depth factor, the logarithm of the power spectrum would be proportional to *-2dk*, and *d* can be obtained from

the slope of the log radially averaged power spectrum. RAPS should be preferably applied on relatively homogenous structures so that the slope clearly breaks in the spectrum (Spector and Grant, 1970). It may yield up to five depth values (Connard et al. 1983; Maus and Dimri, 1996). Note that not only potential field power spectra possess limited depth information, but they are dominated by scaling properties of their source distributions (Maus and Dimri, 1996).

The radial power spectrum is plotted as the natural log of power versus wavenumber. The spectrum can be fit with a series of straight line segments where each line's slope ($m$) is related to the depth of density anomalies ($d = -m / 4\pi$; Spector and Grant, 1970). Line segments corresponding to the lower frequencies (wavenumbers) have information from deeper anomalies. In this study, I have plotted the line segments for each RAPS. Where the slop changes, that point (wavenumber) is considered as a cut-off point. These cut-off points can be used for designing filters (low-pass and high-pass). RAPS is mostly used for the depth estimation. Wavenumber ($k$) is equal to $2\pi$/wavelength ($l$). Therefore, using cut-offs obtained from RAPS I can find the wavelength belonging to the various contributions.

## 6.4 Spectral analysis of some models

In this section, both the 2D power spectrum and the radially averaged power spectrum are applied on some models, especially the McArthur area model.

### 6.4.1 2D power spectrum of a simple model with different line and station spacing

In order to investigate the use of the 2D power spectrum for separating overburden and deeper effects in the McArthur-Millennium area, a simple model (including only a cylinder representing alteration zone from elevation 0 m to 400 m) was first considered. The cylinder is extended from north-east to south-west with a length and a density of 12 km and -0.2 g/cc, respectively. Gravity data was synthetized for three different grids over the cylinder using the forward modelling code of Lelièvre et al. (2011).

The station and profile spacing for the grid shown in Figure 6.12 is 200 m. For the grid in Figures 6.13 and 6.14, the station and profile spacings are 100 m and 500 m, respectively. The direction of profiles in Figures 6.12, 6.13 and 6.14 is north-south and east-west, respectively. Figures 6.12, 6.13 and 6.14 show 2D power spectra for the three grids (with an area 15×15 km) at a fixed elevation of 700m. 2D power spectra are obtained using Oasis Montaj software (2006 and 2007) over different grid cell sizes 10, 20, 50, 100 and 200 m to show that the accuracy of 2D power spectrum depends on these gridding parameters. Note that measurement spacing has also consequences on the Nyquist (Section 6.3).

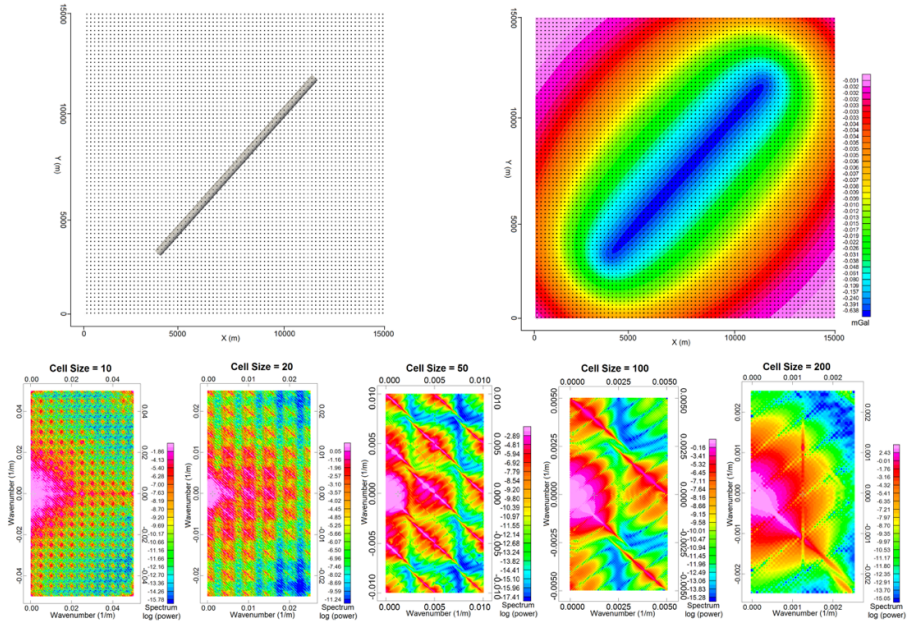


Figure 6.12: Top-left: Stations (black dots) over a cylindrical anomaly (grey body) with a density of -0.2 g/cc; station and profile spacing: 200 m. Top-right: gravity data. Bottom: 2D Power Spectrum for 5 different grid cell sizes 10, 20, 50, 100 and 200 m (gridded by Oasis Montaj).

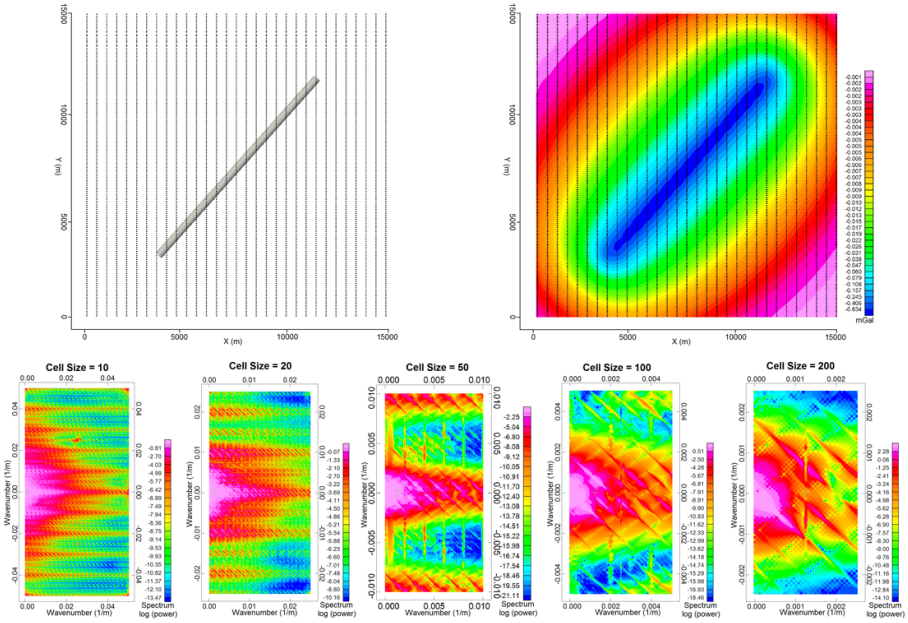


Figure 6.13: Top-left: Stations/profiles (black dots/ N-S lines) over a cylindrical anomaly (grey body) with a density of -0.2 g/cc; station spacing: 100 m; profile spacing: 500 m. Top-right: gravity data. Bottom: 2D Power Spectrum for 5 different grid cell sizes 10, 20, 50, 100 and 200 m (gridded by Oasis Montaj).

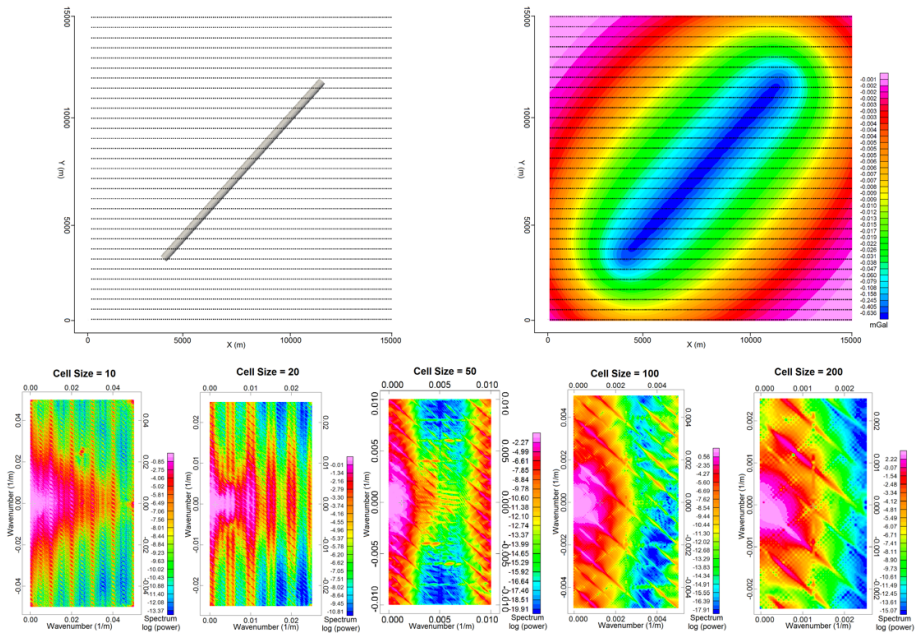


Figure 6.14: Top-left: Stations/profiles (black dots/ E-W lines) over a cylindrical anomaly (grey body) with a density of -0.2 g/cc; station spacing: 100 m; profile spacing: 500 m. Top-right: gravity data. Bottom: 2D Power Spectrum for 5 different grid cell sizes 10, 20, 50, 100 and 200 m (gridded by Oasis Montaj).

In Figures 6.12, 6.13 and 6.14, grid cell sizes 10 m and 200 m show interesting results. For the grid cell size of 10 m, the linear pink parallel zones (high power) correspond to the direction of the survey lines. This indicates that there is a lot of power and hence a lot of structures in those directions. For the grid cell size of 200 m, the linear pink zone (high power; northwest to southeast trending) in the centre of the 2D power spectrum corresponds to the anomaly (cylinder). The power spectra for the small cell size in all three figures look quite different, but the power spectra for the 200 m cell size looks fairly similar for the three cases. This is because the cell size is comparable with the line spacing, which is larger than the station spacing for Figures 6.13 and 6.14. Also, information in the centre of the power spectrum from the 200 m grid cell size is contained within the power spectrum from the 10 m grid cell size.

### 6.4.2 2D power spectrum of the McArthur area model

A 2D power spectrum was generated for the data synthetized in Section 6.2. Synthetic data include free-air gravity data, "free-air data without overburden signature" (FwOB), basement signature gravity data, overburden signature gravity data and alteration signature gravity data (Figures 6.4 and 6.5). Figures 6.15 to 6.19 show 2D power spectra for different grid cell sizes.

Different grid cell sizes show different wavenumber range. For example, in Figures 6.15 to 6.19, it can be seen that grid cell sizes of 10 m and 200 m give wavenumbers up to 0.05 $m^{-1}$ and 0.003 $m^{-1}$, respectively. Thus, the grid cell size of 200 m can hopefully show the structures with the low wavenumbers (high wavelength). The 2D power spectrum for the grid cell size of 10 m shows similar results to that for the grid cell size of 200m when a larger range of "Spectral log (power)" is considered (in our examples, values from -10 to 17 $mGal^2$; a zoom-in to the same wavenumber range as for the 200 m grid cell size power spectrum). Note that the grid cell size has consequences on the Nyquist (Section 6.3).

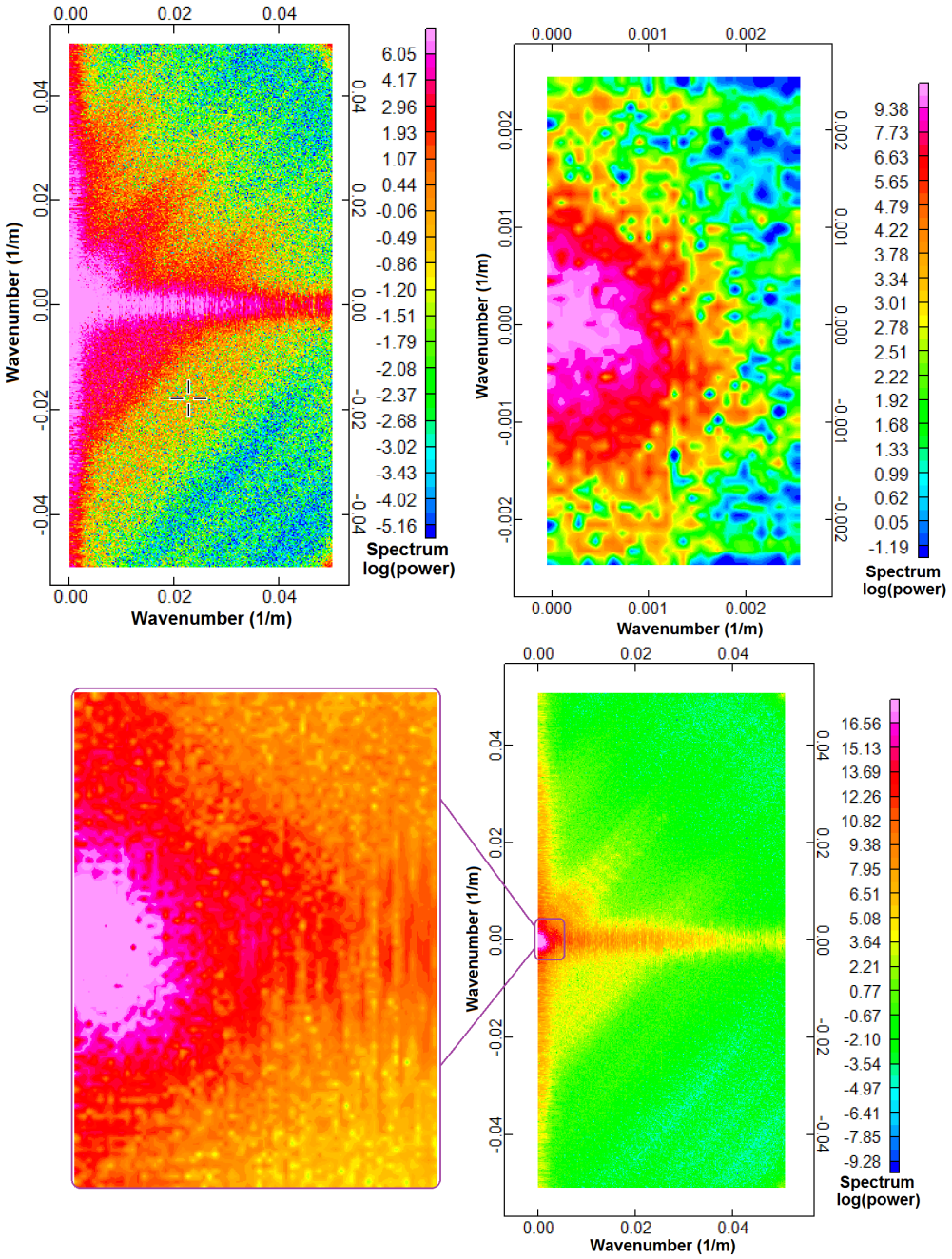


Figure 6.15: 2D power spectrum from free-air data (whole model; Figure 6.4) for grid cell sizes of 10 m (top-left side) and 200 m (top-right side). Rescaled 2D power spectrum from free-air data with a larger range of "Spectral log (power)" for grid cell sizes of 10 m (bottom-right side) and a zoom-in to the central region (bottom-left side; plotted by Oasis Montaj).

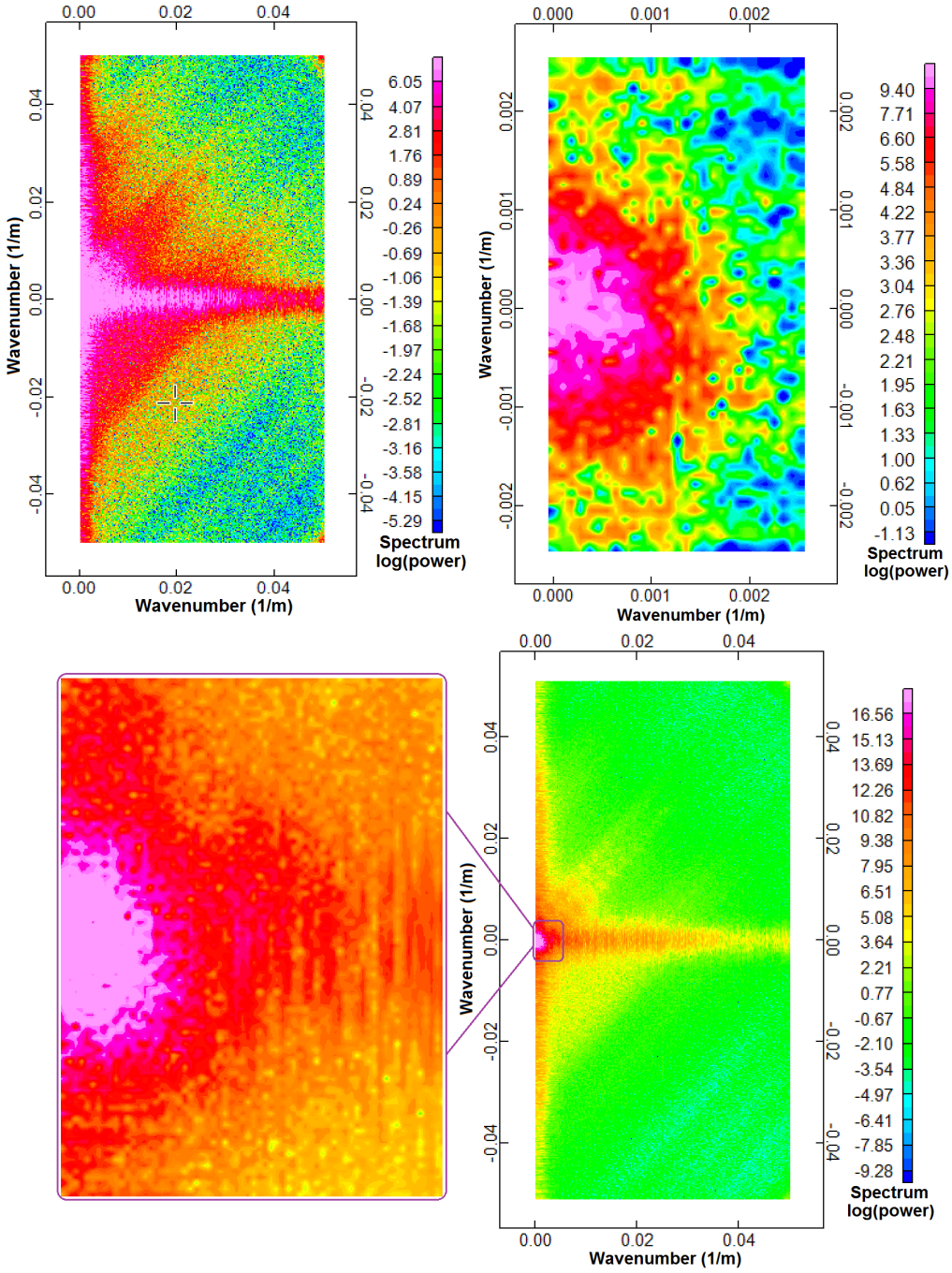


Figure 6.16: 2D power spectrum from overburden signature gravity data (Figure 6.5) for grid cell sizes of 10 m (top-left side) and 200 m (top-right side). Rescaled 2D power spectrum from free-air data with a larger range of "Spectral log (power)" for grid cell sizes of 10 m (bottom-right side) and a zoom-in to the central region (bottom-left side; plotted by Oasis Montaj).

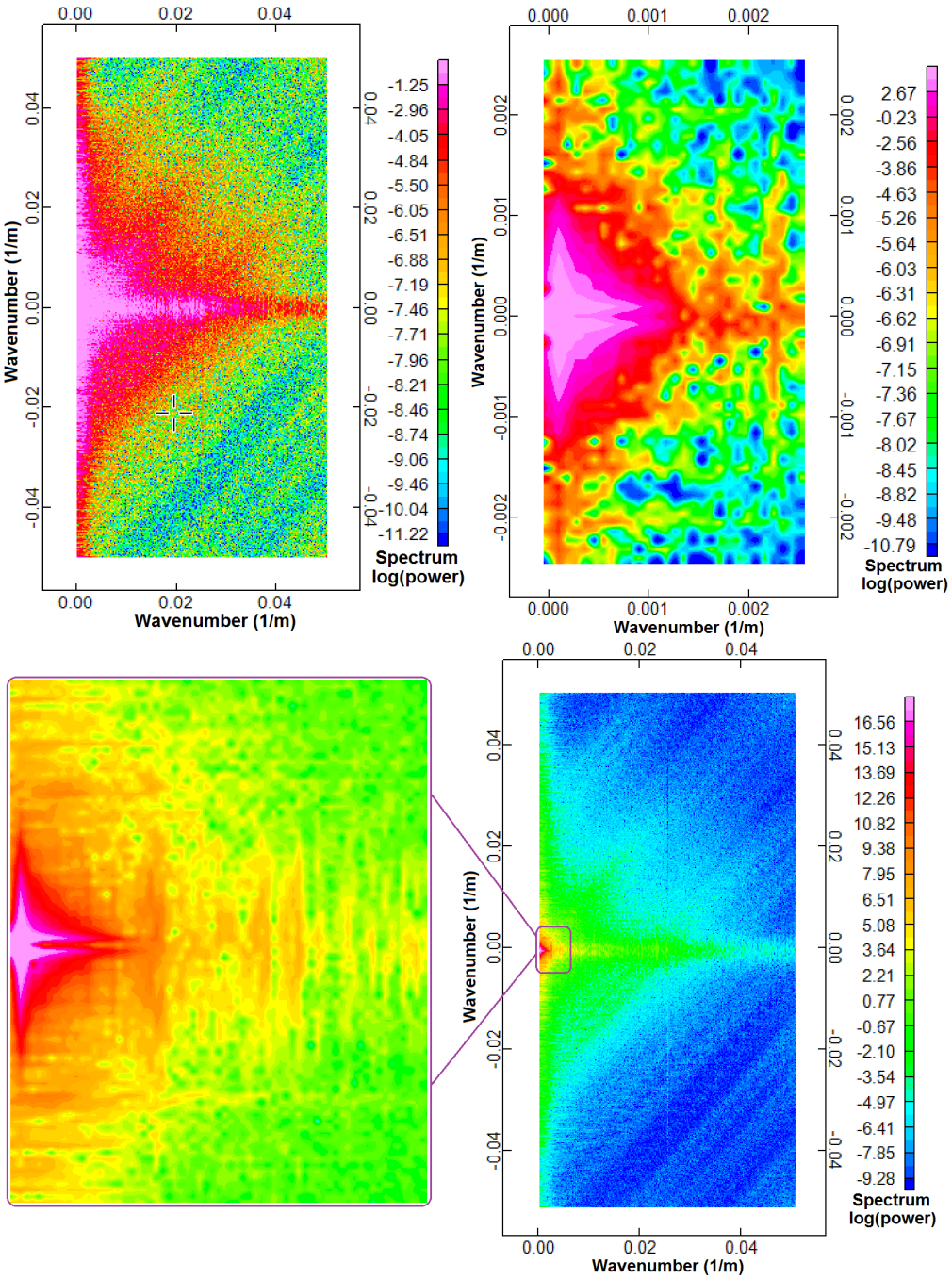


Figure 6.17: 2D power spectrum from basement signature gravity data (Figure 6.5) for grid cell sizes of 10 m (top-left side) and 200 m (top-right side). Rescaled 2D power spectrum from free-air data with a larger range of "Spectral log (power)" for grid cell sizes of 10 m (bottom-right side) and a zoom-in to the central region (bottom-left side; plotted by Oasis Montaj).

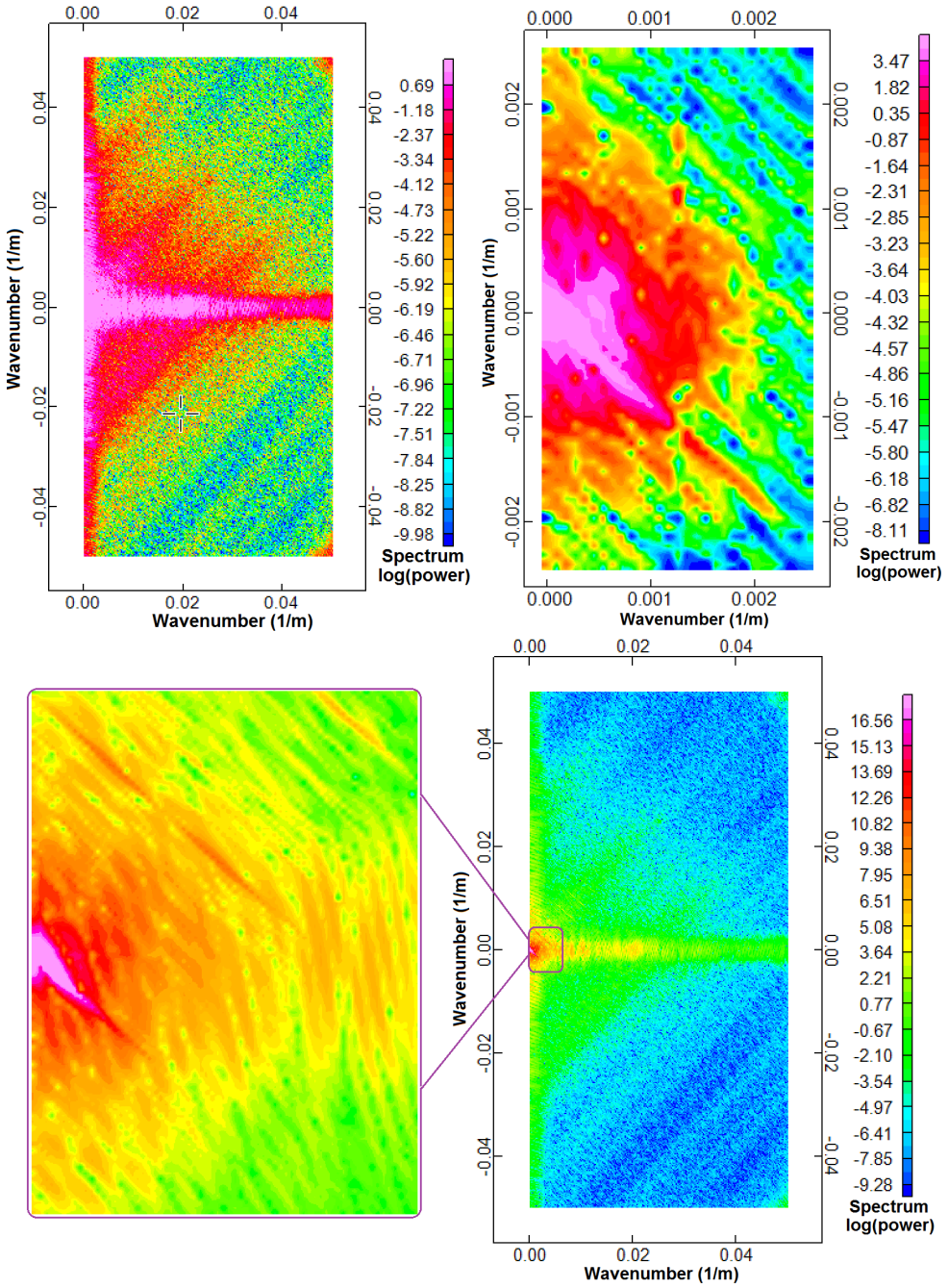


Figure 6.18: 2D power spectrum from alteration signature gravity data (Figure 6.5) for grid cell sizes of 10 m (top-left side) and 200 m (top-right side). Rescaled 2D power spectrum from free-air data with a larger range of "Spectral log (power)" for grid cell sizes of 10 m (bottom-right side) and a zoom-in to the central region (bottom-left side; plotted by Oasis Montaj).

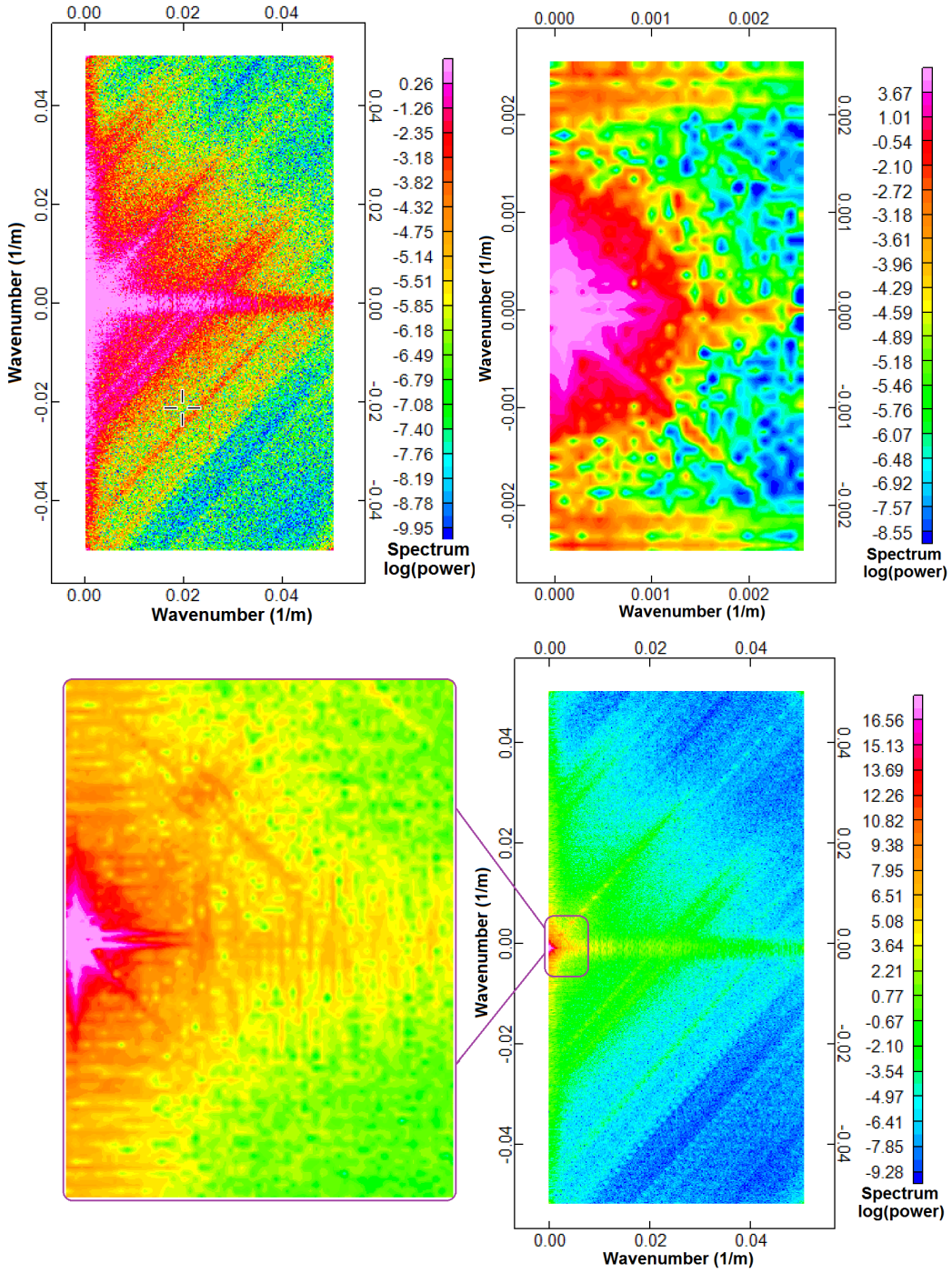


Figure 6.19: 2D power spectrum from FwOB data (Figure 6.5) for grid cell sizes of 10 m (top-left side) and 200 m (top-right side). Rescaled 2D power spectrum from free-air data with a larger range of "Spectral log (power)" for grid cell sizes of 10 m (bottom-right side) and a zoom-in to the central region (bottom-left side; plotted by Oasis Montaj).

For the grid cell size of 10 m, the linear pink parallel zones (high power; northeast to southwest trending) in the centres of the whole 2D power spectra correspond to the direction of the survey lines which makes sense given that I have data every 50 m in this direction but data only every 300 m in the across-line direction. This indicates that there is a lot of power in that direction (and hence a lot of structures should be in that direction). For the grid cell size of 200 m, the linear pink zone (high power; northwest to southeast trending) in the centre of the 2D power spectrum of the alteration signature gravity data corresponds to the alteration zone.

Since free-air data is dominated by the overburden signature (as shown in Chapter 5), the 2D power spectrum corresponding to the free-air data is similar to the overburden signature data. However, drumlins in the Athabasca basin have a northeast to southwest trend, but in this 9×9 km study area this trend cannot be seen clearly enough. So, I don't expect to see clearly this trend in the 2D power spectra.

For the grid cell size of 200 m, as expected, the features in the 2D power spectrum of the FwOB data include the features in both the 2D power spectrum of the alteration gravity data and 2D power spectrum of the basement gravity data. For the grid cell size of 10m, the linear blue and green parallel zones (low power; northeast to southwest trending) in the upper/bottom right corners of the entire 2D power spectra can be due to the 2 factors: "aliasing" or "*sinc* function". According to Section 6.3.1, since the (minimum) station spacing is around 50 m, the sampling rate is around 0.02 samples/metre (or 20 samples/km). So, Nyquist wavenumber is 0.01 samples/metre (or 10 samples/km). It can be seen that those linear blue and green parallel zones are constructed for the wavenumbers greater than

0.01 ($m^{-1}$). Also, according to Figure 6.11 the variations/oscillations in the *sinc* function can be another cause for those linear blue and green parallel zones.

### 6.4.3 Radially averaged power spectrum of the McArthur area model

RAPS are done using Oasis Montaj software (2006) over different grid cell sizes on the synthetized gravity data of the McArthur area (Figures 6.20 to 6.24). For free-air data (Figure 6.20), two RAPS are plotted for grid cell sizes of 20 m and 200 m. The RAPS of 200 m shows the information related to the low wavenumbers better than the RAPS of 20 m, whereas the RAPS of 20 m shows the information related to the high wavenumbers better than the RAPS of 200 m as the smaller grid cell size covers shorter wavelength better than the bigger grid cell size.

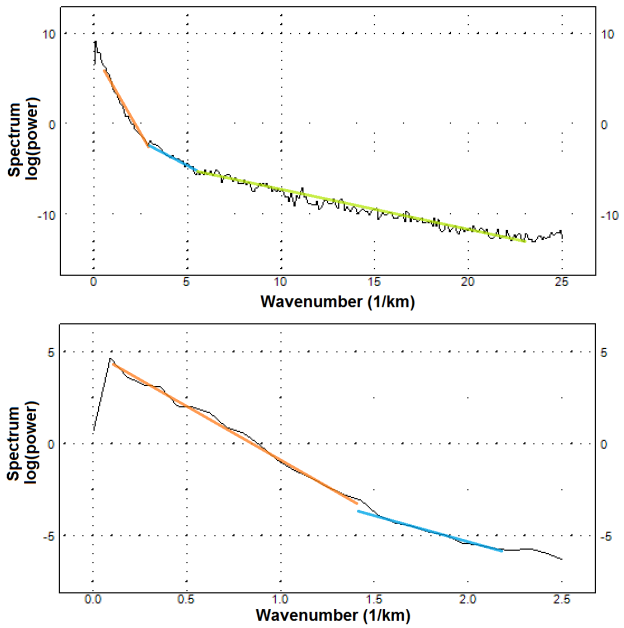


Figure 6.20: Top: RAPS from free-air data for grid cell sizes of 20 m. Colored lines are drawn and fitted in order to find the cut-offs (here 3, 5.5 and 12 $km^{-1}$). Bottom: RAPS from free-air data for grid cell sizes of 200 m. Colored lines are drawn and fitted in order to find the cut-offs (here 1.4 and 2.2 $km^{-1}$; plotted by Oasis Montaj).

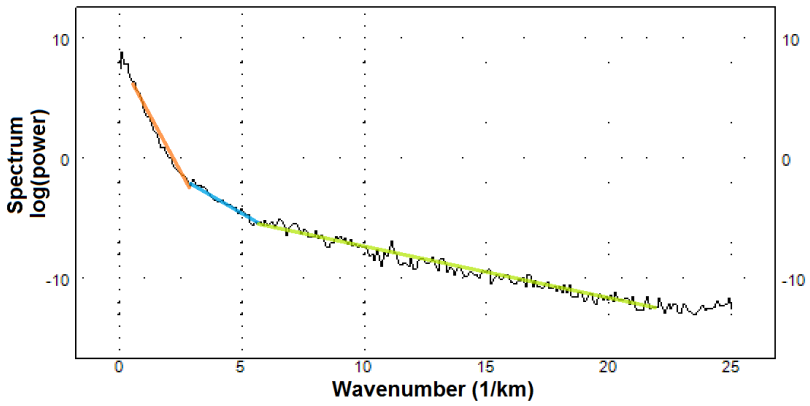


Figure 6.21: RAPS from overburden signature gravity data for grid cell sizes of 20 m. Cut-offs: 3, 5.5 and 12 $km^{-1}$ (plotted by Oasis Montaj).

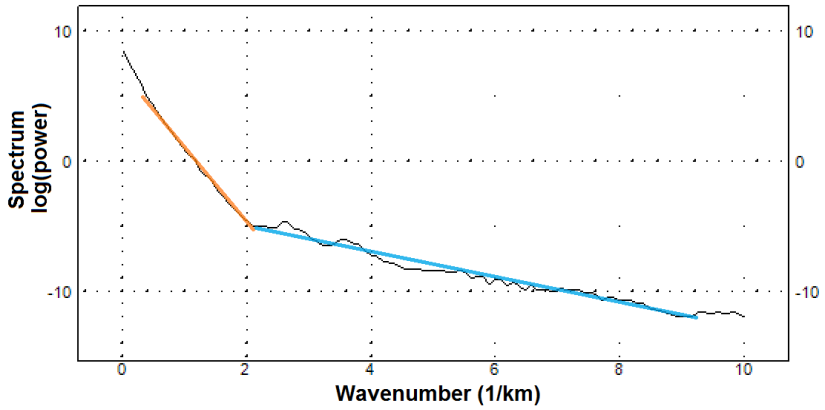


Figure 6.22: RAPS from alteration signature gravity data for grid cell sizes of 50 m. Cut-off: 2.1 $km^{-1}$ (plotted by Oasis Montaj).

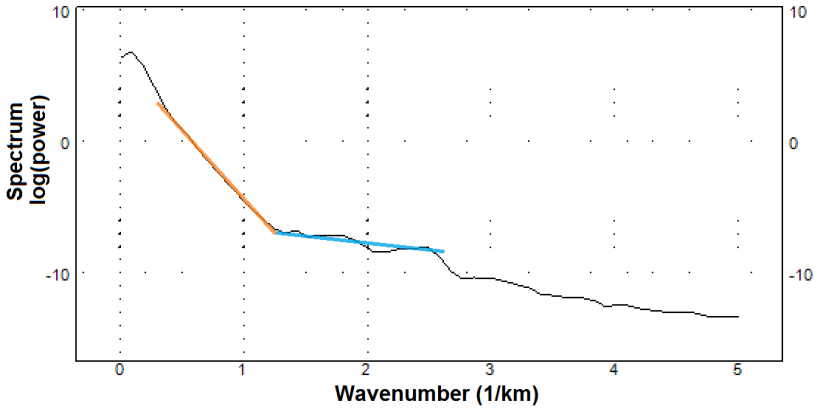


Figure 6.23: RAPS from basement signature gravity data for grid cell sizes of 100 m. Cut-off: 1.3 $km^{-1}$ (plotted by Oasis Montaj).

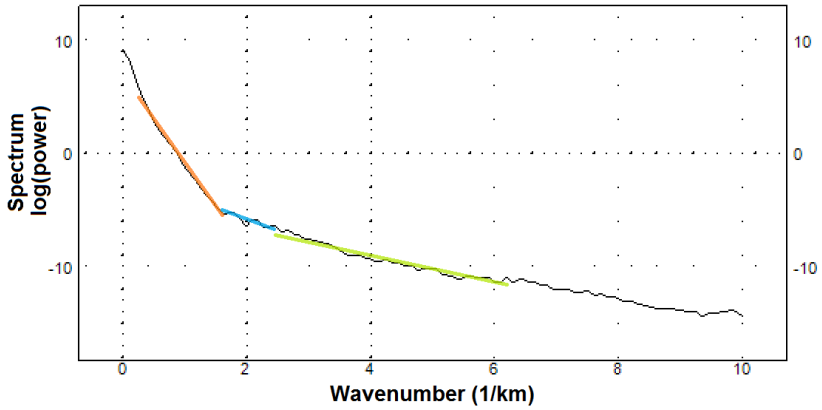


Figure 6.24: RAPS from FwOB data for grid cell sizes of 50 m. Cut-offs: 1.5, 2.5 and 6.2 $km^{-1}$ (plotted by Oasis Montaj).

Calculating the wavelengths ($l$) using the wavenumber ($k$) cut-offs obtained from RAPS (Figures 6.20 to 6.24) is as follows:

**Alteration:** $k$=2.1 => $l$= $2\pi/k$=6.28/2.1=3km

**Basement:** $k$=1.3 => $l$=6.28/1.3=4.8km

**Overburden:** $k$=3 => $l$=6.28/3=2.1km
$k$=5.5 => $l$=6.28/5.5=1.1km
$k$=12 => $l$=6.28/12=0.5km

**FwOB:**

$k$ =1.5 => $l$ =6.28/1.5=4.2km (probably belonging to the basement)
$k$ =2.5 => $l$ =6.28/2.5=2.5km (probably belonging to the alteration)
$k$ =6.2 => $l$ =6.28/6.2=1.01km (probably belonging to the interface between overburden and sandstone)

**Free-air (grid cell size of 200m):**

$k$ =1.4 => $l$ =6.28/1.4=4.5km (probably belonging to the basement)
$k$ =2.2 => $l$ =6.28/2.2=2.85km (probably belonging to the alteration)

**Free-air (grid cell size of 20m):**

$k$ =3 => $l$ =6.28/3=2.1km
$k$ =5.5 => $l$ =6.28/5.5=1.1km (probably belonging to the overburden)
$k$ =12 => $l$ =6.28/12=0.5km (probably belonging to the overburden)

Wavelengths obtained from the cut-off wavenumbers show good correlation with the gravity data plotted in Figures 6.4 and 6.5. The depths (*d*: distance from observation points) obtained from the lines' slopes (*m*) in RAPS using equation $d=-m/4\pi$ are as follows:

**Alteration:** orange line => $d = - m / 4\pi$ = - (y2-y1/x2-x1) / $4\pi$ = - (2.5/-0.4) / $4\pi$
= 6.25 / 12.56 = 0.49 km

**Basement:** orange line => $d$ =-(3.5/-0.4)/$4\pi$=0.69km

**Overburden:** orange line => $d$ =-(4/-1)/$4\pi$ =0.31km
blue line => $d$ =-(2.5/-0.2)/$4\pi$=0.1km
green line => $d$ =-(4.5/-10)/$4\pi$=0.035km

**FwOB:**
orange line => $d$ =-(7/-0.8)/$4\pi$=0.69km (probably belonging to the basement)
blue line => $d$ =-(2/-0.8)/$4\pi$=0.39km (probably belonging to the alteration)
green line => $d$ =-(3/-1.4)/$4\pi$=0.17km (probably belonging to the interface between overburden and sandstone)

**Free-air (grid cell size of 200m):**
orange line => $d$ =-(4/-0.45)/$4\pi$=0.71km (probably belonging to the basement)
blue line => $d$ =-(1.5/-0.45)/$4\pi$=0.27km (probably belonging to the alteration)

**Free-air (grid cell size of 20m):**
orange line => $d$ =-(4/-1)/$4\pi$=0.31km
blue line => $d$ =-(2.5/-0.2)/$4\pi$=0.1km (probably belonging to the overburden)
green line => $d$ =-(4.5/-10)/$4\pi$=0.035km (probably belonging to the overburden)

Note that the depth is defined as the distance from the observation points to the top of the layer or structure. Airborne stations are located at an average elevation of 650 m. Thus, true depths from observation points for the geological structures are as follow: alteration ≈ 300 m; basement ≈ 650 m; overburden ≈ 30 m to 150 m; interface between overburden and sandstone ≈ 150 m. By comparing the depths calculated using RAPS with the true depths, it can be seen that the accuracy between them varies from around 20 m (for the base of overburden) to around 200 m (for the top of alteration zone).

## 6.5 Frequency filtering

Different filtering methods were applied to the entire data-set (Section 6.2). Low-pass filters were applied on the free-air data in order to remove the short wavelengths, and hopefully to obtain a result similar to the "basement signature gravity data" or "FwOB". For this purpose, two consecutive filters were applied using Oasis Montaj software (2006): Directional Cosine Filter and Gaussian Regional/Residual Filter. The Directional Cosine Filter is useful for removing directional features from a grid. The cosine function makes the filter smooth, so directional ringing effects are usually not a problem. The Gaussian filter is another smooth filter that is often used for low-pass or high-pass applications (Oasis Montaj software, 2006). For gridding a value of 50 m is considered for "grid cell size". For the Directional Cosine Filter an angle of 140 degree (Azimuth) is considered. In the Gaussian Regional/Residual Filter, different values from the "cut-off wavelength" are applied for the low-pass filter. According to the RAPS of free-air data, wavelengths less than 2000 m belong to the overburden, and larger wavelengths belong to the basement and alteration zones. As shown in Figure 6.25, different low-pass filters are applied on the free-air data, especially with a cut-off of 2000 m. It was expected that the low-pass filter results would be similar to the "basement signature gravity data" or "FwOB data" but they are not (Figures 6.5 and 6.25). Also, according to the RAPS results, the wavelengths associated with the alteration zone are located between 1000 m and 3000 m. So, a band-pass filter was applied on the free-air data in order to get the alteration gravity response. However, the result obtained from this filter is not good (Figure 6.26).

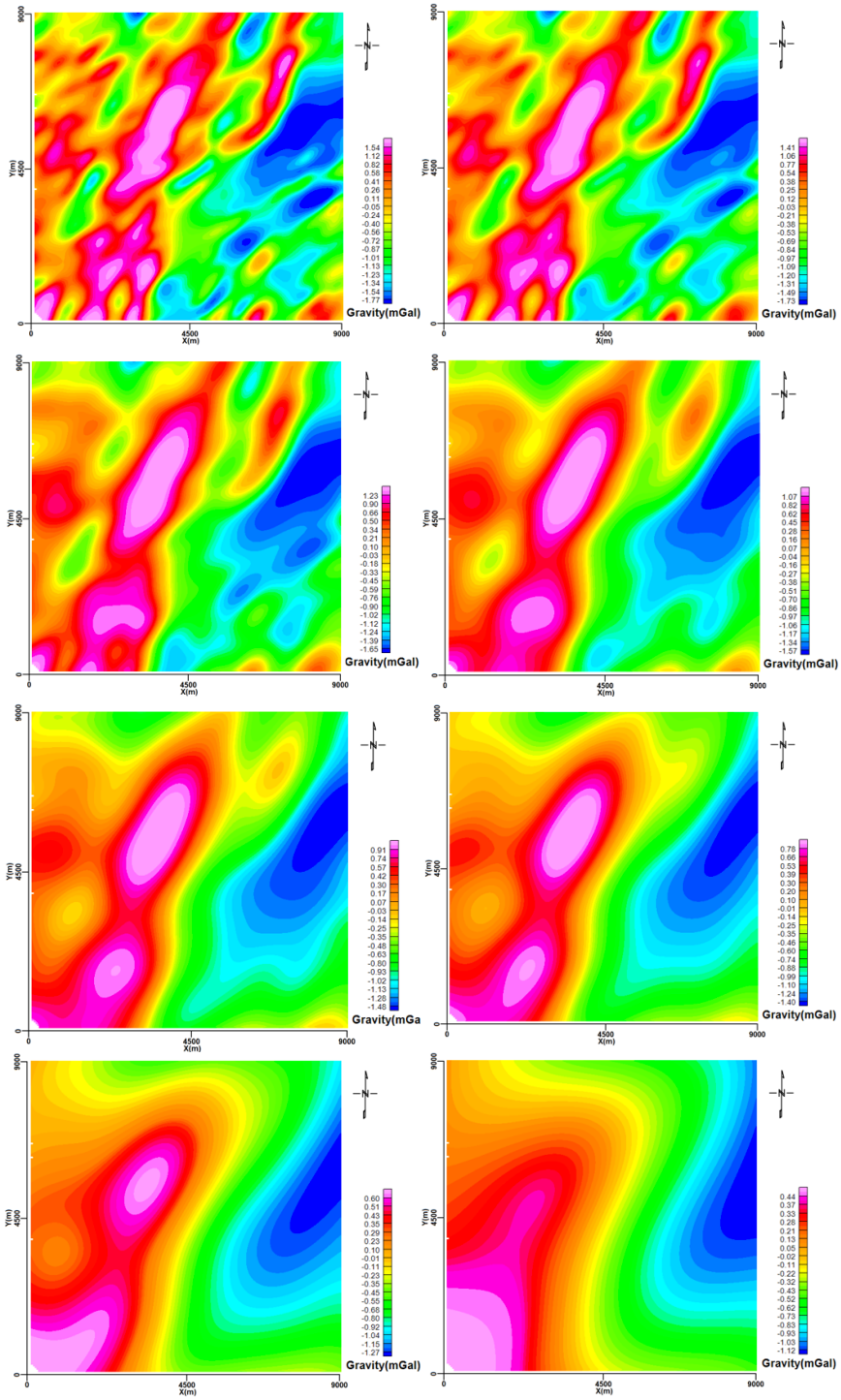


Figure 6.25: Grid of gravity free-air data after applying low-pass filters (from left to right and top to bottom) 500 m, 1000 m, 2000 m, 3000 m, 4000 m, 5000 m, 7000 m and 10000 m (gridded by Oasis Montaj).

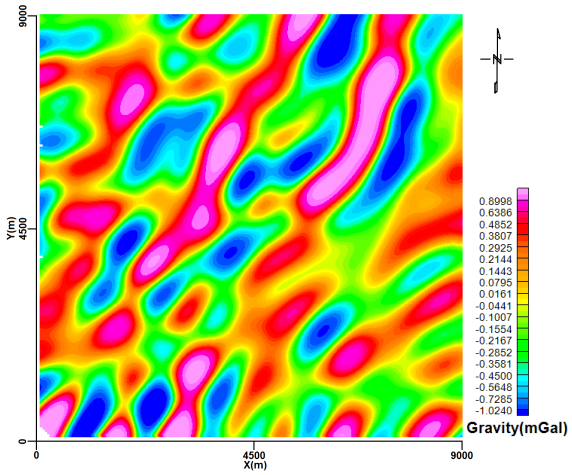


Figure 6.26: Grid of gravity free-air data after applying band-pass filters from 1000 m to 3000 m (gridded by Oasis Montaj).

The results in Figures 6.25 and 6.26 are not as good as hoped. This is probably due to the complicated geological structure in which the gravity data contain a wide range of wavelengths. Especially, the variable thickness of the overburden and the wavelengths associated with that provides a range of wavelengths (less than 2 km; see Section 6.4.3) as well. Therefore, the separation into the contributions coming from the various components of the model based on specific wavelengths is not as easy as expected.

"High-pass" and "derivative in Z-direction" filters were applied on the free-air gravity data as well (Figures 6.27 and 6.28). In "Gaussian Regional/Residual Filter", values of 500 m and 2000 m were applied for the "cut-off wavelength" for the high-pass filter. For "Derivative in Z-direction" filter, different orders (1 and 2) of differentiation were considered. Vertical derivatives can emphasize shorter wavelength features as they accentuate anomalies associated with shallow bodies. Also, they can emphasize the boundaries of target zones (Kearey et al., 2002; Telford et al, 1976).

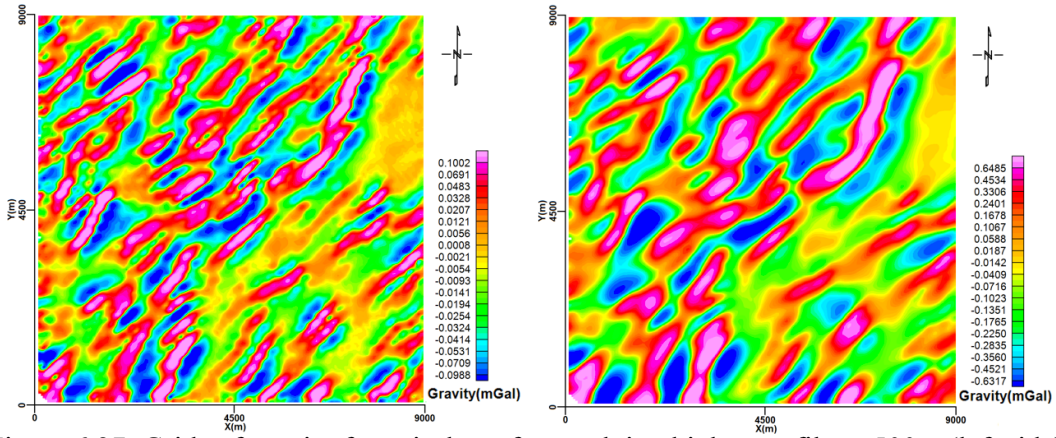


Figure 6.27: Grids of gravity free-air data after applying high-pass filters 500m (left side) and 2000m (right side; gridded by Oasis Montaj).

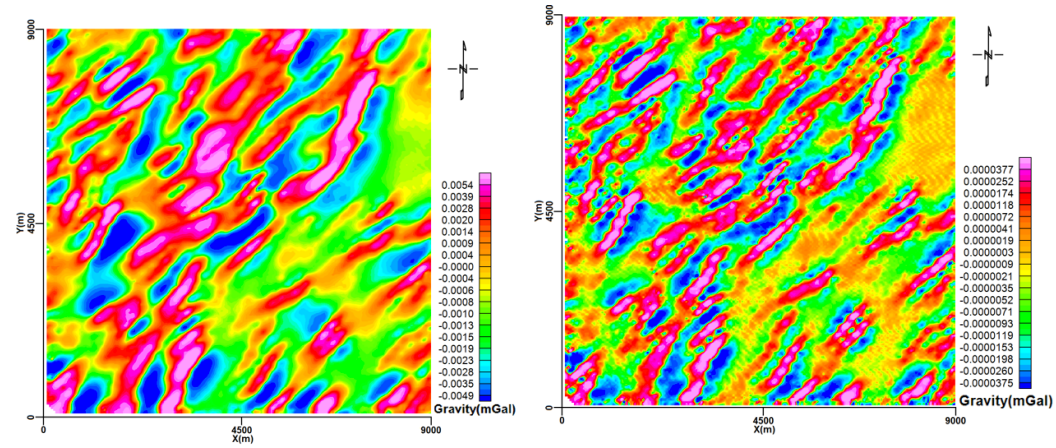


Figure 6.28: Grids of gravity free-air data after applying derivative filter in Z-direction for differentiation orders of 1 (left) and 2 (right; gridded by Oasis Montaj).

Assume that I was able to find the thickness of overburden, and also remove its contribution from the free-air data. Therefore, finally and hopefully I will have a data-set like "FwOB". As mentioned, this data is dominated by variations due to the topography of interface between overburden and sandstone. So, to continue, I will apply different filters (high-pass, band-pass and derivatives) on the "FwOB" in order to detect the portion of alteration zone (Figures 6.29 to 6.31).

Both “high-pass” and “derivative in Z-direction” filters on the FwOB data clearly show the portion of alteration zone in the data which is a stripe (red zone) oriented from the bottom left to the top right (Figures 6.29 and 6.30). The high-pass filter shows good results for values less than 3000m. This has a good correlation with the results obtained from RAPS (Figure 6.29). In Figure 6.31, the band-pass filter results do not show any clear signature related to the alteration zone.

In the next section, I shall apply the various spectral analysis and filtering techniques to real airborne gravity data from the McArthur area.

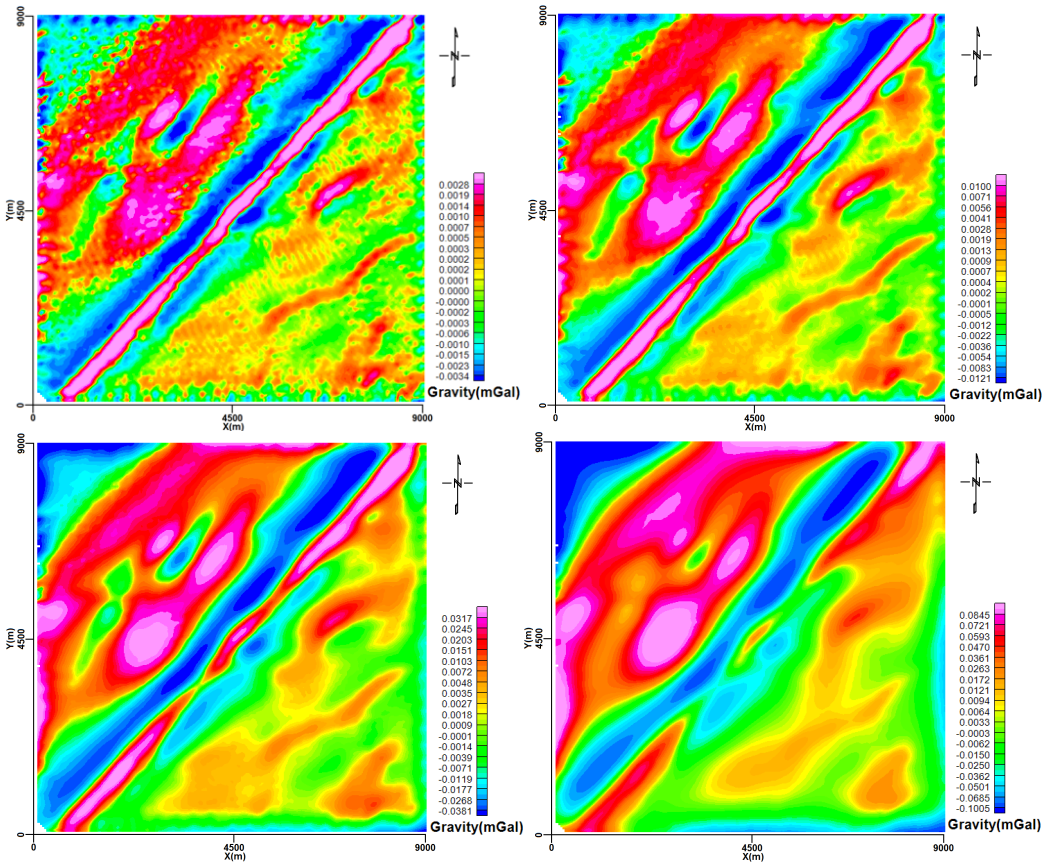


Figure 6.29: Grid of FwOB data after applying high-pass filters 500m (top-left side), 1000m (top-right side), 2000m (bottom-left side) and 4000m (bottom-right side; gridded by Oasis Montaj).

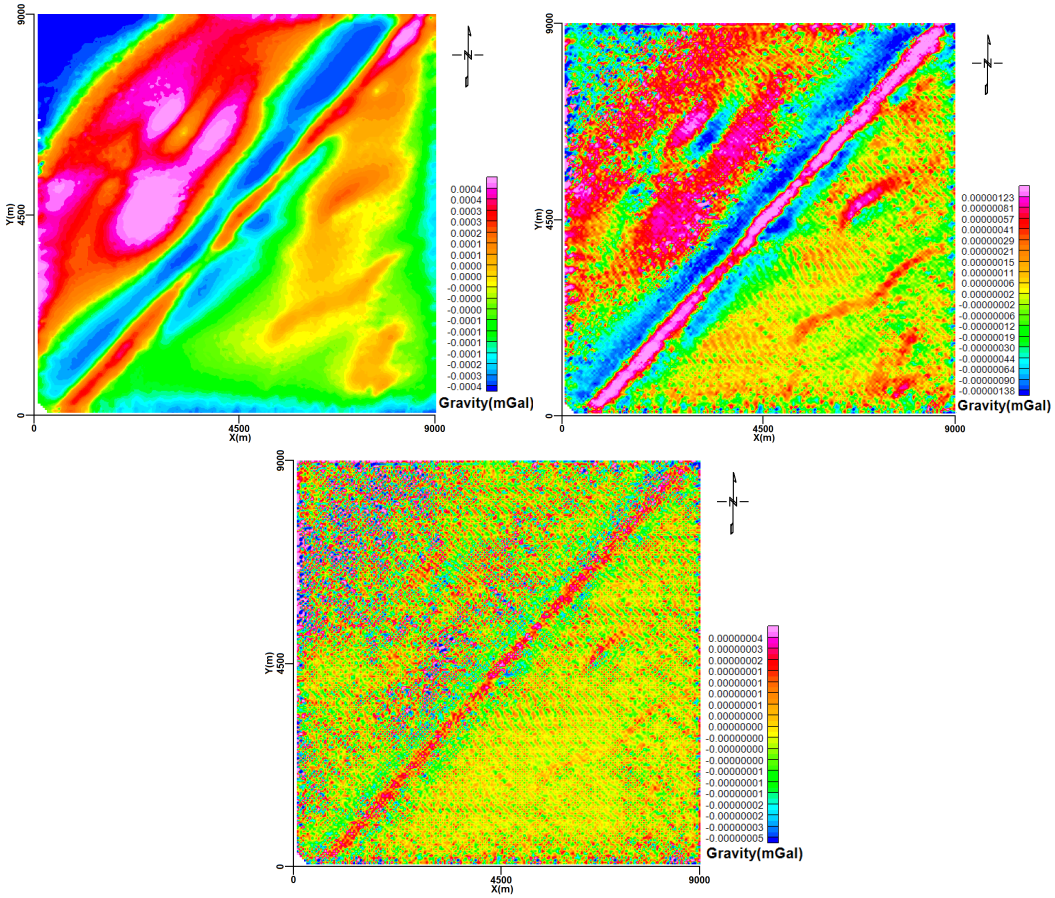


Figure 6.30: Grid of FwOB data after applying derivative filter in Z-direction for differentiation orders of 1 (top-left), 2 (top-right) and 3 (bottom; gridded by Oasis Montaj).

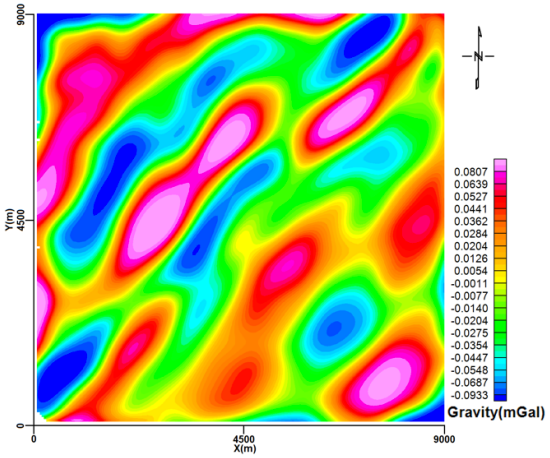


Figure 6.31: Grid of FwOB data after applying band-pass filters from 1000m to 3000m (gridded by Oasis Montaj).

## 6.6 Spectral analysis and filtering of real data

In this section, I will investigate the spectral analysis and filtering tested on the synthetic data on a part of the real airborne Bell gravity data (Figure 6.32; Bell Geospace Limited, 2007; see Section 8.1). I assume that the interface between the overburden and the sandstone constructed using drill-hole data is the best estimation. So, I will calculate the gravity data related to the overburden part at real gravity stations. And, then I subtract it from the real free-air data in order to generate the real estimated FwOB data (Figure 6.32).

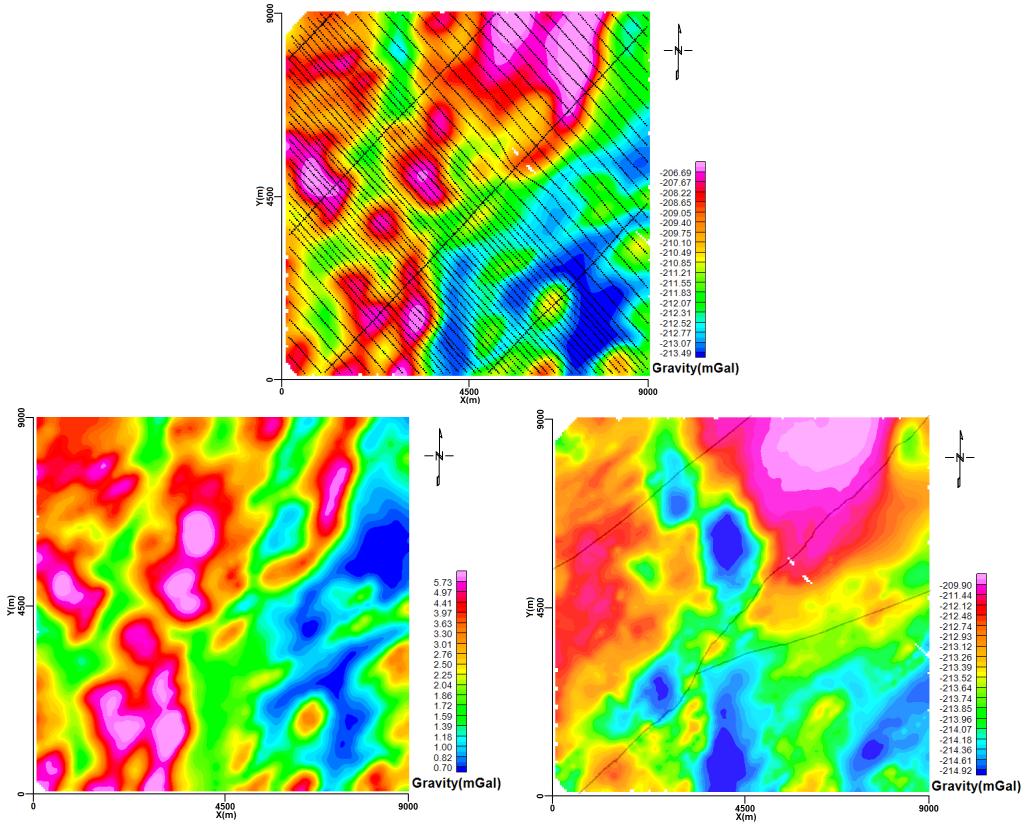


Figure 6.32: Top: Grid (9×9km) of real free-air data along the airborne survey lines (black dots). Number of stations: 7719. Bottom-left: Grid of overburden signature gravity data. Bottom-right: Grid of real gravity free-air data after removing overburden signature (FwOB). Faults are shown by the black lines. Main fault (P2 fault; adapted from CMIC-Footprints project) is shown by a diagonal line started from the bottom left to the top right (gridded by Oasis Montaj).

Figures 6.33 to 6.35 show the 2D power spectrum as well as RAPS of the real free-air data and real estimated FwOB data. “Low-pass” filter and spectral analysis on the free-air data (Figures 6.33 to 6.36) as well as both “high-pass” and “derivative in Z-direction” filters on the real FwOB data (Figures 6.37 and 6.38) were applied. Some of the faults in the basement have been indicated on these images (using Global Mapper software) to indicate possible locations and trends of alteration zones.

For a grid cell size of 5m, the linear pink parallel zones (high power; northeast to southwest trending) in the centre of the whole 2D power spectrum correspond to the direction of the survey lines (Figures 6.33 and 6.34). This indicates that there is a lot of power and hence a lot of structure in the data-set in that direction. For a grid cell size of 20m, and based on the synthetic results of Section 6.4, the linear pink zone (high power; northwest to southeast trending) in the centre of the 2D power spectrum of the free-air gravity data possibly corresponds to the direction of overburden streamlined deposits, and the linear pink zones in FwOB due to variations (e.g. alteration zones) aligned with the faults. But, most likely the northwest-southeast trending features in the power spectra is still due to the survey lines because the larger cell size averages out (aliases) the variation along the flight lines that is happening at the measurement spacing, which is closer than 20m.

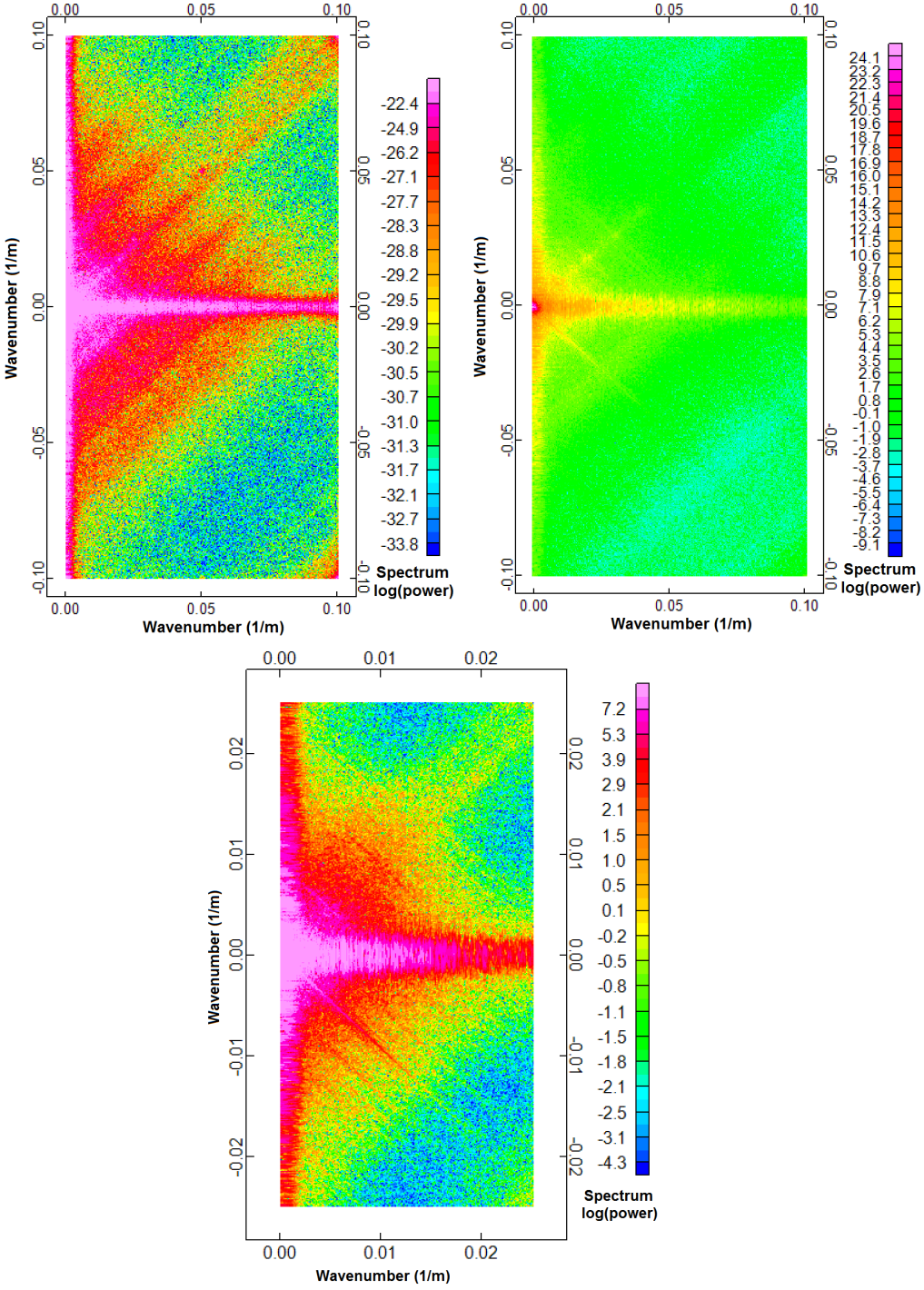


Figure 6.33: 2D power spectra for free-air data for grid cell sizes of 5 m (top-left), for grid cell size of 5 m with a larger range of "Spectrum log (power)" (top-right), and for a grid cell size of 20 m (bottom; gridded by Oasis Montaj).

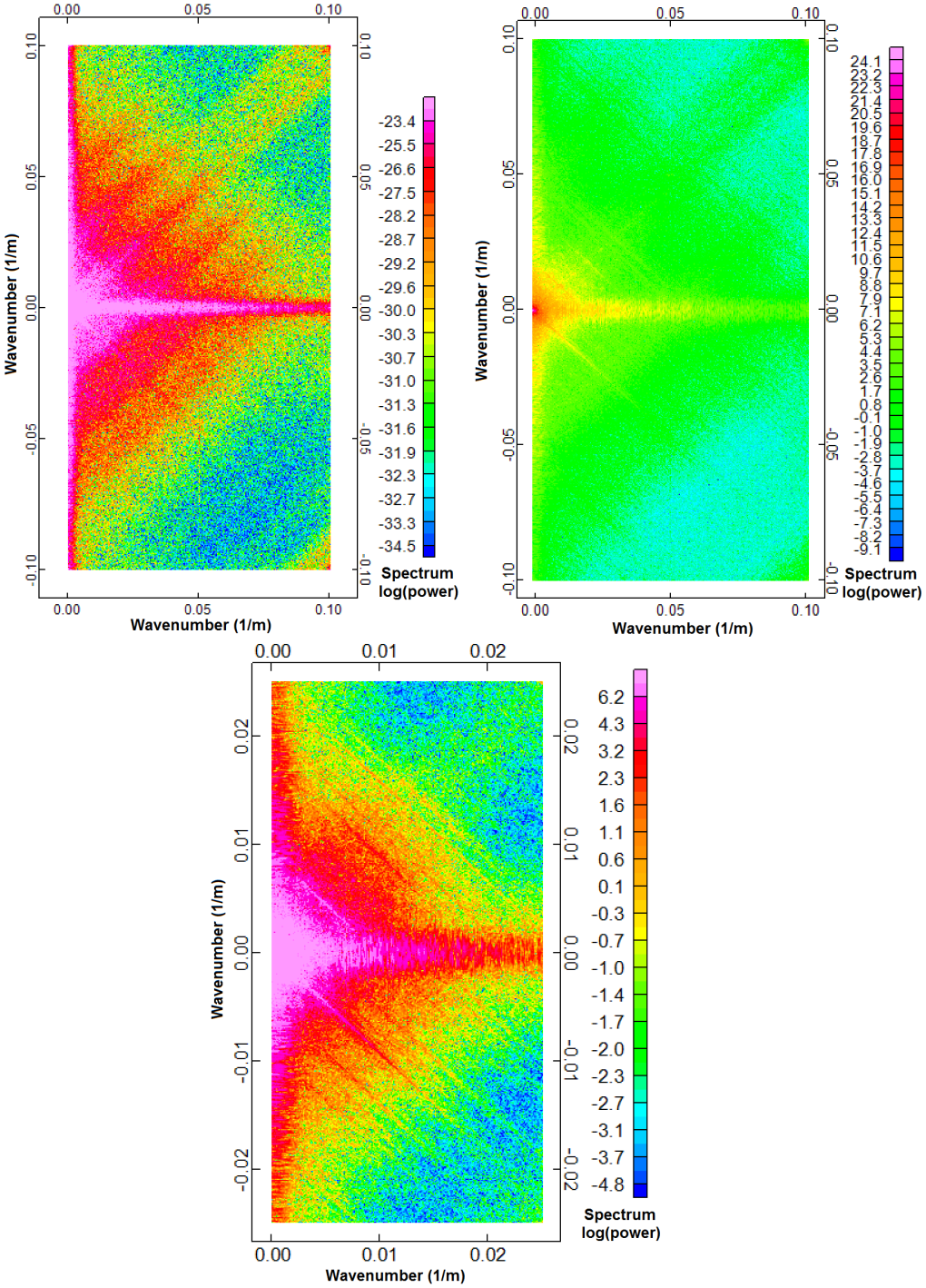


Figure 6.34: 2D power spectra for FwOB data for grid cell sizes of 5 m (top-left), for grid cell size of 5 m with a larger range of "Spectrum log (power)" (top-right), and for a grid cell size of 20 m (bottom; gridded by Oasis Montaj).

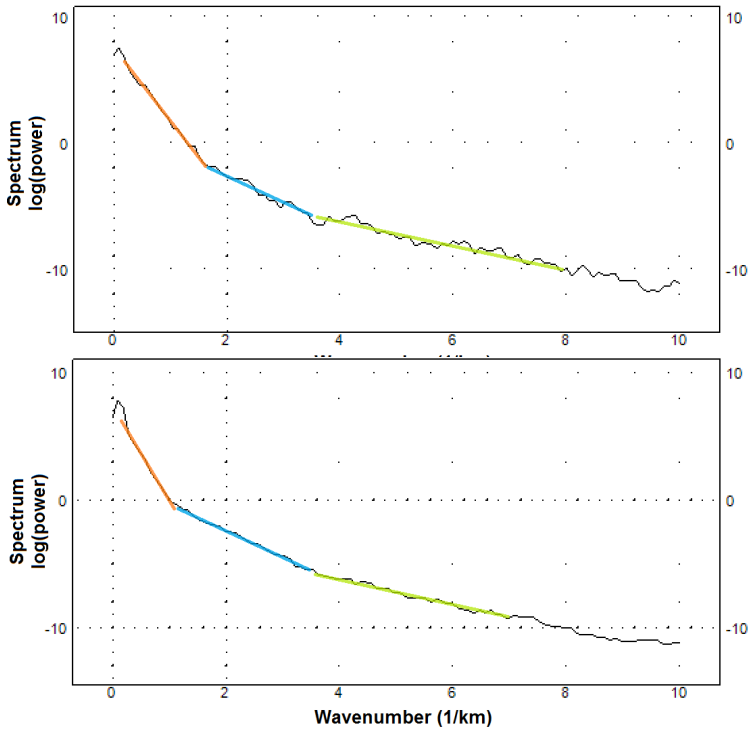


Figure 6.35: Top: RAPS from free-air data for grid cell sizes of 50 m. Colored lines are drawn and fitted in order to find the cut-offs (here 1.5, 3.2 and 8 $km^{-1}$). Bottom: RAPS from FwOB data for grid cell sizes of 50 m. Colored line are drawn and fitted in order to find the cut-offs (here 1.3, 3.3 and 7 $km^{-1}$; gridded by Oasis Montaj).

The following shows the RAPS results for the free-air and FwOB data. Wavenumber ($k$) is equal to $2\pi$/wavelength ($l$). Therefore, using cut-offs obtained from RAPS I can find the wavelength belonging to the various contributions.

**Free-air:**

$k$=1.5 => $l$=4.2km (probably belonging to the basement)
$k$=3.2 => $l$=2km (probably belonging to the alteration)
$k$=8 => $l$=0.8km (wavelengths less than 2km are belonging to the overburden)

**FwOB:**

$k$=1.3 => $l$=4.8km (probably belonging to the basement)
$k$=3.3 => $l$=1.9km (probably belonging to the alteration)
$k$=7 => $l$=0.9km (probably belonging to the interface between overburden and sandstone)

The depths (*d*: distance from observation stations) are obtained from the lines' slopes (*m*) using equation $d=-m/4\pi$ as follow:

**Free-air:**

orange line => $d=-(3/-0.4)/4\pi=0.6$km (probably belonging to the basement)
blue line => $d=-(3/-1)/4\pi=0.24$km (probably belonging to the alteration)
green line => $d=-(2/-2)/4\pi=0.08$km (probably belonging to the overburden)

**FwOB:**

orange line => $d=-(5/-0.6)/4\pi=0.66$km (probably belonging to the basement)
blue line => $d=-(5/-1.9)/4\pi=0.2$km (probably belonging to the alteration)
green line => $d=-(1.5/-1)/4\pi=0.12$km (probably belonging to the interface between overburden and sandstone)

In Figure 6.36, the low-pass filter results for the "real free-air data" for a value of 10000m shows good correlation with the faults in the area. Figure 6.37 shows derivatives in Z-direction for differentiation orders. For these data, the tie-lines were removed from the dataset. The high-pass filter on the real FwOB data for values more than 3000m show variations which have good correlation with the faults (Figure 6.38).

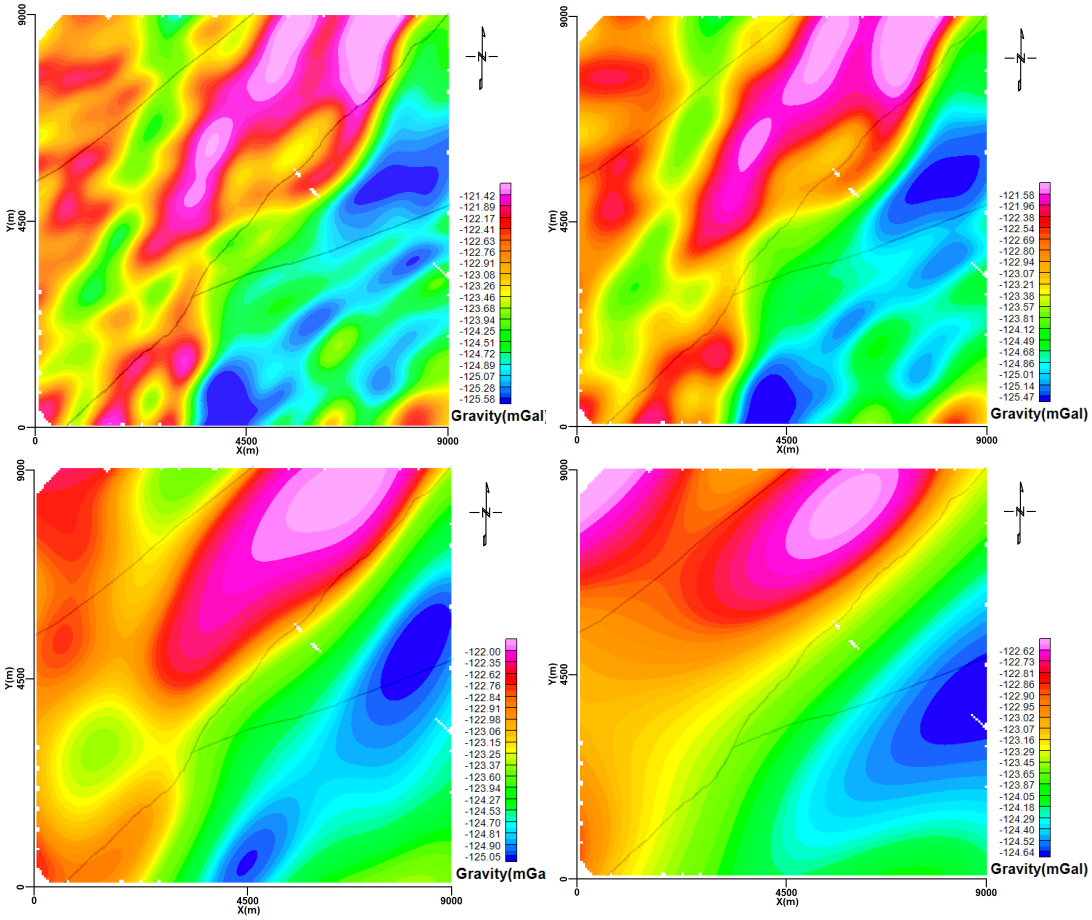


Figure 6.36: Grid of real gravity free-air data after applying low-pass filters 1000m (top-left), 2000m (top-right), 5000m (bottom-left) and 10000m (bottom-right). Faults are shown by the black lines (gridded by Oasis Montaj).

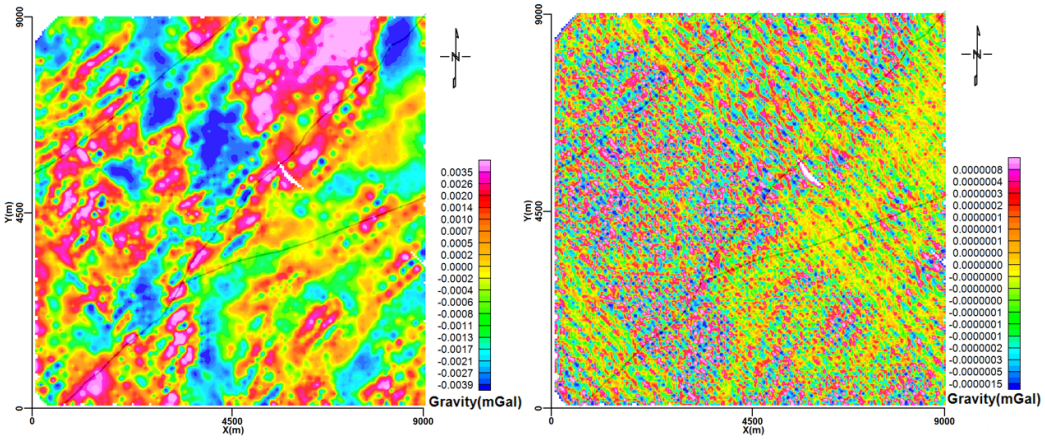


Figure 6.37: Grid of real FwOB data after applying derivative filter in Z-direction for differentiation orders of 1 (left) and 3 (right). Faults are shown by the black lines (gridded by Oasis Montaj).

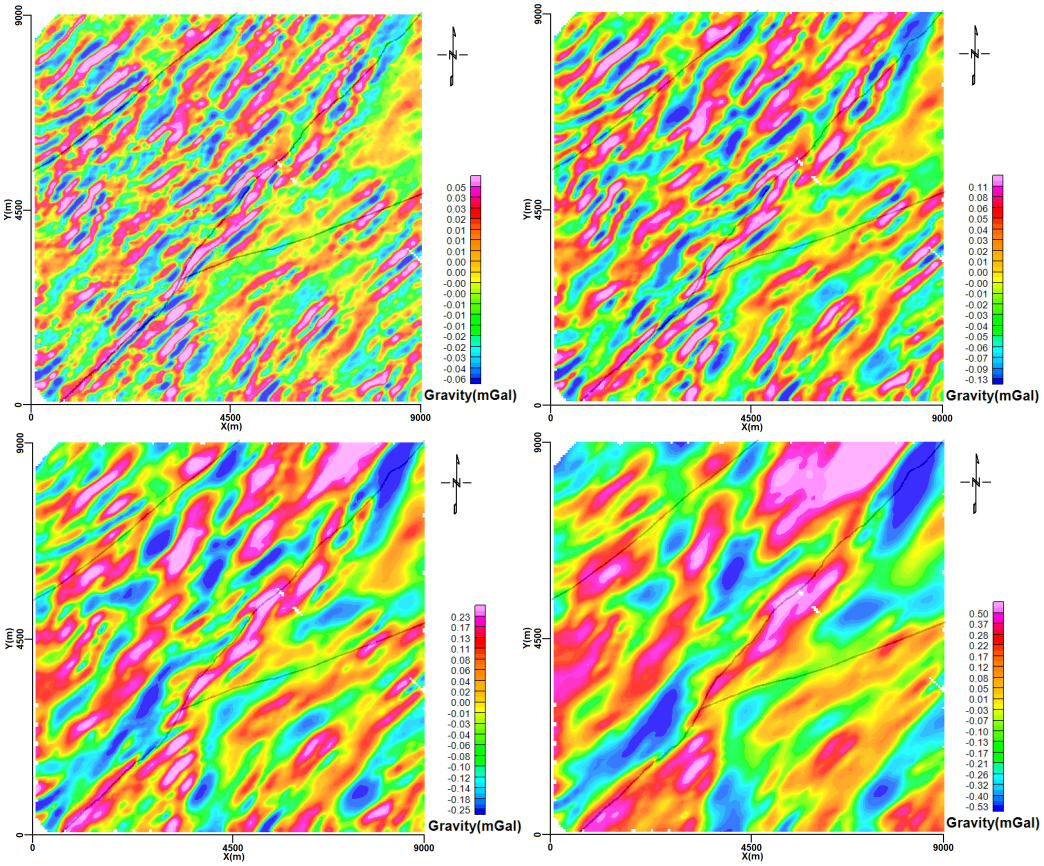


Figure 6.38: Grid of real FwOB data after applying high-pass filters of 500m (top-left), 1000m (top-right), 2000m (bottom-left) and 5000m (bottom-right). Faults are shown by the black lines (gridded by Oasis Montaj).

## 6.7 Conclusion

Free-air gravity data were synthetized for the McArthur area model. Using drill-hole data the base of the overburden is estimated in order to calculate the gravity signature of the overburden. This signature is subtracted from the free-air data to generate FwOB (meaning free-air data without overburden signature) data. Spectral analyses such as 2D power spectrum and radially averaged power spectrum (RAPS) are tested on the synthetic free-air data and FwOB data. The signature of the alteration zone can be seen in the 2D power

spectrum of the FwOB while the 2D power spectrum of the free-air data is dominated by the survey lines and the variations of topography. RAPS gave a good estimation of the wavelength and the depth of the geological structures.

Frequency filtering (low-pass, high-pass, band-pass and vertical derivatives filters) was applied on both synthetic free-air and FwOB data. Filters applied on the free-air data were not useful to detect the alteration zone signature as the data was dominated by the overburden signature. But, high-pass and vertical derivatives applied on the FwOB data showed clearly the alteration zone signature. Also, both spectral analysis and frequency filtering tested by synthetic data were applied on the real free-air data as well. The low-pass filter on real free-air data and the high-pass filter on real FwOB data show good correlations with the faults in the area. Features in the 2D power spectrum of real data are mostly correspond to the direction of the survey lines, overburden streamlined deposits, variations (e.g. alteration zones) aligned with the faults and the variation along the flight lines. The RAPS results for the real free-air and FwOB data estimate the depth to some of structures.

# Chapter 7

# Modelling and Inversion of Seismic Refraction and Gravity Data of the McArthur Area

## 7.1 Introduction

Seismic refraction (see Section 3.4) is one of the best geophysical methods to investigate the interface between shallow layers. It can also yield the seismic velocity of the geological structures between the interfaces (Telford et al. 1976; Sheriff and Geldart, 1995; Kearey et al., 2002). In this research, seismic refraction data were synthetized for a 2D model. Inversion (see Section 4.5) was applied on the synthetic data to find the base of the overburden. The inversion approach used in this research is that of Lelièvre et al. (2012). This uses the minimum structure approach in which an objective function is minimized using a Gauss-Newton method. For the joint inversion, I have mostly used the clustering fuzzy c-mean method in which I can specify a relationship between the physical properties that lies in discrete clusters (Paasche and Tronicke, 2007). 2D joint (as well as independent and constrained) inversion of seismic refraction and gravity data is assessed as a means of reliably mapping overburden thickness, enabling density anomalies from deeper mineralization and alteration to be reconstructed through gravity inversion. Results show

that the seismic refraction data provides an accurate estimation of the base of the overburden in the joint Earth model, which in turn leads to an accurate density distribution in the same model.

In this chapter, 2D models of the McArthur area are made to synthetize the seismic refraction data followed by the inversion of synthetic data to reconstruct the true model. Different earth models will be investigated such as two-layer model and drumlin-shape model. Also, the joint inversion method will be assessed by considering and adding the gravity method. Finally, a constrained gravity inversion will be used to reconstruct the alteration zone by getting help from the independent and joint inversion models of seismic refraction.

## 7.2 Synthetic modelling and inversion of seismic refraction

In this section, synthetic modelling and inversion of seismic refraction data are investigated over different models. Figure 7.1 represents the topography of the McArthur-Millennium corridor. There are many drill-holes in the corridor which are mostly located close to the faults (e.g. P2 fault in McArthur area). A straight survey line is chosen for the modelling along a few drill-holes. In the model, the variation of topography and the base of overburden are obtained from drill-hole data. Inset in Figure 7.1 shows the location of the survey line. The variation of overburden thickness is not only due to the variable topographic surface, which is the outcome of glacial events, but also due to the variable interface between overburden and sandstones (Figure 7.2).

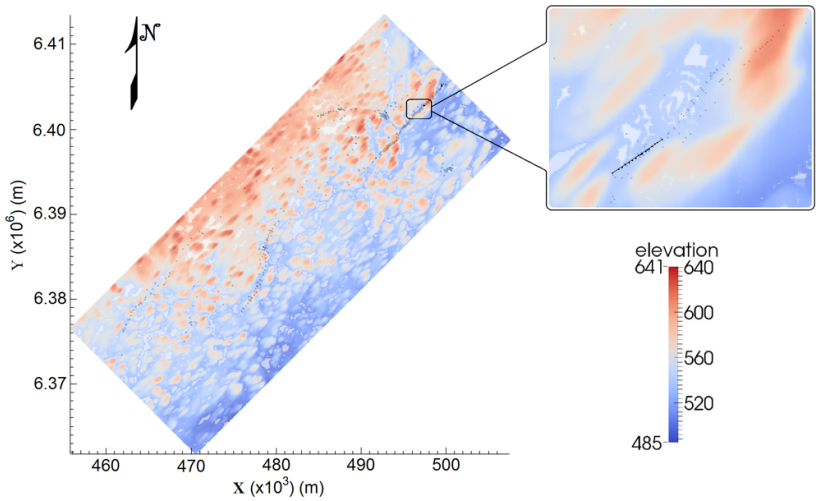


Figure 7.1: Topography of the McArthur-Millennium corridor. Inset shows location of survey line and seismic sources for synthetic modelling study.

### 7.2.1 Two-layer model

A vertical section was made for the synthetic model using real drill-hole data (Figure 7.2). Two layers are considered in which the upper layer is the overburden and the lower layer is sandstones. Appropriate slownesses were specified for these two layers. The overburden and the sandstones have a slowness of 0.00025 s/m and 0.000625 s/m, respectively (see Section 2.5.1). Then, the forward modelling code (Lelièvre et al., 2011; see Section 4.3) run in order to achieve the seismic first arrival travel times data. In order to keep this synthetic modelling similar to the real surveys, distances between receivers (geophones) and sources are 2m and 50m, respectively. In this chapter, using a code of Lelièvre and Farquharson (2015) a Gaussian random noise of standard deviation equal in magnitude to 1% of a datum is added to synthetic traveltime data. Also, Figure 7.2 illustrates the propagation of a wavefront (travel-time contours) belonging to one of the sources, and related seismic rays.

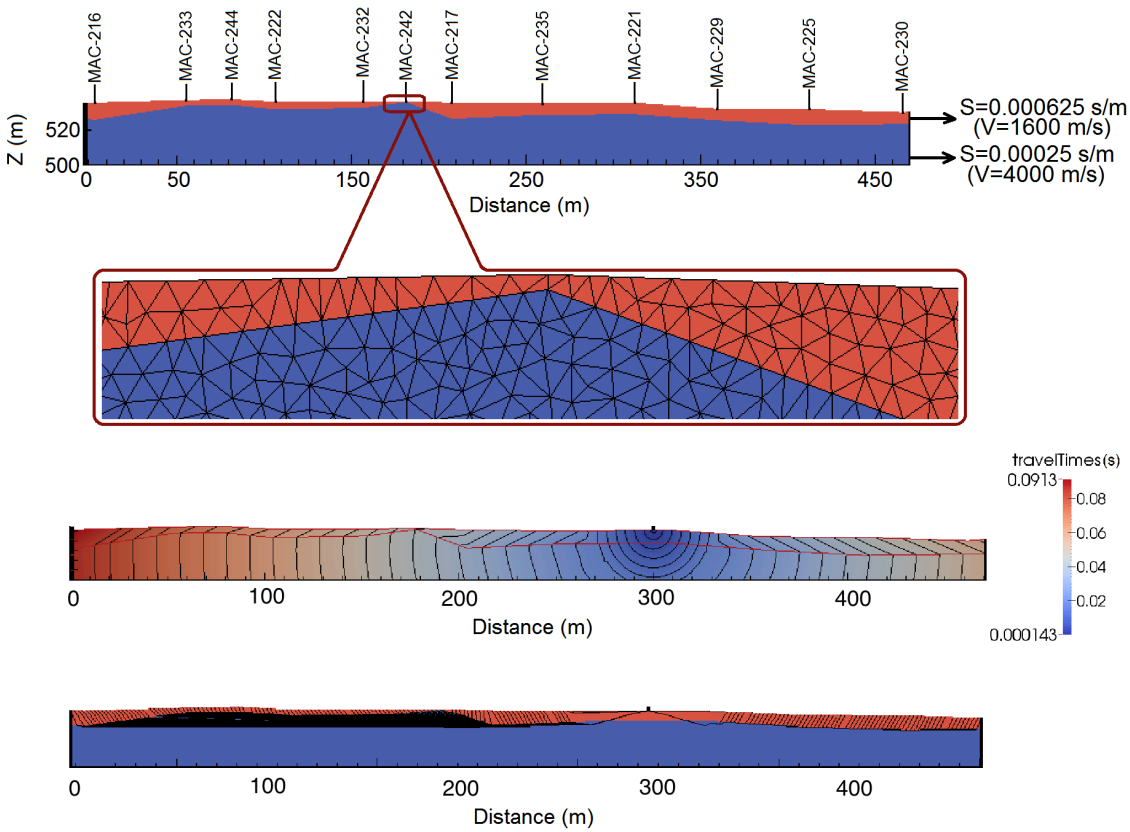


Figure 7.2: Top: model of glacial sediments (red, slow) over sandstone (blue, faster) based on true topography and base of glacial sediments interpolated between boreholes (labelled), and the triangular mesh used for the modelling. Middle: propagation of a wavefront (travel-time contours) belonging to one of the sources. Bottom: seismic traces between receivers and one of the sources.

In the entire inversions in this chapter, for the data misfit, the value of $\omega$ reached 1 while a value less than one is considered for the *chifact* (see Section 4.5). This leads to a desirable fit. Also, a small value of 1.0E-5 is considered for the initial trade-off parameter value. For the inversion of gravity data, the distance weighting is considered. Also, no reference model is considered in the inversions except in the constrained inversions described towards the end of this chapter. The mesh used in the all inversions is laterally a little larger than what is shown in the figures in order to decrease the effect of the edge of the mesh on the computed data.

After considering suitable values for inversion parameters, the inversion code (Lelièvre et al., 2012) was run for the synthetic traveltime data-set using both L2-norm and L1-norm methods (Figure 7.3). The model obtained from the inversion process using the L2-norm displays a good agreement with the true model (Figure 7.3 top panel). But, the interface between the two layers is not sharp and obvious, which is due to the smoothing nature of the L2-based regularization used in this inversion. In order to ameliorate this problem, the L1-based approach was also used (Figure 7.3 bottom panel). As can be seen, small variations in the glacial sediments–sandstones contact are remarkably well reproduced, and the interface sharp. However, the number of iterations (and subsequently the run-time) in the L1-based inversion is much more than the L2-based. The run-time for L2 is around 2 hours (for 11 iterations), while the run-time for L1 is more than 4 hours (for 24 iterations).

Figure 7.4 shows traveltime-distance plots of the refraction data computed for the models constructed by the inversions as well as the synthetic observed refraction data-set provided to the inversion. The fit between the observed and calculated data is good and mostly acceptable. For the L2-norm and the L1-norm, the inversion process started with an $\omega$ value of 1447.3 and 1168.7, and stopped when they reached to 1.042 and 1.028, respectively (see Section 4.5). Models are made of more than 40,000 triangle cells, in which the maximum area of cells is limited to 1 square metre. The advantage of small cells is seen where the thickness of the layers is very small, as it can be seen in Figure 7.2 in the model between 100 m and 200 m. Although small cells increase run-time, they increase the resolution and accuracy. Small cells give the inversion freedom to put interface and changes of slowness where it most wants to without being constrained by cell boundaries. The

interface under the two last stations in both sides is not reconstructed because there is no refracted wave which comes from those parts (see Figure 3.14).

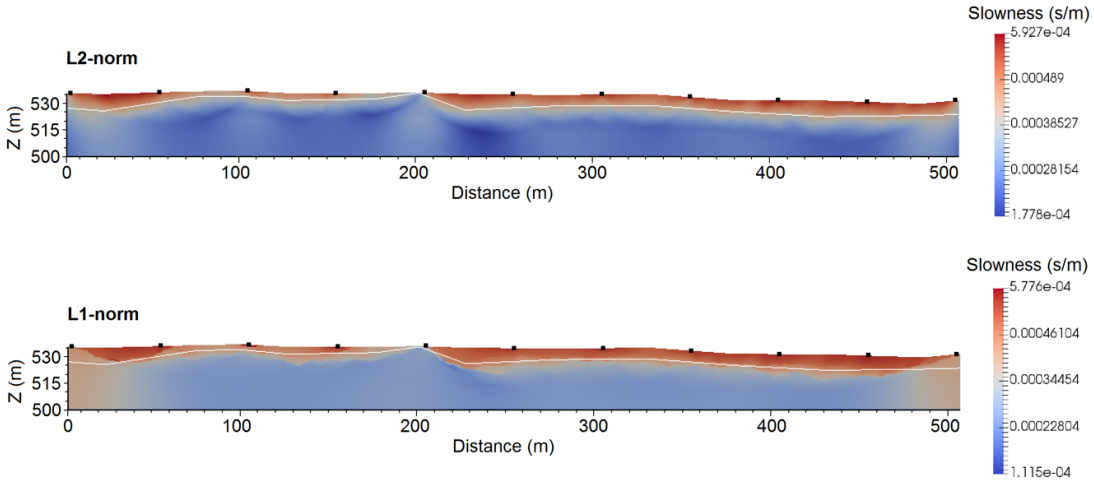


Figure 7.3: Earth model constructed from inversion of synthetic seismic data along the line shown in Figure 7.2 using L2- and L1-norm. Locations of sources indicated by squares. White line indicates the glacial sediments-sandstone contact in the model used to synthesize the data for this example.

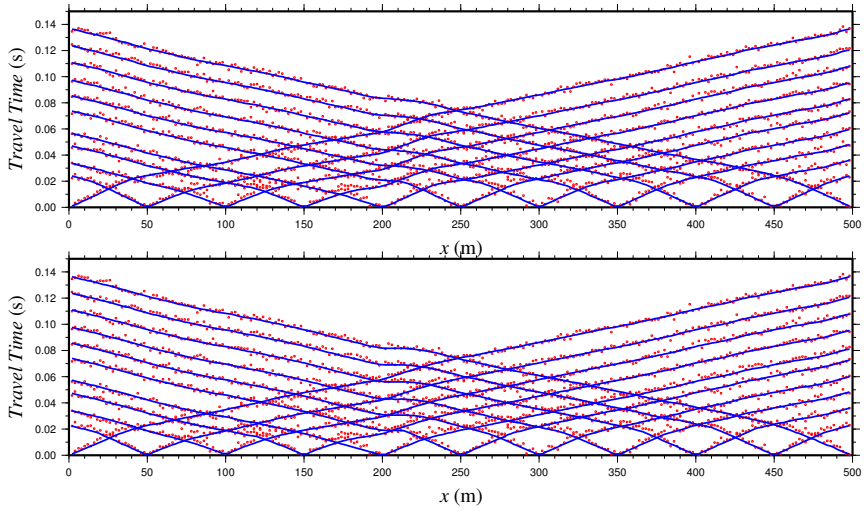


Figure 7.4: Traveltime-distance plot of refraction data belonging to the forward modelling used in the inversion code (red) and data calculated from the inversion model (blue) for both L2-norm (top) and L1-norm (bottom) models in Figure 7.3.

### 7.2.2 Drumlin-shape models

In order to test the modelling and inversion for different structures, a few models were made for drumlin-shape models as the McArthur-Millennium corridor is dominated by streamlined deposits such as drumlins (Figures 7.5, 7.6 and 7.7). Physical properties were kept the same as for the previous model; however, the shape and thickness of overburden is different in these models. The difference between them are in the shape of the interface between glacial sediments and sandstones as the base of the glacial sediments has a topography due to the abrasion caused by glacial motions.

In Figure 7.5, small variations were considered for the interface, whereas Figures 7.6 and 7.7 demonstrate bulge and troughs shapes for the interface, respectively. Forward and inversion modellings for these model were similar to those for the model in Figure 7.3, where distances between receivers (geophones) and sources were kept as 2m and 50m, respectively. It can be seen that inversion results (using L2-norm method) show a good agreement with the true synthetic models, and there is a good fit between observed and calculated data.

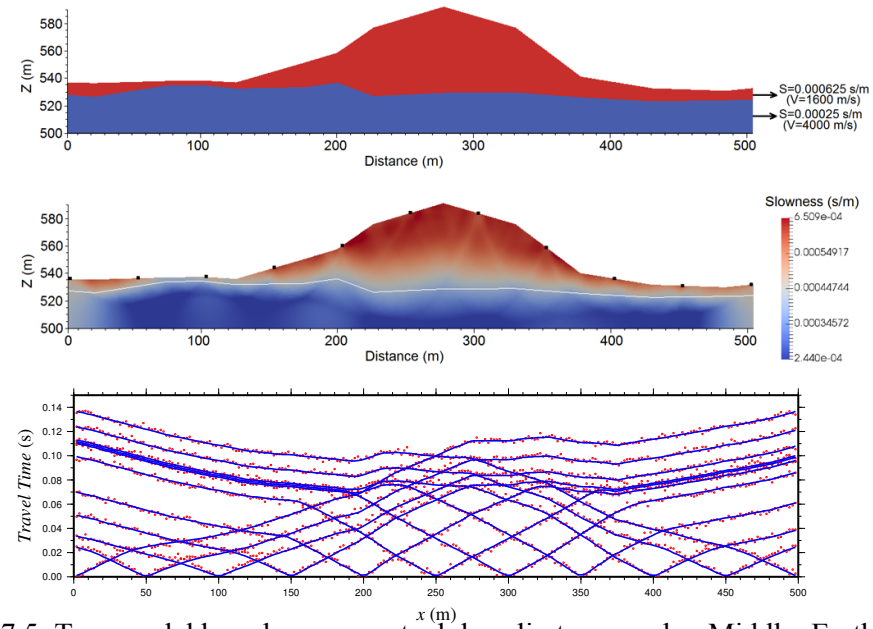


Figure 7.5: Top: model based on conceptual drumlin topography. Middle: Earth model constructed from L2-norm inversion of synthetic seismic data. White line indicates the glacial sediments-sandstone contact. Bottom: Travel-time vs distance plot of refraction data for true model (red) and data calculated from the inversion result (blue).

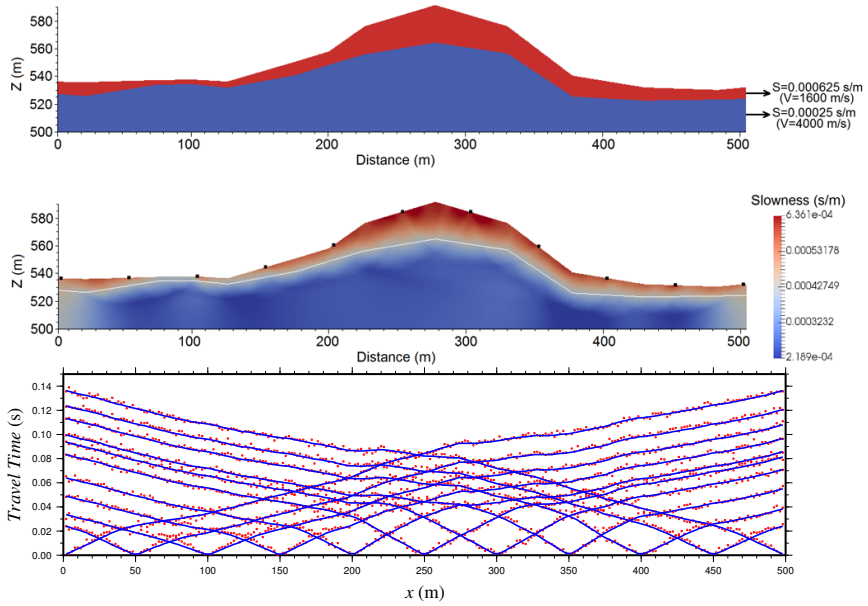


Figure 7.6: Top: Second drumlin model. Middle: Inversion model (L2-norm). Bottom: Travel-time vs distance plot of refraction data for true model (red) and for inversion result (blue).

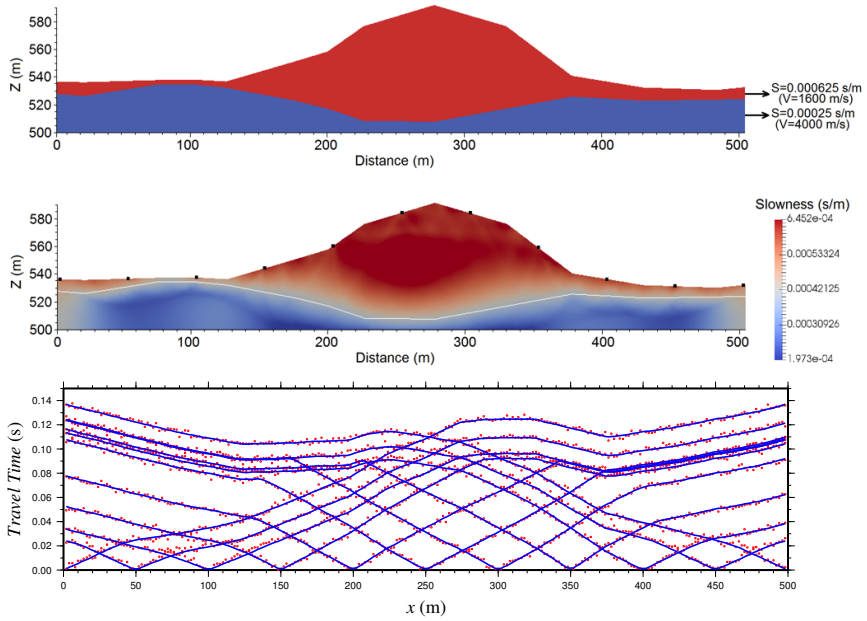


Figure 7.7: Top: Second drumlin model. Middle: Inversion model (L2-norm). Bottom: Travel-time vs distance plot of refraction data for true model (red) and for inversion result (blue).

### 7.2.3 Blind-layer model

A blind layer results from a low-velocity layer in which rays cannot be critically refracted (see Section 2.5.1 and 3.4.3). This leads to an overestimation of the depth to underlying interfaces. The assumption that velocity increases with depth may not be valid always. The real indication of a blind layer in McArthur area is shown in Figure 2.12 where the lower layer in the glacial sediments (which is unconsolidated stratified sand and gravel) can have a less seismic velocity than the upper layer in the glacial sediments (which is unconsolidated stratified tills). Thus, a synthetic model is made for a blind layer case which is represented in Figure 7.8. In this model, distances between receivers (geophones) and sources are 5m and 20m, respectively. The middle layer has a lower velocity than the upper

layer. The difference between observed and calculated data for the inversion illustrates a good fitting, whereas the inversion vertical section shows an overestimation and a very fuzzy, indistinct base of the overburden/blind layer of the depth (see Figure 7.8).

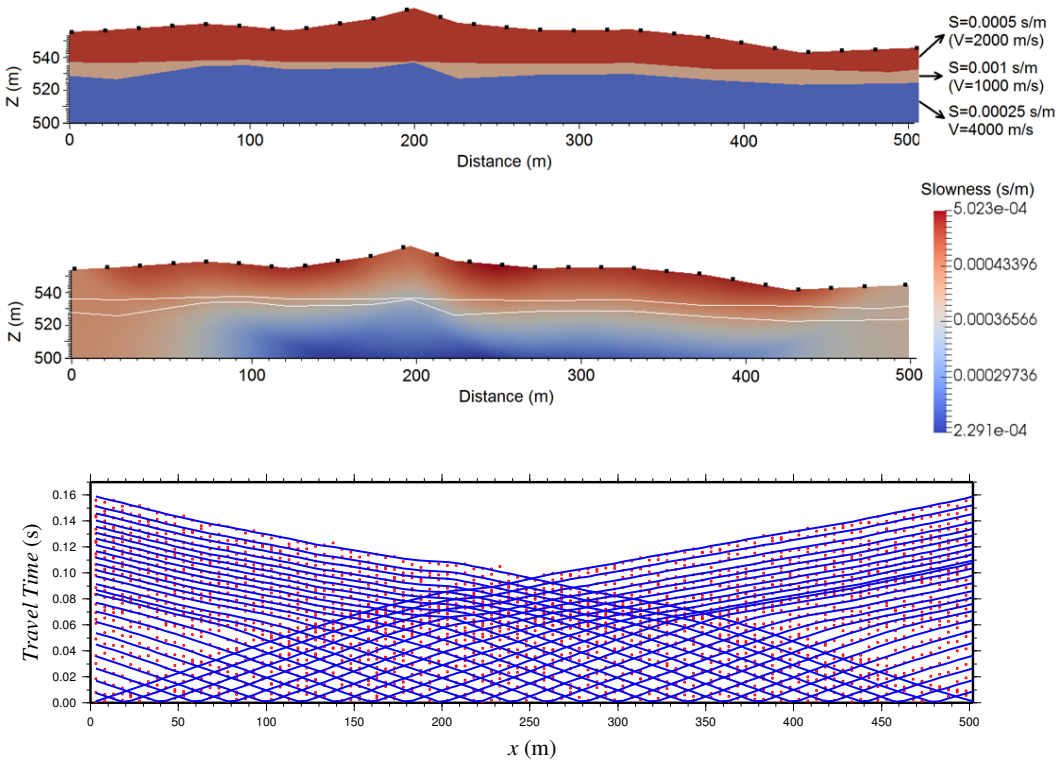


Figure 7.8: Top: model of glacial sediments (red & grey (blind layer)) over sandstone (blue, faster) based on conceptual topography. Middle: Inversion model (L2-norm). Bottom: Travel-time vs distance plot of refraction data for true model (red) and for inversion result (blue).

## 7.3 Joint inversion of synthetic seismic refraction and gravity data

Another effective method to depict the subsurface structure using geophysical data is joint inversion (see Section 4.5). The joint inversion is applied on the same model shown in Figure 7.5. The mesh used for this joint inversion is laterally and vertically a little bit larger

than what is shown in the figures. Two layers are considered in which the upper layer is the glacial sediments (v=1600m/s and d=2g/cc) and the lower layer is sandstone (v=4000m/s and d=2.42g/cc). Using a code of Lelièvre and Farquharson (2015) a Gaussian random noise of standard deviation equal in magnitude to 1% of a datum is added to both synthetic traveltime and gravity data. Figure 7.9 shows results from the independent inversions of gravity data for this drumlin-shaped model using L2-norm. There is a good fit between observed and calculated data. However, the density vertical section in particular does not resemble the true model (Figure 7.9).

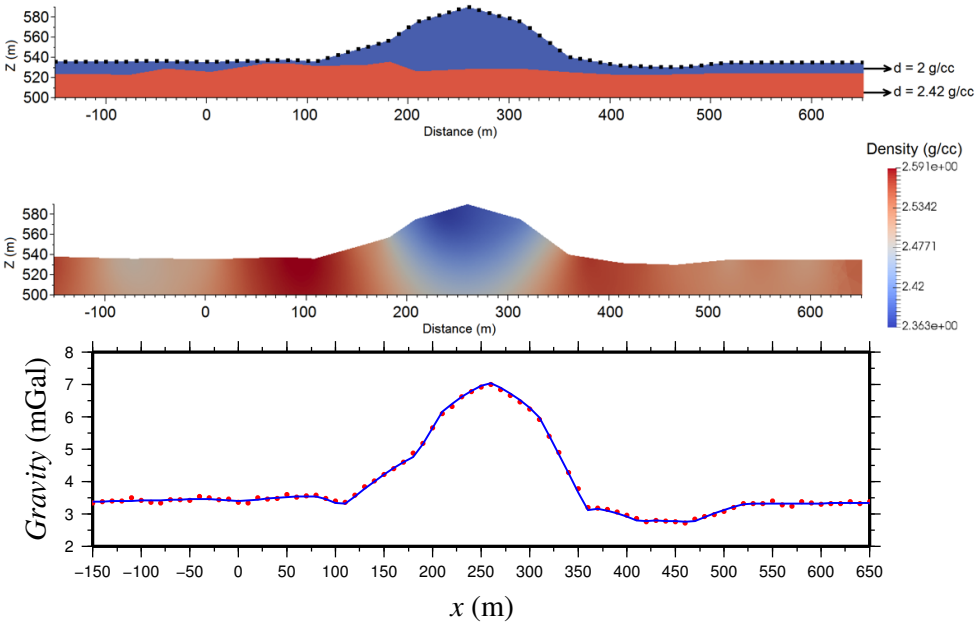


Figure 7.9: Top: model of glacial sediments (d=2g/cc) over sandstone (d=2.42g/cc) based on conceptual topography (drumlin; Figure 7.5). Middle: Earth models constructed from independent inversions (L2-norm) of synthetic gravity data along an 800 m line. Bottom: gravity data for the true model (red) and data calculated from the inversion result (blue).

In order to solve this problem, the joint inversion of seismic refraction and gravity data is used (Figures 7.10 to 7.13). The joint inversion method tries to leverage good seismic sensitivity to the glacial sediments–sandstones contact to build accurate glacial sediments

layer in the density model. It is the simultaneous inversion of two geophysical data-sets (here i.e. seismic refraction and gravity data; see Sections 3.2 and 3.4) to produce a single Earth model. In this chapter, the clustering fuzzy c-mean method is used for the joint inversion method to simultaneously invert the two data sets by including a terms in the objective function which links the two physical properties (see Section 4.5). Because there are two layers in the true model, two clusters are defined with average physical properties corresponding to the two main geological structures: glacial sediments (density=2 g/cc; slowness:0.000625 s/m), sandstone (density=2.42 g/cc; slowness:0.00025 s/m). A coupling factor of $\rho$=1 is considered. Values larger than $\rho$=1 were tested for the coupling factor as well, but the results were not as good as for $\rho$=1. Therefore, they are not shown in this thesis. By increasing the coupling factor, the similarity between the models increases, but the number of iterations (convergence) as well as the run-time will increase. For the joint inversion of gravity and seismic data the JaP is used, and one stage is used for heating the coupling factor (see Section 4.5).

Figure 7.10 shows the model for a coupling factor of $\rho$ =1. The fit between observed and predicted data is good (Figure 7.11), and the approximate location of the interface can be seen. In comparison to the independent inversions, the density model is much improved (Figure 7.9). The variation of the various terms in the objective function (see Section 4.5) for the joint inversion model is shown in Figure 7.12. 237 iterations are done in the "JaP" inversion process (see Section 4.5) of which 82 were used for pre-heating (shown by the grey area in Figure 7.12). The run-time was around 542 hours for a mesh with 468,000 cells.

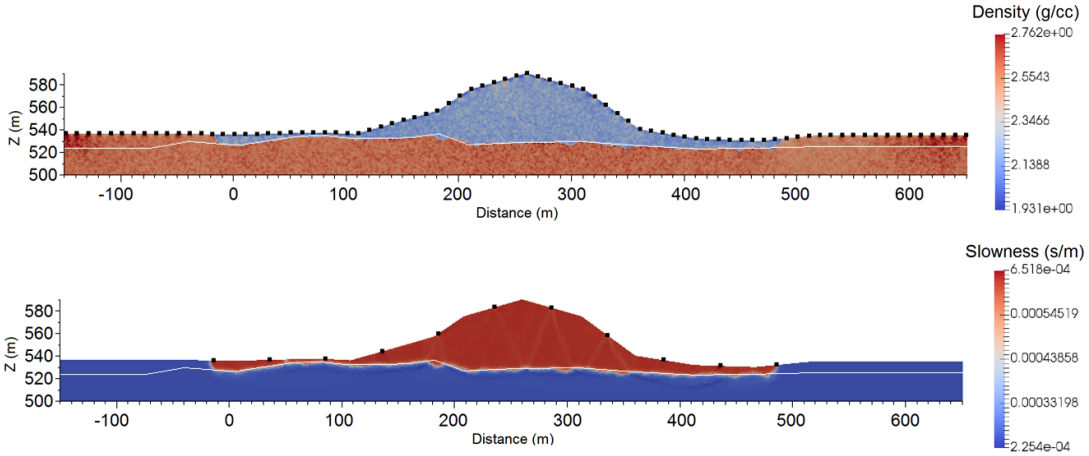


Figure 7.10: Density (top) and slowness (bottom) models constructed from joint inversion of seismic and gravity data (coupling factor $\rho$ =1). Locations of seismic sources and gravity observation locations are indicated by black squares. White line indicates the glacial sediments-sandstone contact.

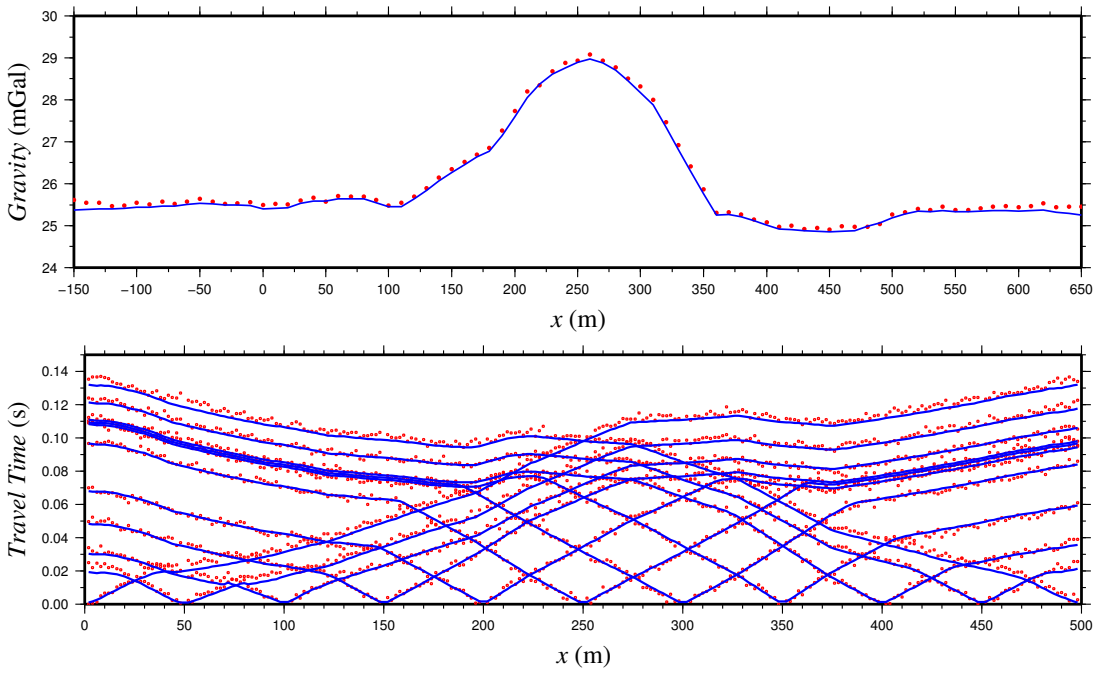


Figure 7.11: Gravity and seismic refraction data for the true model (red) and data for the joint inversion result (blue; $\rho$ =1).

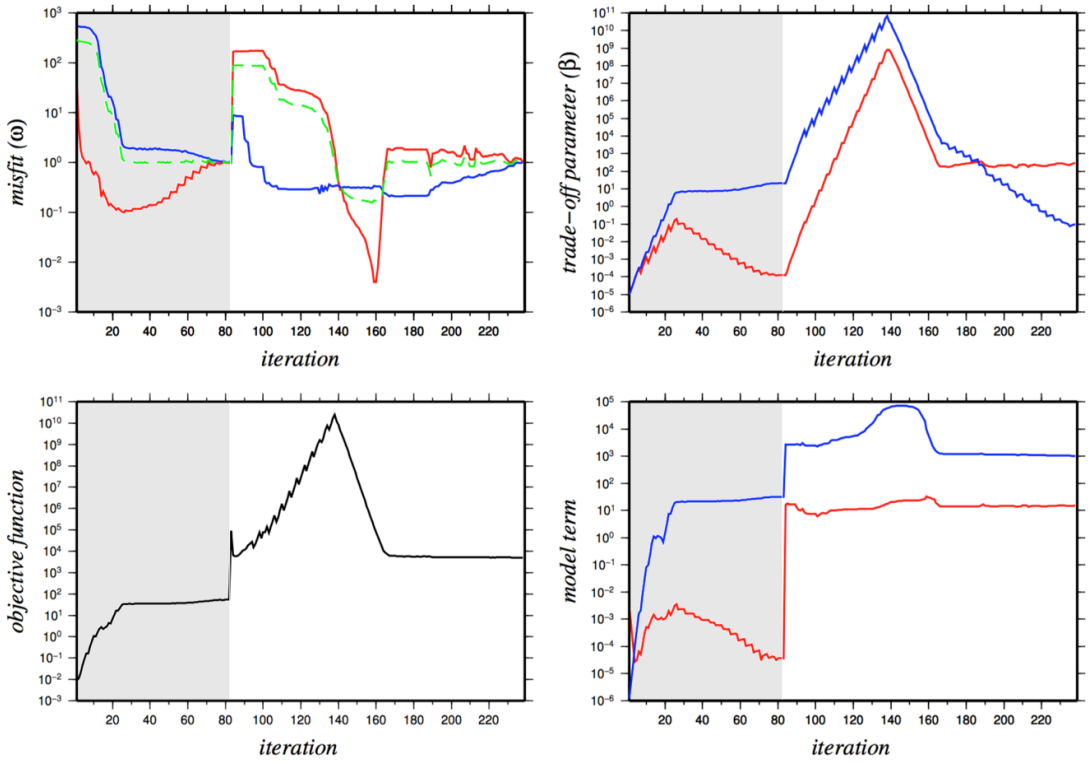


Figure 7.12: Variations of the different parts of the objective function such as data misfit ($\omega$; top-left), trade-off parameter ($\beta$; top-right), objective function ($\mathbf{\Phi}$; bottom-left) and model term ($\phi_m$; bottom-right) at iterations for the joint inversion of gravity (red) and seismic refration (blue) data for $\rho$=1. Green color shows the "average $\omega$" (see Section 4.5). Grey area shows the pre-heating part, and the white area shows the joint inversion part.

Figure 7.13 illustrates the physical properties (slowness versus density) obtained after the independent and joint inversions. Physical properties belonging to each cell are indicated by a blue spot. For the independent inversion, no clusters are generated, while two clusters can be seen for the joint inversion results which represent the physical properties of upper ($S$=0.000625s/m and $d$=2g/cc) and lower ($S$=0.00025s/m and $d$=2.42g/cc) layers.

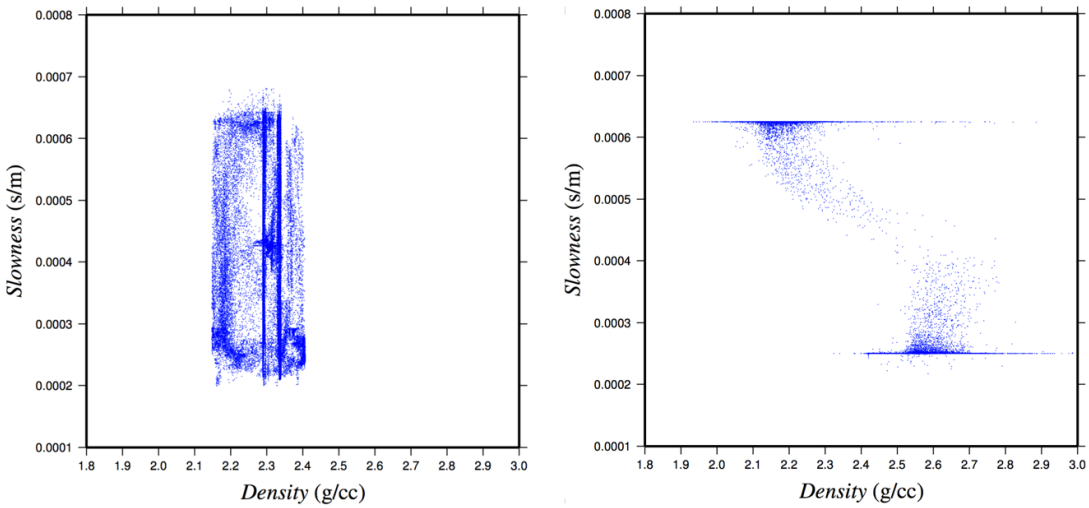


Figure 7.13: Physical properties (slowness versus density) obtained after the joint inversion (right; Figure 7.10) as well as the independent inversions that produced the models in Figures 7.5 and 7.9 (left).

Next, a more complicated model is investigated. For this purpose, a drumlin shaped model with an anomaly is made containing three geological structures: glacial sediments (#1 in Figure 7.14), sandstone (#2 in Figure 7.14) and alteration zone (#3 in Figure 7.14). After considering appropriate physical properties (i.e. density and slowness), seismic first arrival travel-time data as well as gravity data were synthesized using the code of Lelièvre et al. (2011). As it can be seen in Figure 7.15, the seismic data have no chance of seeing the alteration zone as it is too deep in this modelling. The contribution of the different structures to gravity data is shown in Figure 7.16. The extra/difference density of the alteration zone relative to the sandstone (i.e., 0.18 g/cc) increases the magnitude of gravity data as much as 0.2 mGal.

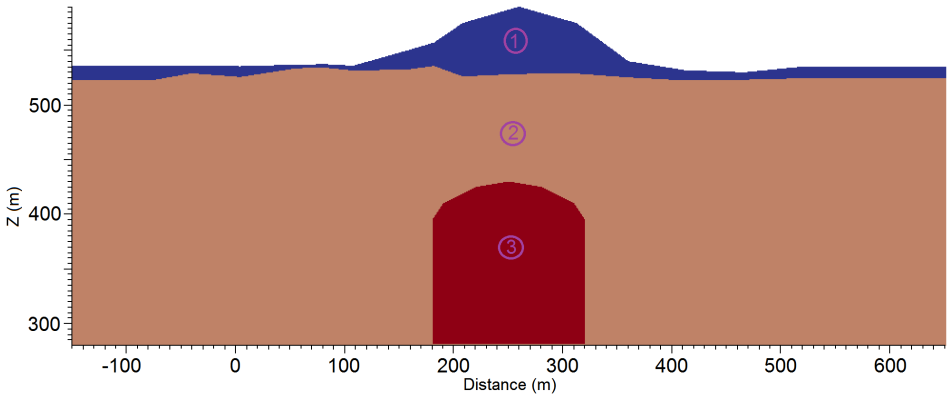


| | Density(g/cc) | Slowness(s/m) |
|---|---|---|
| ① | 2 | 0.000625 |
| ② | 2.42 | 0.00025 |
| ③ | 2.6 | 0.0002 |

Figure 7.14: Drumlin shaped model with an anomaly (alteration zone) at depth.

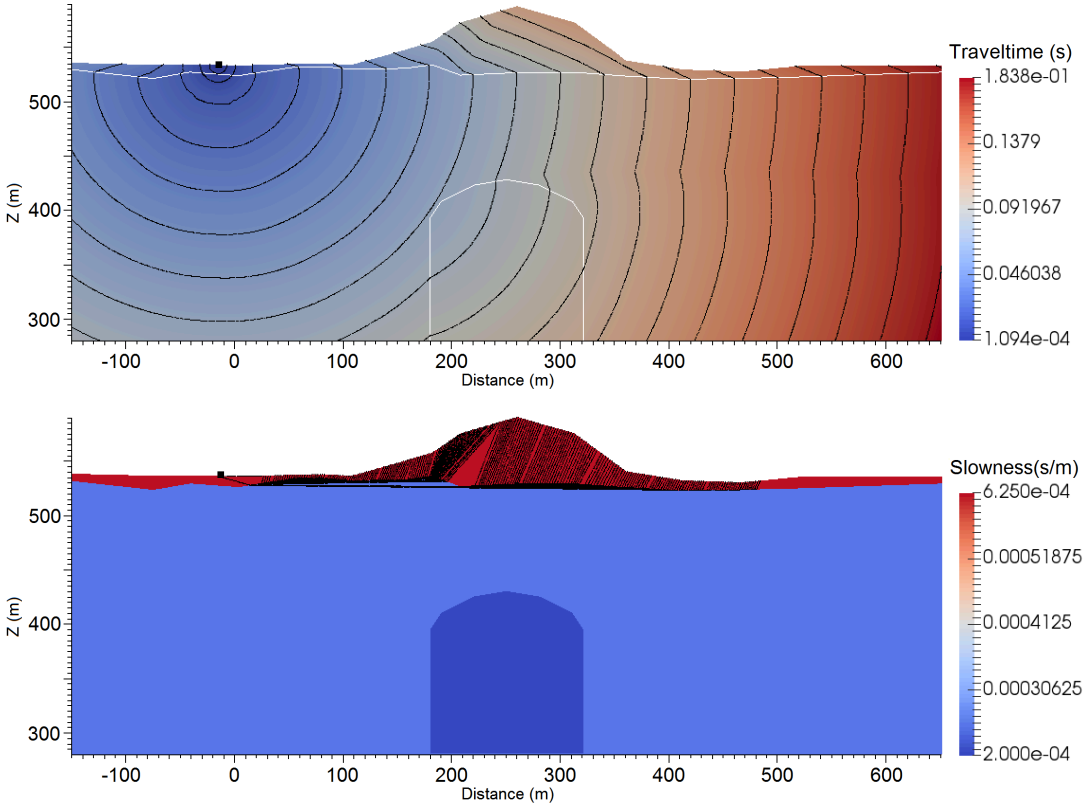


Figure 7.15: Propagation of a wavefront (travel-time contours; top) belonging to the first source from left (black dot), and seismic rays between this source and receivers (bottom).

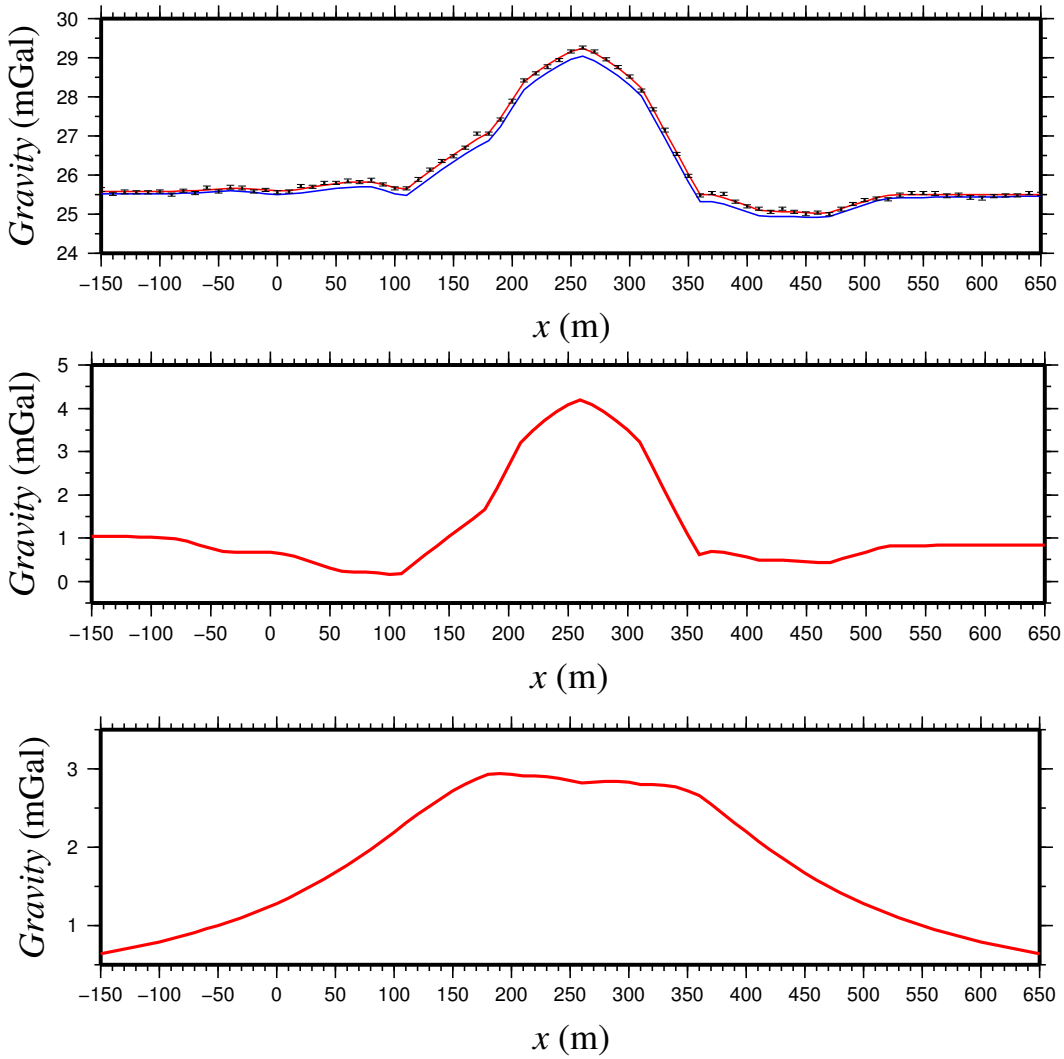


Figure 7.16: Top: red line show gravity data for the model shown in Figure 7.14. Error bars show the the uncertainty and data after adding 1% noise. Blue line shows gravity data for the model shown in Figure 7.14 with only for two layers (alteration zone is removed). Middle: overburden signature. Bottom: alteration zone signature.

Independent inversions were performed for gravity data using L2 norm (Figure 7.17) as well as for seismic data using both L2-norm (Figure 7.18) and L1-norm methods (Figure 7.19) using the code of Lelièvre et al. (2012). The slowness vertical sections show a good agreement with the original model in the upper part of the model. However, the alteration zone is not reconstructed. The density vertical section is not appropriate for any interpretation as expected. The fit between observed and calculated data for all the models is good. The mesh used for the inversion is laterally a little larger than what is shown in the figures in order to decrease the effect of the edge of mesh on the data especially gravity data.

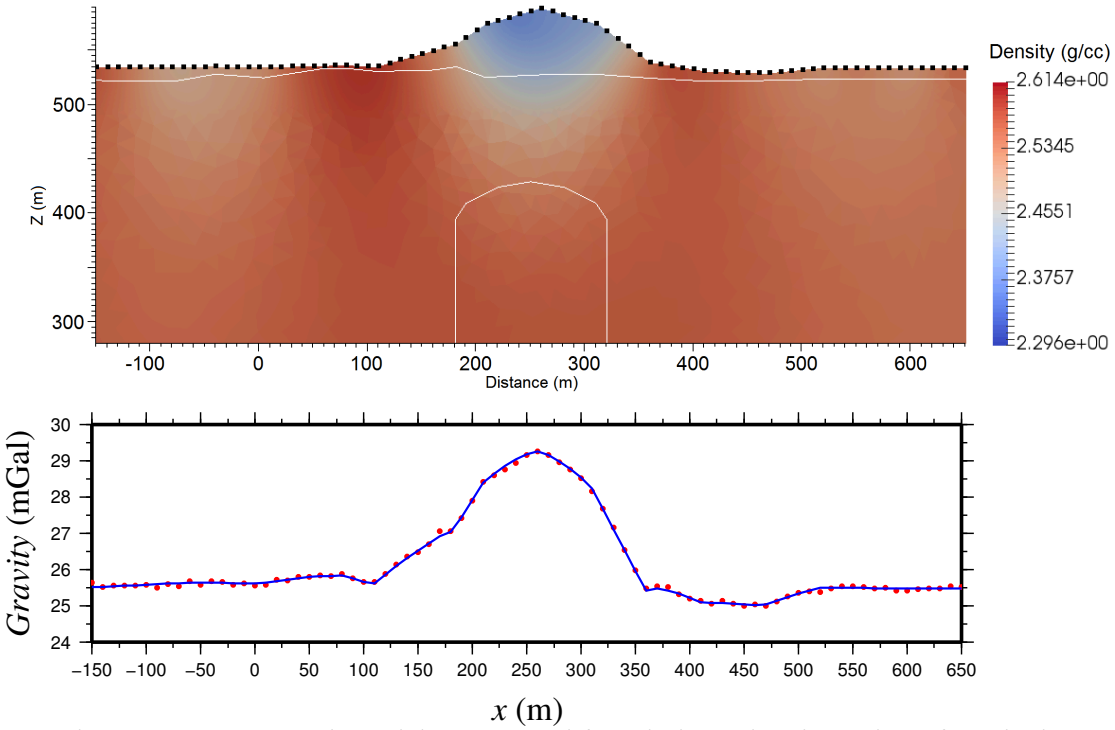


Figure 7.17: Top: Earth model constructed from independent inversion of synthetic gravity data (L2-norm). Bottom: Gravity data for the true model (red) and data calculated from the inversion result (blue).

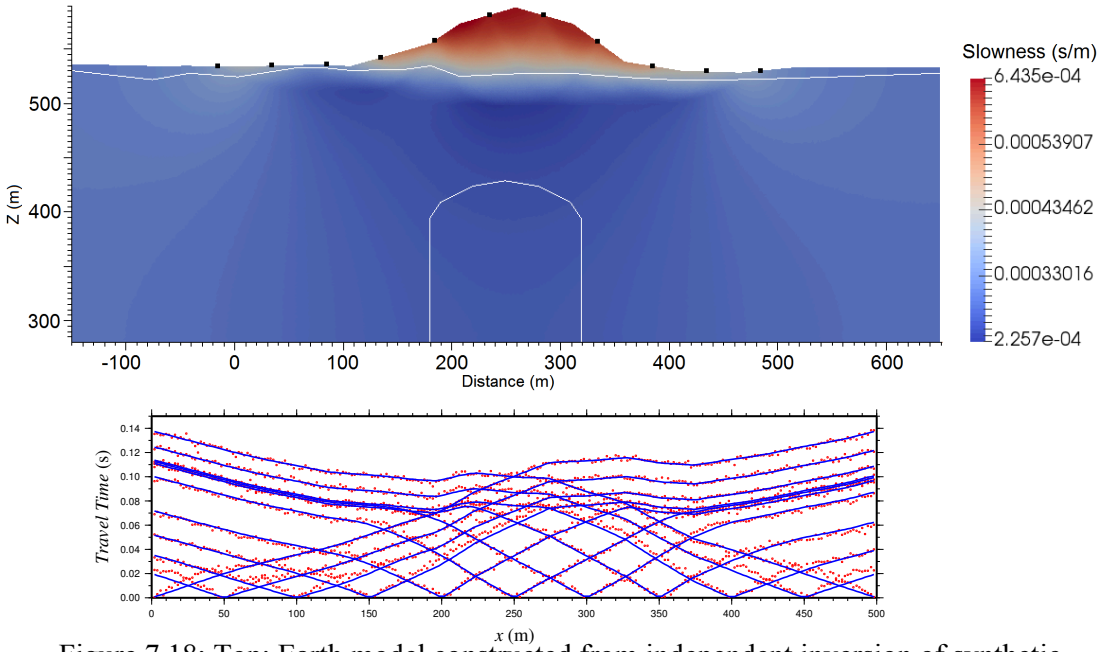


Figure 7.18: Top: Earth model constructed from independent inversion of synthetic seismic data using L2-norm. Bottom: Refraction data for the true model (red) and data calculated from the inversion result (blue).

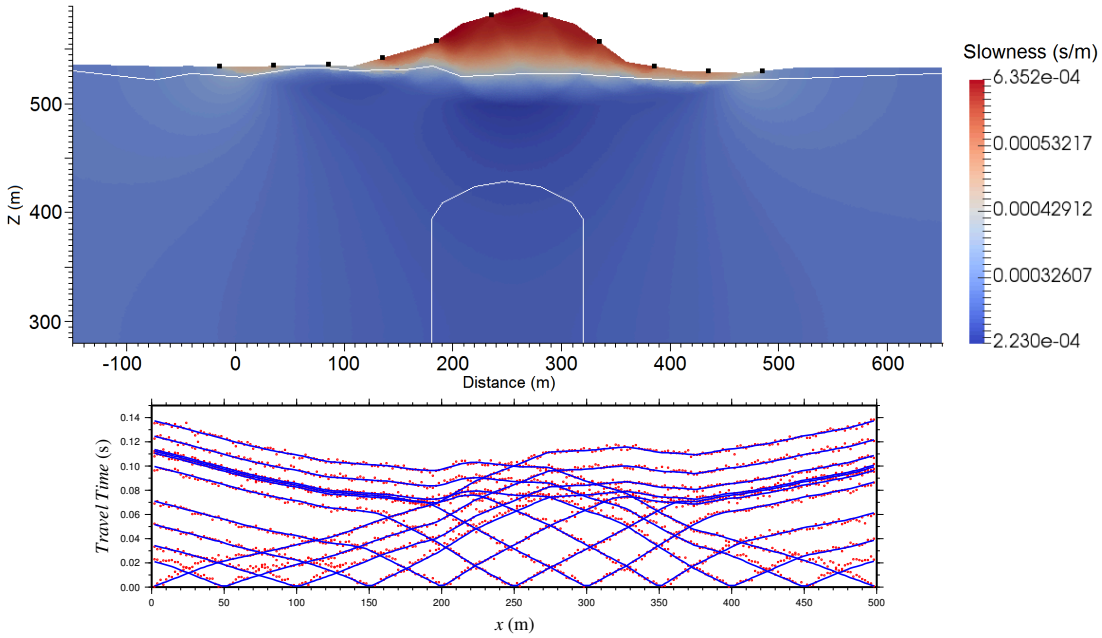


Figure 7.19: Top: Earth model constructed from independent inversion of synthetic seismic data using L1-norm. Bottom: Refraction data for the true model (red) and data calculated from the inversion result (blue).

In order to improve the results, the joint inversion method is used. Figure 7.20 shows the slowness and density models obtained by joint inversion using a coupling factor of $\rho$=1. Two clusters were defined as prior information for the joint inversion, namely, for upper layer: S=0.000625s/m and d=2g/cc; for lower layer: S=0.00025s/m and d=2.42g/cc. However, initially three clusters were considered (alteration zone as the third cluster). This forced the code to generate a third anomaly at depth while there was no signature of alteration zone in the seismic data. This was tested by a model which had no alteration zone but three clusters were considered in the joint inversion. It was seen that an artificial anomaly is constructed in the inversion model for the third cluster (alteration zone). Therefore, in this modelling only two clusters were considered.

81 iterations are done in the "JwP" inversion process in one stage (see Section 4.5). The run-time was around 287 hours. The fit between data is reasonable (Figure 7.21), and the approximate location of the base of the overburden can be clearly seen in Figure 7.20. In comparison to the independent inversion of the gravity and seismic refraction data (Figures 7.17 to 7.19), the density and slowness models are much improved. But, the alteration zone is not yet reconstructed. The variation of the various terms of the objective function (convergence curves) for the joint inversion models are shown in Figure 7.22. Figure 7.23 illustrates the physical properties (slowness versus density) obtained after the joint inversion for the models in Figure 7.20. Physical properties belonging to each cell are indicated by a blue spot (around 468,000 cells). It can be seen that two clusters are made.

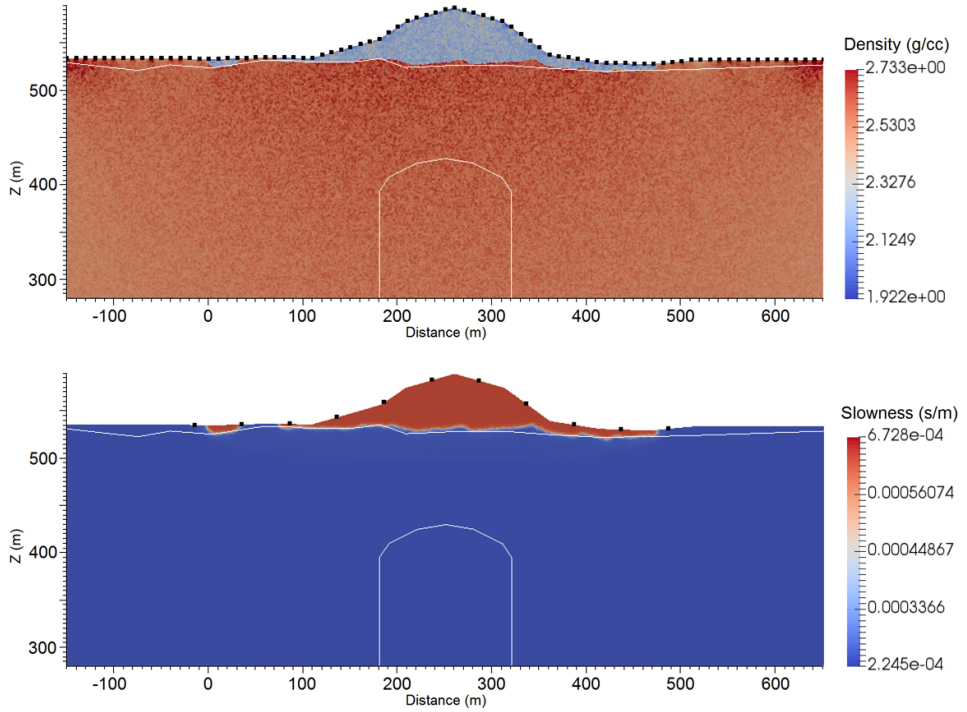


Figure 7.20: Density (top) and slowness (bottom) models constructed from joint inversion of seismic and gravity data (coupling factor $\rho$ =1). Locations of sources are indicated by black squares. White line indicates the glacial sediments-sandstone contact.

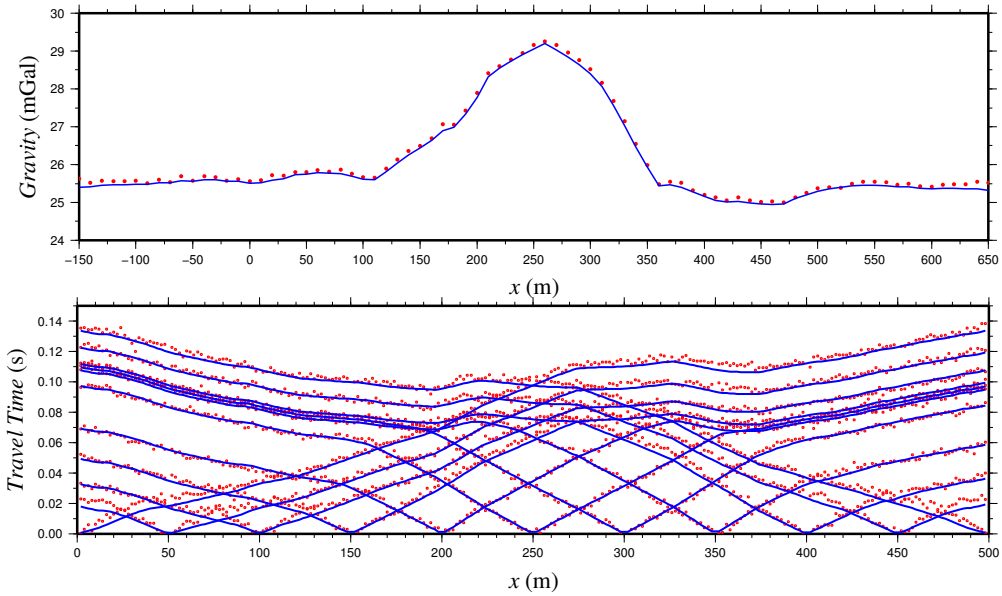


Figure 7.21: Gravity and seismic refraction data for the true model (red) and data for the joint inversion result (blue; $\rho$ =1).

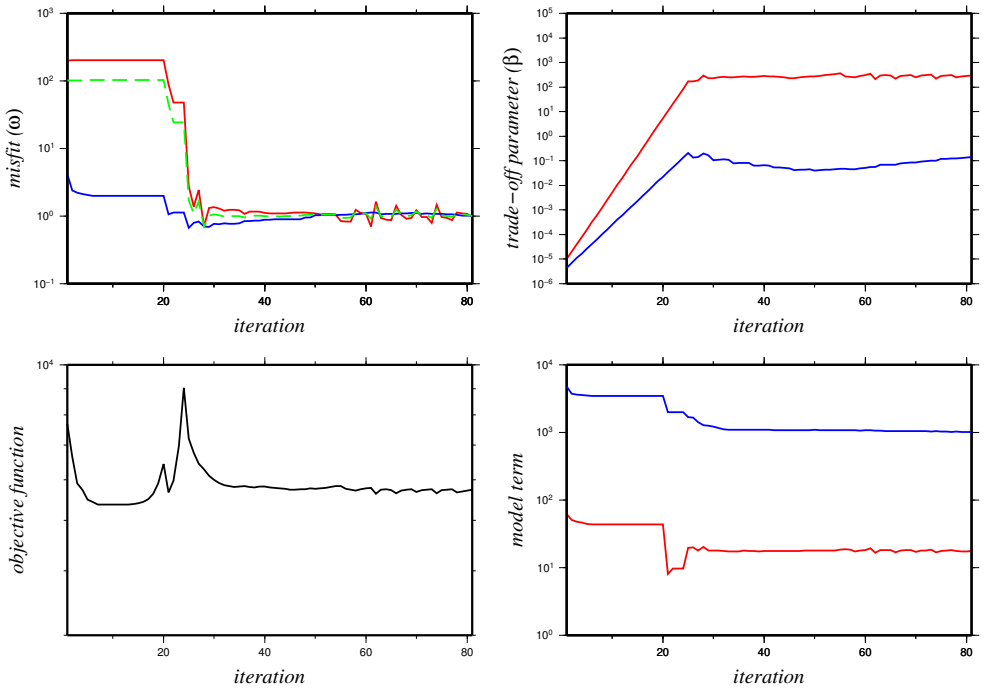


Figure 7.22: Variations of different parts of the objective function such as data misfit ($\omega$; top-left), trade-off parameter ($\beta$; top-right), objective function ($\mathbf{\Phi}$; bottom-left) and model term ($\phi_m$; bottom-right) at iterations for the joint inversion of gravity (red) and seismic refraction (blue) data for $\rho$=1. Green color shows the "average $\omega$" (see Section 4.5). Pre-heating is not used for this joint inversion.

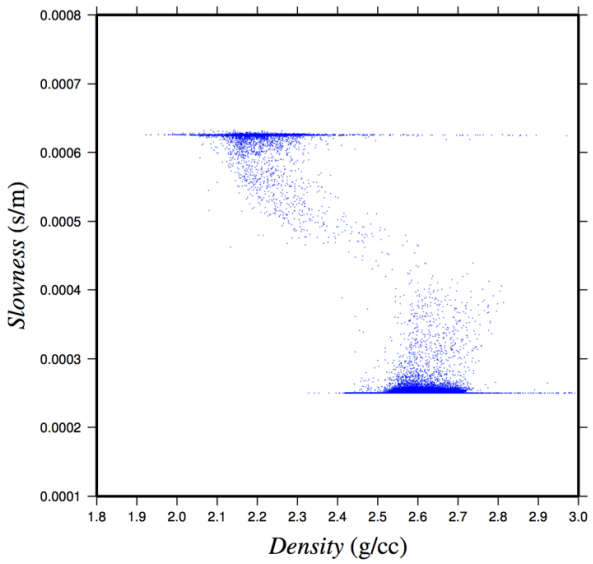


Figure 7.23: Physical properties (slowness versus density) obtained after the joint inversion. Two clusters can be seen which represent the physical properties of overburden (S=0.000625s/m and d=2g/cc) and sandstone (S=0.00025s/m and d=2.42g/cc).

To try to improve the density model at depth, a constrained inversion is performed to compare with the joint inversion (see Section 4.5). For this purpose, the thickness of the overburden structure which is obtained from the joint inversion models (slowness and density) is used as a constraint in an independent gravity inversion. For the constrained inversion, the density of overburden cells (2 g/cc) in the inversion mesh was fixed during the inversion process. This helps the code reconstruct the other geological structures (i.e. alteration zone) below the overburden. Figure 7.24 shows that overburden part has a uniform density, and the alteration zone is made using the constrained independent inversion of gravity data. Alteration zone can be seen in the centre of the model with a small increase in the density between 200m and 300m from the bottom of model to a depth of 400m. This makes sense given how small a contribution it makes to the overall gravity.

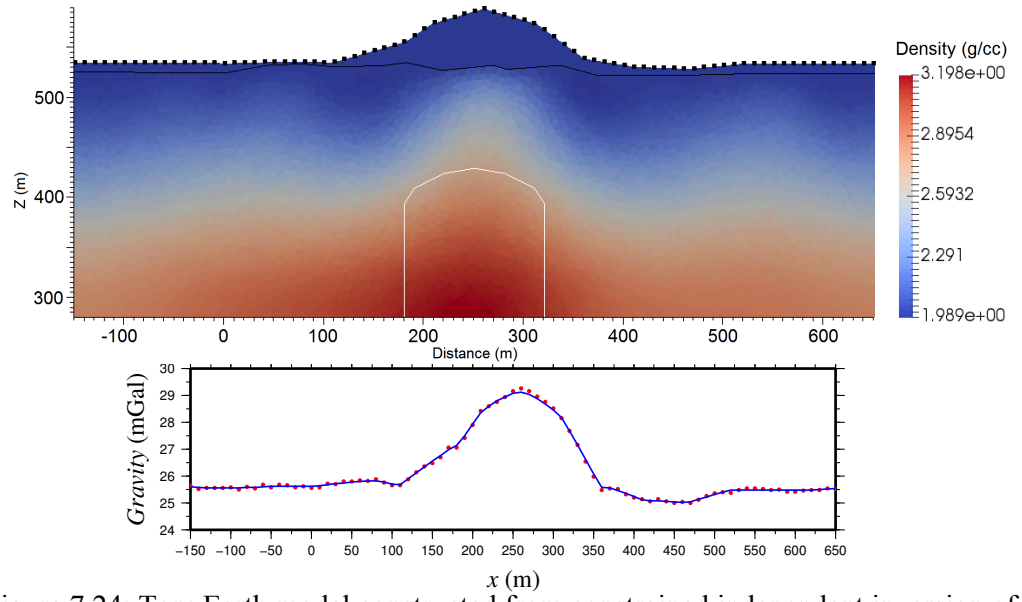


Figure 7.24: Top: Earth model constructed from constrained independent inversion of synthetic gravity data (L2-norm). Black line is the overburden base obtained from joint inversion results used as constraint in the inversion. White line shows the location of the true alteration zone. Bottom: gravity data for the true model (red) and data calculated from the inversion result (blue).

## 7.4 Conclusions

In this chapter, it was shown that the independent inversion of seismic refraction data can be considered one of the best methods for determining the subsurface interfaces while gravity data is poor in this respect. There are many methods to improve the inversion results such as joint and constrained inversions. For this purpose, I initially tested joint inversions for two different coupling factors, and then applied a constrained method on the independent gravity data. For these synthetic modellings, different models relevant to the McArthur area are is generated. The first modelling includes a two-layers model made based on the drill-hole data. Also, a drumlin-shaped model was generated to investigate the effect of topography on the inversions. This model had different scenarios in which the interface between the layers has topography. In addition to a blind layer model, a model was made which include an alteration zone as well. Independent and joint inversions were able to reconstruct the interfaces but not the alteration zone. To try to improve the density model at depth, the constrained inversion was performed on the gravity data. Therefore, I have demonstrated through realistic synthetic examples that the joint inversion of gravity data with seismic refraction data can accurately reconstruct the base of overburden in the joint Earth model, and hence the densities of the overburden and underlying bedrock. Also, the constrained inversion can help to detect the alteration zone at depth. Note that the contribution from the alteration zone in these examples (as in real life) is small, and so it's very ambitious to attempt to try to reconstruct that anomalous density due to the alteration zone (in these examples in particular, as well as in real life). Also, limitations to a real world application (such as station spacing) should be considered as well.

# Chapter 8

# Modelling and Inversion of Magnetic and Gravity Data of the McArthur Area

## 8.1 Introduction

In this chapter, 3D inversion of magnetic and gravity data is performed on both synthetic and real data in order to map overburden thickness as well as the density anomalies from deeper mineralization and basement. For the inversion methods, independent as well as joint and constrained methods will be investigated. For the synthetic modelling, the McArthur area is modelled as the real data cover this area as well. In the Athabasca basin, real gravity and magnetic data are dominated by the variations of topography. Airborne gravity data (Bell Gravity Data; Bell Geospace Limited, 2007; see Section 6.6) as well as airborne magnetic data (Triaxial Magnetic Data; Goldak Airborne Surveys, 2007) are two sets of available data in this project (Figures 8.1 and 8.3).

Bell gravity data, which includes airborne free-air data as well as airborne full tensor gravity gradiometry data (Air-FTG), was acquired over McArthur River, Read Lake and Rabbit Lake areas in the Athabasca Basin by Bell Geospace Limited for Cameco

Corporation in 2007. The data was acquired using the FTG system which is installed in an aircraft. Data contain around 88,700 stations in a total 6568 line kilometres of data, while the station spacing and the profile spacing are around 50 m and 300 m, respectively. A radar altimeter system is deployed to measure the distance between the airplane and the ground. Along with the plane's altitude acquired via GPS, radar altimetry data can be used to produce a digital elevation model (DEM). The free-air data used in this research, was the computed free-air gravity response from vertical integration of the vertical gravity gradient ($G_{zz}$; see Appendix D) anomaly field. All data were de-noised and corrected by Bell Geospace Limited (Bell Geospace Limited, 2007).

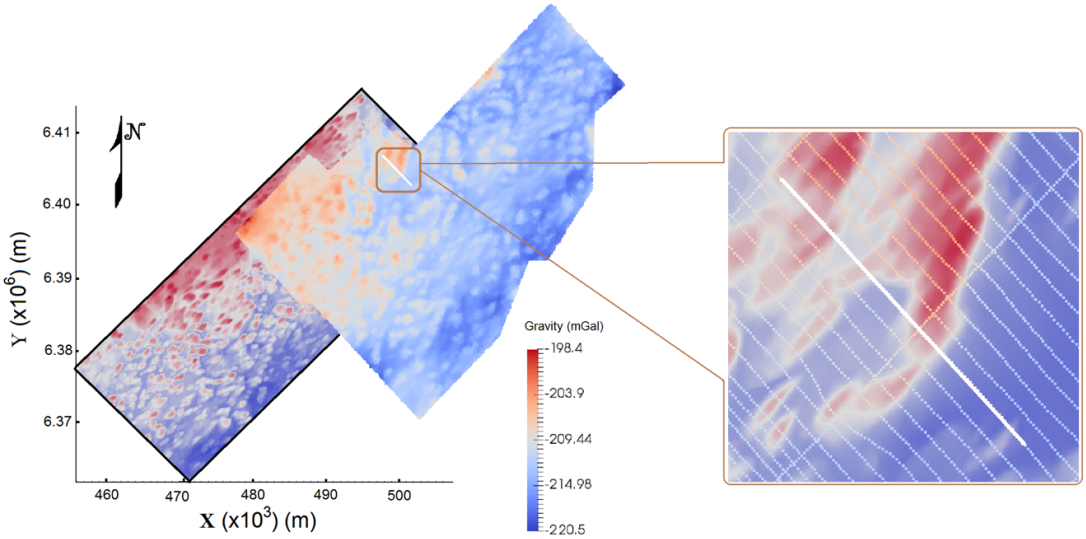


Figure 8.1: Topography of McArthur-Millennium corridor (in the black frame) as well as Bell free-air gravity data (over the north part of area). Inset shows McArthur area (5x5km) as well as gravity profiles (coloured lines) and selected survey line (white line).

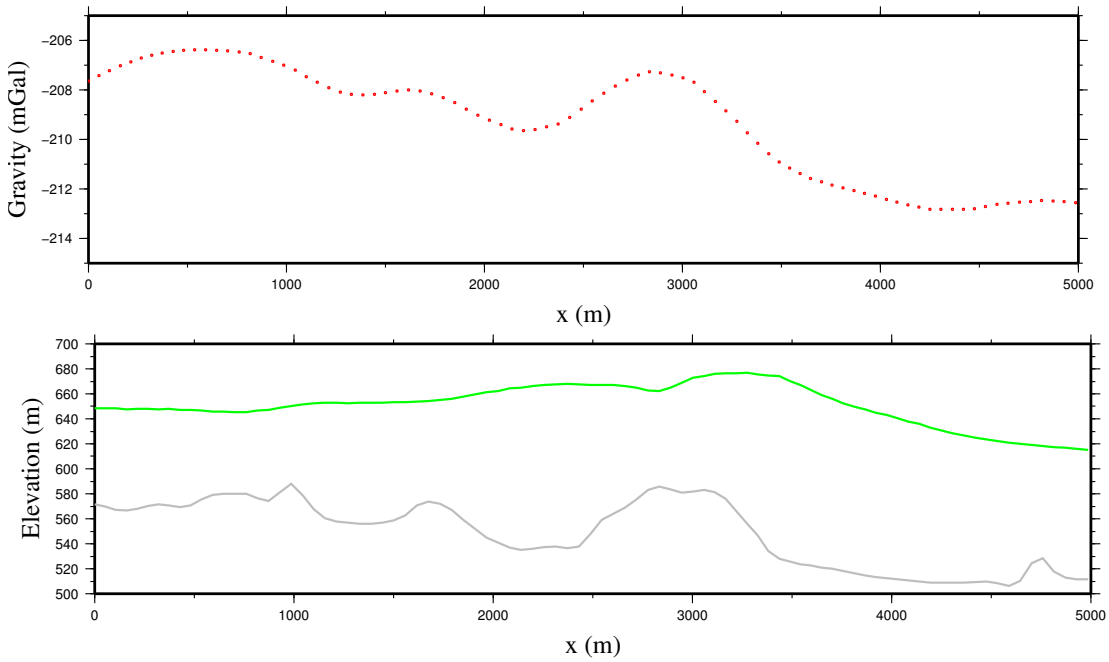


Figure 8.2: Top: gravity data (free-air) along the selected survey line. Bottom: topography under the selected survey line (grey), and airborne flight height (green).

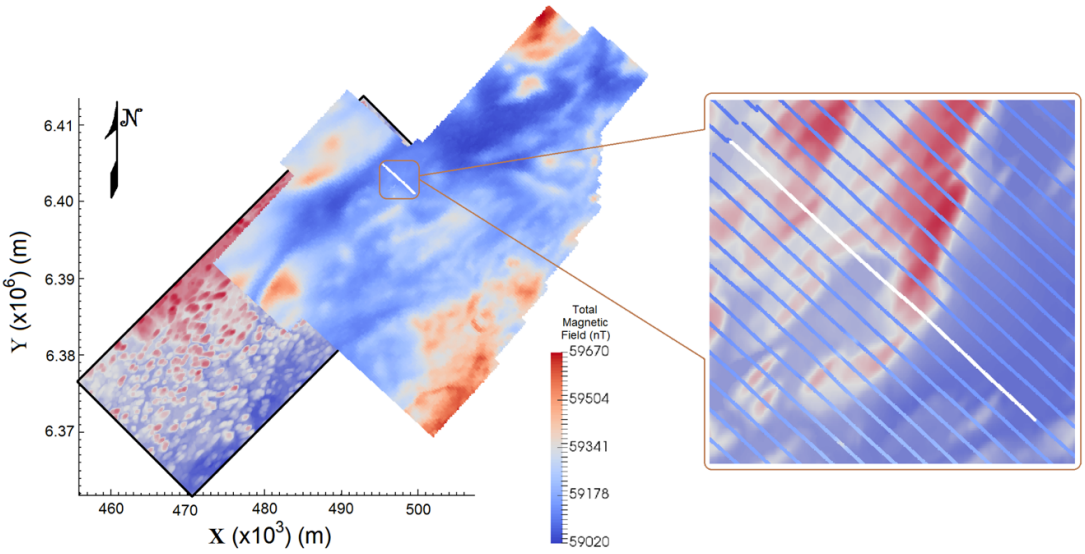


Figure 8.3: Topography of McArthur-Millennium corridor (in the black frame) as well as Triaxial magnetic data (over the north part of area). Inset shows McArthur area (5x5km) as well as magnetic profiles (parallel blue lines) and selected survey line (white line).

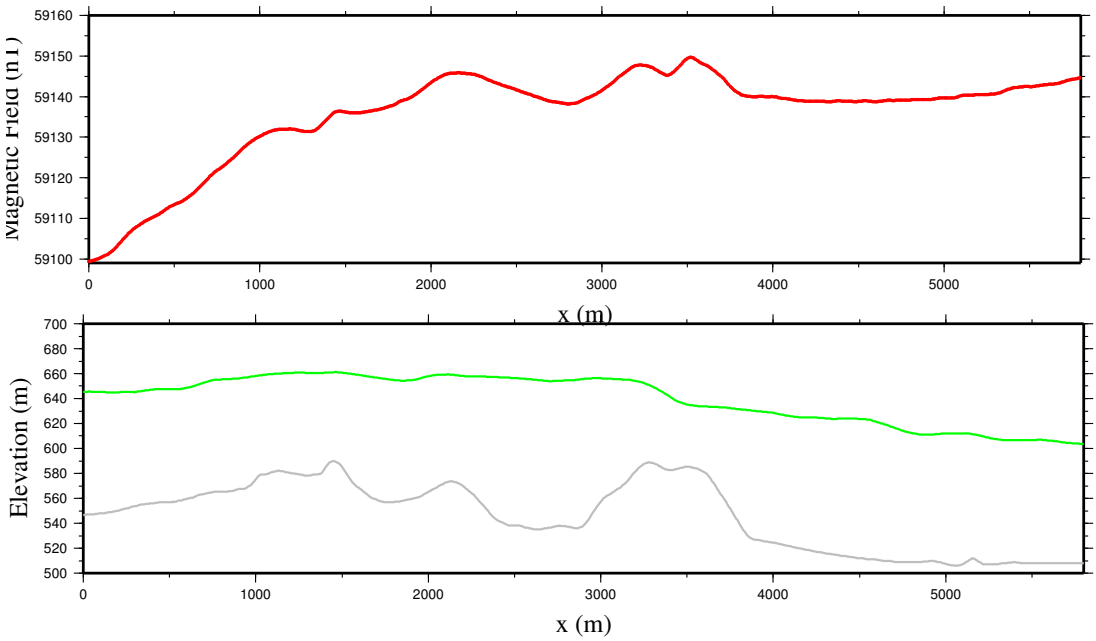


Figure 8.4: Top: total magnetic field strength along a selected survey line. Bottom: topography under the selected survey line (grey), and airborne flight height (green).

Triaxial magnetic data, which includes airborne total magnetic intensity data as well as airborne magnetic gradiometry data (derivative of the field in the three directions), was acquired (and was corrected) over McArthur River and Read Lake in the Athabasca Basin by Goldak Airborne Surveys (Goldak) on behalf of the Cameco Corporation in a total of 5433 line kilometers in March 2007. The data was acquired using Geometrics G-822A optically pumped cesium vapour magnetometer with a sensitivity of 0.005 nT which was installed in an aircraft. Also, for acquiring the diurnal variations, GEM Systems GSM19W proton precession magnetometer with a GPS time base was used as the magnetic base station. Two radar altimeters as well as a GPS system were also installed in the aircraft. Triaxial magnetic data has around 676,500 stations, and the station spacing and the profile spacing are around 7 m and 300 m, respectively. During data acquisition, geomagnetic field

strength in McArthur area was 59500nT, and geomagnetic field declination and inclination were around 12 and 80 degrees, respectively. The magnetic noise did not exceed 1 nT over a distance of 3000 m (Goldak Airborne Surveys, 2007). Parts of survey lines for both magnetic and gravity data are plotted in Figures 8.2 and 8.4. By comparing the variation in data and the topography under the survey lines, the topography signature on the data can clearly be seen.

## 8.2 3D synthetic modelling and inversion

In this section, gravity and magnetic data are synthesized for the McArthur area over a 3D model along a number of profiles (Figures 8.5 to 8.7). The McArthur area was chosen for the modelling as there is plenty of geological, geophysical and physical property data for this area (see Chapter 2). The model is the one based on the work of Wood and Thomas (2007; see Section 3.6) which was first described in Section 5.4. For the basement, different units of granitoid and gneiss rocks are considered (Figure 8.5). The basement is now very relevant to these large magnetic and gravity data-sets unlike the seismic and gravity data-sets considered in Chapter 7. Independent, joint and constrained inversions were performed in order to reconstruct density and susceptibility models. Physical property data as well as drill-hole data were used as constraints in the inversions (see Section 2.5).

405 airborne observation locations at a fixed elevation above sea level of 650m are used for gravity data along 5 profiles with station spacing and profile spacing of 50m and 300m, respectively. The same stations are used for magnetic data. These survey specifications are based on those for the real data-sets (see Section 8.1). In the magnetic modelling (the same

as for the real data), geomagnetic field strength, declination and inclination were considered to be 59500nT, 12 degrees and 80 degrees, respectively.

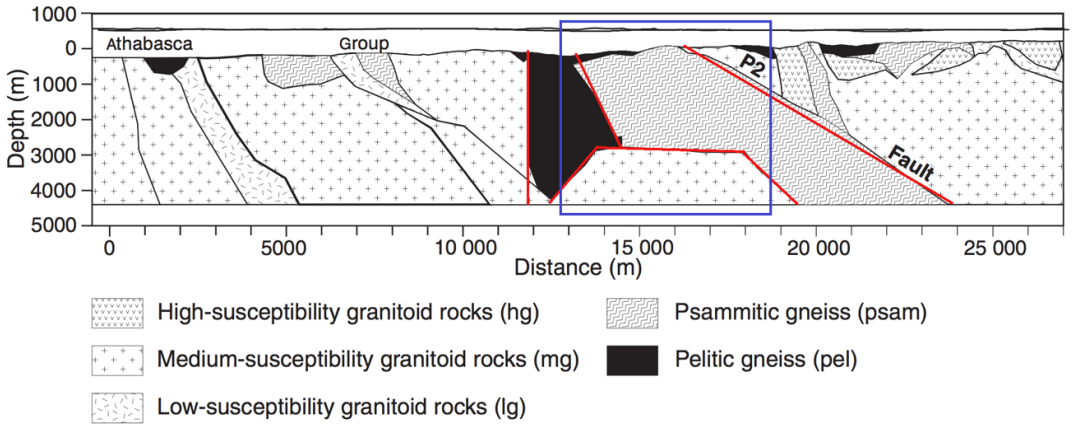


Figure 8.5: McArthur geological section (Thomas and Wood, 2007). Blue square shows the part which forms the basis of the models considered in this research. Red lines show the modeled interfaces between the blocks. Small zones and variations are ignored in the modelling.

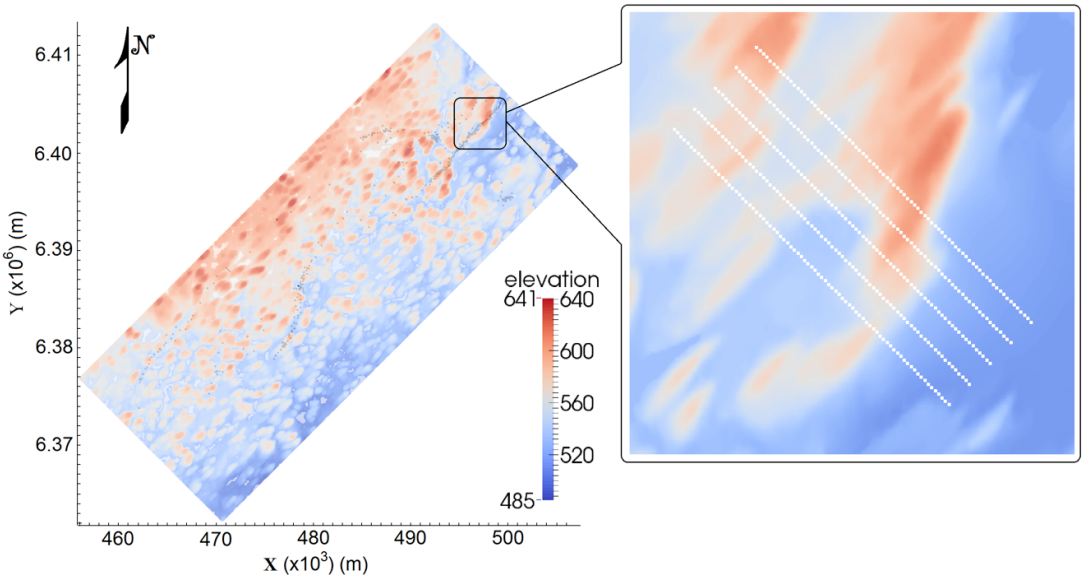


Figure 8.6: Topography of McArthur-Millennium corridor. Inset shows location of survey lines over the (modelled) McArthur area.

The gravity model with the densities of the various geological units is shown in Figure 8.7. The images shown here of the 3D models in this research show the central 5 by 5 km (Figure 8.6). The actual 3D models used for the computations had a size of 500 by 500 km in order to avoid any effect of the edges on the gravity data. The average total thickness of these models was 4850 m.

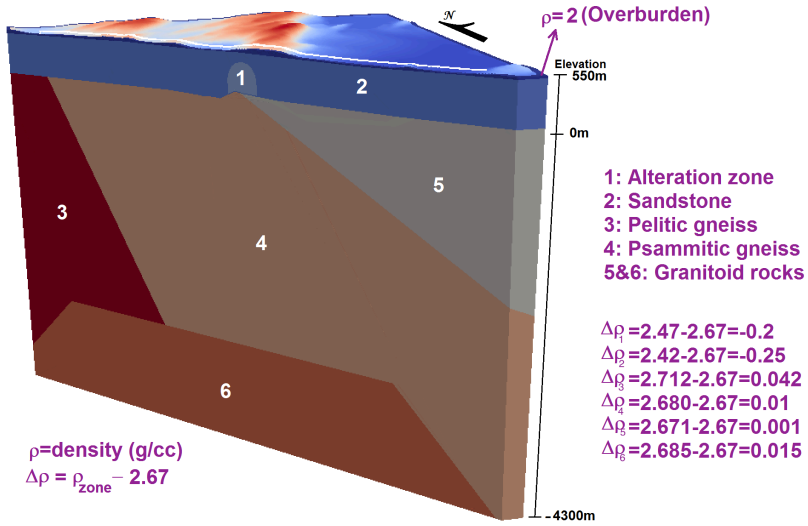


Figure 8.7: Density model including different geological structures based on Wood and Thomas (2007). Basement blocks are adapted from Figure 8.5.

In this model, a cylinder anomaly is considered as an alteration body. Free-air gravity data were computed. As mentioned in Section 5.4, considering the interface between the overburden and sandstone as the reference ellipsoid can be an acceptable choice. The layers (or structures) above the reference ellipsoid have real densities in the model while the layers (or structures) below the reference ellipsoid have relative density. The relative densities are with respect to 2.67 g/cc. Therefore, the overburden has a real density of 2 g/cc whereas the lower layers have a relative density. Figure 8.8 shows the synthetized free-air gravity for the survey lines considered here. This figure also shows the topography, and it is clear

that the free-air data are predominantly affected by the topography.

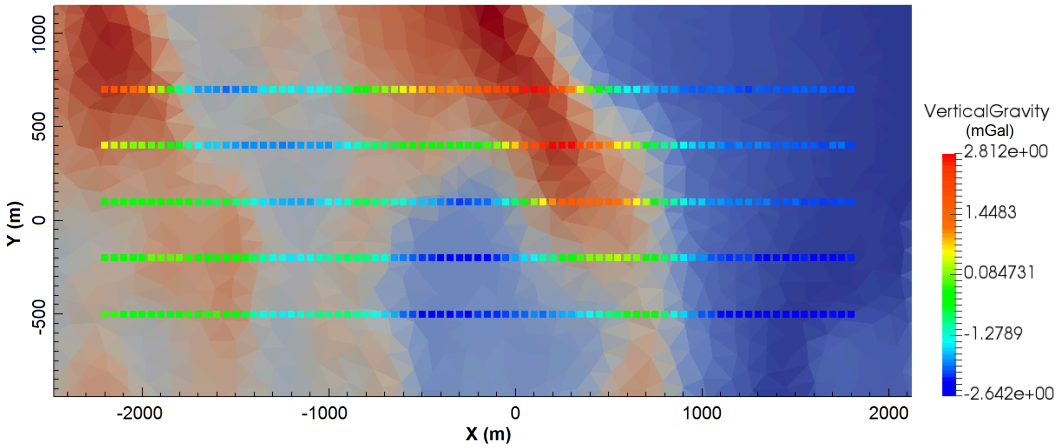


Figure 8.8: Gravity free-air data along the airborne survey lines after adding 1% noise. Number of stations: 405.

The magnetic model with magnetic susceptibilities of the various geological units is shown in Figure 8.9. Magnetic data were computed along the same airborne survey lines used for the gravity modelling. The images of the 3D magnetic models in this research show the central 5 by 5 km. The magnetic susceptibility of the sandstone is approximately zero, so it is expected that the overburden and its variable thickness will strongly influence the magnetic data. Thomas and Wood (2007) considered the overburden as non-magnetic, but I assigned a value of $5\times10^{-3}$ SI for the magnetic susceptibility of overburden based on the CMIC-Footprints database (see Section 2.5.3). Figure 8.10 shows the synthetized magnetic data. Similar to the gravity data, the magnetic data is strongly dominated by variations of topography. Units on the right side of the P2 fault (body #5 in Figure 8.9) have higher magnetic susceptibility values than those on the left side of the P2 fault (bodies #3 and #4 in Figure 8.9). The signature of this difference can be clearly seen in the right sides of the magnetic profiles where the magnetic data is significantly increased. The real

magnetic and gravity data shown in Figures 8.2 and 8.4 demonstrate that the data is not too noisy. Therefore, using a code of Lelièvre and Farquharson (2015), a Gaussian random noise of standard deviation equal in magnitude to 1% of a datum is added to both synthetized gravity and magnetic data.

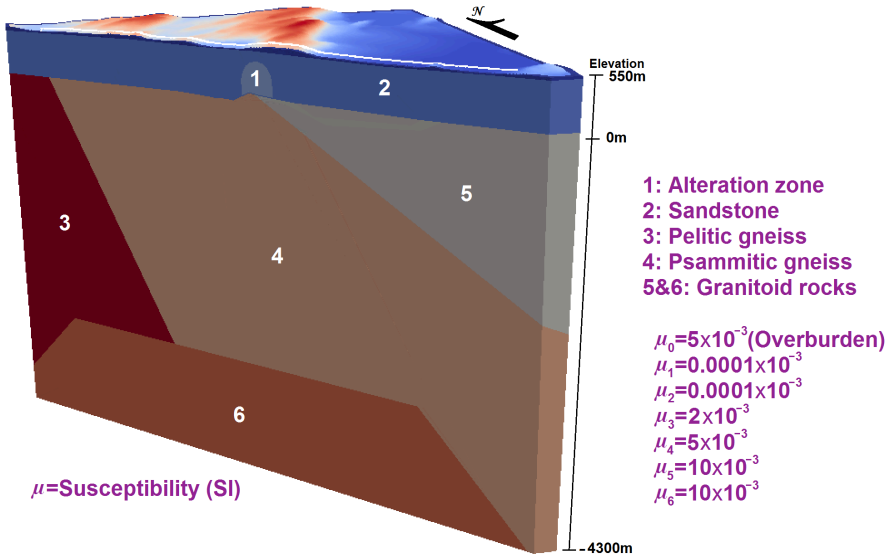


Figure 8.9: 3D magnetic susceptibility model including different geological structures based on Wood and Thomas (2007). Basement blocks are adapted from Figure 8.5.

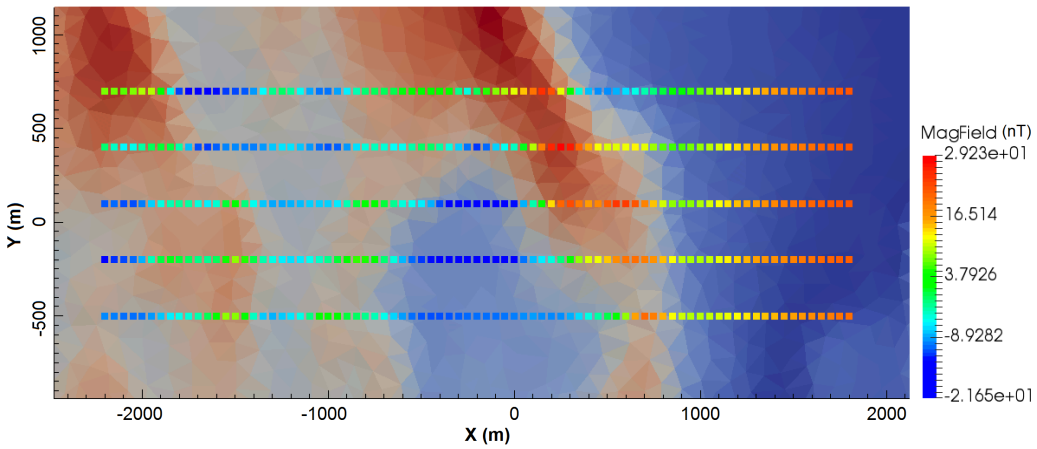


Figure 8.10: Total magnetic intensity along the airborne survey lines after adding 1% noise. Geomagnetic field strength: 59500nT; geomagnetic field declination: 12 degrees; geomagnetic field inclination: 80 degrees; Number of stations: 405.

### 8.2.1 3D independent inversions of synthetic gravity and magnetic data

3D inversions are performed on the synthetized airborne gravity and magnetic data on a mesh shown in Figure 8.11. The smallest tetrahedral cells which are located at the surface have a small edge size of 30 m. As depth increases, the cell size increases. For the data misfit of inversions in this chapter, the value of $\omega$ reached 1 while a value of 0.05 is considered for the *chifact* (see Section 4.5). This means that a desirable fit is obtained. For the distance weighting, a value of 1.0 is assigned for $w_z$ and $w_p$. Also, no reference model was considered in the inversions except in the constrained inversions.

As mentioned, independent inversions were considered first, and then constrained inversions. Finally, the joint inversion was investigated as well as constrained joint inversion. Figures 8.11 and 8.12 show the block used for the inversions as well as the independent inversion results for magnetic and gravity data, respectively. The views of these models are the same as the view of the true model in Figure 8.7 (or 8.9). The mesh used for the independent inversions had about 28,000 tetrahedral cells. The normalized data residuals in Figure 8.13 show there is a good fit between the observed and calculated data.

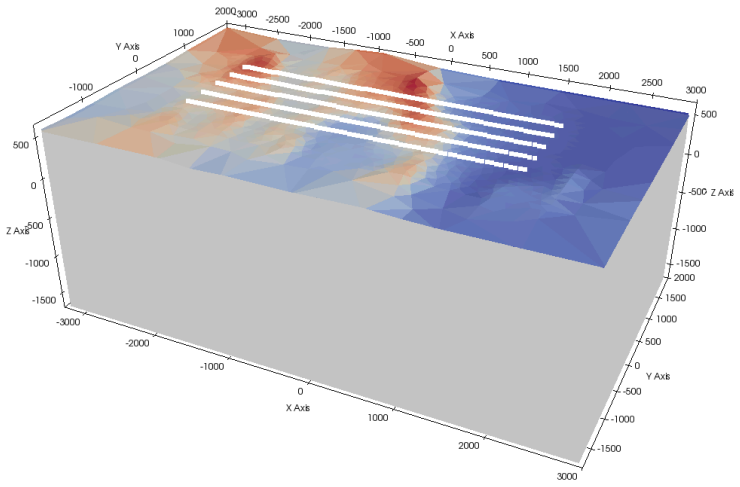


Figure 8.11: Block (rectangular cube ~6×4×2km) with tetrahedral cells used in the inversions. The topography of McArthur area can be seen on the surface as well as the airborne survey lines (white lines).

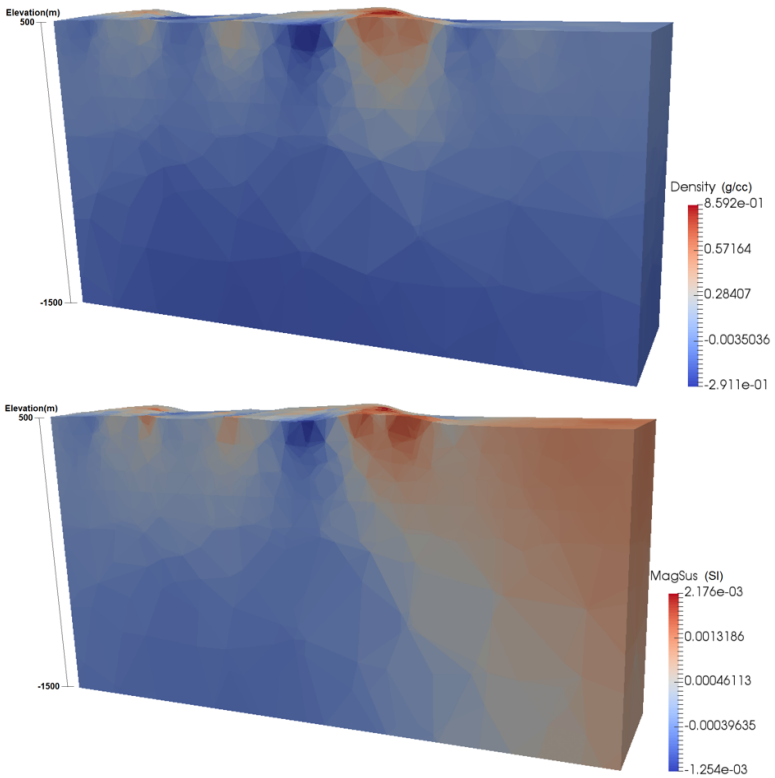


Figure 8.12: Vertical sections of independent gravity (top) and magnetic (bottom) inversion models.

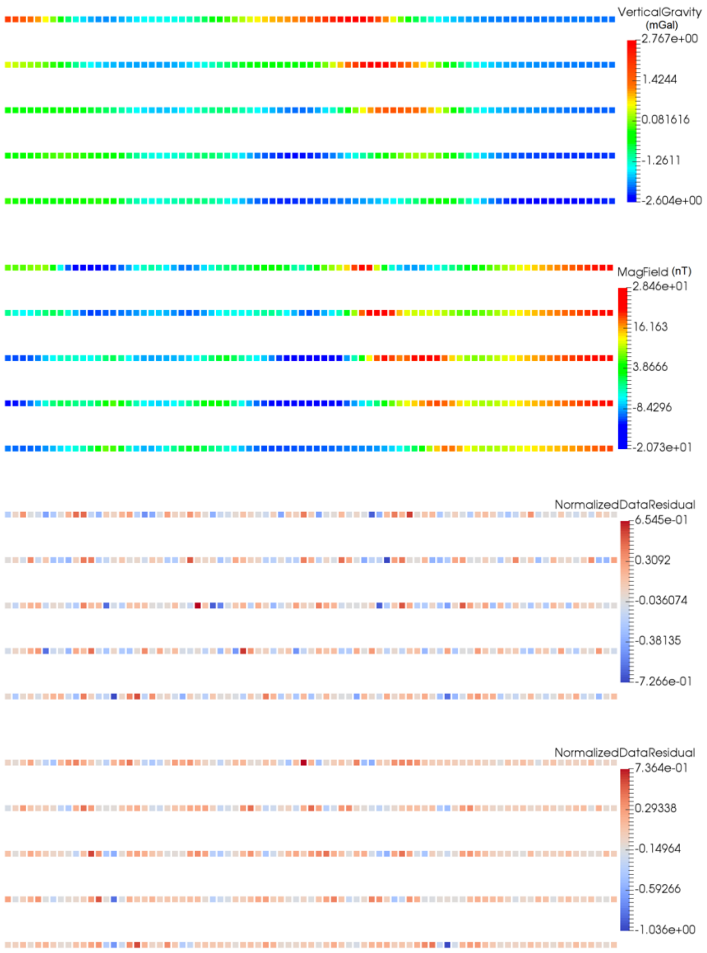


Figure 8.13: From top to bottom: gravity data calculated by the density model constructed by the independent inversion; magnetic data calculated by the susceptibility model constructed by the independent magnetic inversion; normalized data residual for the gravity model; normalized data residual for the magnetic model.

It can be seen that the independent inversions of gravity and magnetic data are not able to construct the true interfaces and geological blocks and layers properly. A reason for the poorness of these results is because of the poor inherent/intrinsic resolution and nonuniqueness of both gravity and magnetic data. Without any other information, there inversion does not really know where to put the density and susceptibility, especially when it should to construct absolute densities above the reference level and relative values below.

Since independent unconstrained inversions are very poor, I move on here to consider constrained inversion. For this purpose, physical property data as well as depth information are used as constraints in the inversions, and for this purpose, a reference model was developed to include 4 layers. From top to bottom these are:

1- A layer that we are confident is all overburden from surface to an elevation above sea level of around 500 m that has fixed physical properties during the inversion process, e.g. here a density value of 2 g/cc and a magnetic susceptibility of $5\times10^{-3}$ SI.

2- A layer that we are unsure of but is either overburden or sandstone from an elevation of 500 m above see level to 450 m. So, for the physical properties a wide range of values is considered as constraint (as lower and upper bounds).

3- A layer that we are confident is all sandstone from an elevation of 450 m to 50 m that has fixed physical properties during the inversion process, e.g. here a relative density value of -0.25 g/cc and a magnetic susceptibility of 0 SI.

4- A layer from 50m to the bottom of the model that we are unsure of but is either sandstone or basement. So, for the physical properties a wide range of values is considered as constraint (as lower and upper bounds).

The mesh used for the constrained independent inversions had about 533,000 tetrahedral cells. The results in Figure 8.14 show the constrained independent inversions for magnetic and gravity models. The constrained independent inversion results are better than the independent inversion results, especially the magnetic model in which the basement shows

the location of the P2 fault rather well. However, they are nevertheless not good reproductions of the true model and not reliable. For example, the basement in the gravity model has a pattern suspiciously similar to the variations of the overburden thickness. Figure 8.15 (top) shows the shallow part of the model for the constrained magnetic inversion. The four layers are shown clearly in this figure. The red layer at the top and the blue layer in the middle are layers that we are confident are all overburden and sandstone, respectively (with fixed physical properties during the inversion process). Constrained results seem interesting, but the truth is that the constructed anomalies in the basement have the same pattern of the overburden variations as can be seen in Figure 8.15 (bottom) in comparison with Figure 8.12. Figure 8.16 shows there is a good fit between the observed and calculated data.

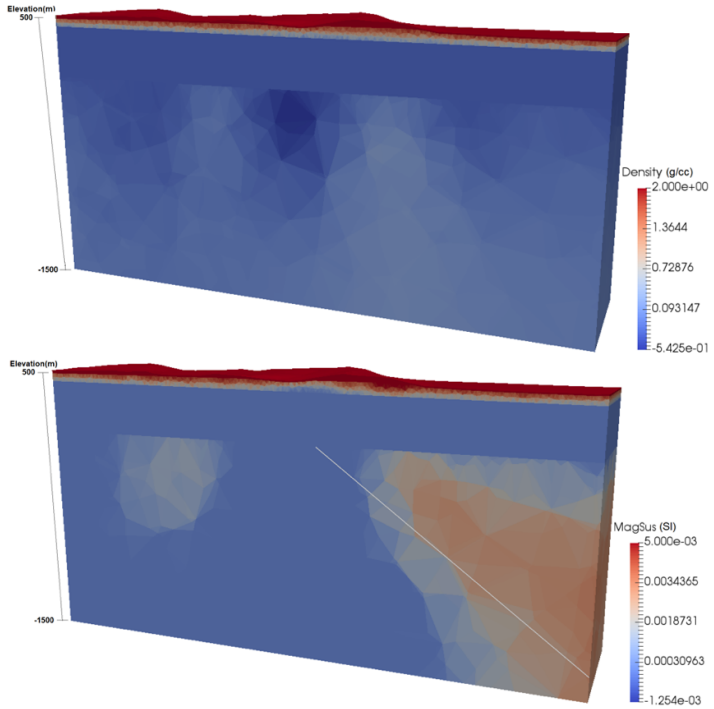


Figure 8.14: Vertical section of constrained independent gravity (top) and magnetic (bottom) inversion models. White line shows the approximate location of the P2 fault.

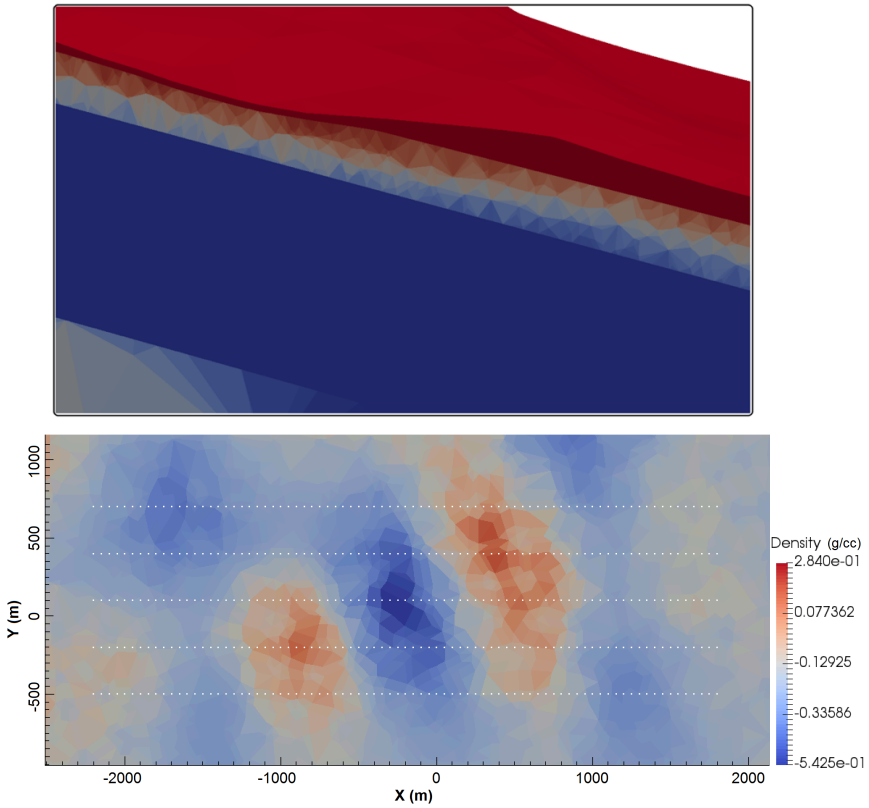


Figure 8.15: Top: a zoom-in on the magnetic section displayed in Figure 8.14 close to the surface. Bottom: a horizontal section of the gravity model at elevation -50 m under the survey lines. White dots show the survey lines.

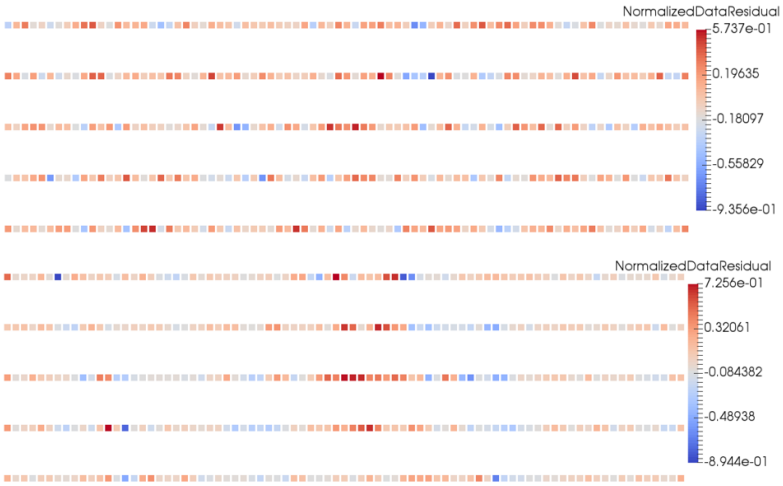


Figure 8.16: Top: normalized data residual for the gravity model. Bottom: normalized data residual for the magnetic model (for constrained independent inversions).

### 8.2.2 3D joint inversion of synthetic gravity and magnetic data

In order to improve the inversion results, joint inversion of gravity and magnetic data using different coupling factors is investigated. Since the results related to different coupling factors were good, the results belonging to $\rho$=10 and $\rho$=1.0E+5 are shown as representing a small value and a large value. For this purpose, two different methods for coupling are used: the correlation method and the clustering fuzzy c-mean method (see Section 4.5). The mesh used for the joint inversions (except constrained) had about 28,000 tetrahedral cells. The JwP is used for all the joint inversions in this chapter, and one stage is used for heating the coupling factor (see Section 4.5). For the joint inversions in this chapter, a value of 700 is considered for the initial value of trade-off parameter. This value was obtained as the final trade-off parameter from a few test runs with an initial trade-off parameter of 1.0. Therefore, the trade-off parameter value rather than going up (see Section 4.5) in the iterations starting from a small value to reach an appropriate value, it oscillates around 700 to find the best value. This can help not only to reduce the number of iterations as well as the run-time but to improve the results. Figures 6.18 and 6.19 show the joint inversion results for the correlation method for the two coupling factors of $\rho$=10 and $\rho$=1.0E+5. A higher coupling factor causes a greater similarity between the gravity and magnetic inversion models (not at the expense of the fit between calculated and observed data), but it increases the run-time as well. The run-times for the joint inversions (correlation method) of $\rho$=10 and $\rho$=1.0E+5 is 1 hour and 27 minutes for 13 iterations and 3 hour and 53 minutes for 38 iterations, respectively. For the results shown in Figures 8.17 and 8.21, the normalized data residuals shown in Figures 8.18 and 8.22 show there is a good fit between

the observed and calculated data. Also, Figures 8.19 and 8.23 show the cross plot of densities and magnetic susceptibilities constructed using the joint inversion. The variations of the various terms of the objective function for the joint inversion model are shown in Figures 8.20 and 8.24.

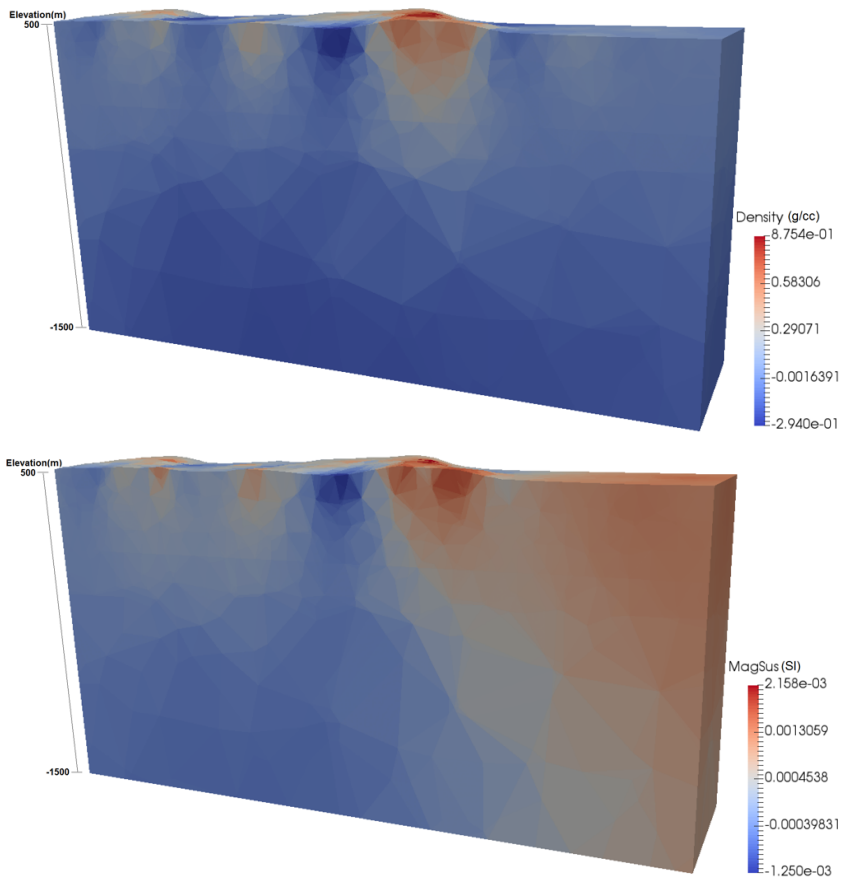


Figure 8.17: Vertical sections of the joint inversion models of gravity (top) and magnetic (bottom) data using correlation method for $\rho$=10.

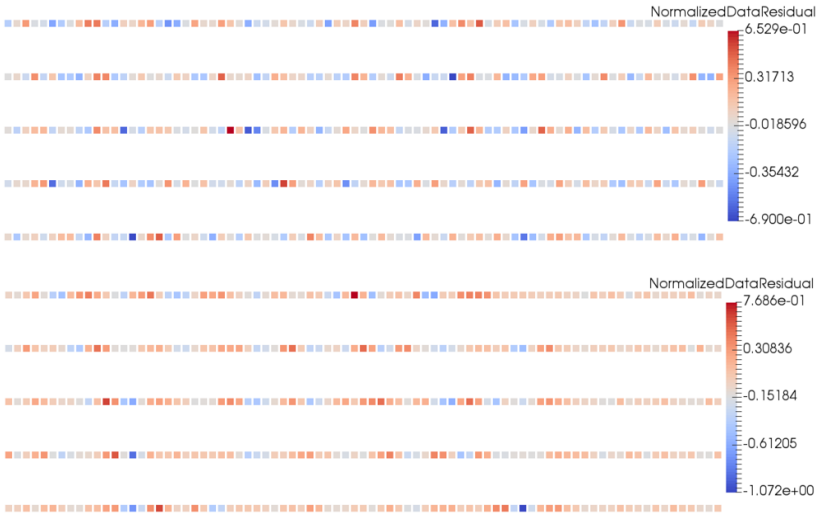


Figure 8.18: Top: normalized data residual for the gravity model. Bottom: normalized data residual for the magnetic model (correlation method for $\rho$=10).

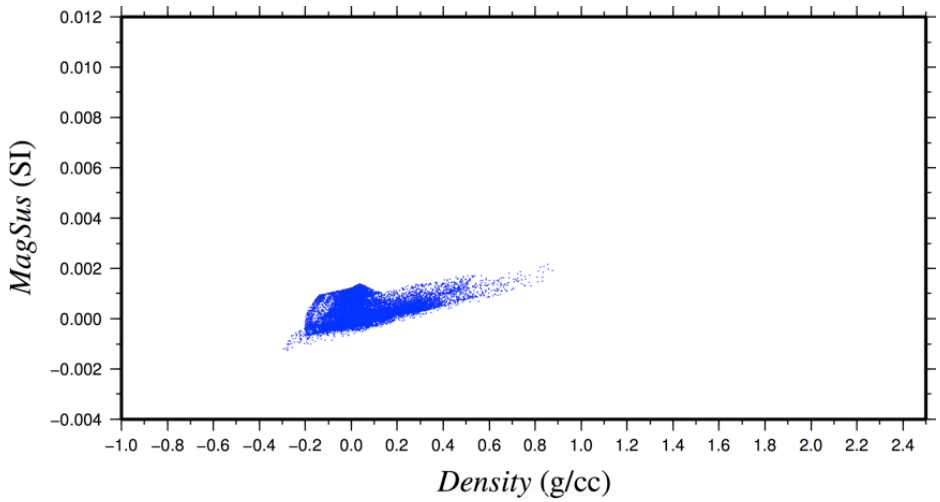


Figure 8.19: Physical properties (magnetic susceptibility versus density) obtained after the joint inversion using the correlation method for $\rho$=10. Each blue dot corresponds to a cell in the inversion mesh.

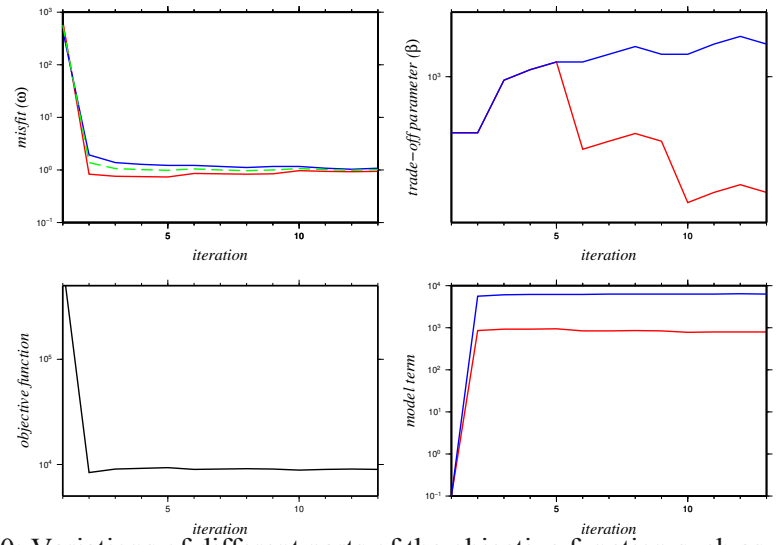


Figure 8.20: Variations of different parts of the objective function such as data misfit ($\omega$; top-left), trade-off parameter ($\beta$; top-right), objective function ($\mathbf{\Phi}$; bottom-left) and model term ($\phi_m$; bottom-right) at iterations for the joint inversion of gravity (red) and magnetic (blue) data using the correlation method for $\rho$=10. Green color shows the "average $\omega$" (see Section 4.5).

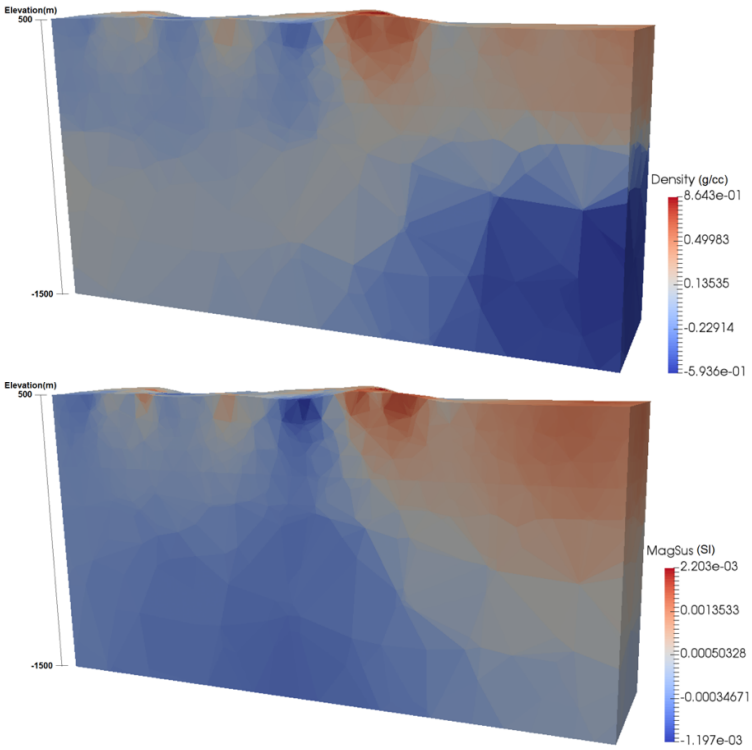


Figure 8.21: Vertical sections of the joint inversion models of gravity (top) and magnetic (bottom) data using correlation method for $\rho$=1.0E+5.

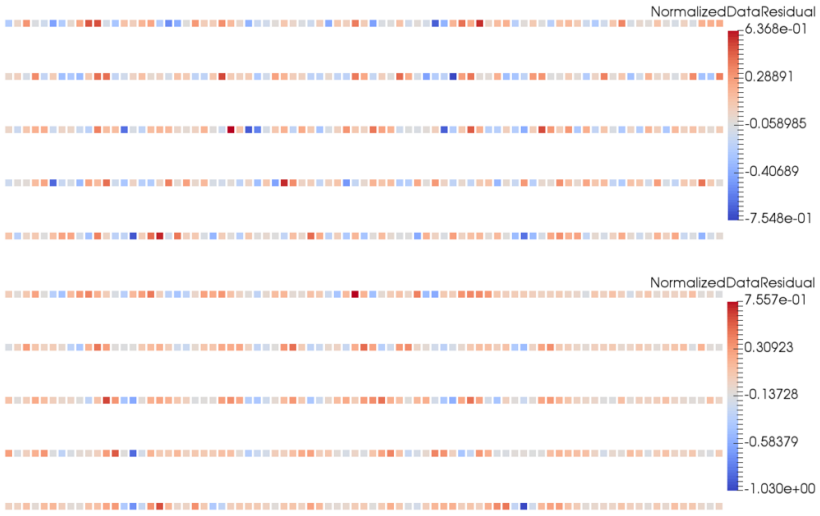


Figure 8.22: Top: normalized data residual for the gravity model. Bottom: normalized data residual for the magnetic model (correlation method for $\rho$=1.0E+5).

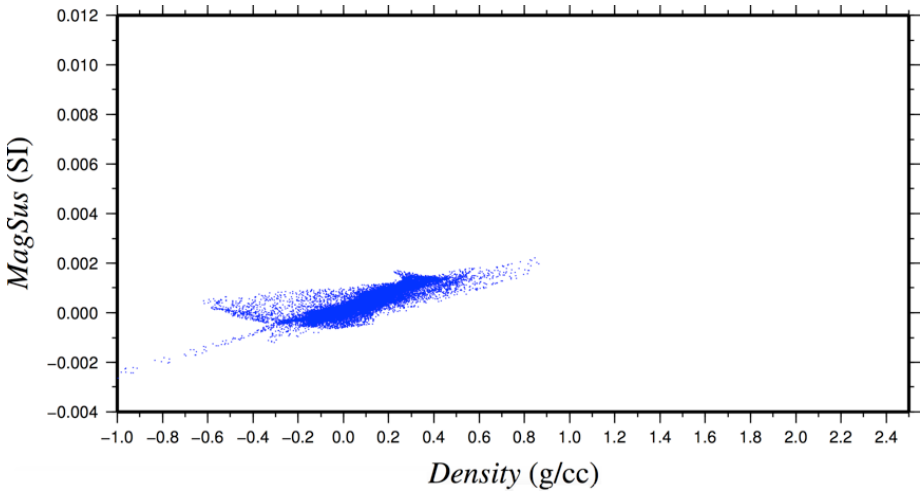


Figure 8.23: Physical properties (magnetic susceptibility versus density) obtained after the joint inversion using the correlation method for $\rho$=1.0E+5. Each blue dot corresponds to a cell in the inversion mesh.

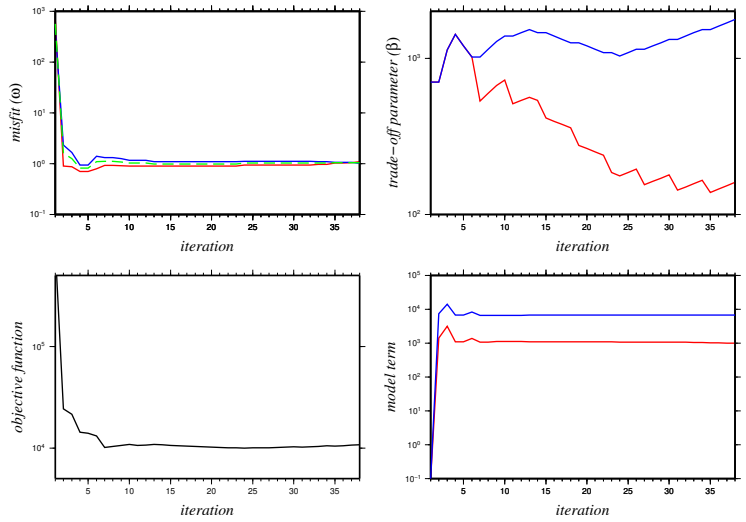


Figure 8.24: Variations of different parts of the objective function such as data misfit ($\omega$; top-left), trade-off parameter ($\beta$; top-right), objective function ($\mathbf{\Phi}$; bottom-left) and model term ($\phi_m$; bottom-right) at iterations for the joint inversion of gravity (red) and magnetic (blue) data using the correlation method for $\rho$=1.0E+5. Green color shows the average "$\omega$".

Joint inversion results from the correlation method do not show good results. In order to improve the inversion results the clustering method is used, for two scenarios: two clusters and three clusters. For the three cluster case I define three different clusters with average physical properties corresponding to the three main geological structures: overburden (density=2 g/cc; MagSus: $4\times10^{-3}$SI), sandstone (relative density=-0.25 g/cc; MagSus: 0SI) and basement (relative density=0.0 g/cc; MagSus: $5\times10^{-3}$SI). For the two cluster case I omit the basement. Figures 8.25 to 8.28 show joint inversion results for a 2 cluster case with a coupling factor of 10, the normalized data residuals, the cross plot of the physical properties (magnetic susceptibility versus density) obtained after the joint inversion, and the variation of the various terms of the objective function, respectively. The constructed model shows much improvement over those from the independent inversions. The run-time was 1 hour and 57 minutes for 13 iterations.

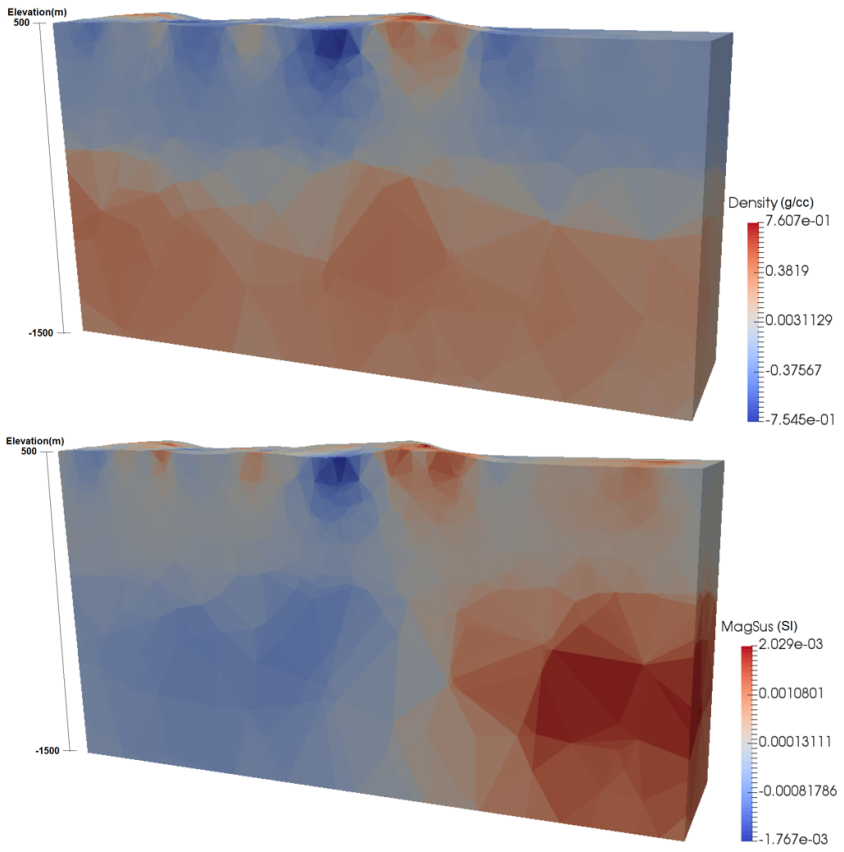


Figure 8.25: Vertical sections of the joint inversion models of gravity (top) and magnetic (bottom) data using clustering method (2 clusters) for $\rho$=10.

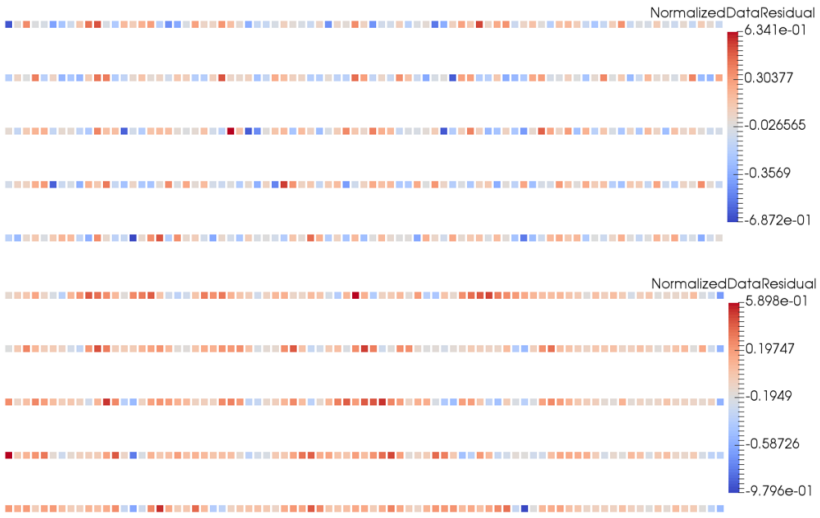


Figure 8.26: Top: normalized data residual for the gravity model. Bottom: normalized data residual for the magnetic model (clustering method; 2 clusters; $\rho$=10).

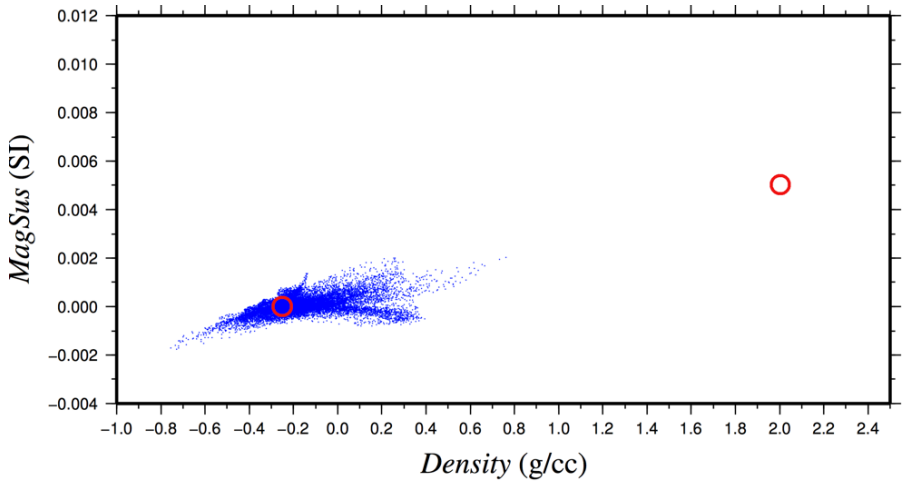


Figure 8.27: Physical properties (magnetic susceptibility versus density) obtained after the joint inversion using the clustering method (2 clusters) for $\rho$=10. Each blue dot corresponds to a cell in the inversion mesh. Red circles: the two initial clusters defined in the joint inversion (from left to right: overburden and sandstone).

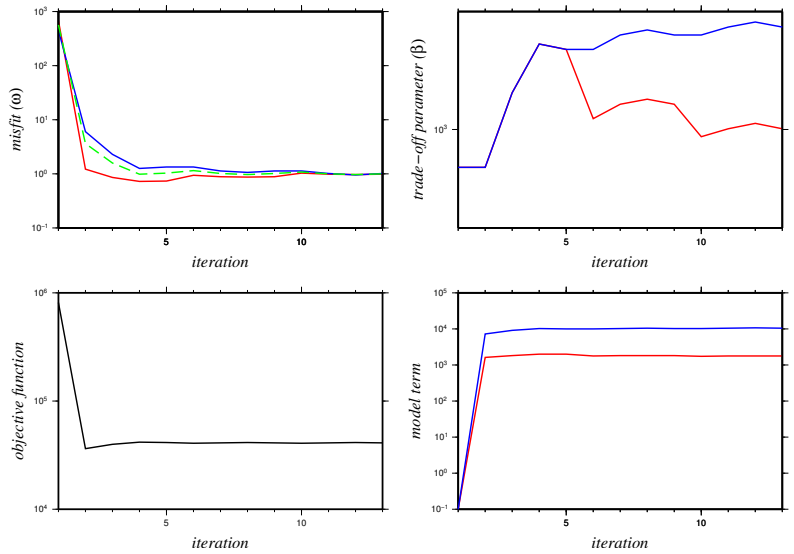


Figure 8.28: Variations of different parts of the objective function such as data misfit ($\omega$; top-left), trade-off parameter ($\beta$; top-right), objective function ($\mathbf{\Phi}$; bottom-left) and model term ($\phi_m$; bottom-right) at iterations for the joint inversion of gravity (red) and magnetic (blue) data using the clustering method (2 clusters) for $\rho$=10. Green color shows the average "$\omega$".

It can be seen that three different layers are somewhat apparent in the joint inversion model (Figure 8.25). The susceptibility is concentrated in the overburden and basement with susceptibility of around 0SI in the middle layer that corresponds to the sandstone. The same situation can be seen in the density model in which the middle zone has a relative density of around -0.25g/cc corresponding to the sandstone layer. Also it can be seen that the magnetic susceptibility on the left side is less than on the right side. These models match reasonably well the true models (see Figure 8.9). The approximate location of the unconformity can be clearly seen. In particular, the clustering joint inversion is able to separate out the susceptibility and density in the basement.

Figures 8.29 and 8.30 show joint inversion results of the synthetic data for a three cluster case with a coupling factor of 10 as well as the normalized data residuals. This clustering does not seem better than for the 2 cluster case, and also the results show only a little improvement over the 2 cluster case. Figures 8.31 to 8.32 show the cross plot of the physical properties (magnetic susceptibility versus density) obtained after the joint inversion, and the variation of the various terms of the objective function, respectively. The run-time was 1 hour and 23 minutes for 13 iterations.

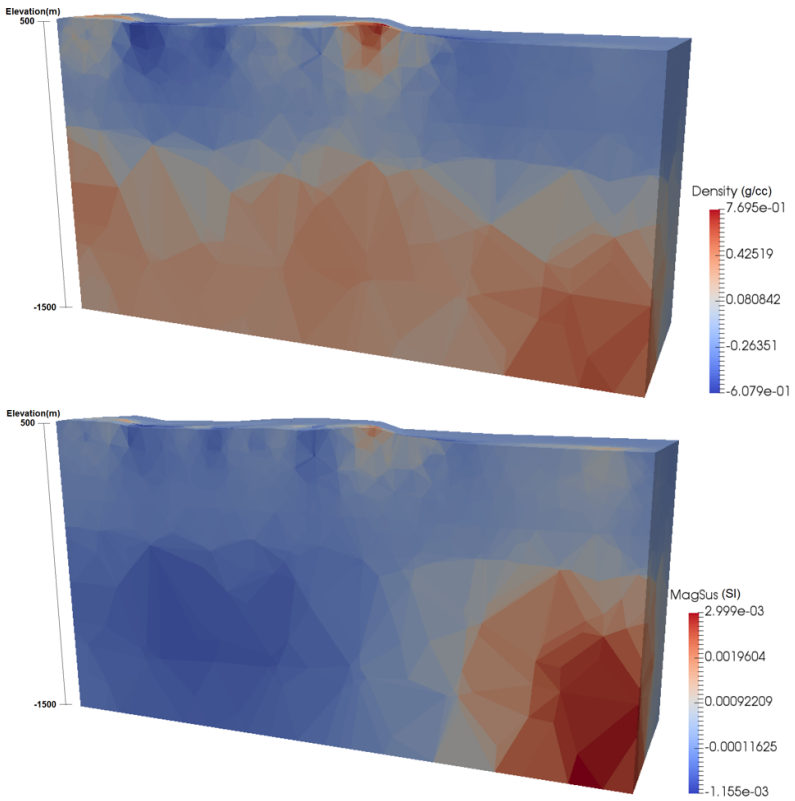


Figure 8.29: Vertical sections of the joint inversion models of gravity (top) and magnetic (bottom) data using clustering method (3 clusters) for $\rho$=10.

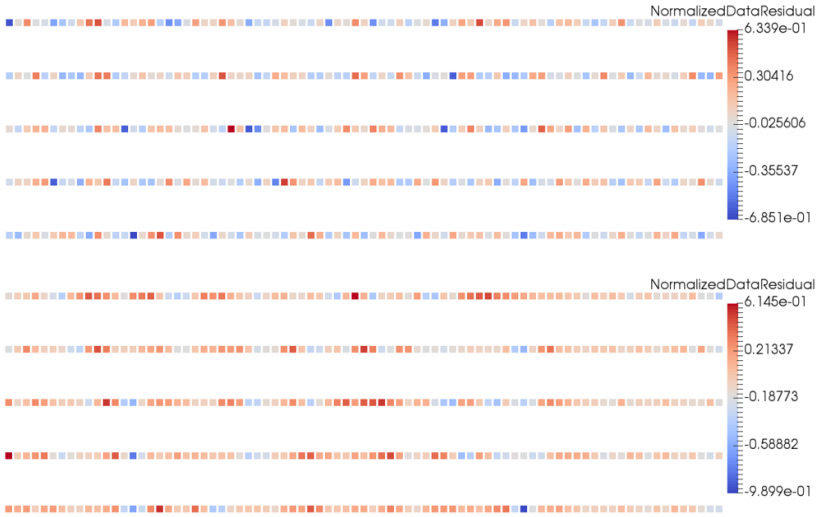


Figure 8.30: Top: normalized data residuals for the gravity model. Bottom: normalized data residual for the magnetic model (clustering method; 3 clusters; $\rho$=10).

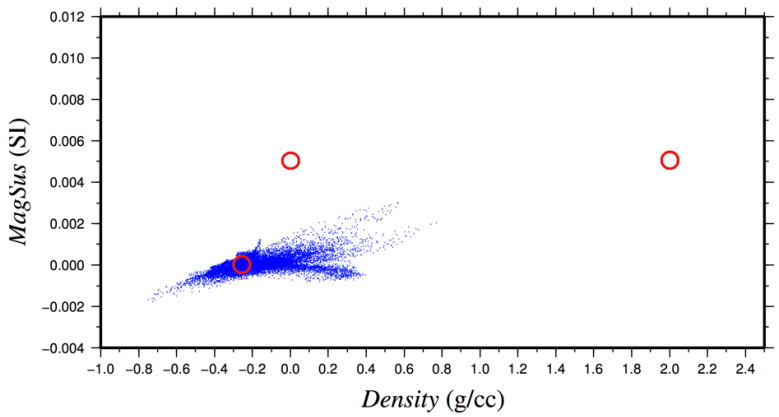


Figure 8.31: Physical properties (magnetic susceptibility versus density) obtained after the joint inversion using the clustering method (3 clusters) for $\rho$=10. Each blue dot corresponds to a cell in the inversion mesh. Red circles: the three clusters defined in the joint inversion (from left to right: sandstone, basement and overburden).

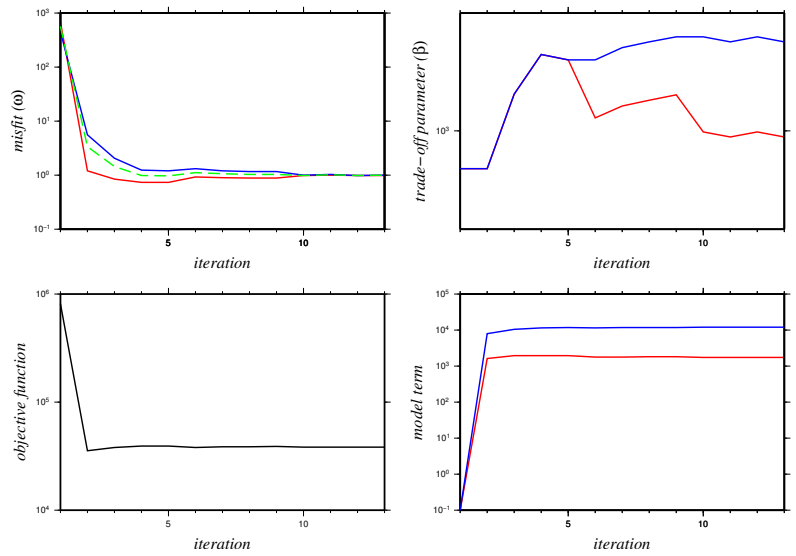


Figure 8.32: Variations of different parts of the objective function such as data misfit ($\omega$; top-left), trade-off parameter ($\beta$; top-right), objective function ($\mathbf{\Phi}$; bottom-left) and model term ($\phi_m$; bottom-right) at iterations for the joint inversion of gravity (red) and magnetic (blue) data using the clustering method (3 clusters) for $\rho$=10. Green color shows the average "$\omega$".

It can be seen that the cluster method can generate the sandstone and basement structure as well as the unconformity location. But the overburden is still not good enough. To solve

this problem, I use the constrained joint inversion. I consider a layer that I am confident is all overburden from surface to an elevation above sea level of around 500m in which the physical properties are fixed during the inversion process (a density value of 2g/cc and a magnetic susceptibility of $5\times10^{-3}$SI). The mesh had about 325,000 tetrahedral cells. The reason that unlike the constrained independent inversion I started with a mesh with 1 constrained layer rather than 2 constrained layers is to reduce the number of cells. Because by increasing the number of cells, the run-time will increase. Therefore, I will initially start with a mesh with 1 constrained layer. If no desired results are obtained, I will try a mesh with 2 constrained layers. Also, since it is the free-air data that is being inverted, it is expected that by constraining the layer/structure which has the absolute density value in the mesh, the code be able to reconstruct other parts of the model as well as the base of overburden.

To achieve better results, the code was initially run for $\rho$=10. The model constructed by this inversion was used as an initial model for the both inversions for $\rho$=1.0E+5 and (again) $\rho$=10. Without considering this approach, the inversion for $\rho$=1.0E+5 stopped after 150 iterations with a run-time of 314 hours. Whereas, by considering this initial model, not only the run-time for $\rho$=1.0E+5 was reduced, but the results for $\rho$=10 were improved. The run-times for the joint inversions of $\rho$=10 and $\rho$=1.0E+5 were 33 hours and 35 minutes for 13 iterations and 48 hours and 12 minutes for 17 iterations, respectively. Figures 8.33 to 8.40 show the results for $\rho$=10 and $\rho$=1.0E+5 for this (1 layer) constrained joint inversion.

For the clustering method, a higher coupling factor gives a better clustering (see Figure

8.39). Thus, it is expected that this gives the better inversion models (but not necessarily always). In this research many models were made to investigate the clustering method, but only a few of them, which represent the range of results, are shown in this thesis. In one of this models, all clusters (6 clusters including overburden, sandstone, politic gneiss, psammitic gneiss, granitoid rocks and alteration zone) were considered for the joint inversion. The results for $\rho$=10 were similar to Figures 8.29 and 8.31. For $\rho$=1.0E+5, the structures reconstructed in the basement were similar to those in Figure 8.37 with sharper boundaries. The only improvement for $\rho$=1.0E+5 was related to the clustering in which all 6 clusters were made. Therefore, as mentioned a higher coupling factor gives a better clustering but not necessarily always the better inversion models.

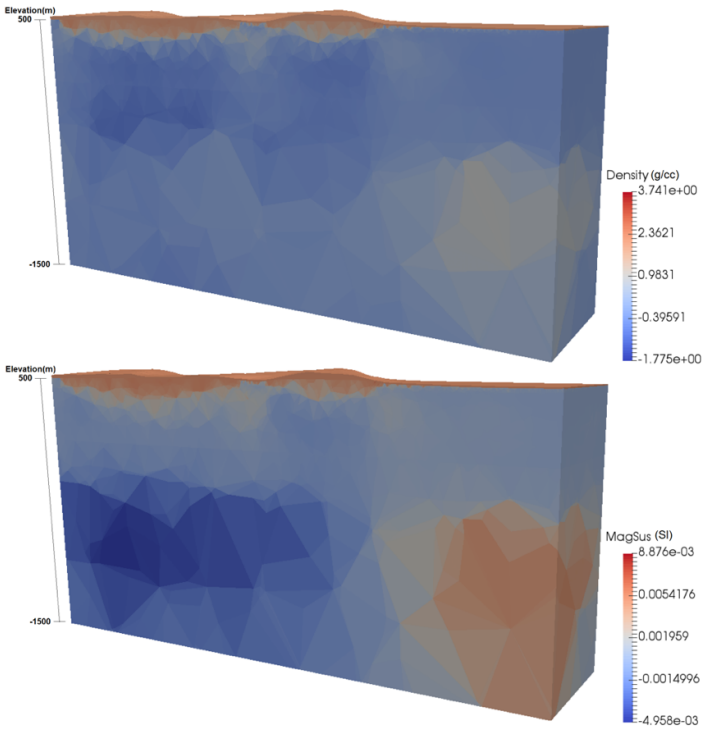


Figure 8.33: Vertical sections of the constrained (1 constraint) joint inversion models of gravity (top) and magnetic (bottom) data using clustering method (2 clusters) for $\rho$=10.

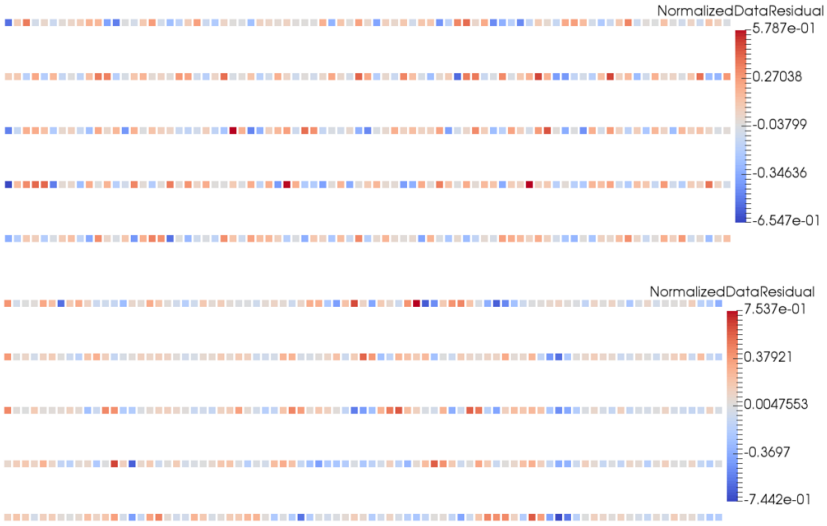


Figure 8.34: Top: normalized data residuals for the gravity model. Bottom: normalized data residual for the magnetic model (1 constraint; 2 clusters; $\rho$=10).

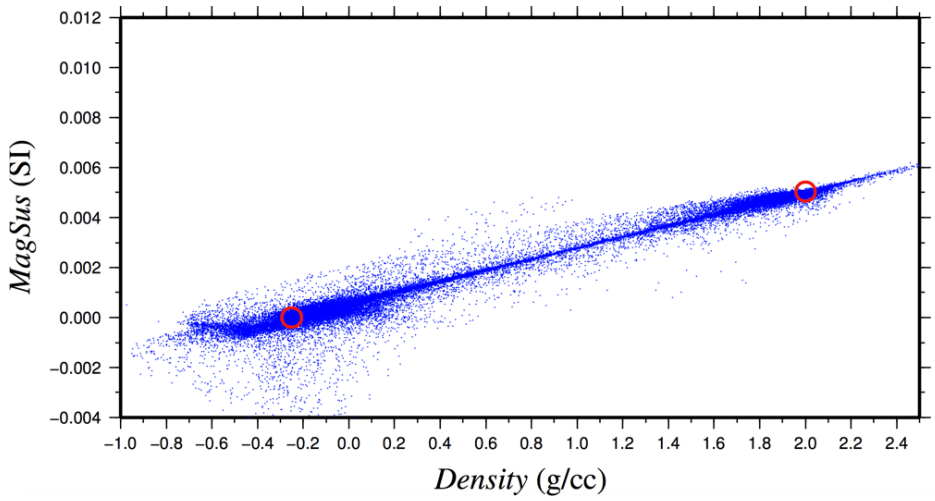


Figure 8.35: Physical properties (magnetic susceptibility versus density) obtained after the constrained (1 constraint) joint inversion. Each blue dot corresponds to a cell in the inversion mesh. Red circles: the two initial clusters defined in joint inversion.

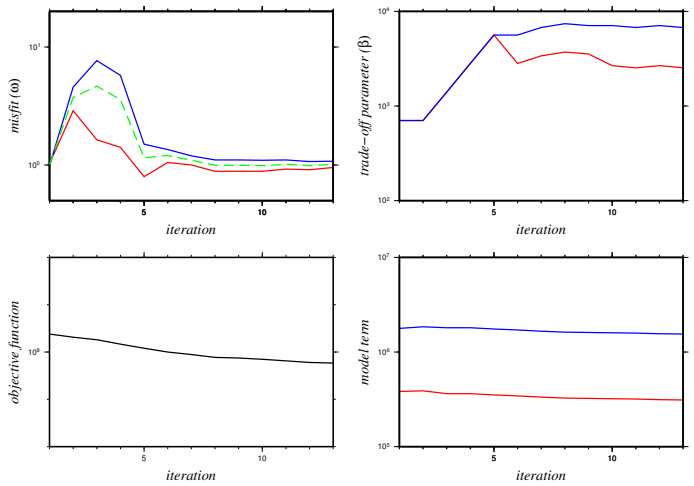


Figure 8.36: Variations of different parts of the objective function such as data misfit ($\omega$; top-left), trade-off parameter ($\beta$; top-right), objective function ($\mathbf{\Phi}$; bottom-left) and model term ($\phi_m$; bottom-right) at iterations for the joint inversion of gravity (red) and magnetic (blue) data using the clustering method (2 clusters; 1 constraint) for $\rho$=10. Green color shows the average "$\omega$".

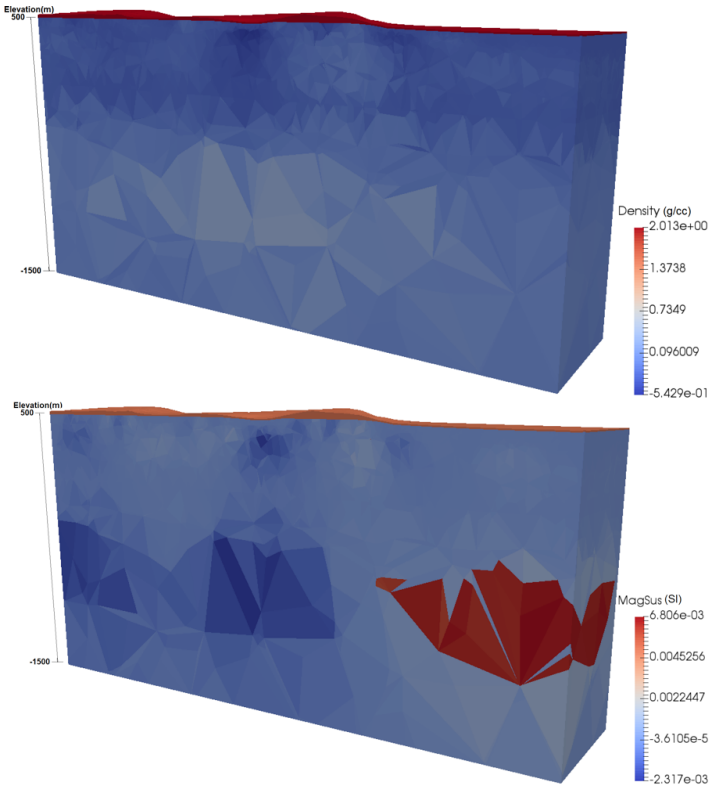


Figure 8.37: Vertical sections of the constrained (1 constraint) joint inversion models of gravity (top) and magnetic (bottom) data using clustering method (2 clusters) for $\rho$=1.0E+5.

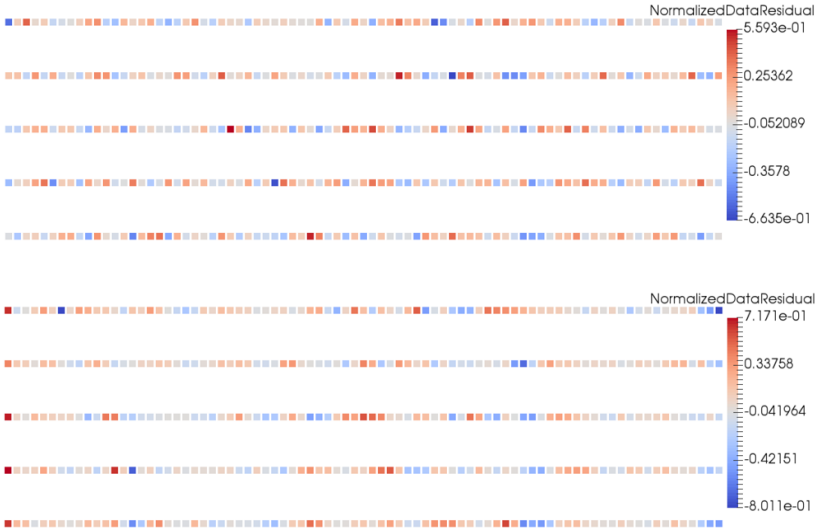


Figure 8.38: Top: normalized data residuals for the gravity model. Bottom: normalized data residual for the magnetic model (1 constraint; 2 clusters; $\rho$=1.0E$^{+5}$).

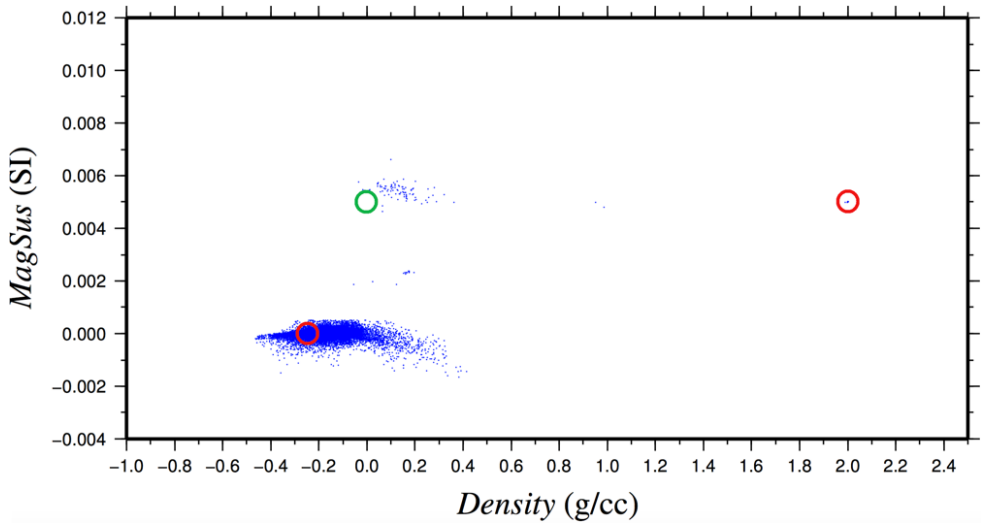


Figure 8.39: Physical properties (magnetic susceptibility versus density) obtained after the constrained (1 constraint) joint inversion. Each blue dot corresponds to a cell in the inversion mesh. Red circles: the two initial clusters defined in joint inversion. Green circle: basement cluster which was omitted in this 2 cluster joint inversion.

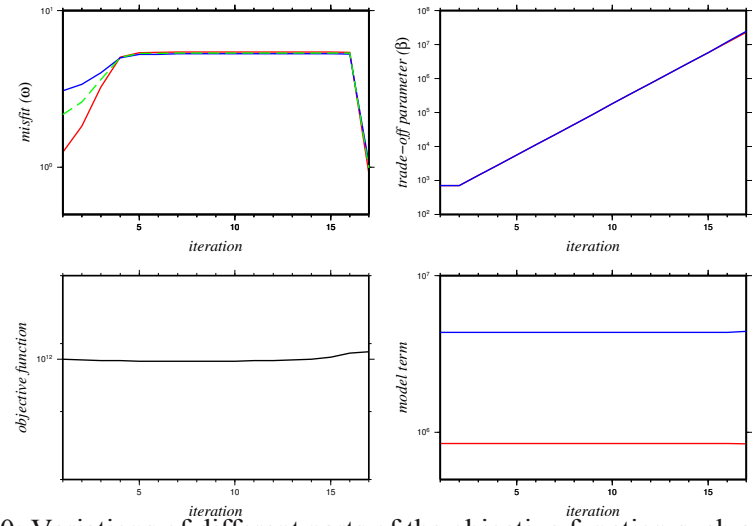


Figure 8.40: Variations of different parts of the objective function such as data misfit ($\omega$; top-left), trade-off parameter ($\beta$; top-right), objective function ($\mathbf{\Phi}$; bottom-left) and model term ($\phi_m$; bottom-right) at iterations for the joint inversion of gravity (red) and magnetic (blue) data using the clustering method (2 clusters; 1 constraint) for $\rho$=1.0E+5. Green color shows the average "$\omega$".

Only two clusters (overburden and sandstone) were considered for the constrained joint inversions. But it can be seen that the clustering for $\rho$=1.0E+5 is better than that for $\rho$=10 as far as it has generated three distinct clusters (for overburden, sandstone and basement). The green circle in Figure 8.39 shows the location of the basement cluster. The clustering for $\rho$=10 is not too good, but the constructed models for $\rho$=10 are a little better than the results for $\rho$=1.0E+5, as the base of overburden is reconstructed better. The results for 3 cluster case are not shown here as they were very similar to the 2 cluster case without any improvement and superiority.

I try to further improve the results. So, Figures 8.41 to 8.45 show the results when two layers with fixed physical properties are constrained during the joint inversion. From top to bottom the layers are:

1- A layer that can confidently be assumed to be the overburden from the surface to an elevation above sea level of around 500m with fixed physical properties during the inversion process: e.g. here a density value of 2g/cc and a magnetic susceptibility of $5\times10^{-3}$SI.

2- A layer that we are unsure of but is either overburden or sandstone from an elevation of 500m to 450m. So, for the physical properties a wide range of values is considered as constraint (as lower and upper bounds; i.e. -100g/cc < density < 100g/cc and -10000SI < magnetic susceptibility < 10000SI).

3- A layer that we are confident is all sandstone from an elevation of 450m to 50m with fixed physical properties: e.g. here a relative density value of -0.25g/cc and a magnetic susceptibility of 0SI.

4- A layer from 50m to the bottom of the model that we are unsure of but is either sandstone or basement. So, for the physical properties a wide range of values is considered as constraint (as lower and upper bounds; i.e. -100g/cc < density < 100g/cc and -10000SI < magnetic susceptibility < 10000SI).

From Figures 8.41 and 8.42, it can be seen that the result for the overburden section has improved in the constrained (with 4 constrained layers) joint inversion results. Similar to the previous model (1 constraint model), an initial model is used in order to improve the results. The run-time for this constrained joint inversion (of $\rho$=10) was 89 hours and 52 minutes for 20 iterations. The mesh had about 533,000 tetrahedral cells.

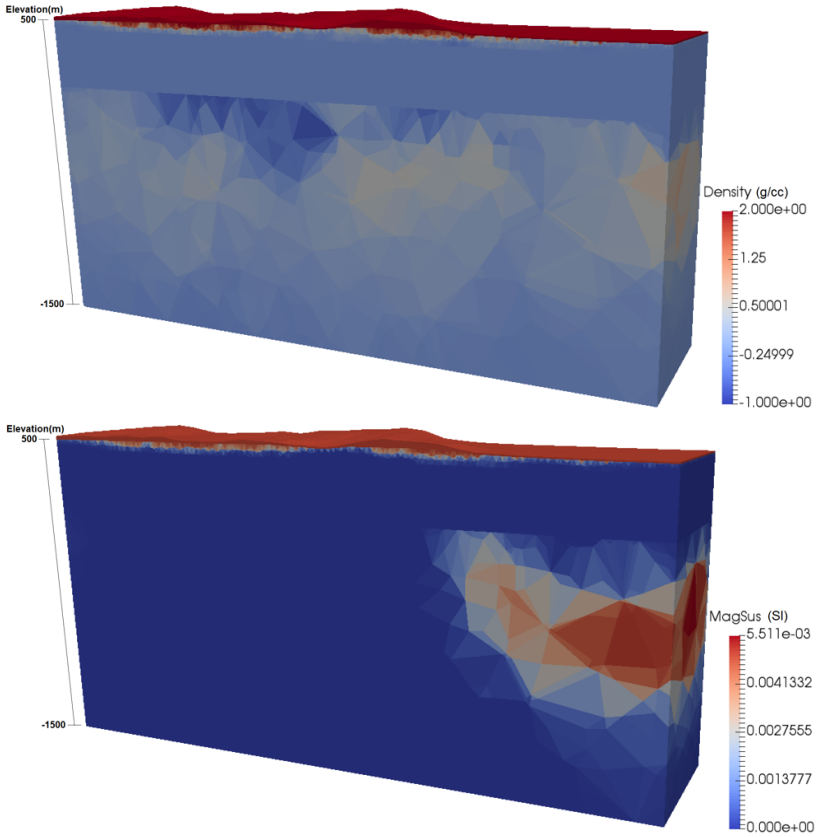


Figure 8.41: Vertical sections of the constrained (4 constraints) joint inversion models of gravity (top) and magnetic (bottom) data using clustering method (2 clusters) for $\rho$=10.

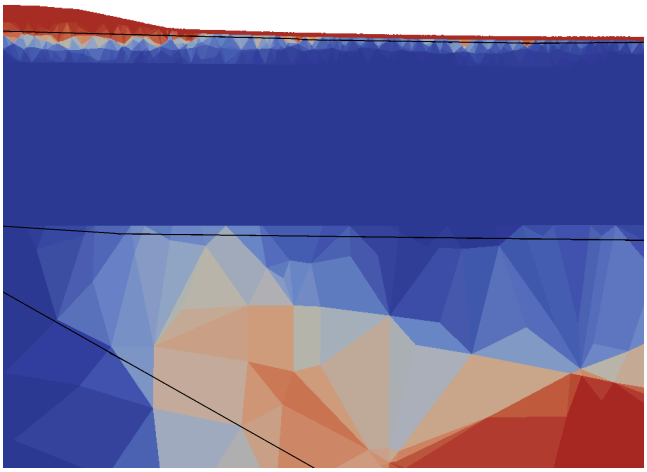

Figure 8.42: Part of the susceptibility model produced by the constrained (4 constraints) joint inversion. Three black lines (from top to bottom): true base of overburden, true unconformity and true P2 fault (true interface between blocks #4 and #5 in the basement).

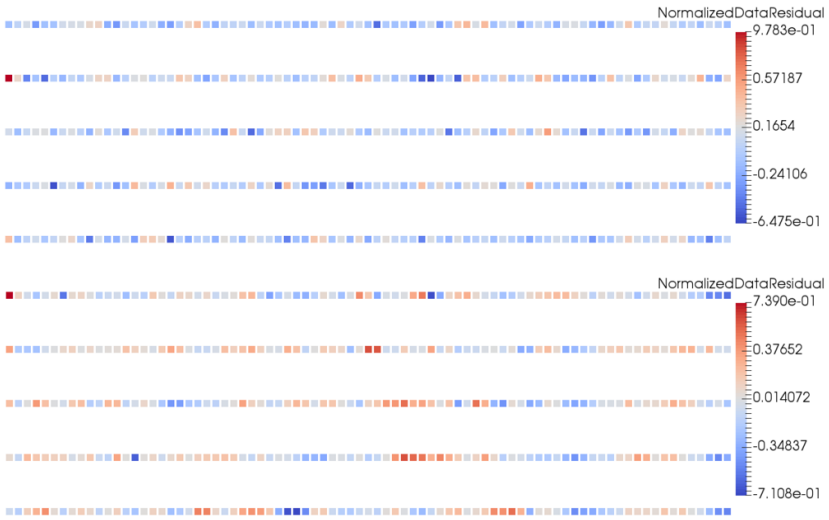


Figure 8.43: Top: normalized data residual for the gravity model. Bottom: normalized data residual for the magnetic model (4 constraints; 2 clusters; $\rho$=10).

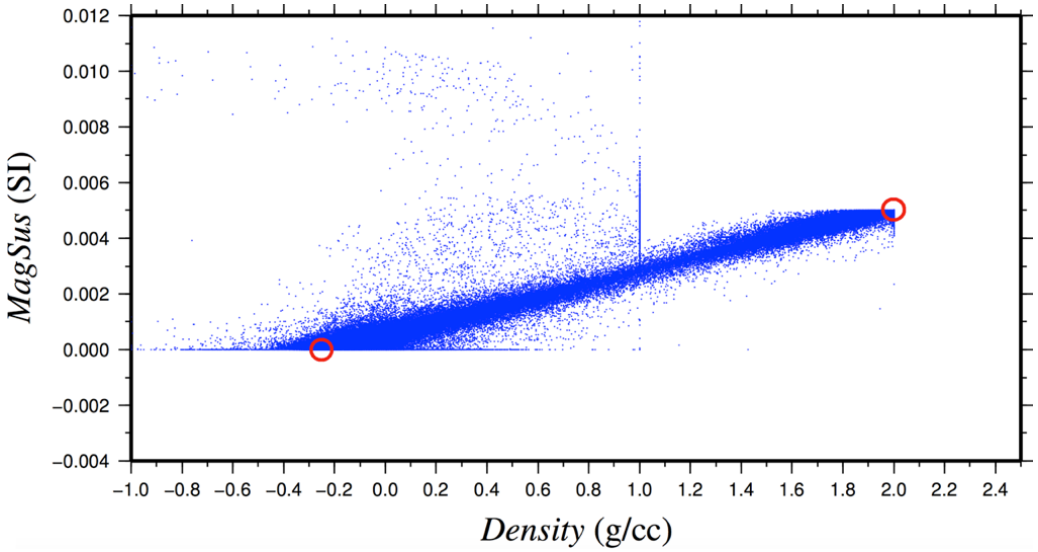


Figure 8.44: Physical properties (magnetic susceptibility versus density) obtained after the constrained (4 constraints) joint inversion. Each blue dot corresponds to a cell in the inversion mesh. Red circles: the two clusters defined in joint inversion.

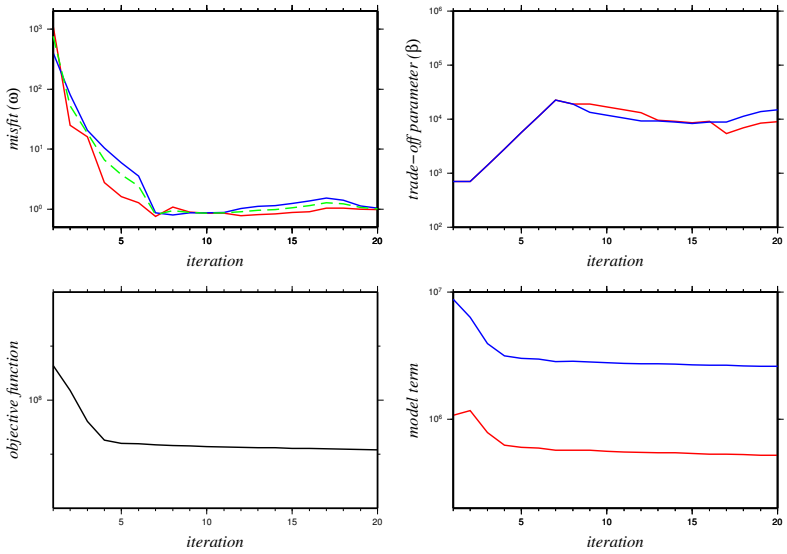


Figure 8.45: Variations of different parts of the objective function such as data misfit ($\omega$; top-left), trade-off parameter ($\beta$; top-right), objective function ($\mathbf{\Phi}$; bottom-left) and model term ($\phi_m$; bottom-right) at iterations for the joint inversion of gravity (red) and magnetic (blue) data using the clustering method (2 clusters; 4 constraints) for $\rho$=10. Green color shows the average "$\omega$".

## 8.3 3D inversion of real gravity and magnetic data

In this section, 3D inversions of real gravity and magnetic data are performed for the McArthur area for a number of profiles. Independent and joint inversions are performed in order to construct density and susceptibility models. Physical property data are used as constraints in the inversions. Similar to the synthetic examples, for the distance weighting, a value of 1.0 is assigned for $w_z$ and $w_p$. Also, a value of 0.05 is considered for the *chifact* value for both magnetic and gravity methods. A value of 1.0 and 700 is considered for the initial trade-off parameter of independent and joint inversions, respectively (see Section 8.2.2). For the inversions, appropriate uncertainties are probably about 5% of the ranges (Van Wijk et al., 2002). Since the gravity data is on [-212.96,-204.45] and the magnetic

data is on [-380.61,-330.71] (after removing the geomagnetic field value = 59500 nT), uncertainty values can be about 0.44mGal and 2.5nT for gravity and magnetic data, respectively. For levelling the data, simply removing the average value of data was the most sensible approach for both gravity and magnetic methods.

A part of the airborne free-air gravity data (from Bell Gravity data-set) as well as airborne total magnetic field data (from Triaxial Magnetic data-set) were selected for the inversion with a station spacing and a profile spacing of around 50 m and 300 m, respectively (Figures 8.46 and 8.47; see Section 8.1). The data are almost in the same locations but not quite (see Figures 8.1, 8.3 and 8.46). During data acquisition, the geomagnetic field strength in McArthur area was 59500nT, and the geomagnetic field declination and inclination were around 12 and 80 degrees, respectively. Figure 8.47 shows that the gravity and magnetic data are strongly dominated by variations of topography. Also, the right side and left side of the magnetic profiles show a decrease and an increase in the magnetic data, respectively. These variations are a part of a long wavelength trend (see also Figure 8.4) which is due to the deep (i.e. basement) structures.

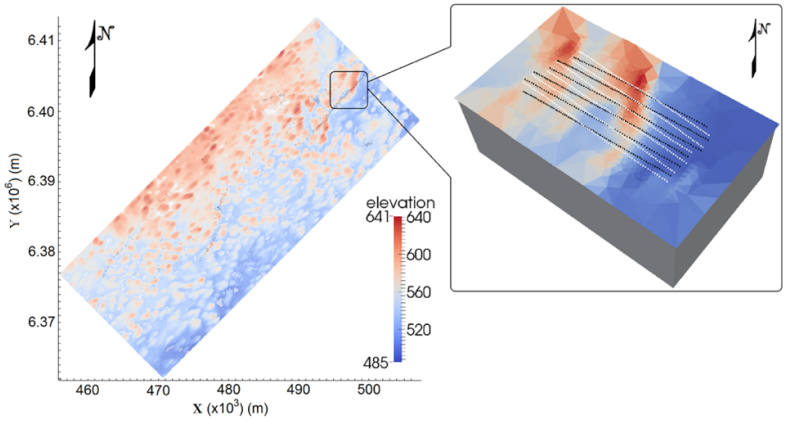

Figure 8.46: Topography of McArthur-Millennium corridor. Inset shows location of magnetic (black) and gravity (white) survey lines.

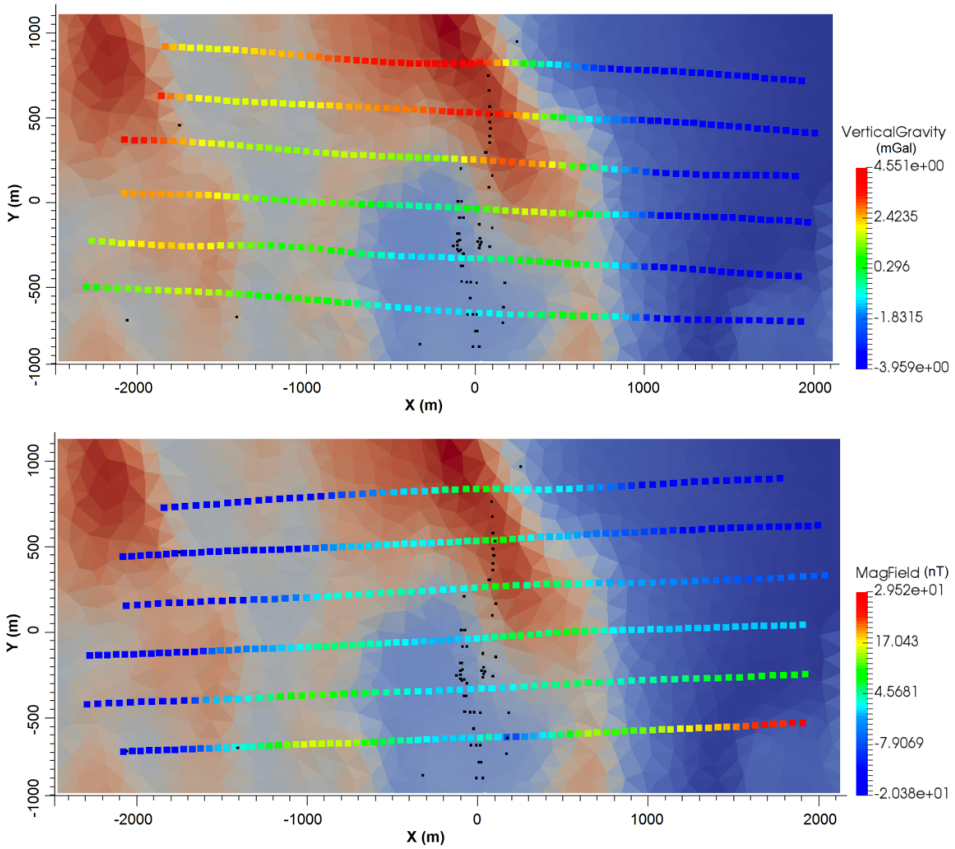


Figure 8.47: Free-air gravity data (top; in mGal) and magnetic data (bottom; in nT) over the McArthur River area (~4×2km). Data are dominated by variations in topography. Black dots show the location of drill-holes. The background image for both panels is elevation (and the same colour scale as in Figure 8.46).

3D inversions were performed for the real airborne gravity and magnetic data on a mesh using the L2-norm method. Similar to the synthetic examples, I started with independent inversions, then I investigated the results of joint inversion as well as constrained joint inversion. Figure 8.48 shows the independent inversion results for magnetic and gravity data. It can be seen that the independent inversions were not able to reconstruct the interface between the overburden and sandstone nor the basement structure. Figure 8.49 shows there is a good fit between the observed and calculated data. The mesh had about 28,000 tetrahedral cells.

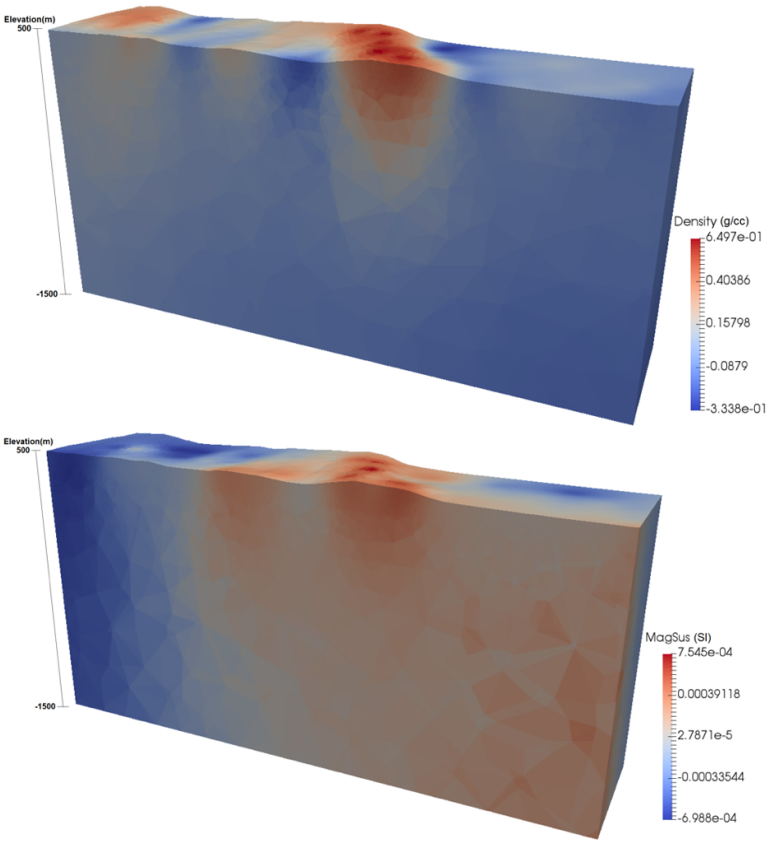


Figure 8.48: Vertical sections of independent gravity (top) and magnetic (bottom) inversion models for the real data.

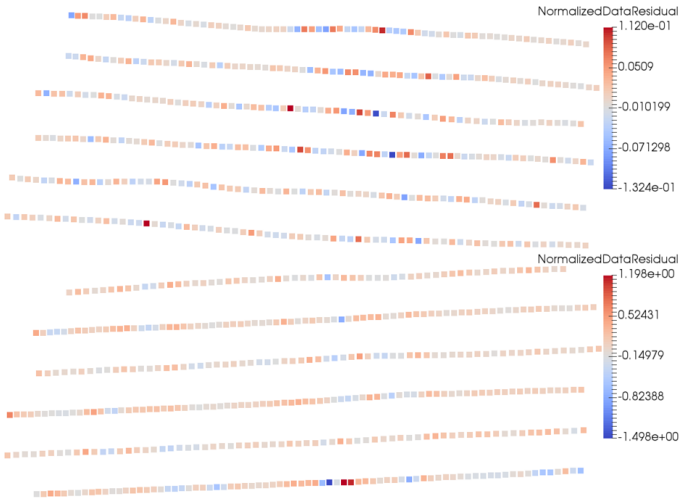


Figure 8.49: Top: normalized data residuals for the gravity model. Bottom: normalized data residuals for the magnetic model (for the independent inversions).

In order to improve the inversion results, joint inversion of gravity and magnetic data using the clustering method for a coupling factor of $\rho$=10 was applied (similar to the synthetic case in Section 8.8.2; Figure 8.25). For this purpose, two clusters were considered in which two different clusters with average physical properties corresponding to the two main geological structures were defined: overburden (density=2 g/cc; MagSus: $4\times10^{-3}$ SI) and sandstone (relative density=-0.25 g/cc; MagSus: 0 SI). For the joint inversion results shown in Figure 8.50, the normalized data residuals shown in Figure 8.51 show there is a good fit between the observed and calculated data. Figure 8.52 shows the cross plot of densities and magnetic susceptibilities constructed using the joint inversion. Also, the variation of the various terms of the objective function for the joint inversion model are shown in Figure 8.53. The run-time for this joint inversion (of $\rho$=10) was 2 hours and 57 minutes for 13 iterations. The mesh had about 28,000 tetrahedral cells.

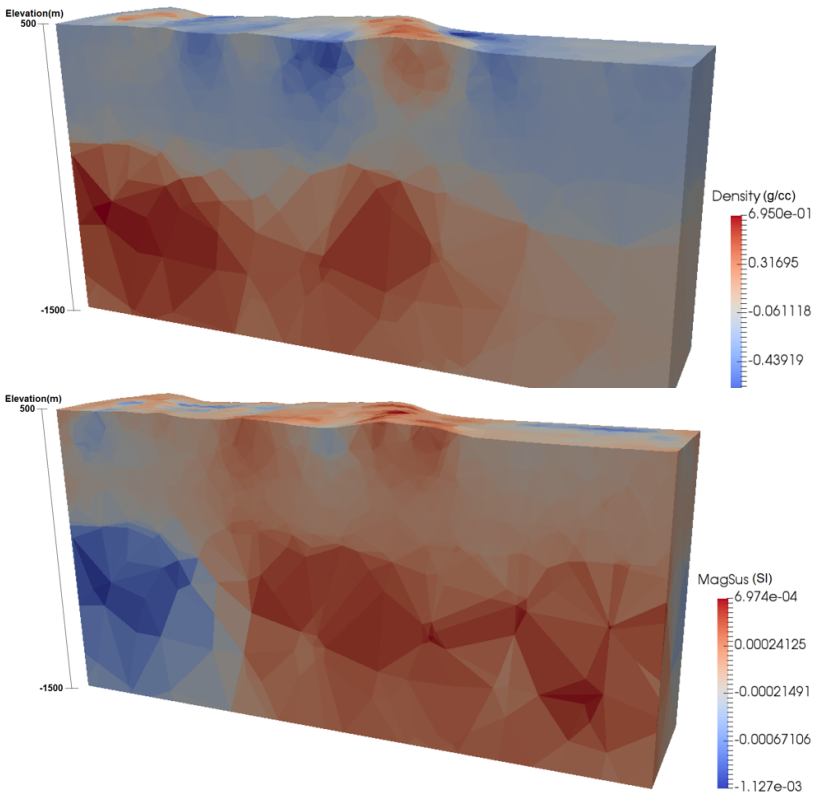


Figure 8.50: Vertical sections of the joint inversion models of real gravity (top) and magnetic (bottom) data using clustering method (2 clusters) for $\rho$=10.

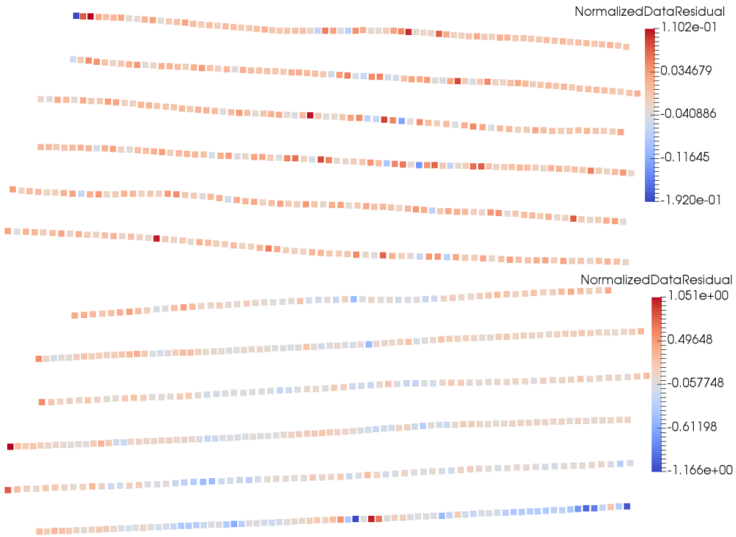


Figure 8.51: Top: normalized data residuals for the gravity model. Bottom: normalized data residuals for the magnetic model (clustering method; 2 clusters; $\rho$=10).

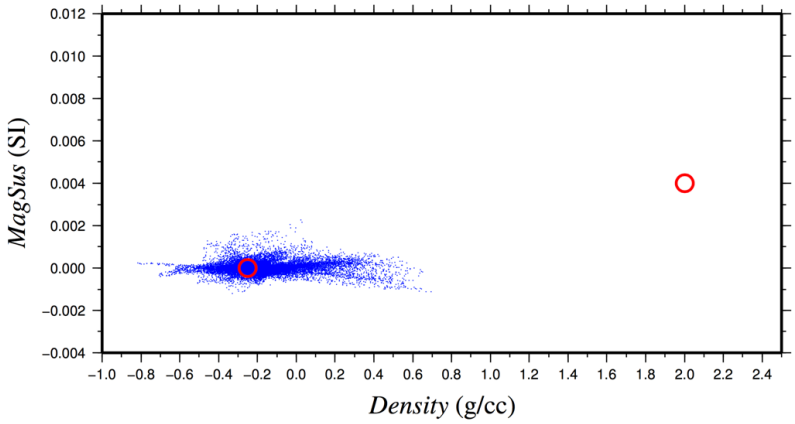


Figure 8.52: Physical properties (magnetic susceptibility versus density) obtained after the joint inversion of real data using the clustering method (2 clusters) for $\rho$=10. Each blue dot corresponds to a cell in the inversion mesh. Red circles: the two clusters defined in the joint inversion (from left to right: overburden and sandstone).

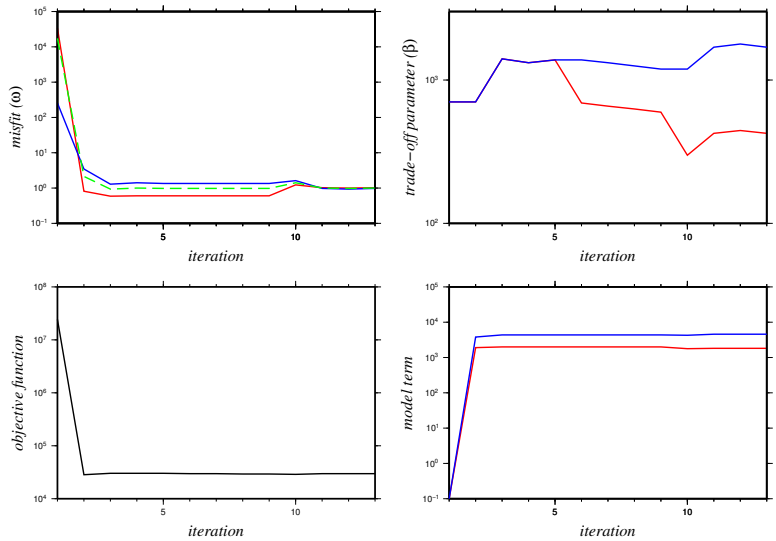


Figure 8.53: Variations of different parts of the objective function such as data misfit ($\omega$; top-left), trade-off parameter ($\beta$; top-right), objective function ($\mathbf{\Phi}$; bottom-left) and model term ($\phi_m$; bottom-right) at iterations for the joint inversion of real gravity (red) and magnetic (blue) data using the clustering method (2 clusters) for $\rho$=10. Green color shows the average "$\omega$".

A susceptibility of around 0 SI is constructed in the middle layer that corresponds to the sandstone (Figure 8.50). The same situation can be seen in the density model in which the middle zone has a relative density of around -0.25 g/cc corresponding to the sandstone layer. The approximate location of the unconformity can be clearly seen. And, in the

basement zone the magnetic susceptibility on the left side is less than on the right side of the basement. As mentioned in Chapter 2, in the McArthur River area the magnetic susceptibility of rocks in the footwall of the P2 fault is less than that of the rocks in the hanging-wall. Therefore, in the inversion results the boundary between the low and high magnetic susceptibly in the basement can be interpreted as the approximate location of the P2 fault. In particular, the clustering joint inversion is able to separate out the susceptibility and density in the basement. But the overburden is still not good enough.

To attempt to solve this problem, I use the 1-layer constrained joint inversion (similar to the synthetic case in Section 8.2.2; Figure 8.33). A layer is considered that can confidently be assumed to be overburden in which the physical properties are fixed during the inversion process (a density value of 2 g/cc and a magnetic susceptibility of $4\times10^{-3}$ SI based on drill-hole information; Figures 8.54 to 8.57). The run-time for this constrained joint inversion (of $\rho$=10) was 49 hours and 34 minutes for 20 iterations. The mesh had about 325,000 tetrahedral cells which is significantly larger than the previous example as defining a narrow layer below the topography (as constraint) cause "tetgen" to generate many (small) refined tetrahedral cells in that region. The 1-layer constrained joint inversion improved the results better than the join inversion method as the base of overburden is reconstructed better.

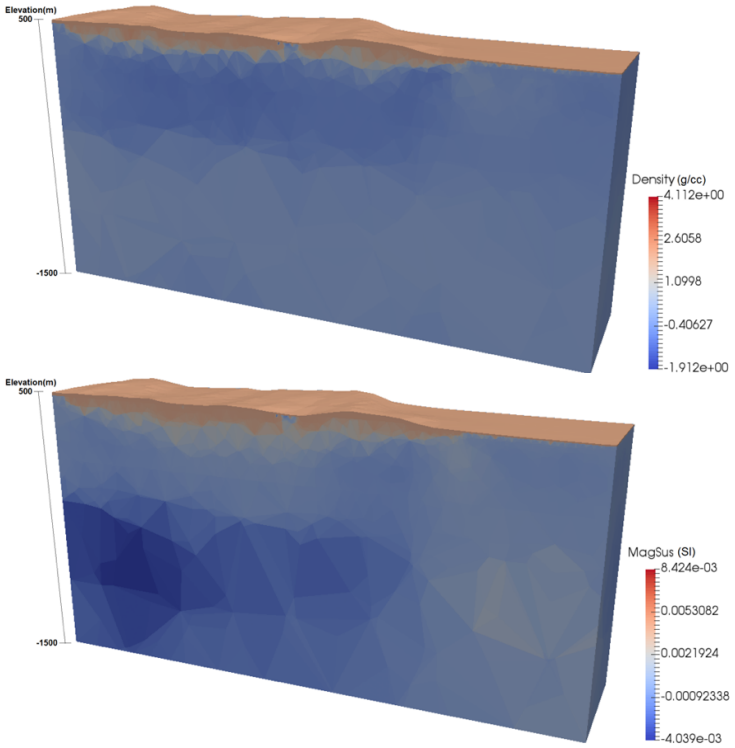


Figure 8.54: Vertical sections of the constrained (1 layer) joint inversion models of real gravity (top) and magnetic (bottom) data using clustering method (2 clusters) for $\rho$=10.

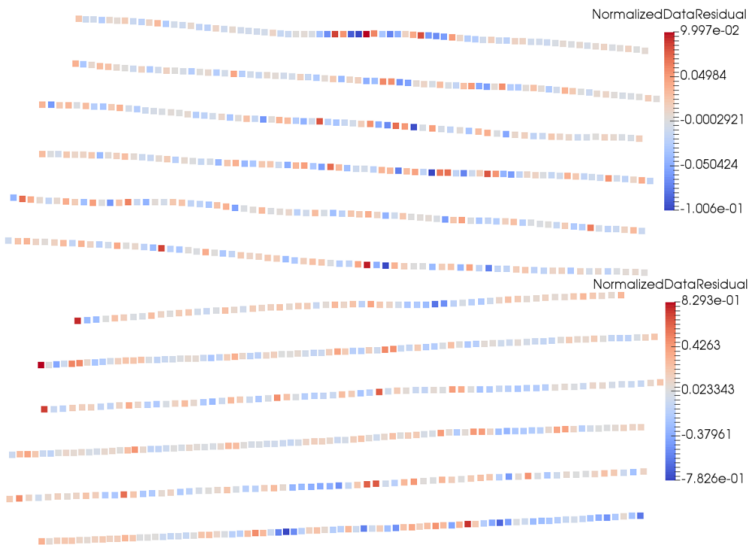


Figure 8.55: Top: normalized data residuals for the gravity model. Bottom: normalized data residuals for the magnetic model (1 constraint/layer; 2 clusters; $\rho$=10).

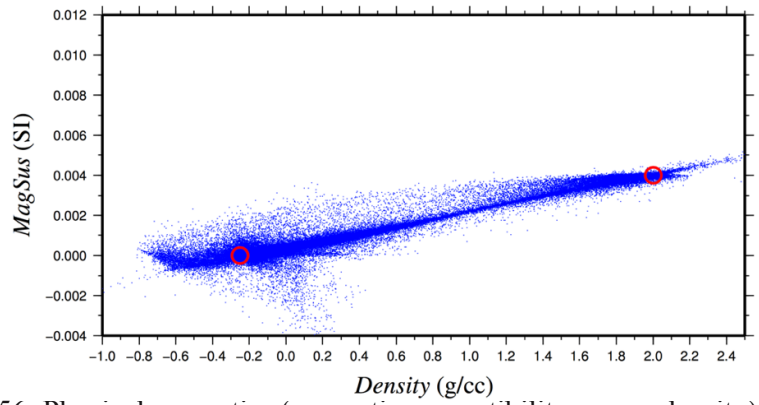


Figure 8.56: Physical properties (magnetic susceptibility versus density) obtained after the constrained (1 layer) joint inversion of real data. Each blue dot corresponds to a cell in the inversion mesh. Red circles: the two clusters defined in joint inversion.

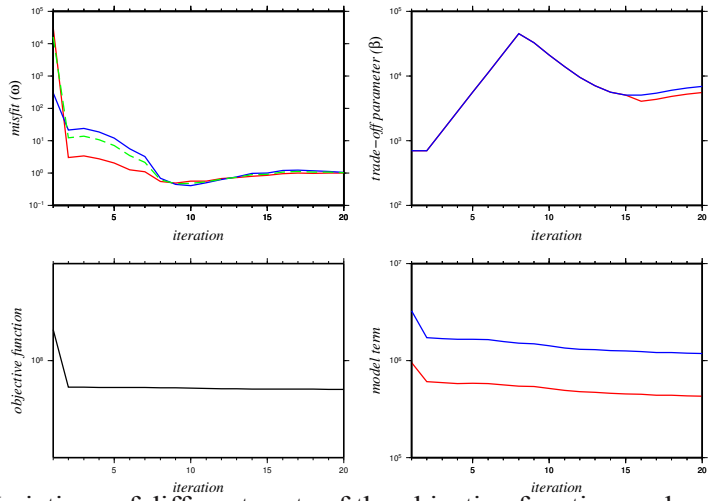


Figure 8.57: Variations of different parts of the objective function such as data misfit ($\omega$; top-left), trade-off parameter ($\beta$; top-right), objective function ($\mathbf{\Phi}$; bottom-left) and model term ($\phi_m$; bottom-right) at iterations for the joint inversion of real gravity (red) and magnetic (blue) data using the clustering method (2 clusters; 1 constraint) for $\rho$=10. Green color shows the average "$\omega$".

I try to further improve the results. The next figures show the results when there are two layers with fixed physical properties during a constrained joint inversion (Figures 8.58 to 8.62). Similar to the synthetic case in Section 8.2.2 (Figure 8.41), the layers in the mesh were as follows: 1- A layer that can safely be assumed to be overburden with fixed physical properties during the inversion process: e.g. here a density value of 2 g/cc and a magnetic

susceptibility of $4\times10^{-3}$ SI. 2- A layer that we are unsure of but is either overburden or sandstone. So, for the physical properties a wide range of values is considered as constraint (as lower and upper bounds). 3- A layer that we are confident is all sandstone from an elevation of 450 m to 50 m with fixed physical properties: e.g. here a relative density value of -0.25 g/cc and a magnetic susceptibility of 0 SI. 4- A layer from 50 m to the bottom of the model that we are unsure of but is either sandstone or basement, and hence for which a wide range of physical property values is considered as constraint (as lower and upper bounds).

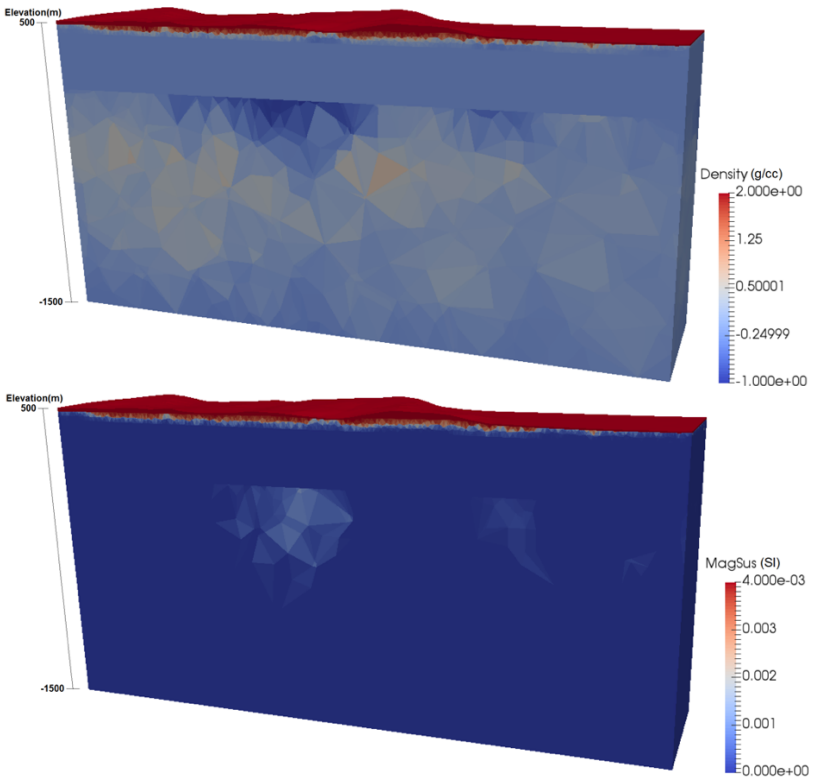


Figure 8.58: Vertical sections of the constrained (2 constraint) joint inversion models of real gravity (top) and magnetic (bottom) data using clustering method (2 clusters) for $\rho$=10.

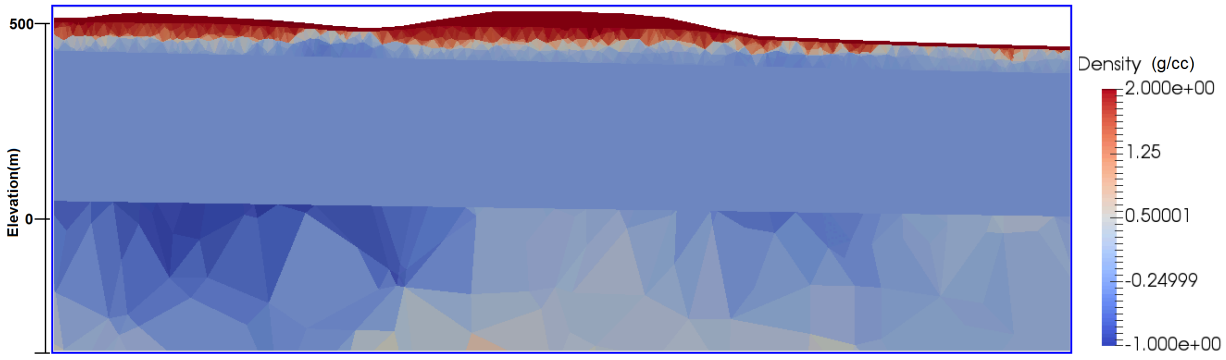


Figure 8.59: Part of the density model produced by the constrained (2 constraints) joint inversion.

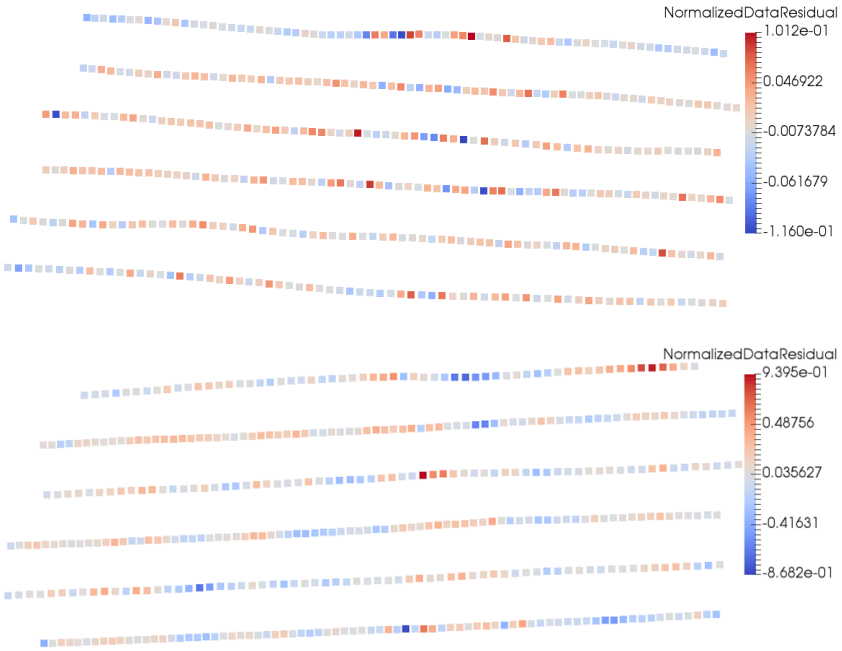


Figure 8.60: Top: normalized data residuals for the gravity model. Bottom: normalized data residuals for the magnetic model (4 constraints; 2 clusters; $\rho$=10).

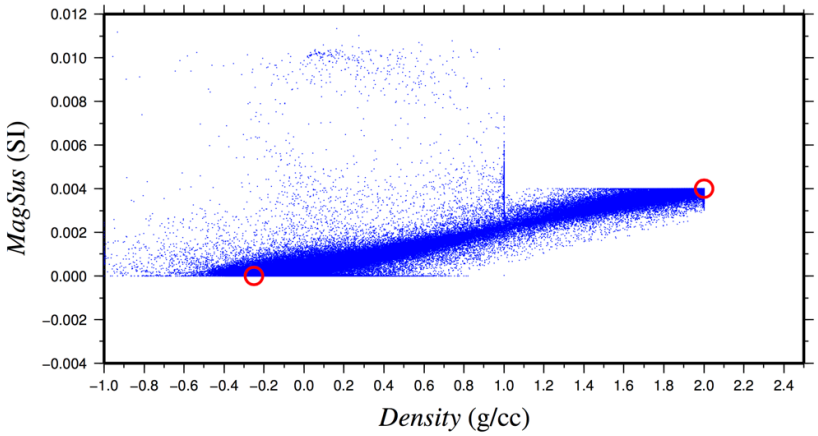


Figure 8.61: Physical properties (magnetic susceptibility versus density) obtained after the constrained (4 constraints) joint inversion of real data. Each blue dot corresponds to a cell in the inversion mesh. Red circles: the two initial clusters defined in joint inversion.

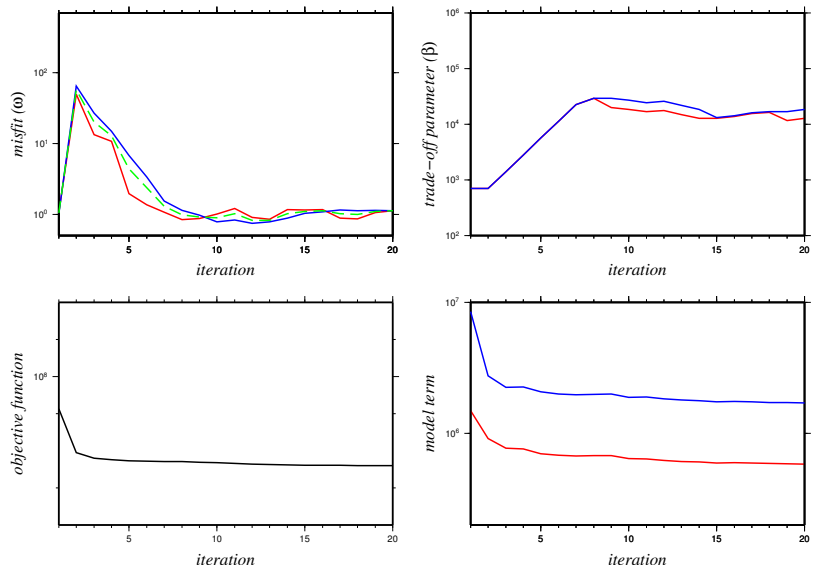


Figure 8.62: Variations of different parts of the objective function such as data misfit ($\omega$; top-left), trade-off parameter ($\beta$; top-right), objective function ($\mathbf{\Phi}$; bottom-left) and model term ($\phi_m$; bottom-right) at iterations for the joint inversion of real gravity (red) and magnetic (blue) data using the clustering method (2 clusters; 4 constraints) for $\rho$=10. Green color shows the average "$\omega$".

The run-time for this constrained joint inversion (of $\rho$=10 with 4 constraints) was 110 hours and 8 minutes for 22 iterations. The mesh had about 533,000 tetrahedral cells which

is larger than the previous example as defining layers/interfaces in the mesh (as/for constraint) cause “tetgen” to generate more refined tetrahedral cells in/around those layers/interfaces. Similar to the synthetic models (see Section 8.2.2), for the constrained inversions an initial model is considered to improve the results and to reduce the run-time. It can be seen that the result for the overburden section has improved in the constrained joint inversion results. Also, most of the reconstructed parts of the overburden are located below the drumlins (Figure 8.59). This can be due to the present of magnetic rocks (only) in the drumlins (see Section 2.5.3). This means that where the magnetic rocks are located a better reconstruction happens in the constrained joint inversion. Also, some depression in the base of the overburden in the reconstructed model can be due to (not enough good) the quality/size of cells.

## 8.4 Conclusions

Independent inversion of gravity and magnetic can be an appropriate method to construct subsurface structures, but not enough good to reconstruct the interfaces in a way similar to the seismic method. There are many methods to improve the inversion results. For this purpose, I initially tested different joint inversions, and then applied a constrained version of join inversion on both synthetic and real data. In order to synthetize the gravity and magnetic data, a model for McArthur area was made including three main strata overburden, sandstone and basement. The basement is made from different blocks.

Independent inversion of gravity and magnetic data did not show good results. For the joint inversion, both correlation and fuzzy c-mean clustering methods were applied on the

synthetic data. For the correlation method, the result had no improvement in comparison with the independent inversions. But, the clustering method showed better results in which the interface between the sandstone and basement was reconstructed. To improve the results, the constraints (from drill-hole data for real data) were applied on the joint inversions to construct the base of the overburden. The constrained joint inversion using the clustering method shows the best results as the interface between the layers are constructed well. A summary of the research in this chapter is shown in Table 8.1. Whole these processes were applied on the real airborne gravity and magnetic data as well. Joint inversion of real data reconstructed the sandstone and basement well. Constrained joint inversion was also applied to the real airborne gravity and magnetic data which improved the (base of) overburden part.

Table 8.1: A summary of the research done in this chapter based on the techniques used for reconstructing the geological structures (overburden, sandstone and basement).

| | Overburden | Sandstone | Basement |
|---|---|---|---|
| **Independent Inversion (gravity data)** | poor | poor | moderate |
| **Independent Inversion (magnetic data)** | poor | poor | moderate |
| **Constrained Independent Inversion (gravity data)** | poor | poor | good |
| **Joint Inversion (correlation method)** | poor | poor | moderate |
| **Joint Inversion (clustering method)** | poor | good | good |
| **Constrained Joint Inversion (clustering method)** | good | good | good |

# Chapter 9

# 3D Modelling and 1D Inversion of Electromagnetic Data (Frequency Domain & Time Domain) of the McArthur Area

## 9.1 Introduction

In this chapter, modelling and inversion of frequency domain (FDEM) and time domain (TDEM) electromagnetic methods are applied for overburden stripping and graphite exploration. As mentioned before, the uranium deposits are often found in the vicinity of conductive graphite in the Athabasca Basin. Also, the overburden can have low resistivity in the Athabasca Basin (see Section 2.5 and 3.6.5). However, I consider different resistivities for it in this research. It was initially thought that EM would be the main method to get overburden thickness, but then it was realized that there is not much of a conductivity contrast for the McArthur-Millennium corridor (adapted from CMIC-Footprints project). The work in this chapter may still be applicable to the Athabasca basin, but certainly relevant to overburden stripping in many other places.

In this chapter, 1D synthetic modelling and inversion of FDEM and TDEM methods will be initially studied for overburden stripping using codes EM1DFM (Farquharson and Oldenburg, 2000) and EM1DTM (Farquharson and Oldenburg, 2006). For the FDEM and TDEM methods, the helicopter-borne DIGHEM and VTEM systems with depth-detection capabilities for conductive anomalies of 150 m and 600 m are investigated, respectively. The DIGHEM system is an on-time system which means it measures the secondary field in the presence of the primary field when the transmitter is emitting five frequencies in the range 900 Hz to 56000 Hz with a sinusoid waveform (Cain, 2000). The VTEM system is an off-time system which means it measures the voltage induced in the receiver loop in time-channels immediately after the current is switched off in the transmitter (Witherly et al., 2004).

Three different scenarios are considered for the modelling: overburden is more conductive than the sandstone; overburden is less conductive than the sandstone; and when there is no good conductivity contrast between overburden and sandstone. Also, for the FDEM method two cases are considered: overburden has magnetic susceptibility; and overburden has no magnetic susceptibility. Also, in this chapter 3D synthetic modelling is performed using a code of Ansari and Farquharson (2014). Then, the 1D inversion is done on the synthetized data to reconstruct the true model. Finally, the 1D inversion is applied to the real VTEM data (see Appendix E for the 1D inversion of real DIGHEM data of Au project).

## 9.2 1D synthetic modelling and inversion of FDEM

1D modelling and inversion of FDEM was done using EM1DFM (using L2-norm; Farquharson and Oldenburg, 2000) for a model with two layers, namely, overburden and sandstone (half-space). Since the depth penetration of FDEM is less than 150 m, only these two layers are considered for the forward modelling. The output of the forward code is the secondary field normalized by the primary field in ppm. A resistivity of 2000 Ohm-m is used for the sandstone. For overburden three scenarios (700 Ohm-m, 1800 Ohm-m and 6000 Ohm-m) are considered. For each of these, three different thicknesses (5m, 25m and 100m) are also considered (see Section 2.5). The scenario for overburden with a resistivity of 1800 Ohm-m is the most representative of the McArthur area in which there is no good conductivity contrast between overburden and sandstone.

For magnetic susceptibility, two values of 0.005 SI and 0 SI are considered for overburden. A value of 0 SI is considered for sandstone. Thus, input files have different resistivity values as well as magnetic susceptibility values. Actually, it is totally relevant to consider non-zero susceptibility given what I know of the overburden in most parts of the Athabasca Basin (see Section 2.5.3). An elevation of 40 m is considered as EM sensor height, and 2% noise is added to the data (Cain, 2000).

The initial model for all the 1D inversions in this chapter is made of layers with different thicknesses increasing from surface to depth with a factor of 1.134. Also, a constrained inversion is applied in order to investigate its effect on the results (see Section 4.5). It is done by using a reference model in which I assume that I know the conductivity of the last

layer in the inversion mesh. So its weight for the reference model is much higher than other layers.

Figures 9.1 to 9.3 show the true models as well as inversion results for the scenarios mentioned above when the magnetic susceptibility of the overburden is 0SI. Also, these figures show the results for the constrained inversions. Figures 9.4 to 9.6 show the results when the magnetic susceptibility of overburden is 5E-3SI. Figures 9.1 to 9.6 involve the results for the three different overburden thicknesses (5 m, 25 m and 100 m) since the variation of the overburden thickness in the McArthur-Millennium corridor is mostly in the range of 5 to 100 m. For the scenario in which the overburden is more conductive than the sandstone, the results are shown in Figures 9.1 and 9.4. Figures 9.2 and 9.5 show the results for the scenario in which there is no good conductivity contrast between overburden and sandstone. Also, Figures 9.3 and 9.6 show the results for the scenario in which the overburden is more resistive than the sandstone.

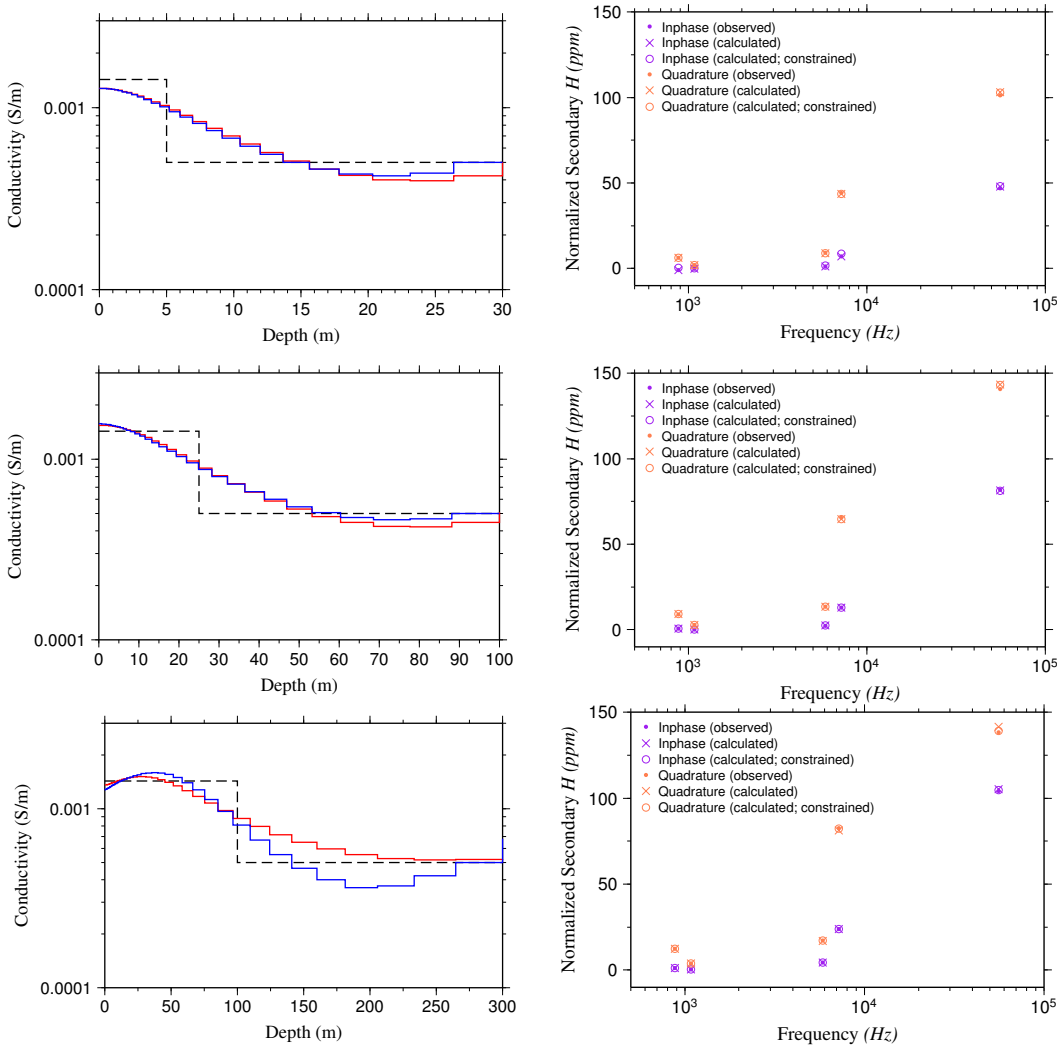


Figure 9.1: Left: true model (black dashed line), the result of inverting the synthetic data set from the true model (red line), and the constrained inversion result (blue line) for the model with the more conductive, non-susceptible overburden. Right: observed and calculated data. Overburden with different thicknesses 5m (top), 25m (middle) and 100m (bottom) is investigated.

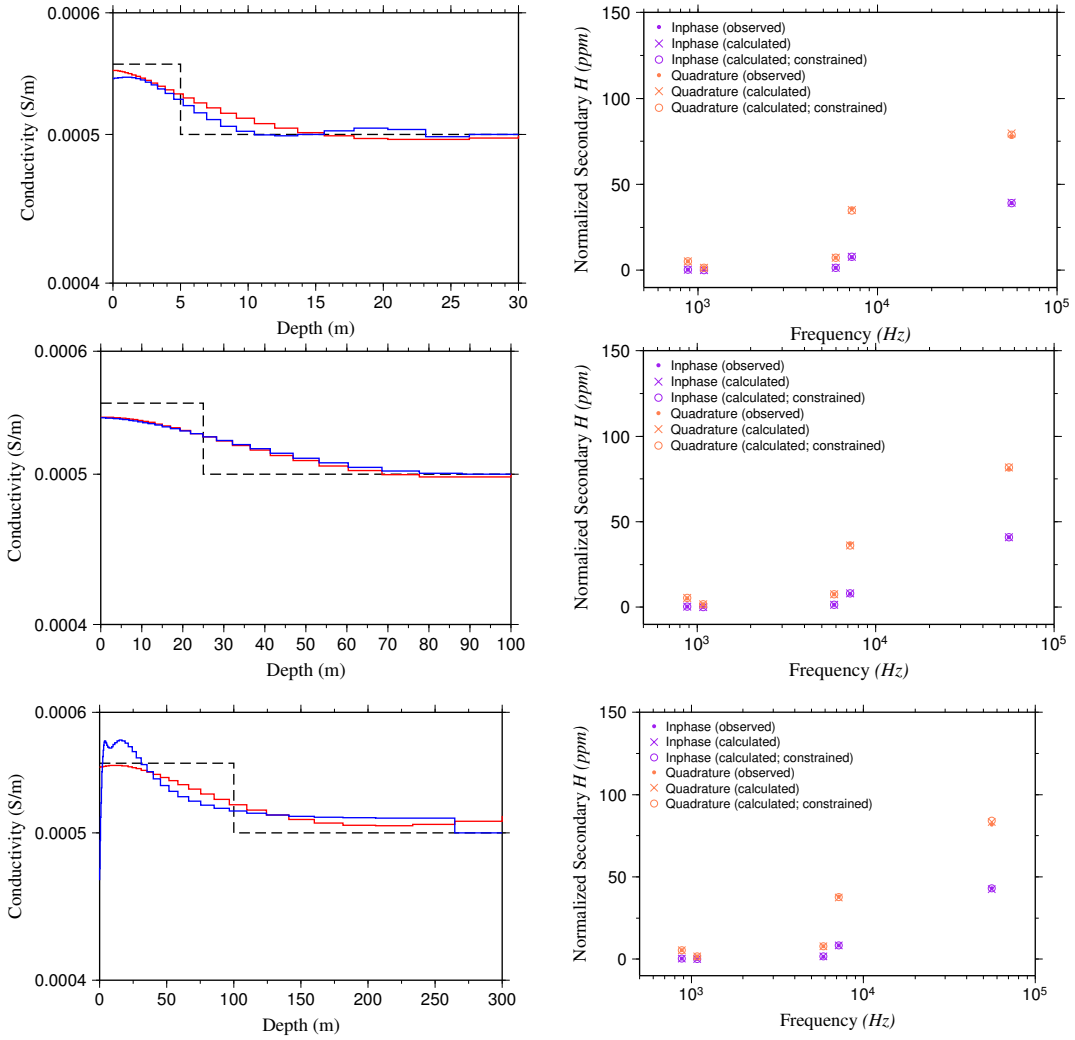


Figure 9.2: Left: true model (black dashed line), the result of inverting the synthetic data set from the true model (red line), and the constrained inversion result (blue line) for the model with the low conductivity contrast and non-susceptible overburden. Right: observed and calculated data. Overburden with different thicknesses 5m (top), 25m (middle) and 100m (bottom) is investigated.

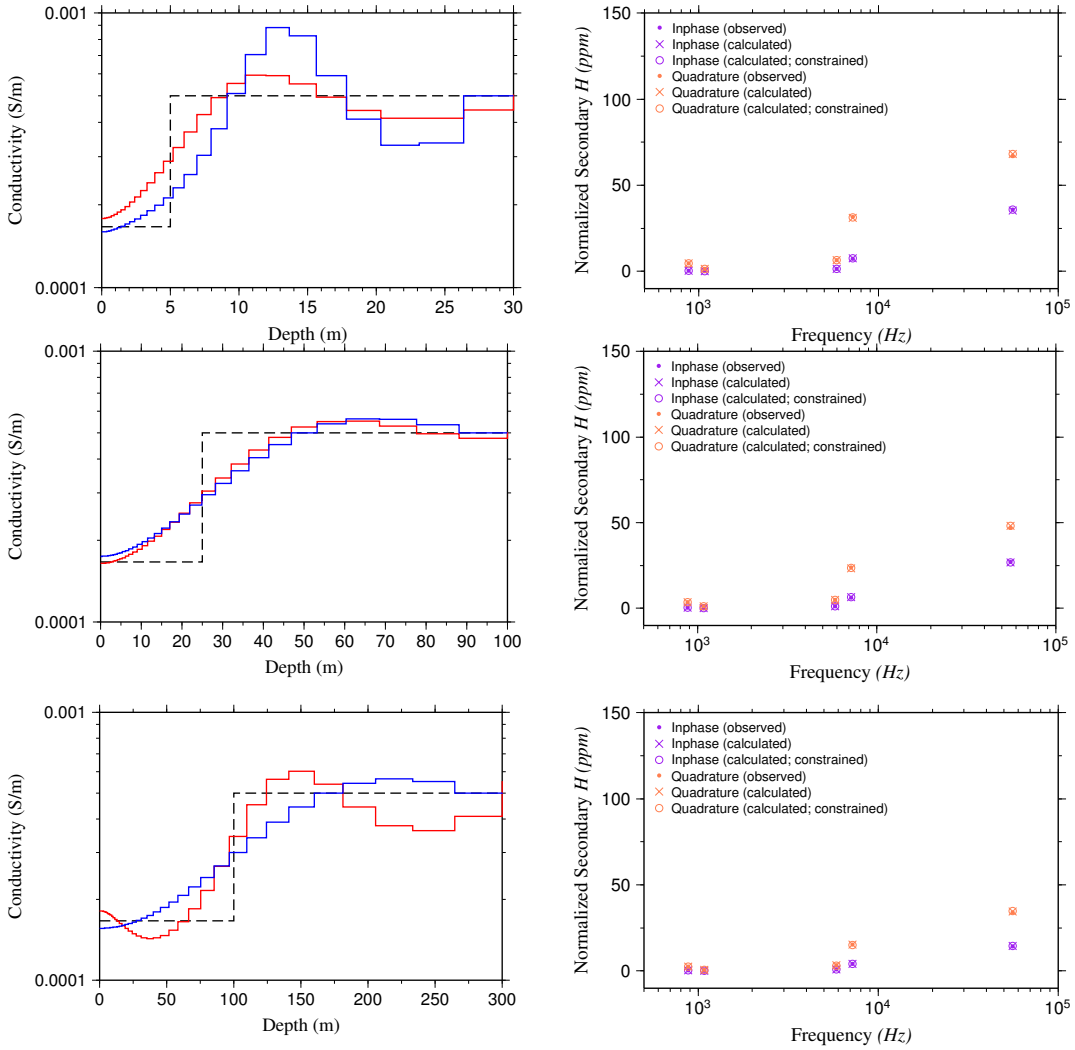


Figure 9.3: Left: true model (black dashed line), the result of inverting the synthetic data set from the true model (red line), and the constrained inversion result (blue line) for the model with the more resistive, non-susceptible overburden. Right: observed and calculated data. Overburden with different thicknesses 5m (top), 25m (middle) and 100m (bottom) is investigated.

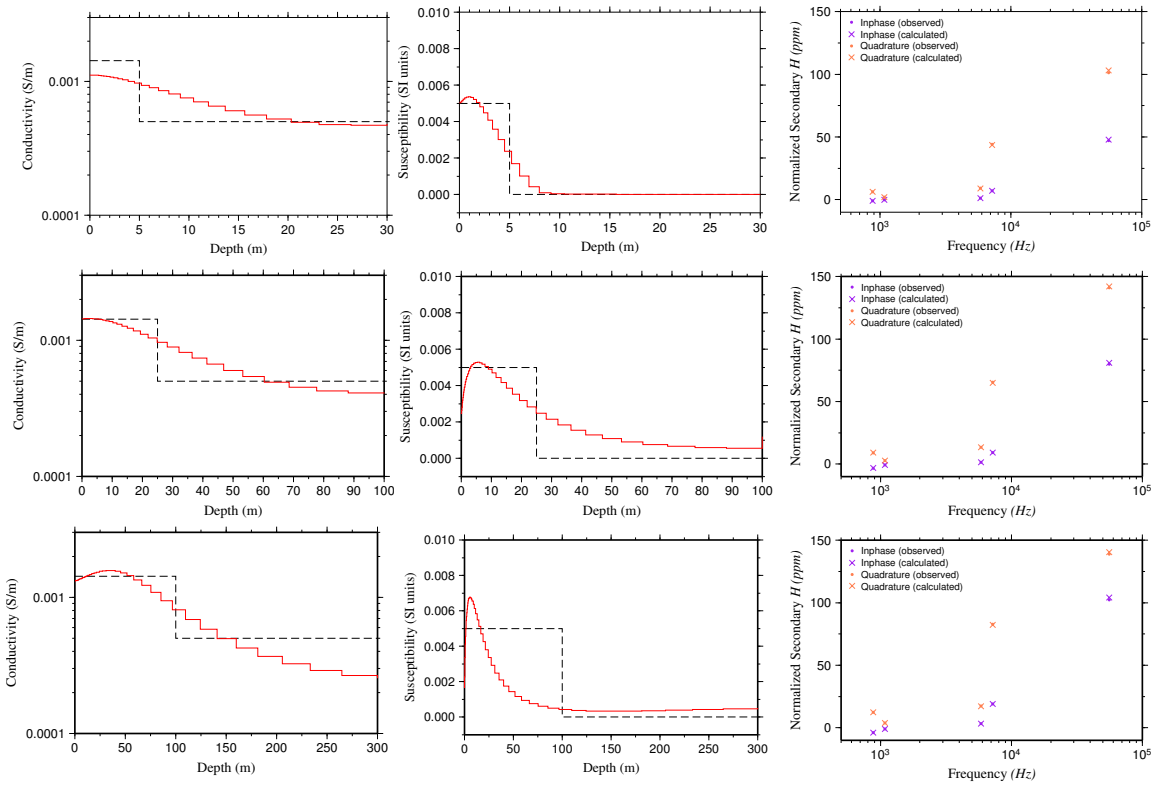


Figure 9.4: Left and middle: True model (black dashed line) and the result of inverting the synthetic data set from the true model (red line) for conductivity and magnetic models. Right: Observed and calculated data. Overburden with different thicknesses 5m (top), 25m (middle) and 100m (bottom) is investigated.

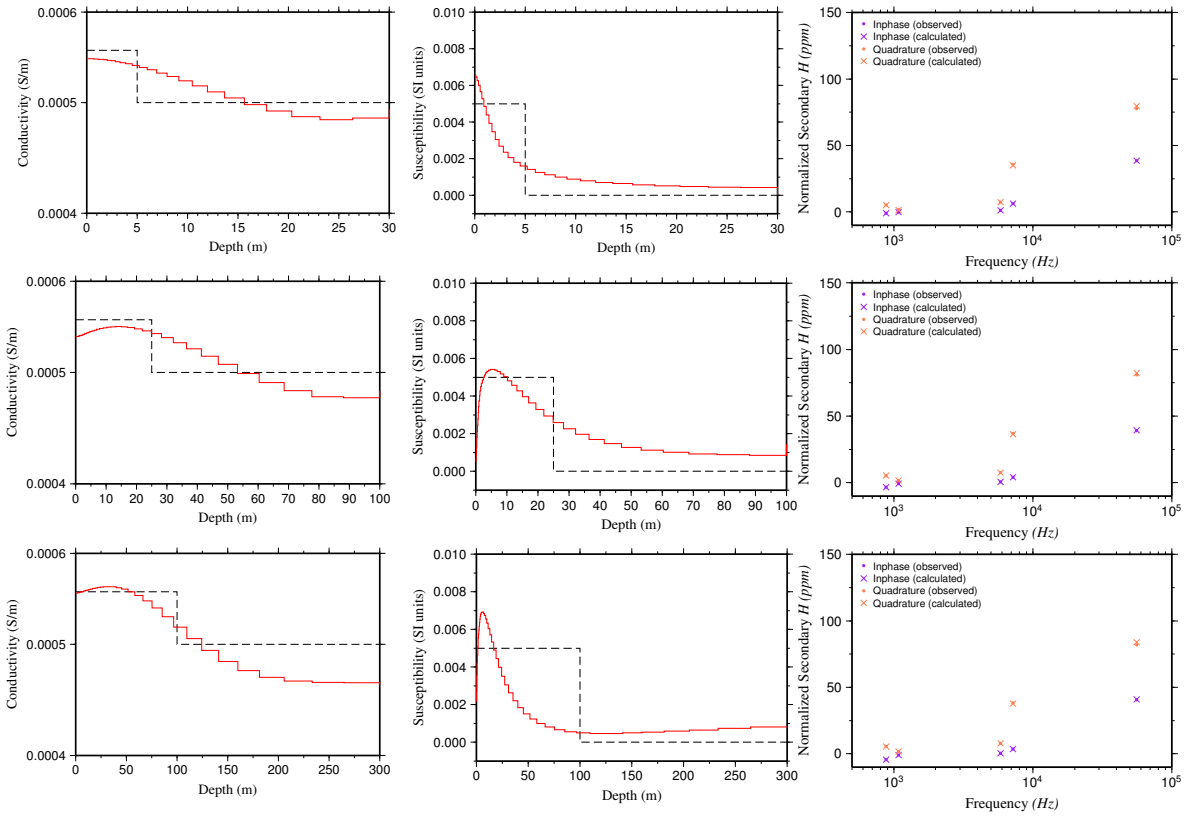


Figure 9.5: Left and middle: True model (black dashed line) and the result of inverting the synthetic data set from the true model (red line) for conductivity and magnetic models. Right: Observed and calculated data. Overburden with different thicknesses 5m (top), 25m (middle) and 100m (bottom) is investigated.

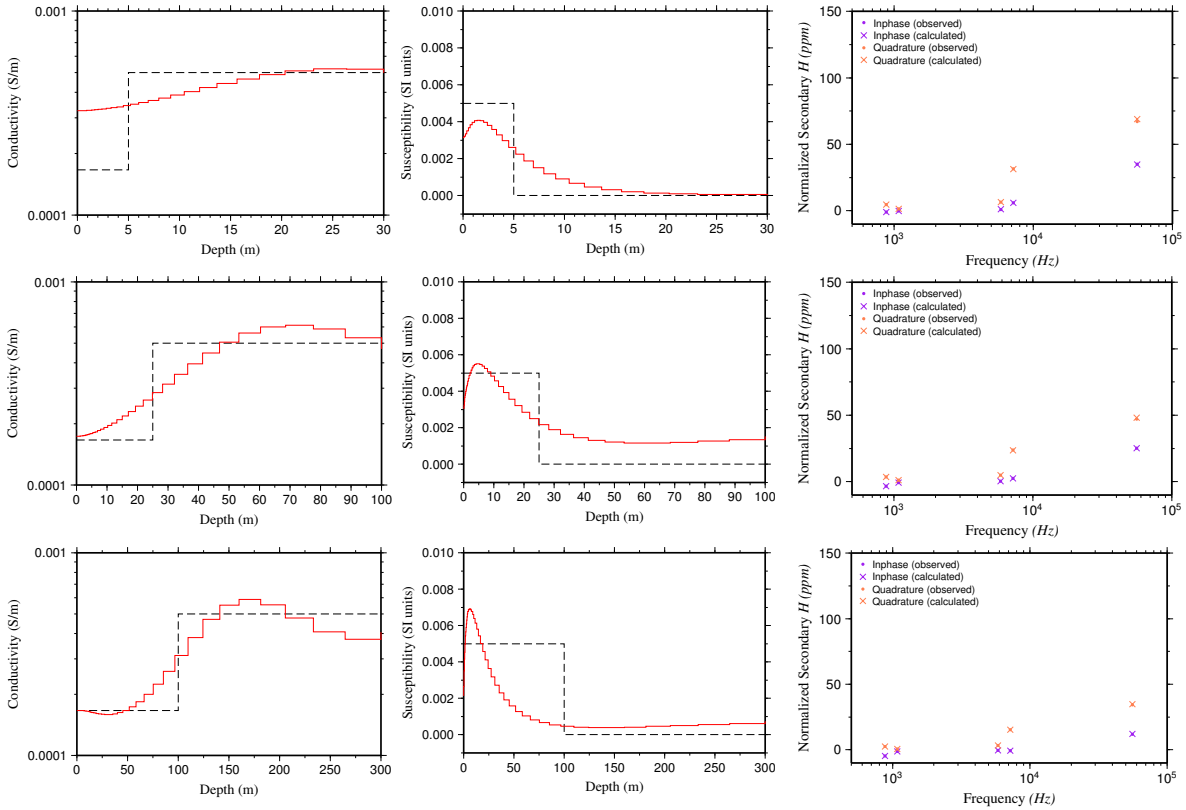


Figure 9.6: Left and middle: True model (black dashed line) and the result of inverting the synthetic data set from the true model (red line) for conductivity and magnetic models. Right: Observed and calculated data. Overburden with different thicknesses 5m (top), 25m (middle) and 100m (bottom) is investigated.

For the constrained inversions, it was expected that the boundary between the layers would be reconstructed better and sharper. However, the results show that in most models it was not helpful. Considering the presence of the magnetic susceptibility in the overburden rocks does not help improve the results. But, in total it can be said that the synthetic modelling and inversion results show that DIGHEM can be used for overburden stripping if there is a conductivity contrast between overburden and sandstones. Also, the variation of the various terms of the objective function for an inversion model are shown in Figure 9.7; all other inversions behave in a similar manner.

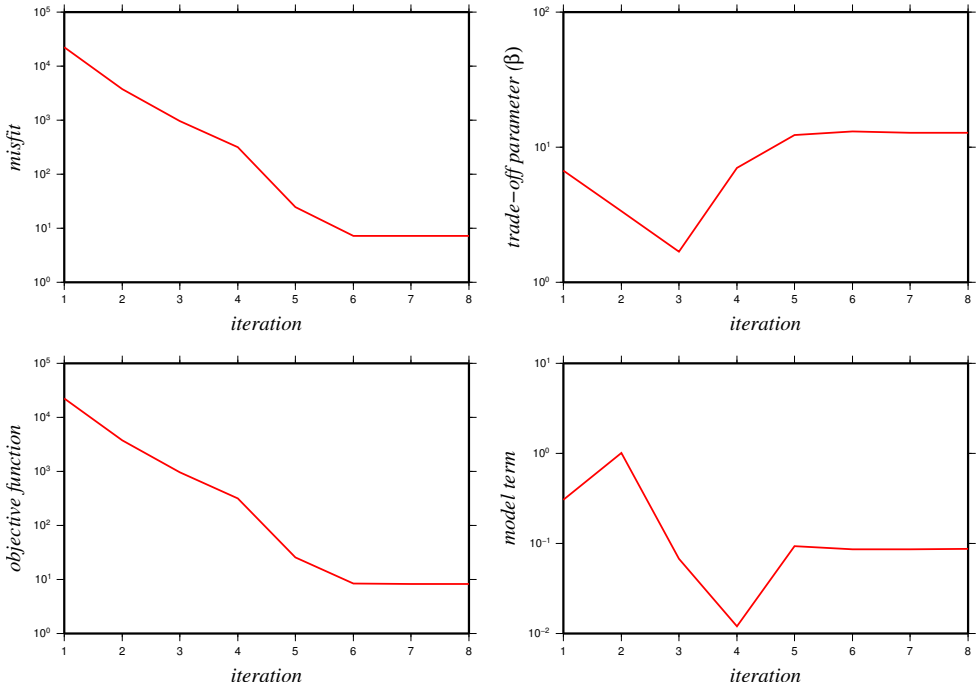


Figure 9.7: Variations of different parts of the objective function such as data misfit ($\phi_d$; top-left), trade-off parameter ($\beta$; top-right), objective function ($\Phi$; bottom-left) and model term ($\phi_m$; bottom-right) at iterations for the inversion of synthetic DIGHEM data of the model in which the overburden thickness and resistivity are 5 m and 700 Ohm-m, respectively.

## 9.3 1D synthetic modelling and inversion of TDEM

1D modelling and inversion of TDEM is done using EM1DTM code (Farquharson and Oldenburg, 2006) for two main scenarios: two layers (overburden and sandstone (half-space); Figures 9.9 to 9.11); and four layers (overburden, sandstone, graphitic zone and basement (half-space)); Figures 9.12 to 9.14). These four layers are considered in the modelling as the uranium deposit in the Athabasca Basin is mostly located close to the graphitic fault and the unconformity between sandstone and basement (see Chapter 2). Also, the investigation depth for TDEM is more than FDEM (see Section 3.5). EM1DTM code is able to invert the data in both methods L1-norm and L2-norm.

In this modelling, sandstone, graphitic zone and basement have resistivities of 2000 Ohm-m, 50 Ohm-m and 20000 Ohm-m, respectively. But, for the overburden three different resistivities (700 Ohm-m, 1800 Ohm-m and 6000 Ohm-m) were considered. For each of them, three different thicknesses (5m, 25m and 100m) were considered as well. In this modelling the graphitic zone has a thickness of 50 m, and 2% noise is added to the data (adapted from CMIC-Footprints reports; McCracken et al., 1984). Note that real graphitic structures/faults are not horizontal (see Section 2.3), however a horizontal graphitic layer is assumed here as that is all the code can handle. I just want to see if the supposedly deeper-seeing VTEM data can indeed see graphitic conductors at depth or not. An elevation of 30 m is considered for the height of EM coils. The current waveform can have different shapes such as half-sine, square, triangular and trapezoidal shape. In this research, the current

waveform for the 1D VTEM modelling has a shape of trapezoid similar to the current waveform of real VTEM data (Figure 9.8). Off-time starts at 5.74 ms.

Figures 9.9 to 9.11 show the true models as well as inversion (L1- and L2- norms) results for the three different resistivities of the overburden when the true model has two layers. Similar to these figures, Figures 9.12 to 9.14 show the results when the true model has four layers. Each figure involves the results for the cases in which the overburden has three different thicknesses.

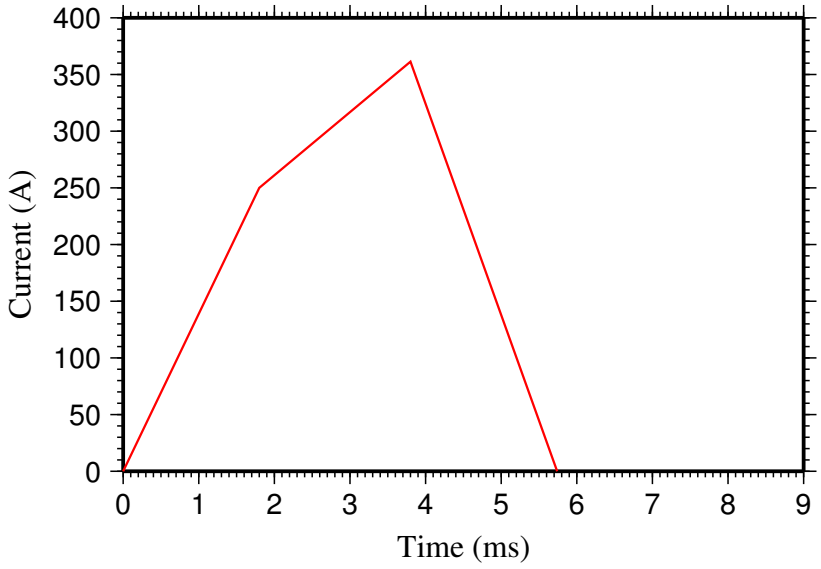


Figure 9.8: Transmitter current waveform for 3D synthetic VTEM modelling.

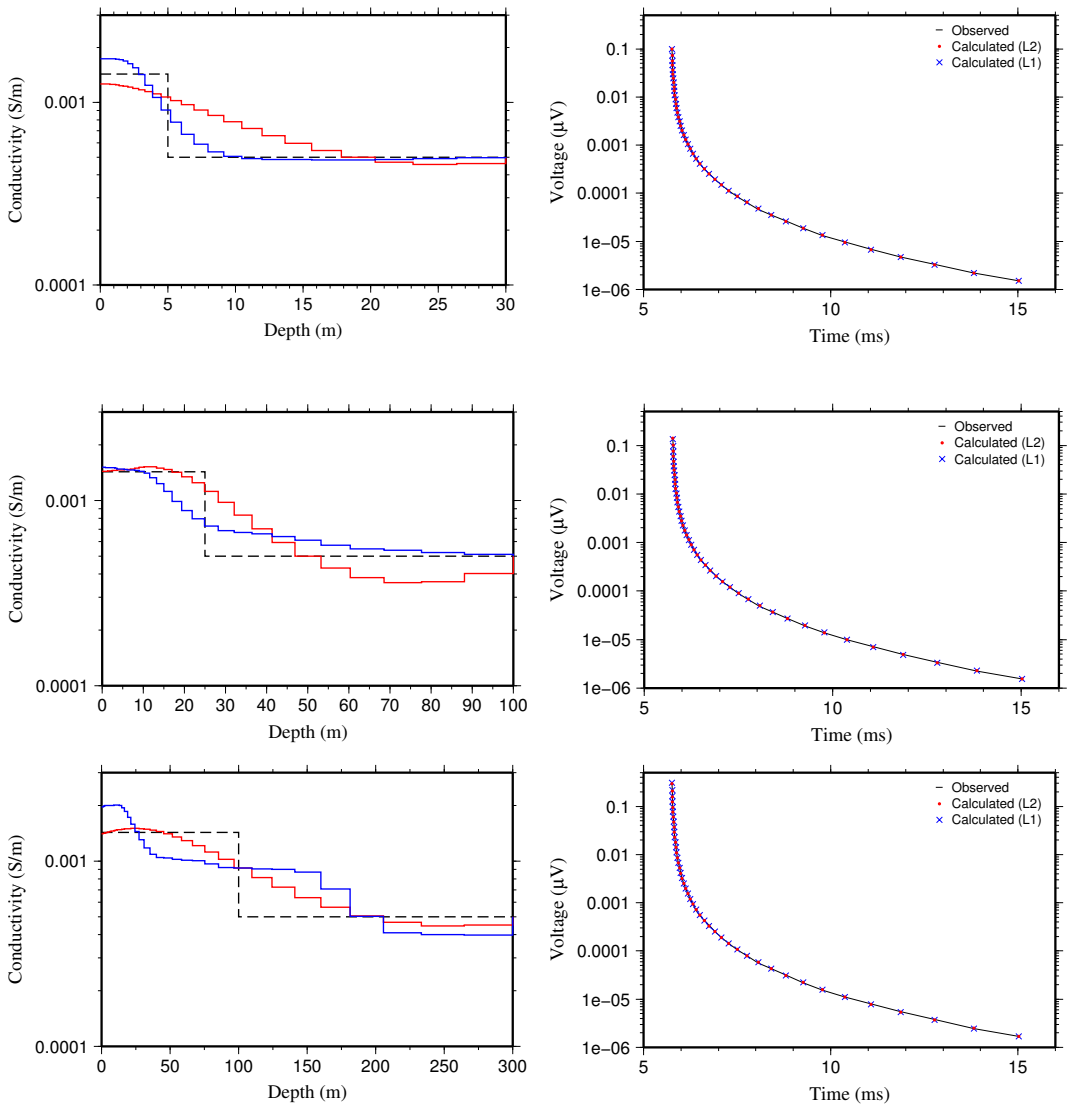


Figure 9.9: Left: true model (black dashed line), and inversion models for L2-norm (red line) and L1-norm (blue line) for the conductive overburden. Right: observed and calculated data. Different thicknesses of overburden 5m (top), 25m (middle) and 100m (bottom) are investigated.

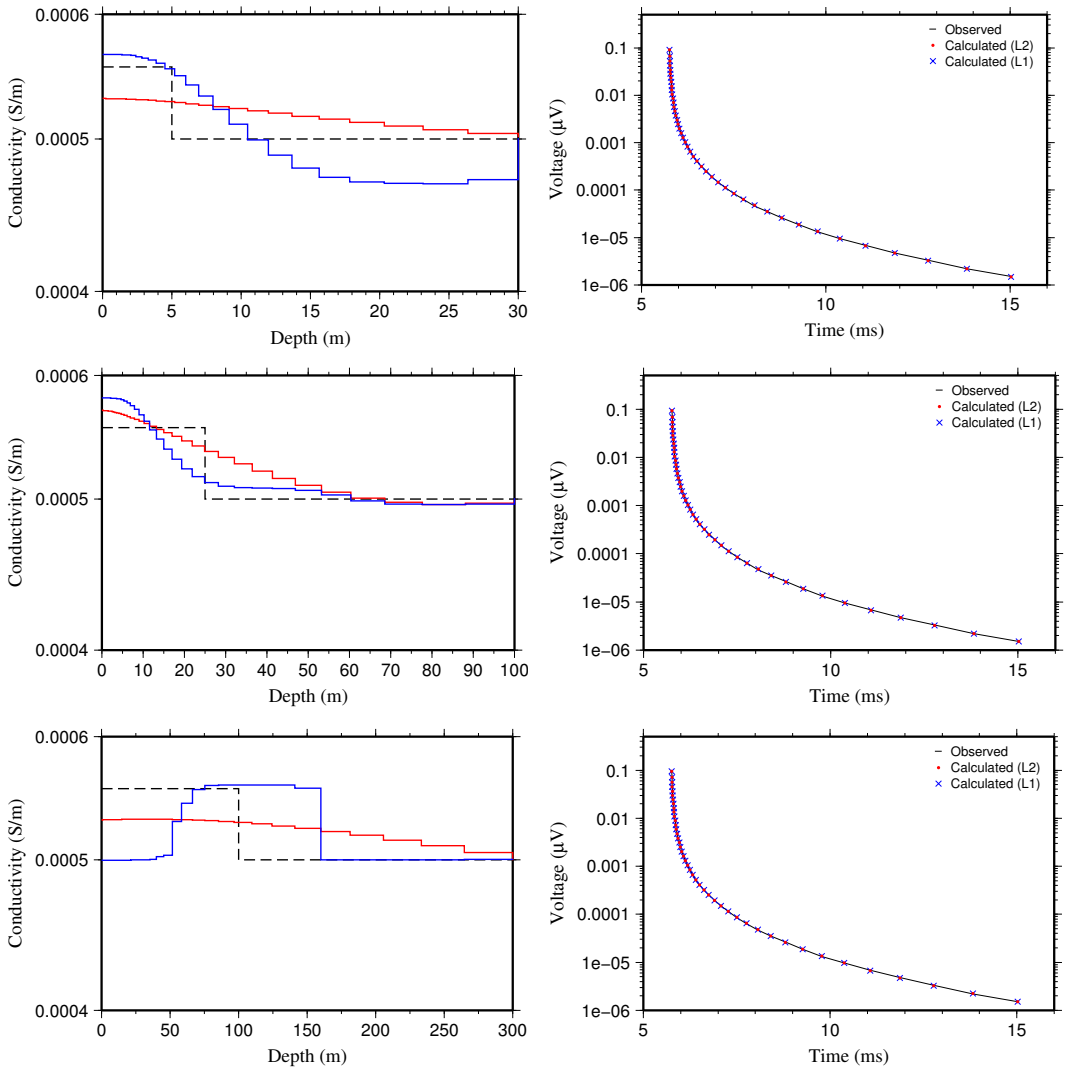


Figure 9.10: Left: true model (black dashed line), and inversion models for L2-norm (red line) and L1-norm (blue line) for a low contrast overburden. Right: observed and calculated data. Different thicknesses of overburden 5m (top), 25m (middle) and 100m (bottom) are investigated.

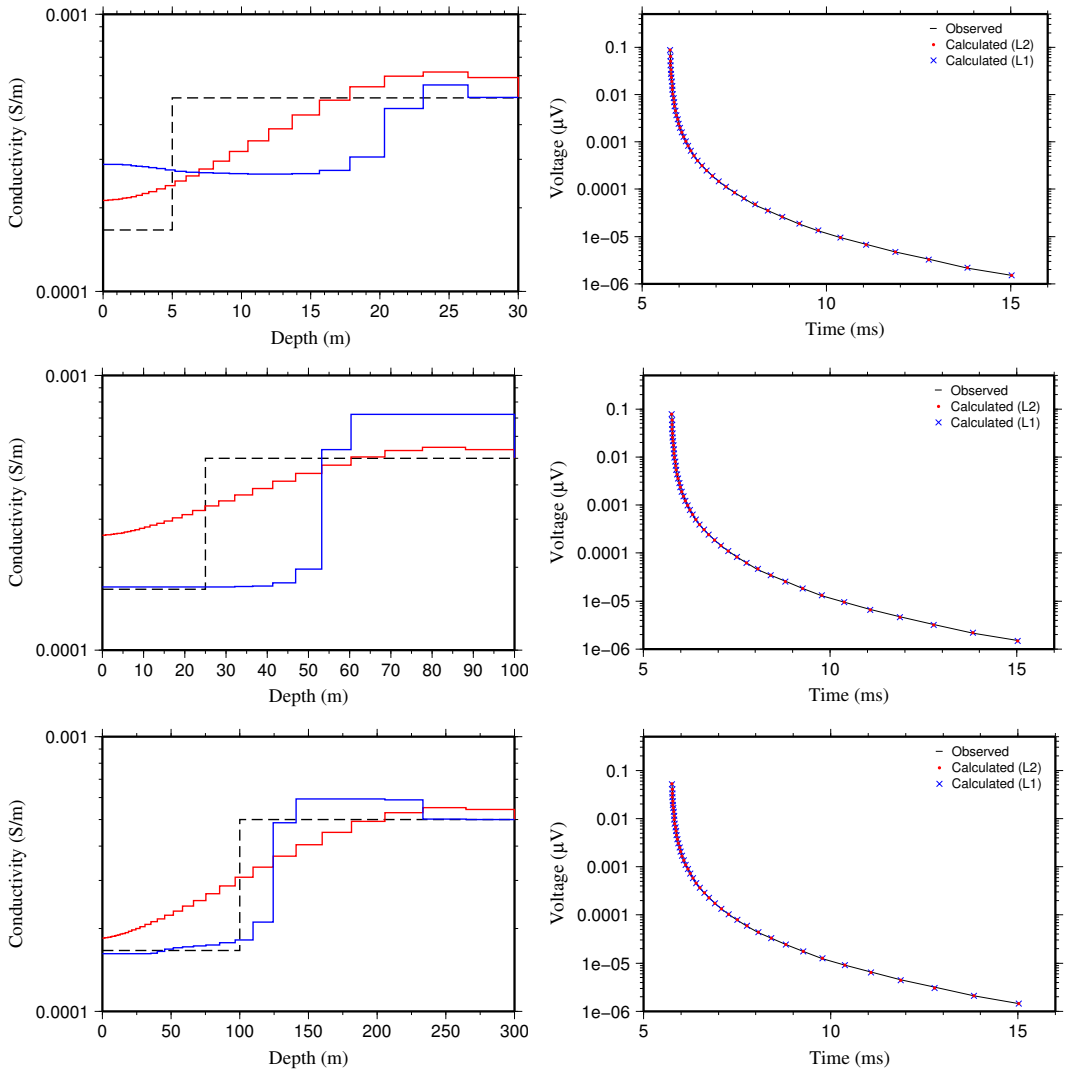


Figure 9.11: Left: true model (black dashed line), and inversion models for L2-norm (red line) and L1-norm (blue line) for resistive overburden. Right: observed and calculated data. Different thicknesses of overburden 5m (top), 25m (middle) and 100m (bottom) are investigated.

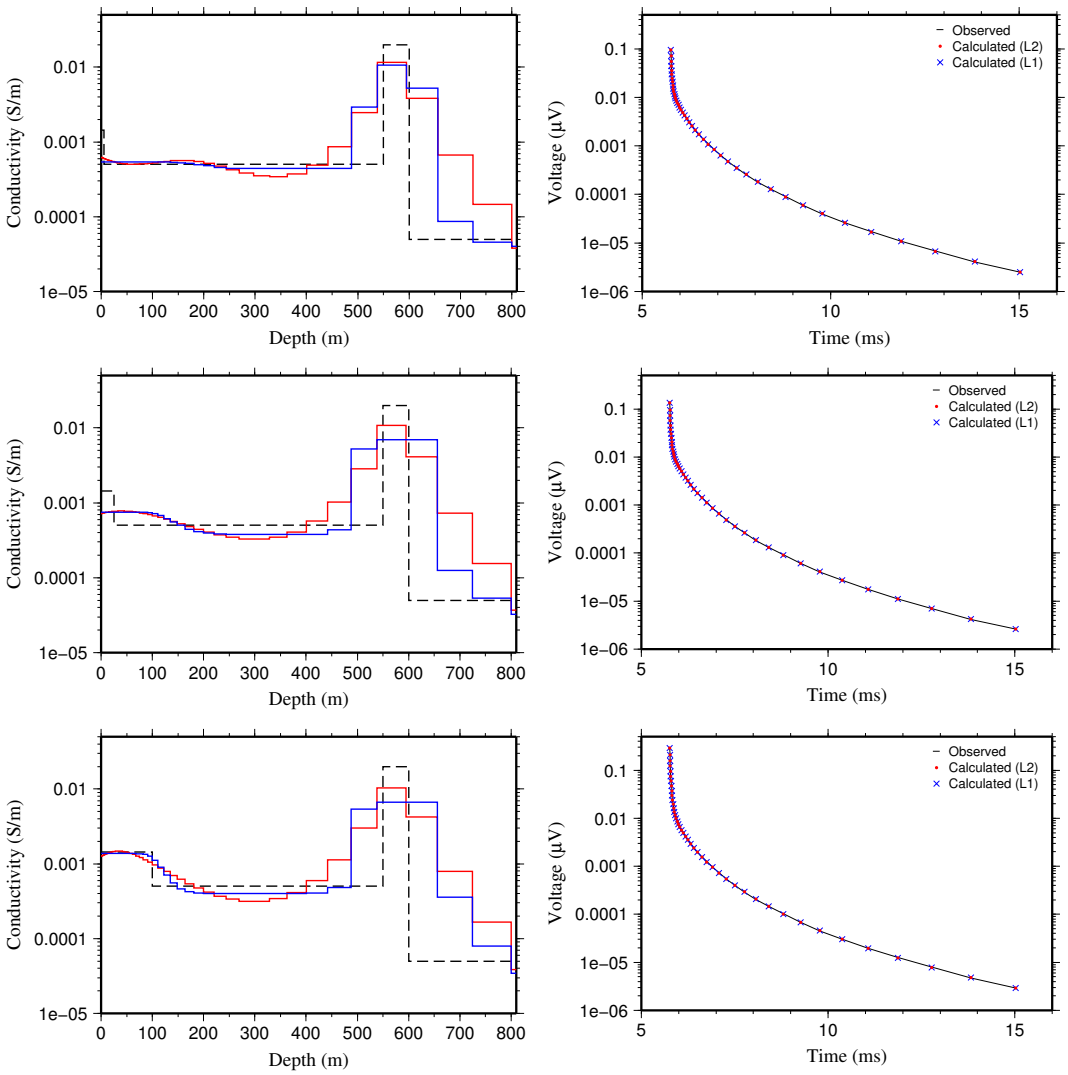


Figure 9.12: Left: true model (black dashed line), and inversion models for L2-norm (red line) and L1-norm (blue line) for the four-layer models with conductive overburden. Right: observed and calculated data. Different thicknesses of overburden 5m (top), 25m (middle) and 100m (bottom) are investigated.

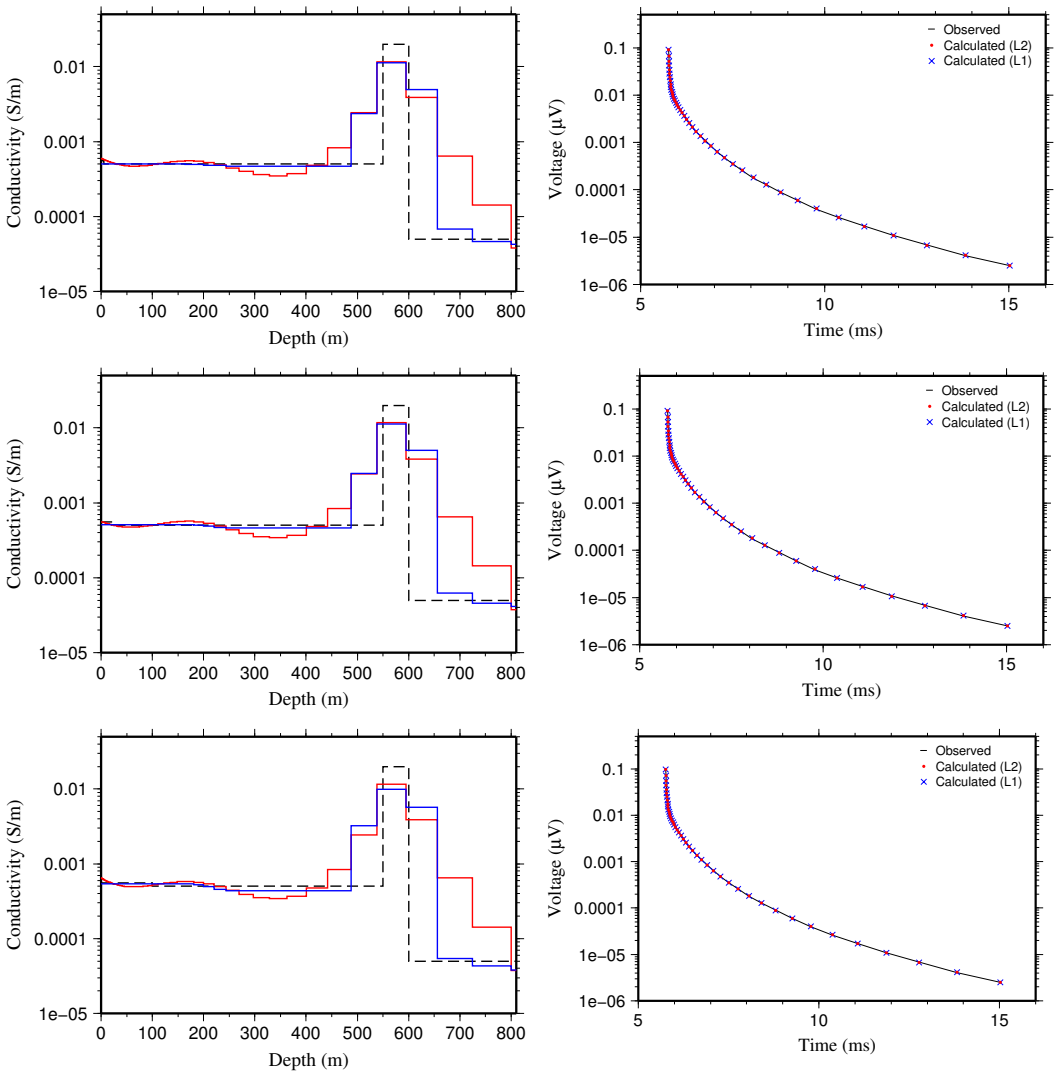


Figure 9.13: Left: true model (black dashed line), and inversion models for L2-norm (red line) and L1-norm (blue line) for the four-layer models with minimal overburden contrast. Right: observed and calculated data. Different thicknesses of overburden 5m (top), 25m (middle) and 100m (bottom) are investigated.

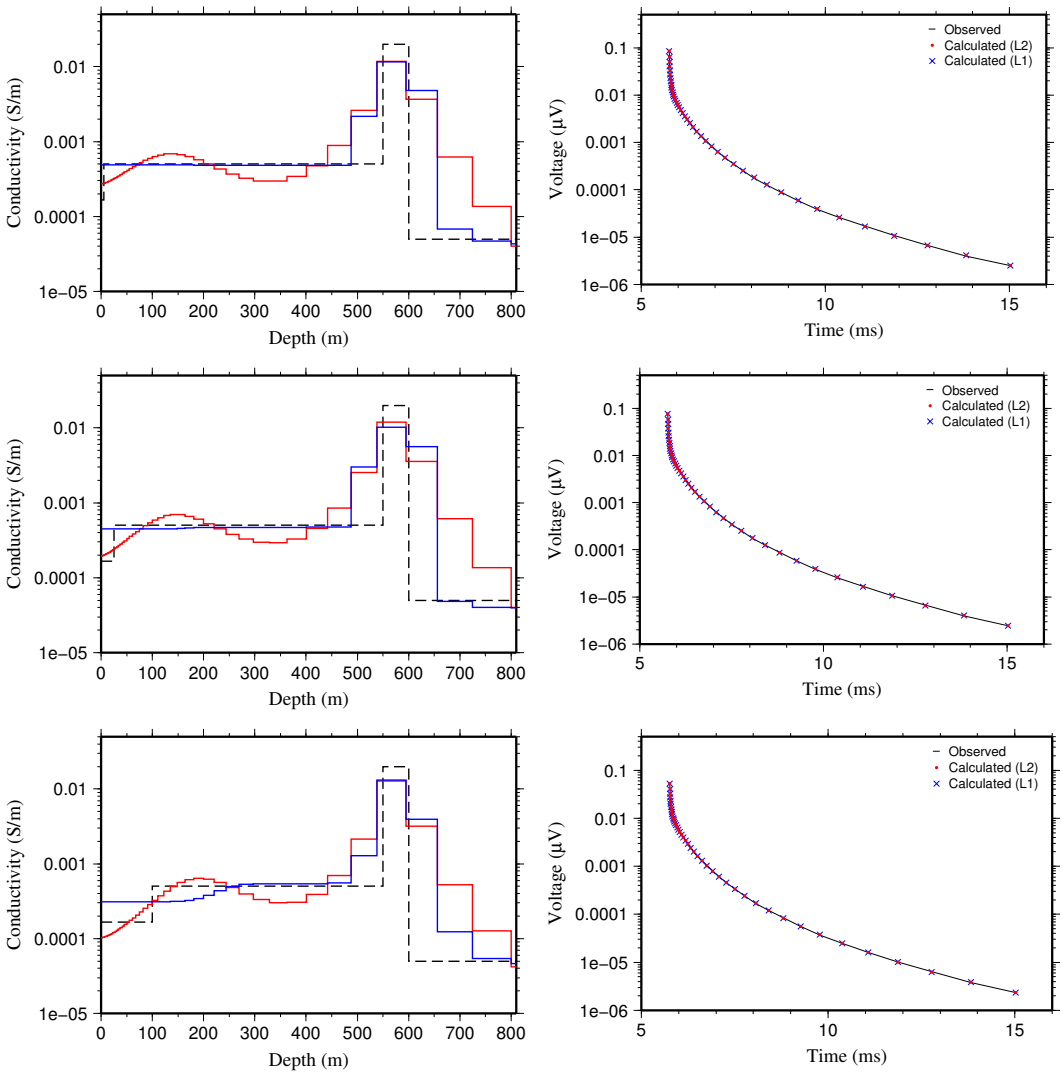


Figure 9.14: Left: true model (black dashed line), and inversion models for L2-norm (red line) and L1-norm (blue line) for the four-layer models with resistive overburden. Right: observed and calculated data. Different thicknesses of overburden 5m (top), 25m (middle) and 100m (bottom) are investigated.

It can be seen that the conductive graphitic zone is reconstructed well in the early-time VTEM inversion results. As expected, by increasing electrical resistivity contrast between layers the inversion results improve. Also, it can be seen that by increasing the conductivity of the layers which are close to the surface, the values of early-times are increasing. And, by increasing the conductivity of the layers at depth, the values of late-times are increasing. The variation of the various terms of the objective function for an inversion model are shown in Figure 9.15; all other inversions behave in a similar manner.

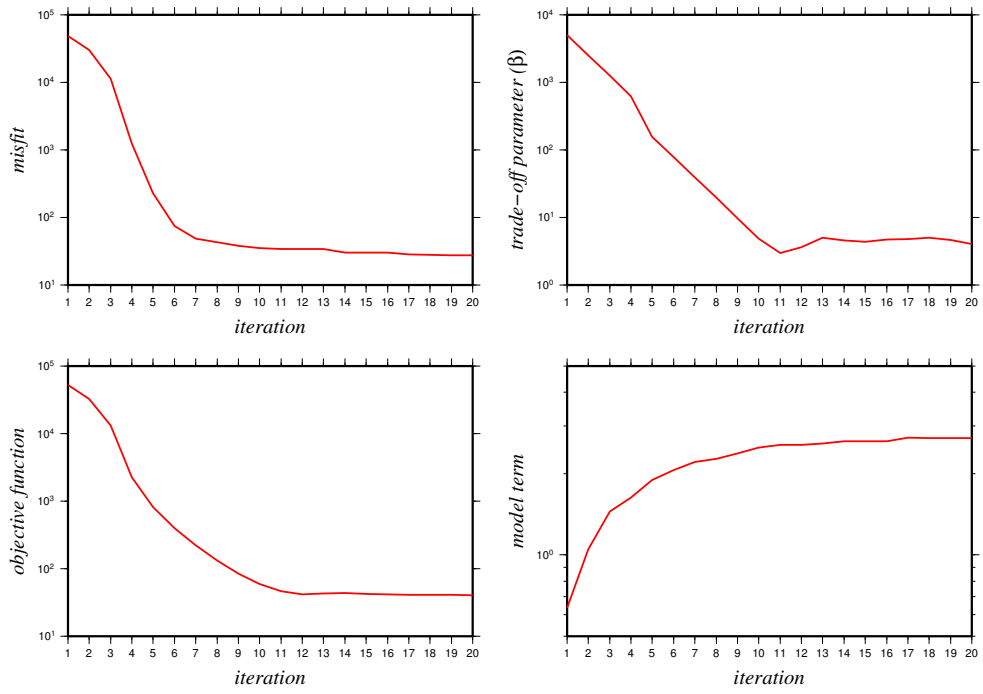


Figure 9.15: Variations of different parts of the objective function such as data misfit ($\phi_d$; top-left), trade-off parameter ($\beta$; top-right), objective function ($\Phi$; bottom-left) and model term ($\phi_m$; bottom-right) at iterations for the inversion (L2-norm) of synthetic VTEM data of the (four layers) model in which the overburden thickness and resistivity are 5 m and 700 Ohm-m, respectively.

## 9.4 3D synthetic modelling and 1D inversion

For 3D modelling, a model (Figures 9.16 and 9.17) was made based on the most recent model in the CMIC-Footprint project (adapted from CMIC-Footprints project; generated by Kevin Ansdell, Ken Wasyliuk and Gerard Zaluski; entered into Gocad by Marc Vallée). The main difference between this model and models used previously in this thesis is in the basement structure in which the geological surfaces were built from recent geological sections and maps. It can be seen that the main geological structures in this model are overburden, sandstone, alteration zone, pelite, psammite, quartzite, granitoid gneiss and graphitic fault. The graphitic fault is the most conductive structure in this model.

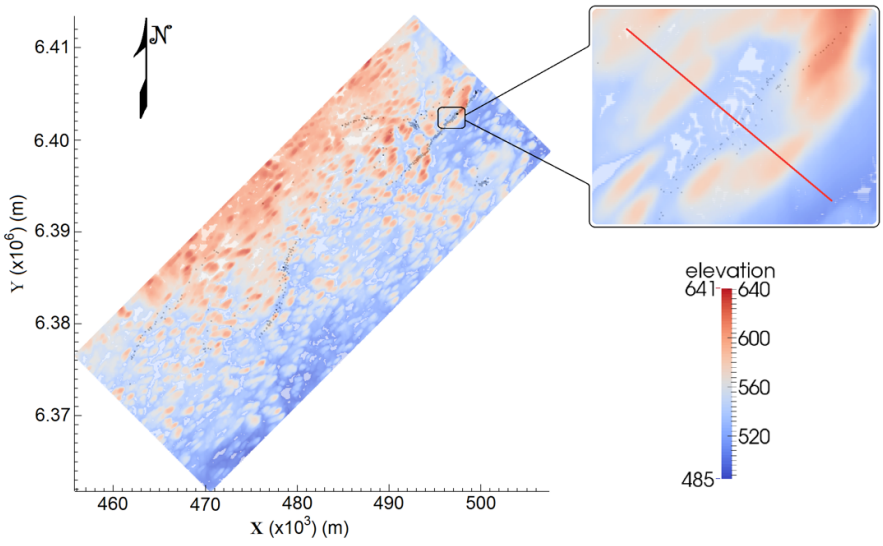


Figure 9.16: Topography of McArthur-Millennium corridor. Inset shows location of survey line (red line) considered for 3D EM modelling.

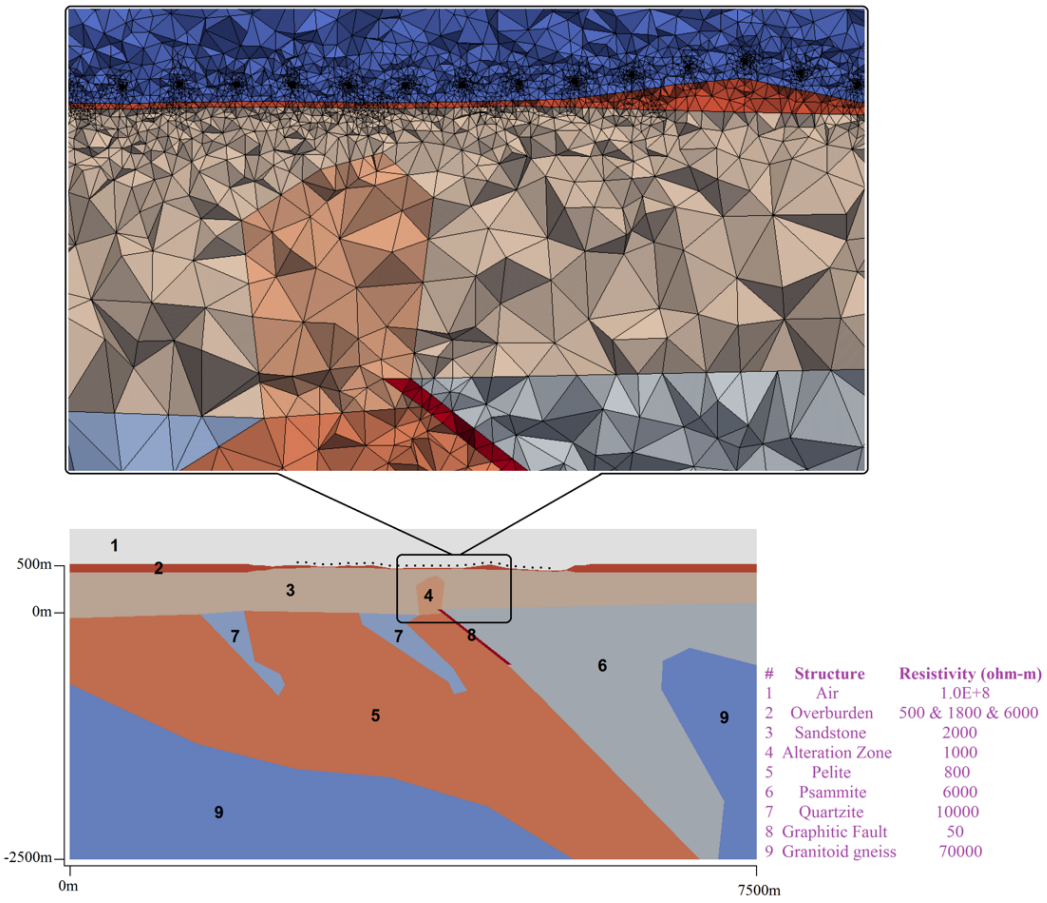


Figure 9.17: Constructed 3D geological structure under the profile (bottom), and tetrahedral mesh (top).

DIGHEM data for three different scenarios, in which overburden has three different resistivities 500, 1800 and 6000 Ohm-m, are calculated using CSEM3DFWD code (Ansari and Farquharson, 2014; see Section 4.4) along a profile with a station spacing of 100m. Also, an elevation of 30 m is considered as EM sensor height. A narrow zone with a thickness of around 40m is considered as graphitic fault with a resistivity of 50 Ohm-m (adapted from CMIC-Footprints reports).

1D inversion was applied to the data. For the inversion of data, a 5% noise is considered as uncertainty as it was added into the data before inversion. Figures 9.18 to 9.20 show the inversion results for the above-mentioned scenarios. DIGHEM data (secondary field normalized by the primary field in ppm) include both in-phase and quadrature parts for five frequencies in the range 880 Hz to 55840 Hz. The fit between observed and calculated data is good. The inversion results show that the overburden base is reconstructed well when there is a good contrast between overburden and sandstone and vice versa. Also, the conductive alteration zone is not reconstructed as it is located at a depth to which the EM fields (at the frequencies considered) are no longer sensitive. In total, the inversion results show that DIGHEM can be used for overburden stripping.

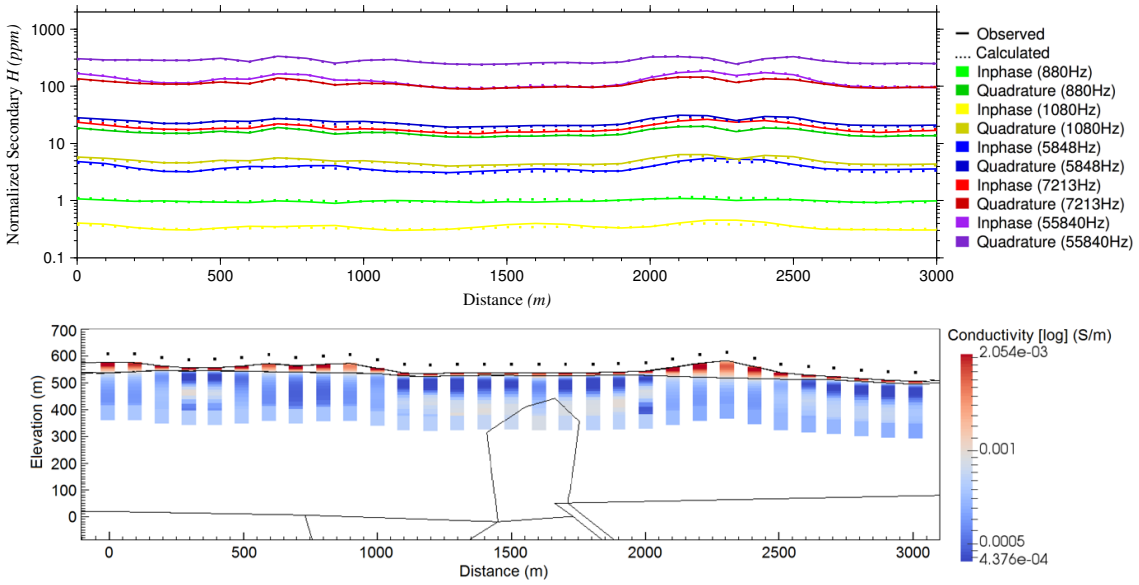


Figure 9.18: Top: observed and calculated data. Bottom: true model (black lines), and 1D inversion results for each station along the profile. True overburden has a resistivity of 500 Ohm-m.

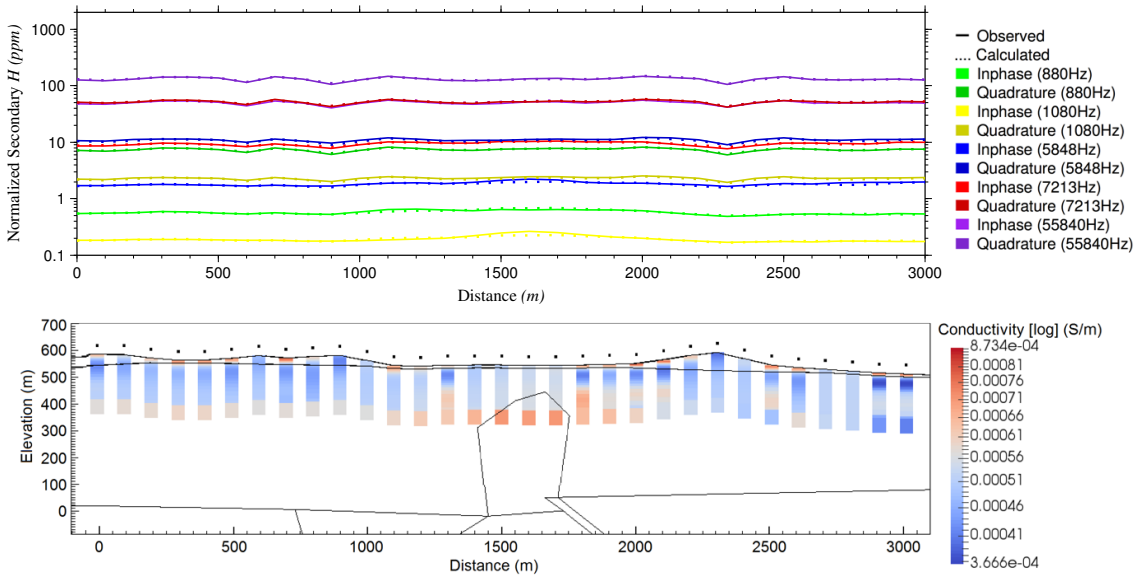


Figure 9.19: Top: observed and calculated data. Bottom: true model (black lines), and 1D inversion results for each station along the profile. True overburden has a resistivity of 1800 Ohm-m.

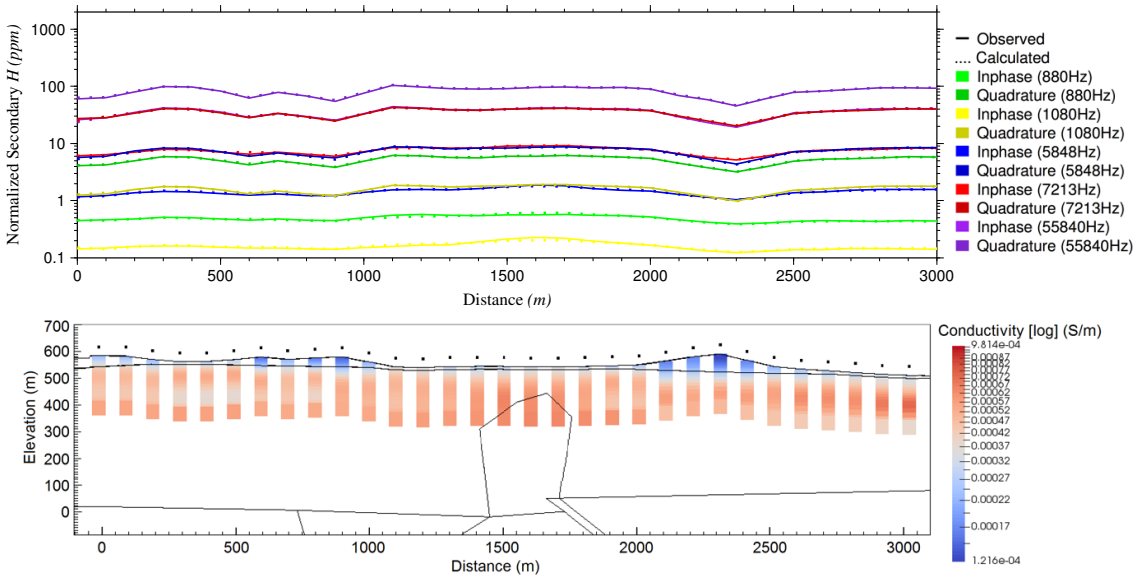


Figure 9.20: Top: observed and calculated data. Bottom: true model (black lines), and 1D inversion results for each station along the profile. True overburden has a resistivity of 6000 Ohm-m.

For 3D VTEM, the same geological model used for DIGHEM was used. Responses were computed initially in the frequency domain using CSEM3DFWD code (Ansari and Farquharson, 2014) along a profile with a station spacing of 100m. Time-domain voltages were calculated using Fourier transform (i.e., dB/dt; see Section 4.4; Newman et al., 1986; Jones et al., 2016) using 160 frequencies over a frequency range from 1 Hz to 100 MHz. VTEM data for three different scenarios were considered, in which overburden has three different resistivities 500, 1800 and 6000 Ohm-m. Also, an elevation of 30m is considered as EM sensor height. A dipole moment and a current of 1 $Am^2$ and 1 A is considered for the modelling, respectively. Since the data are transforming from frequency domain to time domain, the current waveform (by default) has a shape of square (Figure 9.21). Off-time starts at 5.74 ms. 1D inversion is applied on the data. For the inversion of data, a variable range of noise from 0.5% (for early times) to 100% (for late times) is considered as uncertainty (Figure 9.22). Figures 9.23 to 9.25 show the inversion results for the mentioned scenarios. It can be seen that the base of overburden reconstructed by the VTEM method is not as good as the DIGHEM method. But, as the conductivity contrast increases, the inversion results improve.

For EM modelling, the mesh should be refined especially at the receiver points and, in order to have a quality mesh, each tetrahedron should have as close to equal edges and angles as possible. This is possible but by increasing the refinement, the number of cells increases. In order to avoid memory problem, the number of cell cannot be increased (and consequently the refinement) easily. Also, the refinement for the receiver can be controlled by considering a small cell (a fine tetrahedron with the edge size of 1m) at receiver points.

This causes the other cells around the receiver point be small and refined. The maximum refinement was applied in the modelling by considering the limitation of the number of cells (up to one million cells). Nevertheless, responses for very low frequencies were noisy and so some of them were removed before transforming to the time domain. These low frequencies have an effect on the late time measurements.

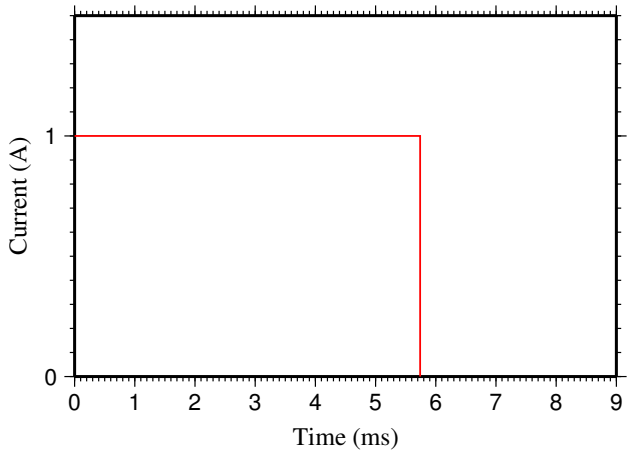


Figure 9.21: Transmitter current waveform for 3D synthetic VTEM modelling.

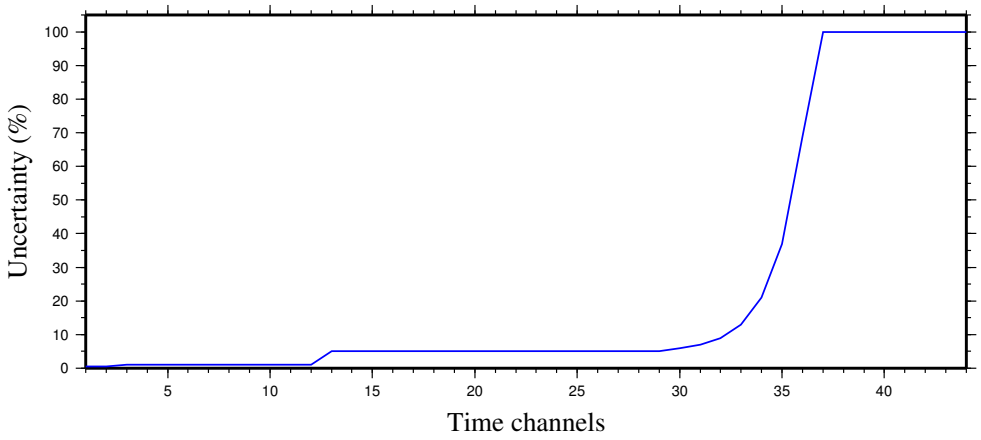


Figure 9.22: Curve shows the uncertainty values in percentage assigned to 44 off-time channels.

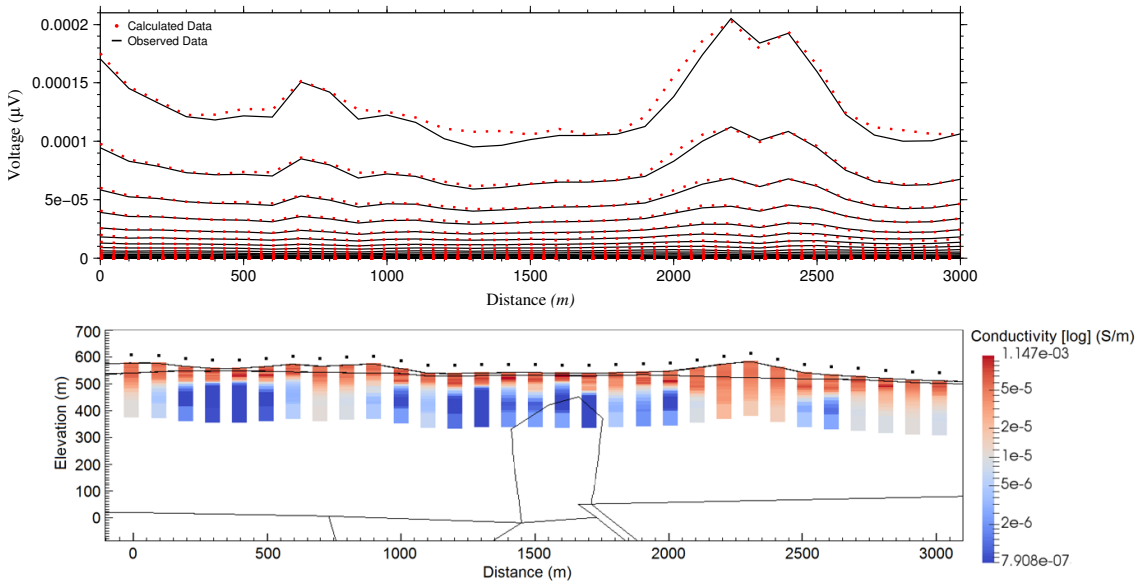


Figure 9.23: Top: observed and calculated data. Bottom: true model (black lines), and 1D inversion results for each station along the profile. True overburden has a resistivity of 500 Ohm-m.

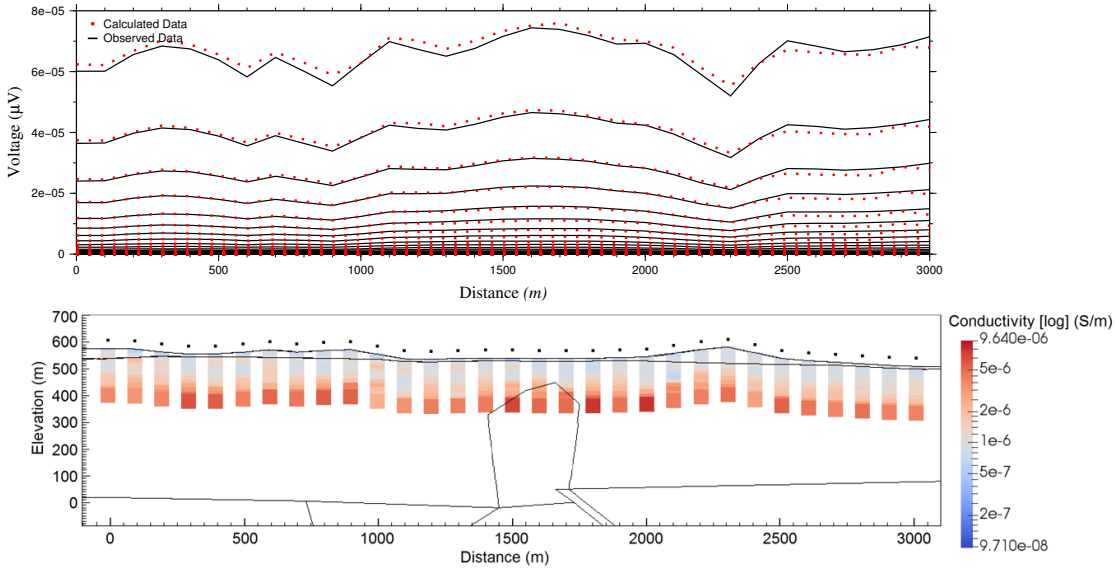


Figure 9.24: Top: observed and calculated data. Bottom: true model (black lines), and 1D inversion results for each station along the profile. True overburden has a resistivity of 1800 Ohm-m.

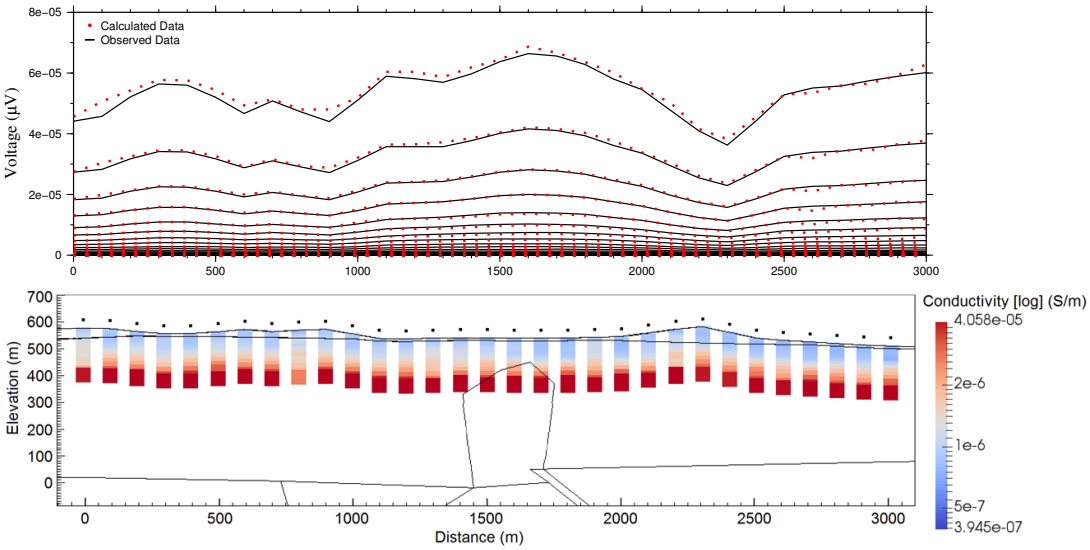


Figure 9.25: Top: observed and calculated data. Bottom: true model (black lines), and 1D inversion results for each station along the profile. True overburden has a resistivity of 6000 Ohm-m.

## 9.5 1D inversion of real VTEM data

1D inversion was applied to the real VTEM data along a part of a profile with 1260 stations over the McArthur River area. VTEM system specifications in CMIC Footprints project were as follows:

**Transmitter**

- Transmitter loop diameter: 35 m
- Effective Transmitter loop area: 3848 $m^2$
- Number of turns: 4
- Transmitter base frequency: 30 Hz
- Peak current: 361.59 A

- Pulse width: 5.74 ms
- Wave form shape: trapezoid
- Peak dipole moment: 1,391,561 nIA
- Average EM Bird terrain clearance: 31 metres above the ground

**Receiver**

- X Coil diameter: 0.32 m
- Number of turns: 245
- Effective coil area: 19.69 $m^2$
- Z-Coil diameter: 1.2 m
- Number of turns: 100
- Effective coil area: 113.04 $m^2$

The transmitter current waveform (first pulse) has a shape of trapezoid, and the off-time starts at 5.74 ms (Figure 9.26). VTEM data (for the time gate number 10) for more than 380,000 stations with a total area coverage of 250 $km^2$ are shown in Figure 9.27. Figure 9.27 also shows the particular line that is inverted.

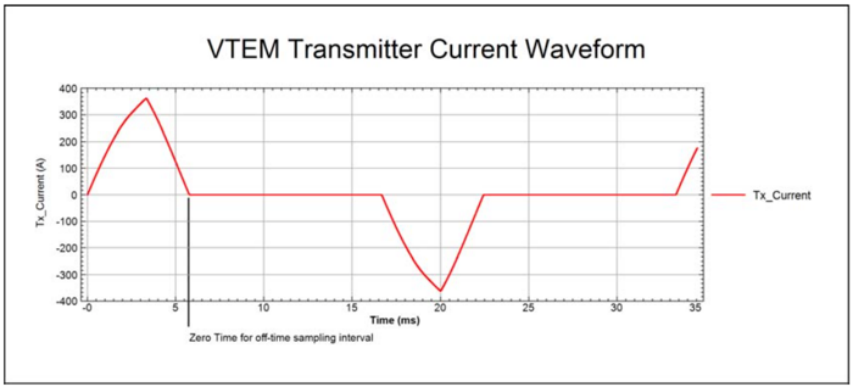


Figure 9.26: Waveform for real VTEM system (Geotech Ltd., 2013).

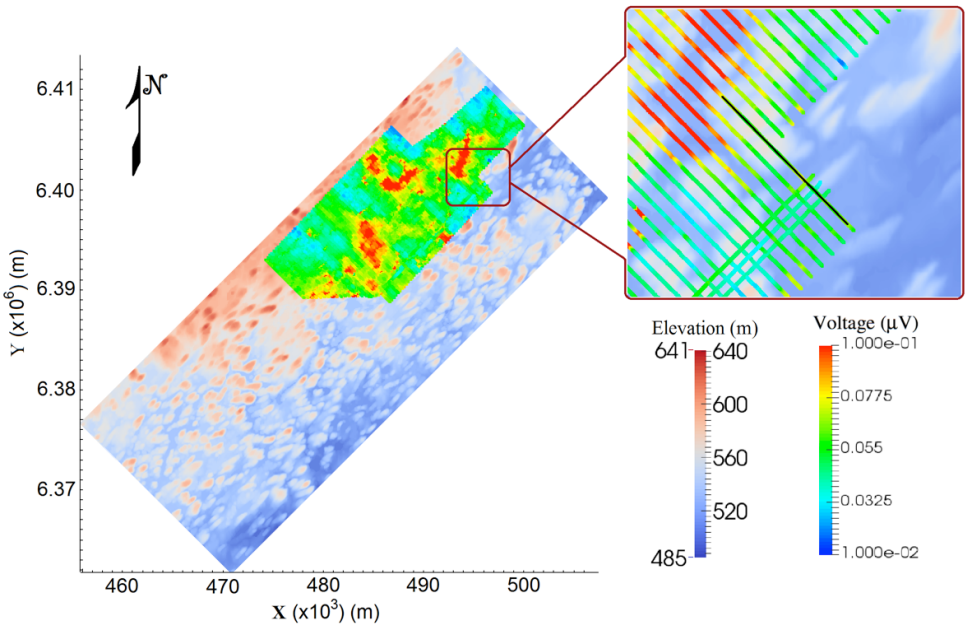


Figure 9.27: VTEM data for the time gate number 10. Inset shows location of survey line (black line) chosen for 1D inversion.

The late-time measurements were noisy. Therefore, the data were filtered using non-linear filtering and smoothing of the data with a moving average filter by Reza Mir (taken from CMIC-Footprints project). 1D inversion using L2-norm was applied on the filtered real VTEM data (Figure 9.28). The same uncertainties applied for the inversion of 3D synthetic data (Figure 9.22) were used for the inversion of real data. There is a similarity between the 1D inversion model and the resistivity depth imaging (RDI) model (adapted from Geotech Ltd., 2013; Figure 9.29). RDI is a quick technique to convert EM profile decay data into an apparent resistivity section, by deconvolving the measured TDEM data. Figures 9.30 and 9.31 respectively show the 1D inversion model and the convergence curves for one of the stations.

The 1D inversion results show three main structures: 1- The first one is a conductive layer at the bottom of the model below -100m elevation which is almost certainly due to the noise in the late-time measurements. This can be explained as follows. An increase in conductivity at depth tends to increase the late-time measurements, and from Figure 9.30 it can be seen that late-time measurements are noisy, and this noise acts to increase the measured values at the late times in a way similar to the effect of a deep conductor. Thus, the inversion code for this data in order to fit the calculated data with the observed data, shift the calculated data to the up. This increase in the value of calculated data is done by generating a (artifact) conductive layer at depth. 2- The second feature is a conductive zone starting from a depth of 0m in the right side of the model between 2000m and 3000m. This zone is located around the P2 fault; thus this can be a signature of the graphitic zone. 3- The third feature is a narrow conductive layer close to the surface. The real location of the interface between overburden and sandstone in shown with a black dot using the data from drill-hole RL-73. Although this conductive layer is close to the interface between overburden and sandstone, there is not a certain geological interpretation for this as there is not a good contrast between the overburden and sandstone. Also, it seems too consistent all the way along the profile to be considered as, for example, a water table.

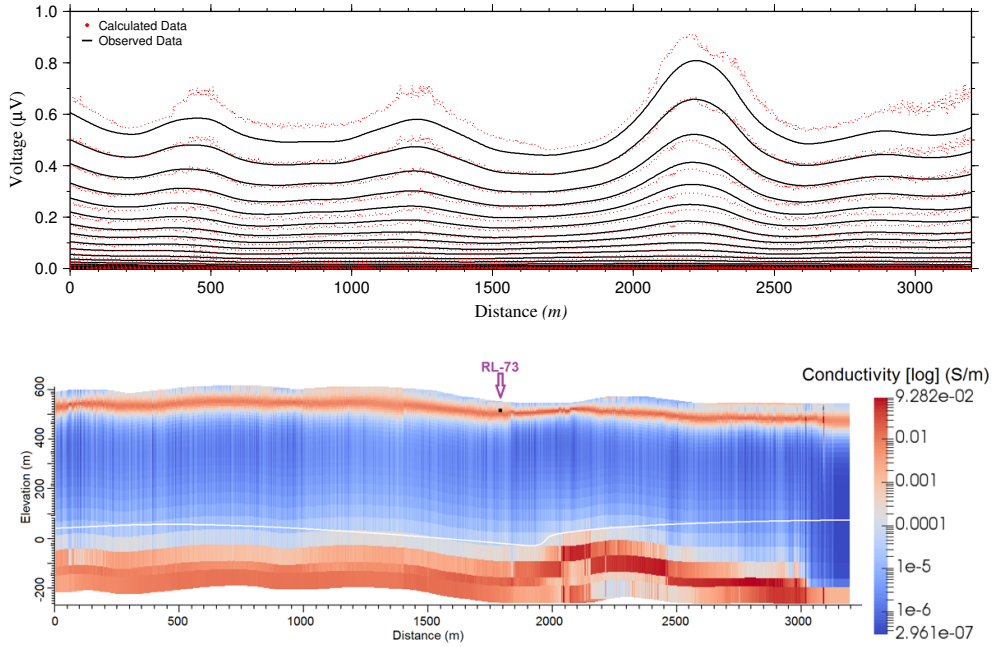


Figure 9.28: Top: real observed and calculated data. Bottom: 1D inversion results for around 1200 stations along a profile. Approximate location of unconformity (white line), and the true location of the overburden base from drill-hole RL-73 (black dot).

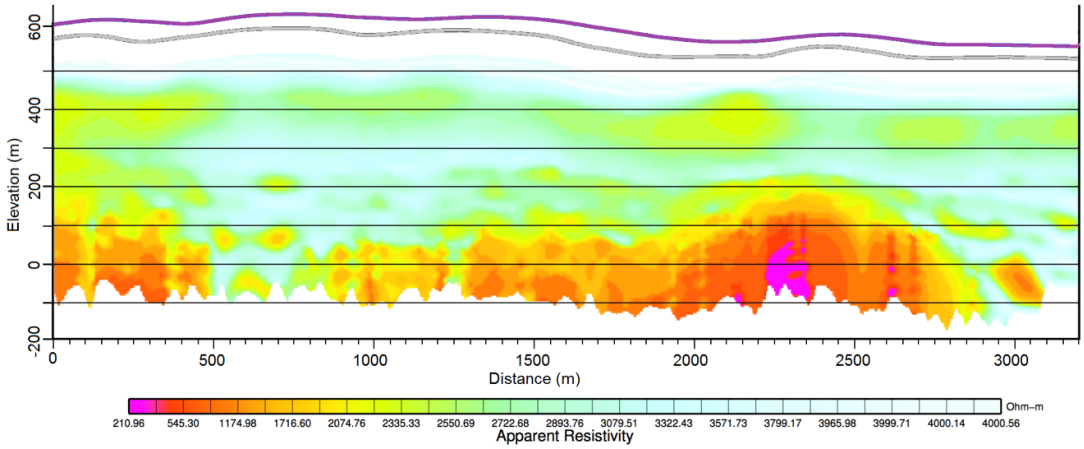


Figure 9.29: Resistivity depth imaging (RDI) done by deconvolving measured TDEM data (Geotech Ltd., 2013). Grey and purple lines on the top show topography and airborne survey line, respectively.

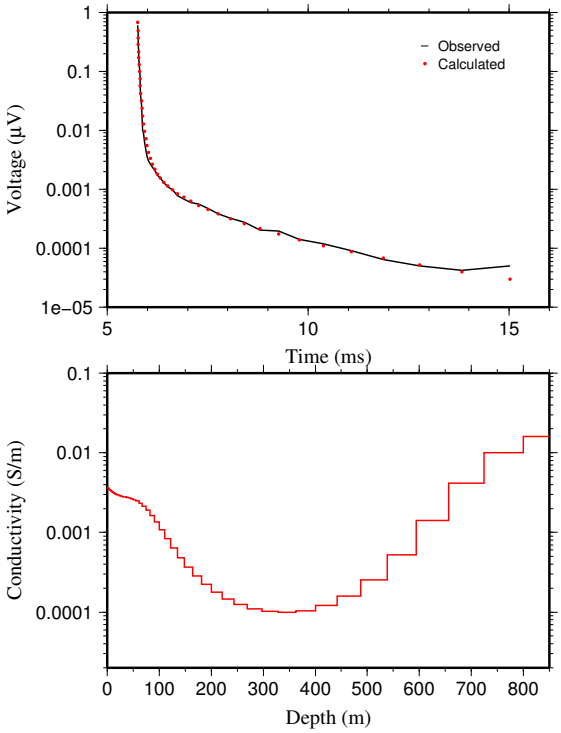


Figure 9.30: Top: observed and calculated data for a station of real VTEM data. Bottom: 1D inversion model.

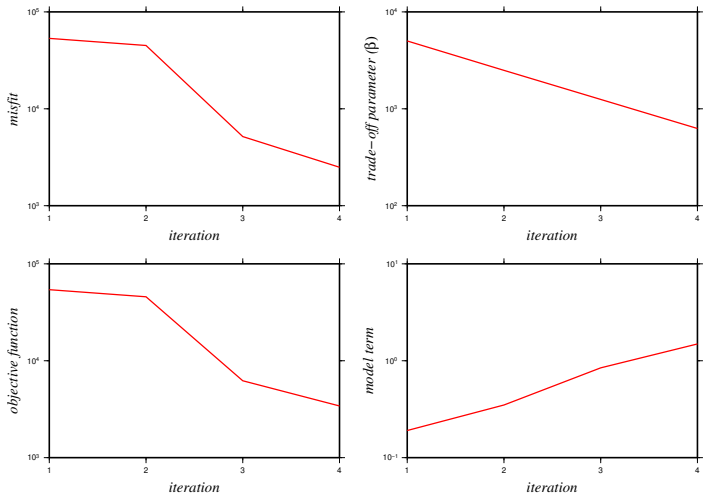


Figure 9.31: Variations of different parts of the objective function such as data misfit ($\phi_d$; top-left), trade-off parameter ($\beta$; top-right), objective function ($\Phi$; bottom-left) and model term ($\phi_m$; bottom-right) at inversion iterations for the model in Figure 9.30.

## 9.6 Conclusions

Electromagnetic method can be used for a wide range of subsurface explorations. EM can be divided in two main categories: frequency domain and time domain. Both of them are investigated in this chapter for airborne cases. For the frequency domain and time domain, DIGHEM and VTEM data were considered, respectively.

1D and 3D forward modelling, and 1D inversion, were considered here. For the 1D DIGHEM case, a model with two layers was investigated in three scenarios in which the upper layer (overburden) had different conductivities. The inversion results show that DIGHEM data is good for overburden stripping. For the 1D VTEM case, two models, one with two layers and the other with four layers, were investigated in three scenarios in which the upper layer (overburden) had different conductivities. Also, DIGHEM and VTEM data were synthetized for a 3D model of the McArthur area. Results showed that DIGHEM data are better than VTEM data for overburden stripping while the VTEM data are better for reconstructing deep conductive structures. 1D inversion was applied on the real VTEM data showed some conductive zones, especially a conductive zone close to the P2 fault which can be related to the graphite fault zone. Other apparent conductive zones are probably due to the noise.

# Chapter 10

# Summary and Conclusion

The Athabasca Basin, Canada, has around 20% of the world's uranium. The uranium deposits are not detectable by direct geophysical methods as they have a small size and are located at depth. But, they are surrounded by large alteration zones which have the potential to be good targets for the gravity method. Also, they are located adjacent to graphitic faults which are good targets for electromagnetic (EM) methods. Seismic can image the unconformity and the basement faults where uranium is mostly deposited.

The focus of this project was on the eastern Athabasca Basin, McArthur-Millennium corridor, which has the world's largest high-grade uranium deposits at depth of 500-800m where basement faults intersect the unconformity. Overburden in the region is dominated with Quaternary glacial deposits. The problem is that the overburden signature in the geophysical data, especially in the gravity data, masks the signature of the other geological structures such as alteration zones. In this research, four geophysical methods (seismic refraction, gravity, magnetic and electromagnetic methods) were investigated for stripping out the overburden response in order to determine the location of the uranium mineralization in the depths with more precision.

Main tactics that were used throughout the thesis were synthetic modelling and inversion

in which models representing the real-life situations were built, data computed for these models, and then these data inverted. Testing was done by considering the various components of the models individually or in various combinations to assess the relative importance of the various contributions to the geophysical data-sets. And of course emphasizing the use and testing and investigation of joint and cooperative inversion methods, especially with information from one data-type helping out the inversion of another data-type. Thus, for the inversion 2D and 3D independent, constrained and joint methods were applied over the McArthur-Millennium site. Also, best inversion methods obtained from synthetic modelling were applied on the available real data. In addition to the modelling and inversion, spectral analysis and filtering were performed on the both synthetic and real gravity data to assess that method's capabilities for identifying and stripping out the contribution from the overburden.

Due to the sensitivity of seismic method to spatial changes of seismic velocities in the subsurface, the independent inversion of the seismic refraction data is a useful method for overburden stripping, whereas the independent gravity inversion is a weak method for this purpose because of reasons such as poor depth resolution as well as the non-uniqueness of interpretation. Thus, joint inversion of gravity and seismic refraction data was tested which was able well to reconstruct the variable thickness of the overburden. The seismic refraction data were essentially enabling the inversion to reconstruct the base of the overburden. After determining the thickness of the overburden using the joint inversion, synthetic modelling showed that the constrained independent inversion of gravity data can illustrate the location of alteration zone at depths. In the synthetic example, the seismic data did not cover the

deep anomaly such as the alteration zone. However, problematic issue such as blind layer and attenuation can be in the seismic refraction data.

Both independent inversions of magnetic and gravity methods are not perfect methods for overburden stripping as these methods have a poor resolution. The joint inversion of magnetic and gravity data was able to reconstruct the basement blocks, the sandstone and the unconformity, however the base of overburden cannot be build well. But, the constrained joint inversion of magnetic and gravity data showed that is a good method for overburden stripping. There are different mathematical methods for the joint inversion, but the best results were obtained using "fuzzy c-mean clustering" method.

EM methods were applied to determine the location of the interface between overburden and sandstone as well as the location of the graphitic faults. For this purpose, both frequency domain (FDEM) and time domain (TDEM) methods were tested. The real scenario considered for FDEM and TDEM methods are airborne DIGHEM and VTEM methods, respectively. Results showed that DIGHEM and VTEM method can be considered as a better method for overburden stripping and detecting the graphitic faults, respectively. Note that there is not a good conductivity contrast between the overburden and the sandstones in the McArthur area that is required to make this work. However, overburden over basement is a little bit of a ubiquitous problem, and often there will be a conductivity contrast, and so the use of EM could work well.

This project as a part of the larger CMIC Footprints project has access to comprehensive geophysical data-sets, physical property data and geological information as well as access

to the results from other researchers in this project. A summary of my research based on the geophysical methods and techniques used in this thesis is shown in Table 10.1.

Table 10.1: A summary of the research done in this thesis.

| | Seismic Refraction (2D) | Gravity (2D) | Gravity (3D) | Magnetics (3D) | DIGHEM (1D/3D) | VTEM (1D/3D) |
|---|---|---|---|---|---|---|
| **Independent Inversion** | Synthetic data only. Successful (for the overburden stripping) if dense shot locations and simple model. | Synthetic data only. Poor results for the overburden stripping. | Synthetic and real data. Poor results for the overburden stripping, and good results for reconstructing the deep structures such as basement. | Synthetic and real data. Poor results for the overburden stripping, and good results for reconstructing the deep structures such as basement. | Synthetic data only. Good results for the overburden stripping (1D and 3D modellings & 1D inversions). | Synthetic and real data. Good results for the overburden stripping if there is a good conductivity contrast. Good results for deep conductive structures such as graphitic faults. |
| **Constrained Independent Inversion** | Not considered. | Synthetic data only. Good for reconstructing the deep structures such as alteration zones (overburden thickness which was constructed using the independent seismic refraction inversion results was considered as the constraint). | Synthetic data only. Poor results for the overburden stripping (based on the drill-hole data, parts of overburden and sandstone thicknesses were considered as constraints). | Synthetic data only. Poor results for the overburden stripping (based on the drill-hole data, parts of overburden and sandstone thicknesses were considered as constraints). | Not considered. | Not considered. |
| **Joint Inversion** | With gravity; synthetic data only. Good (for the overburden stripping) if moderately dense shot locations, and simple model. | With seismic refraction; synthetic data only. Good results for the overburden stripping. | With magnetic; synthetic and real data. Better results than the independent inversions for the overburden stripping, but still not acceptable. Good results for reconstructing the deep structures such as sandstone, unconformity and basement. | With gravity; synthetic and real data. Better results than the independent inversions for the overburden stripping, but still not acceptable. Good results for reconstructing the deep structures such as sandstone, unconformity and basement. | Not considered. | Not considered. |
| **Constrained Joint Inversion** | Not considered. | Not considered. | With magnetic; synthetic and real data. Good results for the overburden stripping as well as for reconstructing the deep structures such as sandstone, unconformity and basement. | With gravity; synthetic and real data. Good results for the overburden stripping as well as for reconstructing the deep structures such as sandstone, unconformity and basement. | Not considered. | Not considered. |
| **Filtering and Spectral Analysis** | N/A | Not considered. | Synthetic and real data. Poor results for the overburden stripping, and good results for the deep structures. | Not considered. | N/A | N/A |

# Bibliography

Aario, R. and Peuraniemi, V., 1992, Glacial dispersal of till constituents in morainic landforms of different types; in Proceedings of the Third International Drumlin Symposium, (ed.) R. Aario and H. Heikkinen; Geomorphology v. 6, p. 9–25.

Alexandre P., K. Kyser, D. Thomas, P. Polito and J. Marlat, 2007. Geochronology of unconformity-related uranium deposits in the Athabasca Basin, Saskatchewan, Canada and their integration in the evolution of the basin. Miner Deposita, DOI 10.1007/s00126-007-0153-3.

Annesley, I.R., Madore, C., and Portella, P., 2005, Geology and thermotectonic evolution of the western margin of the Trans-Hudson Orogen: Evidence from the eastern sub-Athabasca basement, Saskatchewan: Canadian Journal of Earth Sciences, v. 42, p. 573-597.

Ansari, S., and Farquharson, C. G., 2014, 3D finite-element forward modeling of electromagnetic data using vector and scalar potentials and unstructured grids: Geophysics, 79, no. 4, E149–E165.

Averill, S.A., 1976a, Geikie River east, Saskatchewan; overburden drilling report for Conwest Canadian Uranium Exploration, Joint Venture; in Saskatchewan Industry and Resources Mineral Assessment File No. 74H-0017, 71 p.

Bamford, D., Nunn, K., Prodehl, C. and Jacob, B., 1978, LISPB-IV. Crustal structure of northern Britain. Geophys. J. R. astr. Soc., 54, 43–60.

Bell Geospace Limited, 2007, Report of acquisition and processing of Air-FTG data over McArthur river, Read Lake and Rabbit Lake in the Athabasca Basin, Saskatchewan, Canada, 42p.

Bernier, S., 2004, Stratigraphy of the Late Paleoproterozoic Manitou Falls Formation, in the Vicinity of the McArthur River Uranium Deposit, Athabasca Basin, Saskatchewan, Canada: M.Sc. thesis, Laurentian University, Sudbury, Ontario, 184 p.

Bhattacharya B. K., 1966: Two-dimensional harmonic analysis as a tool for magnetic interpretation. Geophysics, 30, 829–857.

Blakely, R.J., 1995, Potential Theory in Gravity and Magnetic Applications. Cambridge University Press, Cambridge.

Börner, R. U., 2010, Numerical modelling in geo-electromagnetics: Advances and challenges: Surveys in Geophysics, 31, 225–245, doi: 10 .1007/s10712-009-9087-x.

Bracewell, R., 1965, The Fourier transform and its applications: McGraw-Hill.

Cain, M. J., 2000, DIGHEM EM/Magnetic survey for Cream Minerals LTD. Nootka island, British Columbia, Fargo Airborne Survey report, 94p.

Campbell, J.E. and Flory, G., 1999, Cameco Corporation: till geochemical and Quaternary geological investigations on the Dawn Lake project properties (part of NTS 64L-4,-5 and 74I-1,-8,-9); in Saskatchewan Industry and Resources Mineral Assessment File No. 74I01-0091, 39 p.

Campbell, J. E., Shieves, R. B. K. and Klassen R. A., 2002. Integrated field investigations of airborne radiometric spectral domains, NEA-IAEA test area, eastern Athabasca Basin: A preliminary report, Summary of Investigations 2002, v2, Saskatchewan Geological Survey, Saskatchewan Industry Resources, Miscellaneous Report 2002-4.2, Paper D-2.

Campbell, J.E., 2007, Quaternary geology of the eastern Athabasca Basin, Saskatchewan; in EXTECH IV, Geological Survey of Canada, Bulletin 588, p. 211–228.

Card, C.D., 2006, Remote predictive map for the basement to the western Athabasca Basin:

Saskatchewan Industry and Resources, Preliminary Geological Map, Open File 2006-45, scale: 1:500 000.

Carter-McAuslan, A., 2013, Joint inversion of geologically realistic, synthetic Earth models. M.Sc. thesis, Memorial University of Newfoundland, St. John's, NL, Canada, 356 p.

Cerveny, V., and Ravindra, R., 1971, Theory of Seismic HeadWaves. University of Toronto Press.

CGG, 2014, HeliFALCON airborne gravity gradiometer survey; Project Number: 14021, Saskatchewan, Canada, 31p.

Clement, W.G., 1972, Basic principles of two-dimensional digital filtering, Geophysical Prospecting, pp. 125-145.

Connard, G., Couch, R. and Gemperle, M., 1983, Analysis of aeromag- netic measurements from the Cascade Range in central Oregon, Geophysics, 48, 376-390.

Cowan, D. R., and Cowan, S., 1993, Separation filtering applied to aeromagnetic data. Exploration Geophysics, v. 24, pp. 429-436.

Craik, D. J., 1995, Magnetism: principles and applications, Wiley, 468p.

Davies, J., Mushayandebvu, M. and Smith, I.R., 2004, Magnetic detection and characterization of Tertiary and Quaternary buried channels; SEG International Exposition and 74th Annual Meeting, Denver, Colorado. p. 734-737.

Derecke, P., 1981, An Introduction to the generalized reciprocal method of seismic refraction interpretation. Geophysics 46: 1508-1518.

Domzalski. W., 1956, Some problems of shallow refraction investigations. Geophysics. Props., vol 4, no:2, 140-166.

Ekblom, H., 1973, Calculation of linear best Lp-approximations, BIT, 13, 292-300.

Ekblom, H., 1987, The L1-estimate as limiting case of an Lp-or Huber-estimate, in Y. Dodge, ed., Statistical data analysis based on the L1-norm and related methods: Elsevier Science Publ. Co., Inc., 109–116.

Everett, M.E., and Meju., M.A., 2005, Near-Surface controlled-source electromagnetic induction: background and recent advances, p.157-184. In Y. Rubin and S.S. Hubbard (ed.) Hydrogeophysics. Springer, Dordrecht, the Netherlands.

Farquharson, C. G., and J. A. Craven, 2009, Three-dimensional inversion of magnetotelluric data for mineral exploration: An example from the McArthur River uranium deposit, Saskatchewan, Canada: Journal of Applied Geophysics, 68, no. 4, 450–458, doi: 10.1016/j.jappgeo.2008 .02.002.

Farquharson, C.G., and Oldenburg, D.W., 1998, Non-linear inversion using general measures of data misfit and model structure: Geophys. J. Int., 134, 213–227.

Farquharson, C.G., and Oldenburg, D.W., 2000, EM1DFM; A Program Library for Forward Modelling and Inversion of Frequency Domain Electromagnetic Data over 1D Structures, Version 1.0, Developed by the UBC- Geophysical Inversion Facility, Department of Earth and Ocean Sciences, University of British Columbia, Vancouver, British Columbia.

Farquharson, C.G., and Oldenburg, D.W., 2004, A comparison of automatic techniques for estimating the regularization parameter in nonlinear inverse problems, Geophysical Journal International, 156, 411–425.

Farquharson, C.G., and Oldenburg, D.W., 2006, EM1DTM; A Program Library for Forward Modelling and Inversion of Time Domain Electromagnetic Data over 1D Structures, version 1.0, Developed by the UBC- Geophysical Inversion Facility, Department of Earth and Ocean Sciences, University of British Columbia, Vancouver,

British Columbia.

Farquharson, C.G, 2008. Constructing piecewise-constant models in multidimensional minimum-structure inversions, Geophysics, 73, K1-K9. (DOI: 10.1190/1.2816650)

Fayek, M., T. M. Harrison, R. C. Ewing, M. Grove and C. D. Coath, 2002a. O and Pb isotope analyses of uranium minerals by ion microprobe and U-Pb ages from the Cigar Lake deposit, Chemical Geology, 185, p. 205- 225.

Fayek, M., and Kyser, K.K., 1997, Characterization of multiple fluid events and rare-earth-element mobility associated with formation of unconformity-type uranium deposits in the Athabasca Basin, Saskatchewan: The Canadian Mineralogist, v. 35, p. 627-658.

Fitterman D. V., and Labson V. F., 2005, 10. Electromagnetic Induction Methods for Environmental Problems. Near-Surface Geophysics: pp. 301-356.

Fowler, C. M. R., 2005, The solid earth: an introduction to global geophysics, Cambridge University Press, 726p.

Fraser, D., 1986, Dighem resistivity techniques in airborne electromagnetic mapping in Airborne Resistivity Mapping, ed. G.J. Palacky; Geological Survey of Canada, Paper 86-22, p. 49-54.

Fulton, R. J., 1995, Geological Survey of Canada, "A" Series Map 1880A, 1 sheet, https://doi.org/10.4095/205040

Furgo Airborne Surveys Corp., 2006, DIGHEM survey for Osisko Exploration Ltd. in Malartic/Cadillac area, Quebec, Canada, 203p.

Gandhi, S.S., 1989, Geology and uranium potential of the Thelon Basin and adjacent basement in comparison with the Athabasca Basin region: Uranium Resources and Geology of North America, Technical Committee Meeting, Saskatoon, Vienna, 1-3 September, 1987, Proceedings, p. 411-428.

Gandhi, S.S., 1995, An overview of the exploration history and genesis of Proterozoic uranium deposits in the Canadian Shield: Exploration and Research for Atomic Minerals, v. 8, p. 1-47.

Geddes, R.S., 1982, The Vixen Lake indicator train Northern Saskatchewan; in Prospecting in Areas of Glaciated Terrain – 1982, (ed.) P.H. Davenport; Canadian Institute of Mining and Metallurgy, p. 264–283.

Geotech Ltd., 2013, Report on a helicopter-borne versatile time domain electromagnetic (VTEM max) and aeromagnetic geophysical survey, Read Lake project, McArthur river mine, Saskatchewan, Canada, 150p.

Gill, P.E., W. Murray & M.H. Wright, 1981. Practical Optimization, Academic Press, London.

Goldak Airborne Surveys, 2007, Technical report on a fixed wing magnetic gradiometer survey over McArthur River and Read Lake in the Athabasca Basin, Saskatchewan, Canada, 22p.

Grant, F. S., and West, G. F., 1965, Interpretation Theory in Applied Geophysics. McGraw-Hill Co., New York.

Györfi, I., Hajnal, Z., White, D.J., Takács, E., Reilkoff, B., Annesley, I.R., Powell, B., and Koch, R., 2007, High-resolution seismic survey from the McArthur River region: contributions to mapping the complex P2 uranium ore zone, Athabasca Basin, Saskatchewan, in Jefferson, C.W., and Delaney, G., eds., EXTECH IV: Geology and Uranium EXploration TECHnology of the Proterozoic Athabasca Basin, Saskatchewan and Alberta: Geological Survey of Canada, Bulletin 588, (also Geological Association of Canada, Mineral Deposits Division, Special Publication 4; Saskatchewan Geological Society, Special Publication 18), p. 397-412.

Haber, E., 1997, Numerical Strategies for the Solution of Inverse Problems, Ph.D. thesis,

University of British Columbia.

Haber, E., and Oldenburg, D.W., 2000, A GCV based method for nonlinear ill-posed problems, Computational Geosciences, 4, 41–63.

Hajnal, Z., E. Takács, D. J. White, I. Györfi, B. Powell, and R. Koch, 2007, Regional seismic signature of the basement and crust beneath the McArthur River mine district, Athabasca Basin, Saskatchewan, in C. W. Jefferson, and G. Delaney, eds., EXTECH IV: Geology and uranium exploration technology of the Proterozoic Athabasca Basin; Saskatchewan and Alberta: Geological Survey of Canada, Bulletin, 588, 389–396.

Hauck, C., Kneisel, C., 2008, Applied Geophysics in Periglacial Environments, Cambridge University Press, 240 pp.

Hinze, W. J., Von Frese, R. R. B., and Saad, A. H., 2013, Gravity and Magnetic Exploration: Principles, Practices and Applications, Cambridge Univ. Press, New York.

Hodges, G., 1999, A world of applications for helicopter electromagnetics to environmental and engineering problems, Proceedings of 12th Annual Symposium on the Application of Geophysics to Environmental and Engineering Problems (SAGEEP).

Hoeve, J., and Quirt, D.H., 1984, Mineralization and Host Rock Alteration in Relation to Clay Mineral Diagenesis and Evolution of the Middle- Proterozoic, Athabasca Basin, northern Saskatchewan, Canada: Saskatchewan Research Council, SRC Technical Report 187, 187 p.

Hoeve, J., and Quirt, D.H., 1987, A stationary redox front as a critical factor in the formation of high-grade, unconformity-type uranium ores in the Athabasca Basin, Saskatchewan, Canada: Bulletin de Minéralogie, v. 110, p. 157-171.

Holladay, S., and Lo, B., 1997, Airborne Frequency-Domain EM- Review and Preview Proceedings of Exploration 97: Fourth Decennial International Conference on Mineral Exploration, pp 505-514.

Hsu, S. K., Sibuet, J.C., Shyu, C.T., 1996, High-resolution detection of geologic boundaries from potential-field anomalies: An enhanced analytic signal technique: Geophysics, 61, 373–386.

Irvine, R. and Witherly, K., 2006, Advances in airborne EM acquisition and processing for uranium exploration in the Athabasca Basin, Canada, SEG/New Orleans 76th Annual Meeting.

Jahandari, H., and Farquharson, C.G., 2014, A finite-volume solution to the geophysical electromagnetic forward problem using unstructured grids. Geophysics 79, E287–E302.

Jahandari, H., 2015, Three-dimensional numerical modelling of gravity and electromagnetic data using unstructured tetrahedral grids, PhD thesis, Memorial University of Newfoundland, St. John's, NL, Canada, 183 p.

Jahandari, H., Ansari, S., and Farquharson, C.G., 2017, Comparison between staggered grid finite–volume and edge–based finite–element modelling of geophysical electromagnetic data on unstructured grid. Journal of Applied Geophysics, V 138, 185-197.

Jain, S., 2014, Fundamentals of Physical Geology, Springer Geology, P 350, DOI: 10.1007/978-81-322-1539-4_1.

Jefferson, C. W., G. Delaney, and R. A. Olson, 2003, EXTECH IV: Athabasca uranium multidisciplinary study of northern Saskatchewan and Alberta, Part 1: Overview and impact: Geological Survey of Canada Current Research, C18, doi: 10.4095/214200.

Jefferson, C. W., D. J. Thomas, S. S. Gandhi, P. Ramaekers, G. Delaney, D. Brisbin, C. Cutts, P. Portella and R. A. Olson, 2007. Unconformity associated uranium deposits, in Jefferson, C.W., and Delaney, G., eds., EXTECH IV: Geology and Uranium EXploration TECHnology of the Proterozoic Athabasca Basin, Saskatchewan and Alberta: Geological Survey of Canada, Bulletin 588 (also Saskatchewan Geological

Society, Special Publication 18; Geological Association of Canada, Mineral Deposits Division, Special Publication 4).

Jin, J., 2002, The finite element method in electromagnetics, 2nd ed.: John Wiley & Sons Inc.

Jones, D., Ansari, S., Farquharson, C. and Hearst, R., 2016, Synthesizing time-domain electromagnetic data for graphitic fault zones and associated uranium deposits in the Athabasca Basin, Canada. SEG Technical Program Expanded Abstracts 2016: pp. 2206-2210.

Juhojuntti, N., Wood, G., Juhlin, C., O'Dowd, C., Dueck, P. and Cosma C., 2012. 3D seismic survey at the Millennium uranium deposit, Saskatchewan, Canada: Mapping depth to basement and imaging post-Athabasca structure near the orebody. GEOPHYSICS, 77(5), WC245-WC258.

Kearey, P., Brooks, M., Hill, I., 2002, An introduction to geophysical exploration. Blackwell Science.

Kyser, K., Hiatt, E., Renac, C., Durocher, K., Holk, G., and Deckart, K., 2000, Diagenetic fluids in Paleo- and Mesoproterozoic sedimentary basins and their implications for long protracted fluid histories, Chapter 10 in Kyser, K., ed., Fluids and Basin Evolution, Short Course Series Volume 28 (Series editor Robert Raeside): Mineralogical Association of Canada, p. 225-262.

LaFehr, T. R., and Nabighian, M. N., 2012, Fundamentals of Gravity Exploration, Geophysical Monograph Series: Society of Exploration Geophysicists, http://dx.doi.org/10.1190/1.9781560803058.

Lankston, R., 1990, High Resolution Refraction Seismic Data Acquisition and Interpretation. In: Geotechnical and Environmental Geophysics, Vol 1, Reviewer and Tutorial, S. Ward (ed.), Investigations in Geophysics No. 5, Society of Exploration

Geophysicists, Tulsa, OK, pp. 45–73.

Legault, J.M., Prikhodko, A., Kumar, H., and Tishin, P., 2011, An improved early-channel VTEM helicopter system for near-surface applications, a paper presented at 24TH SAGEEP symposium and annual meeting of Environment and Engineering Geophysical Society, EEGS, Charleston, SC.

Lelièvre, P. G., C. G. Farquharson, and Hurich, C. A., 2011, Computing first-arrival seismic traveltimes on unstructured 3D tetrahedral grids using the fast marching method: Geophysical Journal International, 184, 885–896, doi: 10.1111/gji.2011.184.issue-2.

Lelièvre, P.G., Farquharson, C.G., Hurich, C.A., 2012. Joint inversion of seismic traveltimes and gravity data on unstructured grids with application to mineral exploration. Geophysics 77, K1-K15.

Lelièvre, P. G., and Farquharson, C. G., 2015, PODIUM: a suite of software utilities for Preparation of Data for Inversion on Unstructured Meshes.

Lelièvre, P. G. and Oldenburg, D. W., 2009, A comprehensive study of including structural orientation information in geophysical inversions, Geophys. J. Int., 178, 623–637.

Li, Y., and Oldenburg, D. W., 1998, 3-D inversion of gravity data: Geophysics, 63, 109–119.

Lim, B.K., Jones, S.J., 1989, Some applications and problems of the seismic refraction technique in civil engineering projects in Malaysia, Geol. Soc. Malaysia, 15, pp95-121.

Madsen, N. K., and R. W. Ziolkowski, 1990, A three-dimensional modified finite volume technique for Maxwell's equations: Electromagnetics, 10, 147–161, doi: 10.1080/02726349008908233.

Marlatt, J., McGill, B., Matthews, R., Sopuck, V., and Pollock, G., 1992, The discovery of the McArthur River uranium deposit, Saskatchewan, Canada, new developments in

uranium exploration, resources, production and demand: International Atomic Energy Agency - Nuclear Energy Agency of the OECD, Vienna, 26-29 August, 1991, Technical Committee Meeting, Proceedings, IAEA TECDOC-650, p. 118-127

Matthews, R., Koch, R., Leppin, M., Powell, B., and Sopuck, V., 1997, Advances in integrated exploration for unconformity uranium deposits in Western Canada; in Proceedings of Exploration 97: Fourth Decennial International Conference on Mineral Exploration, (ed.) A.G. Gubins; GEO F/X, 993-1001, 1068 p.

Maus S. and Dimri V.P., 1996, Depth estimation from the scaling power spectrum of potential field. Geophysical J. International, v. 124, pp. 113–120.

Mavko, G., Mukerji, T., Dvorkin, J., 2009, The Rock Physics Handbook. 2nd ed. Cambridge: Cambridge University Press. p 522.

McCracken, K. G., Pik, J. P., and Harris, R. W., 1984, Noise in EM exploration systems: Explor. Geophys., 15, 169-174.

McGill, B.D., Marlatt, J.L., Matthews, R.B., Sopuck, V.J., Homeniuk, L.A., and Hubregtse, J.J., 1993, The P2 North uranium deposit Saskatchewan, Canada; Exploration Mining Geology, v. 2, p. 321–331.

McMullan, S. R., R. B. Matthews and P. Robertshaw, 1987. Exploration geophysics for Athabasca uranium deposits: Exploration ’87 Proceedings, Ontario Geological Survey, Geophysical Methods: Their application to ore exploration, 3, 547 – 566.

Millard, M.J., 1988, Quaternary geology and drift prospecting Dawn Lake area, northern Saskatchewan; M.Sc. thesis, University of Saskatchewan, Saskatoon, Saskatchewan, 171 p.

Milsom, J., 1989. Field Geophysics, John Wiley & Sons, New York.

Mwenifumbo, C. J., B. E. Elliott, C. W. Jefferson, G. R. Bernius and K. A. Pflug, 2004.

Physical rock properties from the Athabasca Group: designing geophysical exploration models for unconformity uranium deposits, Journal of Applied Geophysics, 55, 117-135.

Mwenifumbo, C.J., Percival, J.B., Bernius, G., Elliott, B., Jefferson, C.W., Wasyliuk, K., and Drever, G., 2007, Comparison of geophysical, mineralogical and stratigraphic attributes in drill holes MAC 218 and RL 88, McArthur River uranium camp, Athabasca Basin, Saskatchewan, in Jefferson, C.W., and Delaney, G., eds., EXTECH IV: Geology and Uranium EXploration TECHnology of the Proterozoic Athabasca Basin, Saskatchewan and Alberta: Geological Survey of Canada, Bulletin 588, (also Geological Association of Canada, Mineral Deposits Division, Special Publication 4; Saskatchewan Geological Society, Special Publication 18) p. 507-520.

Nabighian, M. N. and Macnae, J. C., 1991, Time-domain electromagnetic prospecting methods, in Electromagnetic Methods in Applied Geophysics. Vol. 2, pp. 427-479, ed. Nabighian, M. N., Soc. Expl. Geophys., Tulsa.

Naidu, P. S., 1968, Spectrum of the Potential Field due to Randomly Distributed Sources. Geophysics, v. 33, pp. 337-345.

Naidu, P.S. and Mathew, M.P., 1998, Analysis of geophysical potential fields, A digital signal processing approach. Elsevier Science publishers, Amseterdam, 298p.

Newman, G. A., G. W. Hohmann, and W. L. Anderson, 1986, Transient electromagnetic response of a three-dimensional body in a layered earth: Geophysics, 51, 1608–1627, http://dx.doi.org/10.1190/1.1442212.

Nur, A., Mavko, G., Dvorkin, J., Galmudi, D., 1998, Critical porosity: a key to relating physical properties to porosity in rocks. Leading Edge 17, 357-362.

Oasis Montaj, 2006, Gravity and magnetic software, user manual. Oasis Montaj v 6.4, Geosoft Inc.

Oasis Montaj, 2007, 2-D frequency domain processing of potential field data; user's guide. Oasis Montaj v.6.4. Geosoft Inc.

O'Dowd, C. R., Wood, G. R., Brisbin, D., and Powell, B. W., 2006, Enhancing uranium exploration through seismic methods and potential field modeling at the McArthur River mine site, Saskatchewan, Canada: 76th Annual International Meeting, SEG, Expanded Abstracts, 1253–1257.

Okabe, M., 1979, Analytical expressions for gravity anomalies due to homogeneous polyhedral bodies and translations into magnetic anomalies. Geophysics, Vol. 44, No. 4; P. 730-741.

Okwueze, E.E., 1988, Mapping Bedrock Surface and Lithology with the Seismic Refraction Method in Basement Area. Physics, 26, pp 33-40.

Oldenburg, D. W., and Li, Y., 2005, Inversion for Applied Geophysics: A Tutorial. Near-Surface Geophysics: pp. 89-150. eISBN: 978-1- 56080-171-9

Paasche, H., and J. Tronicke, 2007, Cooperative inversion of 2D geophysical data sets: A zonal approach based on fuzzy c-means cluster analysis: Geophysics, 72, no. 3, A35–A39, doi: 10.1190/1.2670341.

Palmer, D., 1980, The Generalized Reciprocal Method of Seismic Refraction Interpretation, Soc. of Expl. Geophysicists, Tulsa, Oklahoma.

Papoulis, A., 1962, The Fourier integral and its applications: McGraw-Hill.

Pilkington, M., 1989, Variable-depth magnetization mapping: application to the Athabasca Basin, northern Alberta and Saskatchewan, Canada: Geophysics, v. 54, p. 1164-1173.

Powell, B., Wood, G., and Bzdel, L., 2007, Advances in geophysical exploration for uranium deposits in the Athabasca Basin, in Exploration 07 Proceedings Fifth Decennial Conference on Geophysics and Geochemistry of Minerals, ed. B. Milkereit, p. 771-790.

Rainbird, R. H., R. A. Stern, N. Rayner and C. W. Jefferson, 2007. Age, provenance, and regional correlation of the Athabasca Group, Saskatchewan and Alberta, constrained by igneous and detrital zircon geochronology; in Jefferson, C.W., and Delaney, G., eds., EXTECH IV: Geology and Uranium EXploration TECHnology of the Proterozoic Athabasca Basin, Saskatchewan and Alberta: Geological Survey of Canada, Bulletin 588 (also Saskatchewan Geological Society, Special Publication 18; Geological Association of Canada, Mineral Deposits Division, Special Publication 4).

Ramaekers, P., 1981. hudsonian and Helikian basins of the Athabasca Region, northern Saskatchewan, in Proterozoic Basins of Canada, (ed.) F.H.A. Campbell, GSC, paper 81 – 10, 219 – 233.

Ramaekers, P., 1990, Geology of the Athabasca Group (Helikian) in northern Saskatchewan; Saskatchewan Geological Survey, Report 195, 49 p.

Ramaekers, P. and Catuneanu, O., 2004, Development and sequences of the Athabasca Basin, Early Proterozoic, Saskatchewan and Alberta, Canada; in The Precambrian Earth: Tempos and Events, (ed.) P.G. Eriksson, W. Altermann, D.R. Nelson, W.U. Mueller, and O. Catuneanu; Elsevier, Amsterdam, Netherlands, p. 705–723.

Ramaekers, P., Jefferson, C.W., Yeo, G.M., Collier, B., Long, D.G.F., Catuneanu, O., Bernier, S., Kupsch, B., Post, R., Drever, G., McHardy, S., Jiricka, D., Cutts, C., and Wheatley, K., 2007, Revised geological map and stratigraphy of the Athabasca Group, Saskatchewan and Alberta, in Jefferson, C.W., and Delaney, G., eds., EXTECH IV: Geology and Uranium EXploration TECHnology of the Proterozoic Athabasca Basin, Saskatchewan and Alberta: Geological Survey of Canada, Bulletin 588, (also Geological Association of Canada, Mineral Deposits Division, Special Publication 4; Saskatchewan Geological Society, Special Publication 18) p. 155-192.

Rayner, J.N. ,1971, An Introduction to Spectral Analysis. Pion, England.

Redpath, B.B., 1973, Seismic refraction exploration for engineering site investigations,

National Technical Information Service, 63 pp.

Reynolds, J. M., 1997, An Introduction to Applied and Environmental Geophysics. John Wiley & Sons.

Ruzicka, V., 1996, Unconformity associated uranium, Geology of Canada, 8, 197 – 210.

Schön, J.H., 1996, Physical Properties of Rocks: Fundamentals and Principles of Petrophysics (Handbook of Geophysical Exploration Series). Pergamon Press, London.

Schön, J.H., 2011, Physical Properties of Rocks: A Workbook, Elsevier publications, p 494.

Schreiner, B.T., 1983, Quaternary geology of the NEA/IAEA Athabasca test area; in Uranium Exploration in the Athabasca Basin, Saskatchewan, Canada, (ed.) E.M. Cameron; Geological Survey of Canada, Paper 82-11, p. 27–32.

Schreiner, B.T., 1984a, Quaternary geology of the Precambrian Shield, Saskatchewan; Saskatchewan Energy and Mines Report 221, 106 p., 1 map, scale 1:1 000 000.

Shaw, J. and Kvill, D., 1984, A glaciofluvial origin for drumlins of the Livingston Lake area, Saskatchewan, Canadian Journal of Earth Sciences, v. 21, p. 1442–1459.

Sheriff, R. E., Geldart, L. P., 1995, Exploration Seismology (2nd ed.). Cambridge University Press. p. 292.

Shewchuk, J. R., 1996, Triangle: Engineering a 2D Quality Mesh Generator and Delaunay Triangulator, in “Applied Computational Geometry: Towards Geometric Engineering” (Ming C. Lin and Dinesh Manocha, editors), volume 1148 of Lecture Notes in Computer Science, pages 203-222, Springer-Verlag, Berlin.

Shi, D., Milkereit, B., and Sun, L. F., 2014, Elastic and viscoelastic modeling of seismic waves in the Athabasca Basin, Canada. In 2014 SEG Annual Meeting. Society of

Exploration Geophysicists.

Si, H., 2015, "TetGen, a Delaunay-Based Quality Tetrahedral Mesh Generator". ACM Trans. on Mathematical Software. 41 (2), Article 11 (February 2015), 36 pages. DOI=10.1145/2629697 http://doi.acm.org/10.1145/2629697.

Simpson, M.A., 1997, Surficial geology of Saskatchewan; Saskatchewan Energy and Mines–Saskatchewan Research Council, scale 1:1 000 000.

Sjörgen, B., 1984, Shallow refraction seismics. Springer Netherlands. p. VII. 270. DOI: 10.1007/978-94-009-5546-2.

Smith, R. S., Thurston, J. B., Dai, T. F., and MacLeod, I. N., 1998, iSPI —- the improved source parameter imaging method: Geophysical Prospecting, 46, 141–151.

Spector, A., and Grant, F.S., 1970, Statistical models for interpreting aeromagnetic data, Geophysics, v.35, no.2, pp. 293-302.

Sproule, J.C., 1939, The Pleistocene geology of the Cree Lake region, Saskatchewan; Transactions of the Royal Society of Canada, third series, v. 33, sec. 4, p. 101–109.

Stoffa, P.L., and Buhl, P., 1979, Two-ship multichannel seismic experiments for deep crustal studies: expanded spread and constant offset profiles. J. Geophys. Res., 84, 7645–60.

Telford, W. M., Geldart, L. P., Sheriff, R. E., and Keys, D. A., 1976, Applied geophysics. Cambridge University Press.

Thomas, D.J., 1983, Distribution, Geological Controls and Genesis of Uraniferous Pegmatites in the Cree Lake Zone of northern Saskatchewan: M.Sc. thesis, University of Regina, Regina, Saskatchewan, 213 p.

Thomas, D.J., Jefferson, C.W., Yeo, G.M., Card, C., and Sopuck, V., 2002, Introduction;

in Field Trip A1. The Eastern Athabasca Basin and its Uranium Deposits, (ed.) N. Andrade, G. Breton, C.W. Jefferson, D.J. Thomas, G. Tourigny, S. Wilson, and G.M. Yeo; Geological Association of Canada–Mineralogical Association of Canada Guidebook, Saskatoon, Saskatchewan, p. 1–22.

Thomas, M. D. and McHardy, S., 2007. Magnetic insights into basement geology in the area of McArthur River uranium deposit, Athabasca Basin, Saskatchewan, in Jefferson, C.W. and Delaney, G., eds., EXTECH IV: Geology and Uranium EXploration TECHnology of the Proterozoic Athabasca Basin, Saskatchewan and Alberta: Geological Survey of Canada, Bulletin 588 (also Saskatchewan Geological Society, Special Publication 18; Geological Association of Canada, Mineral Deposits Division, Special Publication 4).

Thomas, M.D. and Wood, G., 2007. Geological significance of gravity anomalies in the area of McArthur River uranium deposit, Athabasca Basin, Saskatchewan; in EXTECH IV: Geology and Uranium EXploration TECHnology of the Proterozoic Athabasca Basin, Saskatchewan and Alberta, (ed.) C.W. Jefferson and G. Delaney; Geological Survey of Canada, Bulletin 588, p. 441–464.

Treitel, S., Clement, W.G. and Kaul, R.K., 1971, The spectral determination of depths of buried magnetic basement rocks. Geophysical Journal of the Royal Astronomical Society, v.24, pp. 415–428.

Tuncer, V., Unsworth, M. J., Siripunvaraporn, W. and Craven, J. A., 2006a, Exploration for unconformity type uranium deposits with audio-magnetotelluric data: A case study from the McArthur River Mine, Saskatchewan (Canada), Geophysics, 71 (6), B201 – B209.

Van Wijk, K., J. A. Scales, W. Navidi, and L. Tenorio, 2002, Data and model uncertainty estimation for linear inversion: Geophysical Journal International, 149, 625–632.

Veillette, J. J., 2004, Geologie des Formations en Surface et Histoire Glaciaire, Cadillac,

Quebec. Commission Geologique de Canada, Carte 2019A, Echelle 1/100 000.

Ward, S. M., and G. W. Hohmann, 1988, Electromagnetic Theory for Geophysical Applications, in Electromagnetic Methods in Applied Geophysics, Volume 1, Theory: Society of Exploration Geophysicists, 131–308.

Wares, R. & Burzynski, J., 2011. The Canadian Malartic Mine, Southern Abitibi Belt, Québec, Canada: Discovering and Development of an Archean Bulk-Tonnage Gold Deposit, s.l.: Osisko Mining Corporation.

Weiss, C. J., 2010, Triangulated finite difference methods for global-scale electromagnetic induction simulations of whole mantle electrical heterogeneity: Geochemistry, Geophysics, Geosystems, 11, 1–15, doi: 10.1029/ 2010GC003283.

Wessel, P. and W. H. F. Smith, 1991, Free software helps map and display data, EOS Trans. AGU, 72, 441.

West G. F., and Macnae J. C., 1991, 1. Physics of the Electromagnetic Induction Exploration Method. Electromagnetic Methods in Applied Geophysics: pp. 5-46.

White, D. J., Z. Hajnal, B. Roberts, I. Gyorfi, B. Reilkoff, B. Bellefleur, C. Mueller, S. Woelz, C. J. Mwenifumbo, E. Takacs, D. R. Schmitt, D. Brisbin, C. W. Jefferson, R. Koch, B. Powell and I. Annesley, 2007. Seismic methods for uranium exploration; an overview of EXTECH IV seismic studies at the McArthur River mining camp, Athabasca Basin, Saskatchewan; in Jefferson, C.W., and Delaney, G., eds., EXTECH IV: Geology and Uranium EXploration TECHnology of the Proterozoic Athabasca Basin, Saskatchewan and Alberta: Geological Survey of Canada, Bulletin 588 (also Saskatchewan Geological Society, Special Publication 18; Geological Association of Canada, Mineral Deposits Division, Special Publication 4).

Witherly, K., Irvine, R., and Morrison, E.B., 2004, The Geotech VTEM time domain helicopter EM system, SEG Expanded Abstracts, 23, 1217-1221.

Witherly, K., and Irvine, R, 2006, The VTEM airborne electromagnetic system – benchmarking continuous improvement via repeat surveys over time, SEG Expanded Abstracts, 25, 1273-1277.

Wood, G. and Thomas, M.D., 2002. Modelling of high-resolution gravity data near the McArthur River uranium deposit, Athabasca Basin; in Summary of Investigations 2002, Volume 2, Saskatchewan Geological Survey, Sask. Industry Resources, Misc. Rep. 2002-4.2, CD-ROM, Paper D-16, 9p.

Wright, C., Barton, T., Goleby, B.R., Spence, A.G. and Pester, D., 1990, The interpretation of expanding spread profiles: examples from central and eastern Australia. Tectonophysics, 173, 73–82.

Yeo, G.M., and Delaney, G., 2007, The Wollaston Supergroup, stratigraphy and metallogeny of a Paleoproterozoic Wilson cycle in the Trans- Hudson Orogen, Saskatchewan, in Jefferson, C.W., and Delaney, G., eds., EXTECH IV: Geology and Uranium EXploration TECHnology of the Proterozoic Athabasca Basin, Saskatchewan and Alberta: Geological Survey of Canada, Bulletin 588, (also Geological Association of Canada, Mineral Deposits Division, Special Publication 4; Saskatchewan Geological Society, Special Publication 18) p. 89-118.

Zhang, J. and Toksoz, M.N., (1998), "Nonlinear Refraction Traveltime Tomography," Society of Exploration Geophysicists, Geophysics, Vol. 63, No.5, pp. 1726-1737.

# Appendix A: PODIUM software

PODIUM (Preparation of Data for Inversion on Unstructured Meshes; Lelièvre and Farquharson, 2015) is a package of software. It has many utilities for working with rectilinear meshes. The package helps users to prepare data and models for running forward and inverse modelling programs, and for assessing the results of such modelling. Following are some programs in this package which I have frequently used them in this research:

**add_noise**: It adds noise and/or assigns uncertainties to data (.node or .ele file).

**combine_mesh:** It combines up to 8 mesh files. Mesh file is made from ele and node files.

**combine_node:** It combines up to 8 node files.

**combine_poly:** It combines up to 8 poly files. "poly" file is an input for the "tetgen" and "triangle" codes.

**convert_format:** It is to convert different format of files to each other as follow:

Input file extensions are mandatory:
- Datamine (.pt .tr .ssv)
- Geomatic (.dat .txt etc)
- Geomview (.off)
- Medit (.mesh)
- Gocad solids (.ts .so)
- GSS xyz mag (.xyz etc)
- WSINV3DMT (.model)

Output file extension is optional:
- .node
- .ele
- .vtu

**interpolate_topography:** Topography interpolation at specified points.

**make_obs:** This code creates gridded observation locations and writes them to a "node" file.

**mesh2poly:** Converts .node and .ele files to a .poly file for use with meshing programs.

**mesh2solid:** Converts .node and .ele files to a .tsurf or .tvol file.

**mesh2vtu:** It generates “vtu” file (which is the input file for the “ParaView” software) using “node” and “ele” files.

**node2vtu:** It generates “vtu” file from a “node” file.

**poly2mesh:** It converts a .poly file to .node and .ele files.

**poly2vtu:** It generates “vtu” file from a “poly” file.

**print_coordinates:** Reads data from a file which can be a .node or .ele file, and prints coordinate and attribute range information (minimum, maximum values, etc.).

**remove_trend:** Removes a polynomial trend from (x, y, d) data in a .node file.

**transform_coordinates:** Coordinate transformation of data or a model.

# Appendix B: A 2D forward gravity code

File: /home/mehrdad/Desktop/Forward_Code.f90 Page 1 of 2

```
Program Forward

!################################################################
!2D gravity forward modelling
!by: Mehrdad Darijani
!    March 2014
!==============================
!==============================
!This code is written based on the Okabe's paper: "Okabe, M., 1979, Analytical  expressions for gravity
anomalies due to homogeneous polyhedral bodies and translations into magnetic anomalies, Geophysics, Vol.
44 No. 4, 730-741."
!The file "obspoints.txt" is observation point coordinates. At file "mesh.1.node"  the first column is
number of vertice and two next column are respectively x and z cordinates
!At file "mesh.1.ele" the first column to end are: number of cell and the numbers of its three vertices
!The z axis is considered negative downward while in plotting the mesh in the Paraview software it
consider positive. !The z axis is considered positive upward.(density=g/cm^3)
!The outputs are the coordinates of x-axes of observation points and gravity responces.
!The output, gravity, can be in mgal (by multipying original "gal" to 1000).
!The input coordinates are in meters which will be transformed to cm afterwards in the code.
!################################################################

implicit none
real::g,temp1,temp2,temp3,temp4, temp5, temp6,temp7,temp8,temp9, temp10,sumg,pof
real,dimension(1000000)::xobs,zobs,xvert,zvert,grav,x,z,xx,zz,sinsai,cossai,kn,first,second,&
                    &third,ll,lll,u,gravity,dens
integer,dimension(100000,5)::vert
integer::status,nobs,nvert,h,i,j,k,f,r,ncell

!----------------------------------------
g=6.67384*1.0E-8          !! cm^3/gs^2
!----------------------------------------

!!   Read the observation point from file and count them
nobs=0
open(unit=1, file="obspoints.txt")
    do
    read(1,*,iostat=status)temp1,temp2
    if (status/=0) exit
    nobs=nobs+1
    xobs(nobs)=temp1
    zobs(nobs)=temp2
    end do
!----------------------------------------

!!   Reading the vertice values of cells and count them
open(unit=3, file="mesh.1.node")
do
read(3,*,iostat=status)temp9,temp3,temp4
if (status/=0) exit
nvert=temp9
xvert(nvert)=temp3
zvert(nvert)=temp4
end do
!----------------------------------------

!!   Reading the cell number and its vertices and density
open(unit=5, file="mesh.1.ele")
do
read(5,*,iostat=status)temp10,temp5,temp6,temp7
if (status/=0) exit
ncell=temp10
vert(ncell,1)=temp5
vert(ncell,2)=temp6
vert(ncell,3)=temp7
vert(ncell,4)=vert(ncell,1)
end do
!----------------------------------------
```

```
!!   Reading the density
open(unit=44, file="density.txt")
do f=1,ncell
read(44,*,iostat=status)temp8
if (status/=0) exit
dens(f)=temp8
end do
!----------------------------------------

!!   Find the answer for observation points
do k=1,nobs
  do r=1,ncell

    do i=1,4
      x(i)=(xvert(vert(r,i))-xobs(k))*100
      z(i)=(zvert(vert(r,i))-zobs(k))*100
    end do

    do i=1,4
      sinsai(i)=(x(i+1)-x(i))/sqrt((z(i+1)-z(i))**2+(x(i+1)-x(i))**2)
      cossai(i)=(z(i+1)-z(i))/sqrt((z(i+1)-z(i))**2+(x(i+1)-x(i))**2)
    end do

    do i=1,3
      kn(i)=-sinsai(i)
        do j=i,i+1
          zz(j)=z(j)*cossai(i)+x(j)*sinsai(i)
          xx(j)=-z(j)*sinsai(i)+x(j)*cossai(i)
          pof=zz(j)**2+xx(j)**2
          if (pof==0) then
            first(j)=0
            else
            first(j)=zz(j)*log(pof)
          end if
          if (xx(j)==0) then
            second(j)=0
            else
            second(j)=2*xx(j)*atan(zz(j)/xx(j))
          end if
            third=2*zz(j)
            ll(j)=first(j)+second(j)-third(j)
        end do
          lll(i)=ll(i+1)-ll(i)
        end do

        sumg=0
        do i=1,3
          u(i)=lll(i)*kn(i)
          sumg=sumg+u(i)
        end do
      grav(r)=g*dens(r)*sumg  !*(1.0E3)
      end do

    gravity(k)=0
  do i=1,ncell
    gravity(k)=gravity(k)+grav(i)
  end do
end do
!----------------------------------------

!! Writting the result file
open (unit=10,file="obsdata.txt")
Do h=1,nobs
 write(10,*)xobs(h),gravity(h)
end do
end program
```

# Appendix C: 2D linear inversion of gravity data

**A simple example: 2D linear inversion of gravity data**

A simple example of inversion method is explained in this section (see appendix C for Fortran code). It is a 2D model in which the mesh is made by the triangular cells. The 2D linear equation for the inversion of gravity data using the minimum structure method can be simply defined as (Oldenburg and Li, 2005):

$$\{J^T W_d^T W_d J + \beta W_z^T W_t^T W_t W_z\}\delta m = J^T W_d^T W_d\Big(d^{obs} - d(m)\Big) - \beta W_z^T W_t^T W_t W_z m_0$$

where $\delta m = m - m_0$, $m$ is the unknown matrix containing the density values for cells, and $m_0$is the initial model which can be zero (so the term $\beta W_z^T W_m^T W_m W_z m_0$ can be removed!). Matrix $m$ is

$$m = \begin{bmatrix} m_1 \\ \vdots \\ m_M \end{bmatrix}$$

The data-weighting, $W_d$, is

$$(W_d)_{jj} = \frac{1}{\sigma_j \times d_j}$$

$$W_d = \begin{bmatrix} \frac{1}{\sigma_1 \times d_1} & \cdots & 0 \\ \vdots & \ddots & \vdots \\ 0 & \cdots & \frac{1}{\sigma_N \times d_N} \end{bmatrix}$$

where $W_d$ is an $N \times N$ diagonal matrix whose elements are the reciprocals of the estimates of the standard deviations of the noise ($\sigma_j$) in the observations times by the observed data ($j$th observation station), and $N$ is the number of observation points.

$\boldsymbol{W_t}$ calculates model differences between adjacent grid cells. It is the first-order spatial finite-difference matrix in which each row has two non- zero elements with the same value but different signs that are the reciprocal of the distance between the centroids of two adjacent triangles. Hence, in this matrix, the number of rows would be the number of connections between the centroids and the number of columns is the number of triangles (i.e. $M$). The following equation shows the $W_t$ matrix for a simple example in Figure C1.

$$W_t = \begin{bmatrix} \frac{1}{c_{12}} & \frac{-1}{c_{12}} & 0 & 0 \\ 0 & \frac{1}{c_{23}} & \frac{-1}{c_{23}} & 0 \\ 0 & \frac{1}{c_{24}} & 0 & \frac{-1}{c_{24}} \end{bmatrix}$$

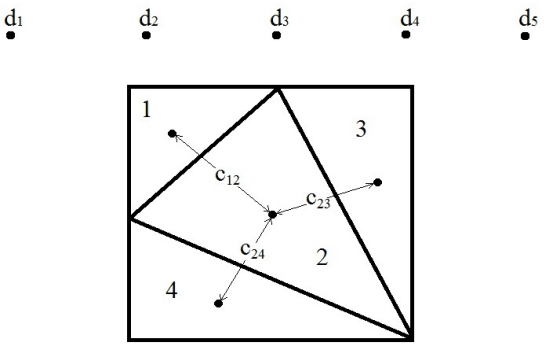


Figure C1: Simple triangular mesh and observation points.

In the potential methods (e.g. gravity and magnetic methods), to allow the code to generate models that have structure at depth, we have to consider a depth weighting. Otherwise, the structures will be reconstructed close to the surface. $W_z$ is the depth

weighting function and an $M \times M$ diagonal matrix, where $M$ is the number of cells, given by

$$(W_z)_{ii} = \frac{1}{(z+z_0)^{v/2}}$$

where $z$ refers to the depth of the centroid of each triangle ($i$th triangle), $v$ is a constant between 0 and 2, and the value of $z_0$ depends on the height of the observation points and size of mesh cells.

$J$ is the Jacobian matrix, containing the first-order derivatives of the gravitational field with respect to all the model parameters and in all the observation points. As you remember, we had the following equation in the chapter 3 for the gravity forward modelling.

$$U_k = \rho \left[ G \sum_{i=1} k^T n_i I_i \right]$$

By comparing this equation with $d = Gm$ (general forward equation), it can be seen that $U$ is the datum at an observation point, $\rho$ is the model parameter (i.e. density) for a cell, and the remaining is the kernel matrix values that make up the Jacobian matrix for respective cell and observation point. Based on Figure 5.10, the following equations show the values in the Jacobian matrix.

$$d_1 = \rho_1 J_{11} + \rho_2 J_{12} + \rho_3 J_{13} + \rho_4 J_{14}$$

$$\vdots \qquad \vdots \qquad \vdots$$

$$d_5 = \rho_1 J_{51} + \rho_2 J_{52} + \rho_3 J_{53} + \rho_4 J_{54}$$

Therefore,

$$J = \begin{bmatrix} J_{11} & \cdots & J_{14} \\ \vdots & \ddots & \vdots \\ J_{51} & \cdots & J_{54} \end{bmatrix}$$

where $J$ is an $N \times M$ matrix. Thus, the Jacobian contains the forward problem.

The inversion equation is tested with synthetic data. The true model was a square anomaly with a density contrast of 1g/cc. The gravity data were synthetized (using the code in appendix B) along a 100m profile with a station spacing of 5m. The data is inverted using my code which is written for the inversion equation over a 2D triangular mesh (see following for Fortran code). For the reconstructed model by the inversion, $v$=1, β=0.1 and $z_0$=0 are considered (Figure C2).

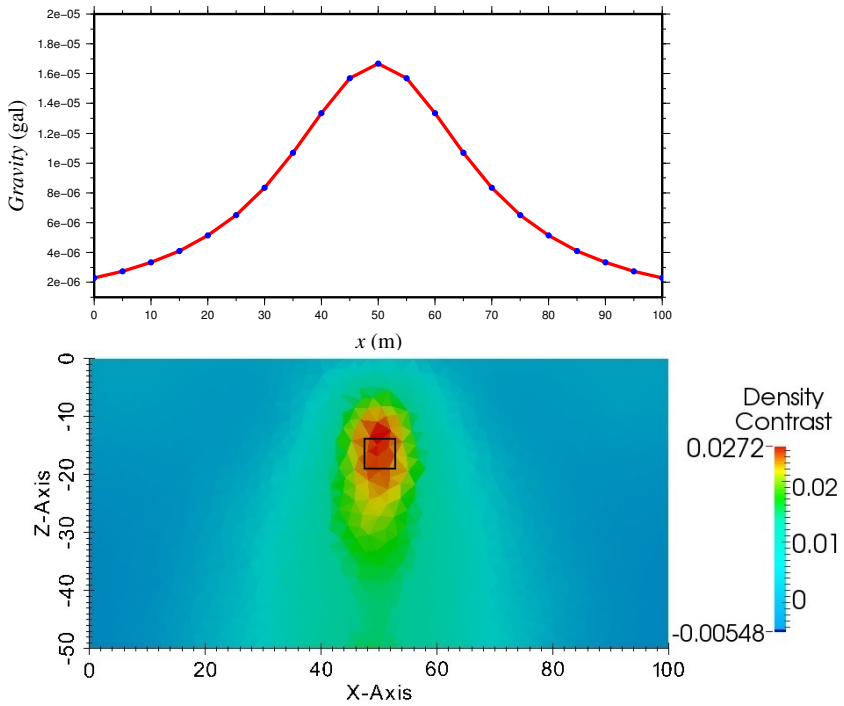


Figure C2: The observed data (blue points), calculated data (red curve) and 2D inversion result for $v$=1, β=0.1 and $z_0$=0. Black square shows the location of the true anomaly.

```
Program Inversion

!#################################################################
!2D linear inversion of gravity data
!by: Mehrdad Darijani
!    2014-04-04
!============================
!============================
!This code is a linear code (without iteration) based on Minimun Structure method (Li and Oldenburg, 1996)
!The file "obspoints.txt" is observation point coordinates. At file "mesh.1.node"  the first column is
number of vertice and two next column are respectively x and z cordinates
!At file "mesh.1.ele" the first column to end are: number of cell and the numbers of its three vertices
!At file "mesh.1.neigh" the first column to end are: number of cell and the numbers of its three neighbors
!The z axis is considered negative downward while in plotting the mesh in the Paraview software it
consider positive.
!#################################################################

implicit none

real(kind=8)::g,sumg,z0,beta,lambda,temp1,temp2,temp3,temp4,temp8,temp16,ooo,temp15,pof,pof1
integer::status,nobs,nvert,ncell,i,i1,i2,i3,i4,nne,i11,temp11,temp9,temp10&
        &,i6,i7,i8,i9,i10,temp5,temp6,temp7,nne1,p,q,i5,k,r,e,j,errorflag
integer,dimension(1000000)::n1,n2,n3
integer,dimension(100000,5)::vert
real(kind=8),dimension(1000000)::x,z,xx,zz,sinsai,cossai,kn,first,second,zobs,xobs&
        &,zvert,xvert,zcen,xcen,d,third,ll,lll,u,grav
real(kind=8),allocatable,dimension(:,:)::obsd,wd,wz,wt,rem,pred,jac,dd,A,B,OO,PP,QQ&
        &,RR,model,fmodel,IA

!----------------------------------------

!write (*,*)'Please enter a number for z0 , Beta and Lambda:
!read (*,*)z0,beta,lambda
z0=0
beta=1
lambda=0.1
!----------------------------------------

!!  Read the observation point from file and counting them
nobs=0
open(unit=1, file="obspoints.txt")
do
  read(1,*,iostat=status)temp1,temp2
  if (status/=0) exit
  nobs=nobs+1
  xobs(nobs)=temp1
  zobs(nobs)=temp2
end do
!----------------------------------------

!!  Reading the vertice coordinates of cells and counting them
open(unit=3, file="mesh.1.node")
do
  read(3,*,iostat=status)temp9,temp3,temp4
  if (status/=0) exit
  nvert=temp9
  xvert(nvert)=temp3
  zvert(nvert)=temp4
end do
!----------------------------------------

!!  Reading the cell number and its vertices
open(unit=5, file="mesh.1.ele")
do
  read(5,*,iostat=status)temp10,temp5,temp6,temp7
  if (status/=0) exit
  ncell=temp10
```

```
  vert(ncell,1)=temp5
  vert(ncell,2)=temp6
  vert(ncell,3)=temp7
  vert(ncell,4)=vert(ncell,1)
end do
!----------------------------------------

!!  Obtaining the centriod coordinates for each cell
do i=1,ncell
  xcen(i)=((xvert(vert(i,1))+xvert(vert(i,2))+xvert(vert(i,3)))/3)
  zcen(i)=((zvert(vert(i,1))+zvert(vert(i,2))+zvert(vert(i,3)))/3)
end do
!----------------------------------------

!!  Forming the Wz matrix
allocate(wz(ncell,ncell))
do i1=1,ncell
  do i2=1,ncell
    if (i1==i2) then
      wz(i1,i2)=1/((zcen(i1)+z0)**(beta/2))
    else
      wz(i1,i2)=0
    end if
  end do
end do
!----------------------------------------

!!  Reading the observed data (data unit:cm/s^2 or gal)
allocate(obsd(nobs,1))
i11=0
open (unit=7, file="obsdata.txt")
do
  read(7,*,iostat=status)temp8,temp16
  if (status/=0) exit
  i11=i11+1
  ooo=temp8
  obsd(i11,1)=temp16
end do
!----------------------------------------

!! Forming the Wd matrix
allocate(wd(nobs,nobs))
do i3=1,nobs
  do i4=1,nobs
    if (i3==i4) then
      wd(i3,i4)=1/(0.05*obsd(i3,1))
    else
      wd(i3,i4)=0
    end if
  end do
end do
!----------------------------------------

nne=0   !number of neighbors
open(unit=13, file="mesh.1.neigh")
do q=1,ncell
  read(13,*,iostat=status)temp11,n1(q),n2(q),n3(q)
  if (status/=0) exit
  if (n1(q)>temp11) then
    nne=nne+1
    d(nne)=sqrt((xcen(temp11)-xcen(n1(q)))**2+(zcen(temp11)-zcen(n1(q)))**2)
  end if
  if (n2(q)>temp11) then
    nne=nne+1
    d(nne)=sqrt((xcen(temp11)-xcen(n2(q)))**2+(zcen(temp11)-zcen(n2(q)))**2)
  end if
  if (n3(q)>temp11) then
```

```
    nne=nne+1
    d(nne)=sqrt((xcen(temp11)-xcen(n3(q)))**2+(zcen(temp11)-zcen(n3(q)))**2)
  end if
end do
!----------------------------------------

!! Forming the Wt matrix
allocate(wt(nne,ncell))
wt=0
nne1=0
do  p=1,ncell
  if (n1(p)>p) then
    nne1=nne1+1
    wt(nne1,p)= 1/(d(nne1))
    wt(nne1,n1(p))= -1/(d(nne1))
  end if
  if (n2(p)>p) then
    nne1=nne1+1
    wt(nne1,p)= 1/(d(nne1))
    wt(nne1,n2(p))= -1/(d(nne1))
  end if
  if (n3(p)>p) then
    nne1=nne1+1
    wt(nne1,p)= 1/(d(nne1))
    wt(nne1,n3(p))= -1/(d(nne1))
  end if
end do
!----------------------------------------

!! Reading the reference model 'rem' (density unit:g/cm^3)  >>>> it can be zero
allocate(rem(ncell,1))
open (unit=11, file="refmodel.txt")
do i5=1,ncell
  read(11,*,iostat=status)temp15
  if (status/=0) exit
  rem(i5,1)=temp15
end do
!----------------------------------------

!! Forming reference model data & jacobian [Forward Modelling Section]
g=6.67384*1.0E-8      ! cm^3/gs^2
allocate(pred(nobs,1),jac(nobs,ncell))
jac=0
do k=1,nobs
  do r=1,ncell
    do e=1,4
      x(e)=(xvert(vert(r,e))-xobs(k))*100
      z(e)=(zvert(vert(r,e))-zobs(k))*100
    end do
    do e=1,4
      sinsai(e)=(x(e+1)-x(e))/sqrt((z(e+1)-z(e))**2+(x(e+1)-x(e))**2)
      cossai(e)=(z(e+1)-z(e))/sqrt((z(e+1)-z(e))**2+(x(e+1)-x(e))**2)
               if (abs(cossai(e))<1.0e-8) then
               cossai(e)=0
               end if
    end do
    do e=1,3
       kn(e)=-sinsai(e)
       do j=e,e+1
          zz(j)=z(j)*cossai(e)+x(j)*sinsai(e)
          xx(j)=-z(j)*sinsai(e)+x(j)*cossai(e)
          pof=zz(j)**2+xx(j)**2
          if (pof==0) then
            first(j)=0
          else
            first(j)=zz(j)*log(pof)
          end if
```

```
          pof1=zz(j)/xx(j)
          if (xx(j)==0) then
            second(j)=0
          else
            second(j)=2*xx(j)*atan(pof1)
          end if
            third=2*zz(j)
            ll(j)=first(j)+second(j)-third(j)
        end do
        lll(e)=ll(e+1)-ll(e)
    end do
    sumg=0
    do e=1,3
    u(e)=lll(e)*kn(e)
    sumg=sumg+u(e)
    end do
    jac(k,r)=g*sumg  !Jacobian
    grav(r)=jac(k,r)*rem(r,1)
  end do
  pred(k,1)=0
  do e=1,ncell
  pred(k,1)=pred(k,1)+grav(e)
  end do
end do
!----------------------------------------

!!  Inversion equation calculations
allocate(dd(nobs,1))
do i6=1,nobs
  dd(i6,1)=obsd(i6,1)-pred(i6,1)
end do
allocate(A(ncell,ncell),OO(ncell,ncell),PP(ncell,ncell),B(ncell,1),QQ(ncell,1),RR(ncell,1))
OO=(matmul(matmul(matmul(transpose(jac),transpose(wd)),wd),jac))
PP=(lambda)*(matmul(matmul(matmul(transpose(wz),transpose(wt)),wt),wz))
QQ=(matmul(matmul(matmul(transpose(jac),transpose(wd)),wd),dd))
RR=(lambda)*(matmul(matmul(matmul(matmul(transpose(wz),transpose(wt)),wt),wz),rem))
do i7=1,ncell
  do i8=1,ncell
    A(i7,i8)=OO(i7,i8)+PP(i7,i8)
  end do
end do
do i9=1,ncell
  B(i9,1)=QQ(i9,1)-RR(i9,1)
end do

allocate(IA(ncell,ncell))
call FINDInv(A,IA,ncell,errorflag) !Finding the inverse of a square matrix
allocate(model(ncell,1),fmodel(ncell,1))

model=(matmul(IA,B))
do i10=1,ncell
  fmodel(i10,1)=rem(i10,1)+model(i10,1)
end do
!----------------------------------------

!! Writting the file of final model
open (unit=20, file="density.txt")
do i10=1,ncell
write(20,*)fmodel(i10,1)
end do

end program

!*****************************************************************************!
!*****************************************************************************!

!Subroutine to find the inverse of a square matrix
```

```
!Author : Louisda16th a.k.a Ashwith J. Rego
!Reference : Algorithm has been well explained in:
!http://math.uww.edu/~mcfarlat/inverse.htm
!http://www.tutor.ms.unimelb.edu.au/matrix/matrix_inverse.html
SUBROUTINE FINDInv(matrix, inverse, n, errorflag)
        IMPLICIT NONE
        !Declarations
        INTEGER, INTENT(IN) :: n          ! n is size of square matrix (n*n)
        INTEGER, INTENT(OUT) :: errorflag  !Return error status. -1 for error, 0 for normal
        REAL(kind=8), INTENT(IN), DIMENSION(n,n) :: matrix   !Input matrix
        REAL(kind=8), INTENT(OUT), DIMENSION(n,n) :: inverse !Inverted matrix

        LOGICAL :: FLAG = .TRUE.
        INTEGER :: i, j, k, l
        REAL(kind=8) :: m
        REAL(kind=8), DIMENSION(n,2*n) :: augmatrix !augmented matrix

        !Augment input matrix with an identity matrix
        DO i = 1, n
            DO j = 1, 2*n
                IF (j <= n ) THEN
                        augmatrix(i,j) = matrix(i,j)
                ELSE IF ((i+n) == j) THEN
                        augmatrix(i,j) = 1
                Else
                        augmatrix(i,j) = 0
                ENDIF
            END DO
        END DO

        !Reduce augmented matrix to upper traingular form
        DO k =1, n-1
            IF (augmatrix(k,k) == 0) THEN
                FLAG = .FALSE.
                DO i = k+1, n
                        IF (augmatrix(i,k) /= 0) THEN
                                DO j = 1,2*n
                                        augmatrix(k,j) = augmatrix(k,j)+augmatrix(i,j)
                                END DO
                                FLAG = .TRUE.
                                EXIT
                        ENDIF
                        IF (FLAG .EQV. .FALSE.) THEN
                                PRINT*, "Matrix is non - invertible"
                                inverse = 0
                                errorflag = -1
                                return
                        ENDIF
                END DO
            ENDIF
                DO j = k+1, n
                        m = augmatrix(j,k)/augmatrix(k,k)
                        DO i = k, 2*n
                                augmatrix(j,i) = augmatrix(j,i) - m*augmatrix(k,i)
                        END DO
                END DO
        END DO

        !Test for invertibility
        DO i = 1, n
                IF (augmatrix(i,i) == 0) THEN
                        PRINT*, "Matrix is non - invertible"
                        inverse = 0
                        errorflag = -1
                        return
                ENDIF
        END DO
```

```
        !Make diagonal elements as 1
        DO i = 1 , n
                m = augmatrix(i,i)
                DO j = i , (2 * n)
                        augmatrix(i,j) = (augmatrix(i,j) / m)
                END DO
        END DO

        !Reduced right side half of augmented matrix to identity matrix
        DO k = n-1, 1, -1
                DO i =1, k
                m = augmatrix(i,k+1)
                        DO j = k, (2*n)
                                augmatrix(i,j) = augmatrix(i,j) -augmatrix(k+1,j) * m
                        END DO
                END DO
        END DO

        !store answer
        DO i =1, n
                DO j = 1, n
                 inverse(i,j) = augmatrix(i,j+n)
                END DO
        END DO
        errorflag = 0

!RETURN
END SUBROUTINE FINDinv
```

# Appendix D: Gravity gradiometry and terrain effect

## Gravity gradiometry theory

Gravity gradiometry measures the variations in the three orthogonal directions of the components of the acceleration due to gravity. The unit of gravity gradient is the Eötvös (E), which is a unit of acceleration divided by distance, and it is equivalent to $10^{-4}$ mGal/m (or $10^{-9}$ $s^{-2}$; LaFehr and Nabighian, 2012). All gradient elements (tensors) are shown in Figure D1. For example, the vertical gravity gradient ($G_{zz}$) represents the rate of change of vertical gravity ($g_z$) with height ($z$), i.e.,

$$G_{zz} = \frac{\partial g_z}{\partial z}$$

Therefore, the gravity field ($g_z$) can be calculated from the gradient tensor by means of integration as well. The output of any integration process lacks an unknown constant of integration, therefore, the absolute value of the gravity field can not be calculated from the gradient tensor (Bell Geospace Limited, 2007). In the airborne gravity, the measure of $g_z$ cannot be acquired to the same precision on the ground because of the aircraft acceleration. But, airborne gravity gradiometry can remove the aircraft motion effects, and deliver gravity data to an accuracy comparable with ground gravity data (CGG, 2014).

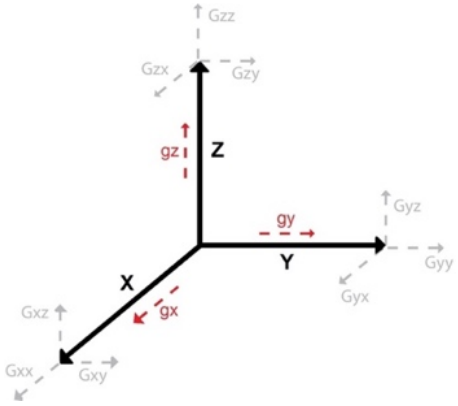


Figure D1: The relationships of the various gravity gradiometry elements (grey colour; adapted from www.wikipedia.org).

The modelled data considered here are compared with real HeliFALCON data (CGG, 2014) from the McArthur-Millennium area. The HeliFALCON gradiometer instrument acquires two elements of the gravity gradient tensor, namely $G_{xy}$ and $G_{uv}$ where $G_{uv}=(G_{xx} - G_{yy})/2$. $G_{xy}$ and $G_{uv}$ data can be transformed into the vertical component of gravity ($g_z$; derived by integrating of $G_{zz}$) by Fourier domain transformation. The $G_{xy}$ and $G_{zz}$ data are selected to plot here. The directly measured $G_{xy}$ data is appropriate for inversion to reconstruct the Earth model, and $G_{zz}$ data is more sensitive to small and shallow structures and has greater spatial resolution than $g_z$ (adapted from CMIC-Footprints project; CGG HeliFALCON gradiometry data report).

## Terrain correction for gravity gradiometry data

Before moving on to consider different models of different realistic and complexity, the terrain correction for gradiometry data is investigated. For this purpose, six components of the gradiometry tensor are synthetized using forward modelling for a model with a uniform density of 1g/cc. The model is generated for a 6x6km area below the HeliFALCON survey

(Figure D2). The model starts from elevation 450m to a surface which concludes a 10x10m dense/refined topography of Millennium area (Figure D3). These synthetized gradiometry data can be considered as the terrain effect.

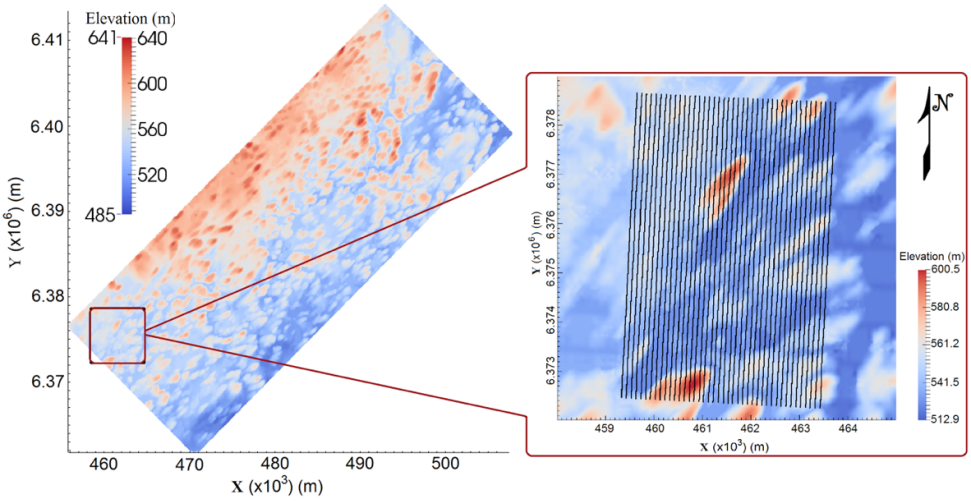


Figure D2: Topography of McArthur-Millennium corridor. Inset shows location of HeliFALCON survey lines (black) over the Millennium area. Tie lines are not shown.

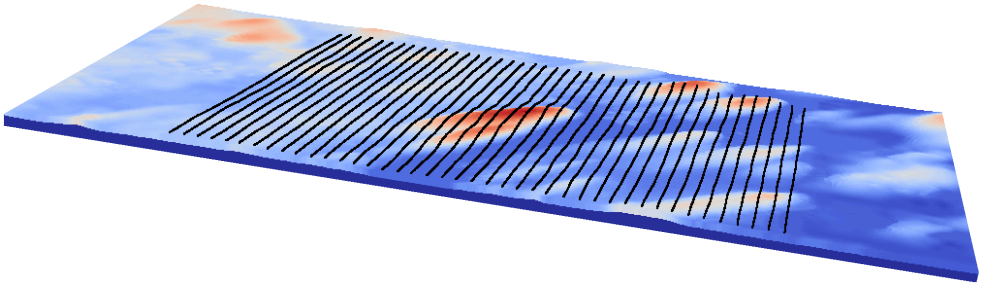

Figure D3: A part of model and HeliFALCON survey lines (black). Color scale is topography.

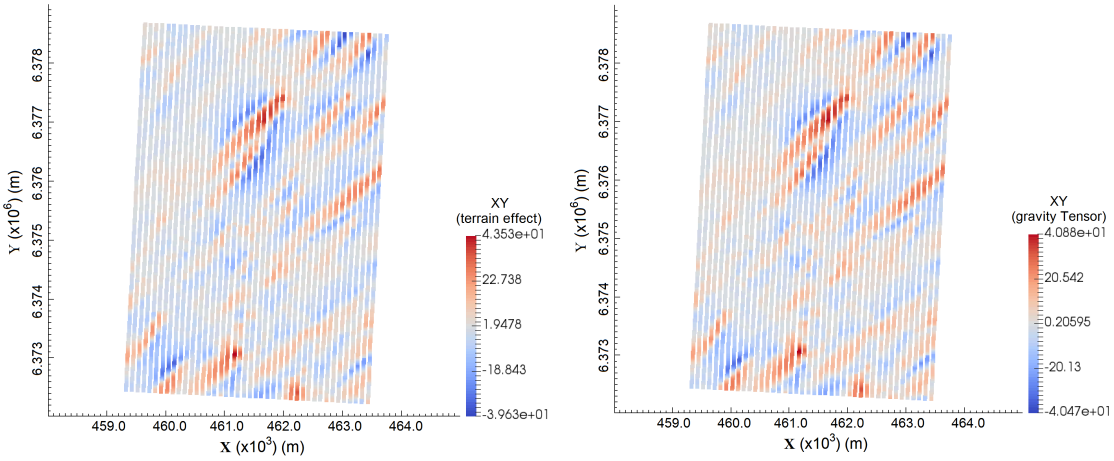


Figure D4: Terrain effect calculated for $G_{xy}$ (left; CGG data) and gravity tensor synthetized for $G_{xy}$ (right) for a density of 1g/cc (i.e. for the model in Figure D3). Unit:

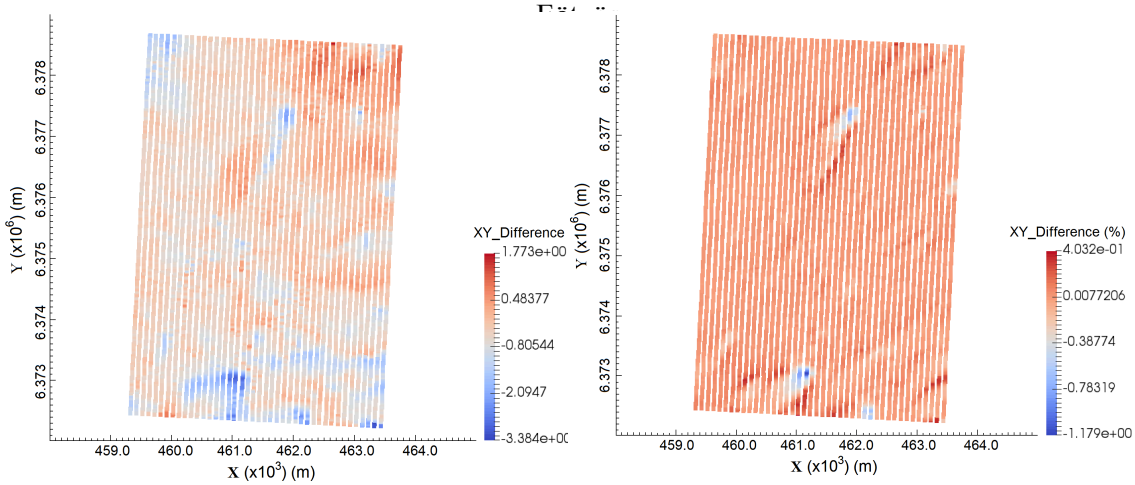


Figure D5: Difference (left) and percentage difference (right) between calculated terrain effect and synthetized gravity tensor for $G_{xy}$ shown in Figure D4. Unit: Eötvös.

For two components $G_{xy}$ and $G_{zz}$, the synthetized data are compared with a terrain effect data which is calculated using a common correction technique by CGG company (CMIC-Footprints project; CGG HeliFALCON gradiometry data report) for a terrain density of 1g/cc (Figures D4, D5, D6 and D7). Results on the next pages show around 5E (i.e. 2%) and 12E (i.e. 8%) differences for $G_{xy}$ and $G_{zz}$ components, respectively.

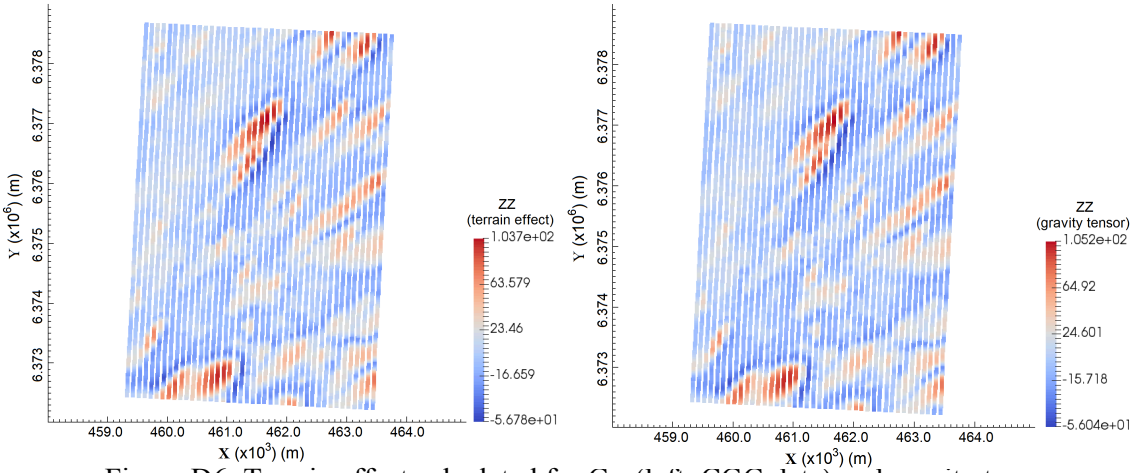


Figure D6: Terrain effect calculated for $G_{zz}$ (left; CGG data) and gravity tensor synthetized for $G_{zz}$ (right) for a density of 1g/cc (i.e. for the model in Figure D3). Unit: Eötvös.

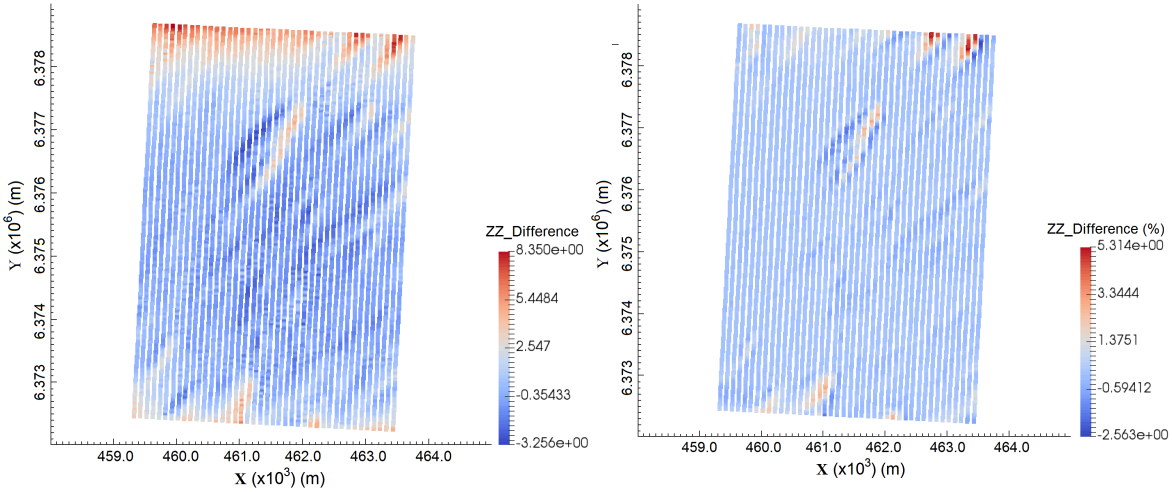


Figure D7: Difference (left) and percentage difference (right) between calculated terrain effect and synthetized gravity tensor for $G_{zz}$. Unit: Eötvös.

A density of 1 g/cc was used to compute the terrain effects and to synthetized the gravity tensors, which can then be simply multiplied by a chosen appropriate density and subtracted from the data. In this research a terrain density of 2 g/cc is chosen. Thus, synthetized $G_{xy}$ and $G_{zz}$ data are multiplied by 2. The results are used as the terrain correction that is applied to the synthetized data-set in the remainder of this section. They will be subtracted from the (CGG's Fourier derived; Figures D8 and D10) $G_{xy}$ and $G_{zz}$ data.

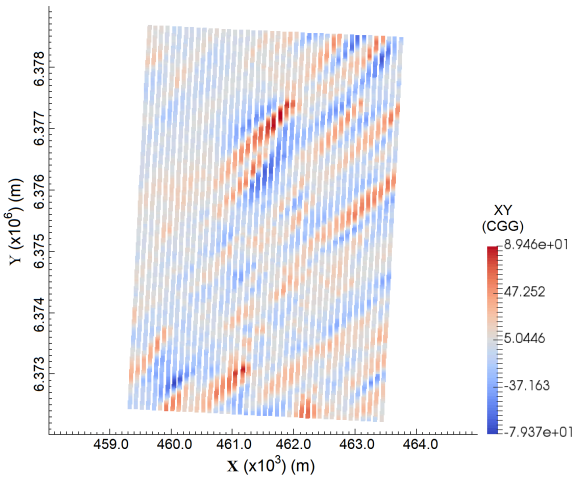


Figure D8: CGG's Fourier derived $G_{xy}$ gradiometry data (no terrain correction applied). Unit: Eötvös.

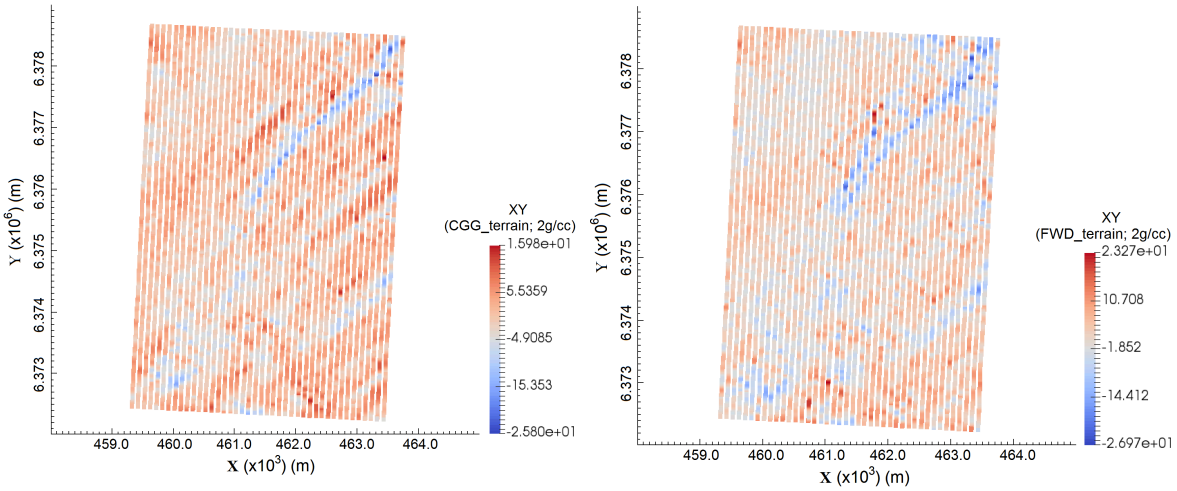


Figure D9: Fourier derived $G_{xy}$ gradiometry data after applying terrain correction performed using a common correction technique by CGG company (left) and using synthetized (forward modelling) terrain data in this research (right). Unit: Eötvös.

The final results will be compared with the (CGG's Fourier derived) terrain-corrected $G_{xy}$ and $G_{zz}$ data in which the terrain correction were computed by a common correction technique (Figures D9 and D11).

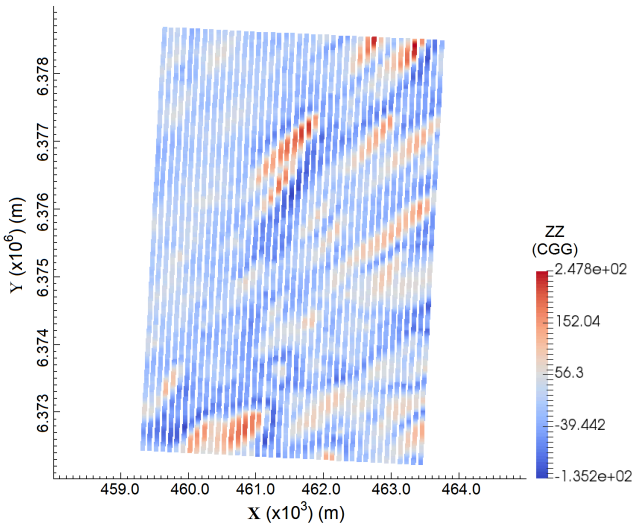


Figure D10: CGG's Fourier derived $G_{zz}$ gradiometry data (no terrain correction applied). Unit: Eötvös.

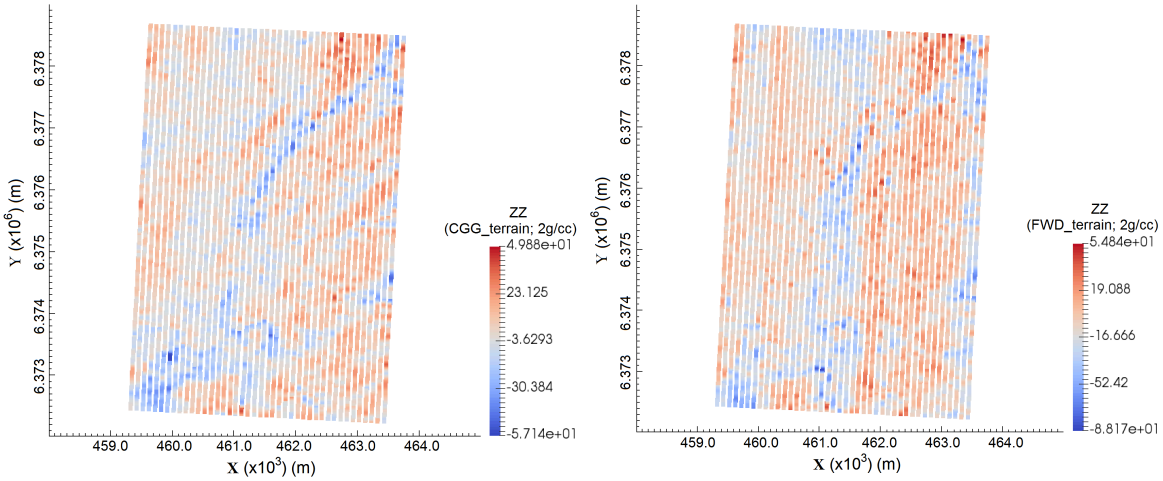


Figure D11: Fourier derived $G_{zz}$ gradiometry data after applying terrain correction performed using a common correction technique by CGG company (left) and using synthetized (forward modelling) terrain data in this research (right). Unit: Eötvös.

It can be seen that the gradiometry data before the terrain correction are highly dominated by the topography signature. By comparing the terrain corrected results, it can be seen that the topography signature in the data which is corrected by our method is highly reduced in comparison with the CGG's data which is corrected by a common terrain correction technique.

# Appendix E: 1D inversion of real DIGHEM data for the Malartic area

## Geological setting

The Canadian Malartic Gold Mine is an open pit mine which is located in Malartic near Val d'Or, Quebec. It is considered as a large-tonnage, low-grade Archean gold deposit in which the mineralization occurs in clastic metasedimentary rocks of the Pontiac Group and in porphyry monzodiorite intrusions. The main ore minerals are native gold accompanied by pyrite as a result of hydrothermal alteration (Wares & Burzynski, 2011). Sedimentary rocks of the Pontiac Group are cut by intrusive rocks include porphyritic quartz monzodiorite and granodiorite, intermediate and felsic dykes, and widespread lamprophyre dykes which are known to show some evidence of hydrothermal alteration (Figure E1). Also, sedimentary rocks are covered by subglacial till, coarse glaciofluvial sediments, and glaciolacustrine fine sediments (Veillette, 2004; Figure E2).

## DIGHEM system

A DIGHEM airborne geophysical survey carried out (and processed) by Furgo Airborne Surveys Corp. for Osisko Exploration Ltd. over the Canadian Malartic Gold Mine in August 2006. Survey coverage consisted of north-south lines of approximately 2485 line-km with a line spacing up to 100 metres and a station spacing of around 3 m. This was accomplished using a DIGHEM electromagnetic system, supplemented by a high

sensitivity cesium magnetometer, a spectrometer and a GPS which were installed in an AS350B(2) turbine helicopter. The helicopter flew at an average of 136 km/h with an EM sensor height of approximately 30 metres (Furgo Airborne Surveys Corp., 2006). DIGHEM system uses five frequencies from 877Hz to 56110Hz with two coil configurations: coaxial (horizontal dipole; 1128Hz and 5087Hz) coil pairs and coplanar (vertical dipole; 877Hz, 7166Hz and 56110Hz) coil pairs. Coil separation (between receiver and transmitter) is 8 m except for 55840Hz which is 6.3 m. Receiver and transmitter coils have a diameter of about half a metre. System measures both in-phase and quadrature parts. I had access to DIGHEM data-set as "Au site" is another research project of the large Canadian Mining Innovation Council (CMIC; www.cmic-footprints.ca) Footprints project.

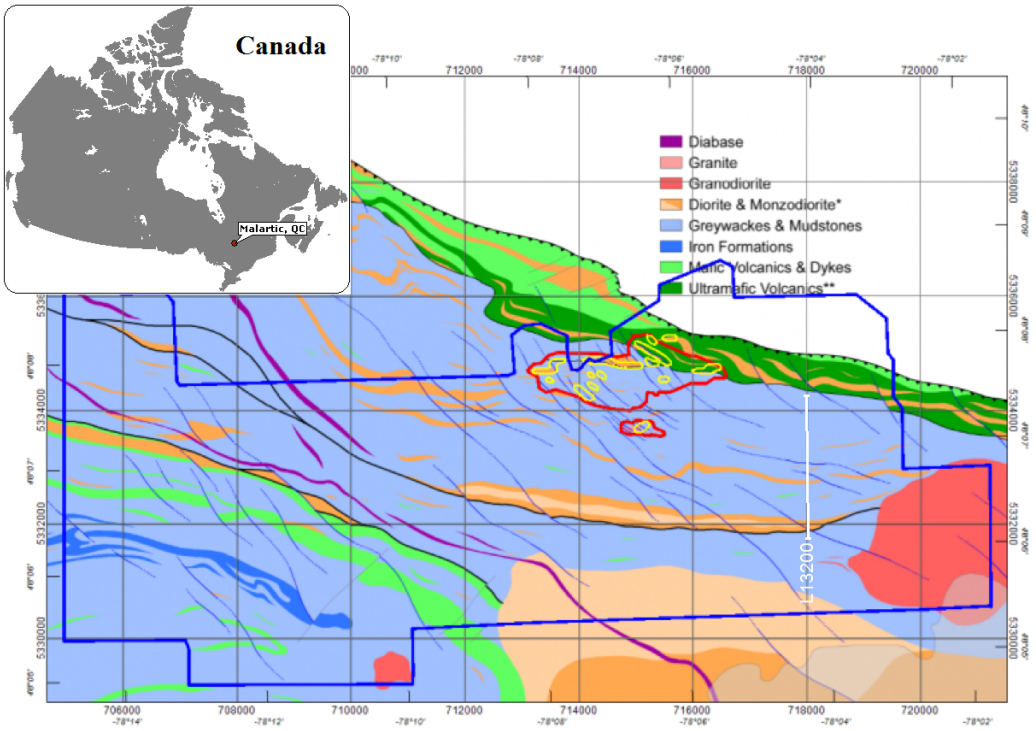


Figure E1: Geology map of the Malartic area. The red outlines show the pit and mining operation areas and the yellow show the zones of mineralization. The DIGHEM survey area is overlaid in blue. White line shows a part of the survey line L13200 which is inverted (taken from CMIC-Footprints project).

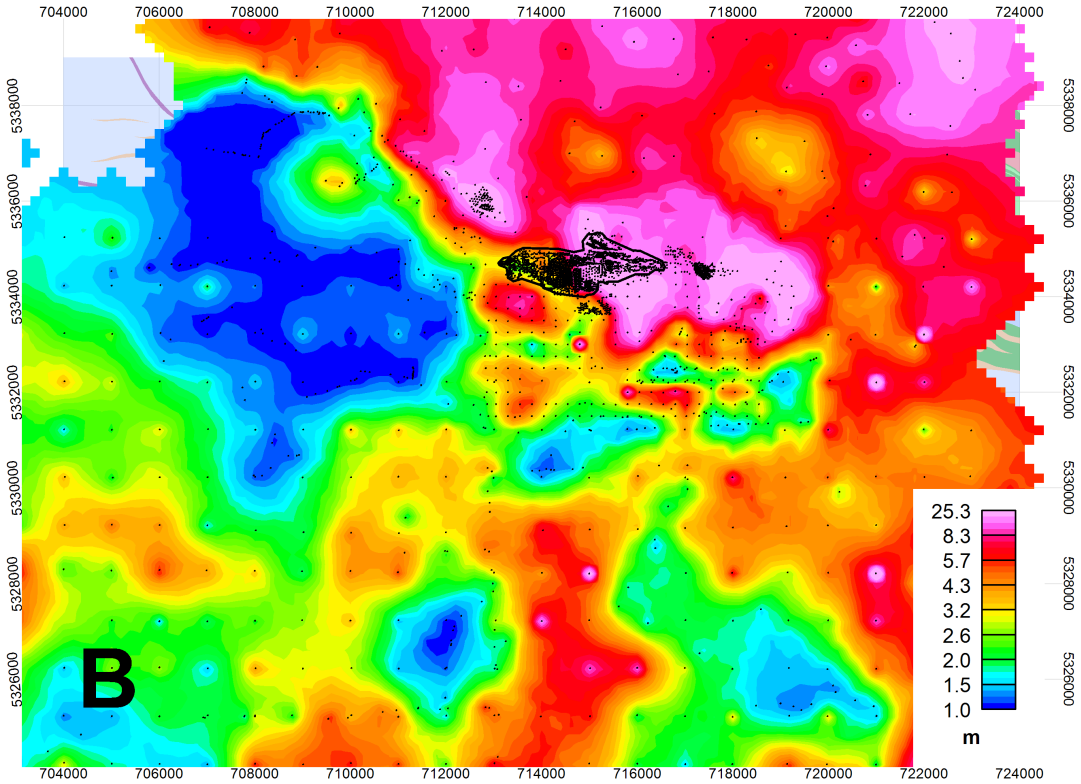


Figure E2: Map of the overburden thicknesses. Black dots show the location of drill-holes. The black outlines show the pit and mining operation area (mapped by Reza Mir; taken from CMIC-Footprints project).

**1D inversion**

Data were slightly filtered by Reza Mir (taken from CMIC-Footprints project). 1D inversion using EM1DFM (using L2-norm; Farquharson and Oldenburg, 2000) was applied to the filtered real DIGHEM data along a part of a profile (L13200) with 805 stations over the Malartic area (Figure E3). Vertical dipole data (877Hz, 7166Hz and 56110Hz) were used for the inversion. Also, a 5% noise is considered as uncertainty. Magnetic data along the (inverted) survey line is shown in Figure E4. Figures E5 and E6 respectively show the 1D inversion model and the convergence curves for one of the stations.

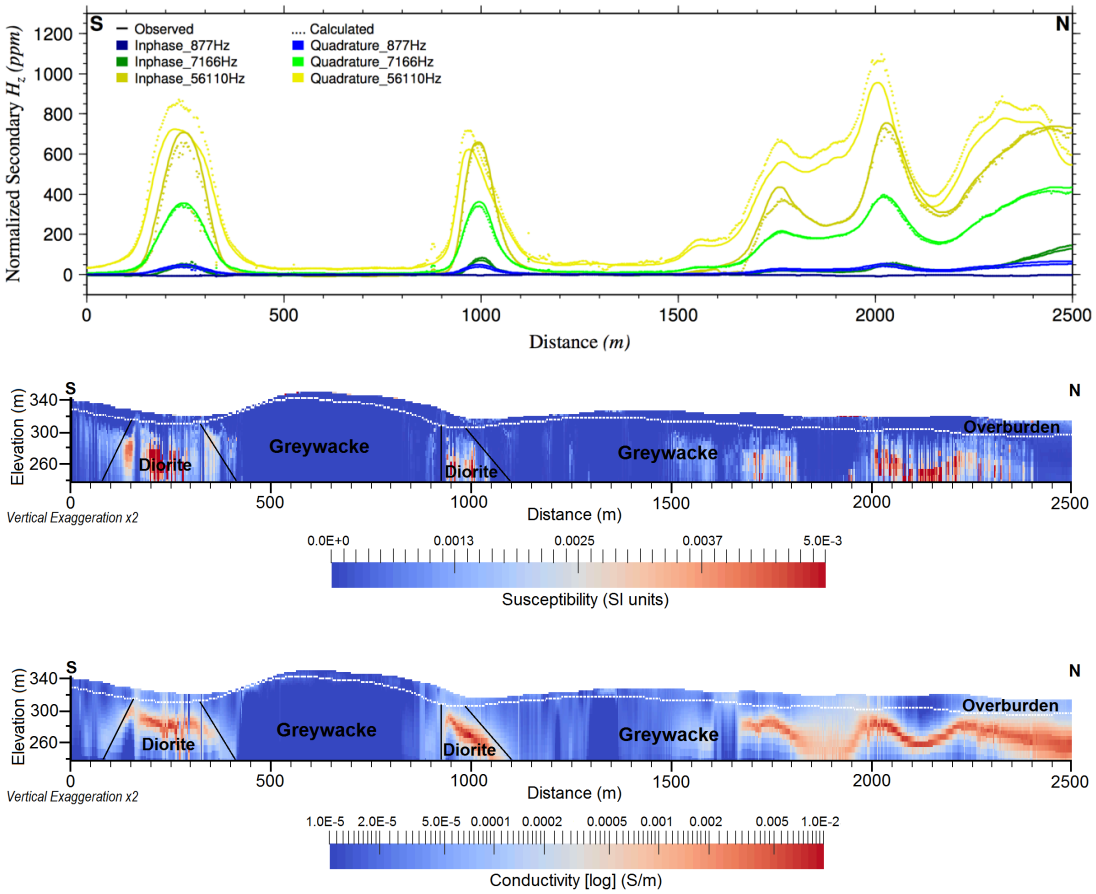


Figure E3: Top: real observed and calculated data. Middle and bottom: 1D inversion results for both magnetic susceptibility and conductivity models. Estimated location of geological structures are shown by black lines. Using drill-hole data, the approximate location of the base of overburden is shown by a white dotted line.

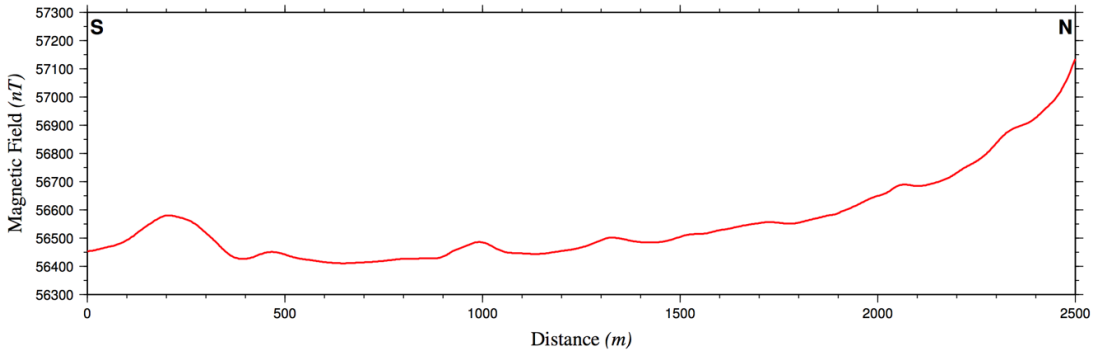


Figure E4: Magnetic data along (inverted) survey line.

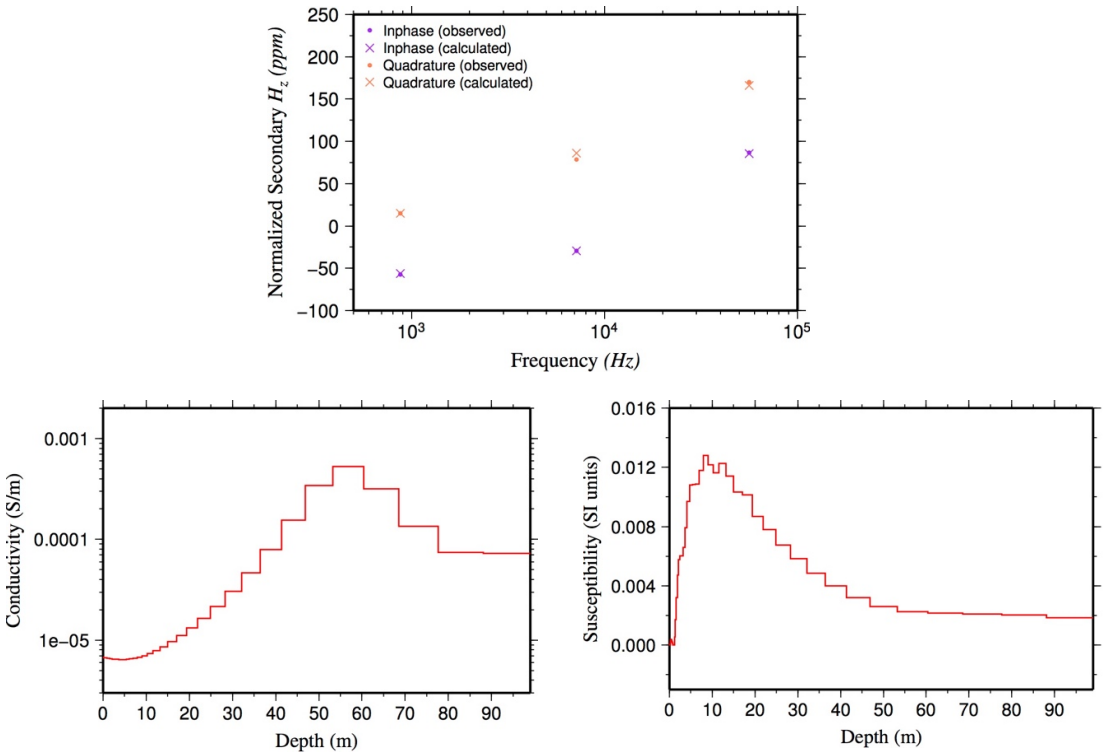


Figure E5: Top: observed and calculated data for a station of real DIGHEM data. Bottom: 1D inversion models.

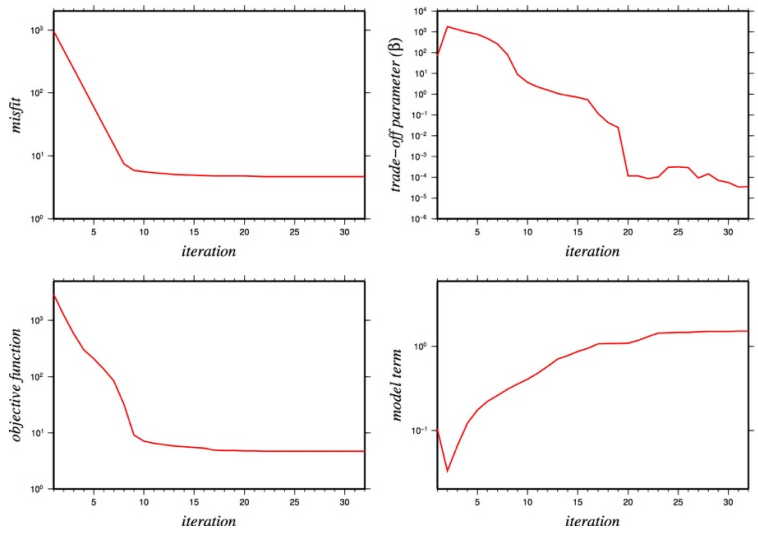


Figure E6: Variations of different parts of the objective function such as data misfit ($\phi_d$; top-left), trade-off parameter ($\beta$; top-right), objective function ($\Phi$; bottom-left) and model term ($\phi_m$; bottom-right) at inversion iterations for the model in Figure E6.

The 1D inversion results show a good match with the geology map (see Figures E1 and E3). It can be seen that the overburden is resistive and non-magnetic along the survey line. Also, two conductive/magnetic structures in the left side of the inversion models are related to the intrusive bodies (Diorite/Monzodiorite). The top of Greywackes in the right side of the inversion model is dominated by a conductive (layered) structure, however Greywacke is resistive in the left side of the inversion model. Also, there is a good match between magnetic data (Figure E4) and EM inversion results. It can be seen that intrusive rocks (e.g. Diorite/Monzodiorite) are magnetic anomalies whereas metasedimentary rocks (e.g. Greywackes) are mostly non-magnetic.